



**HAL**  
open science

# Phenomenology of dark matter particles at the centers of galaxies

Thomas Lacroix

► **To cite this version:**

Thomas Lacroix. Phenomenology of dark matter particles at the centers of galaxies. Astrophysics [astro-ph]. Université Pierre et Marie Curie - Paris VI, 2016. English. NNT : 2016PA066060 . tel-01369006

**HAL Id: tel-01369006**

**<https://theses.hal.science/tel-01369006>**

Submitted on 20 Sep 2016

**HAL** is a multi-disciplinary open access archive for the deposit and dissemination of scientific research documents, whether they are published or not. The documents may come from teaching and research institutions in France or abroad, or from public or private research centers.

L'archive ouverte pluridisciplinaire **HAL**, est destinée au dépôt et à la diffusion de documents scientifiques de niveau recherche, publiés ou non, émanant des établissements d'enseignement et de recherche français ou étrangers, des laboratoires publics ou privés.



THÈSE DE DOCTORAT  
DE L'UNIVERSITÉ PIERRE ET MARIE CURIE

ET DE L'ÉCOLE DOCTORALE D'ASTRONOMIE ET D'ASTROPHYSIQUE  
D'ÎLE-DE-FRANCE (ED 127)

RÉALISÉE À

L'INSTITUT D'ASTROPHYSIQUE DE PARIS

---

Phenomenology of dark matter particles at  
the centers of galaxies

---

présentée par

Thomas LACROIX

et soutenue publiquement le 1er juillet 2016

devant un jury composé de

Pr Pierre SALATI	Université de Savoie	Président du jury
Pr Marc KAMIONKOWSKI	The Johns Hopkins University	Rapporteur
Pr Piero ULLIO	International School for Advanced Studies	Rapporteur
Dr Marco CIRELLI	Université Pierre et Marie Curie	Examinateur
Pr Gabrijela ZAHARIJAŠ	University of Nova Gorica	Examinatrice
Pr Joseph SILK	Université Pierre et Marie Curie	Directeur de thèse
Dr Céline BØHM	Durham University	Co-directrice de thèse



*À la mémoire de Vincent.*



# Acknowledgments

First and foremost I would like to express my deepest gratitude to my supervisors, Joseph Silk and Céline Boehm, for giving me the opportunity to work on very exciting problems and for teaching me so many things both on physics-related and non physics-related topics. Thank you so much Joe for sharing your invaluable experience, for boosting my self-confidence whenever I showed you my results, for making it possible for me to collaborate with so many great people, and for allowing me to attend conferences in wonderful places that I never dreamed to visit before. Merci Céline tout d’abord de m’avoir permis de faire cette thèse, car c’est grâce à toi en premier lieu que j’ai pu faire ce parcours. Ensuite un grand merci pour tous tes précieux conseils notamment sur la rédaction des articles et la recherche en général. Je te suis également extrêmement reconnaissant de m’avoir encouragé et aiguillonné dans les moments où j’avais besoin d’être secoué. Merci de tout coeur de m’avoir accompagné même quand tu avais d’autres choses en tête. J’ai vraiment appris beaucoup sur la vie ces dernières années. Thank you both for guiding and supporting me, and for believing in me.

I would like to address my thanks to my other collaborators: Chiara Arina, Alexander Belikov, Avery Broderick, Anthony Brown, Francesca Calore, Paula Chadwick, Timur Delahaye, Chris Gordon, Jamie Graham, Sadegh Khochfar, Stephen Lloyd, Óscar Macías, Emmanuel Moulin, Paolo Panci, Christoph Weniger. I also wish to thank several people who have been postdocs at IAP or in Marco Cirelli’s group at IPHT, and with whom I have shared good moments and very interesting discussions: Sarah Andreas, Jonathan Davis, Irina Dvorkin, Nico Hamaus, Jens Jasche, Bradley Kavanagh, Thibaut Louis, Filippo Sala and Marco Taoso.

I am also very grateful to the members of my thesis committee, Marco Cirelli, Marc Kamionkowski, Pierre Salati, Piero Ullio and Gabrijela Zaharijaš for doing me the honor of judging my work. Special thanks to the rapporteurs, Marc Kamionkowski and Piero Ullio, for reviewing the manuscript.

Cette thèse a été financée par l’École Normale Supérieure de Lyon et l’Université Pierre et Marie Curie, que je remercie. J’ai également bénéficié de manière significative du projet ERC No. 267117 (DARK) hébergé par l’UPMC, grâce auquel j’ai pu notamment parfaire ma formation et présenter mes résultats en participant à plusieurs écoles d’été, conférences et ateliers. En outre, ce travail a été réalisé dans le cadre du Labex Institut Lagrange de Paris (ILP, référence ANR-10-LABX-63) de l’Idex SUPER, et a ainsi bénéficié d’une aide de l’État gérée par l’Agence Nationale de la Recherche au titre du programme Investissements d’avenir portant la référence ANR-11-IDEX-0004-02. Je remercie en particulier l’ILP de m’avoir permis de participer à l’école d’été “Post-Planck cosmology” aux Houches.

I am indebted to the organizers of the “New Horizons for observational cosmology” summer school (Varenna, Italy), the “Post-Planck cosmology” summer school (Les Houches, France), the “What is the dark matter?” workshop (Stockholm, Sweden), the TeVPA/IDM 2014 conference (Amsterdam, The Netherlands), the “Frontiers of Fundamental Physics 14” conference (Marseille, France), the Amsterdam-Paris-Stockholm meeting (Paris & Amsterdam), the Dark MALT workshop (Munich, Germany)—additional thanks to Anna and Sebastian for showing me around in Munich!—, and the PACIFIC2015 conference (Moorea, French Polynesia), for giving me the opportunity to learn so much and present my work in stimulating environments. Merci également aux organisateurs du GDR Terascale pour les invitations à l’X et à l’IPHT.

En outre, j'ai bénéficié des excellentes conditions de travail offertes par l'IAP, ce dont je suis extrêmement reconnaissant. Je remercie les chercheurs de l'IAP et en particulier ceux que j'ai eu le plaisir de côtoyer : Francis Bernardeau, Frédéric Daigne, Cédric Deffayet, Valérie de Lapparent, Yohan Dubois, Florence Durret, Silvia Galli, Kumiko Kotera, Guilhem Lavaux, Alain Lecavelier des Etangs, Gary Mamon, Patrick Peter, Sébastien Renaux-Petel, Marta Volonteri et Benjamin Wandelt. Merci en particulier à Florence Durret pour son accompagnement au cours de la thèse dans le cadre de l'Ecole Doctorale 127.

Je tiens aussi à remercier les services informatique, administratif et technique de l'IAP. Je voudrais exprimer ma reconnaissance tout particulièrement envers les assistants successifs du projet ERC DARK pour leur aide précieuse : Flora Delamare, Audrey Salmon, Ghita Chilla et Arnaud Sers.

J'en arrive maintenant aux doctorants que j'ai vus défiler à l'IAP au cours de ces quatre années et grâce auxquels la thèse a été encore plus agréable au quotidien ! Merci à Alba, Alice, Caterina, Céline, Charlotte, Clément, Clotilde, Erwan, Federico, Flavien K., Flavien V., Florence, Florent, Florian, Guillaume D., Guillaume P., Hayley, Hélène, Jean, Jean-Baptiste, Jesse, Julia, Laura, Luciana, Maxime, Mélanie, Nicolas C., Nicolas M., Ophélie, Óscar, Pierre, Raphaël, Rebekka, Sandrine, Sébastien, Siwei, Sylvain, Tanguy, Tilman, Vincent B., Vincent V. et Vivien, sans oublier bien sûr les copains des autres labos de la région : Agnès, Aisling, Alexis, Gaëlle, Julian, Julien, Lorène et Lucile. Cette très bonne ambiance parmi les doctorants et les discussions stimulantes y ont été pour beaucoup dans la préservation de ma santé mentale ! Un certain nombre d'entre vous sont devenus mes amis (ceux pour qui c'est réciproque se reconnaîtront !) mais je ne m'étendrai pas plus sur le sujet ici, sauf bien sûr pour vous remercier de tous ces bons moments passés à l'intérieur et à l'extérieur de l'IAP.

Un grand merci également aux copains doctorants du comité d'organisation de la conférence Elbereth des étudiants d'astronomie et d'astrophysique d'Île-de-France : Alan, Anna, Anthony, Aurore, Clément, Jean-Loup, Loïc, Mathieu, Raphaël, Sophie, Tchuu et Vivien. Organiser cette conférence avec vous en 2013 et 2014 a été très enrichissant, et grâce à vous ça n'a pas été que du travail mais aussi beaucoup de plaisir !

Je remercie du fond du cœur mes amis de longue date pour leur soutien toutes ces années : Benoît, Chloé, Christophe, Farid, Florence, Guillaume, Mathieu, Quentin, Romain, Sandrine, Thomas et Victoria. La vie aurait beaucoup moins de piquant sans vous tous ! Un grand merci Chloé pour ton soutien psychologique en temps réel pendant la rédaction du manuscrit.

Enfin, je ne pourrai jamais exprimer suffisamment ma gratitude envers mes parents pour leur soutien inébranlable. Je vous en ai vraiment fait voir de toutes les couleurs pendant tout ce temps ! Et merci aux autres membres de ma famille qui m'ont soutenu.

La fin de cette expérience unique qu'est la thèse est pour moi tout naturellement le moment de faire le point sur les quatre dernières années, sur ce que j'ai gagné et ce que j'ai perdu. Je ne m'étendrai pas sur le sujet ici, néanmoins je souhaite dédier ce travail à la mémoire de Vincent, parti bien trop tôt avant d'avoir lui-même pu débiter sa thèse. J'espère honorer son souvenir en allant au bout de cette aventure.

# Contents

Acknowledgments	v
Introduction	xiii
Physical constants and abbreviations	xv
<b>I Dark matter: from historical evidence to modern searches</b>	<b>1</b>
<b>1 Evidence and candidates for dark matter</b>	<b>3</b>
1.1 Initial evidence for dark matter . . . . .	4
1.1.1 The missing mass problem . . . . .	4
1.1.2 Cosmology . . . . .	7
1.2 Standard dark matter scenario: thermal relics . . . . .	15
1.2.1 Thermal history and freeze-out . . . . .	15
1.2.2 The relic density of dark matter particles . . . . .	16
1.2.3 The “WIMP miracle” . . . . .	17
1.3 Dark matter candidates . . . . .	19
1.3.1 Massive astrophysical compact halo objects . . . . .	19
1.3.2 Particle dark matter . . . . .	20
1.3.3 Small-scale issues of cold dark matter: additional properties, baryonic physics or modified gravity theories? . . . . .	26
<b>2 Overview of standard searches for dark matter particles</b>	<b>29</b>
2.1 Direct detection . . . . .	30
2.1.1 Principle . . . . .	30
2.1.2 Number of expected events . . . . .	31
2.1.3 Status of direct searches . . . . .	33
2.2 Collider searches . . . . .	36
2.2.1 Principle . . . . .	36
2.2.2 Overview of results . . . . .	37
2.2.3 Comment on the tentative 750 GeV excess at LHC . . . . .	39
2.3 Indirect detection: overview of standard searches . . . . .	40
2.3.1 Constraints from the CMB . . . . .	40
2.3.2 Charged antiparticles . . . . .	41
2.3.3 Gamma rays . . . . .	44
2.3.4 Neutrinos . . . . .	48
2.3.5 Summary . . . . .	49

<b>II</b>	<b>Going beyond standard searches for dark matter particles</b>	<b>51</b>
<b>3</b>	<b>Dark matter spikes at the centers of galaxies?</b>	<b>53</b>
3.1	Dark matter profile in galaxies: a debated picture . . . . .	54
3.2	Dark matter spike from adiabatic accretion onto a supermassive black hole . . .	56
3.2.1	Scaling relations . . . . .	56
3.2.2	Semi-analytic derivation using adiabatic invariants . . . . .	57
3.3	Discussion of competing dynamical effects . . . . .	59
3.3.1	Instantaneous black hole growth . . . . .	59
3.3.2	Mergers . . . . .	59
3.3.3	Off-centered black hole formation . . . . .	60
3.3.4	Stellar heating . . . . .	60
3.3.5	Dynamical processes steepening the dark matter profile . . . . .	61
3.4	Summary . . . . .	62
<b>4</b>	<b>Photon emission from electrons and positrons</b>	<b>63</b>
4.1	Radiative processes . . . . .	64
4.2	Flux of secondary photons . . . . .	64
4.2.1	Differential photon intensity . . . . .	64
4.2.2	Volume emissivity . . . . .	65
4.2.3	Emission spectrum . . . . .	65
4.2.4	Example: power-law $e^\pm$ spectrum . . . . .	71
4.3	Electron/positron spectrum $\psi$ accounting for propagation . . . . .	72
4.3.1	Physical processes at play . . . . .	72
4.3.2	Transport equation . . . . .	72
4.3.3	Diffusion zone and parameters . . . . .	73
4.3.4	A qualitative picture of spatial diffusion . . . . .	74
4.3.5	Energy loss rate . . . . .	75
4.3.6	Electron/positron spectrum for negligible spatial diffusion . . . . .	78
4.3.7	Electron/positron spectrum in the presence of spatial diffusion . . . . .	79
<b>III</b>	<b>Secondary gamma-ray emission from electrons and positrons and the <i>Fermi</i> Galactic center excess</b>	<b>85</b>
<b>5</b>	<b>The <i>Fermi</i> excess of gamma-rays at the Galactic center</b>	<b>87</b>
5.1	Properties of the Galactic center excess . . . . .	88
5.2	Interpretations . . . . .	88
5.2.1	Pulsars . . . . .	88
5.2.2	Electron or proton bursts in the Galactic center . . . . .	89
5.2.3	Dark matter annihilations . . . . .	90
5.3	On the importance of secondary electrons and positrons from dark matter . . . .	91
5.3.1	Components of the diffuse gamma-ray emission from dark matter . . . . .	91
5.3.2	New dark matter interpretation of the GeV excess with secondary photon emission . . . . .	92
5.3.3	Further tests . . . . .	96
5.4	Conclusion . . . . .	98
<b>6</b>	<b>The spatial morphology of the secondary emission in the Galactic center gamma-ray excess</b>	<b>101</b>
6.1	Introduction . . . . .	102
6.2	Models for the gamma-ray emission . . . . .	102

6.3	Data analysis . . . . .	104
6.3.1	Data selection . . . . .	104
6.3.2	Analysis methods . . . . .	105
6.4	Models and procedure . . . . .	107
6.5	Results and discussion . . . . .	108
6.5.1	<i>Model I</i> , democratic leptons . . . . .	108
6.5.2	<i>Model II</i> , no electrons . . . . .	109
6.5.3	<i>Model III</i> , millisecond pulsars . . . . .	109
6.6	Conclusions . . . . .	110
<b>IV</b>	<b>Phenomenology of dark matter spikes in the Milky Way</b>	<b>113</b>
<b>7</b>	<b>Probing a dark matter spike at the Galactic center in the presence of spatial electron diffusion</b>	<b>115</b>
7.1	Dark matter spike and electron diffusion . . . . .	116
7.2	Synchrotron emission from a dark matter spike with spatial diffusion . . . . .	116
7.3	Constraining the existence of a dark matter spike . . . . .	117
7.3.1	Morphology of the synchrotron emission: maps of the Galactic center with or without a spike . . . . .	118
7.3.2	Can we distinguish different inner profiles using their synchrotron emission? . . . . .	118
7.3.3	Impact of the magnetic field . . . . .	123
7.3.4	Observability with <i>Planck</i> . . . . .	124
7.4	Conclusion and perspectives . . . . .	126
<b>8</b>	<b>New H.E.S.S. diffuse emission from the Galactic center: a combination of heavy dark matter and millisecond pulsars?</b>	<b>127</b>
8.1	Introduction . . . . .	128
8.2	TeV gamma-rays from pulsars and dark matter annihilations . . . . .	129
8.2.1	Inverse Compton emission from millisecond pulsars . . . . .	129
8.2.2	Annihilation signal from a dark matter spike . . . . .	130
8.3	Explaining the H.E.S.S. diffuse emission . . . . .	132
8.3.1	Spectral morphology . . . . .	132
8.3.2	Spatial morphology . . . . .	132
8.4	Synchrotron emission and X-ray data . . . . .	135
8.5	Conclusion . . . . .	135
<b>V</b>	<b>Probing dark matter spikes in the M87 and Centaurus A galaxies</b>	<b>137</b>
<b>9</b>	<b>Ruling out thermal dark matter with a black hole induced spiky profile in the M87 galaxy</b>	<b>139</b>
9.1	Introduction . . . . .	140
9.2	Diffuse emission in the presence of a dark matter spike in M87 . . . . .	140
9.3	Upper limits on the annihilation cross-section . . . . .	142
9.3.1	Methodology . . . . .	142
9.3.2	Results . . . . .	143
9.3.3	Robustness of our constraints . . . . .	146
9.4	DM spike and jet . . . . .	147
9.4.1	Jet emission . . . . .	147
9.4.2	Upper limits on the annihilation cross-section with spike+jet . . . . .	148
9.4.3	Explaining the TeV data with a dark matter spike . . . . .	149

9.5	Conclusion	152
<b>10</b>	<b>Discovery of a new extragalactic source population of energetic particles</b>	<b>153</b>
10.1	Introduction	154
10.2	Analysis	154
10.3	Interpretation	155
10.3.1	Dark matter	156
10.3.2	Millisecond pulsars	159
10.3.3	Diffused protons	160
10.4	Conclusion	160
<b>11</b>	<b>Probing a dark matter spike at the center of M87 with the Event Horizon Telescope</b>	<b>163</b>
11.1	Introduction: beyond spectral information	164
11.2	The Event Horizon Telescope	164
11.2.1	General features	164
11.2.2	Imaging the shadow of a black hole	164
11.3	Probing dark matter at the center of M87 with the Event Horizon Telescope	166
11.3.1	Electron propagation in the presence of advection	166
11.3.2	Relevance of advection	168
11.3.3	Dark synchrotron intensity in a curved spacetime	168
11.4	Preliminary results	169
11.5	Summary	170
	<b>Conclusion and outlook</b>	<b>171</b>
	<b>Appendices</b>	<b>175</b>
<b>A</b>	<b>Technical details</b>	<b>177</b>
A.1	Integral over the line of sight	178
A.1.1	Projection of a three-dimensional profile over the line of sight	178
A.1.2	Coordinate systems in the Milky Way	179
A.2	Normalization of the dark matter profile in M87 and Centaurus A	179
A.2.1	M87	179
A.2.2	Cen A	180
A.3	Synchrotron self-Compton jet model	181
A.4	Solving the cosmic-ray equation with advection towards the black hole	182
<b>B</b>	<b><i>Fermi</i>-LAT observations and data analysis of Cen A</b>	<b>185</b>
B.1	Description of the data	186
B.2	Models	186
B.3	Spectrum	188
B.4	Systematic error	191
B.5	Luminosity	193
B.6	Variability	193
<b>C</b>	<b>Résumé détaillé en français</b>	<b>195</b>
C.1	Introduction	195
C.2	La matière noire : du contexte historique aux recherches actuelles	195
C.2.1	Historique et candidats de la matière noire	195
C.2.2	Recherches standards	197
C.3	Recherche de la matière noire : au-delà des méthodes standards	197

C.3.1	Des pics de matière noire au centre des galaxies ? . . . . .	197
C.3.2	Émission de photons par des électrons et positrons . . . . .	198
C.4	L'excès <i>Fermi</i> de rayons gamma au centre Galactique . . . . .	198
C.4.1	De l'importance des électrons et positrons produits par la matière noire .	198
C.4.2	Morphologie spatiale de l'émission secondaire et excès au centre Galactique	199
C.5	Phénoménologie des pics de matière noire dans la Voie Lactée . . . . .	199
C.5.1	Recherche d'un pic de matière noire au centre Galactique en présence de diffusion spatiale . . . . .	199
C.5.2	Nouvelle émission diffuse mesurée avec H.E.S.S. au centre Galactique : une combinaison de matière noire lourde et de pulsars milliseconde? . . . . .	199
C.6	A la recherche de pics de matière noire dans les galaxies M87 et Centaurus A . .	200
C.6.1	Exclusion de candidats thermiques en présence d'un pic de matière noire au centre de M87 . . . . .	200
C.6.2	Découverte d'une population extragalactique de particules énergétiques .	200
C.6.3	Recherche d'un pic de matière noire au centre de M87 avec le Télescope de l'Horizon des Événements . . . . .	201
C.7	Conclusion . . . . .	201
<b>Bibliography</b>		<b>203</b>



# Introduction

Unraveling the mystery of dark matter is one of the greatest challenges of modern physics. After a century of unexplained results in astrophysics, and despite tremendous progress in observations, numerical simulations and theory, we still have no idea of the nature of this enigmatic invisible substance. Is dark matter made of new particles or can it be accounted for by an extension of the theory of gravitation? This remains to be established, and there might not be a clear-cut answer.

The leading approach to this long-standing problem considers that dark matter is composed of new exotic particles, whose properties need to be determined. These particles are sought for using a variety of methods, ranging from attempts to produce them in particle colliders, to the study of their collisions with nuclei in dedicated experiments, through indirect characterization via putative signatures in astrophysical observations, induced by dark matter annihilation or decay. In this regard, the dark matter problem pertains to the field of astroparticle physics, which is at the interface of astrophysics, particle physics and cosmology.

In this thesis, I tackle some aspects of indirect searches for dark matter particles. This approach is complementary to direct detection or collider experiments (which will also be described in the course of this manuscript), in that in principle, the discovery of a dark matter particle could only be claimed if confirmed simultaneously by these independent techniques. Indirect searches are an extremely promising avenue to elucidate the nature of dark matter, considering the variety of astrophysical observables that we have at our disposal nowadays, with more yet to come in the near future. I find indirect searches all the more fascinating as they touch upon a very wide range of topics in physics. This approach to the dark matter problem goes beyond its primary purpose, namely to characterize unknown particles. There is indeed an actual feedback of indirect searches on non-exotic astrophysics, since we need to significantly improve our understanding of astrophysical processes to uncover a putative dark matter contribution, which calls for new instruments with unprecedented capabilities.

Astroparticle physics and more specifically indirect dark matter searches now benefit from tremendous progress regarding observations, over the entire electromagnetic spectrum, and including alternative messengers like neutrinos. The advent of new telescopes with tremendous sensitivity and angular resolution, both ground-based and in space, has revolutionized the field, especially at high energies.

Therefore, going beyond standard searches in the context of these technological advances, in order to better characterize the properties of dark matter, was the main motivation of this thesis. More specifically, I have focused on the highly debated issue of the dark matter density profile in the inner regions of galaxies, exploring in particular the phenomenology of dark matter spikes, i.e. strong enhancements of the dark matter density at the centers of galaxies from accretion of dark matter particles onto supermassive black holes. I have explored new probes of dark matter at the centers of galaxies, focusing in particular on the Milky Way, but more importantly on other galaxies in which the phenomenology of dark matter annihilation has not been explored, such as Messier 87 (M87) and Centaurus A (Cen A).

This manuscript is divided in five parts. In Part **I**, I review the evidence and the main candidates for dark matter, as well as the results of standard searches. Then in Part **II** I discuss the approaches I have adopted to go beyond standard searches, and I present the tools I have used and developed to model dark matter signatures. Finally, Parts **III**, **IV** and **V** are dedicated

to the presentation of the results I have obtained. Technical details can be found in the Appendices.

The thesis work presented in this manuscript has led to the following publications:

1. Lacroix T., Boehm C. and Silk J., *Probing a dark matter density spike at the Galactic center*, *Phys. Rev. D* **89**, 063534 (2014), [arXiv:1311.0139](#)
2. Lacroix T., Boehm C. and Silk J., *Fitting the Fermi-LAT GeV excess: On the importance of including the propagation of electrons from dark matter*, *Phys. Rev. D* **90**, 043508 (2014), [arXiv:1403.1987](#)
3. Lacroix T., Boehm C. and Silk J., *Ruling out thermal dark matter with a black hole induced spiky profile in the M87 galaxy*, *Phys. Rev. D* **92**, 043510 (2015), [arXiv:1505.00785](#)
4. Lacroix T., Macias O., Gordon C., Panci P., Boehm C. and Silk J., *The Spatial Morphology of the Secondary Emission in the Galactic Center Gamma-Ray Excess*, ArXiv e-prints (2015), *Phys. Rev. D* **93**, 103004 (2015), [arXiv:1512.01846](#)
5. Brown A. M., Boehm C., Graham J., Lacroix T., Chadwick P. M. and Silk J., *Discovery of a new extragalactic source population of energetic particles*, ArXiv e-prints (2016), [arXiv:1603.05469](#)
6. Lacroix T., Silk J., Moulin E. and Boehm C., *New H.E.S.S. diffuse emission from the Galactic center: a combination of heavy dark matter and millisecond pulsars?*, ArXiv e-prints (2016), [arXiv:1603.05977](#)

# Physical constants and abbreviations

**Table 1** – List of physical constants used in this thesis. Their values can be found in the National Institute of Standards and Technology ([NIST](#)) database.

Physical constants	Name
$\alpha_{\text{em}}$	fine-structure constant
$c$	speed of light in a vacuum
$e$	elementary charge
$\epsilon_0$	vacuum permittivity
$G$	Newton's constant
$h$	Planck constant
$\hbar \equiv h/(2\pi)$	reduced Planck constant
$k_{\text{B}}$	Boltzmann constant
$m_e$	electron mass
$\mu_0$	vacuum permeability
$\sigma_{\text{T}}$	Thomson cross-section

**Table 2** – List of abbreviations used in this thesis.

Abbreviation	Meaning
3D	three-dimensional
AGN	active galactic nuclei
ALP	axion-like particle
BAO	baryon acoustic oscillations
BBN	Big-Bang nucleosynthesis
BH	black hole
CDM	cold dark matter
Cen A	Centaurus A
CL	confidence level
CMB	cosmic microwave background
CP	charge-parity
DGB	diffuse Galactic background
DM	dark matter
d.o.f.	degree of freedom
DZ	diffusion zone
EW	electroweak
fov	field of view
$\gamma$ -ray	gamma-ray
GC	Galactic center
GCE	Galactic center excess

Continued on next page

**Table 2** – continued from previous page

Abbreviation	Meaning
GUT	Grand Unified Theory
h.c.	Hermitian conjugate
IACT	imaging atmospheric Čerenkov telescope
IC	inverse Compton
ICS	inverse Compton scattering
IGRB	isotropic gamma-ray background
IR	infrared
ISM	interstellar medium
ISRF	interstellar radiation field
KK	Kaluza-Klein
LHS	left-hand side
LKP	lightest Kaluza-Klein particle
LSP	lightest supersymmetric particle
l.o.s.	line of sight
M87	Messier 87
MACHO	massive astrophysical compact object
MAX	maximum
MIN	minimum
MED	median
MSP	millisecond pulsar
MSSM	minimal supersymmetric standard model
MW	Milky Way
NFW	Navarro-Frenk-White
PBH	primordial black hole
QCD	quantum chromodynamics
RHS	right-hand side
SD	spin-dependent
SED	spectral energy distribution
Sgr A*	Sagittarius A*
SI	spin-independent
SIDM	self-interacting dark matter
SM	Standard Model
SMBH	supermassive black hole
SSC	synchrotron self-Compton
SUSY	supersymmetry
TS	test statistic
UED	universal extra dimensions
UR	ultrarelativistic
UV	ultraviolet
WDM	warm dark matter
WIMP	weakly interacting massive particle
WISP	weakly interacting slim particle

## Part I

# Dark matter: from historical evidence to modern searches



# Chapter 1

## Evidence and candidates for dark matter

We start off by giving an overview of the historical observations that promoted the dark matter conundrum to one of the most fundamental problems of astroparticle physics, before discussing the standard dark matter scenario and the main possible candidates.

### Contents

---

<b>1.1</b>	<b>Initial evidence for dark matter</b> . . . . .	<b>4</b>
1.1.1	The missing mass problem . . . . .	4
1.1.2	Cosmology . . . . .	7
<b>1.2</b>	<b>Standard dark matter scenario: thermal relics</b> . . . . .	<b>15</b>
1.2.1	Thermal history and freeze-out . . . . .	15
1.2.2	The relic density of dark matter particles . . . . .	16
1.2.3	The “WIMP miracle” . . . . .	17
<b>1.3</b>	<b>Dark matter candidates</b> . . . . .	<b>19</b>
1.3.1	Massive astrophysical compact halo objects . . . . .	19
1.3.2	Particle dark matter . . . . .	20
1.3.3	Small-scale issues of cold dark matter: additional properties, baryonic physics or modified gravity theories? . . . . .	26

---

## 1.1 Initial evidence for dark matter

### 1.1.1 The missing mass problem

#### 1.1.1.1 Historical introduction: dynamics of stars and galaxies

Throughout the history of mankind, philosophers and natural scientists have wondered about the very nature of matter, from the infinitely small to the infinitely large. However, it was only in the early 20th century that the astronomical community started to study more quantitatively the possible existence of significant amounts of invisible matter on the scales of galaxies and beyond. This revolution was allowed by tremendous progress made both on the observation and theory sides, and marked the dawning of a new era in astronomy.

**The early days – local dynamics.** In the early 20th century, Thomson (Lord Kelvin) pioneered the search for invisible matter in the Milky Way by applying thermodynamical arguments to stellar systems, in an attempt to quantify the amount of ‘dark bodies’ (Kelvin, 1904). Based on the fact that Lord Kelvin’s approximate estimate of the velocity dispersion of stars was of the same order as the observed one, Poincaré argued in 1906 that the amount of invisible matter—for which he coined the expression *dark matter*—had to be smaller than that of visible matter (Poincaré & Vergne, 1911).

In the early 1930s, improving upon seminal works by Kapteyn (1922), Jeans (1922) and Lindblad (1926), Oort studied the kinematics of stars in the Solar neighborhood to determine the gravitational potential, and concluded that the mass in the Galactic plane must be larger than the mass of visible matter in order to explain stellar motions (Oort, 1932). However, at first this result could not be unambiguously confirmed: in 1989 Kuijken and Gilmore deduced the local surface mass density of identified matter, by using photometric and spectroscopic data for a sample of K dwarfs to determine vertical dynamics of the stellar population in the solar neighborhood, and including the observed amount of interstellar gas as well. They found no significant missing mass (Kuijken & Gilmore, 1989). Since then, as reviewed in Read (2014), the characterization of the local density of invisible matter has been extensively studied and refined, for instance in Bovy & Tremaine (2012), qualitatively confirming Oort’s result.

**Galaxy clusters.** It was also in the 1930s that Zwicky published his ground-breaking results. Zwicky measured the velocity dispersion of individual galaxies in the Coma cluster. Applying the virial theorem—which relates the gravitational potential energy to the kinetic energy of stars—to the cluster, he demonstrated that the mass of the cluster was about 400 times larger than the visible mass inferred from the luminosities of galaxies (see Zwicky, 1933, or Zwicky, 2009, for the English translation; see also Zwicky, 1937). The expression *dark matter* (DM) was made popular by Zwicky to refer to this invisible form of matter associated with the apparent missing mass. This pioneering work is widely held as one of the most famous milestones in the history of the dark matter problem.

**Rotation curves.** In the 1970s, the missing mass problem became even more compelling with studies of the rotation curves of spiral galaxies, characterizing the rotation speed of the disk as a function of galactocentric radius. Several groups obtained rotation curves extending to large radii. Rubin and Ford measured the optical rotation curve of the Andromeda (M31) galaxy by spectroscopy of ionized hydrogen (HII) emission regions (Rubin & Ford, 1970), thanks to the spectrograph developed by Ford in the 1960s which yielded data of unprecedented quality. Subsequently, by comparing rotation curves obtained by measuring the Doppler shift of the 21-cm line—associated with the hyperfine transition of neutral atomic hydrogen—in gas clouds, with predictions based on the mass distribution derived from photometry, several authors obtained flat rotation curves at large radii and started to suggest the need for non-luminous matter (Freeman,

1970; Rogstad & Shostak, 1972). Actually, from Newton’s law, for ordinary matter concentrated at the center of a galaxy, the rotation speed is predicted to fall off with the radius  $r$  as  $r^{-1/2}$ , so that flat rotation curves at large radii require the support of a halo of unseen material.

Roberts, Whitehurst and Rots were the ones who actually made the community realize the fundamental implications of flat rotation curves in terms of invisible matter (Whitehurst & Roberts, 1972; Roberts & Rots, 1973). In this context, Roberts stated the importance of radio observations of the 21-cm line which allow for measurements of rotation speeds at larger radii than optical observations (Roberts, 1975), strengthening the case for flat rotation curves (Krumm & Salpeter, 1977). Two influential papers then highlighted the common features of the missing mass problem in galaxies and clusters (Einasto et al., 1974; Ostriker et al., 1974). By the end of the 1970s, the evidence for halos of invisible matter had become overwhelming, partly thanks to Rubin’s and Bosma’s groups who independently showed that most galaxies in their samples had approximately flat rotation curves at large radii, well beyond the optical radius (Rubin et al., 1980; Bosma & van der Kruit, 1979). These papers remain the most famous, despite being only milestones in a series of ground-breaking works and relying only on optical data.

These fascinating results are illustrated beautifully by the rotation curve of the NGC 6503 galaxy, from Begeman et al. (1991), shown in Fig. 1.1. The flatness of galactic rotation curves therefore implies the existence of an extended halo of invisible matter to support the rotation of stars and gas at large radii. Due to difficulties inherent to our location in our own galaxy, translating into large uncertainties on the Milky Way’s rotation curve and the distribution of ordinary matter, historically most studies have focused on other galaxies. However, for a recent analysis of the rotation curve of the Milky Way, relying on recent data, and for a discussion of the implications in terms of DM, see Iocco et al. (2015).

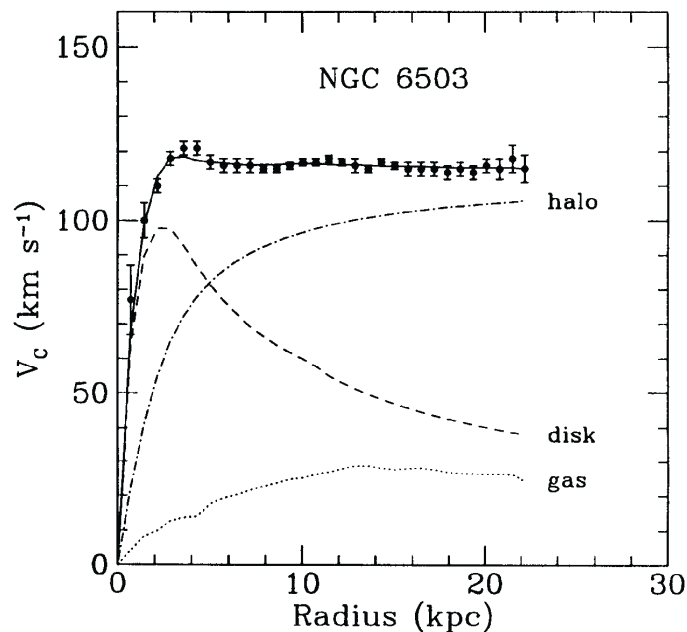


**Figure 1.1** – Rotation curve of NGC 6503 from Begeman et al. (1991), showing the flattening at large radii, indicative of the existence of a dark halo.

**Stabilizing stellar disks.** Finally, pioneering the use of N-body simulations in the 1970s, Ostriker and Peebles showed that a halo of dark matter was necessary to stabilize self-gravitating disks (Ostriker & Peebles, 1973).

### 1.1.1.2 Gravitational lensing

The phenomenon of gravitational lensing—i.e. the deflection of photons due to the curving of spacetime caused by a massive object—provides the most spectacular manifestations of the missing mass or dark matter problem. For a review of gravitational lensing see e.g. [Massey et al. \(2010\)](#).

**Strong lensing.** The gravitational lensing effect is most readily observable for light rays passing close to a very massive object, like a galaxy or a galaxy cluster. In the associated *strong lensing* regime, photons are significantly deflected and follow different paths to the observer, leading to the formation of multiple images. In particular, if the source is aligned with an axisymmetric lens, light rays are equally deflected all around the lens, so that by symmetry the resulting image is a ring, referred to as the *Einstein ring*. The radius of the Einstein ring is proportional to the square root of the projected mass of the lens. In the presence of a small offset between the source and the lens, or for a more complex lens, the Einstein ring is replaced by a series of arcs. The positions and shapes of arcs, arclets and multiple images are used to set tight constraints on the mass distribution of massive objects, in particular clusters of galaxies (see e.g. [Fort & Mellier, 1994](#)).

The first observation of a strong gravitational lens was achieved with the Jodrell Bank MkIA radio telescope in 1979 ([Walsh et al., 1979](#)), finding evidence for the double image of a quasar. This was followed by a number of observations from other ground-based telescopes, leading to a database of strong lenses. Then the Hubble Space Telescope (HST) launched in 1990 revolutionized the field, leading to a large number of high-resolution observations of many arcs and multiple images, as illustrated with the image of the Abell 2218 cluster shown in Fig. 1.2.



**Figure 1.2** – Image of the Abell 2218 galaxy cluster from the Hubble Space Telescope (HST), showing arcs caused by strong gravitational lensing of background galaxies due to the mass of the cluster. Credit: NASA/ESA.

Reconstructing the masses of galaxy clusters via strong lensing measurements reveals that the visible mass cannot account for the significant bending of light revealed by observations, again pointing to a dominant dark matter component and confirming Zwicky’s findings. Besides, Zwicky had foreseen that gravitational lensing would prove essential to weight galaxy clusters.

**Weak lensing.** For light rays that do not pass close to a massive object, the deflection is much weaker, so that the magnification and distortion of background sources are too small to be detectable for individual objects. This is referred to as the *weak lensing* regime. In particular, although the shear distortion affects the shape of background galaxies, these changes are much less significant than the intrinsic dispersion in shapes. This requires a statistical treatment of the lensed sources. If the Universe is indeed isotropic, intrinsic projected shapes of galaxies average

out to circular. Then, adjacent background galaxies are sheared by approximately the same amount, which results in an average elliptical shape from which the shear field can be inferred statistically. This in turn allows the gravitational potential of the lens projected along the line of sight to be reconstructed, and from there one obtains a map of the projected mass distribution of the lens (see e.g. [Hoekstra et al., 2013](#)).

Applying this technique to the cluster merger 1E0657-558, commonly known as the “Bullet Cluster”, led to what is held as one of the most convincing pieces of evidence for weakly interacting dark matter ([Markevitch et al., 2004](#); [Clowe et al., 2004, 2006](#)). Fig. 1.3 shows a composite image of the cluster merger. Two concentrations of galaxies are observed in optical light, X-ray emitting hot gas in both clusters is represented in red, and the mass distributions of the clusters reconstructed from weak lensing are shown in blue. Most of the mass corresponds to non-luminous matter, while the hot gas makes up most of the ordinary matter. The striking feature in this observation is the large offset between the dark matter and gas distributions of each cluster, with the gas found to lag behind the dark matter which coincides with the galaxies behaving as collisionless particles. This shows that the gas is slowed by the ram pressure induced by the electromagnetic interaction, while the dark matter must be collisionless, i.e. not self-interacting.



**Figure 1.3** – Composite image of the cluster merger 1E0657-558. This object is commonly known as the “Bullet Cluster”, although the term “bullet” actually refers to the smaller cluster moving away from the larger one. Credit for the composite image: X-ray: NASA/CXC/CfA/[Markevitch \(2006\)](#); Lensing Map: NASA/STScI; ESO WFI; Magellan/U.Arizona/[Clowe et al. \(2006\)](#); Optical: NASA/STScI; Magellan/U.Arizona/[Clowe et al. \(2006\)](#).

More recently, detailed simulations have been performed to accurately model the lensing properties as well as multi-wavelength observations of the Bullet Cluster, in order to better characterize the merger and ultimately derive more robust constraints in particular on DM ([Lage & Farrar, 2014](#)).

## 1.1.2 Cosmology

In this section, we review the cosmological evidence for DM, and discuss its crucial importance for the self-consistency of the standard cosmological model.

### 1.1.2.1 The standard cosmological model

Here we summarize the main elements of the standard cosmological model, relevant in the context of DM. For a detailed review and derivation of the equations, see e.g. [Peebles \(1980\)](#). The standard model of cosmology is based on the *Einstein equations of general relativity*, which relate the energy content of the Universe to its geometry, and the *cosmological principle*, which states

that the Universe is homogeneous and isotropic, i.e. has the same properties at every point in space and in every direction (this is observed in practice at large scales, i.e. above  $\sim 100$  Mpc).

From the assumptions of homogeneity and isotropy, the only possible form for the metric of spacetime  $g_{\mu\nu}$  is the Friedmann-Lemaître-Robertson-Walker metric (Friedmann, 1922; Lemaître, 1927; Robertson, 1929, 1935, 1936a,b; Walker, 1937), defined by the line element

$$ds^2 = g_{\mu\nu}dx^\mu dx^\nu = -dt^2 + a(t)^2 \left( \frac{dr^2}{1 - kr^2} + r^2 d\Omega^2 \right), \quad (1.1)$$

where  $t$  be the cosmic time and  $a$  the cosmic scale factor, normalized to unity at the present epoch,  $a_0 \equiv a(t_0) = 1$ . From there, the redshift  $z$  is defined by  $a = 1/(1+z)$ .  $k$  is the reduced curvature parameter, equal to  $-1$ ,  $0$  or  $1$  respectively for an open, flat or closed universe. We consider units such that  $c = 1$ . In the following, dots represent derivatives with respect to  $t$ .

The self-consistent evolution of spacetime is then described by the Einstein equations:

$$R_{\mu\nu} - \frac{1}{2}g_{\mu\nu}R = -8\pi GT_{\mu\nu} + \Lambda g_{\mu\nu}, \quad (1.2)$$

where  $R_{\mu\nu}$  and  $R$  are respectively the Ricci tensor and scalar—contractions of the Riemann curvature tensor derived from the metric.  $G$  is Newton's gravitation constant. The left-hand side of Eq. 1.2 characterizes the geometry, whereas the right-hand side represents the energy content of the Universe, with  $T_{\mu\nu}$  the stress-energy tensor.  $\Lambda$  is the cosmological constant which is added in order to account for the acceleration of cosmic expansion at the present epoch. To be compatible with the cosmological principle, the cosmological fluid (including matter and radiation) must have the stress-energy tensor of a perfect fluid:

$$T_{\mu\nu} = (\rho + P)U_\mu U_\nu - g_{\mu\nu}P, \quad (1.3)$$

where  $\rho = \rho_m + \rho_r$  is the sum of the matter and radiation energy densities, and  $P$  is the pressure. Finally, the Einstein equations lead to the Friedmann equations:

$$H^2 = \frac{8\pi G}{3}\rho - \frac{k}{a^2} + \frac{\Lambda}{3}, \quad (1.4)$$

$$\frac{\ddot{a}}{a} = -\frac{4\pi G}{3}(\rho + 3P) + \frac{\Lambda}{3}, \quad (1.5)$$

where  $H \equiv \dot{a}/a$  is the Hubble parameter. From Eq. 1.4, also referred to as the Hubble equation, we can see that for a flat universe ( $k = 0$ ), the total energy density today  $\rho_{\text{tot}} \equiv \rho + \rho_\Lambda$ , with  $\rho_\Lambda = \Lambda/(8\pi G)$ , is equal to

$$\rho_{\text{crit}} \equiv \frac{3H_0^2}{8\pi G}, \quad (1.6)$$

referred to as the critical density, with  $H_0 \equiv H(t_0)$ . Abundances of the various constituents today are expressed for convenience in units of  $\rho_{\text{crit}}$ :

$$\Omega_i = \frac{\rho_i(t_0)}{\rho_{\text{crit}}}. \quad (1.7)$$

The Hubble equation can thus be rewritten in such a way as to show the evolution of the various constituents of the Universe with  $a$  or equivalently  $z$ :

$$E(z) \equiv \frac{H^2(z)}{H_0^2} = \Omega_r(1+z)^4 + \Omega_m(1+z)^3 + \Omega_k(1+z)^2 + \Omega_\Lambda, \quad (1.8)$$

where  $\Omega_k \equiv -k/H_0^2$ . As we will see in the following, cosmological observations indicate that matter is mostly made of DM, which is therefore a crucial ingredient of the standard cosmological model, the Lambda-cold-dark-matter ( $\Lambda$ CDM) model.

### 1.1.1.2 The cosmic microwave background

The cosmic microwave background (CMB), fossil light of the Big Bang, gives perhaps the strongest case for DM.

**Characterization.** The physical origin of the CMB was actually understood in 1948 (Gamow, 1948; Alpher & Herman, 1948), but it was not until the 1960s that its importance was fully realized, thanks to the work of Dicke, Peebles, Roll and Wilkinson (Dicke et al., 1965). In the early Universe, the primordial plasma was in thermal equilibrium due to particle interactions. In particular, the Universe was opaque due to scattering of photons off of charged particles. When cosmic expansion allowed the temperature to decrease sufficiently (down to  $\sim 3000$  K) for electrons to combine with atomic nuclei, the Universe became transparent and photons started to stream freely. CMB photons were therefore emitted at that time, known as the time of recombination, and we receive them today as a largely isotropic signal, in agreement with the cosmological principle.

Penzias and Wilson accidentally detected the CMB in 1964 (Penzias & Wilson, 1965) as an irreducible diffuse background in the radio telescope at Bell Labs, and were subsequently awarded the Nobel Prize in 1978 for the discovery, thanks to the interpretation given in Dicke et al. (1965).

Reflecting the thermal equilibrium in the early Universe, the CMB is the physical object closest to a perfect blackbody in nature, with a spectrum very well described by the Planck spectrum

$$B_\nu = \frac{2h\nu^3}{c^2} \frac{1}{e^{h\nu/k_B T_{\text{CMB}}} - 1}, \quad (1.9)$$

with a temperature  $T_{\text{CMB}} = 2.72548 \pm 0.00057$  (Fixsen, 2009), as demonstrated with very good accuracy with the Far Infrared Absolute Spectrophotometer (FIRAS) on board the Cosmic Background Explorer (COBE) satellite (Fixsen et al., 1996). The low temperature of the CMB observed today is simply the result of cosmic expansion, with a redshift of recombination of  $z^* = 1090.06 \pm 0.30$  (Ade et al., 2015b).

Actually, the CMB is not perfectly isotropic, due to primordial quantum fluctuations imprinted in temperature anisotropies. The latter turn out to be the most important property of the CMB for cosmology, and are quantified by

$$\Theta(\hat{n}) = \frac{T(\hat{n}) - \langle T \rangle}{\langle T \rangle}, \quad (1.10)$$

where  $\hat{n}$  is a direction in the sky and  $\langle T \rangle$  the average temperature on the sky. The temperature fluctuations are very small, of order  $10^{-5}$ , hence the need to subtract the average temperature. They are further masked by the dipole anisotropy induced by the motion of the Solar system with respect to the CMB rest frame, and towards the boundary of the constellations of Crater and Leo, at a velocity of  $369 \pm 0.9$  km s $^{-1}$  (Hinshaw et al., 2009).

Maps of the CMB temperature fluctuations have been obtained with increasing angular resolution thanks to satellite experiments, namely the balloon-borne BOOMERANG experiment (Ruhl et al., 2003; Masi et al., 2006), COBE (Bennett et al., 1996), the Wilkinson Microwave Anisotropy Probe (WMAP) (Bennett et al., 2013) and more recently *Planck*. The latter has achieved a very good angular resolution of a few arcmin. The *Planck* map from Ade et al. (2015a), obtained after removing Galactic foregrounds is shown in Fig. 1.4.

To extract information from this map, the temperature fluctuations are decomposed on the sphere of the sky using spherical harmonics  $Y_{\ell m}$ :

$$\Theta(\hat{n}) = \sum_{\ell=0}^{\infty} \sum_{m=-\ell}^{+\ell} a_{\ell m} Y_{\ell m}(\hat{n}). \quad (1.11)$$

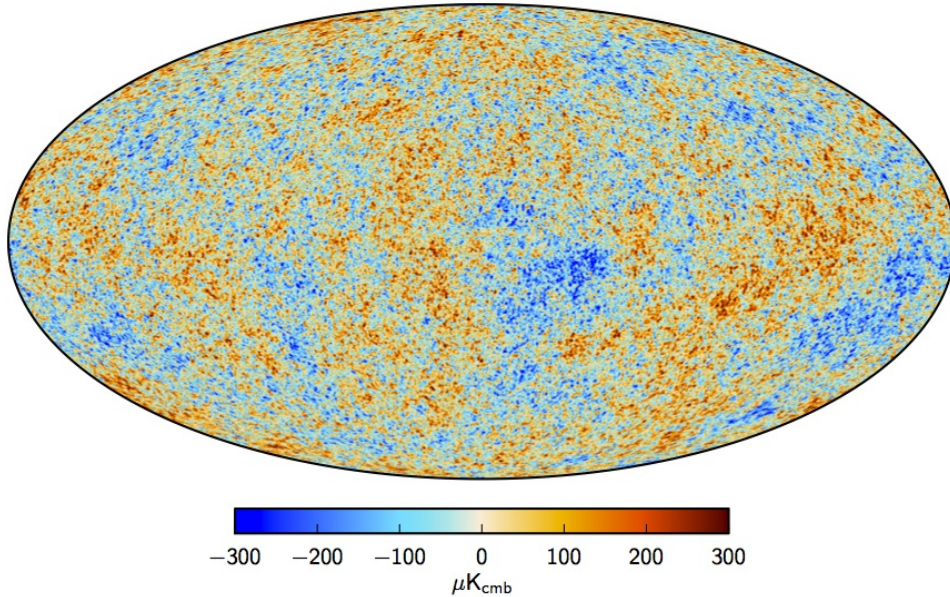


**Figure 1.4** – *Planck* map of the CMB temperature fluctuations from Ade et al. (2015a), obtained with a Mollweide projection of the celestial sphere.

Assuming statistical isotropy, the covariance between the  $a_{\ell m}$  coefficients is diagonal and reads  $\langle a_{\ell m} a_{\ell' m'}^* \rangle = C_\ell \delta_{\ell\ell'} \delta_{mm'}$ . In this case, the cross-correlation of the temperature fluctuations in two directions  $\hat{n}$  and  $\hat{n}'$  can be written as an expansion over Legendre polynomials  $P_\ell$ , and is entirely characterized by the  $C_\ell$  coefficients which depend only on the multipoles  $\ell$ :

$$\langle \Theta(\hat{n}) \Theta(\hat{n}') \rangle = \sum_{\ell=0}^{\infty} \frac{2\ell+1}{4\pi} C_\ell P_\ell(\cos \theta), \quad (1.12)$$

where  $\theta$  is the angle between the two directions  $\hat{n}$  and  $\hat{n}'$ , defined by  $\hat{n} \cdot \hat{n}' = \cos \theta$ .  $C_\ell$  represents the power spectrum of the CMB temperature fluctuations, and characterizes the correlation between the fluctuations in two directions of the sky separated by an angle  $\theta \sim 180^\circ/\ell$ . For convenience, the rescaled power spectrum  $\mathcal{D}_\ell \equiv \ell(\ell+1)C_\ell/2\pi$  is usually displayed instead of  $C_\ell$ , as shown in Fig. 1.5. The data are very well reproduced by the base  $\Lambda$ CDM model which features six parameters, namely the baryon abundance today  $\Omega_b h^2$ , the cold DM abundance today  $\Omega_c h^2$ , the angular sound horizon  $\theta^*$  at  $z = z^*$ , the Thomson scattering optical depth  $\tau$  due to reionization of the Universe, the power-law index  $n_s$  and the normalization  $A_s$  (at  $k_0 = 0.05 \text{ Mpc}^{-1}$ ) of the scalar primordial power spectrum.

The CMB power spectrum contains a wealth of cosmological information and is a central element in modern cosmology, as discussed e.g. in Peter & Uzan (2009). However, here we only focus on aspects of the CMB that are directly relevant to the DM problem. The detailed shape of the peaks of the CMB spectrum turns out to be closely related to the abundances of baryonic and dark matter.

**Baryon acoustic oscillations.** The most important feature in the CMB power spectrum is the series of *acoustic oscillations* (Silk, 1968; Peebles & Yu, 1970; Sunyaev & Zeldovich, 1970). In the CMB power spectrum, acoustic peaks have a period of  $\Delta l_s \sim 300$ , which reveals the existence of a correlation between fluctuations separated by  $\theta^* \sim 0.6^\circ$ . These oscillations originate from relativistic acoustic waves in the tightly coupled primordial photon-baryon plasma, caused by perturbations and propagating under the effect of radiation pressure. In the simple case of a single density fluctuation, a spherical shell of baryons is driven outwards by radiation pressure

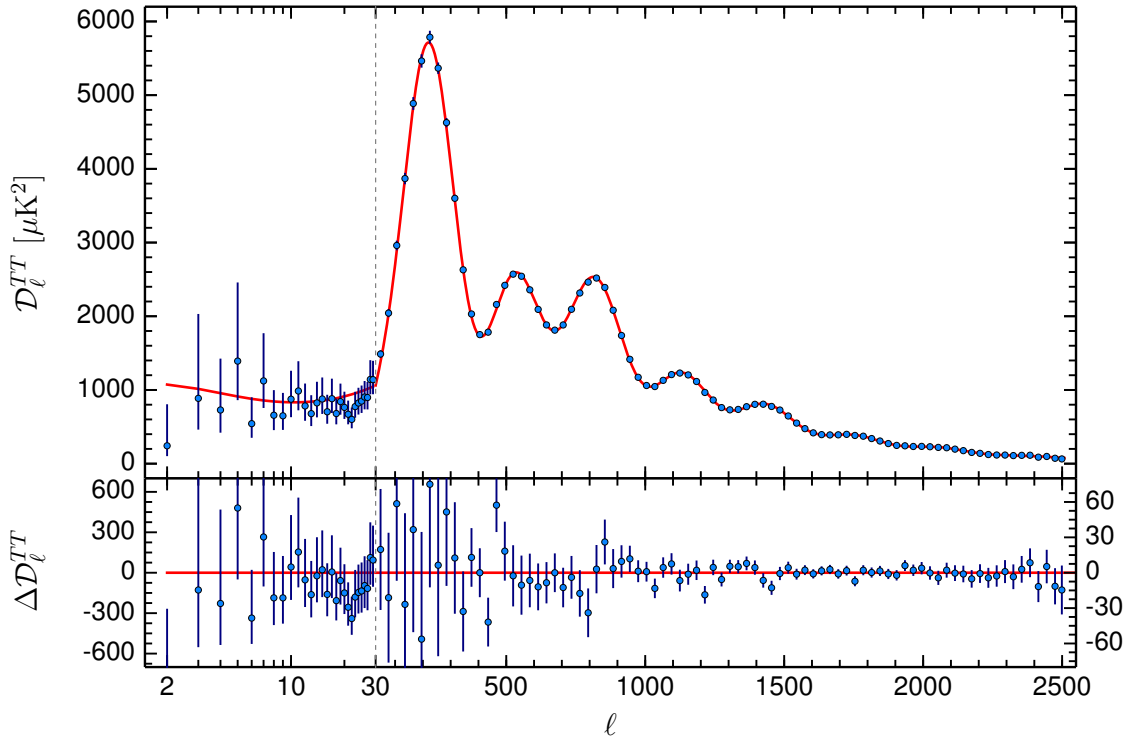


**Figure 1.5** – Temperature power spectrum of the CMB from *Planck* (Ade et al., 2015b). This plot shows the remarkable agreement between the predictions of the standard cosmological model with six parameters ( $\Omega_b h^2$ ,  $\Omega_c h^2$ ,  $\theta^*$ ,  $\tau$ ,  $n_s$ ,  $A_s$ ) and the *Planck* data, with the small residuals shown in the lower panel.

and propagates at the speed of sound (see e.g. Eisenstein & Hu, 1998; Bassett & Hlozek, 2010)

$$c_s(z) = \frac{c}{\sqrt{3(1 + R(z))}}, \quad R(z) = \frac{3\Omega_b}{4\Omega_\gamma} \frac{1}{1 + z}. \quad (1.13)$$

Then, once photons and baryons decouple at the time of recombination, baryons no longer feel the radiation pressure, so that a standing spherical shell of baryons remains around a central DM overdensity. The radius of the spherical shell is given by the sound horizon, i.e. the distance traveled by the acoustic wave between its creation and the end of the Compton drag epoch—during which baryons were dragged by photons via radiation pressure—which occurs slightly after recombination, at a redshift  $z_{\text{drag}} = 1059.62 \pm 0.31$  (Ade et al., 2015b). The comoving radius of the spherical shell is given by the comoving sound horizon at the end of the drag epoch,  $r_{\text{drag}} \equiv r_s(z_{\text{drag}})$ , where

$$r_s(z) = \int_z^\infty c_s(z') \frac{dz'}{H(z')}. \quad (1.14)$$

The comoving radius of the spherical shell of baryons is actually very close to the comoving sound horizon at recombination,  $r^* \equiv r_s(z^*)$ .

Under the effect of gravity, the baryonic and DM densities evolve together, resulting in a density profile with a small peak at  $r_{\text{drag}}$ , so that today galaxies are more likely to be observed with a separation corresponding to this radius (Cole et al., 2005; Eisenstein et al., 2005). This peak in the correlation function in real space translates into oscillations in Fourier space, or similarly in spherical harmonic space, hence the name *baryon acoustic oscillations* (BAO). In practice, the density profile is the result of many perturbations, so that the BAO scale can only be measured statistically, as a stronger correlation between overdensities separated by this characteristic scale. The first acoustic peak in the CMB power spectrum was detected with

BOOMERANG (Mauskopf et al., 2000), and the peaks at higher multipoles were subsequently reported by WMAP and *Planck*. For a review of BAO see e.g. Eisenstein & Hu (1998); Bassett & Hlozek (2010).

Physically, BAO give a strong case for DM, since in the absence of a form of matter that does not interact with photons, initial perturbations would be washed out by radiation pressure, leaving no trace of any characteristic correlation scale (Boehm et al., 2002). In the CMB power spectrum, the preferred angular separation between fluctuations therefore corresponds to the apparent BAO scale at recombination, defined by  $\theta^* = r^*/[(1+z^*)D_A(z^*)]$ , with  $D_A$  the physical angular diameter distance.<sup>1</sup> The CMB power spectrum sets strong constraints on the cosmological parameters, especially through the acoustic peaks. In particular, the cosmic abundances measured with *Planck* using the information from temperature and polarization are (Ade et al., 2015b):<sup>2</sup>

$$\Omega_m = 0.3156 \pm 0.0091, \quad (1.16)$$

$$\Omega_c h^2 = 0.1198 \pm 0.0015, \quad (1.17)$$

$$\Omega_b h^2 = 0.02225 \pm 0.00016, \quad (1.18)$$

with  $h = H_0/(100 \text{ km s}^{-1} \text{ Mpc}^{-1})$  and  $H_0 = 67.27 \pm 0.66 \text{ km s}^{-1} \text{ Mpc}^{-1}$ . This in turn constrains the comoving BAO scale:  $r_{\text{drag}} \approx r^* \approx 150 \text{ Mpc}$ .

**Damping of oscillations on small scales and structure formation.** Another crucial feature of the CMB power spectrum is the damping of oscillations on small scales (i.e. high  $\ell$ ). This is due to the fact that the primordial photon-baryon fluid is not a perfect fluid, since photons can actually diffuse over a certain distance, determined by the properties of the plasma, before being Compton scattered by electrons. Density fluctuations on scales smaller than this diffusion length are washed out, which makes the CMB more isotropic below these scales. This results in a damping of acoustic oscillations in the CMB power spectrum. This effect is referred to as *diffusion damping* or *Silk damping* (Silk, 1968). Were all the matter baryonic, the high- $\ell$  acoustic peaks of the CMB would be completely suppressed, which is obviously not the case considering the observed CMB power spectrum which features eight acoustic peaks. As a result, to counteract the effect of Silk damping, matter must be made of a significant non-baryonic component,<sup>3</sup> which does not interact strongly with photons. The degree of interaction actually allowed by the observed CMB power spectrum and structure formation was discussed in detail in Boehm et al. (2001, 2002, 2005); Boehm & Schaeffer (2005), and more recently in Wilkinson et al. (2014a,b); Boehm et al. (2014b); Schewtschenko et al. (2015a,b); Escudero et al. (2015). In particular, the coupling of DM to photons (and neutrinos) induces *collisional damping* of small-scale DM fluctuations.

Additionally, the measurement of eight acoustic peaks in the CMB power spectrum is generally held as evidence in favor of cold DM particles, i.e. non relativistic well before decoupling of matter and radiation, otherwise density fluctuations on small scales would have been washed out by the free streaming of hot (i.e. relativistic) DM particles. The cold dark matter (CDM) scenario is therefore the standard paradigm to explain the formation of large-scale structures (Peebles, 1982; Blumenthal et al., 1984; Davis et al., 1985) and galaxies (Peebles, 1984; Blumenthal et al., 1982). In the absence of interactions, this favors massive DM particles, typically above the keV range. However, models of collisionless warm dark matter (WDM) models corresponding to particles

<sup>1</sup>The physical angular diameter distance is given by

$$D_A(z) = \frac{c}{H_0(1+z)} \int_0^z \frac{dz'}{E(z')}. \quad (1.15)$$

<sup>2</sup>In the following we use  $\Omega_{\text{DM}} h^2 \equiv \Omega_c h^2$ .

<sup>3</sup>Throughout this work we use the term ‘baryonic’ to refer to ordinary matter—including for instance leptons which are not baryons—, as opposed to DM.

with keV masses (Olive & Turner, 1982; Bond et al., 1982; Schaeffer & Silk, 1988), or DM models with non-negligible but not too large interactions with radiation (Boehm et al., 2001), can also be indistinguishable from CDM regarding the CMB power spectrum, while providing a richer phenomenology than CDM on small scales. In particular, DM-photon interactions induce a certain amount of free streaming of the DM particles even after decoupling from photons, which is another source of damping and can be constrained by observations of small-scale structure (Boehm et al., 2001, 2002, 2005, 2014b; Boehm & Schaeffer, 2005; Wilkinson et al., 2014a,b; Schewtschenko et al., 2015a,b; Escudero et al., 2015).

**Summary.** To conclude, CMB observations show that DM—along with dark energy in the form of a cosmological constant  $\Lambda$ —are the fundamental ingredients of the standard model of cosmology, referred to as the  $\Lambda$ CDM model. DM is therefore a dominant component of the Universe, with standard abundances of collisionless cold DM derived from the CMB power spectrum, corresponding to about 26–27% of the energy budget of the Universe, and approximately 85% of matter in the Universe.

### 1.1.2.3 Structure formation and numerical simulations

Dark matter is the crucial ingredient of structure formation, allowing for the survival of perturbations evidenced by the temperature fluctuations in the CMB. It turns out that the amount of baryonic matter is insufficient to explain the formation of structures: DM is needed to steepen the gravitational potential and maintain perturbations before recombination.

The success of the  $\Lambda$ CDM paradigm is illustrated by the comparison of numerical N-body simulations—based on this scenario and on cosmological parameters derived from the CMB—like *Millennium* (Springel et al., 2005) with maps of the large-scale structure obtained by various galaxy redshift surveys, namely the CfA redshift survey (de Lapparent et al., 1986; Geller & Huchra, 1989), the 2dFGRS (Colless et al., 2001), and the SDSS (York et al., 2000). The very good agreement is shown in Fig. 1.6, taken from Springel et al. (2006), in which semi-analytic models are used to describe the formation and evolution of visible components on top of the DM distribution.

### 1.1.2.4 Baryon acoustic oscillations in large scale structure at low redshift

BAO were not only detected in the CMB anisotropies but also in the spatial distribution of galaxies at low redshift with the SDSS (Eisenstein et al., 2005) and 2dFGRS (Cole et al., 2005) galaxy surveys.

A more recent characterization of BAO in the large-scale structure at low redshift, independent of the CMB, has been obtained with the Baryon Oscillation Spectroscopic Survey (BOSS). Shown in the left panel of Fig. 1.7 is the correlation function calculated from the BOSS DR11 CMASS galaxy sample, which corresponds to an effective redshift  $z = 0.57$  (Anderson et al., 2014). The BAO peak is clearly visible at  $\sim 100h^{-1}$  Mpc  $\approx 150$  Mpc, which is the expected physical BAO scale at low redshift in the  $\Lambda$ CDM model. The power spectrum of the same galaxy sample, divided by a smooth power spectrum without BAO, is presented in the right panel of Fig. 1.7, clearly showing the presence of oscillations.

The measurement of the BAO scale at low redshift therefore provides an independent characterization of the matter content of the Universe, and thus gives additional evidence for DM.

### 1.1.2.5 Big Bang nucleosynthesis

The production of light chemical elements in the early Universe is referred to as primordial nucleosynthesis (or Big Bang nucleosynthesis, BBN). The understanding of the physical processes

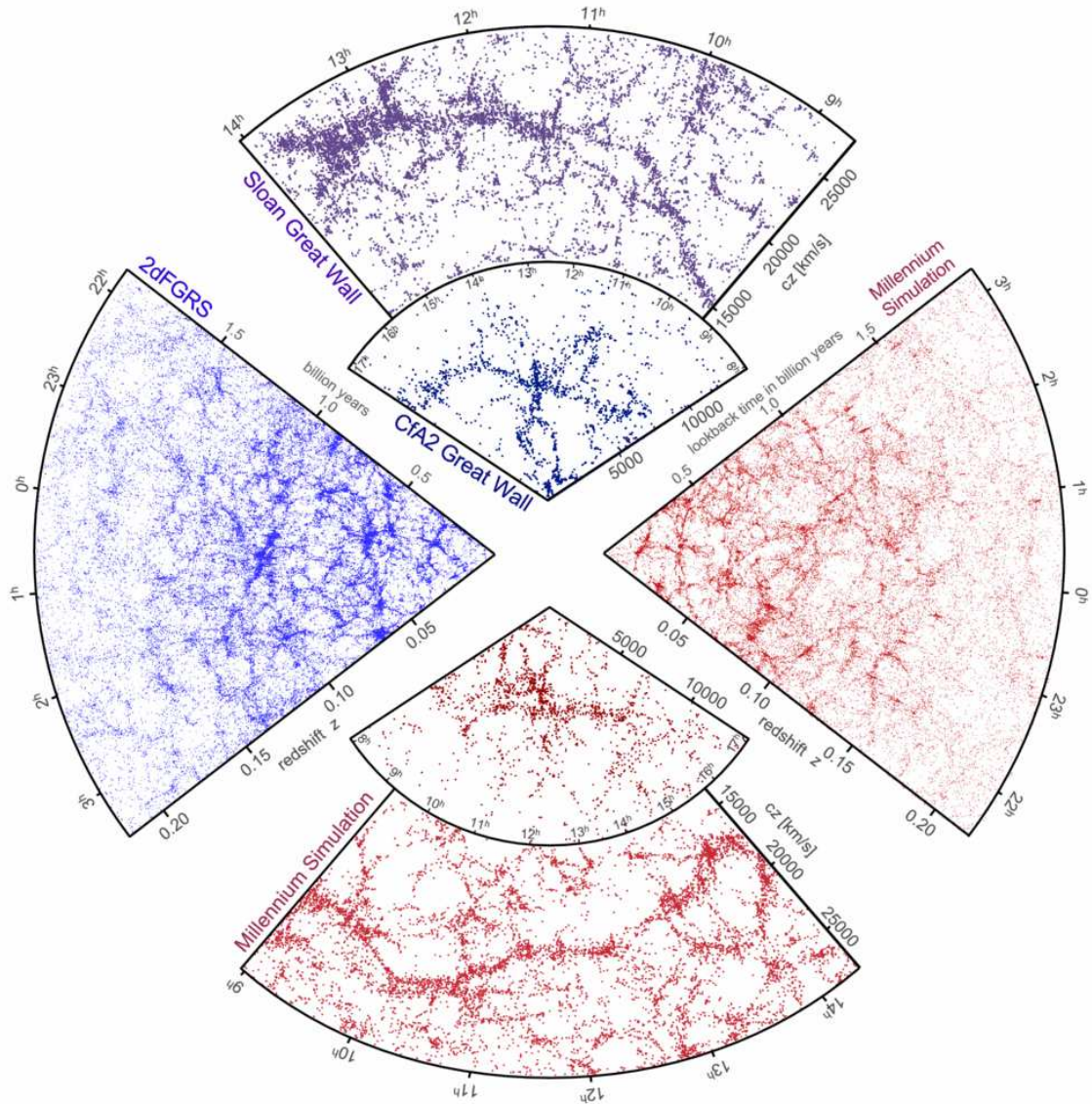


**Figure 1.6** – Comparison of the predictions of the Millennium simulation with observational results of the CfA, 2dFGRS and SDSS galaxy redshift surveys, demonstrating the validity of the  $\Lambda$ CDM paradigm at large scales. This figure is taken from [Springel et al. \(2006\)](#). Semi-analytic models are used to describe the formation and evolution of galaxies on top of the DM distribution.

involved dates back to [Hayashi \(1950\)](#); [Alpher et al. \(1953\)](#); [Hoyle & Taylor \(1964\)](#); [Peebles \(1966a,b\)](#); [Wagoner et al. \(1967\)](#). For reviews see e.g. [Sarkar \(1996\)](#); [Olive et al. \(2000\)](#); [Peter & Uzan \(2009\)](#). BBN proceeds through a chain of nuclear reactions involving neutrons,  $^1\text{H}$ ,  $\text{D}\equiv^2\text{H}$ ,  $\text{T}\equiv^3\text{H}$ ,  $^3\text{He}$ ,  $^4\text{He}$ ,  $^7\text{Be}$  and  $^7\text{Li}$ . The baryon-to-photon ratio  $\eta \equiv n_b/n_\gamma$  is too small for 3-body or 4-body processes to have a sizable probability to occur. Therefore, the key process is the formation of deuterium (D) which is a 2-body process ( $n+p \rightarrow \text{D}+\gamma$ ) occurring below  $T \sim 1$  MeV. Other elements can only form after deuterium. However, deuterium has a low binding energy of  $\sim 2.2$  MeV, so other elements like  $^4\text{He}$  can only form below  $\sim 0.1$  MeV, i.e. when the density of photons  $n_\gamma$  has sufficiently decreased, since at higher temperature deuterium nuclei are readily photo-dissociated. As a result, primordial abundances depend critically on  $\eta$ .

Determining the primordial abundances is difficult since light elements have been reprocessed via nuclear reactions throughout the evolution of the Universe. Consequently, abundances must be measured in low-metallicity astrophysical environments, as pristine as possible.

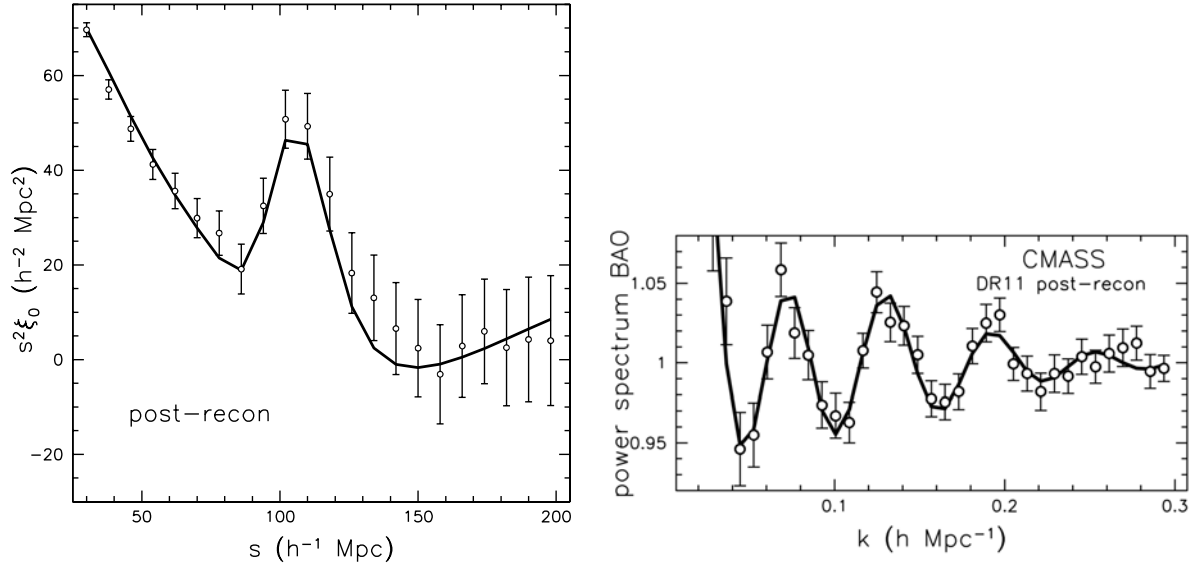


**Figure 1.7 – Left panel:** Correlation function of galaxies from the BOSS DR11 CMASS sample, clearly showing the BAO peak (Anderson et al., 2014). The solid curve represents the best-fit BAO model. **Right panel:** Power spectrum of galaxies from the BOSS DR11 CMASS sample, divided by a smooth power spectrum without BAO (Anderson et al., 2014). The solid curve represents the best-fit BAO model.

In the end, BBN gives  $\eta \sim 6 \times 10^{-10}$  and is an independent way of measuring the baryon abundance  $\Omega_b$ , indirectly providing additional evidence for DM. Additionally, BBN sets strong constraints on deviations from the standard model of cosmology (Malaney & Mathews, 1993) and on new physics beyond the standard model of particle physics (Sarkar, 1996).

## 1.2 Standard dark matter scenario: thermal relics

Determining the production mechanism of DM particles is of crucial importance to understand their microphysics. Many scenarios have been considered in the literature, including thermal production (e.g. Lee & Weinberg, 1977; Binétruy et al., 1984a,b; Bouquet & Salati, 1987; Griest, 1988, 1989; Srednicki et al., 1988; Kolb & Turner, 1990; Kamionkowski & Turner, 1990; Drees & Nojiri, 1993; Chung et al., 1999) and non-thermal production (e.g. Kawasaki et al., 1996; Enqvist & McDonald, 1998; Jeannerot et al., 1999; Covi et al., 1999; Moroi & Randall, 2000; Lin et al., 2001; Covi et al., 2001; Fujii & Hamaguchi, 2002; Khalil et al., 2002; Allahverdi & Drees, 2002; Torrente-Lujan, 2002). Thermal production is the central assumption of the standard DM picture. See e.g. the review in Baer et al. (2015) for a discussion of DM production mechanisms.

In the standard DM scenario, DM particles are thermal relics of the Big Bang, which means that they were thermally produced in the early Universe, i.e. produced from particles in thermal equilibrium. As discussed in the following, the most popular thermal relics are massive and coupled to SM particles via the weak interaction, and no asymmetry is assumed between DM particles and antiparticles.

### 1.2.1 Thermal history and freeze-out

The evolution of the number density  $n$  of DM particles in thermal and chemical equilibrium in the early Universe is governed by the Boltzmann equation (Hut, 1977; Lee & Weinberg, 1977;

Kolb & Turner, 1990):

$$\frac{dn}{dt} = -3Hn - \langle\sigma v\rangle (n^2 - n_{\text{eq}}^2) \quad (1.19)$$

where  $H$  is the Hubble parameter,  $\langle\sigma v\rangle$  the thermal average of the annihilation cross-section of DM particles times relative velocity, and  $n_{\text{eq}}$  is the equilibrium number density of DM particles. The first term on the right-hand side of Eq. (1.19) accounts for the dilution of the number density of particles due to cosmic expansion, whereas the second term accounts for the fact that the number of particles is further reduced by annihilations.

DM particles are initially in thermal and chemical equilibrium via annihilations with their antiparticles into lighter SM particles. The inverse reaction actually takes place as long as the temperature is high enough for the lighter particles to annihilate into the heavier ones. During that phase, the number density  $n$  is equal to the equilibrium density  $n_{\text{eq}}$  and the number of particles  $na^3$  is constant.

Then, as the temperature drops below the mass of the DM particles  $m_{\text{DM}}$ , DM particles become non-relativistic, and the thermal energy becomes insufficient to fuel the inverse reaction. As a result, the number density  $n$ , which still follows  $n_{\text{eq}}$ , starts to decrease exponentially, because of the Boltzmann factor which appears in the non-relativistic limit. Consequently, the annihilation rate per particle  $\Gamma_{\text{ann}} = n\langle\sigma v\rangle$  starts decreasing.

When  $\Gamma_{\text{ann}}$  becomes equal to the Hubble parameter  $H$ , DM particles chemically decouple from the thermal bath. This is referred to as *freeze-out*. We denote by  $T_{\text{F}}$  the temperature corresponding to the moment of freeze-out. As  $T$  drops below  $T_{\text{F}}$ , the DM particles can no longer annihilate efficiently, considering that the characteristic time scale of the reaction  $\Gamma_{\text{ann}}^{-1}$  is now greater than the expansion rate of the Universe  $H$ .  $na^3$  remains constant from freeze-out onwards, which gives the relic abundance of DM particles today.

### 1.2.2 The relic density of dark matter particles

Before attempting to solve the Boltzmann equation, one can simplify it using the conservation of entropy (which derives from the conservation of the stress-energy tensor). The entropy per comoving volume reads (see e.g. Kolb & Turner, 1990)

$$s = \frac{2\pi^2 g_* T^3}{45}, \quad (1.20)$$

with  $g_*$  is the number of relativistic degrees of freedom of the DM particles.  $g_*$  is a slowly varying function of the temperature, so its variations are neglected here. The change of variables  $Y = n/s$  absorbs the expansion term and leads to a convenient form of the Boltzmann equation. With  $sa^3 = \text{cst}$  and  $\dot{\ } \equiv d/dt$ , Eq. (1.19) therefore becomes:

$$s\dot{Y} = -\langle\sigma v\rangle s^2(Y^2 - Y_{\text{eq}}^2), \quad (1.21)$$

with  $Y_{\text{eq}} = n_{\text{eq}}/s$ . Now we define

$$x = \frac{m_{\text{DM}}}{T}. \quad (1.22)$$

In the radiation dominated era, which is the relevant regime here, the Hubble parameter reads

$$H = \left(\frac{4\pi^3 g_*}{45}\right)^{1/2} \frac{m_{\text{DM}}^2}{M_{\text{Pl}}} \frac{1}{x^2}, \quad (1.23)$$

where  $M_{\text{Pl}} = 1.22 \times 10^{19}$  GeV is the Planck mass. Moreover, in this regime we have  $t = 1/2H$ . Differentiating this expression leads to  $dx/dt = Hx$  and the Boltzmann equation eventually takes on the following simplified form:

$$\frac{dY}{dx} = -C \langle\sigma v\rangle \frac{1}{x^2} (Y^2 - Y_{\text{eq}}^2), \quad (1.24)$$

where  $C \equiv m_{\text{DM}} M_{\text{Pl}} (\pi g_*/45)^{1/2}$ . However, Eq. (1.24) it is a Ricatti type equation and cannot be solved analytically. Nevertheless, the late-time value of the density can be obtained analytically. The equilibrium distribution is given by

$$Y_{\text{eq}}(x) = \frac{45g}{4\pi^4 g_*} x^2 K_2(x), \quad (1.25)$$

with  $g$  the number of internal degrees of freedom of the particle and  $K_2$  the modified Bessel function of the second kind. Therefore, due to the exponential decrease of  $Y_{\text{eq}}$  in the non-relativistic regime corresponding to  $x \gg 1$ ,  $Y_{\text{eq}}^2$  can be neglected with respect to  $Y^2$ . To highlight the dependence of the relic density on the annihilation cross-section, we assume the simplest case in which the latter is dominated by the s-wave contribution—i.e. independent of the velocity. Therefore we consider  $\langle\sigma v\rangle$  independent of the temperature. Separating the variables and integrating between freeze-out  $x_{\text{F}}$  and  $+\infty$  ( $T \rightarrow 0$ ), we obtain:

$$\frac{1}{Y_{\text{F}}} - \frac{1}{Y_0} = -\frac{C \langle\sigma v\rangle}{x_{\text{F}}}. \quad (1.26)$$

Consequently, with  $Y_0 \ll Y_{\text{F}}$ , the number density today is:

$$Y_0 = \frac{x_{\text{F}}}{m_{\text{DM}} M_{\text{Pl}} \left(\frac{\pi g_*}{45}\right)^{1/2} \langle\sigma v\rangle}. \quad (1.27)$$

From there, the relic abundance of DM particles is given by  $\Omega_{\text{DM}} = \rho_0/\rho_{\text{crit}}$  where the critical density is  $\rho_{\text{crit}} = 1.0539 \times 10^{-5} h^2 \text{ GeV cm}^{-3}$ . With  $\rho_0 = m_{\text{DM}} n_0 = m_{\text{DM}} s_0 Y_0$ —where  $s_0 = 2889.2 \text{ cm}^{-3}$  is the entropy today—we obtain:

$$\Omega_{\text{DM}} h^2 = 1.04 \times 10^9 x_{\text{F}} g_*^{-1/2} \left(\frac{M_{\text{Pl}}}{\text{GeV}}\right)^{-1} \left(\frac{\langle\sigma v\rangle}{\text{GeV}^{-2}}\right)^{-1}. \quad (1.28)$$

Considering that no exact expression of  $Y$  can be found, and to visualize the behaviour of the solution for different values of the cross-section, the Boltzmann equation needs to be solved numerically. Eq. (1.24) is a stiff equation, so it cannot be solved by standard techniques, but it requires the use of an implicit method such as the Adams-Moulton method that allows to account for the rapid variations of the solution. Fig. 1.8 shows the evolution of  $Y$  normalized to its initial value, as a function of  $x$ , for three different values of  $\langle\sigma v\rangle$ :  $3 \times 10^{-27} \text{ cm}^3 \text{ s}^{-1}$ ,  $3 \times 10^{-26} \text{ cm}^3 \text{ s}^{-1}$  and  $3 \times 10^{-25} \text{ cm}^3 \text{ s}^{-1}$ . Below the freeze-out temperature,  $Y_{\text{eq}}$  keeps on decreasing exponentially while  $Y$  quickly reaches a constant.

### 1.2.3 The “WIMP miracle”

The last ingredient needed to fully determine the relic abundance given in Eq. (1.28) is the freeze-out temperature  $x_{\text{F}}$ . The freeze-out temperature is defined by the equality  $n \langle\sigma v\rangle = H$ . Now,  $n \approx n_{\text{eq}}$  since  $n$  only starts differing from  $n_{\text{eq}}$  at freeze-out. Taking

$$n_{\text{eq}} = g \left(\frac{m_{\text{DM}} T}{2\pi}\right)^{3/2} \exp\left(-\frac{m_{\text{DM}}}{T}\right) \quad (1.29)$$

for the equilibrium density in the non-relativistic regime and  $H$  given by Eq. (1.23), we obtain:

$$x_{\text{F}} = \ln \left( \frac{\langle\sigma v\rangle g m_{\text{DM}} M_{\text{Pl}}}{2^{5/2} \pi^3} \left(\frac{45}{g_*}\right)^{1/2} x_{\text{F}}^{1/2} \right) \quad (1.30)$$

The freeze-out temperature can be estimated by solving this equation by iteration. We have  $g = 1$ , and at the freeze-out temperature  $g_* \approx 92$ . For masses close to the electroweak scale,  $x_{\text{F}}$

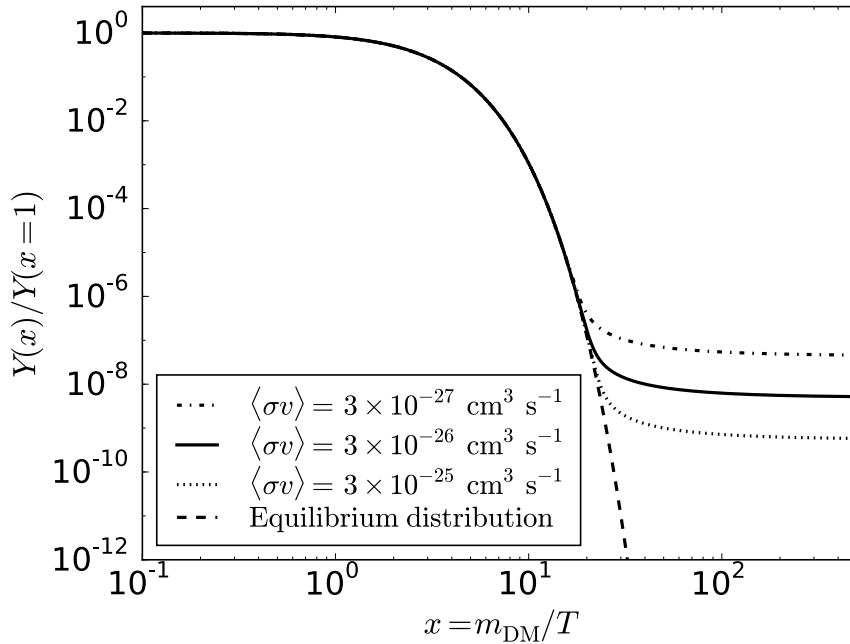


**Figure 1.8** – Solution of the Boltzmann equation for three values of  $\langle\sigma v\rangle$ :  $3 \times 10^{-27} \text{ cm}^3 \text{ s}^{-1}$  (dot-dashed),  $3 \times 10^{-26} \text{ cm}^3 \text{ s}^{-1}$  (solid) and  $3 \times 10^{-25} \text{ cm}^3 \text{ s}^{-1}$  (dotted). The dashed curve represents the equilibrium density  $Y_{\text{eq}}$ . The density quickly reaches a constant after freeze-out which occurs at  $x_{\text{F}} \sim 20$ .

is of the order of 20. From there it is convenient to use an order of magnitude approximation of Eq. (1.28):

$$\Omega_{\text{DM}} h^2 \approx 0.1 \frac{3 \times 10^{-26} \text{ cm}^3 \text{ s}^{-1}}{\langle\sigma v\rangle}, \quad (1.31)$$

which clearly shows that for  $\langle\sigma v\rangle \approx 3 \times 10^{-26} \text{ cm}^3 \text{ s}^{-1}$ , referred to as the *canonical* cross-section, the relic density of DM particles reproduces the DM abundance measured e.g. with *Planck*,  $\Omega_{\text{DM}} h^2 = 0.1198 \pm 0.0015$ .<sup>4</sup> This corresponds to a cross-section  $\sigma \approx 1 \text{ pb}$ , characteristic of the weak interaction.<sup>5</sup> The cosmological abundance therefore requires DM particles to be *weakly interacting massive particles (WIMPs)*. This famous result is referred to as the “WIMP miracle”. It is quite remarkable since it shows that starting from the only assumption of DM particles in thermal equilibrium via annihilations into SM particles, it is possible to determine the nature of their interactions, using only the cosmological abundance of DM, without any specific particle physics model. Of course, one must be careful, without experimental proof, this might just be a coincidence. However, relic density constraints serve as a preliminary consistency test for DM models.

We note that the relic density of thermally produced DM candidates also constrains their mass, with an approximate upper bound of 340 TeV found using partial-wave unitarity (Griest & Kamionkowski, 1990). Additionally, theoretical lower bounds of a few GeV can be set (Hut, 1977; Lee & Weinberg, 1977), but they can be evaded if DM particles interact with ordinary matter via the exchange of a new light gauge boson (Boehm & Fayet, 2004), so that robust lower limits must in fact rely on experimental constraints, like *Planck* observations which lead to an  $\mathcal{O}(\text{MeV})$  lower bound (Boehm et al., 2013).

In the most general case, the annihilation cross-section depends on the velocity. Usually,  $\sigma v$

<sup>4</sup>See however Steigman et al. (2012) for a more precise analytic calculation of the canonical value of the annihilation cross-section in particular in the low-mass range  $m_{\text{DM}} \lesssim 10 \text{ GeV}$ .

<sup>5</sup>1 pb =  $10^{-12} \text{ b}$  and 1 b =  $10^{-24} \text{ cm}^2$ .

is approximated by a non-relativistic expansion in powers of  $v^2$ :

$$\sigma v = a_0 + a_2 v^2 + \mathcal{O}(v^4), \quad (1.32)$$

where  $a_0$  and  $a_2$  are independent of  $v$  and characterize s-wave and p-wave annihilation processes, respectively. This introduces an additional dependence on  $x_F$  in Eq. (1.28). However, such an expansion is not always valid, for instance in the presence of resonances, as discussed in [Jungman et al. \(1996\)](#); [Gondolo & Gelmini \(1991\)](#). In the most general case the following expression should be used instead ([Gondolo & Gelmini, 1991](#)):

$$\langle \sigma v \rangle = \frac{1}{8m_{\text{DM}}^4 T K_2^2(m_{\text{DM}}/T)} \int_{4m_{\text{DM}}^2}^{\infty} (s - 4m_{\text{DM}}^2) \sqrt{s} \sigma(s) K_1\left(\frac{\sqrt{s}}{T}\right) ds, \quad (1.33)$$

where  $K_1$  and  $K_2$  are modified Bessel functions of the second kind. So in the general case, the Boltzmann equation must be solved numerically to obtain the relic density. In addition, resonance effects in the annihilation process, as well as co-annihilation of the DM particle with heavier particles from a putative dark sector can lead to significant enhancements of the thermally averaged cross-section ([Edsjö & Gondolo, 1997](#)). The numerical codes [MicrOMEGAs](#) ([Bélanger, 2002](#)) and [DarkSUSY](#) ([Gondolo et al., 2004](#)) compute the relic density for DM arising from physics beyond the SM, in particular for supersymmetric candidates.

## 1.3 Dark matter candidates

We now move on describe the main DM candidates, including but not restricted to WIMPs.

### 1.3.1 Massive astrophysical compact halo objects

As an alternative to the WIMP scenario, [Petrou \(1981\)](#) and [Paczynski \(1986\)](#) pointed out that DM could be made of faint astrophysical compact objects, such as black holes, neutron stars, brown dwarfs and free-floating planets, collectively referred to as massive astrophysical compact halo objects (MACHOs). These objects have been searched for through gravitational microlensing, which is slightly different from weak and strong lensing. In this case, images cannot be resolved and the only effect of the deviation of light from a background star due to the passage of a compact object is a transient amplification of the flux from the star.

Improving upon previous results based on the [EROS](#), [MACHO](#), [OGLE](#), [MOA](#) and [SuperMACHO](#) microlensing surveys, the [EROS-2](#) experiment has placed tight constraints on the fraction of the mass of the Milky Way halo that can consist of MACHOs. More specifically, the [EROS-2](#) results rule out MACHOs in the mass range

$$0.6 \times 10^{-7} M_{\odot} < m_{\text{MACHO}} < 15 M_{\odot} \quad (1.34)$$

as the main component of the MW dark halo ([Tisserand et al., 2007](#); [Moniez, 2009](#)).

Primordial black holes (PBHs) are a particular class of MACHOs, which may have formed in the early Universe from gravitational collapse of density fluctuations, as originally proposed by [Hawking \(1971\)](#). PBHs are good DM candidates since they are cold and weakly interacting, while they do not require an extension of the Standard Model of particle physics. Evaporation would have prevented PBHs with masses  $\lesssim 10^{15}$  g from surviving until the present epoch ([Hawking, 1975](#)), and PBHs in the mass range  $10^{15}$  g  $\lesssim m_{\text{PBH}} \lesssim 10^{17}$  g are excluded since the photons they would produce would overshoot the extragalactic  $\gamma$ -ray background ([Carr et al., 2010](#)). Finally PBHs with masses  $\gtrsim 10^{24}$  g are ruled out by various probes including microlensing (the bounds on MACHOs are also valid for PBHs) and cosmology, namely BBN ([Carr et al., 2010](#)) and spectral distortions of the CMB ([Ricotti et al., 2008](#)). The latter exclude PBHs as DM for  $m_{\text{PBH}} \gtrsim M_{\odot}$ .

Yet, until recently, the mass range  $10^{17} \text{ g} \lesssim m_{\text{PBH}} \lesssim 10^{24} \text{ g}$ , i.e.  $10^{-16} M_{\odot} \lesssim m_{\text{PBH}} \lesssim 10^{-9} M_{\odot}$ , was poorly constrained.

However, [Pani & Loeb \(2014\)](#) showed that PBHs can disrupt neutron stars after being tidally captured in close encounters, and the observation of old neutron stars rules out PBHs in the remaining allowed mass range.

All these results indicate that MACHOs (including PBHs) are unlikely to account for the entire DM component of the Universe. However, this may not be the end of the story, considering the possibility of evading the CMB and microlensing constraints with massive PBHs (i.e. with masses of a few tens of  $M_{\odot}$ ), suggested in [Clesse & García-Bellido \(2015\)](#). The recent detection of gravitational waves from a BH merger by Advanced LIGO ([Abbott et al., 2016](#)) has been suggested to be a hint for DM in the form of massive PBHs, and sets constraints on the properties of such candidates ([Bird et al., 2016](#); [Clesse & García-Bellido, 2016](#)). Future gravitational wave observations will be instrumental in testing PBH scenarios of DM.

### 1.3.2 Particle dark matter

In this section, we give an overview of DM candidates provided by particle physics.

The Standard Model (SM) of particle physics has been extremely successful in explaining the data from colliders with very high precision. We now summarize its properties. For a review of the SM see e.g. [Altarelli \(2013\)](#).

The SM is a non-Abelian gauge field theory based on the symmetry group  $SU(3)_C \otimes SU(2)_L \otimes U(1)_Y$ . The  $SU(3)_C$  group of quantum chromodynamics (QCD) describes the strong interaction through the color charge  $C$ .  $SU(2)_L \otimes U(1)_Y$  characterizes the electroweak (EW) interaction, which unifies the electromagnetic and weak interactions ([Glashow, 1961](#); [Weinberg, 1967](#); [Salam, 1968](#)). The hypercharge  $Y = 2(Q - T_3)$ , where  $Q$  is the electric charge and  $T_3$  the weak isospin, is the generator of the  $U(1)_Y$  group.

Matter is made of fermions, namely quarks ( $u, d, c, s, t, b$ ) and leptons ( $e, \mu, \tau, \nu_e, \nu_{\mu}, \nu_{\tau}$ ). Fermions are arranged in left-handed  $SU(2)_L$  doublets and right-handed  $SU(2)_L$  singlets, as shown in [Fig. 1.9](#). The  $L$  subscript denotes the fact that only left-handed fermions (or right-handed anti-fermions) are sensitive to the weak interaction. The primes in [Fig. 1.9](#) refer to gauge eigenstates, which are related to mass eigenstates via the Cabibbo-Kobayashi-Maskawa (CKM) matrix for down-type quarks, and via the Pontecorvo-Maki-Nakagawa-Sakata (PMNS) matrix for neutrinos. Each particle has its own antiparticle, with same mass and opposite quantum numbers.

$$\begin{array}{cccccc}
 \left( \begin{array}{c} \nu'_e \\ e \end{array} \right)_{L,1/6}^{-1/2} & \left( \begin{array}{c} \nu'_\mu \\ \mu \end{array} \right)_{L,1/6}^{-1/2} & \left( \begin{array}{c} \nu'_\tau \\ \tau \end{array} \right)_{L,1/6}^{-1/2} & e_R^{-1} & \mu_R^{-1} & \tau_R^{-1} \\
 \left( \begin{array}{c} u \\ d' \end{array} \right)_{L,g,1/6} & \left( \begin{array}{c} c \\ s' \end{array} \right)_{L,g,1/6} & \left( \begin{array}{c} t \\ b' \end{array} \right)_{L,g,1/6} & \begin{array}{c} u_{R,g}^{2/3} \\ d_{R,g}^{-1/3} \end{array} & \begin{array}{c} c_{R,g}^{2/3} \\ s_{R,g}^{-1/3} \end{array} & \begin{array}{c} t_{R,g}^{2/3} \\ b_{R,g}^{-1/3} \end{array} \\
 \left( \begin{array}{c} u \\ d' \end{array} \right)_{L,r,1/6} & \left( \begin{array}{c} c \\ s' \end{array} \right)_{L,r,1/6} & \left( \begin{array}{c} t \\ b' \end{array} \right)_{L,r,1/6} & \begin{array}{c} u_{R,r}^{2/3} \\ d_{R,r}^{-1/3} \end{array} & \begin{array}{c} c_{R,r}^{2/3} \\ s_{R,r}^{-1/3} \end{array} & \begin{array}{c} t_{R,r}^{2/3} \\ b_{R,r}^{-1/3} \end{array} \\
 \left( \begin{array}{c} u \\ d' \end{array} \right)_{L,b,1/6} & \left( \begin{array}{c} c \\ s' \end{array} \right)_{L,b,1/6} & \left( \begin{array}{c} t \\ b' \end{array} \right)_{L,b,1/6} & \begin{array}{c} u_{R,b}^{2/3} \\ d_{R,b}^{-1/3} \end{array} & \begin{array}{c} c_{R,b}^{2/3} \\ s_{R,b}^{-1/3} \end{array} & \begin{array}{c} t_{R,b}^{2/3} \\ b_{R,b}^{-1/3} \end{array}
 \end{array}$$

**Figure 1.9** – List of fermions of the SM, arranged in left-handed doublets and right-handed singlets ([Murayama, 2000](#)). For each field, the superscript indicates the hypercharge  $Y$ , while the subscripts represent the chirality ( $L$  or  $R$ ) and the color charge  $C = g, r, b$ .

The  $SU(2)_L \otimes U(1)_Y$  symmetry is spontaneously broken into  $U(1)_Q$  (with  $Q = T_3 + Y/2$ ) through the Higgs mechanism ([Englert & Brout, 1964](#); [Higgs, 1964a,b, 1966](#); [Guralnik et al., 1964](#); [Kibble, 1967](#)). The resulting Goldstone bosons mix with the massless gauge bosons  $W^1$ ,

$W^2$ ,  $W^3$  and  $B$  to give the three massive gauge bosons  $W^+$ ,  $W^-$  and  $Z^0$  which mediate the weak interaction, the massless mediator of electromagnetism (the photon,  $\gamma$ ) and one massive scalar particle, the Higgs boson  $h$ . The mediators of the strong interaction are 8 massless gluons.

In spite of its phenomenological success, the SM does not provide any viable DM candidate.<sup>6</sup> Moreover, most of the parameters of the SM do not have a fundamental explanation. In this sense the SM of particle physics is similar to the concordance model of cosmology. The DM problem turns out to be extremely puzzling in both contexts. The SM may turn out to be a low-energy effective theory in the framework of a more fundamental underlying theory, which signals the need for extensions of the SM.

In the following we give an overview of the main DM candidates beyond the SM. For reviews see e.g. Bertone et al. (2005); Bergström (2009); Bertone (2013).

### 1.3.2.1 Neutrinos

**Light neutrinos: hot DM.** SM neutrinos are massless. However, neutrino oscillations require neutrinos to be massive, and therefore call for an extension of the SM. Adding a regular Dirac mass term  $\mathcal{L}_{\text{mass}}^{\text{D}} = -m_{\text{D}}\bar{\nu}_L N_R + \text{h.c.}$  for neutrinos (similar to the mass terms of quarks and other leptons) requires to introduce right-handed neutrinos  $N_R$ , which do not exist in the SM and have never been detected, so their mass can be very large, way above the electroweak scale:  $M \gg \Lambda_{\text{EW}} \sim 246$  GeV. If they exist, they are singlets of all interactions, and therefore referred to as *sterile neutrinos*, as opposed to left-handed neutrinos which are active. For reviews see e.g. Asaka et al. (2005); Mohapatra et al. (2007); Boyarsky et al. (2009); Atre et al. (2009); Abazajian et al. (2012). Based on the electrical neutrality of neutrinos, the simplest extension of the SM assumes that neutrinos are Majorana particles (i.e. they are their own antiparticle). As a result, one can add to the Lagrangian a Majorana mass term for the right-handed neutrino  $\mathcal{L}_{\text{mass}}^{\text{M}} = 1/2 M N_R^{\text{T}} C^{\dagger} N_R + \text{h.c.}$ , which is allowed by gauge invariance. We consider the simple case of one left-handed neutrino and one sterile neutrino. In this case, the global mass term reads

$$\mathcal{L}_{\text{mass}} = \frac{1}{2} \begin{pmatrix} \bar{\nu}_L & \bar{N}_R^c \end{pmatrix} \underbrace{\begin{pmatrix} 0 & m_{\text{D}} \\ m_{\text{D}} & M \end{pmatrix}}_{\mathcal{M}} \begin{pmatrix} \nu_L^c \\ N_R \end{pmatrix} + \text{h.c.} \quad (1.35)$$

The mass matrix  $\mathcal{M}$  has two different eigenvalues,  $M$  and  $m_{\text{D}}^2/M$ , and the associated eigenstates approximately coincide with  $N_R$  and  $\nu_L$ , respectively. Therefore, the two masses are related, and if the mass  $M$  of the sterile neutrino is very large, the mass  $m_{\text{D}}^2/M$  of the left-handed neutrino is very small ( $m_{\text{D}}$  is typically of order  $\Lambda_{\text{EW}}$ ). This is referred to as the *seesaw mechanism* (Minkowski, 1977; Gell-Mann et al., 1979; Yanagida, 1979). If  $M \sim 10^{15}$  GeV, corresponding to the Grand Unified Theory (GUT) scale, then  $m_{\nu} \sim 0.01$  eV. In practice, the Lagrangian of Eq. (1.35) can be generalized to the three generations of left-handed neutrinos and to an arbitrary number of sterile neutrinos, which is only constrained by the fact that it must be at least 2 in order to account for neutrino oscillations.

Therefore neutrinos are massive, but are they viable DM candidates? The contribution of light neutrinos to the energy density of the Universe is given by (Gershtein & Zeldovich, 1966)

$$\Omega_{\nu} h^2 = \frac{\sum_i m_{\nu_i}}{94 \text{ eV}}. \quad (1.36)$$

However, the upper limit from *Planck* on the sum of neutrino masses, assuming three species, is  $\sum_i m_{\nu_i} < 0.49$  eV using the temperature and polarization power spectra (Ade et al., 2015b). Consequently, light neutrinos can account for less than 10% of DM. In any event, light neutrinos are relativistic so they would be hot DM, and could not account for all the DM, otherwise

<sup>6</sup>The stable H dibaryon ( $sudd\bar{s}\bar{u}$ ) has nevertheless been proposed as a possible exotic DM candidate within the SM (Farrar, 2003).

structure formation would be severely suppressed on small scales. Finally, a massive but light neutrino is excluded as the dominant constituent of DM since to explain the rotation curve of galaxies the neutrino mass must satisfy

$$m_\nu \geq 120 \left( \frac{100 \text{ km s}^{-1}}{\sigma} \right)^{1/4} \left( \frac{1 \text{ kpc}}{r_c} \right) \text{ eV}, \quad (1.37)$$

where  $\sigma$  is the velocity dispersion and  $r_c$  the core radius (Tremaine & Gunn, 1979). However, considering the bound from cosmology, light neutrinos clearly do not fulfill this condition, but sterile neutrinos could, since they are expected to be heavier.

**Sterile neutrinos: warm DM.** Here we discuss the viability of sterile neutrinos as DM candidates as proposed in Dodelson & Widrow (1994); Shi & Fuller (1999); Abazajian et al. (2001a,b); Dolgov & Hansen (2002). For reviews see e.g. Asaka et al. (2005); Boyarsky et al. (2009). Sterile neutrinos are produced mainly through active-sterile oscillations. Their contribution to the energy budget of the Universe is

$$\Omega_N h^2 \sim 0.1 \sum_I \sum_{\alpha=e,\mu,\tau} \left( \frac{\Theta_{\alpha I}^2}{10^{-8}} \right) \left( \frac{M_I}{1 \text{ keV}} \right)^2, \quad (1.38)$$

where  $\Theta_{\alpha I} \sim m_{D,\alpha}/M_I$  represents the mixing between active and sterile neutrinos, and the index  $I$  labels sterile neutrinos which are viable DM candidates, i.e. which are stable over the age of the Universe  $\sim 4 \times 10^{17}$  s. A sterile neutrino  $N_I$  decays into an active neutrino  $\nu_\alpha$  (with  $\alpha = e, \mu, \tau$ ) and a photon, and the associated lifetime is

$$\tau_{N_I} = 5 \times 10^{26} \left( \frac{M_I}{1 \text{ keV}} \right)^{-5} \left( \frac{\bar{\Theta}_I^2}{10^{-8}} \right)^{-1} \text{ s}, \quad (1.39)$$

where  $\Theta_{\alpha I} = \bar{\Theta}_I$  for the three families of active neutrinos. The sterile neutrino lifetime sets constraints on their parameter space. Sterile neutrinos have masses typically in the keV range, so they are warm DM candidates. They are therefore constrained by cosmology, since they cannot be too light lest they suppress structures on small scales. Moreover, their mass range is further constrained by X-ray observations. As a result, sterile neutrinos are limited to the narrow mass range

$$2 \text{ keV} \lesssim M_I \lesssim 5 \text{ keV}. \quad (1.40)$$

Although sterile neutrinos have a less rich phenomenology than WIMPs, which makes them generally less popular, the interest in these DM candidates was recently rekindled by the 3.5 keV line reported in X-ray observations with the XMM-Newton satellite of the Andromeda galaxy and the Perseus cluster (Bulbul et al., 2014; Boyarsky et al., 2014) and the Galactic center (Jeltema & Profumo, 2015), although these lines may simply originate from known plasma lines, as discussed in Jeltema & Profumo (2015).

### 1.3.2.2 Supersymmetric WIMPs

Supersymmetry (SUSY) is the flagship of physics beyond the SM. SUSY started to be developed in the 1970s (Golfand & Likhtman, 1971; Volkov & Akulov, 1973; Wess & Zumino, 1974), to solve most of the unexplained issues of the SM, by symmetrizing fermion and boson fields. For a general review of SUSY, see e.g. Haber & Kane (1985), and Jungman et al. (1996) in the context of DM.

SUSY provides a solution to the hierarchy problem, which manifests itself by the huge difference between the EW scale ( $\sim 100$  GeV) and the Planck scale ( $\sim 10^{19}$  GeV). More specifically, radiative corrections to the mass of the Higgs boson due to its interaction with SM

particles should make it much heavier than 125 GeV. SUSY provides a solution by introducing superpartners (also called sparticles) which differ in spin by 1/2 with the corresponding SM particles. If SUSY was an exact symmetry, superpartners would be degenerate in mass with particles, thus exactly canceling the quadratic divergence of the Higgs mass in the high-energy cut-off scale of the theory. However, this is not what is observed in nature, so SUSY must be broken. It was actually shown that SUSY can be spontaneously broken (Fayet & Iliopoulos, 1974; Fayet, 1975a; O’Raifeartaigh, 1975). In practice, experimentally no supersymmetric particles have been detected in colliders, so superpartners must have larger masses than SM particles. Still, the introduction of superpartners replaces the quadratic divergence by a logarithmic divergence, provided the breaking of SUSY is soft, i.e. the mass difference between SM fields and superpartners is at most a few TeV. In this case the naturalness of the Higgs mass is maintained. Another initial motivation for SUSY was that it allowed for the unification of fundamental interactions—including gravitation—at the GUT scale, which is one of the main goals of theoretical physics. However, once SUSY is broken, this problem is no longer solved and unification is only approximate.

The simplest realization of SUSY is the minimal supersymmetric standard model (MSSM), which introduces one superpartner for each SM particle (Dimopoulos & Georgi, 1981). Quarks and leptons acquire scalar superpartners, squarks  $\tilde{q}$  and sleptons  $\tilde{l}$ , respectively. The fermionic superpartners of massless gauge bosons are the bino  $\tilde{B}^0$ , winos  $\tilde{W}^0, \tilde{W}^\pm$  and gluinos  $\tilde{g}$ . Finally, in order to give mass to both up-type and down-type quarks and remain consistent with the underlying supersymmetry, the standard Higgs sector must be supplemented by a second Higgs doublet. This results in four higgsino fermionic superpartners  $\tilde{H}_u^0, \tilde{H}_d^0, \tilde{H}_u^\pm$  and  $\tilde{H}_d^\pm$ . The four electrically neutral fermionic sparticles  $\tilde{B}^0, \tilde{W}^0, \tilde{H}_u^0$  and  $\tilde{H}_d^0$  mix to give the four neutral mass eigenstates, referred to as the neutralinos  $\tilde{\chi}_1^0, \tilde{\chi}_2^0, \tilde{\chi}_3^0$  and  $\tilde{\chi}_4^0$ , while  $\tilde{W}^\pm, \tilde{H}_u^\pm$  and  $\tilde{H}_d^\pm$  mix to give the charginos  $\tilde{\chi}_1^\pm$  and  $\tilde{\chi}_2^\pm$ .

In order to avoid baryon number violating processes such as proton decay, SUSY features an additional discrete symmetry (Fayet, 1977; Farrar & Fayet, 1978) called  $R$ -parity, and associated with a new conserved multiplicative quantum number,

$$R = (-1)^{3(B-L)+2S}, \quad (1.41)$$

where  $B$  is the baryon number,  $L$  the lepton number and  $S$  the spin. As a result,  $R = +1$  for SM particles and  $R = -1$  for sparticles. Therefore, sparticles can only be created or annihilated in pairs when interacting with SM particles. But more importantly, a sparticle can only decay into a final state with an odd number of sparticles, which results in the stability of the lightest supersymmetric particle (LSP). Provided it is electrically neutral and does not carry any color charge, the LSP is a viable DM candidate. For a discussion of the LSPs that are viable DM candidates from theoretical, cosmological and experimental arguments, see e.g. Ellis et al. (1984). The leading candidate turns out to be the lightest neutralino  $\tilde{\chi}_1^0$ . With weak interactions and a mass expected in the TeV range, it clearly satisfies relic density constraints. In principle, sneutrinos, superpartners of SM neutrinos, and the gravitino, superpartner of the graviton, are also viable supersymmetric DM candidates. However, the sneutrino is ruled out since the associated scattering cross-section with SM particles is too high and is thus excluded by direct-detection experiments (Falk et al., 1994), described in Sec. 2.1. As for the gravitino, it is very difficult to observe since it has essentially only gravitational interactions (Feng et al., 2003), although its decay may have interesting consequences.

The MSSM is hard to constrain due to a very large number parameters, namely 18 for the SM plus 106 (e.g. Haber, 1998), hence the difficulty to find evidence for a supersymmetric DM candidate in colliders. It is however possible to constrain the MSSM by coupling it with a minimal supergravity model, leading to the minimal supergravity (mSUGRA) model (Nilles, 1984) or the constrained MSSM (CMSSM, Kane et al., 1994) with 18+5 parameters. Extensions of the MSSM (like the next-to-minimal supersymmetric standard model, NMSSM, Fayet, 1975b) contain even more particles and free parameters, with potentially additional DM candidates.

### 1.3.2.3 WIMPs from Universal Extra Dimensions

The notion of extra dimensions was originally introduced by Kaluza in an attempt to unify electromagnetism and gravity (Kaluza, 1921). Although the Universe seems to consist of  $3 + 1$  dimensions, Kaluza postulated the existence of a fifth dimension. Klein subsequently suggested that this extra dimension could be compactified on very small scales, thus hiding it from observations (Klein, 1926).

Despite the fact that the original Kaluza-Klein proposal has undergone significant changes and refinements, the common idea of models of extra dimensions is that our  $3+1$  spacetime is embedded in a higher-dimensional  $3 + \delta + 1$  spacetime, referred to as the bulk, with  $\delta$  the number of extra dimensions.

In models of Universal Extra Dimensions (UED) developed more recently, all SM fields are allowed to propagate in the bulk (Appelquist et al., 2001). The simplest UED model postulates one extra dimension, compactified on some scale  $R_c$ . This is shown to result in the quantization of the momentum of particles propagating in the bulk in units of  $p^2 \sim 1/R_c^2$ . Therefore, all SM fields have a series (or tower) of Kaluza-Klein (KK) modes  $X^{(n)}$  that represent excitations of the SM fields  $X$ . From the point of view of the four-dimensional world, these KK modes appear as a series of states with masses given at tree level by  $m_{X^{(n)}} = \sqrt{(n/R_c)^2 + m_{X^{(0)}}^2}$ , where  $m_{X^{(0)}}$  is the zero-mode mass, i.e. the mass of the ordinary SM particle. All the states in a KK tower have the same quantum numbers as the zero mode.

UED models feature a symmetry, KK parity, which is analogous to  $R$ -parity in supersymmetry. In particular, KK parity stabilizes the lightest KK particle (LKP), which makes it a viable DM candidate. One can show that the LKP is the first KK excitation  $B^{(1)}$  of the weak hypercharge gauge boson. For this DM candidate, the annihilation cross-section was computed in Servant & Tait (2003) and reads

$$\sigma v = 0.6 \left( \frac{m_{B^{(1)}}}{1 \text{ TeV}} \right)^2 \text{ pb}, \quad (1.42)$$

and relic density constraints yield a mass of order  $0.5\text{--}1$  TeV (Servant & Tait, 2003; Cheng et al., 2002).

DM candidates from extra dimensions are very interesting since they provide an example of a vector WIMP. They also have very promising phenomenological implications, in particular since they are expected to be important sources of positrons. For a detailed review of the theory of UED and the resulting DM phenomenology, see e.g. Hooper & Profumo (2007).

### 1.3.2.4 Axions and other very light dark matter candidates

Here we briefly discuss much lighter DM candidates, the most prominent one being the QCD axion. For reviews see e.g. Peccei (2008); Sikivie (2008); Ringwald (2012); Marsh (2015). Theoretically, QCD allows for a term violating the CP (charge-parity) symmetry in the Lagrangian:

$$\mathcal{L}_\theta = \frac{\alpha_s}{8\pi} \theta G_{\mu\nu}^a \tilde{G}^{a\mu\nu}, \quad (1.43)$$

with  $\alpha_s$  the strong coupling constant and  $\theta$  a fundamental parameter expected to be of order 1.  $G_{\mu\nu}^a$  is the gluon field strength tensor and  $\tilde{G}^{a\mu\nu} = 1/2 \epsilon^{\mu\nu\alpha\beta} G_{\alpha\beta}^a$ , with  $\epsilon^{\mu\nu\alpha\beta}$  the completely antisymmetric pseudo-tensor. The most stringent constraint on  $\theta$  comes from the upper bound on the electric dipole moment of the neutron  $d_n$ , with  $|d_n| \sim 3 \times 10^{-16} |\theta| e \text{ cm}$  (Baluni, 1979; Crewther et al., 1979). The current experimental limit is  $|d_n| < 3 \times 10^{-26} e \text{ cm}$  (Baker et al., 2006), which leads to  $|\theta| \lesssim 10^{-10}$ . The unnatural smallness of the fundamental parameter  $\theta$  is known as the *strong CP problem*.

This can be solved by a small extension of the Standard Model, as proposed by Peccei and Quinn (Peccei & Quinn, 1977a,b). The idea is to introduce an additional global symmetry  $U(1)_{\text{PQ}}$ , spontaneously broken at high energy in the early Universe. The introduction of the

symmetry effectively replaces the static CP-violating parameter  $\theta$  by a dynamical field  $a$ , the axion. The CP-violating term in the Lagrangian is then proportional to  $\theta + a/f_a$  (where  $f_a$  is the axion decay constant), which relaxes to zero when the symmetry is broken, therefore solving the strong CP problem (Peccei & Quinn, 1977a,b). The axion field  $a$  is a pseudo Nambu-Goldstone boson of this spontaneously broken symmetry.

More specifically, axions are produced at the Peccei-Quinn (PQ) phase transition which occurs at temperature  $T \sim f_a \gg \Lambda_{\text{QCD}}$ , where  $\Lambda_{\text{QCD}} \sim 200$  MeV is the QCD scale. As long as  $T \gg \Lambda_{\text{QCD}}$ , the strong CP problem is irrelevant, so the axion field can take any value. In addition the axion is massless in this regime. When the Universe cools down to  $T \sim \Lambda_{\text{QCD}}$  via cosmic expansion, the axion acquires a mass due to non-perturbative QCD effects (Weinberg, 1978),

$$m_a = 6 \mu\text{eV} \left( \frac{10^{12} \text{ GeV}}{f_a} \right), \quad (1.44)$$

which tilts the axion potential, causing the axion to roll towards the minimum  $-f_a\theta$ . However, this process is not instantaneous, and the axion field actually oscillates to its final value. These coherent oscillations form a zero-momentum condensate which contributes to the energy density of the Universe, giving a present axion relic density of (Fox et al., 2004; Sikivie, 2008)

$$\Omega_a h^2 \sim 0.3 \left( \frac{f_a}{10^{12} \text{ GeV}} \right)^{\frac{7}{6}}. \quad (1.45)$$

The value of the axion decay constant needed to saturate the abundance of DM measured with *Planck* is  $f_a \sim 10^{11}$  GeV, which corresponds to  $m_a \sim 10$   $\mu\text{eV}$ . Therefore QCD axions are very light, but they behave as CDM since they were produced non-thermally. Had they been produced thermally, they would behave as hot DM.

QCD axions are a well-motivated example of very light DM candidates, referred to as weakly interacting slim particles (WISPs). Ultralight axions, with masses of order  $10^{-22}$  eV, have also been suggested as DM candidates arising from string theory (Arvanitaki et al., 2010). Other WISPs include axion-like particles (ALPs) and dark photons (see e.g. Ringwald, 2012). ALPs generalize QCD axions, but they are more massive and do not solve the strong CP problem.

### 1.3.2.5 Other candidates

There is a wealth of alternative DM candidates with very diverse properties. Here we only give a few examples. Some are expected to be light, e.g. in the MeV–10 GeV range. For instance, a 1–100 MeV scalar candidate has been proposed (Boehm et al., 2004a; Boehm & Fayet, 2004). Others are regular WIMPs, like in the inert Higgs doublet model in which the DM mass must be either smaller than  $m_W \sim 80$  GeV or between  $\sim 500$  GeV and a few tens of TeV (Ma, 2006; Barbieri et al., 2006), or in the Minimal DM model which gives masses in the TeV range (Cirelli et al., 2006). Finally, some candidates can be very heavy like WIMPZILLAS (with masses of order the scale of inflation) produced non-thermally in the early Universe (Kolb et al., 1999).

The asymmetric DM scenario considers the existence of an asymmetry between DM particles and antiparticles (Nussinov, 1985), similar to the asymmetry observed in the baryonic sector, based on the abundances that are of the same order of magnitude  $\Omega_m \sim 5\Omega_b$ , leading to a  $\sim 5$  GeV DM candidate. The existence of asymmetric DM would suggest a common formation process of baryons and DM. Such a non self-conjugate DM candidate would have a negligible annihilation rate today. For a review see e.g. Petraki & Volkas (2013).

Self-interacting DM (SIDM) has also been proposed (Carlson et al., 1992; Machacek et al., 1993; de Laix et al., 1995; Spergel & Steinhardt, 2000). It can have interesting consequences at the center of galaxies as discussed in Sec. 1.3.3. The DM-DM scattering cross-section has been however constrained using cosmological simulations (Yoshida et al., 2000), observational

properties of supermassive black holes (Hennawi & Ostriker, 2002) and strong lensing (Miralda-Escudé, 2002; Wyithe et al., 2001; Meneghetti et al., 2001). More recently, observations of the Bullet cluster have led to very stringent constraints on the self-scattering cross-section,  $\sigma/m_{\text{DM}} < 0.7 \text{ cm}^2 \text{ g}^{-1}$  (Randall et al., 2008).

### 1.3.3 Small-scale issues of cold dark matter: additional properties, baryonic physics or modified gravity theories?

Although DM particles are very appealing, the only unambiguous evidence we have for them so far is gravitational. The question is whether DM particles really exist, or whether modified gravity theories, i.e. extensions of general relativity, could account for all the observations that have been held as evidence for DM.

An argument in favor of alternatives to the particle DM scenario comes from the issues on small scales which may indicate the limits of the CDM paradigm (for a review see e.g. Brooks, 2014):

- *The cusp/core controversy:* DM-only N-body simulations predict a steeply rising DM density towards the center of galaxies, typically following the Navarro-Frenk-White (NFW) profile, corresponding to  $\rho(r) \propto r^{-1}$ , which is the prototype of a cusp. However, observations seem to favor shallower density profiles or even constant density cores. See the discussion in Chapter 3.
- *The missing satellite problem:* DM-only simulations predict more satellites than we actually observe in the Milky Way (Moore et al., 1999a; Klypin et al., 1999).
- *The “Too Big To Fail” problem:* DM-only simulations predict satellites that are too dense to have failed to form stars, still they have not been observed (Boylan-Kolchin et al., 2011; Tollerud et al., 2012; Collins et al., 2014).
- The existence of bulgeless disk galaxies (van den Bosch et al., 2001; Dutton, 2009).

Alternatives to the cold DM scenario involving DM particles with different properties can solve some of these issues. In particular, the missing satellite problem—and potentially the Too Big To Fail problem as well—can be solved by collisionless WDM (Lovell et al., 2014), or CDM interacting with radiation (Boehm et al., 2014b), which lead to damping of small-scale fluctuations, as discussed in Sec. 1.1.2.2. However, these scenarios would produce too small cores to settle the cusp/core controversy (Macciò et al., 2012).

Actually, SIDM was invoked to solve the cusp/core problem via dynamical heating of the inner regions of galaxies through DM-DM elastic scattering (Spergel & Steinhardt, 2000). Initial SIDM models assumed a velocity-independent scattering cross-section, but were subsequently abandoned since they violated observational constraints, leading for instance to overflattened galaxy clusters compared to observations (Miralda-Escudé, 2002). To evade these constraints, ad hoc velocity-dependent cross-sections parametrized in powers of  $1/v$  have been explored, in particular with numerical simulations (Vogelsberger et al., 2012). In spite of promising results, whether SIDM can also deal with the satellite issues is a matter of debate. It has been suggested that SIDM can solve the Too Big To Fail problem (Rocha et al., 2013), although in a very narrow region of the allowed parameter space for SIDM according to Zavala et al. (2013), while no fine tuning is necessary according to Elbert et al. (2015). Furthermore, semi-analytic calculations (D’Onghia & Burkert, 2003) and dedicated SIDM simulations (Rocha et al., 2013; Zavala et al., 2013) suggest that SIDM cannot get rid of the missing satellite problem. In the end, numerical simulations are going to be crucial to fully assess the potential of SIDM to solve the small-scale issues of CDM, but exploring the full range of possible models is still computationally expensive. In this context, semi-analytic models are very useful, as shown by recent results suggesting

that SIDM may universally solve the mass deficit problem, from dwarf galaxies to clusters, and provide stringent constraints on the underlying microphysics (Kaplinghat et al., 2016).

However, all the small-scale crises of CDM arise from DM-only predictions. It turns out that small scales are where feedback processes from baryons have a crucial importance. It turns out that including baryons in numerical simulations, and accounting for localized baryonic feedback on DM via e.g. supernova explosions, can solve—at least for dwarf galaxies—the missing satellite and Too Big Too Fail problems (Zolotov et al., 2012; Di Cintio et al., 2013; Arraki et al., 2014), the cusp/core problem (see the discussion in Chapter 3), and even explain observations of bulgeless disk galaxies (Governato et al., 2010). This shows that realistic numerical simulations can be reconciled with observations, solving the small-scale CDM controversies. However, baryonic physics involves complex processes, which have not been fully characterized yet. The problem is made even more complex when jointly simulating SIDM and baryons, which is however very promising to probe the properties of DM (Vogelsberger et al., 2014).

At the end of the day, baryonic feedback and SIDM seem to indicate the need for a certain amount of fine tuning in the CDM picture. These fine-tuning problems can be in principle addressed by modified gravity theories. MODified Newtonian Dynamics (MOND) is an example of such an extension of the standard picture of gravity (Milgrom, 1983a,b,c). It was built on a phenomenological basis to account for the missing mass problem in galaxies without invoking DM. MOND introduces a modification of Newtonian dynamics at very low accelerations, which are typical of galaxies. See also Milgrom (2015) for a review. The tensor-vector-scalar (TeVeS) theory of gravity (Bekenstein, 2004, 2005) is a relativistic generalization of MOND. However, it turns out that modified gravity theories proposed as an alternative to DM are not able to reproduce the CMB data after the third acoustic peak (Skordis et al., 2006). Moreover, several modified gravity theories still need a DM component to be fully self-consistent. In the end, both particle DM and modified gravity approaches need to be carefully investigated, since they may have complementary domains of validity.



## Chapter 2

# Overview of standard searches for dark matter particles

In this chapter, we describe the three strategies used to search for DM particles: direct detection which attempts to observe DM-nucleus scattering, production at colliders, and indirect detection which exploits astrophysical observations. We focus more specifically on standard searches, relying on the results of large collaborations.

### Contents

---

<b>2.1</b>	<b>Direct detection</b>	<b>30</b>
2.1.1	Principle	30
2.1.2	Number of expected events	31
2.1.3	Status of direct searches	33
<b>2.2</b>	<b>Collider searches</b>	<b>36</b>
2.2.1	Principle	36
2.2.2	Overview of results	37
2.2.3	Comment on the tentative 750 GeV excess at LHC	39
<b>2.3</b>	<b>Indirect detection: overview of standard searches</b>	<b>40</b>
2.3.1	Constraints from the CMB	40
2.3.2	Charged antiparticles	41
2.3.3	Gamma rays	44
2.3.4	Neutrinos	48
2.3.5	Summary	49

---

The efficient annihilations expected in the early Universe from the WIMP miracle point to a non-gravitational four-particle weak interaction between DM particles (denoted as  $\chi$ ) and SM particles. As illustrated in Fig. 2.1, this provides the various avenues to search for DM:

- direct detection, corresponding to scattering between DM and ordinary matter,  $\chi\text{SM} \rightarrow \chi\text{SM}$ ,
- collider searches, which attempt to produce DM particles through the collisions of SM particles,  $\text{SM SM} \rightarrow \chi\chi$
- indirect detection, associated with present-day annihilations,  $\chi\chi \rightarrow \text{SM SM}$ .

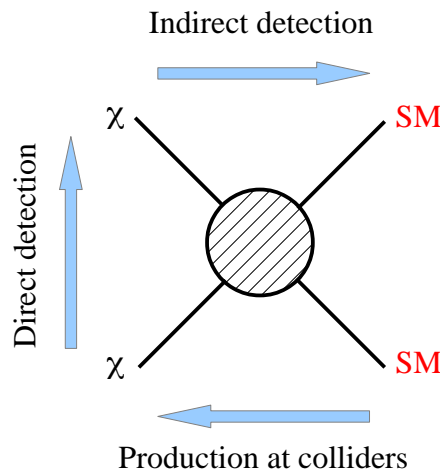


**Figure 2.1** – Diagram of the connection between the various ways of searching for DM, through a four-particle interaction between DM and SM particles.

In this chapter, we give an overview of these three channels, before focusing on specific aspects of indirect detection in the framework of this thesis in the following chapters.

## 2.1 Direct detection

### 2.1.1 Principle

If WIMPs are indeed coupled with ordinary matter not only gravitationally, but also through the weak interaction, they can be searched for on Earth using dedicated ultra-sensitive detectors. These experiments are designed to detect the recoil of a target nucleus hit by an incoming DM particle. This approach is referred to as *direct detection*. For reviews see e.g. [Jungman et al. \(1996\)](#); [Baudis \(2012\)](#); [Panci \(2014\)](#); [Schumann \(2015\)](#).

Due to the extremely low event rates associated with the scattering of a nucleus by a DM particle, backgrounds are very high. Direct detection experiments are therefore located in deep underground laboratories to be shielded from cosmic muons, which produce neutrons that in turn induce nuclear recoils. Radioactivity from the environment is also critical and is dealt with by embedding the detector in shielding material. The detector itself is made of low-background material, but this does not entirely suppress the contamination. Therefore direct detection experiments exploit the self-shielding capabilities of the target material, by using a fiducial region and rejecting events occurring close to the surface, where background events are expected to dominate. Finally, radioactivity leads to electron recoils, and it is often possible to discriminate

between electron and nuclear recoils. Ultimately, direct-detection experiments rely on very precise determination and control of backgrounds.

We now briefly outline the predictions of the number of events in a given detector, before summarizing the status of direct searches.

### 2.1.2 Number of expected events

**Event rate.** The differential event rate per nuclear recoil energy  $E_R$  for WIMP-nucleus elastic scattering is given by (Jungman et al., 1996; Lewin & Smith, 1996)

$$\frac{dR}{dE_R} = \frac{M\rho_\odot}{m_N m_{\text{DM}}} \int_{v_{\min} \leq |\vec{v}| \leq v_{\text{esc}}} v \frac{d\sigma}{dE_R} f(\vec{v}) d\vec{v}, \quad (2.1)$$

with  $M$  the total target mass,  $m_N$  the mass of target nuclei,  $\rho_\odot$  the WIMP density in the solar neighborhood,  $m_{\text{DM}}$  the WIMP mass, and  $d\sigma/dE_R$  the differential WIMP-nucleus scattering cross-section.  $\vec{v}$  is the WIMP velocity,  $v = |\vec{v}|$ , and  $f(\vec{v})$  is the normalized WIMP velocity distribution function in the Earth frame, with  $v_{\text{esc}} \approx 544 \text{ km s}^{-1}$  the escape velocity from the Galactic halo. The WIMP velocity is usually modeled as a Maxwell-Boltzmann distribution in the Galactic rest frame, but this assumption has been questioned since the velocity distribution is a significant source of uncertainty for direct detection experiments. The recoil energy of the nucleus is related to the momentum transfer  $q$  and the WIMP velocity  $v$  through

$$E_R = \frac{q^2}{2m_N} = \frac{\mu_N^2 v^2}{m_N} (1 - \cos \theta), \quad (2.2)$$

where  $\theta$  is the scattering angle in the WIMP-nucleus center-of-mass frame and  $\mu_N$  the WIMP-nucleus reduced mass:

$$\mu_N = \frac{m_N m_{\text{DM}}}{m_N + m_{\text{DM}}}. \quad (2.3)$$

The minimum velocity is given by

$$v_{\min} = \sqrt{\frac{m_N E_{\text{th}}}{2\mu_N^2}}, \quad (2.4)$$

with  $E_{\text{th}}$  the energy threshold of the detector.

Considering that the de Broglie wavelength of WIMPs in the 10 GeV–1 TeV mass range is larger than the diameter of most nuclei, the scattering amplitudes on nucleons in the target nucleus add coherently. For the heaviest nuclei like Xe or WIMPs in the tail of the velocity distribution, the loss of coherence is accounted for through nuclear form factors which lead to a suppression in the event rate. To account for the unknown interactions between DM particles and baryonic matter, in general the WIMP-nucleus scattering cross-section is expressed as the sum of two terms, corresponding to spin-independent (SI) interactions (for a scalar coupling<sup>1</sup>) and spin-dependent (SD) interactions (for an axial-vector coupling):

$$\frac{d\sigma}{dE_R} = \frac{m_N}{2\mu_N^2 v^2} \left[ \sigma_{\text{SI}} F_{\text{SI}}^2(E_R) + \sigma_{\text{SD}} F_{\text{SD}}^2(E_R) \right], \quad (2.5)$$

with  $F_{\text{SI}}$  and  $F_{\text{SD}}$  the nuclear form factors for SI and SD interactions (which can be found e.g. in Baudis (2012)).

It turns out that many more terms appear in the differential scattering cross-section when moving to a more model-independent approach relying on non-relativistic operators, in the framework of an effective field theory of direct detection (Fitzpatrick et al., 2013). In particular,

<sup>1</sup>Generally, a vector coupling, which would lead to an additional contribution to the SI cross-section, is not included, since it corresponds to non-Majorana DM particles and is as such not relevant in the context of the leading supersymmetric WIMP candidates.

this new formalism introduces additional nuclear form-factors to describe DM-nucleus interactions, leading to angular-momentum dependent, and spin- and angular-momentum dependent interactions. Although this novel approach is very promising to set more general constraints on DM-nucleus scattering and is going to be extensively used in the future, in the following we restrict the discussion to the more traditional method focusing on the SI and SD terms to describe the results of direct-detection experiments.

**Spin-independent interactions.** The SI scattering cross-section in the zero momentum transfer limit (corresponding to coherent scattering) can be expressed in terms of the SI WIMP-nucleon cross-section  $\sigma_{\text{SI}}^{\text{p,n}}$ :

$$\sigma_{\text{SI}} = \sigma_{\text{SI}}^{\text{p,n}} \frac{\mu_{\text{N}}^2}{\mu_{\text{p,n}}^2} \frac{(Zf_{\text{p}} + (A - Z)f_{\text{n}})^2}{f_{\text{p,n}}^2}, \quad (2.6)$$

where  $f_{\text{p}}$  and  $f_{\text{n}}$  are the effective WIMP-proton and WIMP-neutron couplings,  $\mu_{\text{n}} \approx \mu_{\text{p}}$  the WIMP-nucleon reduced mass,  $Z$  the atomic number and  $A$  the mass number of the target nucleus.  $f_{\text{p}}$  and  $f_{\text{n}}$  are usually assumed to be equal, so that the SI cross-section scales with  $A^2$ :

$$\sigma_{\text{SI}} = \sigma_{\text{SI}}^{\text{n}} \frac{\mu_{\text{N}}^2}{\mu_{\text{n}}^2} A^2, \quad (2.7)$$

showing that heavy target nuclei offer better detection prospects. The WIMP-nucleon SI cross-section  $\sigma_{\text{n}}$  is used to compare the results obtained with different target materials, and is the quantity used to plot constraints on the SI scattering cross-section.

**Spin-dependent interactions.** The SD cross-section in the zero momentum transfer limit depends on the total spin  $J$  of the target nucleus via

$$\sigma_{\text{SD}} = \sigma_{\text{SD}}^{\text{p,n}} \frac{\mu_{\text{N}}^2}{\mu_{\text{p,n}}^2} \frac{4J + 1}{3} \frac{[a_{\text{p}} \langle S_{\text{p}} \rangle + a_{\text{n}} \langle S_{\text{n}} \rangle]^2}{a_{\text{p,n}}^2}, \quad (2.8)$$

where  $\sigma_{\text{SD}}^{\text{p,n}}$  are the SD WIMP-proton and WIMP-neutron cross-sections, which are convenient quantities to compare the results of different experiments.  $\langle S_{\text{p,n}} \rangle = \langle J | \hat{S}_{\text{p,n}} | J \rangle$  is the expectation value of the total proton or neutron spin operator in the nucleus, derived from nuclear models, and  $a_{\text{p,n}}$  the effective WIMP-proton and WIMP-neutron couplings in a given theoretical model for WIMP interactions. The  $A^2$  dependence that was present for the SI case has been replaced by a dependence on the total spin  $J$ , so that heavy nuclei are not necessarily more sensitive to SD interactions.

The SD cross-section is maximal if the target nucleus has an unpaired proton or/and neutron. This restricts the possible targets that one can use to achieve a good sensitivity to SD interactions. Target nuclei used in practice only have an odd number of protons or neutrons, so that results are given in terms of the proton-only or neutron-only cases, i.e. in terms of  $\sigma_{\text{SD}}^{\text{p}}$  or  $\sigma_{\text{SD}}^{\text{n}}$ .

**Number of events.** Finally, the total number of events that should be observed during a live-time  $T$  is given by integrating the event rate over all measurable nuclear recoil energies

$$N = T \int_{E_{\text{th}}}^{\infty} \epsilon(E_{\text{R}}) \frac{dR}{dE_{\text{R}}} dE_{\text{R}}, \quad (2.9)$$

where  $\epsilon(E_{\text{R}})$  is the efficiency of the detector. The efficiency at the detector threshold  $E_{\text{th}}$  is a critical ingredient in direct detection experiments, and limits in practice the sensitivity to low-mass WIMPs which induce small nuclear recoils.

### 2.1.3 Status of direct searches

We now give an overview of the main results of direct-detection experiments.

#### 2.1.3.1 Spin-independent interactions

**Current situation.** Four anomalies—i.e. excesses of events above backgrounds—have been reported in the past few years from crystal detectors, namely DAMA/LIBRA (Bernabei et al., 2010), CoGeNT (Aalseth et al., 2013), CRESST (Angloher et al., 2012), and CDMS (Agnese et al., 2013a,b). These excesses created much of a stir in the DM community, since they can be interpreted as hints for  $\sim 10$  GeV WIMPs and are depicted as closed contours in the spin-independent parameter space (Fig. 2.2).

However, these anomalies have been challenged by a significant number of null results, leading to upper limits on the WIMP-nucleon cross-section at 90% confidence level (CL), as shown in Fig. 2.2. Since the SI cross-section scales with  $A^2$ , the sensitivity of SI searches is maximal for detectors containing heavy nuclei, such as  $^{131}_{54}\text{Xe}$ , with a high atomic number that offers very good self-shielding capabilities. Actually, very strong constraints have been set by XENON100 (Aprile et al., 2011, 2012) and LUX (Akerib et al., 2014). In particular, the best limit to date is given by LUX, which excludes a WIMP-nucleon SI scattering cross-section as low as  $7.6 \times 10^{-46}$  cm<sup>2</sup> at a WIMP mass of 33 GeV.

These very strong constraints are complemented by a wealth of other experiments. Liquid noble gas detectors have demonstrated excellent capabilities for direct detection. With heavy nuclei, xenon targets are optimal, as demonstrated by XENON100 and LUX. This preference dates back to the older XENON10 results (Angle et al., 2011), and the more recent ones from ZEPLIN-III (Akimov et al., 2012) and PandaX-I (Xiao et al., 2014) which are at the same level. Argon targets are starting to be used, with the DarkSide-50 experiment (Agnes et al., 2015). Exclusion limits have also been derived by the superheated droplet detector SIMPLE (Felizardo et al., 2012) and the bubble chamber COUPP (Behnke et al., 2012). The initial four anomalies are also challenged by crystal detectors like EDELWEISS (Armengaud et al., 2011). Moreover, the CDMS excess was not confirmed by CDMSlite (Agnese et al., 2014a), CDMS-II (Ahmed et al., 2010, 2011). Additionally, the CRESST excess was not confirmed by the CRESST-II upgrade, and upper limits were derived instead (Angloher et al., 2014, 2015). Finally, the DAMIC experiment exploits a different technology, namely charge-coupled devices (CCDs), and is becoming an important player in the game with good sensitivity to GeV WIMPs. No events were detected above backgrounds in the first run, leading to an exclusion limit (Barreto et al., 2012), updated in 2015 (Aguilar-Arevalo et al., 2015). Low-mass WIMPs have also been searched for by the first stage of the SuperCDMS experiment at the Soudan Underground Laboratory, with a non-detection leading to an upper limit of  $1.2 \times 10^{-42}$  cm<sup>2</sup> at 8 GeV (Agnese et al., 2014b).

To conclude, only the DAMA/LIBRA excess and marginally the CoGeNT anomaly—although the latter has not been confirmed by an independent analysis of the CoGeNT data (Davis et al., 2014)—remain, but are in strong tension with all other direct-detection experiments. However, this is not the end of the story, since models reconciling anomalies and null results can be found, as discussed e.g. in Arina et al. (2015).

**The future.** Several existing experiments are going to be upgraded in the next future, with significant improvements in sensitivity: LUX 300 live days (Faham, 2014), SuperCDMS at the SNOLAB facility (Scorza, 2013), and DarkSide-50 (Aalseth et al., 2015). The current results of the XMASS experiments are not competitive yet (Abe et al., 2013a), but a great increase in sensitivity is expected once backgrounds are reduced (Ichimura, 2015).

In the long run, the field is going to be dominated by ton-scale detectors, which are either under commissioning like DEAP-3600 (Amaudruz et al., 2014), being constructed like XENON1T

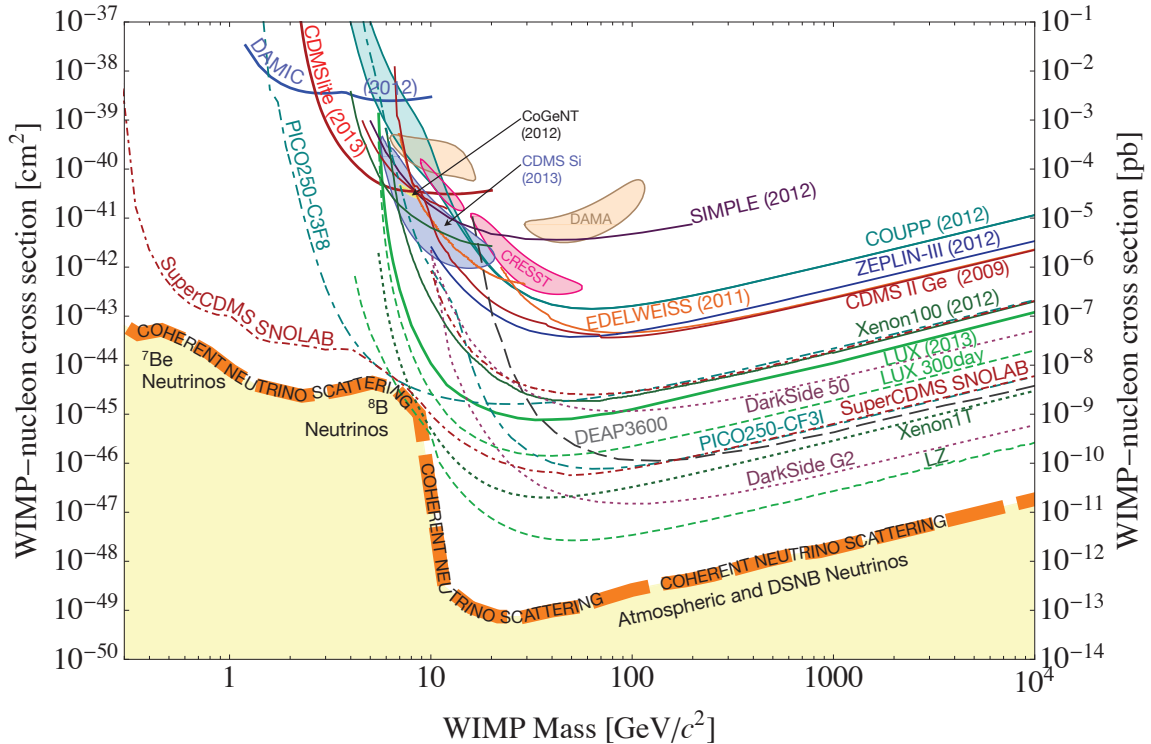


**Figure 2.2** – Compilation of excess contours and current limits at 90% CL on the *spin-independent* WIMP-nucleon scattering cross-section (solid lines) and projected sensitivities (dashed and dot-dashed lines). The yellow shaded region represents the neutrino floor, i.e. the irreducible background from solar and atmospheric neutrinos, as well as from the diffuse supernova neutrino background. This figure is taken from [Cooley \(2014\)](#), and the references corresponding to the various limits are given in the text.

([Aprile, 2012](#)), or in the design phase like LZ ([Akerib et al., 2015](#)), PICO-250 ([Bou-Cabo, 2014](#)), and DarkSide-G2 ([Aalseth et al., 2015](#)).

As shown in Fig. 2.2, ton-scale detectors will be sensitive to coherent neutrino-nucleus scattering, and will directly detect neutrinos from the Sun, the atmosphere, as well as the diffuse supernova neutrino background. This *neutrino floor* will become an irreducible background for direct detection experiments ([Billard et al., 2014](#)). For a discussion of the sensitivity of ton-scale detectors to neutrinos see e.g. [Baudis et al. \(2014\)](#).

To deal with this new type of background, direct detection will have to rely on directional experiments, such as DRIFT ([Battat et al., 2015](#)) and D<sup>3</sup> ([Ross, 2014](#)). For a review of directional detection, see e.g. [Mayet & Billard \(2013\)](#). This technique exploits the variation of the direction of the WIMP wind—which is due to the motion of the Earth in the Galactic rest frame—due to the rotation of the Earth on its axis. As no background is associated with this effect, directional detection is a very promising way to look for WIMPs, without the limitation induced by neutrino-nucleus scattering.

At the low-mass end, beam-dump experiments, which attempt to produce a relativistic beam of DM particles out of electron or proton collisions with a fixed target and then detect the DM particles via DM-nucleus scattering, have the potential to directly probe sub-GeV DM ([Izaguirre et al., 2013](#); [Diamond & Schuster, 2013](#)). This is illustrated in [Batell et al. \(2014\)](#), in which strong constraints were derived using the results of a beam-dump experiment performed at the SLAC National Accelerator Laboratory in 1980–1982. The case for a future beam-dump experiment dedicated to searching for MeV–GeV DM particles at Jefferson Lab is discussed in [Izaguirre et al. \(2014\)](#); [Battaglieri et al. \(2014\)](#).

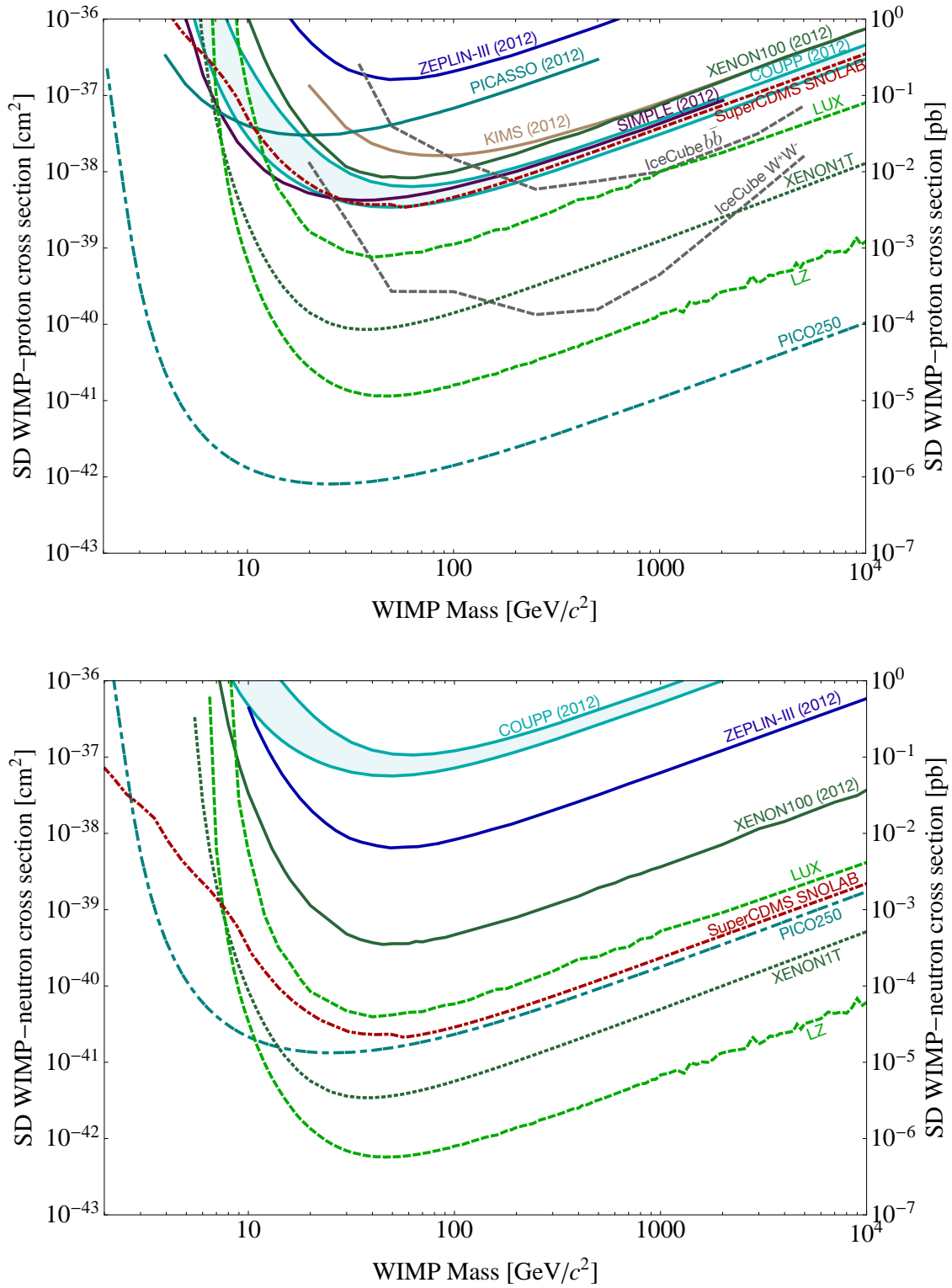


**Figure 2.3** – Compilation of current upper limits at 90% CL on the *spin-dependent* WIMP-nucleon scattering cross-section (solid lines except for the IceCube results, depicted as dashed grey lines) and projected sensitivities (dashed and dot-dashed lines), for WIMP-proton interactions (**top panel**) and WIMP-neutron interactions (**bottom panel**). This figure is taken from [Cushman et al. \(2013\)](#), and the references corresponding to the various limits are given in the text.

### 2.1.3.2 Spin-dependent interactions

**Current situation.** Here we briefly review the current status of spin-dependent searches. The general situation is that no excesses that could be interpreted as WIMP-nucleus SD scattering have been detected. For SD interactions, the cross-section scales with the spin parameter  $(J+1)/J [a_p \langle S_p \rangle + a_n \langle S_n \rangle]^2$ , which gives a significant contribution only for nuclei with unpaired protons or neutrons, and is maximal for  $^{19}\text{F}$ . For SD interactions, neutrons and protons can contribute differently to the total spin, so in practice results are expressed in terms of coupling of WIMP to neutrons or protons only. Currently the most stringent limits on the SD WIMP-neutron scattering cross-section are given by xenon detectors XENON100 (Aprile et al., 2013) and ZEPLIN-III (Lebedenko et al., 2009; Akimov et al., 2012), while the strongest limits on the WIMP-proton SD cross-section are given by experiments containing  $^{19}\text{F}$ , namely the bubble chamber COUPP (Behnke et al., 2012), and the superheated droplet experiments PICASSO (Archambault et al., 2012) and SIMPLE (Felizardo et al., 2012). The crystal detector KIMS (Kim et al., 2012) and searches for neutrinos from the Sun with the IceCube detector (Aartsen et al., 2013a) have also yielded stringent limits on the SD WIMP-proton cross-section. The DRIFT directional detector (Battat et al., 2015) has started to set limits on the SD WIMP-proton scattering cross-section, not competitive yet.

**The future.** The future of SD searches is going to rest with the SuperCDMS upgrade of the CDMS experiment, as well as with ton-scale xenon detectors (XENON1T and LUX) and the ton-scale bubble chamber experiment PICO, which results from the merger of PICASSO and COUPP. Current and projected constraints are summarized in Fig. 2.3.

### 2.1.3.3 Searches for axions and axion-like particles

Axions are also searched for directly, but with a different principle of detection. Axions are primarily detected via the Primakoff effect (Primakoff, 1951), which consists in the axion-photon conversion in a magnetic field perpendicular to the axion momentum. Dedicated experiments exploit this effect, like ADMX, which uses a microwave cavity placed in strong magnets (Shokair et al., 2014). So far, only null results have been obtained, leading to constraints on the axion-photon coupling constant  $g_{A\gamma}$ . Some direct-detection experiments mentioned before also exploit the Primakoff effect, thanks to a well oriented magnetic field. This is the case for crystal experiments such as EDELWEISS (Armengaud et al., 2013) and DAMA (Bernabei et al., 2001).

Liquid gas detectors are insensitive to  $g_{A\gamma}$ , so they rely on the axio-electric effect, looking for axions and ALPs converted into electrons. For a review of constraints on the axion-electron coupling  $g_{Ae}$  with DM direct-detection experiments, see Aprile et al. (2014). These searches have already set strong constraints on the DM axion regime.

Other dedicated axion experiments searching for photons that should not be detectable—were it not for the Primakov effect—are in progress, such as light-shining-through-walls experiments, solar helioscopes, and studies of the transparency of the Universe to  $\gamma$ -rays. For a recent review of searches for axions and ALPs see Graham et al. (2015).

## 2.2 Collider searches

### 2.2.1 Principle

The discovery of the SM Higgs boson with the ATLAS (Aad et al., 2012) and CMS (Chatrchyan et al., 2012a) experiments at the Large Hadron Collider (LHC) has demonstrated the success of the Standard Model (SM) of particle physics. This success in probing the weak scale has paved the way for potential discoveries in beyond-the-Standard-Model physics. This is particularly relevant in the context of DM.

Collider searches have a good sensitivity to low-mass DM candidates—contrary to direct-detection experiments—, since colliders readily produce large amounts of light particles. However, due to their extremely weak couplings with ordinary matter, DM particles escape the detector and therefore can only be detected in the form of missing transverse energy or momentum, denoted as  $\cancel{E}_T$  or  $\cancel{p}_T$ , respectively. In practice, DM particles are expected to be produced along with SM particles. This leads to a characteristic signature consisting of SM particles recoiling against invisible particles identified by a large  $\cancel{E}_T$ . In practice, events producing invisible particles are identified by the emission—denoted as  $X$ —of jets (from quarks or gluons), photons,  $W$  or  $Z$  bosons via initial state radiation, so that the processes of interest are

$$pp \rightarrow \chi\chi X. \quad (2.10)$$

The difficulty lies in discriminating between DM events and SM processes which also produce jets, and to properly identify the particles that are radiated. All this requires a careful selection of events using well-defined kinematical criteria for optimal background rejection.

The modern approach to interpret results of DM searches with colliders consists in relating the production rate in colliders to the scattering and annihilation rates in direct and indirect DM searches, using effective field theories, with effective operators that model the coupling of DM particles to SM particles, corresponding to the four-particle interaction represented in Fig. 2.1. These operators are given e.g. in Goodman et al. (2010).

### 2.2.2 Overview of results

Here we summarize the main results of DM searches with ATLAS and CMS, based on the review of current LHC constraints in light of the 7 and 8 TeV runs in Askew et al. (2014). For constraints on DM in the specific context of SUSY, see Peskin (2015). See also Goodman et al. (2010) for older constraints from the Tevatron collider. No significant excesses over backgrounds in ATLAS and CMS have been observed in the channels relevant for DM.

**Mono-photon searches.** Searches for final states containing one photon and large  $\cancel{E}_T$  have been searched for with ATLAS at 7 TeV (Aad et al., 2013a) and CMS at 7 and 8 TeV (Chatrchyan et al., 2012b). For this analysis, the strongest background comes from  $Z(\rightarrow \nu\nu) + \gamma$  production. The null results in terms of constraints on the DM-nucleon scattering cross-section are shown in Fig. 2.4, for the SI and SD cases, for the D1, D5, D8 or D9 operators, corresponding to DM candidates that are Dirac fermions. These non-detections confirm early results obtained by the DELPHI (Abreu et al., 2000), ALEPH (Heister et al., 2003), L3 (Achard et al., 2004) and OPAL (Abbiendi et al., 2000) experiments at the Large Electron-Positron (LEP) collider.

**Mono-jet searches.** Backgrounds in this channel are dominated by final states involving SM particles and jets, but the difficulty comes from  $Z(\rightarrow \nu\nu) + \text{jet}$ , which is an irreducible background. The absence of significant excess over backgrounds in ATLAS (Aad et al., 2013b) and CMS (Chatrchyan et al., 2012c) at 7 and 8 TeV is interpreted in terms of limits on the DM-nucleon scattering cross-section, as shown in Fig. 2.5.

**Mono- $W/Z$  searches.** Searches for production of DM with  $W$  or  $Z$  bosons have been performed with ATLAS, studying hadronic decay of the bosons  $W/Z \rightarrow \text{jet} + \cancel{E}_T$  (Aad et al., 2013c) and leptonic decay of the  $Z$  boson  $Z \rightarrow ll + \cancel{E}_T$  (Aad et al., 2014a). The CMS Collaboration has studied the leptonic decay  $W \rightarrow l\nu + \cancel{E}_T$  (Chatrchyan et al., 2013). The results in terms of upper limits on the DM-nucleon scattering cross-section are shown in Fig. 2.6.

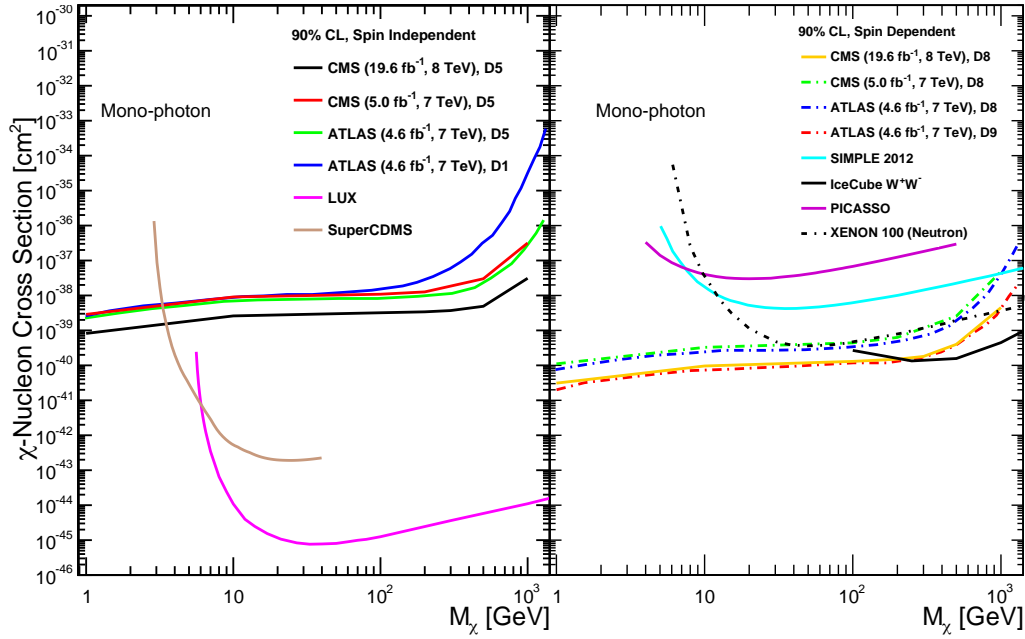


**Figure 2.4** – Constraints from mono-photon searches with ATLAS and CMS: upper limits at 90% CL on the DM-nucleon scattering cross-section for SI interactions (**left**) and SD interactions (**right**). To compare the LHC results with direct-detection constraints, the DM-SM coupling is modeled by the D1, D5, D8 or D9 operators, which apply to DM candidates that are Dirac fermions. This figure is taken from [Askew et al. \(2014\)](#).

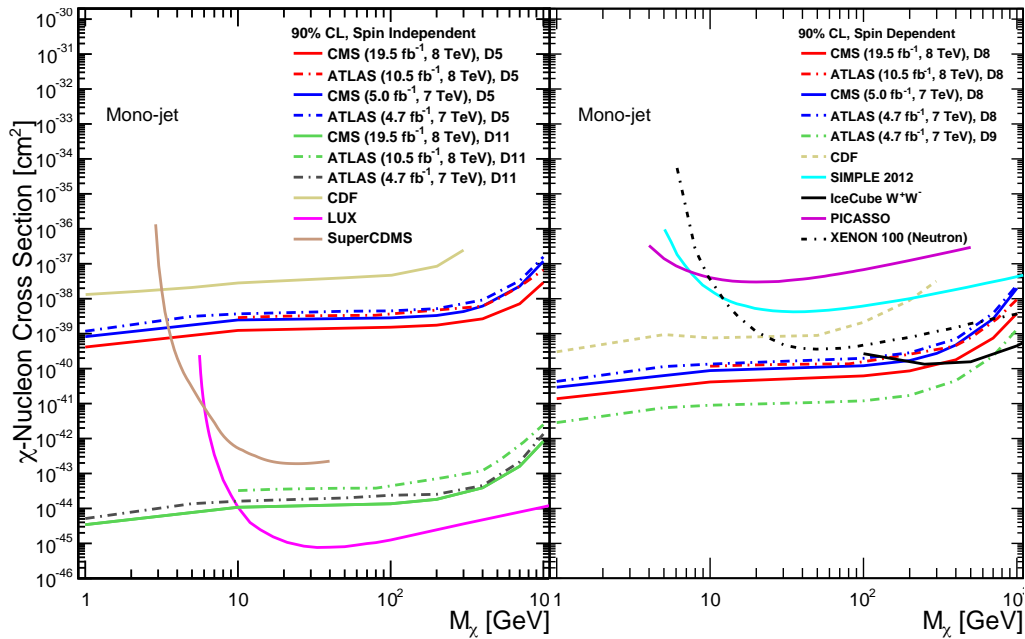


**Figure 2.5** – Constraints from mono-jet searches with ATLAS and CMS: upper limits at 90% CL on the DM-nucleon scattering cross-section for SI interactions (**left**) and SD interactions (**right**). To compare the LHC results with direct-detection constraints, the DM-SM coupling is modeled by the D5, D8, D9 and D11 operators, which apply to DM candidates that are Dirac fermions. This figure is taken from [Askew et al. \(2014\)](#).

**Invisible decay of Higgs bosons.** Now that the Higgs boson has been fully characterized at LHC, its decay into invisible particles can be used to set constraints on DM. Both ATLAS ([Aad](#)

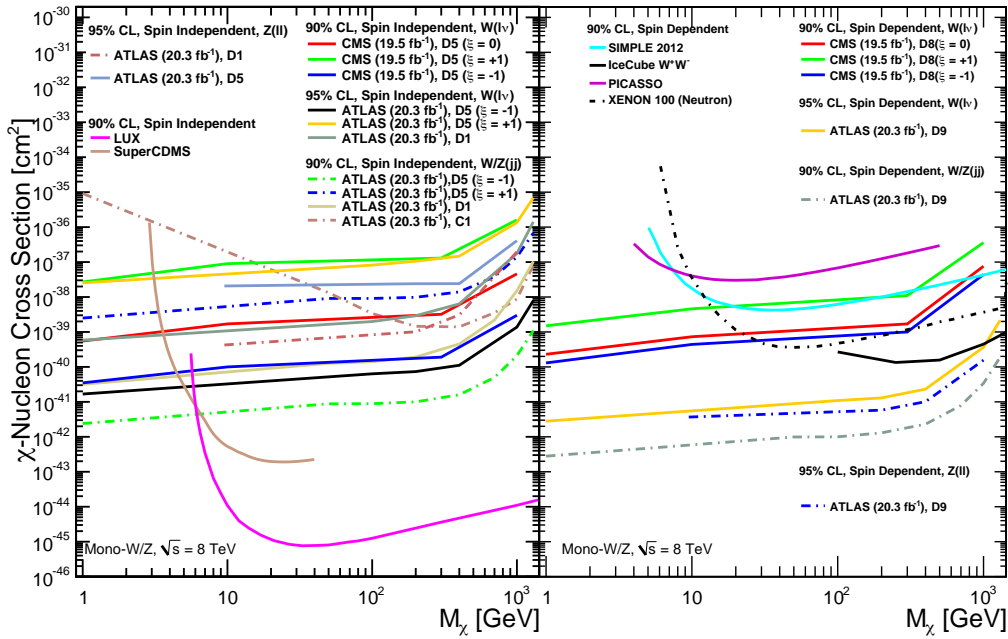


**Figure 2.6** – Constraints from mono-W/Z searches with ATLAS and CMS: upper limits at 90% CL on the DM-nucleon scattering cross-section for SI interactions (**left**) and SD interactions (**right**). To compare the LHC results with direct-detection constraints, the DM-SM coupling is modeled by the D1, D5, D8, D9 operators for Dirac fermions, and the C1 operator for complex scalars. This figure is taken from [Askew et al. \(2014\)](#).

[et al., 2014b, 2015a](#)) and CMS ([Chatrchyan et al., 2014](#)) have searched for invisible Higgs decay using events in which a Higgs boson is produced along with a  $Z$  boson. Additionally, ATLAS has combined measurements of Higgs decay into all visible channels to constrain the branching ratio into invisible states to less than 23% ([Aad et al., 2015a](#)).

No significant deviation from backgrounds has been reported. In this case, the null results are interpreted in terms of limits on the DM-nucleon cross-section using the Higgs portal model, a simple model in which the Higgs boson mediates the interaction between DM and SM particles, as shown in [Fig. 2.7](#), based on [Aad et al. \(2014b\)](#); [Chatrchyan et al. \(2014\)](#).

**Summary.** To conclude, collider searches therefore set much stronger limits on the DM-nucleon scattering cross-section below  $\sim 10$  GeV than direct detection, although limits from colliders are strongly model-dependent. This illustrates the complementarity of the various types of searches for DM. Although the LHC Run 1 has shown no evidence of DM, only time will tell what the Run 2, at higher energy and luminosity, will uncover.

### 2.2.3 Comment on the tentative 750 GeV excess at LHC

It turns out that preliminary results from the ATLAS ([Aad et al., 2015b](#)) and CMS ([Chatrchyan et al., 2015](#)) Collaborations for the LHC Run 2 at 13 TeV hint at a resonance in the diphoton channel with a peak around  $m_{\gamma\gamma} \approx 750$  GeV. The excess can be interpreted as the two-body decay of a new 750 GeV particle, which might turn out to be a portal between the Standard Model and a new sector.

The statistics is far from sufficient yet, but were it to be confirmed, this result would mark the dawning of a new era for physics beyond the Standard Model. For now the data does not allow for the discrimination between a narrow and wide resonance, but if a large width were confirmed, this would point to tree-level coupling of the new particle to DM, as discussed e.g. in [D’Eramo et al. \(2016\)](#).

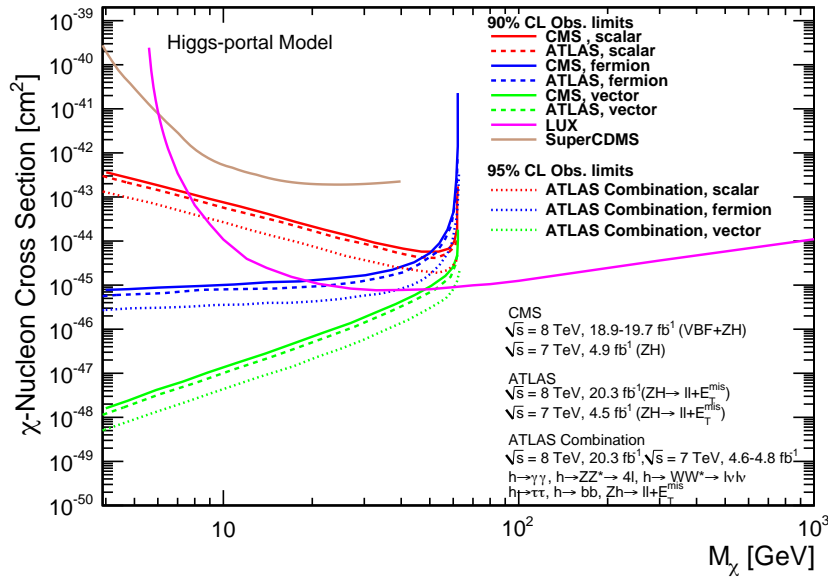


**Figure 2.7** – *Constraints from invisible Higgs decay with ATLAS and CMS*: null results are interpreted as upper limits on the DM-nucleon scattering cross-section using the Higgs portal model, for scalar, fermionic or vector DM candidates. This figure is taken from [Askew et al. \(2014\)](#).

## 2.3 Indirect detection: overview of standard searches

Indirect DM searches are complementary to the previous two approaches, and rely on astrophysical observations to detect the SM products of DM annihilation (e.g. [Gunn et al., 1978](#); [Stecker, 1978](#); [Silk & Srednicki, 1984](#); [Stecker et al., 1985](#); [Hagelin & Kane, 1986](#); [Bergström et al., 1998](#); [Bouquet et al., 1989](#); [Jungman & Kamionkowski, 1994, 1995](#); [Bergström et al., 1998](#)), or decay when considering unstable candidates like the gravitino (e.g. [Buchmüller et al., 2007](#); [Ibarra & Tran, 2008a,b](#); [Ishiwata et al., 2008](#); [Covi et al., 2009](#)). Most searches actually focus on annihilating DM which is expected to lead to more compelling signatures, and on WIMPs. More specifically, DM annihilation produces pairs of particles-antiparticles from the Standard Model, namely quarks ( $q$ ), leptons ( $l$ ), vectors bosons ( $W$ ,  $Z$ ,  $\gamma$ ) and Higgs bosons ( $h$ ). In turn, these SM particles lead, through decay and hadronization cascades, to the production of positrons ( $e^+$ ), antiprotons ( $\bar{p}$ ), antinuclei ( $\bar{N}$ ),  $\gamma$ -ray photons ( $\gamma$ ) and neutrinos ( $\nu$ ). This is represented schematically by

$$\chi\chi \longrightarrow q\bar{q}, l^+l^-, W^+W^-, ZZ, \gamma\gamma, hh \longrightarrow e^\pm, \bar{p}, \bar{N}, \gamma, \nu, \quad (2.11)$$

where the second step will be discussed in more detail for the species of interest in the following. Charged antiparticles, photons and neutrinos can then be searched for using astrophysical observations. The difficulty lies in being able to discriminate between the signatures of these DM annihilation products and sometimes poorly constrained astrophysical backgrounds from cosmic rays, i.e. energetic charged particles. For recent reviews of indirect detection see e.g. [Salati \(2014\)](#); [Cirelli \(2015\)](#).

### 2.3.1 Constraints from the CMB

DM annihilations or decays in the early Universe can affect the standard history of the Universe. In particular, electrons, positrons and photons produced in DM annihilations or decays heat and ionize the medium, which affects the recombination history and leads to changes in the temperature and polarization power spectra of the CMB anisotropies (see e.g. [Chen & Kamionkowski, 2004](#);

Padmanabhan & Finkbeiner, 2005). The strongest constraints come from the *Planck* results and exclude the thermal s-wave (velocity independent) cross-section at 95% CL for masses below 10–40 GeV, depending on the annihilation channel (Ade et al., 2015b; Slatyer, 2016). For p-wave annihilation, the velocity-suppressed cross-section reads  $\sigma v = a_2 v^2$ , where  $a_2$  is a constant. In that case, CMB anisotropies are affected by the enhancement of the cross-section associated with the velocity boost induced by DM clustering at late time. For p-wave annihilation, the constraints are much less stringent than for s-wave annihilation, with limits orders of magnitude above the value of  $a_2 \sim 10^{-25} \text{ cm}^3 \text{ s}^{-1}$  required to explain the relic abundance (Diamanti et al., 2014).<sup>2</sup>

CMB anisotropies can also be used to constrain DM-radiation interactions (Boehm et al., 2001, 2002; Boehm & Schaeffer, 2005; Wilkinson et al., 2014a,b), where radiation refers to photons or neutrinos. The coupling of DM to radiation induces free-streaming and collisional damping for DM particles. The amount of induced damping is constrained by the high- $\ell$  multipoles of the CMB power spectrum.

In addition to anisotropies, distortions of the CMB frequency spectrum caused by energy injection (Zeldovich & Sunyaev, 1969) can be used to constrain the annihilation cross-section or the lifetime of DM particles (e.g. Salati, 1985; Hu & Silk, 1993, and see Chluba & Sunyaev, 2012; Chluba, 2016, for recent updates), as well as the DM-photon and DM-electron scattering cross-sections (Ali-Haïmoud et al., 2015).

### 2.3.2 Charged antiparticles

DM-induced charged antiparticles are very good probes of exotic physics (e.g. Bergström et al., 1999). Astrophysical backgrounds for antimatter species correspond to *secondary* cosmic rays, coming from the spallation of *primary* cosmic rays on the gas in the interstellar medium, where ‘primary’ refers to cosmic rays directly injected in the ISM by sources.

Charged antiparticles are affected by the interstellar magnetic field and propagate in the galaxy in the same way as other cosmic rays. Their propagation is modeled as a diffusion-loss process described in detail in Sec. 4.3.2, and is a key ingredient to compute background fluxes at the Earth, where charged antiparticles are detected in space-based or ground-based experiments.

#### 2.3.2.1 Positrons

**Positron excess.** A very spectacular anomaly is the *positron excess*, characterized by a rise in the positron fraction above  $\sim 10$  GeV. The positron fraction is defined as  $\Phi_{e^+}/(\Phi_{e^+} + \Phi_{e^-})$ , where  $\Phi_{e^+}$  and  $\Phi_{e^-}$  are the numbers per unit surface, time, energy and solid angle, respectively of positrons and electrons, at the Earth’s position. The first hints of a rising positron fraction came from the balloon-borne HEAT instrument (Barwick et al., 1997) and the prototype AMS-01 of the AMS detector (Aguilar et al., 2007). These hints were reinforced by the discovery of a rising positron fraction up to a positron energy of 100 GeV with the PAMELA mission (Adriani et al., 2009a, 2013a), and up to 200 GeV with the *Fermi* Large Area Telescope (LAT) on board the *Fermi* Gamma-ray Space Telescope satellite (Ackermann et al., 2012a). The PAMELA positron rise has been confirmed by the high-precision results of the AMS-02 detector on board the International Space Station, extending the previously available data up to 300 GeV (Aguilar et al., 2013; Accardo et al., 2014). Fig. 2.8 shows a summary of the data on the positron fraction discussed above.

The positron fraction is expected to decrease with the energy for a population of secondary positrons (Moskalenko & Strong, 1998). Therefore, the rise in the positron fraction corresponds to an excess of positrons above known backgrounds. This reveals the existence of a source of primary positrons. As a result, this initially sparked significant excitement in the DM community, since this primary source could actually be DM annihilations (Bergström et al., 2008). If the

<sup>2</sup> $a_2$  is homogeneous to  $\sigma v$  for  $v$  in units of the speed of light.

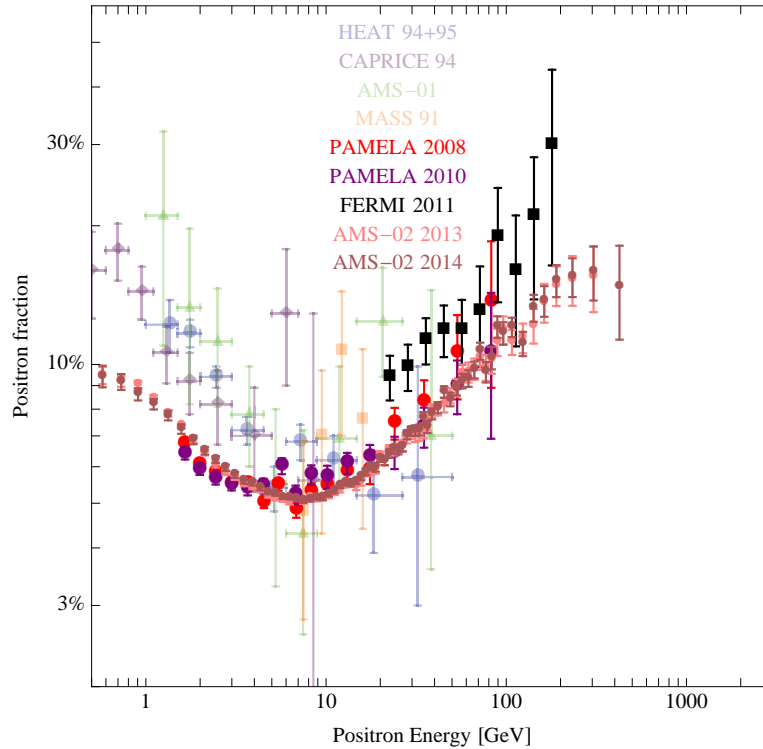


**Figure 2.8** – Positron fraction as a function of energy, showing a spectacular excess backgrounds above  $\sim 10$  GeV. Older data from the balloon-borne CAPRICE (Boezio et al., 2001) and MASS (Grimani et al., 2002) experiments are also included. This figure is taken from Cirelli (2015).

positron excess is interpreted in terms of DM annihilations, with conservative assumptions on the modeling of positron propagation, the best fit to the positron fraction data is obtained for a TeV DM candidate annihilating to leptons (to evade the constraints on annihilation into quarks from antiprotons discussed in Sec. 2.3.2.2) with a cross-section of  $\sim 10^{-23} \text{ cm}^3 \text{ s}^{-1}$  (Cholis & Hooper, 2013; Boudaud et al., 2015a; Cirelli, 2015). This is three orders of magnitude above the thermal value. While this can be reconciled with the DM relic abundance via Sommerfeld enhancement effects or non-thermal production of DM (Madhavacheril et al., 2014), this makes the DM interpretation of the positron excess somehow unnatural. But more importantly, a cross-section this large is excluded by the CMB constraints (Ade et al., 2015b; Slatyer, 2016), although these constraints can be evaded for p-wave DM annihilation (Diamanti et al., 2014), as discussed in Sec. 2.3.1, or if clumpiness in the DM distribution boosts the local annihilation rate significantly. Decaying DM has also been suggested as a possible explanation of the positron anomaly (Ibarra & Tran, 2009); see Ibarra et al. (2013) for a review.

Ultimately, the positron excess is more likely to originate from one or several nearby pulsars (Hooper et al., 2009). See e.g. Cholis & Hooper (2013); Boudaud et al. (2015a) for even more recent discussions of the pulsar interpretation. This illustrates the difficulty of identifying a clear-cut DM signal in the presence of unconstrained astrophysical sources. Due to their similarities, discriminating between signatures of pulsars and DM is especially difficult. This is critical in the context of  $\gamma$ -rays, as we will discuss in Chapter 5.

**Line searches.** By searching for lines in the otherwise a priori smooth positron spectrum measured with AMS-02, several groups have derived stringent constraints on DM annihilating into leptons, in particular  $e^\pm$  and  $\mu^\pm$ . These upper limits exclude the thermal s-wave cross-section below  $m_{\text{DM}} \lesssim 100$  GeV for the  $e^+e^-$  and  $\mu^+\mu^-$  channels (Bergström et al., 2013; Ibarra et al., 2014; Bringmann et al., 2014).

### 2.3.2.2 Antiprotons

The flux of antiprotons has been measured by PAMELA (Adriani et al., 2009b, 2010, 2013b). In 2015, the AMS collaboration released the ratio of the fluxes of antiprotons to protons (Kounine, 2015).<sup>3</sup> The AMS-02 data are shown in Fig. 2.9, along with the PAMELA 2012 data. A benchmark model of the secondary component seems to lead to a discrepancy with the observed  $\bar{p}/p$  ratio above a kinetic energy of  $\sim 100$  GeV, thus possibly pointing to a primary source of antiprotons like DM annihilation. However, once astrophysical uncertainties are fully accounted for, the prediction for the astrophysical component becomes compatible with the data (Giesen et al., 2015; Evoli et al., 2015; Kappl et al., 2015). More specifically, secondary  $\bar{p}$  and  $p$  are produced by spallation of primary cosmic rays on the gas in the interstellar medium, so the  $\bar{p}$  and  $p$  fluxes are sensitive to uncertainties on the injection spectrum of primaries, and on the nuclear cross-sections associated with the spallation process. The  $\bar{p}/p$  ratio is also affected by propagation in the Galaxy, and in the solar system through the interaction of the particles with the solar magnetic field, a process referred to as solar modulation.

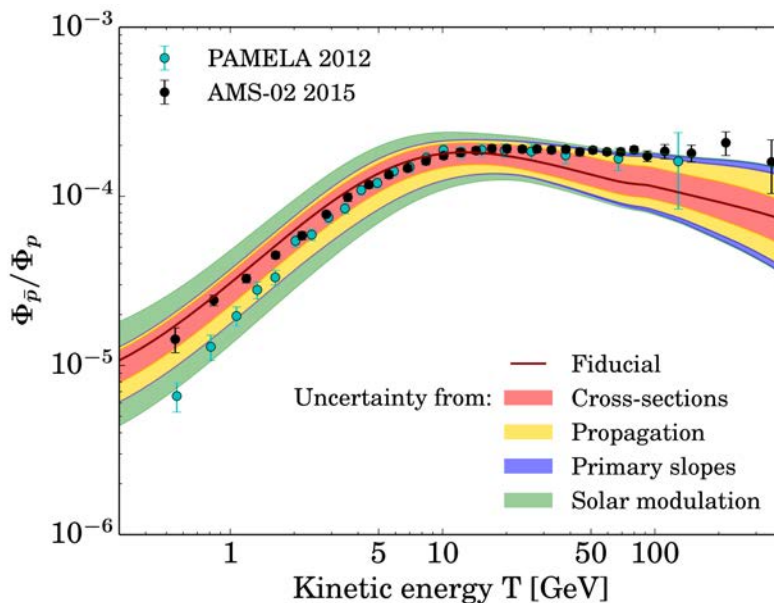


**Figure 2.9** – Ratio of antiproton to proton flux as a function of kinetic energy. The PAMELA 2012 data points (Adriani et al., 2013b) are shown along with the AMS-02 2015 data points. The black solid line corresponds to a benchmark model of the astrophysical background. The red, yellow, blue and green shaded areas represent the uncertainties induced by the modeling of nuclear cross-sections, propagation, source injection spectra and solar modulation, respectively. Once all these uncertainties are accounted for, the astrophysical background can be reconciled with the data. This figure is taken from Giesen et al. (2015).

As a result, contrary to positrons, no unambiguous excess over astrophysical backgrounds has been found in the antiproton data. This can be used to set constraints on DM annihilation (and decay). Since antiprotons are more readily produced from quarks, the  $b\bar{b}$  channel is the most constraining. The  $W^+W^-$  channel is also very constraining (Bélanger et al., 2012; Hryczuk et al., 2014). In particular, the thermal s-wave cross-section is excluded below  $\sim 150$  GeV for the  $b\bar{b}$  channel, for benchmark DM profile and propagation set-up, using PAMELA (Boudaud et al., 2015b) and AMS-02 (Giesen et al., 2015). This is of course sensitive to the uncertainty on the DM profile, but shows the very good potential of antiprotons as DM probes.

<sup>3</sup>AMS days at CERN, April 15-17, 2015.

### 2.3.2.3 Antinuclei

Antideuteron nuclei  $\bar{D}$  (also referred to as antideuterons) can be produced by the coalescence of an antiproton  $\bar{p}$  and an antineutron  $\bar{n}$  with aligned momenta with similar norms, and are very good probes for DM annihilations or decays (Donato et al., 2000). Indeed, although the DM-induced  $\bar{D}$  flux is expected to be much smaller than other cosmic-ray fluxes, it also peaks in the low kinetic energy region which is essentially background-free. The current sensitivity of cosmic-ray detectors is not good enough to detect antideuterons from DM, and only an upper limit has been derived (Fuke et al., 2005) using the balloon-borne BESS experiment. However, the prospects for detection are fairly good after five years of AMS-02 data taking and three 35-day flights of the GAPS balloon-borne experiment (von Doetinchem et al., 2015).

Searches for heavier antinuclei, especially antihelium, are also in principle promising due to very low astrophysical backgrounds at low kinetic energies. However, considering the very low probability of coalescence of a large number of antinucleons, the resulting DM-induced fluxes are about 2–3 orders of magnitude below the sensitivity of AMS-02, but might be within reach of GAPS (Cirelli et al., 2014b; Carlson et al., 2014).

### 2.3.3 Gamma rays

The field of  $\gamma$ -ray observation has been revolutionized by the advent of *Fermi*-LAT (Atwood et al., 2009) and imaging atmospheric Čerenkov telescopes (IACTs), namely the High Energy Stereoscopic System (H.E.S.S.), the Major Atmospheric Gamma-ray Imaging Čerenkov (MAGIC) telescope and the Very Energetic Radiation Imaging Telescope Array System (VERITAS), as discussed in Hillas (2013). IACTs detect the Čerenkov light emitted by charged particles of the electromagnetic showers initiated in the atmosphere by an incoming  $\gamma$ -ray, and allow the direction of the photon to be reconstructed.

In addition to numerous observations of astrophysical objects, the very good energy and angular resolution of these instruments has made it possible to test the WIMP paradigm, making  $\gamma$ -rays one of the most prominent DM probes, confirming early studies showing their potential (Bergström & Snellman, 1988; Zhang Jian-Zu, 1989; Giudice & Griest, 1989; Bouquet et al., 1989; Berezhinsky et al., 1992; Urban et al., 1992; Bergström & Kaplan, 1994; Jungman & Kamionkowski, 1995; Bergström et al., 1998).

As outlined briefly at the beginning of Sec. 2.3, in the standard picture DM particles directly annihilate (i.e. at tree level) into pairs of quarks, leptons, Higgs and weak gauge bosons. The subsequent hadronization and further decays produces photons mostly via neutral pion decay. This leads to a continuous spectrum of  $\gamma$ -rays up to the DM mass. Final state radiation from charged annihilation products also leads to the production of  $\gamma$ -rays, with a sharp cut-off at the DM mass. The  $\gamma$ -ray emission resulting from these processes is referred to as *prompt emission*, since the whole process is essentially instantaneous. This is particularly useful since the spatial morphology of prompt  $\gamma$ -ray emission traces exactly the DM profile. The prompt spectrum is obtained in practice using event generators like PYTHIA (Sjöstrand et al., 2006). Throughout this thesis, we use the interpolations provided in Cirelli et al. (2011) and the associated website.<sup>4</sup>

We note that prompt emission also results from virtual internal bremsstrahlung, which is essentially the emission of a photon by a virtual charged mediator of the annihilation process (Bringmann et al., 2008), but contrary to final state radiation, the corresponding  $\gamma$ -ray spectrum is model-dependent. As a result, in general internal bremsstrahlung is not included in standard computations of the prompt spectrum such as the one in Cirelli et al. (2011), and we disregard it to remain model-independent in our calculations.

Here we summarize the status of standard  $\gamma$ -ray searches for DM. For dedicated reviews, see e.g. Bringmann & Weniger (2012); Conrad et al. (2015).

<sup>4</sup>A Poor Particle Physicist Cookbook for Dark Matter Indirect Detection (PPPC 4 DM ID).

### 2.3.3.1 Prompt gamma-ray spectrum from DM annihilation

In this section, we provide the formalism used to estimate the flux of prompt  $\gamma$ -rays from DM annihilation, used both for general indirect DM searches and in the context of this thesis.

For one DM particle, the annihilation rate with another particle is  $\Gamma_{\text{ann}} = n_{\text{DM}} \langle \sigma v \rangle$  where  $n_{\text{DM}} = \rho/m_{\text{DM}}$  is the DM number density, with  $\rho$  the DM energy density. Therefore the total annihilation rate per unit volume is proportional to  $n_{\text{DM}}^2$ , and the photon emissivity is the product of the total annihilation rate with the number of photons emitted per annihilation. Note that for decaying DM, the decay rate is proportional to  $\rho$  instead of  $\rho^2$ , so the prospects for detection of decay products are much worse than for annihilating DM. For this reason, most searches focus on DM annihilation, and this is what we have done throughout this work.

The differential intensity of prompt  $\gamma$ -ray photons from DM annihilation channel  $f$ , isotropically radiated through solid angle  $d\Omega$  in direction  $\theta$ , is then obtained by integrating the prompt emissivity over the line of sight (l.o.s.) coordinate  $s$ :

$$\left. \frac{dn_f}{dE_\gamma d\Omega} \right|_{\text{prompt}} = \frac{1}{4\pi} \frac{\langle \sigma v \rangle_f}{\eta m_{\text{DM}}^2} \frac{dN_{\gamma,f}}{dE_\gamma} \int_{\text{l.o.s.}} \rho^2(\vec{x}(s, \theta)) ds, \quad (2.12)$$

where  $\vec{x}(s, \theta)$  is the location of the emission region.<sup>5</sup>  $dN_{\gamma,f}/dE_\gamma$  is the  $\gamma$ -ray spectrum per annihilation for channel  $f$ , in practice computed and tabulated for various DM masses e.g. in [Cirelli et al. \(2011\)](#), including electroweak corrections that become increasingly important at high energies.  $\langle \sigma v \rangle_f$  is the DM annihilation cross-section into this final state. The factor  $\eta$  accounts for the fact that the number of annihilations is half the number of DM particles annihilated, hence  $\eta = 2$  for self-conjugate DM (i.e. if DM is a real scalar or a Majorana fermion). For non self-conjugate DM (i.e. for a complex scalar or a Dirac fermion), the annihilation rate would be divided by another factor 2, since particles can only annihilate with antiparticles in that case, which would lead to  $\eta = 4$ . Throughout this work, we consider self-conjugate DM, so we take  $\eta = 2$ .

The differential flux of prompt  $\gamma$ -rays is then obtained by integrating the differential intensity over the region of interest associated with a solid angle  $\Delta\Omega$ :

$$\left. \frac{dn_f}{dE_\gamma} \right|_{\text{prompt}} = \int_{\Delta\Omega} \left. \frac{dn_f}{dE_\gamma d\Omega} \right|_{\text{prompt}} d\Omega. \quad (2.13)$$

In the context of DM searches, the  $\gamma$ -ray flux given in Eq. (2.13) is often expressed as a product of two factors:

$$\left. \frac{dn_f}{dE_\gamma} \right|_{\text{prompt}} = \phi_f^{\text{PP}}(E_\gamma) \times J(\Delta\Omega), \quad (2.14)$$

where  $\phi_f^{\text{PP}}$  contains the information from particle physics through

$$\phi_f^{\text{PP}}(E_\gamma) = \frac{1}{4\pi} \frac{\langle \sigma v \rangle_f}{\eta m_{\text{DM}}^2} \frac{dN_{\gamma,f}}{dE_\gamma}, \quad (2.15)$$

and  $J(\Delta\Omega)$  is referred to as the  $J$ -factor and accounts for the DM profile:<sup>6</sup>

$$J(\Delta\Omega) = \int_{\Delta\Omega} \int_{\text{l.o.s.}} \rho^2(\vec{x}) ds d\Omega. \quad (2.16)$$

For distant targets outside the MW, the  $J$ -factor can be conveniently approximated by

$$J(\Delta\Omega) \approx \frac{1}{d^2} \int_{V_{\Delta\Omega}} \rho^2(\vec{x}) dV_{\Delta\Omega}, \quad (2.17)$$

<sup>5</sup>In the MW, the direction is described by the longitude  $l$  and latitude  $b$  with respect to the GC, see Appendix [A.1.2](#).

<sup>6</sup>We note that in the Milky Way, the  $J$ -factor is computed by normalizing the DM density to  $\rho_\odot$ .

with  $d$  the distance to the target and  $V_{\Delta\Omega}$  the volume of the region associated with  $\Delta\Omega$ .

Considering that the inner part of the DM profile in galaxies is essentially unconstrained, the  $J$ -factor can vary significantly from one profile to another, and depends critically on the inner slope of the profile. This is therefore a major source of uncertainty in DM searches with  $\gamma$ -rays.

### 2.3.3.2 Overview of gamma-ray searches

**Line searches.** In addition to the continuum emission described above, loop-level annihilation of DM particles into  $\gamma X$ —where  $X = \gamma, Z, h$  or an additional new neutral state—would lead to a line in the  $\gamma$ -ray spectrum at  $E_\gamma = m_{\text{DM}}(1 - m_X^2/(4m_{\text{DM}}^2))$ . In particular, for annihilation into two photons, this gives a line at the DM mass. A line feature is held to be a smoking-gun signature of DM, since it cannot be mimicked by astrophysical sources, in which for instance atomic lines are expected to be emitted only up to X-rays, and nuclear lines up to the MeV range. Sharp line-like  $\gamma$ -ray features are also expected to be produced by virtual internal bremsstrahlung, or cascade decays (see [Bringmann & Weniger, 2012](#), and references therein).

For this reason, a tentative  $\gamma$ -ray line at  $\sim 130$  GeV in the *Fermi* data from the GC sparked a lot of excitement in the DM community in 2012 ([Bringmann et al., 2012](#); [Weniger, 2012](#); [Su & Finkbeiner, 2012](#)). Although the line was initially reported with a significance of  $\sim 3\sigma$ , since then the significance has decreased—while it should have increased for a real signal—pointing to a statistical fluke. Moreover, the 130 GeV line was also detected in the  $\gamma$ -ray spectrum of the Earth limb (the edge of the atmosphere), which means that the line would be partly due to instrumental systematics ([Ackermann et al., 2013](#)).

The DM interpretation of the tentative 130 GeV line is even more constrained by the non-detection of  $\gamma$ -ray lines in the H.E.S.S. data at the GC ([Abramowski et al., 2013](#); [Kieffer et al., 2015](#)), or in the *Fermi* data from the GC or the MW halo ([Ackermann et al., 2015d](#)), clusters ([Anderson et al., 2016](#)), and in the MAGIC data from dwarf MW satellites ([MAGIC Collaboration & Ibarra, 2014](#)).

Another very intriguing spectral feature is the 511 keV line at the GC first reported in 1978 in the data of a balloon-borne  $\gamma$ -ray experiment flown over Australia ([Leventhal et al., 1978](#)) and many subsequent experiments, culminating with the SPI spectrometer on board the INTEGRAL satellite ([Jean et al., 2003](#); [Churazov et al., 2005](#); [Knödlseeder et al., 2005](#); [Jean et al., 2006](#); [Weidenspointner et al., 2006](#)). SPI/INTEGRAL observations showed that the line was due to the decay of positronium atoms, but the origin of the electrons and positrons involved is a mystery. The significance of the detection has been reinforced more recently by an analysis of 11 years of INTEGRAL data ([Siegert et al., 2016](#)). The line was suggested to originate from MeV DM ([Boehm et al., 2004c](#)), although this explanation appears to be excluded by the latest CMB and BBN data ([Wilkinson et al., 2016](#)). The origin of the 511 keV line, in light of the associated high luminosity in the Galactic bulge and the spherical symmetry of the dominant component of the emission,<sup>7</sup> remains unexplained.

**Searches for continuum emission from DM.** The continuum prompt emission from DM annihilation and marginally decay has been searched for by the various operating  $\gamma$ -ray telescopes, in different regions of the sky carefully chosen to reach a compromise between high DM density and significant astrophysical backgrounds. Although most searches focus on the model-independent prompt component, in some cases more stringent constraints have been obtained by including secondary  $\gamma$ -rays emitted by electrons and positrons from DM annihilations or decays when interacting with the ISM through inverse Compton scattering or bremsstrahlung. Secondary photon emission from electrons and positrons, and their importance in going further than standard searches, will be discussed in detail in Chapter 4 and subsequent chapters. We now briefly summarize the main searches in the most relevant regions of the sky.

<sup>7</sup>A disk-like component has also been reported.

**Positive signals.** Amid non-detections, several features have emerged that may be hints of DM particles. First, an excess of GeV  $\gamma$ -rays from the GC has been reported in the *Fermi*-LAT data by several groups. This GeV excess will be discussed in detail in Part III, in the context of this thesis. Additionally, see Chapter 10 for the presentation of a hardening in the  $\gamma$ -ray spectrum of the core of the Centaurus A galaxy that we reported in [Brown et al. \(2016\)](#).

**Null results.** Here we give an overview of the studies that have found no significant evidence for a residual signal above backgrounds:

- *Galactic center:* DM annihilation signals have been searched for in the GC region by H.E.S.S., focusing on a  $1^\circ$  region around the GC, excluding the Galactic plane ([Abramowski et al., 2011a](#); [Lefranc & Moulin, 2015](#)). This is a difficult endeavor, considering the potentially large number of unresolved sources like millisecond pulsars (typically  $\sim 10^3$ ) within  $10^\circ$  of the GC, as suggested by point-source analyses ([Lee et al., 2016](#)).
- *Milky Way halo:* The *Fermi*-LAT Collaboration has studied the extended halo of the MW (tens of degrees wide), searching for prompt and IC emission from DM ([Ackermann et al., 2012a](#)).
- *Milky Way satellites:* Satellite galaxies of the MW, which are mainly dwarf spheroidals (dSphs), are prime targets for DM searches since they are expected to be DM-dominated, with low  $\gamma$ -ray backgrounds due to their lack of standard astrophysical sources. Dwarf satellites have been the objects of a significant number of studies, using MAGIC ([MAGIC Collaboration & Ibarra, 2014](#)), H.E.S.S. ([Abramowski et al., 2014](#)), 6 years of *Fermi* data ([Ackermann et al., 2015a](#)), a combined analysis of data from *Fermi* and the Dark Energy Survey (DES) ([Drlica-Wagner et al., 2015](#)), VERITAS ([Zitzer, 2015](#)), and a combination of *Fermi* and MAGIC data ([Rico et al., 2015](#); [MAGIC Collaboration et al., 2016](#)). These studies have resulted in non-detections, cutting deep into the DM annihilation parameter space. Searches with *Fermi*-LAT for DM satellites predicted in DM-only N-body simulations have also yielded null results ([Ackermann et al., 2012b](#)).
- *Globular clusters:* These are dense stellar clusters present in the MW halo. These objects are not DM-dominated but they may have formed in DM subhalos, so that remnants of the progenitor halos can be searched for. In addition, adiabatic contraction of the DM profile induced by baryons may lead to an enhancement of annihilation signals. Such signals have been searched for by H.E.S.S. ([Abramowski et al., 2011b](#)).
- *Galaxy clusters:* They have been scrutinized by *Fermi* ([Ackermann et al., 2010, 2015b](#)), H.E.S.S. ([Abramowski et al., 2012](#)), and VERITAS ([Arlen et al., 2012](#)), searching for evidence for DM annihilation.
- *Isotropic  $\gamma$ -ray background:* Finally, signatures of DM annihilations in halos at all redshifts have been searched for with *Fermi*-LAT in the isotropic gamma-ray background (IGRB), which is the residual in the extragalactic  $\gamma$ -ray background after subtracting resolved extragalactic sources ([Ackermann et al., 2015c](#)).

To summarize the consequences of non-detections, the most stringent constraints on DM particles with masses smaller than  $\sim 1$  TeV come from the 6-year study of dwarfs with *Fermi*-LAT, with upper limits excluding at 95% confidence level the canonical thermal s-wave annihilation cross-section for  $m_{\text{DM}} \lesssim 150$  GeV ([Ackermann et al., 2015a](#)). Above  $\sim 1$  TeV the strongest limits come from the H.E.S.S. study of the GC ([Abramowski et al., 2011a](#); [Lefranc & Moulin, 2015](#)). Concerning light DM, the Imaging Compton Telescope (COMPTEL), sensitive to  $\gamma$ -rays in the 0.8–30 MeV range, was used to exclude candidates with masses in the MeV–GeV range, unless the associated annihilation cross-section is p-wave suppressed ([Boehm et al., 2004a](#)).

**The future of  $\gamma$ -ray observations and DM searches.** Significant increases in sensitivity and resolution (both angular and in energy) are expected thanks to the next generation of IACTs like the Čerenkov Telescope Array (CTA) (see Acharya et al., 2013, and e.g. Wood et al., 2013, for indirect detection prospects), the High Altitude Water Čerenkov Observatory (HAWC, see Abeyssekara et al., 2014; Harding & Dingus, 2015, for DM prospects), and the Large High Altitude Air Shower Observatory (LHAASO). These very powerful instruments will cut deeper into the parameter space of heavy DM. In particular CTA should be able to probe the canonical annihilation cross-section up to a few tens of TeV.

### 2.3.4 Neutrinos

Neutrinos are very good astrophysical probes since they travel unimpeded over very large distances due to their very weak interactions with matter, and therefore point directly to their sources. This is especially interesting in the context of DM indirect detection. DM annihilation (or decay) leads to the production of neutrinos through the same hadronization and decay cascades that produce for instance photons. However, due to the weakness of their interactions, as of today neutrinos can only be detected through the Čerenkov light emitted by the showers of particles (especially muons) that are produced when they interact in the detector or its vicinity.<sup>8</sup> As is the case for  $\gamma$ -rays, the axis of the Čerenkov cone allows the direction of the incoming neutrino to be reconstructed. The main background for neutrino detection comes from atmospheric muons, so just like direct-detection experiments, neutrino detectors are located under ice (IceCube; Abbasi et al., 2011), water (ANTARES, Baikal), or mountains (Super-Kamiokande, Baksan). To further reduce the muon background, these experiments focus on upgoing neutrinos that have traversed the Earth.

So far, searches for DM annihilations from the MW halo by IceCube (Aartsen et al., 2015) and from the GC by ANTARES (Adrián-Martínez et al., 2015) have yielded null results, leading to upper limits on the annihilation cross-section that are starting to be competitive with  $\gamma$ -ray constraints at large DM masses. Prospects for DM detection with the future KM3NeT telescope are discussed in Coyle (2008).

Another promising avenue is to search for DM-induced neutrinos from the center of the Sun (Press & Spergel, 1985; Srednicki et al., 1987; Bouquet et al., 1987). For sufficiently large scattering cross-sections with baryonic matter, DM particles can lose energy and become gravitationally bound, leading to an accumulation of DM in the core of the Sun. Subsequent DM annihilations lead to the production of neutrinos that can escape from the Sun and travel to the Earth unhindered. Therefore, this process probes both DM scattering and annihilation. In the absence of any detection of neutrinos from the center of the Sun, IceCube (Aartsen et al., 2013a), ANTARES (Adrián-Martínez et al., 2013) and Super-Kamiokande (Choi et al., 2015) have been able to set strong constraints mainly on the SD WIMP-proton cross-section, but also competitive constraints on SI interactions. In particular the limits derived from the IceCube results are even more stringent than the LUX ones, as shown in Fig. 2.3, although neutrino constraints are model-dependent since they are obtained for specific assumptions on the annihilation process.

Similarly, the non-detection of neutrinos from annihilation of DM particles captured at the center of the Earth by e.g. IceCube (Kunnen, 2015) constrains the SI scattering cross-section, with great potential for  $m_{\text{DM}} \sim 50$  GeV due to resonant capture on the most abundant elements (Sivertsson & Edsjö, 2012).

Finally, a short comment on the observation of PeV neutrinos by IceCube (Aartsen et al., 2013b) is in order. This discovery opens up a new path to test very heavy DM scenarios. For instance, a decaying PeV DM candidate may be at the origin of these very energetic neutrinos (Murase et al., 2015), and of the hardness of the spectrum of the diffuse isotropic  $\gamma$ -ray background (Eichler et al., 2016).

<sup>8</sup>In the near future, ton-scale direct-detection experiments should become sensitive to neutrino-nucleus coherent scattering, as discussed in Sec. 2.1.

### 2.3.5 Summary

The current status of indirect searches for DM discussed above is summarized in Fig. 2.10, taken from Cirelli (2015). Fig. 2.10 shows the most stringent constraints in the DM annihilation cross-section vs DM mass for the main probes described in this section, namely  $\gamma$ -rays, antiprotons, the CMB and neutrinos. The upper limits are shown for the  $\mu^+\mu^-$ ,  $b\bar{b}$  and  $W^+W^-$  channels, representative of final states containing leptons, quarks and weak gauge bosons respectively. Limits have been rescaled to account for the different assumptions made in their derivation.

This summary plot shows that the natural scale for the DM annihilation cross-section is now probed by several independent methods, and the standard thermal WIMP scenario is starting to be under pressure below  $\sim 100$  GeV for quark final states which arise naturally in the context of supersymmetry.

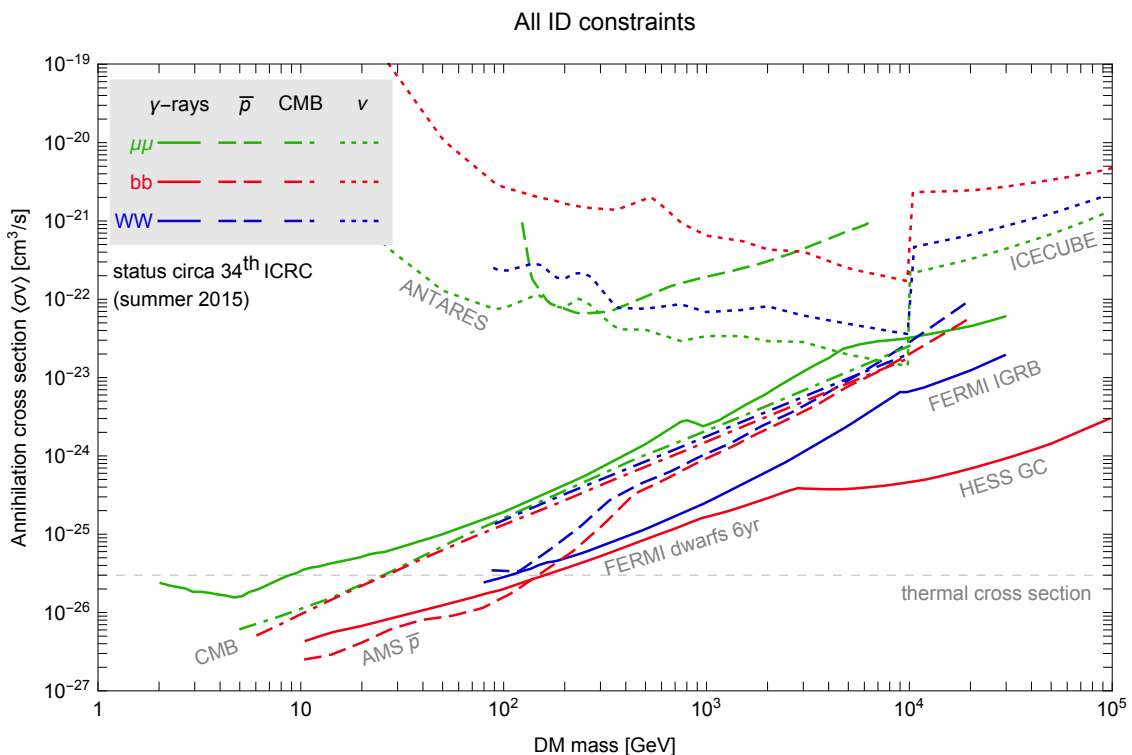


**Figure 2.10** – Summary of the most stringent upper limits on the DM annihilation cross-section vs DM mass (Cirelli, 2015). Some limits have been rescaled to account for the different assumptions e.g. on the DM profile (see Cirelli, 2015, for more details), and conservative limits were used when several results were available.

These bounds correspond to ‘standard’ indirect searches, mostly carried out by large collaborations. Indirect detection has been the object of a wealth of additional more ‘exotic’ studies, which probe different regions of the DM parameter space. For instance DM annihilation or decay can disrupt the standard results of nucleosynthesis in the early Universe, affecting the formation of light chemical elements through e.g. photodissociation (Sarkar, 1996; Jedamzik & Pospelov, 2009).

In this thesis, we go beyond the standard approach, exploring two aspects of indirect searches for DM:

- we perform a detailed study of secondary photon emission from electrons and positrons produced in DM annihilations;
- we explore the phenomenology of supermassive black hole-induced DM spikes—i.e. very strong enhancement of the DM density—at the centers of galaxies.

These aspects will be described in Part II, before presenting the results of the various projects carried out during this thesis. Part III will be dedicated to the *Fermi* GeV excess at the GC, and Parts IV and V to the phenomenology of spikes.

## Part II

# Going beyond standard searches for dark matter particles



## Chapter 3

# Dark matter spikes at the centers of galaxies?

The knowledge of the dark matter density profile in galaxies is crucial to make accurate predictions for indirect searches. However, in spite of tremendous theoretical, numerical and observational progress, the dark matter profile is still plagued by very large uncertainties, especially regarding its inner slope. In this chapter, after giving an overview of the current knowledge on dark matter profiles, we discuss the plausible existence of supermassive black hole-induced dark matter spikes at the centers of galaxies. Dark matter spikes lead to very strong DM signatures in astrophysical observations and are at the heart of this thesis.

### Contents

---

<b>3.1</b>	<b>Dark matter profile in galaxies: a debated picture</b>	<b>54</b>
<b>3.2</b>	<b>Dark matter spike from adiabatic accretion onto a supermassive black hole</b>	<b>56</b>
3.2.1	Scaling relations	56
3.2.2	Semi-analytic derivation using adiabatic invariants	57
<b>3.3</b>	<b>Discussion of competing dynamical effects</b>	<b>59</b>
3.3.1	Instantaneous black hole growth	59
3.3.2	Mergers	59
3.3.3	Off-centered black hole formation	60
3.3.4	Stellar heating	60
3.3.5	Dynamical processes steepening the dark matter profile	61
<b>3.4</b>	<b>Summary</b>	<b>62</b>

---

### 3.1 Dark matter profile in galaxies: a debated picture

In spite of extensive studies both on the observational and simulation sides, there is still no consensus today on the DM profile in galaxies, especially on its inner slope.

Numerical N-body simulations are extremely useful to model the evolution of structures through gravitational clustering. Standard simulations focus on the evolution of DM without including baryonic processes, and are therefore referred to as DM-only simulations. Moreover, they rely on the CDM paradigm. Early results pointed to a universal DM profile following a power law of slope 1 in the central parts of galactic halos, known as the Navarro-Frenk-White (NFW) profile (Navarro et al., 1996a, 1997):

$$\rho_{\text{NFW}}(r) = \rho_0 \left(\frac{r}{r_0}\right)^{-1} \left(1 + \frac{r}{r_0}\right)^{-2}, \quad (3.1)$$

where  $\rho_0$  and  $r_0$  are respectively a scale density and a scale radius. This profile is actually a special case of a more general parametrization (Zhao, 1996; Hernquist, 1990), often referred to as the generalized NFW profile:

$$\rho_{\text{NFW}_{\text{gen}}}(r) = \rho_0 \left(\frac{r}{r_0}\right)^{-\gamma} \left[1 + \left(\frac{r}{r_0}\right)^\alpha\right]^{-\frac{\beta-\gamma}{\alpha}}, \quad (3.2)$$

where  $\alpha$ ,  $\beta$  and  $\gamma$  parametrize the slope. It turns out that several groups have found DM profiles deviating sometimes significantly from the original NFW profile. Typical examples of special cases of the generalized NFW profile with slopes differing from  $\gamma = 1$  are the Moore et al. profile with  $\gamma = 1.5$  (Fukushige & Makino, 1997; Moore et al., 1999b) and the Diemand et al. profile for which  $\gamma = 1.16$  (Diemand et al., 2004). These are all examples of DM *cusps*, i.e. DM profiles following steep power laws towards the center of galactic halos.

Actually, even on the simulation side, the picture is still unclear. In particular, the Einasto profile, which does not follow a power law in the inner region but becomes shallower towards the center, has been emerging as a better parametrization than cusps in more recent numerical simulations (Navarro et al., 2004; Merritt et al., 2006; Springel et al., 2008; Navarro et al., 2010):

$$\rho_{\text{Ein}}(r) = \rho_0 \exp\left(-\frac{2}{\alpha} \left[\left(\frac{r}{r_0}\right)^\alpha - 1\right]\right). \quad (3.3)$$

The value of the  $\alpha$  parameter usually depends on the simulation, but 0.17 has emerged as a benchmark value.

On the other side, observations of galactic rotation curves seem to favor very shallow DM profiles or even constant density *cores* (Burkert, 1995; Kravtsov et al., 1998; Salucci & Burkert, 2000; Borriello & Salucci, 2001; Binney & Evans, 2001; de Blok et al., 2001; de Blok & Bosma, 2002; Simon et al., 2003; Weldrake et al., 2003; Kuzio de Naray et al., 2006; Gentile et al., 2007; Spano et al., 2008; Trachternach et al., 2008; de Blok et al., 2008; Oh et al., 2011), although cusps cannot systematically be ruled out by measurements of rotation curves, depending on the mass of the galaxy (van den Bosch et al., 2000; Swaters et al., 2003). The Kravtsov et al. profile, for which  $\gamma \sim 0.4$  (Kravtsov et al., 1998), is an example of a shallow density profile parametrized by the generalized NFW functional form. Examples of cored profiles are the non-singular isothermal sphere (see e.g. Bahcall & Soneira, 1980; Begeman et al., 1991), which is a special case of the generalized NFW profile with  $\gamma = 0$ , and the Burkert profile (Burkert, 1995):

$$\rho_{\text{Bur}}(r) = \rho_0 \left(1 + \frac{r}{r_0}\right)^{-1} \left[1 + \left(\frac{r}{r_0}\right)^2\right]^{-1}. \quad (3.4)$$

The uncertainty on the DM profile at sub-kpc scales is illustrated in Fig. 3.1 for the case of the MW. The corresponding values of  $\alpha$ ,  $\beta$ ,  $\gamma$  and  $r_0$  for the typical profiles described here are given in Table 3.1, while for each profile  $\rho_0$  is determined by the condition  $\rho(r_\odot) = \rho_\odot$ .

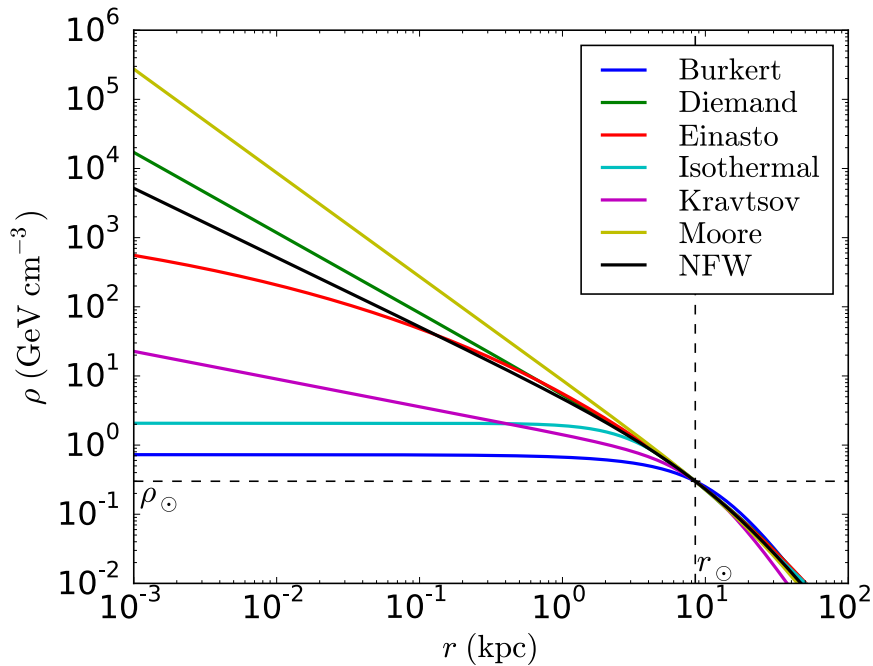


**Figure 3.1** – Illustration of the variety of possible DM profiles on sub-kpc scales in the MW.

The cusp/core controversy is still unresolved, although baryonic feedback may reconcile the results of numerical simulations and observations by reducing the DM density at the center of halos through supernova-driven gas bulk motions and galactic winds (Navarro et al., 1996b; Read & Gilmore, 2005; de Souza et al., 2011; Pontzen & Governato, 2012; Teyssier et al., 2013; Di Cintio et al., 2014). This has a dramatic effect especially for dwarf galaxies, with cusps readily turned into cores. However, this effect seems to depend on the characteristics of galaxies, in particular the stellar-to-halo mass ratio (Di Cintio et al., 2014). Including baryonic physics in simulations is therefore essential but requires to model even more complex processes related for instance to gas dynamics and radiative transfer, which makes such simulations computationally expensive. Moreover, although baryonic processes are likely to have a significant impact on DM profiles, it is not even clear yet whether these processes eventually soften or steepen DM profiles, and this is a matter of debate. In particular, while baryonic feedback seems to flatten DM profiles, adiabatic contraction of baryons has been suggested to produce steeper DM profiles (Blumenthal et al., 1986). On top of that, alternatives to the CDM scenario like self-interacting DM can also address the cusp/core problem, but this has yet to be investigated in more detail in conjunction with baryonic feedback. For a discussion of prospects see e.g. Brooks (2014).

**Table 3.1** – Parameters of the DM profiles shown in Fig. 3.1, based on Bertone et al. (2005); Cirelli et al. (2011).

	$\alpha$	$\beta$	$\gamma$	$r_0$ (kpc)
Burkert	–	–	–	12.67
Diemand	1	3	1.16	30.28
Einasto	0.17	–	–	28.44
Isothermal	2	2	0	3.5
Kravtsov	2	3	0.4	10
Moore	1.5	3	1.5	28
NFW	1	3	1	20

The inner slope of DM profiles is of the utmost importance in indirect searches for DM which

crucially depend on the DM profile via annihilation or decay processes. Uncertainties on the DM profile therefore introduce large systematic uncertainties in DM searches. This problem is made even more severe by the fact that neither numerical simulations nor observations are sensitive to the DM profile below parsec scales, which is of critical importance since the very inner region of galactic halos is critical for indirect DM signals, especially for annihilating DM for which fluxes depend quadratically on the DM density. This is what we focus on in the remainder of this chapter. In particular, we discuss the case for very steep DM profiles in the very inner regions of galaxies induced by the growth of a SMBH at the centers of DM halos.

## 3.2 Dark matter spike from adiabatic accretion onto a supermassive black hole

There is strong evidence for the presence of SMBHs with masses in the range  $M_{\text{BH}} \sim 10^6 - 10^{9.5} M_{\odot}$  at the center of most galaxies (see e.g. [Kormendy & Ho, 2001](#)). In the MW, the determination of the Keplerian orbits of S2 stars very close to the GC provided a measurement of the mass of the central BH, Sgr A\*:  $M_{\text{BH}} \approx 4.3 \times 10^6 M_{\odot}$  ([Gillessen et al., 2009](#)).

BHs at the center of galaxies can grow adiabatically—i.e. slowly compared to the dynamical timescale of order the period of typical orbits on parsec scales—from a small seed, via accretion of gas, stars and DM. It turns out that the adiabatic growth of a BH inside a population of stars was shown to enhance the density of stars ([Peebles, 1972a](#); [Young, 1980](#); [Quinlan et al., 1995](#)). Several authors investigated a similar enhancement in the DM density, referred to as a *spike*, caused by the adiabatic growth of a SMBH in a DM distribution. [Ipser & Sikivie \(1987\)](#) found that a DM spike with density  $\propto r^{-3/2}$  was formed from an initial isothermal DM distribution, while [Gondolo & Silk \(1999\)](#) studied the much more dramatic enhancement of a power-law cusp, which we discuss in the following.

### 3.2.1 Scaling relations

To understand the formation of a spike via adiabatic accretion onto a SMBH, we first make use of the scaling arguments introduced in [Quinlan et al. \(1995\)](#). Let  $\rho_i(r) \propto r^{-\gamma}$  be the initial distribution of DM particles assumed to be on circular orbits, with a BH that grows adiabatically at the center. The slow process of accretion onto this BH induces no torque on the DM particles, so that the angular momentum of each particle is conserved. This results in the conservation of  $rv(r)$ , where  $v(r) = (GM(r)/r)^{1/2}$  is the circular velocity of a DM particle, with  $M(r)$  the total mass (sum of the masses of the DM halo and the BH) enclosed within radius  $r$ . Therefore conservation of angular momentum for a DM particle, with initial and final orbit radii  $r_i$  and  $r_f$  respectively, gives

$$r_i M_i(r_i) = r_f M_f(r_f). \quad (3.5)$$

Additionally, conservation of the DM mass  $M_i^{\text{DM}}(r_i) = M_f^{\text{DM}}(r_f)$  can be expressed as

$$\int_0^{r_i} \rho_i(r) r^2 dr = \int_0^{r_f} \rho_f(r) r^2 dr, \quad (3.6)$$

with  $\rho_f(r) \propto r^{-\gamma_{\text{sp}}}$  the final DM profile, assumed to follow a power law. Eq. (3.6) leads to

$$r_i^{3-\gamma} \propto r_f^{3-\gamma_{\text{sp}}}. \quad (3.7)$$

Moreover, the total mass enclosed in the initial orbit is dominated by the DM halo,  $M_i(r_i) \approx M_i^{\text{DM}}(r_i) \propto r_i^{3-\gamma}$ , while in the final state the orbit of the DM particle is much closer to the BH, so that  $M_f(r_f) \approx M_{\text{BH}}$ . This gives

$$r_i^{4-\gamma} \propto r_f. \quad (3.8)$$

Putting Eqs. (3.7) and (3.8) together, one finds that the final DM density profile has a slope

$$\boxed{\gamma_{\text{sp}} = \frac{9 - 2\gamma}{4 - \gamma}}. \quad (3.9)$$

For  $0 < \gamma < 2$ , corresponding to the range of slopes expected from simulations and/or observations, the slope of the spike lies between 2.25 and 2.5.

It is interesting to note that the slope of a spike strongly depends on the behavior of the initial phase-space distribution (Quinlan et al., 1995), and not only on the spatial density. More specifically, if  $f_i$  diverges for  $E_i = \Phi_i(0)$  as  $f_i \sim (E_i - \Phi_i(0))^{-n}$ , then the final spike profile is

$$\rho_f(r) \propto r^{-A}, \quad A = \frac{3}{2} + n \left( \frac{2 - \gamma}{4 - \gamma} \right). \quad (3.10)$$

For  $\gamma > 0$ , the value of  $n$  is such that one recovers the spike slope of Eq. (3.9), but for  $\gamma \rightarrow 0$ , the final profile is smoother. However, even for a non-singular density profile, the spike slope can be as high as 2. As discussed in Ullio et al. (2001), this can be illustrated by two cored profiles,  $\rho_i(r) \propto (a^2 + r^2)^{-1}$  (isothermal sphere) and  $\rho_i(r) \propto (a + r)^{-2}$ , for which the phase-space distributions are respectively non-singular and singular. The resulting spikes have slopes 1.5 and 2 respectively.

### 3.2.2 Semi-analytic derivation using adiabatic invariants

The scaling result of Eq. (3.9) was confirmed by a more quantitative approach in Gondolo & Silk (1999), relying on the assumption of the adiabatic growth of a BH at the center of a spherically symmetric self-gravitating DM distribution with a profile  $\rho_i(r) \propto \rho_0 (r/r_0)^{-\gamma}$ , with  $\gamma > 0$ .

Under the assumption of adiabaticity, the gravitational potential varies slowly, so that the DM phase-space distribution  $f(E, L)$ , where  $E$  is the energy and  $L$  the angular momentum, is conserved:

$$f_i(E_i, L_i) = f_f(E_f, L_f). \quad (3.11)$$

This is used to derive the final density profile after the growth of the BH:

$$\rho_f(r) = \int_{E_f^{\min}}^0 dE_f \int_{L_f^{\min}}^{L_f^{\max}} dL_f \frac{4\pi L_f}{r^2 v_r} f_f(E_f, L_f), \quad (3.12)$$

where the radial velocity reads

$$v_r = \left[ 2(E - \Phi(r)) - \frac{L^2}{r^2} \right]^{1/2}, \quad (3.13)$$

with  $\Phi$  is the gravitational potential, determined by the Poisson equation  $\nabla^2 \Phi = 4\pi G \rho$ . For the bounds of the energy integral in Eq. (3.12), the contribution of unbound orbits—for which  $E_f > 0$ —is neglected, and  $E_f^{\min} = -GM/r(1 - 4R_S/r)$  where the second term accounts for particles captured by the BH, with  $R_S = 2GM_{\text{BH}}/c^2$  the Schwarzschild radius of the BH. For the angular momentum, the lower bound also accounts for this effect,  $L_f^{\min} = 2cR_S$ , while the upper bound reads  $L_f^{\max} = [2r^2(E_f + GM_{\text{BH}}/r)]^{1/2}$ .

Moreover, in a spherically symmetric system the angular momentum  $L$  and the radial action  $J_r$  are adiabatic invariants:

$$L_i = L_f, \quad J_{r,i}(E_i, L_i) = J_{r,f}(E_f, L_f), \quad (3.14)$$

with

$$J_r(E, L) = \oint v_r dr, \quad (3.15)$$

where the integral is performed over one orbit.

The initial phase-space function  $f_i(E_i, L_i)$  is known, so in order to find the final distribution  $f_f(E_f, L_f)$ , one needs to express  $E_i$  as a function of  $E_f$  using the conservation of the radial action. In the initial state, the radial action is determined by the initial profile  $\rho_i(r) = \rho_0 (r/r_0)^{-\gamma}$ . In the final state, the BH is assumed to dominate the gravitational potential, so  $\Phi_f \approx -GM_{\text{BH}}/r$ . This assumption is justified since we are interested in a region close enough to the BH. Under this assumption, the radial action in the final state can be computed analytically and reads  $J_{r,f}(E_f, L_f) = 2\pi[-L_f + GM_{\text{BH}}(-2E_f)^{-1/2}]$ . The initial radial action can be computed numerically or interpolated (Gondolo & Silk, 1999), and the final result is obtained by performing the double integral in Eq. (3.12). The final profile, valid up to the spike radius  $R_{\text{sp}}$ , is thus given by

$$\rho_{\text{sp}}(r) \equiv \rho_f(r) = \rho_{\text{R}} g_{\gamma}(r) \left( \frac{r}{R_{\text{sp}}} \right)^{-\gamma_{\text{sp}}}, \quad (3.16)$$

where

$$\gamma_{\text{sp}} = \frac{9 - 2\gamma}{4 - \gamma}, \quad R_{\text{sp}} = \alpha_{\gamma} r_0 \left( \frac{M_{\text{BH}}}{\rho_0 r_0^3} \right)^{\frac{1}{3-\gamma}}, \quad \rho_{\text{R}} = \rho_0 \left( \frac{R_{\text{sp}}}{r_0} \right)^{-\gamma}. \quad (3.17)$$

The factor  $g_{\gamma}(r)$  which accounts for capture of DM particles by the BH, and the normalization  $\alpha_{\gamma}$ , are found numerically:  $g_{\gamma}(r) \approx (1 - 4R_{\text{S}}/r)^3$ ,  $\alpha_{\gamma} \approx 0.293\gamma^{4/9}$  for  $\gamma \ll 1$  and  $\alpha_{\gamma} \approx 0.1$  for  $\gamma \sim 1$ .

However, it turns out that for annihilating DM, there is a maximal density at the center, which we refer to as the saturation density, determined by the Boltzmann equation  $\partial\rho/\partial t = -\langle\sigma v\rangle\rho^2/m_{\text{DM}}$ :

$$\rho_{\text{sat}} = \frac{m_{\text{DM}}}{\langle\sigma v\rangle t_{\text{BH}}}, \quad (3.18)$$

where  $t_{\text{BH}}$  is the age of the BH, which is conservatively of the order of the age of the Universe  $\sim 10^{10}$  yr. The resulting profile has a saturation plateau of radius

$$r_{\text{sat}} = R_{\text{sp}} \left( \frac{\rho_{\text{sp}}(R_{\text{sp}})}{\rho_{\text{sat}}} \right)^{1/\gamma_{\text{sp}}}. \quad (3.19)$$

Therefore the global DM profile in the presence of an adiabatic spike is given by<sup>1</sup>

$$\rho(r) = \begin{cases} 0 & r < 4R_{\text{S}} \\ \frac{\rho_{\text{sp}}(r)\rho_{\text{sat}}}{\rho_{\text{sp}}(r) + \rho_{\text{sat}}} & 4R_{\text{S}} \leq r < R_{\text{sp}} \\ \rho_{\text{halo}}(r) & r \geq R_{\text{sp}}, \end{cases} \quad (3.20)$$

with  $\rho_{\text{halo}}(r) \propto \rho_0 (r/r_0)^{-\gamma}$ . In practice in this work we often take the spike radius  $R_{\text{sp}}$  as a free parameter, considering the uncertainties affecting the spike, as discussed in Sec. 3.3.

The case of the MW is illustrated in Fig. 3.2 for various initial halo profiles, namely a non-singular isothermal sphere, leading to a spike slope  $\gamma_{\text{sp}} = 1.5$ , and power-law profiles with  $\gamma = 0.01, 0.1, 1, 2$ , leading to spike slopes  $\gamma_{\text{sp}}$  between 2.25 and 2.5. Additionally, the saturation plateau due to DM annihilations is shown, for  $\rho_{\text{sat}} = 10^8 M_{\odot} \text{pc}^{-3}$ , corresponding to  $m_{\text{DM}} = 50 \text{ GeV}$  and  $\langle\sigma v\rangle = 3 \times 10^{-26} \text{ cm}^3 \text{ s}^{-1}$ .

Throughout this work we consider the halo profile outside the spike to be given by the NFW profile, corresponding to a power law with slope  $\gamma = 1$  below kpc scales:

$$\rho_{\text{halo}}(r) = \rho_0 \left( \frac{r}{r_0} \right)^{-1} \left( 1 + \frac{r}{r_0} \right)^{-2}, \quad (3.21)$$

<sup>1</sup>The cut-off at  $4R_{\text{S}}$  was introduced in Gondolo & Silk (1999) to account for capture of DM particles by the BH, without using a full general relativistic treatment. When considering the Schwarzschild metric, the inner cut-off becomes  $2R_{\text{S}}$  (Sadeghian et al., 2013), so the spike can in principle reach smaller radii.

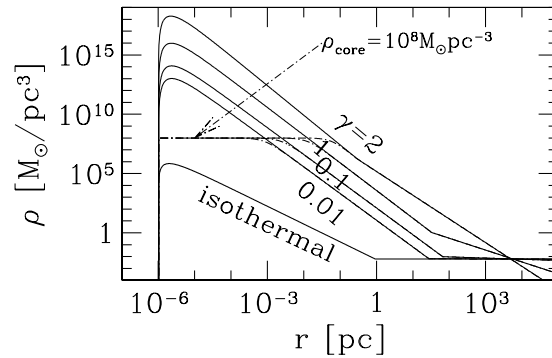


**Figure 3.2** – Examples of spike profiles in the inner region of the MW, grown from various initial halo profiles, namely a non-singular isothermal sphere, leading to a spike slope  $\gamma_{\text{sp}} = 1.5$ , and power-law profiles with  $\gamma = 0.01, 0.1, 1, 2$ , leading to spike slopes  $\gamma_{\text{sp}}$  between 2.25 and 2.5. DM annihilation limits the density at the center. For  $m_{\text{DM}} = 50$  GeV and  $\langle\sigma v\rangle = 3 \times 10^{-26}$  cm<sup>3</sup> s<sup>-1</sup>, the maximal DM density is  $\rho_{\text{core}} \equiv \rho_{\text{sat}} = 10^8 M_{\odot} \text{pc}^{-3}$ . Figure from [Gondolo & Silk \(1999\)](#).

with a scale radius  $r_0 = 20$  kpc and  $\rho_0$  determined in the Milky Way by the condition  $\rho_{\text{halo}}(r_{\odot}) = \rho_{\odot}$ , where we take  $\rho_{\odot} = 0.3$  GeV cm<sup>-3</sup> ([Bovy & Tremaine, 2012](#)). For  $\gamma = 1$ , the spike slope is  $\gamma_{\text{sp}} = 7/3$ , which we use as a benchmark value.

### 3.3 Discussion of competing dynamical effects

The existence of DM spikes is however debated since they can be significantly affected by dynamical effects, which have been neglected in the standard derivation presented in Sec. 3.2. Moreover, the simplified adiabatic spike model assumes that the BH formed exactly at the center of the DM halo. We now discuss the effect of relaxing these assumptions.

#### 3.3.1 Instantaneous black hole growth

If the growth of the BH was instantaneous, i.e. happened too fast to be considered adiabatic, then the inner DM energy density profile would behave instead as  $\rho(r) \propto r^{-4/3}$  ([Ullio et al., 2001](#)). The physical reason is the following. For sudden BH growth, the final orbit of a DM particle is a very eccentric ellipse, whereas in the adiabatic scenario the final orbit is circular, with a much smaller radius than the initial orbit. Therefore, adiabatic growth of the BH results in DM particles spending most of their time close to the BH—leading to a very strong enhancement of the DM density in the inner region—, while in the case of instantaneous growth of the BH, due to their elliptical orbits DM particles spend most of their time at larger radii than in the adiabatic case, which leads to a shallower DM profile.

#### 3.3.2 Mergers

Mergers between halos containing SMBHs can also destroy DM spikes. Such mergers create SMBH binaries which induce a kinetic heating of DM particles, expelling them from the central region. Numerical simulations show that this process leads to a much shallower power-law density profile  $\rho(r) \propto r^{-1/2}$  ([Merritt et al., 2002](#)).

However, the MW is unlikely to have suffered such mergers in its recent past, as evidenced by the quiet history of the thick disk since the only major merger which occurred about 12 Gyr ago and is likely to have led to the formation of the bulge and the SMBH ([Wyse, 2001](#)). In the end, the formation of spikes is closely related to the history of a galaxy, which implies that spikes may at least have formed in some galaxies.

As a matter of fact, the resolution of the simulations used to derive the  $r^{-1/2}$  profile was not sufficient to study sub-parsec scales, so the picture may actually change in the very inner region which turns out to be the most interesting in terms of spikes and annihilation signals.

### 3.3.3 Off-centered black hole formation

Additionally, the SMBH may not have formed exactly at the center of the DM halo, but may have grown instead from a BH seed brought in by a merger of progenitor halos, and then spiraled in to the center. The effect on the DM profile depends on the mass of the seed  $M_{\text{BH}}^{\text{S}}$ . On the one hand, if the seed is massive, i.e. a sizable fraction of the final BH mass, typically  $M_{\text{BH}}^{\text{S}} \gtrsim M_{\text{BH}}/10$ , then the spiral-in to the center results in a weak cusp  $\rho(r) \propto r^{-1/2}$  (Nakano & Makino, 1999; Ullio et al., 2001) regardless of the initial halo profile. On the other hand, adiabatic growth of a low-mass seed with typically  $M_{\text{BH}}^{\text{S}} \gtrsim 10^{-2} M_{\text{BH}}$  leads to a strong enhancement of the DM density at the center, with the  $r^{-1/2}$  weak cusp appearing only at very small radii. For the MW, the resulting profile for an initial NFW profile is essentially indistinguishable from the adiabatic spike if the saturation density due to DM annihilation is  $\gtrsim 10^8 M_{\odot} \text{pc}^{-3}$ , as illustrated in Fig. 3.3.

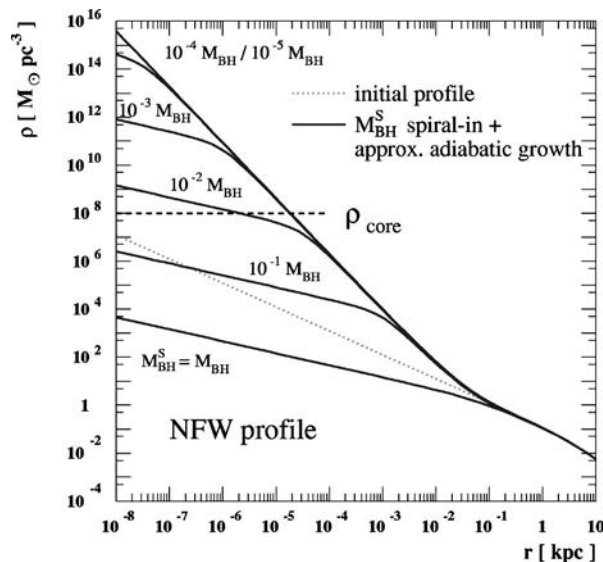


**Figure 3.3** – Effect of an off-centered BH seed of mass  $M_{\text{BH}}^{\text{S}}$  which spirals in to the center and grows adiabatically to the present-day mass of the SMBH  $M_{\text{BH}}$  on an initial NFW halo profile in the MW. Figure from Ullio et al. (2001).

However, as discussed in Ullio et al. (2001), due to the low efficiency of dynamical friction, a low-mass BH seed does not have enough time to spiral in, unless it formed close enough to the center of the DM distribution, typically within 50 pc of the GC for the MW.

### 3.3.4 Stellar heating

Finally, even if an adiabatic spike with  $\gamma_{\text{sp}} = (9 - 2\gamma)/(4 - \gamma)$  could form, the process of dynamical relaxation by DM scattering off stars can smooth down the spike and lead to a DM equilibrium profile,  $\rho(r) \propto r^{-3/2}$  (Gnedin & Primack, 2004; Merritt, 2004). The detailed study of the time evolution of a spike performed in Merritt (2004) suggests that stellar heating should reduce the spike slope to  $\gamma_{\text{sp}} \sim 1.8$  after  $\sim 10$  Gyr, down to the equilibrium value of  $3/2$  after  $\sim 20$  Gyr.

However, this effect varies significantly from one galaxy to another, depending on the dynamical properties of the stellar core (Vasiliev & Zelnikov, 2008), which are defined in terms

of the dynamical relaxation time (Binney & Tremaine, 1987)

$$t_r = \frac{0.34\sigma^3}{G^2 m_* \rho_* \ln \Lambda}, \quad (3.22)$$

where  $\sigma$  is the velocity dispersion of the stellar population,  $m_* \approx M_\odot$  is the typical mass of stars,  $\rho_*$  the stellar mass density and  $\ln \Lambda \approx 15$  the standard Coulomb logarithm. We can relate the relaxation time in the sphere of gravitational influence of the BH using simple scaling relations. First of all the radius of gravitational influence of the BH is defined by (Peebles, 1972b)

$$r_h = \frac{GM_{\text{BH}}}{\sigma^2}. \quad (3.23)$$

Moreover, the velocity dispersion is tightly correlated with the mass of the central BH, via the  $M_{\text{BH}}-\sigma$  relation (Ferrarese & Ford, 2005):

$$M_{\text{BH}} \approx 5.72 \times 10^6 M_\odot \left( \frac{\sigma}{100 \text{ km s}^{-1}} \right)^{4.86}. \quad (3.24)$$

The gravitational influence radius can therefore be expressed as

$$r_h \approx 2 \text{ pc} \left( \frac{M_{\text{BH}}}{4.3 \times 10^6 M_\odot} \right)^{0.59}. \quad (3.25)$$

To order of magnitude, the density of stars within  $r_h$  is  $\rho_* \sim M_*(r_h)/r_h^3$  and the stellar mass  $M_*(r_h)$  within the sphere of influence of the BH is of order  $M_{\text{BH}}$ . As a result, the dynamical relaxation time within  $r_h$  is given to good approximation by

$$t_r \sim 2 \times 10^9 \text{ yr} \left( \frac{M_{\text{BH}}}{4.3 \times 10^6 M_\odot} \right)^{1.4}. \quad (3.26)$$

The relaxation time for  $r < r_h$  turns out to be essentially independent of  $r$  (see e.g. Merritt, 2004).

Consequently, for the MW which harbors a SMBH of mass  $M_{\text{BH}} = 4.3 \times 10^6 M_\odot$ , the relaxation time  $t_r \sim 2$  Gyr is smaller than the age of the Universe given by the Hubble time  $H_0^{-1} \sim 10^{10}$  yr. Therefore the effect of stellar heating of a DM spike at the GC cannot be ruled out a priori, although the spike may not have had enough time to relax to the equilibrium profile with slope  $3/2$ , as discussed in Merritt (2004).

However, as shown by Eq. (3.26), galaxies with much bigger central BHs than Sgr A\* are dynamically young. This is perfectly illustrated by the giant elliptical galaxy radio galaxy M87 which harbors a central SMBH of mass  $M_{\text{BH}} = 6.4 \times 10^9 M_\odot$  (Gebhardt & Thomas, 2009). Therefore, the relaxation time in the core of M87 is of order  $t_r \sim 10^5$  Gyr which is much larger than the age of the Universe, so M87 is dynamically young. As a result, a spike formed at early times is much more likely to have survived dynamical heating up to the present epoch in M87 than in the MW.<sup>2</sup> Consequently, M87 is a very promising target for searches for annihilation signals from DM spikes and we devote it a significant part of this thesis.

### 3.3.5 Dynamical processes steepening the dark matter profile

We now review other dynamical processes that can have the opposite effect of making the DM profile steeper, potentially strengthening the case for the formation and survival of adiabatic spikes.

<sup>2</sup>A similar result was found in Vasiliev & Zelnikov (2008) for other galaxies like dwarfs.

### 3.3.5.1 Baryonic processes steepening the dark matter profile

Here we discuss mechanisms by which baryons can increase the central DM density, and whether these processes can support the survival of spikes.

**Adiabatic contraction of baryons.** Dissipative infall of baryons at the center of a galaxy can be modeled as an adiabatic contraction process and has been shown to enhance the DM density (Blumenthal et al., 1986). Therefore a priori this tends to go in the direction of the adiabatic DM spike. However, as discussed in Ullio et al. (2001), adiabatic contraction of baryons only enhances the DM density at intermediate scales, i.e. from a few pc to a few kpc, while small scales remain dominated by the BH. Therefore this effect does not dramatically affect the central spike.

**Collisional regeneration of DM cusps.** Stellar heating, which can smooth out a DM spike as discussed previously, can also steepen the DM profile after depletion of the central region by a merger (Merritt et al., 2007), provided the galaxy is old enough to have formed a Bahcall-Wolf stellar cusp  $\rho_* \propto r^{-7/4}$  via two-body relaxation (Bahcall & Wolf, 1976). This is referred to as collisional regeneration, which leads to the formation of an equilibrium cusp again with  $\rho(r) \propto r^{-3/2}$ , still shallower than the adiabatic spike.

### 3.3.5.2 Other effects strengthening the case for DM spikes

Several possibilities may lead to a significant increase in the mass of stars and DM in the central region to large values, possibly up to  $M_{\text{BH}}$ , thus making the survival of a spike more likely:

- DM self-interactions, which would initially reduce the density but eventually lead the galactic core to collapse (Ostriker, 2000);
- efficient replenishment of the loss cone, i.e. the cone of orbits that lead to capture by the BH, from a stellar cusp with  $\rho(r) \propto r^{-2}$  (Zhao et al., 2002);
- if the potential in the central region is not axisymmetric but triaxial, stars are mostly on box orbits and thus pass near the central BH much more often than in the axisymmetric case, which leads to chaotic orbits and eventually to enhanced stellar feeding rates of the BH (Norman & Silk, 1983; Gerhard & Binney, 1985). This may also lead to enhanced accretion of DM to counteract the depopulation of chaotic orbits (Merritt & Poon, 2004).

## 3.4 Summary

The DM profile in the very inner region of galaxies is shaped by many competing processes. In particular, there is a complex interplay of baryons and DM. Therefore, although the existence of SMBH-induced DM spikes at the centers of galaxies is debated, in light of our discussion it is very plausible and does not necessarily require finely tuned conditions. More dedicated numerical simulations accounting for as many of these processes as possible would greatly help to assess more quantitatively the probability of formation and survival of DM spikes in galaxies.

With the advent of high angular resolution telescopes from the radio to  $\gamma$ -ray bands, it is now possible to explore the phenomenology of DM spikes in the context of annihilating DM particles, as discussed e.g. in Gondolo & Silk (1999); Bertone et al. (2001, 2002); Aloisio et al. (2004); Regis & Ullio (2008); Belikov et al. (2012); Belikov & Silk (2014) for the case of the MW, and in our work as discussed in the following chapters. Most of this thesis is devoted to studying the phenomenology and observability of spikes, at the GC but also in other galaxies which are essentially unexplored in this regard. This allows us to go beyond standard searches for DM.

## Chapter 4

# Photon emission from electrons and positrons

Standard indirect searches for DM with photons focus on prompt  $\gamma$ -ray emission from DM annihilations. However, electrons and positrons are also produced in DM annihilations and actually lead to very interesting signatures through secondary photon emission processes resulting from their interaction with the interstellar medium. In this chapter we provide the technical background of this thesis regarding the modeling of secondary photon emission from electrons and positrons, from the transport equation to emission spectra, through energy losses.

### Contents

---

<b>4.1</b>	<b>Radiative processes</b>	<b>64</b>
<b>4.2</b>	<b>Flux of secondary photons</b>	<b>64</b>
4.2.1	Differential photon intensity	64
4.2.2	Volume emissivity	65
4.2.3	Emission spectrum	65
4.2.4	Example: power-law $e^\pm$ spectrum	71
<b>4.3</b>	<b>Electron/positron spectrum <math>\psi</math> accounting for propagation</b>	<b>72</b>
4.3.1	Physical processes at play	72
4.3.2	Transport equation	72
4.3.3	Diffusion zone and parameters	73
4.3.4	A qualitative picture of spatial diffusion	74
4.3.5	Energy loss rate	75
4.3.6	Electron/positron spectrum for negligible spatial diffusion	78
4.3.7	Electron/positron spectrum in the presence of spatial diffusion	79

---

## 4.1 Radiative processes

Accelerated charged particles radiate photons, and we now briefly overview the physical processes by which electrons and positrons, injected by DM annihilation or other astrophysical sources, emit high-energy photons (for a review see e.g. [Rybicki & Lightman, 1979](#); [Longair, 2011](#)):

- *Inverse Compton scattering*: the scattering process between an electron and a photon is generally known as Compton scattering. More specifically, Compton scattering actually refers to the case in which a high-energy photon transfers energy and momentum to a stationary electron.<sup>1</sup> However, the process of interest in the context of this work is inverse Compton scattering, in which a high-energy electron scatters a low-energy photon of the interstellar radiation field (ISRF) to high energies. Although strictly speaking inverse Compton scattering does not produce a new photon, the energy of the low-energy photon of the interstellar radiation field increases significantly, so that in practice this is equivalent to the production of a new high-energy photon.<sup>2</sup>
- *Bremsstrahlung*: electrons also emit photons by interacting with atoms and ions of the interstellar gas via Coulomb scattering. This process is referred to as bremsstrahlung (i.e. braking radiation). This process can actually be considered as an inverse Compton scattering process, with a virtual photon corresponding to the Coulomb field of the particle (atom, ion or electron) scattering the incoming high-energy electron.
- *Synchrotron radiation*: by interacting with the ambient magnetic field, high-energy electrons and positrons radiate photons: this is known as the synchrotron process. It can also be seen as the inverse Compton scattering of virtual photons associated with the magnetic field.

## 4.2 Flux of secondary photons

In this section, we describe the procedure used to compute fluxes of photons radiated by electrons and positrons injected in the interstellar medium.

### 4.2.1 Differential photon intensity

For any radiative process, in the absence of absorption,<sup>3</sup> the differential intensity or energy spectrum of photons isotropically radiated through the solid angle  $d\Omega$  is evaluated by integrating the volume emissivity  $j$  for the process of interest (power per unit volume and energy) over the line of sight (l.o.s.) coordinate  $s$  (see e.g. [Rybicki & Lightman, 1979](#), for a textbook presentation of radiative transfer). Therefore, the differential energy spectrum for IC scattering or bremsstrahlung reads

$$\boxed{\left. \frac{dn}{dE_\gamma d\Omega} \right|_{\text{IC,brems}}} = \frac{1}{E_\gamma} \int_{\text{l.o.s.}} \frac{j_{\text{IC,brems}}(E_\gamma, \vec{x})}{4\pi} ds, \quad (4.1)$$

which is a number of photons per unit surface, time, energy and solid angle.  $\vec{x}$  is the position in the galaxy and  $E_\gamma$  the photon energy. The differential energy spectrum is usually multiplied by  $E_\gamma^2$  to obtain a power per unit surface and solid angle.

For synchrotron radiation—which usually involves lower photon energies than IC and bremsstrahlung—it is customary to express the emissivity in terms of the emitted photon frequency  $\nu$ , related to the photon energy via  $E_\gamma = h\nu$ . The synchrotron emissivity  $j_{\text{syn}}$  is written

<sup>1</sup>In the simpler Thomson scattering process, the photon is scattered without change of energy.

<sup>2</sup>Of course at the same time the low-energy background is depleted of one photon.

<sup>3</sup>Absorption will be discussed whenever it is relevant.

as a power per unit volume and frequency and the equivalent of the differential spectrum is the specific intensity  $I_\nu$  at photon frequency  $\nu$ , which reads:

$$I_{\nu,\text{syn}} = \int_{\text{l.o.s.}} \frac{j_{\text{syn}}(\nu, \vec{x})}{4\pi} ds. \quad (4.2)$$

For any radiative process, the specific intensity turns out to be equivalent to the differential spectrum, with the following relation between these two quantities:

$$\nu I_\nu = E_\gamma^2 \frac{dn}{dE_\gamma d\Omega}. \quad (4.3)$$

The differential spectrum is commonly used in the context of  $\gamma$ -rays, while the specific intensity appears more naturally when considering multi-wavelength spectral energy distributions involving the radio band.

### 4.2.2 Volume emissivity

The emissivity is obtained by convolving the  $e^\pm$  spectrum  $\psi$  (number density per unit energy) and the emission spectrum  $P$ , i.e. the differential power radiated into photons (radiated power per unit photon energy or frequency), for the radiative process of interest (see e.g. Longair, 2011; Rybicki & Lightman, 1979):

$$j_{\text{IC,brems}}(E_\gamma, \vec{x}) = N_e \int_{E_\gamma}^{E_e^{\text{max}}} P_{\text{IC,brems}}(E_\gamma, E_e, \vec{x}) \psi(E_e, \vec{x}) dE_e, \quad (4.4)$$

$$j_{\text{syn}}(\nu, \vec{x}) = N_e \int_{m_e}^{E_e^{\text{max}}} P_{\text{syn}}(\nu, E_e, \vec{x}) \psi(E_e, \vec{x}) dE_e. \quad (4.5)$$

The  $N_e$  factor—equal to 2 in all the cases of interest in this work—accounts for the contribution of both positrons and electrons. In particular a positron is always simultaneously produced with an electron in DM annihilations.  $E_e^{\text{max}}$  is the maximum energy of the  $e^\pm$  distribution. For DM annihilation, and in the absence of acceleration processes,  $E_e^{\text{max}} = m_{\text{DM}}$ . The lower bounds of the integrals in Eqs. (4.4) and (4.5) are determined by kinematics. For the IC and bremsstrahlung processes, the radiated photon cannot carry away more than the energy of the incoming electron, so the minimum  $e^\pm$  energy is essentially the energy of the emitted photon  $E_\gamma$ . For synchrotron radiation, the emitted photon has a much smaller energy than the electron, so in principle the lower bound is  $m_e$ , although in practice the lower bound is set by the cut-off in the synchrotron emission spectrum (see Sec. 4.2.3.3).

The main two ingredients necessary to compute the emissivity are therefore:

- the  $e^\pm$  spectrum  $\psi$ . We describe how  $\psi$  is shaped by propagation in the interstellar medium in Sec. 4.3;
- the emission spectrum for the radiative process of interest, which we discuss in Sec. 4.2.3.

### 4.2.3 Emission spectrum

The derivation of the emission spectrum for IC scattering, bremsstrahlung and synchrotron is fairly cumbersome. Therefore, we refer the reader to the thorough treatment presented in Blumenthal & Gould (1970) and we provide the important formulas that are used throughout this thesis. We consider highly relativistic electrons and positrons, which have  $\gamma_e \gg 1$ .

### 4.2.3.1 Inverse Compton scattering

**General results.** For IC scattering, we summarize the main elements of the derivation presented in [Blumenthal & Gould \(1970\)](#), following the reformulation presented in [Cirelli & Panci \(2009\)](#). The IC isotropic emission spectrum for an electron of energy  $E_e$  is given by the rate  $dN/(dt dE_\gamma^0 dE_\gamma)$  of scattering on background photons of energy  $E_\gamma^0$  into photons of energy  $E_\gamma$ , times the energy exchanged in a scattering  $E_\gamma - E_\gamma^0$ , integrated over all initial photon energies :

$$P_{\text{IC}}(E_\gamma, E_e, \vec{x}) = \int (E_\gamma - E_\gamma^0) \frac{dN}{dt dE_\gamma^0 dE_\gamma} dE_\gamma^0. \quad (4.6)$$

The scattering rate is computed from the full scattering cross-section and reads

$$\frac{dN}{dt dE_\gamma^0 dE_\gamma} = \frac{3\sigma_{\text{TC}}}{4\gamma_e^2} \frac{n(E_\gamma^0, \vec{x})}{E_\gamma^0} \left[ 2q \ln q + q + 1 - 2q^2 + \frac{1-q}{2} \frac{(\Gamma q)^2}{1+\Gamma q} \right], \quad (4.7)$$

with

$$\Gamma = \frac{4\gamma_e E_\gamma^0}{m_e c^2}, \quad q = \frac{\epsilon}{\Gamma(1-\epsilon)}, \quad \epsilon = \frac{E_\gamma}{E_e}. \quad (4.8)$$

In Eq. (4.7),  $n(E_\gamma^0, \vec{x})$  is the sum of the number densities per unit energy for the different components of the background photon bath. The kinematics of the scattering process leads to the following bounds for the final photon energy  $E_\gamma$ :

$$E_\gamma^0 \leq E_\gamma \leq E_e \frac{\Gamma}{1+\Gamma}, \quad (4.9)$$

which implies for  $q$ :

$$\frac{1}{4\gamma_e} \leq q \leq 1, \quad (4.10)$$

with  $1/(4\gamma_e) \ll 1$  in the relativistic regime that we consider here. The initial photon energy can be rewritten in terms of  $q$ ,

$$E_\gamma^0(q) = \frac{E_\gamma}{4q\gamma_e^2(1-\epsilon)}, \quad (4.11)$$

and this relation is used as a change of variable to rewrite the integral over  $E_\gamma^0$  in Eq. (4.6). The general result for the IC emission spectrum reads (in terms of  $\epsilon$  instead of  $\Gamma$ )

$$P_{\text{IC}}(E_\gamma, E_e, \vec{x}) = \frac{3\sigma_{\text{TC}}}{4\gamma_e^2} \int_{1/4\gamma_e^2}^1 (E_\gamma - E_\gamma^0(q)) \frac{n(E_\gamma^0(q), \vec{x})}{q} \times \left[ 2q \ln q + q + 1 - 2q^2 + \frac{1}{2} \frac{\epsilon^2}{1-\epsilon} (1-q) \right] dq. \quad (4.12)$$

An interesting regime is defined by the Thomson limit in which the energy of the initial photon in the electron rest frame is much smaller than the electron mass. This corresponds to  $\Gamma \ll 1$ , which also translates into  $\epsilon \ll 1$ . In that case, the photon energy is unchanged by the scattering. The  $q$  variable is replaced by  $y = E_\gamma/(4\gamma_e^2 E_\gamma^0)$ , and the emission spectrum is given in the Thomson regime by

$$P_{\text{IC}}^{\text{Th}}(E_\gamma, E_e, \vec{x}) = \frac{3\sigma_{\text{TC}}}{4\gamma_e^2} E_\gamma \int_0^1 \frac{n(E_\gamma^0(y), \vec{x})}{y} [2y \ln y + y + 1 - 2y^2] dy. \quad (4.13)$$

The Thomson limit is valid for not too high-energy electrons, typically below 100 GeV. For very high energy electrons, i.e. when  $\Gamma$  becomes of order 1, Klein-Nishina corrections corresponding to the last term in the integrand in Eq. (4.12) start to become important. The main characteristics of the IC spectrum can be understood in the Thomson regime. Klein-Nishina corrections must be included, but they only significantly change the picture at very high energies.

**Emission spectrum and interstellar radiation field.** In order to get some insight, a simpler formula can be obtained for the emission spectrum in the Thomson limit, by considering a monochromatic background radiation field with energy  $E_0$ . For simplicity we disregard the spatial dependence of the radiation field. The number density per unit energy of background photons can thus be written in terms of a delta function in energy:

$$n(E_\gamma^0(y), \vec{x}) = n_0 \delta(E_\gamma^0(y) - E_0), \quad (4.14)$$

with  $n_0$  a normalization factor corresponding to the number density. This can be reformulated in terms of  $y$ , so that the IC emission spectrum in the Thomson limit and for a monochromatic background radiation field reads

$$P_{\text{IC,mono}}^{\text{Th}} = 3\sigma_{\text{T}}cn_0 \frac{E_\gamma}{4\gamma_e^2 E_0} f_{\text{IC}}\left(\frac{E_\gamma}{4\gamma_e^2 E_0}\right), \quad (4.15)$$

where  $f$  characterizes the spectrum in the Thomson limit:

$$f_{\text{IC}}(y) = 2y \ln y + y + 1 - 2y^2. \quad (4.16)$$

The resulting emission spectrum is shown in Fig. 4.1. It peaks around  $y \sim 1$ , which means that the energy of the scattered photon is given by  $E_\gamma \sim \gamma_e^2 E_0$ .

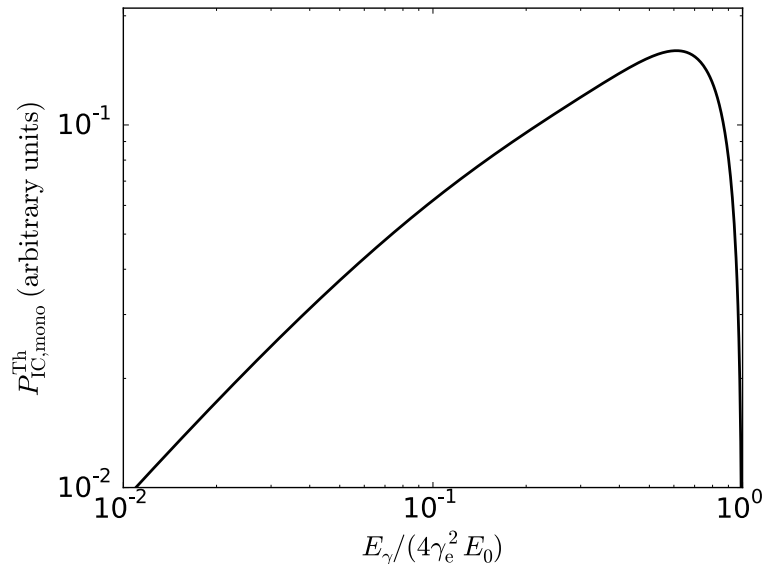


**Figure 4.1** – IC emission spectrum in the Thomson limit, for a monochromatic background photon field. The spectrum peaks at  $E_\gamma \sim \gamma_e^2 E_0$ , where  $E_0$  is the energy of background photons.

In reality, the background radiation field is not monochromatic but consists of several components: the CMB, optical (and possibly UV) stellar radiation and IR photons from absorbed and reprocessed UV radiation by dust. The photon number density at the GC as a function of energy, based on maps provided in the GALPROP cosmic-ray propagation code (Vladimirov et al., 2011; Porter et al., 2008), is shown in Fig. 4.2. As discussed in Sec. 4.3.5.1, where we describe the derivation of energy losses, most of the time we use GALPROP as a reference for the properties of the interstellar medium.

The CMB has a blackbody spectrum, while for the other components this is only an approximation, which nevertheless works fairly well (Cirelli & Panci, 2009). This turns out to be very useful when computing the IC energy loss rate, since it allows for an analytic computation (Sec. 4.3.5.1). The emission spectrum for a realistic component of the ISRF still peaks around  $E_\gamma \sim \gamma_e^2 E_0$ , but is broader than in the monochromatic case. However, the monochromatic case illustrates the main characteristics of the emission from a given component of the photon field.

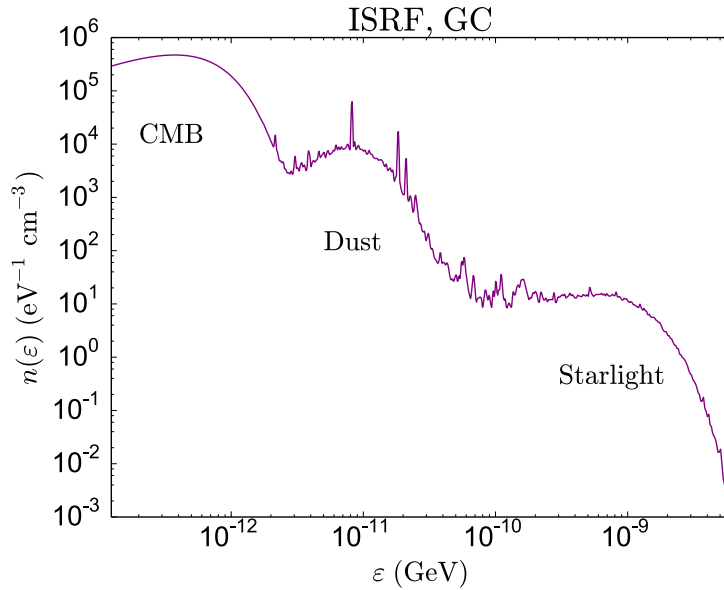


**Figure 4.2** – ISRF spectrum at the GC, extracted from GALPROP, showing the contributions from the CMB, IR emission from dust, and starlight.

#### 4.2.3.2 Bremsstrahlung

The bremsstrahlung emission spectrum is the sum of the contributions from neutral and ionized gas, and reads (see [Blumenthal & Gould, 1970](#), and e.g. [Cirelli et al., 2013](#), for a reformulation):

$$P_{\text{brems}}(E_\gamma, E_e, \vec{x}) = cE_\gamma \sum_a n_a(\vec{x}) \frac{d\sigma_a}{dE_\gamma}(E_\gamma, E_e), \quad (4.17)$$

where  $a$  runs over the species of interest, and the differential cross section is given by

$$\frac{d\sigma_a}{dE_\gamma}(E_\gamma, E_e) = \frac{3\alpha_{\text{em}}\sigma_{\text{T}}}{8\pi E_\gamma} \left[ \left( 1 + \left( 1 - \frac{E_\gamma}{E_e} \right)^2 \right) \phi_{1,a} - \frac{2}{3} \left( 1 - \frac{E_\gamma}{E_e} \right) \phi_{2,a} \right], \quad (4.18)$$

with  $\alpha_{\text{em}}$  the fine structure constant.  $\phi_{1,a}$  and  $\phi_{2,a}$  are scattering functions that characterize the scattering system. The interstellar medium is mostly composed of neutral hydrogen (atomic HI and molecular H<sub>2</sub>). In the MW, helium (He) contributes at the level of about 10% of hydrogen ([Asplund et al., 2006](#); [Cirelli et al., 2013](#)). Finally, ionized hydrogen (HII) is also present but is only important in the context of large scale emission ([Cirelli et al., 2013](#)), which is not the case of interest here. We still include it in this presentation for completeness. Heavier elements are negligible. Therefore  $a = \text{H, He or HII}$ .

For neutral matter, the dependence of the scattering functions is fairly complicated. However, throughout this work we only focus on the ultra-relativistic regime— $e^\pm$  energies of interest are typically larger than 0.1 GeV—in which the scattering functions are actually constant and take the following values ([Blumenthal & Gould, 1970](#)):

$$\phi_{1,\text{H}} = 45.79, \quad \phi_{2,\text{H}} = 44.46, \quad \phi_{1,\text{He}} = 134.6, \quad \phi_{2,\text{He}} = 131.4, \quad \phi_{(1,2),\text{H}_2} \approx 2\phi_{(1,2),\text{H}}. \quad (4.19)$$

For ionized matter the scattering functions read

$$\phi_{1,\text{ion}}(E_\gamma, E_e) = \phi_{2,\text{ion}}(E_\gamma, E_e) = 4Z(Z+1) \left[ \ln \left( \frac{2E_e}{m_e c^2} \left( \frac{E_e - E_\gamma}{E_\gamma} \right) \right) - \frac{1}{2} \right], \quad (4.20)$$

with  $m_e$  the electron mass and  $Z = 1$  for hydrogen.

Therefore, the bremsstrahlung emission spectrum can be rewritten in the following more explicit form:

$$P_{\text{brems}}(E_\gamma, E_e, \vec{x}) = cE_\gamma \left[ (n_{\text{HI}}(\vec{x}) + 2n_{\text{H}_2}(\vec{x})) \frac{d\sigma_{\text{H}}}{dE_\gamma}(E_\gamma, E_e) + n_{\text{He}}(\vec{x}) \frac{d\sigma_{\text{He}}}{dE_\gamma}(E_\gamma, E_e) + n_{\text{HII}}(\vec{x}) \frac{d\sigma_{\text{HII}}}{dE_\gamma}(E_\gamma, E_e) \right]. \quad (4.21)$$

The bremsstrahlung emission spectrum varies weakly in terms of  $E_\gamma$  and  $E_e$ .

#### 4.2.3.3 Synchrotron radiation

**General formula for a given pitch angle.** The synchrotron power per unit frequency for a single electron, in a uniform magnetic field of intensity  $B$ , reads (see [Blumenthal & Gould, 1970](#); [Rybicki & Lightman, 1979](#); [Longair, 2011](#))

$$P_{\text{syn},\alpha}(\nu, E_e) = \frac{1}{4\pi\epsilon_0} \frac{\sqrt{3}e^3 B \sin \alpha}{m_e c} F\left(\frac{\nu}{\nu_{c,\alpha}(E_e)}\right), \quad (4.22)$$

where  $m_e$  is the electron mass,  $e$  the elementary charge,  $\epsilon_0$  the vacuum permittivity,  $\alpha$  is the pitch angle of the electron with respect to the magnetic field axis, and the synchrotron spectrum is characterized by

$$F(t) = t \int_t^\infty K_{5/3}(u) du, \quad (4.23)$$

where  $K_{5/3}$  is the modified Bessel function of order  $5/3$ . The critical frequency for pitch angle  $\alpha$  reads

$$\nu_{c,\alpha} = \frac{3eE_e^2 B \sin \alpha}{4\pi m_e^3 c^4} = \frac{3}{2} \gamma_e^2 \nu_g \sin \alpha, \quad (4.24)$$

with  $\nu_g = eB/(2\pi m_e)$  the nonrelativistic gyrofrequency.

**Average spectrum.** The spectrum presented here corresponds to a uniform magnetic field. The validity of this assumption actually depends on the scale of interest, as discussed in [Longair \(2011\)](#). On small scales, the effect of magnetic irregularities is discussed by comparing the scale of magnetic fluctuations with the characteristic length scale of the trajectory of the electron, defined by the gyroradius  $r_g = p \sin \alpha / (eB)$ , i.e. the radius of the helical path performed by the electron around the local magnetic field axis.  $p$  is the momentum of the electron. If the scale of variation of the magnetic field is much smaller than the gyroradius, the electron is not sensitive to the fine structure of the field but only to the mean uniform component. However, magnetic fluctuations with a scale of the order of the gyroradius lead to significant changes in pitch angle. These fluctuations are either caused by irregularities in the magnetic field or by magnetic instabilities created by the streaming of high-energy particles. They can be safely assumed to be random, so that for a distribution of high-energy electrons, the distribution of pitch angles is expected to be random. Moreover, any high-energy electron is randomly scattered in pitch angle during its propagation. Therefore, the relevant quantity is the average synchrotron spectrum:

$$P_{\text{syn}}(\nu, E_e) = \frac{1}{4\pi\epsilon_0} \frac{\sqrt{3}e^3 B}{m_e c} F_i\left(\frac{\nu}{\nu_c(E_e)}\right), \quad (4.25)$$

where the isotropic synchrotron spectrum  $F_i$  is obtained by averaging the synchrotron spectrum over an isotropic distribution of pitch angles  $\mathcal{P}(\alpha) d\alpha = 1/2 \sin \alpha d\alpha$ :

$$F_i(x) = \frac{1}{2} \int_0^\pi F\left(\frac{x}{\sin \alpha}\right) \sin^2 \alpha d\alpha. \quad (4.26)$$

To simplify the numerical treatment of the angle average,  $F_i$  can be accurately approximated by

$$F_i(x) = ax^d \exp\left(-\sqrt{\frac{x}{b}} - \frac{x}{c}\right), \quad (4.27)$$

where  $x = \nu/\nu_c$  and the best-fit parameters are  $a = 1.85201316$ ,  $b = 3.67724877$ ,  $c = 1.08835947$ , and  $d = 0.33558632$ .  $F_i$  is plotted in Fig. 4.3. Finally, the critical frequency corresponding to the average spectrum is defined by

$$\nu_c = \frac{3eE_e^2 B}{4\pi m_e^3 c^4} = \frac{3}{2}\gamma_e^2 \nu_g. \quad (4.28)$$

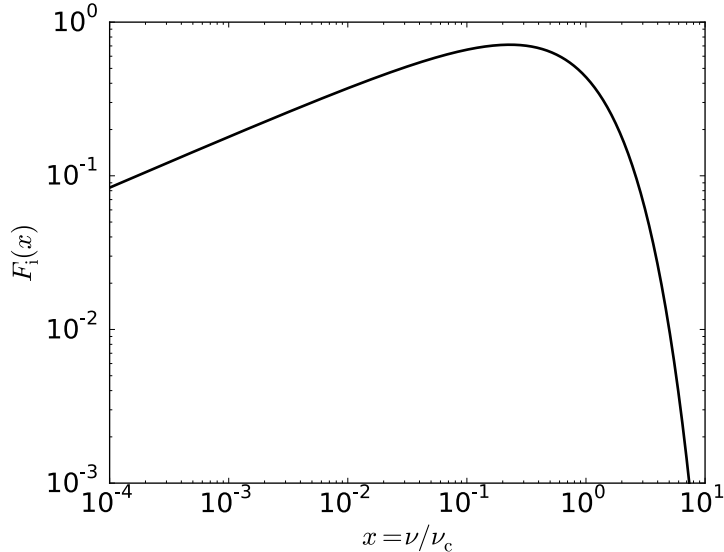


**Figure 4.3** – Synchrotron spectrum averaged over an isotropic distribution of pitch angles. Synchrotron emission peaks at  $x \sim 1$ .

**Spatial dependence.** Additionally, the magnetic field is expected to vary on galactic scales. Large-scale variations of the mean magnetic field are then simply encoded in the magnetic field profile  $B(\vec{x})$ , determined either theoretically or by fitting observations. Therefore, the general expression for the synchrotron spectrum reads

$$P_{\text{syn}}(\nu, E_e, \vec{x}) = \frac{1}{4\pi\epsilon_0} \frac{\sqrt{3}e^3 B(\vec{x})}{m_e c} F_i\left(\frac{\nu}{\nu_c(E_e, \vec{x})}\right). \quad (4.29)$$

The synchrotron spectrum peaks near  $x \sim 1$ , so the frequency of the emitted photon is  $\nu \sim \nu_c$ , with  $\nu_c \sim \gamma_e^2 \nu_g$ . This is very similar to the result obtained for IC scattering and illustrates how synchrotron radiation corresponds to an electron IC scattering a virtual photon of frequency  $\nu_g$ .

**Importance of the magnetic field.** Synchrotron emission critically depends on galactic magnetic fields, which have a complex structure, both in terms of intensity and direction (see e.g. Jansson et al., 2009; Sun & Reich, 2010; Pshirkov et al., 2011; Beck, 2011; Jansson & Farrar, 2012a,b). In general the magnetic field in a galaxy can be divided into a turbulent, randomly oriented field, and a large-scale ordered or regular field. The regular component can be characterized by measuring the linear polarization of synchrotron radiation, while the unpolarized synchrotron intensity probes the total field. Throughout this thesis, we use measurements of unpolarized synchrotron emission and we focus on the strength  $B$  of the total magnetic field, for which we discuss relevant models in chapters pertaining to our results (see Parts III, IV and V).

#### 4.2.4 Example: power-law $e^\pm$ spectrum

Power-law spectra are ubiquitous in high-energy astrophysics. For instance, the energy spectra of cosmic rays—in particular cosmic-ray electrons—can be described by power laws (see e.g. Longair, 2011). Even for electrons and positrons injected e.g. by DM annihilations, the resulting spectrum after accounting for propagation in the galaxy is close to a power law. Let us consider a power-law spectrum for electrons  $\psi(E_e) \propto E_e^{-p}$ . Here for simplicity we only focus on the spectral dependence of the radiated photon spectra  $dn/dE_\gamma$ . In practice, we use the following qualitative results as consistency tests of our numerical results.

**Inverse Compton scattering.** As discussed in Sec. 4.2.3.1, the IC emission spectrum peaks at  $E_\gamma \approx \gamma_e^2 E_0$  for a monochromatic background photon field of energy  $E_0$ . To work out the spectral dependence of the radiated photon spectrum, we can approximate the IC emission spectrum with a delta function,  $P_{\text{IC,mono}}^{\text{Th}} \propto \delta(E_\gamma/(\gamma_e^2 E_0) - 1)$ , which becomes in terms of  $E_e$

$$P_{\text{IC,mono}}^{\text{Th}}(E_\gamma, E_e) \propto E_\gamma^{1/2} \delta\left(E_e - m_e \left(\frac{E_\gamma}{E_0}\right)^{1/2}\right). \quad (4.30)$$

From Eq. (4.4), the emissivity is given by

$$j_{\text{IC}}(E_\gamma) \propto E_\gamma^{1/2} \int E_e^{-p} \delta\left(E_e - m_e \left(\frac{E_\gamma}{E_0}\right)^{1/2}\right) dE_e \propto E_\gamma^{-\frac{p-1}{2}}. \quad (4.31)$$

As a result, for the differential energy spectrum of the emission we have

$$\left.\frac{dn}{dE_\gamma}\right|_{\text{IC}} \propto E_\gamma^{-\frac{p+1}{2}}. \quad (4.32)$$

**Synchrotron radiation.** Similarly, for synchrotron radiation we have

$$P_{\text{syn}}(\nu, E_e) \propto \delta\left(\frac{\nu}{\nu_c} - 1\right), \quad (4.33)$$

so that

$$I_{\nu,\text{syn}} \propto \nu^{-\frac{p-1}{2}}. \quad (4.34)$$

Using the relation between specific intensity and energy spectrum (Eq. (4.3)), we see that the photon spectra from IC and synchrotron have the same power-law dependence, with a flux  $\nu I_\nu \propto \nu^{-\frac{p-3}{2}}$ .

**Bremsstrahlung.** The bremsstrahlung emission spectrum depends weakly on  $E_e$  and  $E_\gamma$ , so that the emissivity reads

$$j_{\text{brems}}(E_\gamma) \propto \int_{E_\gamma}^{\infty} E_e^{-p} dE_e \propto E_\gamma^{-p+1}, \quad (4.35)$$

and the differential energy spectrum is given by

$$\left.\frac{dn}{dE_\gamma}\right|_{\text{brems}} \propto E_\gamma^{-p}. \quad (4.36)$$

Therefore, the emitted photon spectrum has the same power-law form as the electron spectrum.

### 4.3 Electron/positron spectrum $\psi$ accounting for propagation

#### 4.3.1 Physical processes at play

Here we summarize the complex interplay of physical processes that govern cosmic-ray propagation in the interstellar medium (see e.g. [Strong et al., 2007](#), for a review). Cosmic rays are randomly scattered by irregularities in the galactic magnetic field, which results in a motion corresponding to a diffusion process. Magnetic irregularities are actually moving, so that cosmic rays are scattered by magneto-hydrodynamical waves. This leads to an additional effect of stochastic acceleration, referred to as diffusive reacceleration, which is modeled as diffusion in momentum space. Cosmic rays are also transported by convection e.g. in galactic winds or in accretion flows around SMBHs. As they propagate, energetic charged particles lose energy through radiative or ionization processes. They can also lose or gain energy respectively through adiabatic expansion or compression in a convection flow. Additionally, radioactive nuclei decay, but this is not relevant for electrons and positrons. Finally, cosmic-ray nuclei are subject to spallation, i.e. interactions with interstellar matter that lead to the production of lighter particles. Spallation does not affect electrons and positrons. However, secondary electrons and positrons are produced by spallation, mainly of protons and helium nuclei on hydrogen and helium nuclei (see e.g. [Delahaye et al., 2009](#)). Here ‘secondary’ refers to particles that are not produced directly in the source, contrary to primaries. In practice, throughout this work we focus on primary electrons and positrons produced by DM annihilations (or millisecond pulsars in some cases), and we disregard secondaries.

All these processes can be encoded in the cosmic-ray transport equation, the partial differential equation that governs the energy spectrum  $\psi$ .

#### 4.3.2 Transport equation

We now describe the standard derivation of the cosmic-ray transport equation, which follows the textbook approach for the derivation of diffusion equations (see e.g. [Longair, 2011](#); [Lavallo et al., 2007](#)). We start out by writing the continuity equation for  $\psi(E, \vec{x}, t)$  accounting for spatial diffusion, convection, energy losses (seen as convection in energy space), and injection of particles with a source term  $q(E, \vec{x}, t)$ :

$$\frac{\partial \psi}{\partial t} = -\vec{\nabla} \cdot \vec{j}_{\text{diff}} - \vec{\nabla} \cdot \vec{j}_{\text{conv}} - \frac{\partial j_E}{\partial E} + q. \quad (4.37)$$

The spatial diffusion current  $\vec{j}_{\text{diff}}$  accounts for spatial diffusion and is therefore related to the gradient of the density via Fick’s law:

$$\vec{j}_{\text{diff}} = -K(E, \vec{x}) \vec{\nabla} \psi, \quad (4.38)$$

where  $K$  is the spatial diffusion coefficient. The convection current is simply given by:

$$\vec{j}_{\text{conv}} = \psi \vec{v}, \quad (4.39)$$

with  $\vec{v}(\vec{x})$  the velocity field of the flow. The third term on the right-hand side of Eq. (4.37) corresponds to the divergence in energy of the particle current in energy space  $j_E$ , associated with energy losses. Energy losses can be seen as convection in energy space, so that the associated current—i.e. the number of particles passing through  $E$  per unit time (and volume)—reads

$$j_E = \psi \frac{dE}{dt}, \quad (4.40)$$

where  $dE/dt$  is equivalent to a flow velocity in energy space. In practice the energy-loss rate is defined as

$$b_{\text{tot}}(E, \vec{x}) = -\frac{dE}{dt}, \quad (4.41)$$

so that  $b_{\text{tot}}$  is positive when the particle loses energy.  $b_{\text{tot}}$  is actually the sum of the contribution from radiative losses, ionization losses and the energy loss or gain due to adiabatic expansion or compression in the convection flow, as discussed in Sec. 4.3.5.

Using the expressions for the various currents, and omitting the variables for simplicity, Eq. (4.37) becomes:

$$\frac{\partial \psi}{\partial t} = \vec{\nabla} \cdot (K \vec{\nabla} \psi - \vec{v} \psi) + \frac{\partial}{\partial E} (b_{\text{tot}} \psi) + q. \quad (4.42)$$

In principle, using the formalism of the Fokker-Planck equation, one can show that the transport equation features an additional term corresponding to diffusive reacceleration, i.e. diffusion in momentum space (Blandford & Eichler, 1987; Schlickeiser, 2002). However, for electrons and positrons, diffusive reacceleration is actually negligible with respect to energy losses (Salati, 2007; Delahaye et al., 2009). Similarly, convection can be neglected for electrons and positrons, except close to the central BH, where the amplitude of the velocity field of the accretion flow can be of the same order of magnitude as synchrotron losses. This particular case will be discussed in Chapter 11.

In practice, to make the resolution of Eq. (4.42) tractable, we assume the diffusion coefficient  $K$  to be homogeneous, so that  $K(E, \vec{x}) = K(E)$ . Moreover, based on the results of numerical simulation of particle propagation in turbulent magnetic fields (Casse et al., 2002),  $K$  is generally parametrized by a power law in energy (see e.g. Delahaye et al., 2008)

$$K(E) = K_0 \left( \frac{E}{1 \text{ GeV}} \right)^\delta. \quad (4.43)$$

The assumption of homogeneity is a simplification considering that for instance the diffusion coefficient is essentially unconstrained in the GC region and might thus be quite different from the diffusion coefficient in the solar neighborhood (as discussed e.g. in Regis & Ullio, 2008). However, the assumption of a homogeneous diffusion coefficient is justified by the fact that throughout this work we focus on one particular region—namely the GC—so a large-scale spatial variation in the diffusion coefficient would not significantly affect our results.<sup>4</sup>

Finally, one can assume that a steady state is reached if the source term corresponds to continuous injection of particles. This is typically what is expected in the situations of interest in this work, namely for electrons and positrons injected by DM annihilations or a population of millisecond pulsars. Then the diffusion-loss equation for electrons and positrons reads

$$\boxed{K \nabla^2 \psi + \frac{\partial}{\partial E} (b_{\text{tot}} \psi) + q = 0.} \quad (4.44)$$

### 4.3.3 Diffusion zone and parameters

Let us now discuss more specifically some features of spatial diffusion. Radio observations have revealed the presence of a *magnetic halo* around galaxies, as shown in the left panel of Fig. 4.4 (see e.g. Krause, 2009), which implies the existence of a region of space where cosmic rays are confined by the galactic magnetic field. This region is called the *diffusion zone*. Considering the shape of observed magnetic halos around other galaxies, we follow the usual approach in which the diffusion zone of the MW is modeled as a flat cylinder of radius denoted as  $R_{\text{gal}}$ —of the order of magnitude of the radius of the optical disk—and half-height  $L$  defined with respect to the Galactic plane. The usual value for the radius in the literature is  $R_{\text{gal}} = 20 \text{ kpc}$  (see e.g. Delahaye et al., 2008).

Spatial diffusion of cosmic rays in the interstellar medium is therefore governed by three parameters: the half-height  $L$  of the diffusion zone, as well as the normalization of the diffusion

<sup>4</sup>See Chapter 6 where we compare our method with a numerical code which assumes an inhomogeneous diffusion coefficient.

coefficient  $K_0$  and its energy dependence  $\delta$ , as seen in Eq. (4.43). The diffusion parameters are constrained by cosmic-ray measurements at the position of the Earth, especially the boron-to-carbon (B/C) ratio and fluxes of radioactive nuclei (Maurin et al., 2001, 2002; Putze et al., 2010). In particular, the sets of diffusion parameters compatible with measurements of the B/C ratio and giving the minimal (MIN), median (MED) and maximal (MAX) antiproton fluxes from supersymmetric DM (Donato et al., 2004) are used as references:

$$\begin{aligned} \text{MIN} : L &= 1 \text{ kpc}, K_0 = 0.0016 \text{ kpc}^2 \text{ Myr}^{-1}, \delta = 0.85, \\ \text{MED} : L &= 4 \text{ kpc}, K_0 = 0.0112 \text{ kpc}^2 \text{ Myr}^{-1}, \delta = 0.7, \\ \text{MAX} : L &= 15 \text{ kpc}, K_0 = 0.0765 \text{ kpc}^2 \text{ Myr}^{-1}, \delta = 0.46. \end{aligned} \quad (4.45)$$

In practice, we use the MED set as a benchmark model, whereas the MIN and MAX are used to bracket the uncertainty from diffusion.<sup>5</sup>

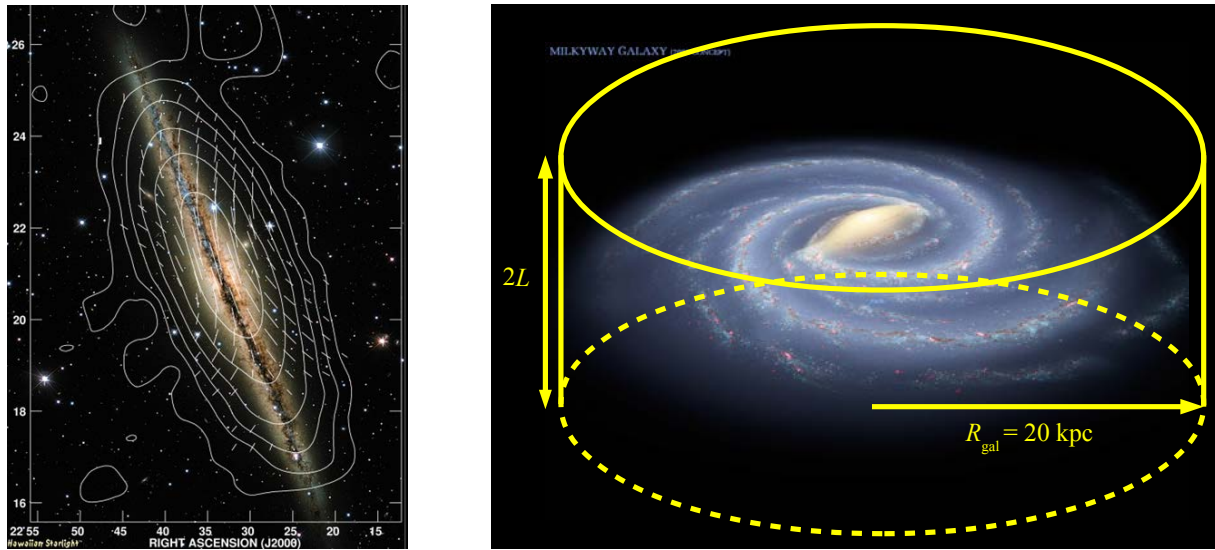


**Figure 4.4 – Left panel:** Optical image of the edge-on NGC 891 galaxy taken with the Canada-France-Hawaii telescope, overlaid with contours of the radio emission at 3.6 cm observed with the 100-m Effelsberg telescope and magnetic field lines shown as dashed lines. Credit: Max Planck Institute for Radio Astronomy, M. Krause & CFHT/Coelum. See also Krause (2009). **Right panel:** Schematic representation of the diffusion zone of cosmic rays as a flat cylinder of radius  $R_{\text{gal}}$  and half-thickness  $L$ , on top of an artist view of the MW.

#### 4.3.4 A qualitative picture of spatial diffusion

Here we describe very qualitatively the effect of spatial diffusion on a given source term. Let  $R$  and  $E$  be characteristic length and energy scales, respectively. Then  $\nabla^2 \sim 1/R^2$  and  $\partial/\partial E \sim 1/E$ , so that in terms of characteristic scales

$$\frac{K}{R^2}\psi + \frac{b_{\text{tot}}}{E}\psi + q = 0. \quad (4.46)$$

Therefore, the diffusion term shapes the spectrum at all scales below a certain length scale defined by  $R \lesssim (KE/b_{\text{tot}})^{1/2}$ . This length scale is in fact to order of magnitude the distance traveled by

<sup>5</sup>We note that these parameters would have to be updated to account for new data from AMS-02, and the standard picture may change. It turns out that due in particular to its very small value of  $L$ , the MIN set is already in tension with the positron data (Lavalle et al., 2014; Di Mauro et al., 2014), radio observations (Di Bernardo et al., 2013; Bringmann et al., 2012b; Orlando & Strong, 2013; Fornengo et al., 2014), and seems to be disfavored by observations of  $\gamma$ -rays (Ackermann et al., 2012c) and antiprotons (Giesen et al., 2015).

the particle during propagation, which we define more rigorously in Sec. 4.3.7.3. In the regime where diffusion dominates, the diffusion-loss equation becomes approximately  $K\nabla^2\psi = -q$ , so that if  $q \propto r^{-\beta}$ —as is typically the case for DM annihilation or decay—then  $\psi \propto r^{2-\beta} + \text{cst.}$  Consequently, for  $r \rightarrow 0$ ,  $\psi$  is either flat (the constant contribution dominates for  $\beta \leq 2$ ) or flatter than the initial distribution by 2 powers (for  $\beta > 2$ ). Of course this is oversimplified since the dependences on space and energy are in fact coupled, but this shows that diffusion flattens the spatial source profile below a diffusion scale determined by the injection energy. The spatial distribution of electrons is therefore depleted in the central part, and extends to larger distances than the initial distribution.

### 4.3.5 Energy loss rate

Energy losses have a crucial importance since they shape the final  $e^\pm$  distribution. In particular if they are large enough, they can counteract spatial diffusion by making  $e^\pm$  lose their energy in place. As a result, it is essential to model the energy loss rate as accurately as possible.

In the most general case, the total energy loss rate  $b_{\text{tot}}(E_e, \vec{x})$  is the sum of the contributions from radiative processes—synchrotron, IC and bremsstrahlung—as well as Coulomb and ionization losses, and adiabatic losses and gains respectively from expansion and compression flows:

$$b_{\text{tot}} = b_{\text{syn}} + b_{\text{IC}} + b_{\text{brems}} + b_{\text{ion}} + b_{\text{Coul}} + b_{\text{ad}}. \quad (4.47)$$

We now describe each term in more detail.

#### 4.3.5.1 Radiative processes

The energy loss rate for radiative processes can be evaluated by performing the integral of the differential emission spectrum over all possible emitted photon energies or frequencies (see e.g. Longair, 2011).

**Inverse Compton scattering.** The IC loss rate is given in full generality by

$$b_{\text{IC}}(E_e, \vec{x}) = \int_0^{E_e} P_{\text{IC}}(E_\gamma, E_e, \vec{x}) dE_\gamma. \quad (4.48)$$

In the Thomson regime, where  $E_\gamma \ll E_e$ , this yields

$$b_{\text{IC}}^{\text{Th}}(E_e, \vec{x}) = \frac{4}{3} \sigma_{\text{T}} c u_{\text{rad}}(\vec{x}) \gamma_e^2, \quad (4.49)$$

where  $u_{\text{rad}}$  is the energy density of the background radiation field, given by

$$u_{\text{rad}}(\vec{x}) = \int_0^\infty \varepsilon n(\varepsilon, \vec{x}) d\varepsilon, \quad (4.50)$$

where  $\varepsilon \equiv E_\gamma^0$  is a simplified notation for the energy of background photons. From the ISRF maps extracted from GALPROP, the ISRF energy density in the GC region is  $\sim 22 \text{ eV cm}^{-3}$ , and the IC energy loss rate in the Thomson limit becomes

$$b_{\text{IC}}^{\text{Th}}(E_e, \vec{x}) \approx 2.24 \times 10^{-15} \left( \frac{u_{\text{rad}}(\vec{x})}{22 \text{ eV cm}^{-3}} \right) \left( \frac{E_e}{1 \text{ GeV}} \right)^2 \text{ GeV s}^{-1}. \quad (4.51)$$

This clearly shows the  $E_e^2$  dependence of the IC losses in the Thomson regime. However, this limit turns out to be valid only up to  $\sim 100 \text{ GeV}$ , as discussed in Sec. 4.3.5.4, so at higher energies one must use the general formula in Eq. (4.48). However, in the general case there is no analytic formula for the IC loss rate. Therefore, to make the calculation of the spatial and

energy dependences of the IC loss rate in the general case less cumbersome, one can tabulate the values of the IC losses based on the ISRF from GALPROP maps.

However, it can also be convenient to use an alternative method, which provides more insight into the energy dependence of the IC loss rate and gives an interpolation in energy of the IC loss rate. This method was introduced in [Cirelli & Panci \(2009\)](#), and relies on the fact that the ISRF can be well approximated by a sum of black bodies (or more generally greybodies which have a smaller emissivity). However, it is mostly suitable when studying a specific region of the sky, like the GC, otherwise it becomes cumbersome to repeat the procedure that we describe now for each location.

Different regimes arise depending on the energy of the background photon in the center of momentum frame, as discussed in [Sec. 4.2.3.1](#). More quantitatively, to distinguish between the various regimes, one may use the parameter  $\Gamma$  or equivalently for a blackbody, for which the temperature  $T$  is well defined,

$$\alpha_T \equiv \frac{\gamma_e k_B T}{m_e c^2}. \quad (4.52)$$

The low energy regime ( $\alpha_T \ll 1$ ) corresponds to the Thomson limit, while high energies ( $\alpha_T \gg 1$ ) are associated with the extreme Klein-Nishina regime. In both limits analytic expressions of the loss rate can be found, while in the intermediate regime, the loss rate is interpolated using the parametrization described in [Delahaye et al. \(2010\)](#). The corresponding energy loss rate for a blackbody at temperature  $T$  is given by

$$b_{\text{IC},T}^{\text{bb}}(E_e) = \begin{cases} \frac{4}{3} \sigma_T c w_{\text{bb}} \gamma_e^2 & \alpha_T < 3.8 \times 10^{-4} \\ A \frac{E_e^2 (k_B T)^4}{\alpha_T} \exp \left[ \sum_{i=0}^5 c_i (\ln \alpha_T)^i \right] & 3.8 \times 10^{-4} \leq \alpha_T \leq 1.8 \times 10^3 \\ \frac{\sigma_T (m_e c k_B T)^2}{16 \hbar^3} \left[ \ln \left( \frac{4 \gamma_e k_B T}{m_e c^2} \right) - 1.9805 \right] & \alpha_T > 1.8 \times 10^3, \end{cases} \quad (4.53)$$

where  $A \approx 1 \text{ GeV}^{-5} \text{ s}^{-1}$  is a normalization coefficient and  $w_{\text{bb}}(T) = \pi^2 (k_B T)^4 / (15 (\hbar c)^3)$  is the energy density of a blackbody. The parametrization of the loss rate in the intermediate regime is characterized by the coefficients

$$c_i = \left\{ 74.77, -0.1953, -9.97 \times 10^{-2}, 4.352 \times 10^{-3}, 3.546 \times 10^{-4}, -3.01 \times 10^{-5} \right\}. \quad (4.54)$$

Now, equation (4.53) is valid for a blackbody distribution of photons. However, the only true blackbody is the CMB. Every other component  $k$  is approximated by a greybody spectrum characterized by an energy density  $w_k (\leq w_{\text{bb}})$  and a temperature  $T_k$ . The resulting total photon density  $n$  of the ISRF entering into the expression of the IC emission spectrum  $P_{\text{IC}}$  (see [Eq. \(4.12\)](#)) is then

$$n(\varepsilon) = \sum_k \frac{15 w_k}{\pi^4 (k_B T_k)^4} \frac{\varepsilon^2}{e^{\frac{\varepsilon}{k_B T_k}} - 1}. \quad (4.55)$$

To adapt the loss rate for black bodies ([Eq. \(4.53\)](#)) to these greybody distributions, one thus needs to multiply them by the factor  $w_k / w_{\text{bb}}$  (equal to 1 for the CMB). As a result, the total energy loss rate for inverse Compton scattering reads

$$b_{\text{IC}}(E_e) = \sum_k \frac{w_k}{w_{\text{bb}}(T_k)} b_{\text{IC},T_k}^{\text{bb}}(E_e). \quad (4.56)$$

**Bremsstrahlung.** For bremsstrahlung we have:

$$b_{\text{brems}}(E_e, \vec{x}) = \int_0^{E_e} P_{\text{brems}}(E_\gamma, E_e, \vec{x}) dE_\gamma. \quad (4.57)$$

Using Eq. (4.21), the bremsstrahlung loss rate can be written as the sum of the contributions from ionized and neutral gas,  $b_{\text{brems}} = b_{\text{brems,I}} + b_{\text{brems,N}}$ , where

$$b_{\text{brems,I}}(E_e, \vec{x}) = \alpha_{\text{em}} \frac{3\sigma_{\text{TC}}}{2\pi} n_{\text{HII}}(\vec{x}) Z(Z+1) \left( \ln \left( \frac{2E_e}{m_e} \right) - \frac{1}{3} \right) E_e, \quad (4.58)$$

with  $Z = 1$  for hydrogen, and

$$b_{\text{brems,N}}(E_e, \vec{x}) = \alpha_{\text{em}} \frac{3\sigma_{\text{TC}}}{8\pi} E_e \left[ (n_{\text{HI}}(\vec{x}) + 2n_{\text{H}_2}(\vec{x})) \left( \frac{4}{3}\phi_{1,\text{H}} - \frac{1}{3}\phi_{2,\text{H}} \right) + n_{\text{He}}(\vec{x}) \left( \frac{4}{3}\phi_{1,\text{He}} - \frac{1}{3}\phi_{2,\text{He}} \right) \right]. \quad (4.59)$$

The bremsstrahlung loss rate is thus essentially proportional to the  $e^\pm$  energy. In practice, at the GC the contributions from helium and ionized hydrogen are negligible, so that

$$b_{\text{brems}}(E_e, \vec{x}) \approx 4.5 \times 10^{-15} \left( \frac{n_{\text{HI}}(\vec{x}) + 2n_{\text{H}_2}(\vec{x})}{5.6 \text{ cm}^{-3}} \right) \left( \frac{E_e}{1 \text{ GeV}} \right) \text{ GeV s}^{-1}. \quad (4.60)$$

**Synchrotron.** The synchrotron loss rate reads

$$b_{\text{syn}}(E_e, \vec{x}) = \int_0^\infty P_{\text{syn}}(\nu, E_e, \vec{x}) d\nu, \quad (4.61)$$

Computing this integral leads to the well-known formula for the synchrotron energy loss rate for an isotropic distribution of electron pitch angles, corresponding to a randomly oriented magnetic field (see e.g. Longair, 2011):

$$b_{\text{syn}}(E_e, \vec{x}) = \frac{4}{3} \sigma_{\text{TC}} \frac{B(\vec{x})^2}{2\mu_0} \gamma_e^2, \quad (4.62)$$

where  $\mu_0$  is the vacuum permeability. This expression reflects the analogy with the IC loss rate in the Thomson limit. Numerically, this gives

$$b_{\text{syn}}(E_e, \vec{x}) \approx 2.53 \times 10^{-16} \left( \frac{B(\vec{x})}{10 \mu\text{G}} \right)^2 \left( \frac{E_e}{1 \text{ GeV}} \right)^2 \text{ GeV s}^{-1}. \quad (4.63)$$

#### 4.3.5.2 Coulomb interactions

Electrons and positrons ionize atoms in the interstellar gas via the Coulomb interaction. The main contribution comes from ionization of atomic hydrogen, and the associated loss rate in the relativistic regime is adapted from the Bethe-Bloch formula and reads (Ginzburg, 1979)

$$b_{\text{ion}}(E_e, \vec{x}) \approx 7.7 \times 10^{-18} \left( \frac{n_{\text{H}}(\vec{x})}{1 \text{ cm}^{-3}} \right) (3 \ln \gamma_e + 20) \text{ GeV s}^{-1}. \quad (4.64)$$

Coulomb interaction of electrons and positrons with free electrons in the ambient plasma lead to additional energy losses (Ginzburg, 1979):

$$b_{\text{Coul}}(E_e, \vec{x}) \approx 7.7 \times 10^{-18} \left( \frac{n_e(\vec{x})}{1 \text{ cm}^{-3}} \right) \left[ \ln \left( \frac{\gamma_e}{n_e(\vec{x})/1 \text{ cm}^{-3}} \right) + 73.6 \right] \text{ GeV s}^{-1}. \quad (4.65)$$

In most cases, especially for the GC region where radiative processes dominate, ionization and Coulomb losses turn out to be negligible at the energies of interest, as discussed in Sec. 4.3.5.4.

#### 4.3.5.3 Adiabatic losses and gains

Finally, in an expansion or accretion flow, the gas of electrons and positrons suffers adiabatic losses or gains of energy, respectively. The associated momentum loss rate reads (see e.g. Longair, 2011)

$$\frac{dp}{dt} = -\frac{1}{3}(\vec{\nabla} \cdot \vec{v})p, \quad (4.66)$$

where  $\vec{v}$  is the velocity field of the expansion or accretion flow. The loss rate can be expressed in the ultra-relativistic regime as an energy loss rate in the following way:

$$\frac{dE}{dt} = -\frac{1}{3}(\vec{\nabla} \cdot \vec{v})E, \quad (4.67)$$

and  $b_{\text{ad}} \equiv -dE/dt$ . Adiabatic losses are relevant for instance in the context of convection winds, but as discussed previously the resulting energy losses of electrons and positrons are negligible compared to radiative losses. However, in the accretion flow, very close to the central SMBH, energy gains can be substantial, sometimes of the order of e.g. synchrotron losses even for large magnetic fields, as discussed in Chapter 11. Nevertheless, in most cases in the MW this effect is negligible since one studies the GC region ‘at large’, typically above sub-milliparsec scales.

#### 4.3.5.4 Comparison of the various loss rates

The various energy loss rates from radiative and Coulomb processes are graphically compared in Fig. 4.5. We show the loss rates at the GC, which is the region of interest in this work. We rely on ISRF and gas distributions extracted from GALPROP, which serve as a reference and as such were used for instance in Buch et al. (2015); Cirelli et al. (2013). For the magnetic field we use a benchmark value of  $10 \mu\text{G}$  (Strong et al., 2000), corresponding in particular to the magnetic field at the GC in GALPROP. The Coulomb loss rate is plotted for a typical free electron density of  $n_e = 1 \text{ cm}^{-3}$  (Boehm et al., 2010). The IC loss rate is shown using both the general expression and the Thomson limit, which illustrates the validity of the latter up to  $\sim 100 \text{ GeV}$ . The radiative processes therefore dominate over the entire range of interest, i.e. above  $\sim 0.1 \text{ GeV}$ . Above  $\sim 10 \text{ GeV}$ , due to its linear dependence in  $E_e$ , bremsstrahlung becomes subdominant with respect to synchrotron and IC. In this work, we have often used GALPROP losses for consistency, but in the framework of a semi-analytic method that does not rely on GALPROP to compute the  $e^\pm$  spectrum and photon fluxes, as discussed in Sec. 4.3.7.

We now move on to the resolution of the diffusion-loss equation, in order to determine the  $e^\pm$  spectrum  $\psi$  accounting for propagation.

#### 4.3.6 Electron/positron spectrum for negligible spatial diffusion

When energy losses dominate over diffusion, the diffusion-loss equation reduces to:

$$\frac{\partial}{\partial E}(b_{\text{tot}}\psi) = -q, \quad (4.68)$$

Here the energy and spatial dependences decouple, so Eq. (4.68) can be readily integrated—with the reasonable assumption that  $\psi$  vanishes at very high energies—to give

$$\psi(E, \vec{x}) = \frac{1}{b_{\text{tot}}(E, \vec{x})} \int_E^\infty q(E_{\text{inj}}, \vec{x}) dE_{\text{inj}}. \quad (4.69)$$

For electrons and positrons injected by DM annihilation into channel  $f$ , the source term is given by the product of the total annihilation rate (already discussed in Sec. 2.3.3.1) with the

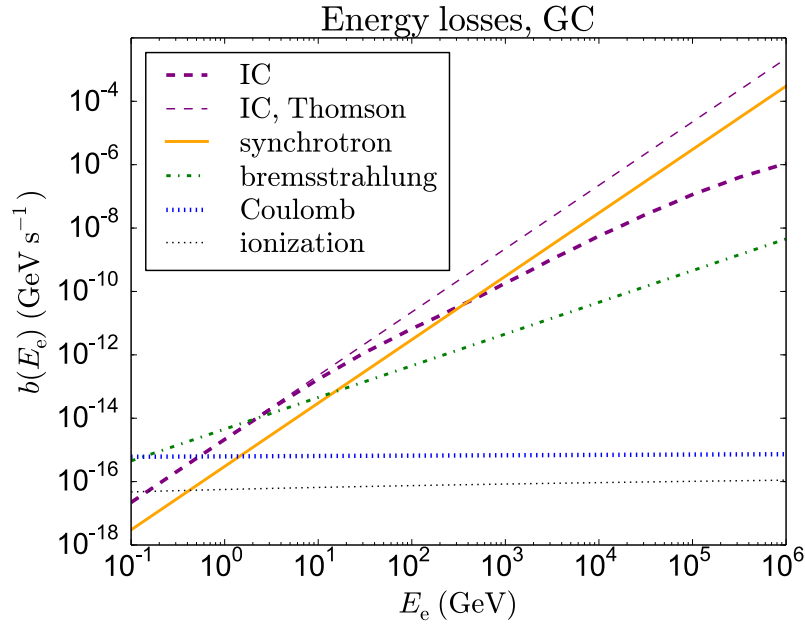


**Figure 4.5** – Comparison of the various loss rates in the GC region. ICS (purple dashed line), synchrotron (orange solid line) and bremsstrahlung (green dot-dashed line) dominate over ionization (black thin dotted line) and Coulomb losses (blue thick dotted line) above 0.1 GeV which is the energy range of interest in this work.

injection spectrum, i.e. the number of electrons or positrons produced per single annihilation,  $dN_{e,f}/dE_{inj}$ :

$$q_f(E_{inj}, \vec{x}) = \frac{\langle \sigma v \rangle_f}{\eta} \left( \frac{\rho(\vec{x})}{m_{DM}} \right)^2 \frac{dN_{e,f}}{dE_{inj}}. \quad (4.70)$$

As a result, for DM annihilation into channel  $f$ , the  $e^\pm$  spectrum in the presence of energy losses, but for negligible diffusion, is given by

$$\psi_{DM,f}(E, \vec{x})|_{\text{no diffusion}} = \frac{1}{b_{tot}(E, \vec{x})} \frac{\langle \sigma v \rangle_f}{\eta} \left( \frac{\rho(\vec{x})}{m_{DM}} \right)^2 \int_E^{m_{DM}} \frac{dN_{e,f}}{dE_{inj}} dE_{inj}. \quad (4.71)$$

In practice, we make use of the injection spectra  $dN_{e,f}/dE_{inj}$  computed and tabulated for various DM masses in [Cirelli et al. \(2011\)](#), which include electroweak corrections, increasingly important at high energy.

### 4.3.7 Electron/positron spectrum in the presence of spatial diffusion

Several techniques exist in the literature to solve the transport equation. [GALPROP](#), which relies on an implicit iteration scheme ([Strong & Moskalenko, 1998](#)), [DRAGON](#) which is based on [GALPROP](#) and introduces an inhomogeneous diffusion coefficient, and [PICARD](#) ([Kissmann, 2014](#)), all use fully numerical methods, while [USINE](#) ([Putze, 2011](#)) and the method presented in [Lavalle et al. \(2007\)](#); [Delahaye et al. \(2008\)](#) are based on a semi-analytic approach. With a minimum step size of 10 pc due to the resolution of gas maps, numerical codes like [GALPROP](#) do not have the spatial resolution needed to zoom in on the GC and account for very sharply peaked source terms. Therefore we have used the semi-analytic method presented in [Lavalle et al. \(2007\)](#); [Delahaye et al. \(2008\)](#), and modified it to treat very steep spatial source profiles.

This semi-analytic approach relies on the assumption of homogeneous energy losses, which is justified when studying a given region of the Galaxy. In particular, we are interested in the GC

region. Therefore, in the rest of Sec. 4.3.7, we consider  $b_{\text{tot}}(E, \vec{x}) \equiv b_{\text{tot}}(E)$ . We now describe the method.

#### 4.3.7.1 Reformulation of the diffusion-loss equation

To solve the diffusion-loss equation, we perform a change of variables by replacing the energy  $E$  by a pseudo-time  $\tilde{t}$  defined by the following relation (see Lavallo et al., 2007; Delahaye et al., 2008, in which the authors made use of a trick described in Baltz & Edsjö, 1999):

$$\frac{d\tilde{t}}{dE} = -\frac{1}{K_0} \frac{K(E)}{b_{\text{tot}}(E)}. \quad (4.72)$$

This corresponds to turning the process of energy loss of electrons or positrons during propagation into an evolution in pseudo-time. Then, with the following changes of variables:

$$\begin{aligned} \tilde{\psi} &= b_{\text{tot}}\psi, \\ \tilde{q} &= \frac{K_0}{K} b_{\text{tot}}q, \end{aligned} \quad (4.73)$$

Eq. (4.44) becomes formally equivalent to the heat equation:

$$\frac{\partial \tilde{\psi}}{\partial \tilde{t}} - K_0 \nabla^2 \tilde{\psi} = \tilde{q}. \quad (4.74)$$

#### 4.3.7.2 Green's function solution

This equation can then be solved using the usual approach using the formalism of Green's functions. More specifically, the solution is expressed in terms of the propagator—or Green's function— $\tilde{G}$  of Eq. (4.74):

$$\tilde{\psi}(\tilde{t}, \vec{x}) = \int_0^{\tilde{t}} d\tilde{t}_{\text{inj}} \int d\vec{x}_{\text{inj}} \tilde{G}(\vec{x}, \tilde{t} \leftarrow \vec{x}_{\text{inj}}, \tilde{t}_{\text{inj}}) \tilde{q}(\tilde{t}_{\text{inj}}, \vec{x}_{\text{inj}}), \quad (4.75)$$

which becomes, when returning to the original quantities:

$$\psi(E, \vec{x}) = \int_E^\infty dE_{\text{inj}} \int d\vec{x}_{\text{inj}} G(\vec{x}, E \leftarrow \vec{x}_{\text{inj}}, E_{\text{inj}}) q(E_{\text{inj}}, \vec{x}_{\text{inj}}), \quad (4.76)$$

with

$$G(\vec{x}, E \leftarrow \vec{x}_{\text{inj}}, E_{\text{inj}}) = \frac{1}{b_{\text{tot}}(E)} \tilde{G}(\vec{x}, \tilde{t} \leftarrow \vec{x}_{\text{inj}}, \tilde{t}_{\text{inj}}). \quad (4.77)$$

#### 4.3.7.3 Diffusion zone and boundary conditions for the propagator

Here we make use of the results of Lavallo et al. (2007) on the propagator accounting for the existence of a diffusion zone which introduces boundary conditions. In particular, outside the diffusion zone, cosmic rays are no longer confined by the magnetic field and can escape freely. This is modeled by assuming that  $\psi$  vanishes at the boundaries.

Without any boundary conditions,  $\tilde{G}$  would be given by the usual expression for the propagator of the heat equation, in three dimensions, for infinite space:

$$\tilde{G}_{\text{free}}(\tilde{t}, \vec{x} \leftarrow \tilde{t}_{\text{inj}}, \vec{x}_{\text{inj}}) = \frac{1}{(4\pi K_0 \tilde{\tau})^{3/2}} \exp\left(-\frac{(\vec{x} - \vec{x}_{\text{inj}})^2}{4K_0 \tilde{\tau}}\right), \quad (4.78)$$

where  $\tilde{\tau} = \tilde{t} - \tilde{t}_{\text{inj}}$  is the typical time it takes the energy of an electron or positron to decrease from  $E_{\text{inj}}$  to  $E$  during propagation. The associated *diffusion length*, denoted as  $\lambda_D$ , represents the distance traveled by an electron or positron during propagation and is related to  $\tilde{\tau}$  via:

$$\lambda_D = \sqrt{4K_0 \tilde{\tau}}. \quad (4.79)$$

Explicitly, in terms of the injection and final energies, the diffusion length is obtained by integrating Eq. (4.72) and reads

$$\lambda_{\text{D}}(E, E_{\text{inj}}) = 2 \left( \int_E^{E_{\text{inj}}} \frac{K(E')}{b_{\text{tot}}(E')} dE' \right)^{1/2}. \quad (4.80)$$

We can now rewrite the dependence of the propagator in terms of  $\lambda_{\text{D}}$ :

$$\tilde{G}(\tilde{t}, \vec{x} \leftarrow \tilde{t}_{\text{inj}}, \vec{x}_{\text{inj}}) \equiv \tilde{G}(\lambda_{\text{D}}, \vec{x}, \vec{x}_{\text{inj}}). \quad (4.81)$$

In fact, one must account for the boundaries of the diffusion zone, which leads to a different propagator from that corresponding to infinite space. First, considering that the observer is located at  $d_{\text{obs}} \equiv r_{\odot} \approx 8.5$  kpc from the GC (Gillessen et al., 2009) and since cosmic rays originate mostly from the central regions, it is safe to assume that the radial boundary at  $R_{\text{gal}} = 20$  kpc has a negligible impact on the spectrum, especially for a medium half-thickness  $L$ . Even for a half-thickness of 15 kpc corresponding to the MAX set, the effect is small (Delahaye et al., 2008). This infinite slab hypothesis allows one to write the propagator as the product of two independent factors corresponding to horizontal and vertical propagation,

$$\tilde{G}(\lambda_{\text{D}}, \vec{x}, \vec{x}_{\text{inj}}) = \frac{1}{\lambda_{\text{D}}^2 \pi} \exp\left(-\frac{(x - x_{\text{inj}})^2 + (y - y_{\text{inj}})^2}{\lambda_{\text{D}}^2}\right) \tilde{V}(\lambda_{\text{D}}, z, z_{\text{inj}}), \quad (4.82)$$

with  $\vec{x}_{\text{inj}}$  the position of injection and  $\vec{x}$  the position after propagation. Here these positions are specified by Cartesian coordinates  $x_{\text{inj}}, y_{\text{inj}}, z_{\text{inj}}$ , and  $x, y, z$  respectively.  $\tilde{V}$  is the vertical contribution to the propagator, for which different regimes arise, as discussed next.

If the diffusion length of a cosmic ray is small enough, the particle does not feel the influence of the boundaries at  $z = \pm L$ . Said more quantitatively, if  $\lambda_{\text{D}}^2 \ll L^2$  the free propagator is a very good approximation:

$$\tilde{V}(\lambda_{\text{D}}, z, z_{\text{inj}}) = \frac{1}{\lambda_{\text{D}} \sqrt{\pi}} \exp\left(-\frac{(z - z_{\text{inj}})^2}{\lambda_{\text{D}}^2}\right). \quad (4.83)$$

In the opposite regime, when  $\lambda_{\text{D}}^2 \gg L^2$ , the propagation is sensitive to the vertical boundaries. As a result, the vertical propagator must be computed differently. However, the diffusion equation can be seen as a Schrödinger equation in imaginary time, so the diffusion equation can be interpreted as describing the evolution of a particle in the diffusion zone, which plays the part of an infinite potential well between  $z = -L$  and  $z = +L$ . The vertical propagator may then be expanded as a series over the eigenfunctions of the associated Hamiltonian,

$$\tilde{V}(\lambda_{\text{D}}, z, z_{\text{inj}}) = \frac{1}{L} \sum_{n=1}^{\infty} \left[ \exp\left(-\frac{\lambda_{\text{D}}^2 k_n^2}{4}\right) \varphi_n(z_{\text{inj}}) \varphi_n(z) + \exp\left(-\frac{\lambda_{\text{D}}^2 k'_n{}^2}{4}\right) \varphi'_n(z_{\text{inj}}) \varphi'_n(z) \right], \quad (4.84)$$

where the wave functions  $\varphi_n$  and  $\varphi'_n$  are, respectively, even and odd:  $\varphi_n(z) = \sin(k_n(L - |z|))$  and  $\varphi'_n(z) = \sin(k'_n(L - z))$ , with the wave vectors defined as  $k_n = (n - 1/2) \pi/L$  and  $k'_n = n\pi/L$ . When the diffusion length is large enough, the series in Eq. (4.84) can be truncated to less than 100 terms. We have used 0.5 kpc as the limiting value between these two regimes.

#### 4.3.7.4 General expression for the spectrum

Knowing the propagator  $\tilde{G}$  in principle determines the solution. Specifying the source term for DM annihilation, the solution given in Eq. (4.76) becomes:<sup>6</sup>

$$\psi_{\text{DM},f}(E, \vec{x}) = \frac{\kappa_f}{b_{\text{tot}}(E)} \int_E^{\infty} \tilde{I}_{\vec{x}}(E, E_{\text{inj}}) \frac{dN_{e,f}}{dE_{\text{inj}}} dE_{\text{inj}}, \quad (4.85)$$

<sup>6</sup>We note that for a pure  $e^+e^-$  final state without radiative corrections, the injection spectrum is monochromatic, i.e.  $dN_{e,e}/dE_{\text{inj}} = \delta(E_{\text{inj}} - m_{\text{DM}})$ , so that the flux accounting for propagation takes on a simplified form:  $\psi_{\text{DM},e}(E, \vec{x}) = \kappa_e/b_{\text{tot}}(E) \tilde{I}_{\vec{x}}(E, m_{\text{DM}})$ . We used this as a consistency test in our calculations.

where  $\tilde{I}_{\vec{x}}(E, E_{\text{inj}}) \equiv \tilde{I}_{\vec{x}}(\lambda_{\text{D}}(E, E_{\text{inj}}))$  is called the *halo function* and contains all the information on propagation through the diffusion length  $\lambda_{\text{D}}$  defined previously (see Eq. (4.79)):

$$\tilde{I}_{\vec{x}}(E, E_{\text{inj}}) = \int_{\text{DZ}} \tilde{G}(\lambda_{\text{D}}(E, E_{\text{inj}}), \vec{x}, \vec{x}_{\text{inj}}) \left( \frac{\rho(\vec{x}_{\text{inj}})}{\rho_{\odot}} \right)^2 d\vec{x}_{\text{inj}}, \quad (4.86)$$

where the integral is performed over the diffusion zone (DZ). The normalization factor in Eq. (4.85),

$$\kappa_f = \frac{\langle \sigma v \rangle_f}{\eta} \left( \frac{\rho_{\odot}}{m_{\text{DM}}} \right)^2, \quad (4.87)$$

is defined by writing the source term as

$$q_f = \kappa_f \left( \frac{\rho}{\rho_{\odot}} \right)^2 \frac{dN_{e,f}}{dE_{\text{inj}}}, \quad (4.88)$$

with the injection spectrum  $dN_{e,f}/dE_{\text{inj}}$  tabulated in Cirelli et al. (2011).

The halo function is therefore the crucial element needed to compute the  $e^{\pm}$  spectrum in the presence of spatial diffusion. However, this turns out to be more difficult than it seems. Actually, depending on the value of  $\lambda_{\text{D}}$  relative to the distance from the GC, the propagator can become very sharply peaked. Moreover, the DM profile is also very sharply peaked, especially when considering spiky profiles. Consequently, if the sampling of the integrand is not done properly, the divergence is completely missed, and the halo function is underestimated. In particular, the sharpness of the propagator requires a dedicated treatment detailed in the following.

#### 4.3.7.5 Green's functions vs alternative methods

**Fourier-Bessel expansion.** The diffusion-loss equation can also in principle be solved using the Fourier-Bessel expansion approach, which relies on an expansion of the source term  $q$  as a series of cosines and Bessel functions (Delahaye et al., 2008). The main element of the expansion is the factor  $j_0(\alpha_i r_{\text{cyl}}/R_{\text{gal}})$ , where  $j_0$  is the zeroth-order Bessel function of the first kind and  $\alpha_i$  the  $i$ th zero of  $j_0$  (with  $r_{\text{cyl}} = \sqrt{x^2 + y^2}$  in terms of Cartesian coordinates). The problem is that  $j_0(\alpha_i r_{\text{cyl}}/R_{\text{gal}})$  goes to 1 when the argument (and therefore  $r_{\text{cyl}}$ ) goes to 0, i.e. toward the GC. The source term therefore appears to be constant while the DM halo profile continues to increase with small values of the radius. To prevent the argument of  $j_0$  from falling to zero too rapidly, one needs to sum over a large number of Bessel zeros  $\alpha_i$ . So unless one uses a huge number of Bessel modes, the expansion cannot account for steep profiles on small scales, which leads to a halo function that is greatly underestimated at the center. However, taking, for example,  $10^9$  modes results in an unacceptably long computing time.

The Green's function approach allows us to avoid this difficulty, since we can define three different regimes for  $\lambda_{\text{D}}$  (depending on the distance to the GC) to which the integration step can be adapted.

**Partial differential equation for  $\tilde{I}$ .** There is actually another technique to compute  $\tilde{I}$  (Rothstein et al., 2009), which consists in rewriting the transport equation as a partial differential equation for  $\tilde{I}$  and solving it numerically (Rothstein et al., 2009) or analytically (Cirelli et al., 2011). This third method is in principle fast and efficient since  $\tilde{I}$  can be computed only once for a given profile, but it is not convenient in our case because the radial dependence of spiky profiles leads to a stiff equation that requires an extremely large number of steps to be solved accurately, and there is no alternative in this case to reduce the computing time.

#### 4.3.7.6 Computing the halo function with Green's functions for a steep source term

**Trick for the propagator.** This section is adapted from (Lacroix et al., 2014a) where we presented our new method, never shown before in the literature. This technique consists in computing the halo function at small scales by exploiting the three different regimes that arise for the horizontal and vertical components of the propagator, depending on the value of  $\lambda_D$  relative to  $r_{\text{cyl}} = \sqrt{x^2 + y^2}$  and  $z$ .

First of all, in the regime of small  $\lambda_D$ , i.e. for  $\lambda_D \ll r_{\text{cyl}}$  or  $\lambda_D \ll z$ , the horizontal and vertical components of the propagator become extremely sharply peaked. In this case, a huge number of integration steps would be required to capture the peak in the integral. However, the halo function has an analytic limit for  $\lambda_D$  going to zero. In fact, for  $\lambda_D \rightarrow 0$ , the propagator  $G(\vec{x}, E \leftarrow \vec{x}_{\text{inj}}, E_{\text{inj}})$  becomes a delta function of space,  $\delta(\vec{x} - \vec{x}_{\text{inj}})$ .<sup>7</sup> Consequently, taking the limit of Eq. (4.86) for  $\lambda_D$  going to 0, or equivalently  $E$  going to  $E_{\text{inj}}$ , leads to

$$\tilde{I}_{\vec{x}}(\lambda_D) \xrightarrow{\lambda_D \rightarrow 0} \left( \frac{\rho(\vec{x})}{\rho_{\odot}} \right)^2, \quad (4.90)$$

which is equal to 1 at the Sun's position ( $\tilde{I}_{\odot} = 1$ ) and very large (depending on the type of spike that we consider) at the GC. Therefore, to solve the problem of the sharply peaked propagator missed by the integral for  $\lambda_D \ll r_{\text{cyl}}$  or  $\lambda_D \ll z$ , we have imposed by hand the condition displayed in Eq. (4.90) in this regime. This way we ensure that the value of  $\tilde{I}$  is correct when cosmic rays do not propagate.

In the intermediate regime, when the propagators are peaked but with finite widths, we compute the spatial integrals over such widths instead of integrating over the whole range of values of  $r_{\text{inj}}$  or  $z_{\text{inj}}$ . This is essential since the analytic limit is no longer a good approximation in this regime, and unless one uses a huge number of points, the integration procedure over the whole range once again misses the peak. Finally, for larger values of  $\lambda_D$ , i.e. when  $\lambda_D \sim r_{\text{cyl}}$  or  $\lambda_D \sim z$ ,  $\tilde{I}$  is computed by doing the complete integrals over the diffusion zone.

**Example: DM spike.** Using this adaptive procedure enables us to derive the halo function at the GC, in particular for a spiky DM profile. Shown in Fig. 4.6 (left panel) are the corresponding curves for the NFW profile and the NFW+spike profile, where we assume  $R_{\text{sp}} = 1$  pc,  $\langle \sigma v \rangle = 3 \times 10^{-26} \text{ cm}^3 \text{ s}^{-1}$ ,  $m_{\text{DM}} = 10$  GeV, and the MED parameter set given in Eq. (4.45). As can be seen in this figure, the reconstruction works well, since the numerical solution reaches the plateau corresponding to the analytical solution when  $\lambda_D \rightarrow 0$ . The relative error between the numerical and analytical solutions is smaller than the percent level, as shown by the small step at roughly  $10^{-7}$  kpc.

In the right panel of Fig. 4.6, we also reproduce the halo function at the Sun's position ( $\tilde{I}_{\odot}$ ) as a function of  $\lambda_D$  for the NFW profile (given in Delahaye et al., 2008). We also show the halo function at the Sun for a NFW+spike profile with  $R_{\text{sp}} = 1$  pc. In this plot we have assumed the MED parameter set,  $\langle \sigma v \rangle = 3 \times 10^{-26} \text{ cm}^3 \text{ s}^{-1}$  and  $m_{\text{DM}} = 10$  GeV.

Fig. 4.6 illustrates the main characteristics of the diffusion process. On the one hand, for  $\lambda_D \gtrsim |\vec{x}|$ , the halo function falls off steeply to zero (approximately as  $\lambda_D^3$ ), showing that the central part of the source distribution (at radii smaller than the diffusion length) is depleted of electrons due to diffusion. On the other hand, for  $\lambda_D \lesssim |\vec{x}|$  we have  $\tilde{I}_{\vec{x}} = (\rho(\vec{x})/\rho_{\odot})^2$ , which illustrates the fact that the source profile is essentially unaffected over scales larger than  $\lambda_D$ , since electrons cannot diffuse over distances larger than the diffusion length. Finally, the peak for  $\lambda_D \approx |\vec{x}|$  visible in the right panel of Fig. 4.6 corresponds to the peak of the DM distribution

<sup>7</sup>We recall that

$$\frac{1}{\lambda_D^3 \pi^{3/2}} \exp\left(-\frac{\vec{x}^2}{\lambda_D^2}\right) \xrightarrow{\lambda_D \rightarrow 0} \delta(\vec{x}). \quad (4.89)$$

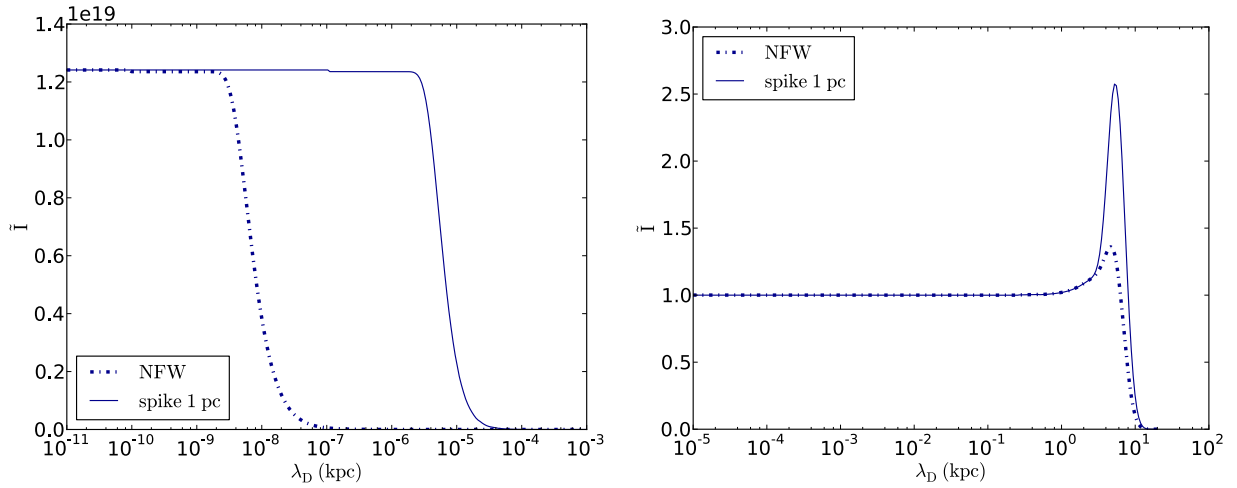


**Figure 4.6** – Halo function at the GC (**left panel**) and at the position of the Sun (**right panel**), as a function of the diffusion length, for the NFW profile (dashed-dotted line) and the NFW+spike profile with  $R_{sp} = 1$  pc (solid line). The MED parameter set is used.

at the GC. The left panel represents the halo function at the GC, so the peak in the DM profile coincides with the fall-off in  $\lambda_D$ .

Armed with this very precise treatment of the halo function for very small  $\lambda_D$  and very small distances from the GC, and the resulting spectrum of primary electrons and positrons accounting for propagation, we can now estimate secondary photon emission from electrons and positrons injected in particular by DM spikes.

## Part III

# Secondary gamma-ray emission from electrons and positrons and the *Fermi* Galactic center excess



## Chapter 5

# The *Fermi* excess of gamma-rays at the Galactic center

Several independent groups have reported evidence in the *Fermi*-LAT data of an extended excess of  $\gamma$ -rays above the diffuse Galactic background (DGB), from a few degrees around the GC (Goodenough & Hooper, 2009; Vitale et al., 2009; Hooper & Goodenough, 2011; Hooper & Linden, 2011; Abazajian & Kaplinghat, 2012, 2013; Gordon & Macías, 2013; Abazajian et al., 2014; Daylan et al., 2016; Calore et al., 2015a; Ajello et al., 2015). In the following, we refer to this feature equally as the *Fermi* GeV excess, the GeV excess, or the GC excess (GCE). In this chapter, we first give an overview of the properties of the GeV excess, and we describe the main possible explanations. Then, based on the spectrum of the GCE, we show that accounting for secondary photon emission from electrons and positrons produced in DM annihilations is crucial and can utterly change the interpretation of the GCE.

### Contents

---

<b>5.1</b>	<b>Properties of the Galactic center excess . . . . .</b>	<b>88</b>
<b>5.2</b>	<b>Interpretations . . . . .</b>	<b>88</b>
5.2.1	Pulsars . . . . .	88
5.2.2	Electron or proton bursts in the Galactic center . . . . .	89
5.2.3	Dark matter annihilations . . . . .	90
<b>5.3</b>	<b>On the importance of secondary electrons and positrons from dark matter . . . . .</b>	<b>91</b>
5.3.1	Components of the diffuse gamma-ray emission from dark matter . . . . .	91
5.3.2	New dark matter interpretation of the GeV excess with secondary photon emission . . . . .	92
5.3.3	Further tests . . . . .	96
<b>5.4</b>	<b>Conclusion . . . . .</b>	<b>98</b>

---

## 5.1 Properties of the Galactic center excess

The spectrum of the GC excess is characterized by a bump peaking around 1–3 GeV. The excess is found to be approximately spherically symmetric,<sup>1</sup> with an intensity which drops like  $\sim \theta^{-2\gamma+1}$  where  $\theta$  is the angle from the GC, and  $\gamma \sim 1.2$ . This corresponds to a volume emissivity dropping with radius  $r$  from the GC like  $r^{-2\gamma}$ .<sup>2</sup> The excess has also been found to extend out as far as  $\sim 10^\circ$  (Hooper & Slatyer, 2013; Daylan et al., 2016).

There is some debate over how much the excess is affected by systematic errors, which are dominated by uncertainties in the DGB model. Although the excess is generally claimed to be robust with respect to systematics (Gordon & Macías, 2013; Macías & Gordon, 2014; Daylan et al., 2016; Zhou et al., 2015; Calore et al., 2015b), some authors argue that the residuals can be partly or even totally absorbed in the DGB (Gaggero et al., 2015a; Carlson et al., 2015; Ajello et al., 2015), or can be an artifact of emission from the Galactic plane (de Boer et al., 2015). Building more accurate models of the DGB, relying for instance on non-standard cosmic-ray propagation (Gaggero et al., 2015b) will be crucial to settle this question.

## 5.2 Interpretations

In this section, we review the leading explanations of the GC excess,<sup>3</sup> under the assumption that it cannot be absorbed in a more complex DGB model.

### 5.2.1 Pulsars

Millisecond pulsars (MSPs) are rapidly rotating neutron stars with periods of order 1–10 ms, much shorter than normal pulsars. The favored model suggests that MSPs are old pulsars that have been spun up by accretion from a binary companion (see e.g. Bhattacharya & van den Heuvel, 1991; Lorimer, 2008, for reviews). This is supported by observations, with a large proportion of MSPs found in binaries, contrary to normal pulsars which are mostly single neutron stars. The production of high-energy  $\gamma$ -rays by rotation-powered pulsars is not well understood at present. However, all models involve electrostatic acceleration in the magnetosphere and the production of electron-positron pairs emitting photons via curvature, inverse Compton and synchrotron radiation. These photons produce in turn more electron-positron pairs, resulting in a cascade that shapes the final  $\gamma$ -ray emission (see e.g. Harding et al., 2007). This mechanism leads typically to a signature in the GeV range.

It turns out that the GeV excess may be accounted for by a population of  $\sim 10^3$ – $10^4$  MSPs, as pointed out in Abazajian (2011); Abazajian & Kaplinghat (2012); Wharton et al. (2012); Abazajian & Kaplinghat (2013); Gordon & Macías (2013); Mirabal (2013); Abazajian et al. (2014); Gordon & Macías (2014); Macías & Gordon (2014); Yuan & Zhang (2014); Petrović et al. (2015). In particular, the spectrum of the GCE can be well reproduced by a power-law with exponential cut-off, which is the characteristic spectrum of observed  $\gamma$ -ray pulsars (Abdo et al., 2013). From the analysis of Gordon & Macías (2013), the best fit to the spectral data points for a power law with exponential cut-off is:

$$\frac{dn}{dE_\gamma} = \mathcal{K} \left( \frac{E_\gamma}{E_0} \right)^{-\Gamma} \exp \left( -\frac{E_\gamma}{E_{\text{cut}}} \right), \quad (5.1)$$

with  $E_0 = 1.176$  GeV,  $\mathcal{K} = 2.5 \times 10^{-7} \pm 4 \times 10^{-8} \text{ cm}^{-2} \text{ s}^{-1} \text{ GeV}^{-1}$ ,  $\Gamma = 1.6 \pm 0.2$  and  $E_{\text{cut}} = 4 \pm 1.5$  GeV. A log parabola spectrum gives an equally good fit:

$$\frac{dn}{dE_\gamma} = N_0 \left( \frac{E_\gamma}{E_0} \right)^{-[\alpha_0 + \beta_0 \log(E_\gamma/E_0)]}, \quad (5.2)$$

<sup>1</sup>The spherical symmetry has been however questioned in Yang & Aharonian (2016).

<sup>2</sup>See Appendix for the analytic projection of a power-law profile along the line of sight.

<sup>3</sup>It has been argued that the GCE may be due to the central point source (Boyarsky et al., 2011).

with  $N_0 = 1.96_{-0.17}^{+0.18} \times 10^{-7} \text{ cm}^{-2} \text{ s}^{-1} \text{ GeV}^{-1}$ ,  $\alpha_0 = 1.92_{-0.15}^{+0.13}$ , and  $\beta_0 = 0.32_{-0.09}^{+0.10}$ . Shown in Fig. 5.1 are these two best-fit spectra, multiplied by  $E_\gamma^2$ , with the power law with exponential cut-off represented by a black dashed line, and the log parabola by a blue solid line, along with the spectral points derived in Gordon & Macías (2013). These very similar functional forms are typical parametrizations of the  $\gamma$ -ray spectrum from a population of MSPs.

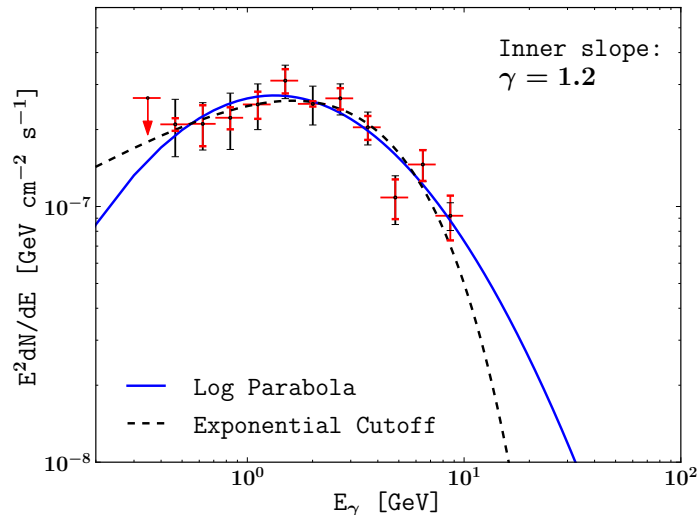


**Figure 5.1** – Two typical parametrizations of the  $\gamma$ -ray spectrum from MSPs that reproduce very well the spectral points of the GCE: a power law with exponential cut-off (black dashed line), and a log parabola (blue solid line). This figure is taken from Gordon & Macías (2013).

Although the spectral signature of the GCE can be very well reproduced by MSPs, there is some debate on the spatial morphology induced by MSPs, especially on whether the subsequent emission could successfully extend out as far as  $\sim 10^\circ$  (Hooper et al., 2013; Cholis et al., 2015a; Petrović et al., 2015; Linden, 2015) given the small number of pulsars that have already been resolved by *Fermi*-LAT (Abdo et al., 2013; Cholis et al., 2014). Nevertheless, these conclusions rely on assumptions made on the luminosity function of MSPs and the treatment of point sources. In this context, the MSP hypothesis has been reinforced by several more recent papers (Bartels et al., 2015; Brandt & Kocsis, 2015; Lee et al., 2015, 2016).

In addition to the spatial extension of the signal, the MSP scenario is supported by observations showing that the favored progenitors of MSPs, namely low-mass X-ray binaries, follow a  $r^{-2.4}$  profile consistent with the observed morphology of the GCE (e.g. Yuan & Zhang, 2014).

Finally, it turns out that young pulsars—provided they are however sufficiently evolved to have hard enough spectra and to reach high latitudes—have also been invoked as an alternative explanation of the GCE (O’Leary et al., 2015). Young pulsars have the advantage of being better characterized than MSPs, so they allow for more definite predictions than MSPs which suffer from larger uncertainties in their modeling.

### 5.2.2 Electron or proton bursts in the Galactic center

Another scenario is an injection of electrons (Petrović et al., 2014) or protons (Carlson & Profumo, 2014) in a burst or series of bursts, from a putative active past of the GC. After injection, the particles propagate in the Galaxy via spatial diffusion and convection. Electrons emit  $\gamma$ -rays by inverse Compton scattering on the ISRF, while interactions of protons with interstellar gas lead to the production of neutral pions which subsequently decay into  $\gamma$ -ray photons.

However, for old bursts, protons have time to diffuse out to large distances, which leads to a  $\gamma$ -ray signature extended along the Galactic plane, i.e. correlated with the gas density. This is inconsistent with the spherical symmetry of the GCE and disfavors this scenario.

Electron bursts would lead to a spherically symmetric signal, and would therefore in principle not be in tension with observations. However, a viable model accounting for all the features of the GCE seems to require several bursts and a significant amount of fine-tuning (Cholis et al., 2015b).

### 5.2.3 Dark matter annihilations

The GeV excess is of great interest to the DM indirect detection community since it can be readily interpreted in terms of annihilations of DM particles with masses in the range 10–100 GeV into a variety of channels (Goodenough & Hooper, 2009; Hooper & Goodenough, 2011; Hooper & Linden, 2011; Abazajian & Kaplinghat, 2012, 2013; Gordon & Macías, 2013; Macías & Gordon, 2014; Abazajian et al., 2014; Daylan et al., 2016; Calore et al., 2015a). The DM model favored in the literature corresponds to a  $\sim 30$  GeV candidate annihilating into  $b\bar{b}$ . In that case the prompt  $\gamma$ -ray emission reproduces the spectral bump at 1–3 GeV, as shown in Fig. 5.2.

The morphology of the excess is also well reproduced for a DM profile going as  $r^{-\gamma}$  at the GC, with  $\gamma \sim 1.2$ . This is steeper than the standard NFW profile—which has a slope of 1—derived from DM-only N-body simulations, but it could be explained for instance by adiabatic contraction of the DM halo induced by baryonic infall (Blumenthal et al., 1986).

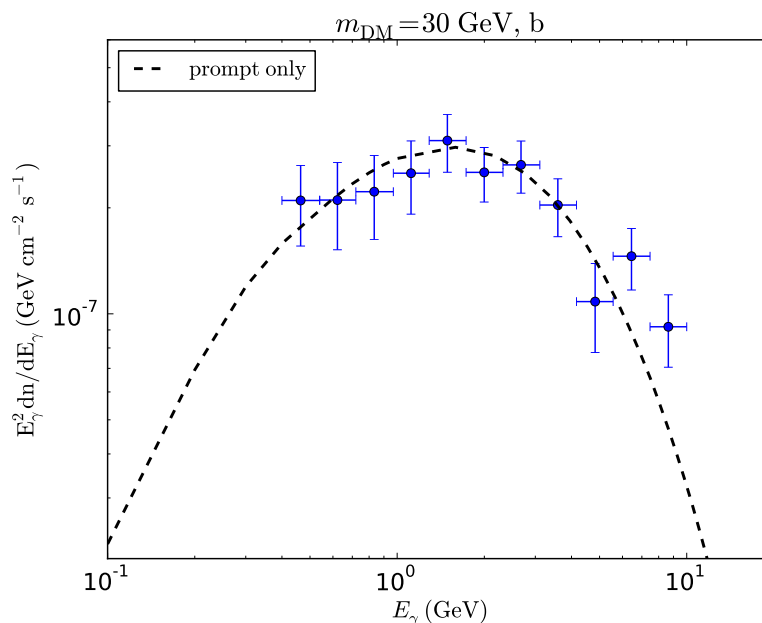


**Figure 5.2** – Spectrum of the GCE in the  $7^\circ \times 7^\circ$  region around the GC. The blue points are the residuals in the *Fermi*-LAT data extracted by Gordon & Macías (2013). The black dashed line represents prompt emission for annihilations of 30 GeV DM particles into 100%  $b\bar{b}$ , with a best-fit cross-section of  $\approx 2 \times 10^{-26} \text{ cm}^3 \text{ s}^{-1}$ .

In spite of the promises it holds in terms of new physics, there is debate as to whether the DM explanation of the GCE is ruled out or confirmed by other probes, in particular *Fermi*-LAT observations of dwarf satellites of the MW (Calore et al., 2015a; Abazajian & Keeley, 2015; Geringer-Sameth et al., 2015a; Ackermann et al., 2015a; Geringer-Sameth et al., 2015b) and antiprotons (Cirelli et al., 2014a; Bringmann et al., 2014; Hooper et al., 2015). For now, no strong conclusions can be drawn in either direction, due to large uncertainties on the modeling side, leaving DM annihilations as a possible origin of the GCE. We now discuss the DM scenario in more detail, focusing on secondary photon emission from DM-induced electrons and positrons.

### 5.3 On the importance of secondary electrons and positrons from dark matter

This section is adapted from Lacroix et al. (2014b). As discussed e.g. in Hooper & Linden (2011); Gordon & Macías (2013), although leptonic channels can contribute to some extent to the GCE, a large fraction of  $b$  quarks in the final state is generally favored. Pure leptonic final states were discarded due to the resulting hard prompt spectra, as discussed in Gordon & Macías (2013).

However, these conclusions were obtained by only accounting for the prompt  $\gamma$ -ray emission originating from these channels. Abazajian et al. (2014) and Daylan et al. (2016) also included the bremsstrahlung contribution from electrons generated by the showering of the  $b\bar{b}$  final state, but they disregarded IC emission. Furthermore, they did not account for spatial diffusion.

Here we show that the  $\gamma$ -ray emission from IC scattering and bremsstrahlung should definitely not be neglected as it typically induces a signal in the energy range where the excess has been observed. The importance of the contribution from inverse Compton scattering was argued in Ackermann et al. (2012a) in the general context of constraints on DM annihilations from the diffuse Galactic  $\gamma$ -ray emission. However, here we show that these contributions from diffused electrons do not simply induce corrections to the  $\gamma$ -ray spectrum, but in fact they drastically change the DM interpretation of the excess. More specifically, it turns out that one can account for the entire spectrum of the GCE with a pure leptonic final state.

#### 5.3.1 Components of the diffuse gamma-ray emission from dark matter

We consider the same DM halo profile as in Gordon & Macías (2013), namely the generalized NFW profile:

$$\rho(r) = \rho_{\odot} \left( \frac{r}{r_{\odot}} \right)^{-\gamma} \left( \frac{1 + \left( \frac{r}{r_s} \right)^{\alpha}}{1 + \left( \frac{r_{\odot}}{r_s} \right)^{\alpha}} \right)^{-\frac{\beta-\gamma}{\alpha}}, \quad (5.3)$$

with  $\alpha = 1$ ,  $\beta = 3$ ,  $\gamma = 1.2$ ,  $\rho_{\odot} = 0.36 \text{ GeV cm}^{-3}$  and  $r_s = 23.1 \text{ kpc}$ .<sup>4</sup>

For prompt emission, the intensity  $dn_f/(dE_{\gamma}d\Omega)|_{\text{prompt}}$  for final state  $f$  is given by Eq. (2.12), while for ICS and bremsstrahlung, the intensity  $dn_f/(dE_{\gamma}d\Omega)|_{\text{IC,brems}}$  is computed following the procedure described in Chapter 4, accounting for spatial diffusion as detailed in Sec. 4.3.7.

Energy losses are dominated by IC, bremsstrahlung, and synchrotron:  $b_{\text{tot}} = b_{\text{IC}} + b_{\text{brems}} + b_{\text{syn}}$ . We consider homogeneous losses, but this is a valid assumption since we focus on a small region around the GC. In this project, we consider for simplicity only neutral hydrogen which is the dominant gas component. The bremsstrahlung loss rate depends on the number density  $n_{\text{gas}} \equiv n_{\text{HI}} + 2n_{\text{H}_2}$  in the region of injection of the electrons. In this chapter, we use a conservative approach and we only consider values of  $\mathcal{O}(1) \text{ cm}^{-3}$  for  $n_{\text{gas}}$ . A higher gas number density would increase the bremsstrahlung losses and accordingly the confinement of the electrons. Consequently this would increase the bremsstrahlung emission and reduce the IC contribution. As for IC losses, we use the procedure described in Sec. 4.3.5.1, which consists in fitting the ISRF spectrum with several greybody spectra corresponding to the different components (CMB, starlight, IR from dust). The corresponding parameters of the ISRF components are given in Table 5.1. The IC loss rate  $b_{\text{IC}}$  is then computed for the different components in the different energy regimes as presented in Sec. 4.3.5.1. To apply this method, we use the spectral energy distribution (SED) of the ISRF at the GC from GALPROP (Porter et al., 2008). Considering that the electron

<sup>4</sup>We put a cutoff in the profile at the Schwarzschild radius of the SMBH at the GC,  $R_s = 4.2 \times 10^{-7} \text{ pc}$ . This value is about the same as the saturation radius from annihilations. We checked the consistency of this cutoff with the literature by reproducing the results of Gordon & Macías (2013); Hooper & Linden (2011) for prompt emission. In practice a cutoff at a slightly larger scale does not make any difference in the results since the angular resolution of *Fermi*-LAT is not good enough.

propagation scale is smaller than 2 kpc in the energy range considered in this study, we average the SED on a cylinder of radius and half-height of 2 kpc centered on the GC.

**Table 5.1** – Temperatures  $T$  and energy densities  $w$  obtained by fitting the spectral energy distribution of the ISRF with greybody spectra. The parameters of the blackbody spectrum of the CMB are also displayed.

	$T$ (K)	$w$ (GeV cm <sup>-3</sup> )
CMB	2.725	$2.602 \times 10^{-10}$
IR	$4.231 \times 10^1$	$6.841 \times 10^{-10}$
Starlight	$2.669 \times 10^2$	$1.214 \times 10^{-10}$
	$3.176 \times 10^3$	$3.317 \times 10^{-9}$
	$6.373 \times 10^3$	$2.745 \times 10^{-9}$
	$2.437 \times 10^4$	$7.746 \times 10^{-10}$

To compare the importance of the different components, we use a  $7^\circ \times 7^\circ$  region corresponding to the region of interest of [Gordon & Macías \(2013\)](#). The fluxes from prompt emission, IC or bremsstrahlung, for annihilation channel  $f$  from the squared  $7^\circ \times 7^\circ$  region are obtained by integrating the corresponding intensities over the field of view:

$$E_\gamma^2 \frac{dn_f}{dE_\gamma} = 4 \int_0^{\theta_{\text{fov}}} \int_0^{\theta_{\text{fov}}} E_\gamma^2 \frac{dn_f}{dE_\gamma d\Omega} \cos b db dl, \quad (5.4)$$

where  $l$  and  $b$  are respectively the longitude and the latitude, and  $\theta_{\text{fov}} = 3.5^\circ$  defines the field of view. This corresponds to the flux expected for a given annihilation channel. Finally, to get the total flux, we sum and weight the different channels (leptons, leptons+ $b$  quarks,  $b\bar{b}$ ).

### 5.3.2 New dark matter interpretation of the GeV excess with secondary photon emission

We can now estimate the relative importance of the diffuse  $\gamma$ -ray emission generated through the propagation of secondary (and primary)  $e^\pm$  with respect to prompt emission, and how this additional contribution affects the fit to the GCE. We consider three specific scenarios in which DM particles annihilate either into 100% leptons, a mixture of leptons and  $b\bar{b}$  or 100%  $b\bar{b}$ . Throughout this section, and especially in the figures, “leptons” refers to a mixture of the  $e^+e^-$ ,  $\mu^+\mu^-$ ,  $\tau^+\tau^-$  channels, with 1/3 of the annihilations into each of these channels.

To make our point, we choose fixed benchmark values of the parameters describing the interstellar medium (in particular the magnetic field and gas density) and allow the annihilation cross-section to vary. For simplicity, we assume the same value of the annihilation cross-section for all the final states considered in this section. In principle one should scan over all possible free parameters (including in fact the magnetic field and gas density) but since we are mainly interested in showing that  $\sim 10$  GeV DM annihilating into leptons fits the data very well if one accounts for spatial diffusion and  $\gamma$ -rays emitted by DM-induced electrons, we keep a simplified setup with  $B = 3 \mu\text{G}$  and  $n_{\text{gas}} = 3 \text{ cm}^{-3}$ .

The data are taken from [Gordon & Macías \(2013\)](#) and correspond to a  $7^\circ \times 7^\circ$  region. Different data sets were obtained e.g. in [Hooper & Linden \(2011\)](#); [Abazajian et al. \(2014\)](#); [Daylan et al. \(2016\)](#), depending on assumptions on the background sources that are being subtracted from the data, but the implications of these different results on our best-fit parameters are beyond the scope of the project presented here.

In [Fig. 5.3](#), we compare the contributions from prompt emission, IC and bremsstrahlung, for a pure democratic leptonic channel. As one can readily see, IC emission is particularly important at low energy (below 1 GeV) while bremsstrahlung emission is important at intermediate energies (1–10 GeV). Also, as pointed out already in previous work ([Gordon & Macías, 2013](#)), prompt

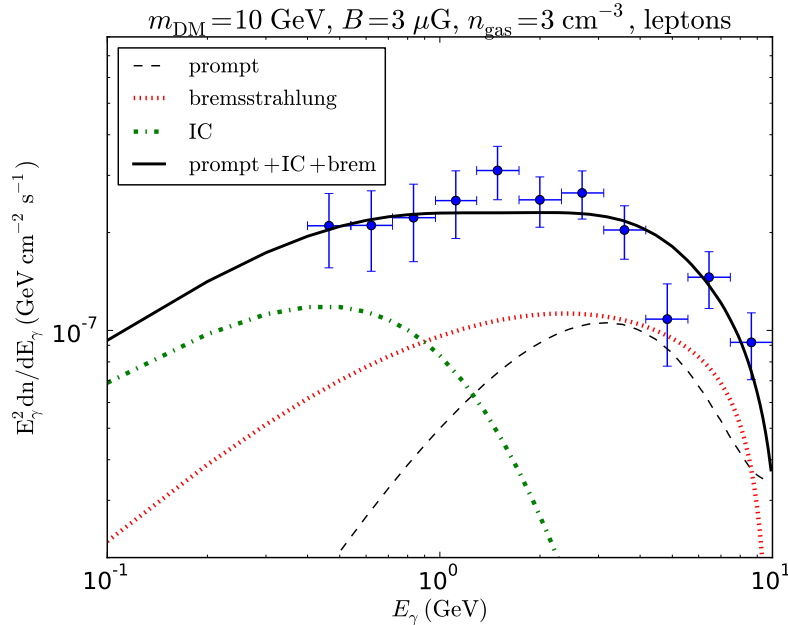


**Figure 5.3** – Spectrum of the GCE in the  $7^\circ \times 7^\circ$  region around the GC. The blue points are the residuals in the *Fermi*-LAT data extracted in [Gordon & Macías \(2013\)](#). The contributions from prompt emission (black dashed), IC (green dot-dashed) and bremsstrahlung (red dotted) from 10 GeV DM democratically annihilating into leptons add up to give a very good fit to the data, as shown by the black solid line. The best-fit cross-section is  $\langle\sigma v\rangle \approx 0.9 \times 10^{-26} \text{ cm}^3 \text{ s}^{-1}$ .

emission alone cannot account for the data for the leptonic channel. However, our work shows that the sum of the three components (prompt, IC and bremsstrahlung) actually provides an excellent fit.

We compare the best fits obtained with prompt emission only and with the contribution from IC and bremsstrahlung, for a pure democratic leptonic final state in [Fig. 5.4](#), and a scenario containing 90% leptons and 10%  $b\bar{b}$  quarks in [Fig. 5.5](#). The importance of the IC and bremsstrahlung contributions is less crucial when DM can annihilate into  $b\bar{b}$ . Nevertheless, these IC and bremsstrahlung components significantly improve the quality of the fit.

To make a more quantitative statement, we define the goodness-of-fit by the criterion  $\chi^2 < 29.6$ , which gives a p-value greater than  $10^{-3}$  ([Beringer et al., 2012](#)), corresponding to 11 data energy bins and one free parameter,  $\langle\sigma v\rangle$ . Note that in our analysis we combine in quadrature the statistical and systematic errors provided in [Gordon & Macías \(2013\)](#). For prompt emission with only leptons, the best fit is obtained for  $\langle\sigma v\rangle \approx 2 \times 10^{-26} \text{ cm}^3 \text{ s}^{-1}$ , with  $\chi^2 = 41.93$ , which is a bad fit. However, we obtain a  $\chi^2$  of 10.21 for a cross-section of  $0.9 \times 10^{-26} \text{ cm}^3 \text{ s}^{-1}$  once we include the IC and bremsstrahlung contributions. This demonstrates the importance of accounting for the  $\gamma$ -ray emission from propagated electrons. Note that the error bars on the cross-section at the  $1\sigma$  level are of the order of  $0.1 \times 10^{-26} \text{ cm}^3 \text{ s}^{-1}$ .

For the channel with 90% leptons + 10%  $b\bar{b}$ , the difference is smaller than for leptons only, but the  $\chi^2$  is nevertheless reduced from 16.46 (with a best-fit cross-section of  $2.1 \times 10^{-26} \text{ cm}^3 \text{ s}^{-1}$ ) down to 9.57 (with a best-fit cross-section of  $0.9 \times 10^{-26} \text{ cm}^3 \text{ s}^{-1}$ ) when including IC and bremsstrahlung. Therefore, in such a scenario, both spectra with or without the IC and bremsstrahlung contributions fit well the data, but there is a clear preference for the total spectrum.

Shown in [Fig. 5.6](#) are the best fits for the prompt spectrum and the total spectrum in the case of a 30 GeV DM particle annihilating into 100%  $b\bar{b}$ . The corresponding best-fit values of the annihilation cross-section are not very different:  $\langle\sigma v\rangle \approx 2.2 \times 10^{-26} \text{ cm}^3 \text{ s}^{-1}$  for prompt emission (with  $\chi^2 = 11.24$ ), and  $\langle\sigma v\rangle \approx 2 \times 10^{-26} \text{ cm}^3 \text{ s}^{-1}$  for the total emission (with  $\chi^2 = 11.98$ ). In

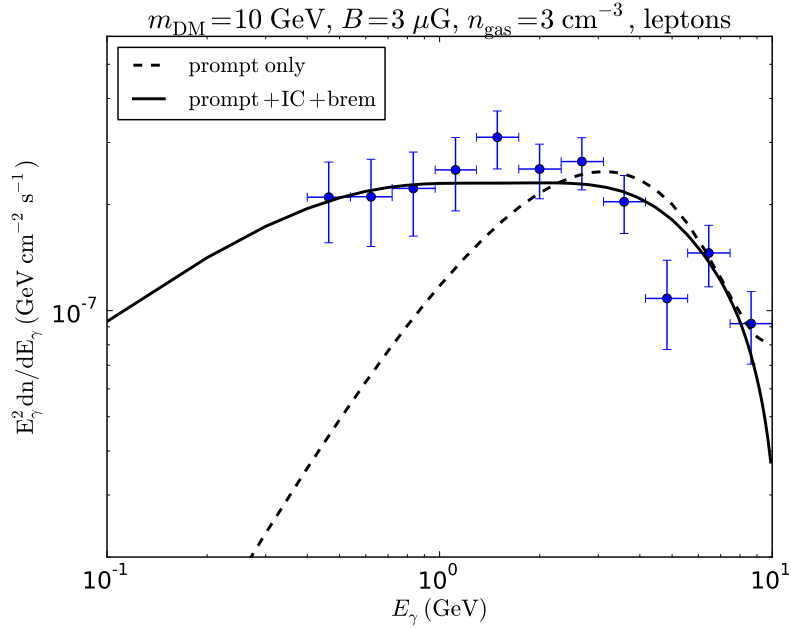


**Figure 5.4** – Best fits to the spectrum of the GCE for democratic annihilations of 10 GeV DM particles into leptons. The best fit is shown for prompt  $\gamma$ -ray emission only, and with the three contributions from prompt, IC and bremsstrahlung. The corresponding best-fit cross-section for the total spectrum is  $\langle\sigma v\rangle \approx 0.9 \times 10^{-26} \text{ cm}^3 \text{ s}^{-1}$ . When fitting the data with only prompt  $\gamma$ -rays, the cross-section is  $\approx 2 \times 10^{-26} \text{ cm}^3 \text{ s}^{-1}$ . Including the  $\gamma$ -ray emission from diffused  $e^\pm$  significantly improves the fit.

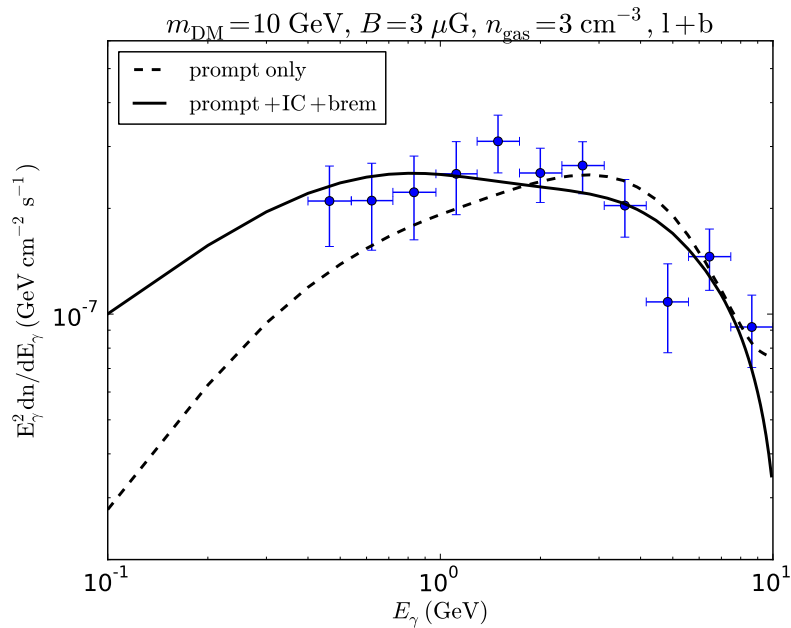


**Figure 5.5** – Best fits to the spectrum of the GCE for annihilations of 10 GeV DM particles into 90% leptons and 10%  $b$  quarks. The best fit is shown for prompt  $\gamma$ -ray emission only (dashed line), and with the three contributions from prompt, IC and bremsstrahlung (solid line). The corresponding best-fit cross-section for the total spectrum is about the same as for leptons only,  $\langle\sigma v\rangle \approx 0.9 \times 10^{-26} \text{ cm}^3 \text{ s}^{-1}$ . The cross-section for prompt emission only is  $\approx 2.1 \times 10^{-26} \text{ cm}^3 \text{ s}^{-1}$ .

this case, the contributions from IC and bremsstrahlung are subdominant, except at low energy. This is due to the fact that the IC and bremsstrahlung emission spectra take large values for

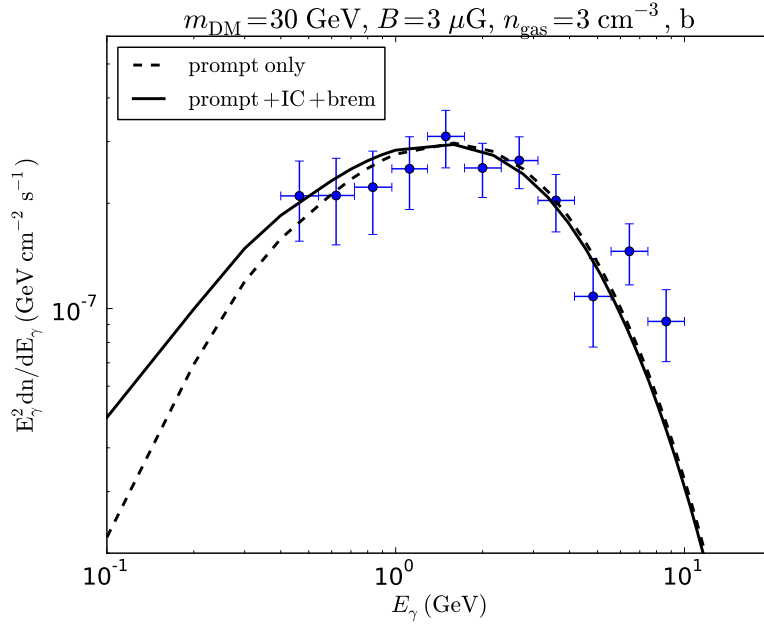


**Figure 5.6** – Best fits to the spectrum of the GCE for annihilations of 30 GeV DM particles into 100%  $b\bar{b}$ . Including the contributions from IC and bremsstrahlung does not significantly affect the spectrum, except at low energies. The best-fit cross-section in both cases is of the order of  $2 \times 10^{-26} \text{ cm}^3 \text{ s}^{-1}$ .

electron energies close to the DM mass ( $E_e$  must be much greater than the observed energy  $E_\gamma$ ). Electrons originating from  $b\bar{b}$  have a softer injection spectrum, unlike those originating from leptonic annihilation channels, which have a harder spectrum, peaking closer to the DM mass. Hence, looking at the  $\gamma$ -ray spectrum at lower energies could be a good way to test whether the  $b\bar{b}$  channel, which is usually claimed to be the preferred channel, indeed agrees with other data sets from the GC.

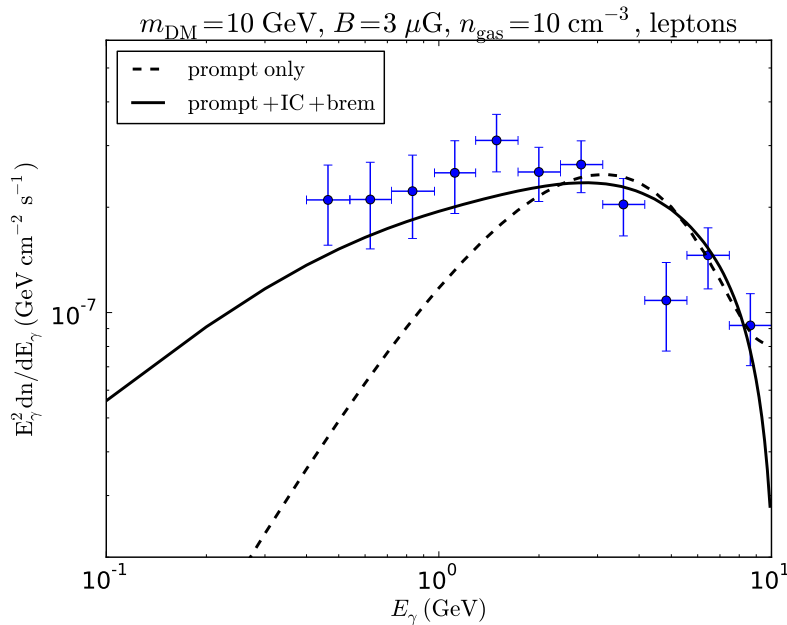


**Figure 5.7** – Best fits to the spectrum of the GCE for democratic annihilations of 10 GeV DM particles into leptons, with a gas density of  $10 \text{ cm}^{-3}$ .

So far, we have shown that taking  $B = 3 \mu\text{G}$  and  $n_{\text{gas}} = 3 \text{ cm}^{-3}$  leads to a very good fit to the data with the total spectrum, particularly for the leptonic channel. It turns out that this conclusion is fairly robust with respect to changes in these parameters. For instance, taking  $B = 10 \mu\text{G}$ —which may be more consistent with the value close to the GC—leads to a small global shift of the IC and bremsstrahlung contributions (due to greater losses). The resulting best fit is only slightly affected, with  $\chi^2 = 10.35$  and  $\langle\sigma v\rangle \approx 0.9 \times 10^{-26} \text{ cm}^3 \text{ s}^{-1}$  for the leptonic channel. When taking a greater value for  $n_{\text{gas}}$ , namely  $10 \text{ cm}^{-3}$ , the resulting spectrum is harder but still provides a very good fit to the data, with  $\chi^2 = 16.6$  and  $\langle\sigma v\rangle \approx 0.6 \times 10^{-26} \text{ cm}^3 \text{ s}^{-1}$ , as shown in Fig. 5.7.

Finally, the diffusion model introduces an additional uncertainty, which is quantified by the MIN and MAX sets of propagation parameters and degenerated with the cross-section (although changing the diffusion parameters mostly affects the low-energy end of the spectrum, since the prompt contribution remains fixed). This uncertainty is shown in Fig. 5.8. The hatched area is bounded by the spectra for the MIN and MAX sets (respectively at the top and the bottom of the band) computed with the best-fit cross-section obtained with the MED set. Hence the uncertainty on the diffusion model translates into an error on the best-fit value for the cross-section. The corresponding values for the MIN and MAX sets are  $\langle\sigma v\rangle_{\text{MIN}} \approx 0.7 \times 10^{-26} \text{ cm}^3 \text{ s}^{-1}$  and  $\langle\sigma v\rangle_{\text{MAX}} \approx 1.2 \times 10^{-26} \text{ cm}^3 \text{ s}^{-1}$ .

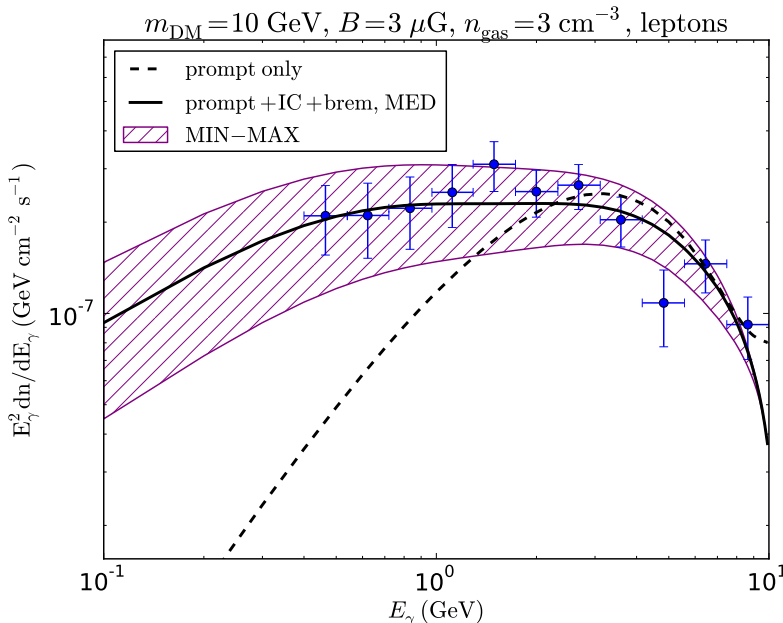


**Figure 5.8** – Best fits to the spectrum of the GCE for democratic annihilations of 10 GeV DM particles into leptons. The purple hatched area represents the uncertainty on the best fit for the total spectrum including IC and bremsstrahlung due to the uncertainty on the diffusion model. The band is bracketed by the fluxes for the MIN and MAX sets, at the top and the bottom, respectively.

### 5.3.3 Further tests

#### 5.3.3.1 Discussion of constraints from the AMS-02 data

We found two best fits in the leptonic case: one corresponding to the democratic scenario ( $\chi^2 = 10.21$ ) and one without electrons and with branching ratios of about 2/3 into  $\mu^+\mu^-$  and 1/3 into  $\tau^+\tau^-$  ( $\chi^2 = 14.22$ ). For the latter case the fit requires a cross-section of  $1.4 \times 10^{-26} \text{ cm}^3 \text{ s}^{-1}$ . The democratic scenario is however in tension with the limits on the annihilation cross-section into  $e^+e^-$  derived from the AMS-02 data in Bergström et al. (2013); Ibarra et al. (2014); Bringmann

et al. (2014), which essentially exclude annihilations into  $e^+e^-$  with cross-sections close to the thermal value in the low-mass range of interest here. These limits also exclude branching ratios into  $\mu^+\mu^-$  larger than 0.25 (Bringmann et al., 2014).

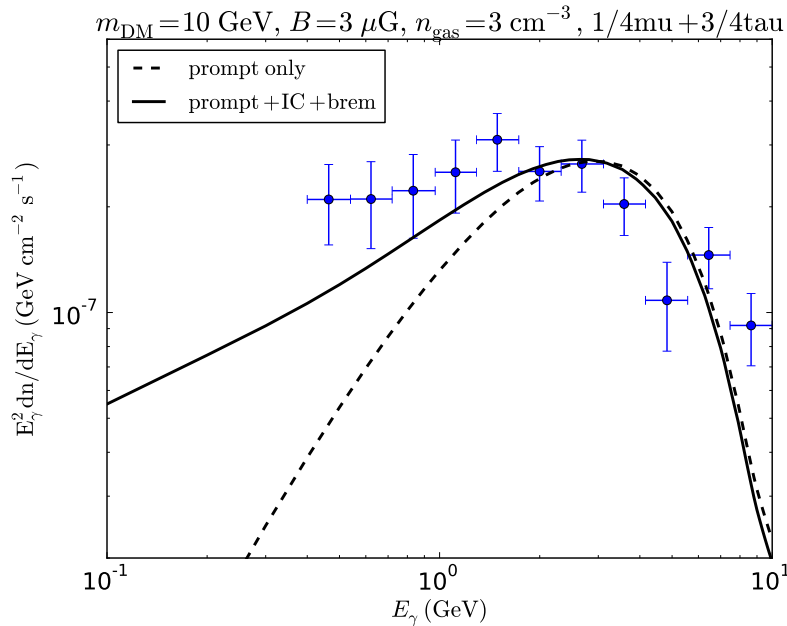


**Figure 5.9** – Best fits to the spectrum of the GCE for annihilations of 10 GeV DM particles with branching ratios of 0.25 into  $\mu^+\mu^-$  and 0.75 into  $\tau^+\tau^-$ . The best-fit cross-section is  $\approx 1 \times 10^{-26} \text{ cm}^3 \text{ s}^{-1}$ .

The constraints from Bringmann et al. (2014) were obtained by searching for tiny deviations from a power-law background that empirically fits the AMS-02 data. These limits would probably be less stringent if one relaxes the assumption of a smooth background. However, as shown in Fig. 5.9, when taking these constraints into account, we find that the effect of IC and bremsstrahlung becomes less significant than for a larger branching ratio into muons, but it is still definitely relevant. The associated best-fit cross-section for a branching ratio into muons of 0.25 is  $\langle\sigma v\rangle \approx 1 \times 10^{-26} \text{ cm}^3 \text{ s}^{-1}$  and we find  $\chi^2 = 27.3$ , which corresponds to a marginally good fit.

### 5.3.3.2 Spatial morphology

The spatial morphology of the diffuse emission in the case of the democratic leptonic scenario depends on the observed energy. In Fig. 5.10, we show the expected  $\gamma$ -ray flux as a function of latitude (or similarly longitude) for three different energies (0.1 GeV, 1.0 GeV and 9.5 GeV). As one can see, secondary electrons can induce a significant excess of  $\gamma$ -rays at low energies (below a few GeV) with respect to prompt emission. This contribution leads to a significant flux up to a few tens of degrees which is in agreement with Daylan et al. (2016), where the authors found that the excess extends out to at least  $12^\circ$ .

Below 1 GeV (typically 0.1 GeV), the diffusion contribution dominates over the contribution from prompt emission. Between  $3^\circ$  and  $12^\circ$ , we find that our model is well fitted by a power law with index 1.34, which is very close to the index of 1.4 that one obtains for prompt emission only, corresponding to a DM profile with a power-law index of 1.2. Therefore, in this energy range our model is consistent with the morphology of the prompt emission found in the literature (see e.g. Daylan et al., 2016). However, at such low energies (i.e., essentially 0.1 GeV), the diffusion contribution leads to a spatial intensity profile between  $\mathcal{O}(0.1)$  and  $\mathcal{O}(1)^\circ$  that is shallower than the profile from prompt emission. At 1 GeV and for the same angular region, the tension is much

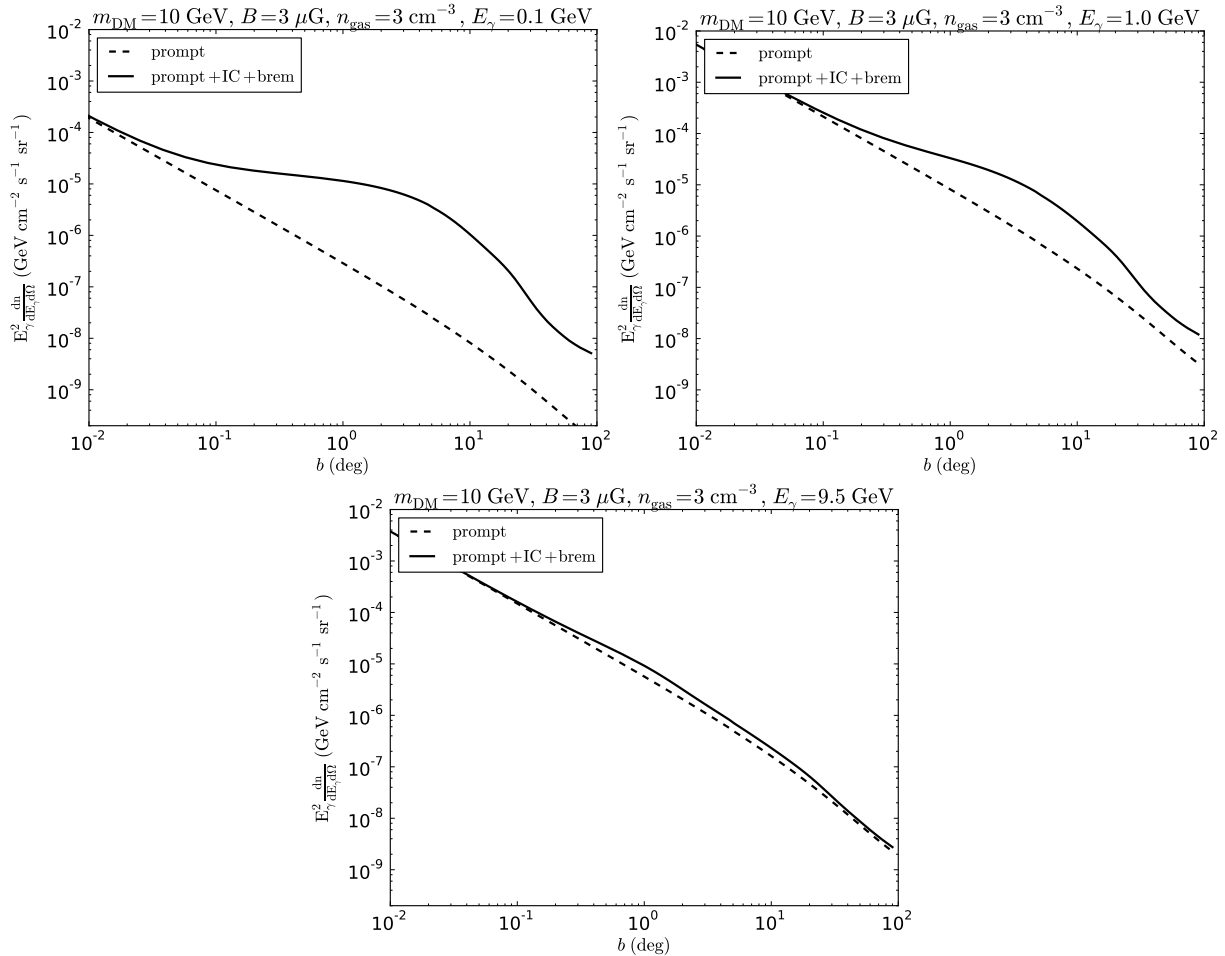


**Figure 5.10** –  $\gamma$ -ray intensity from DM annihilating exclusively into leptons democratically, as a function of latitude  $b$ , for three values of the  $\gamma$ -ray energy  $E_\gamma$ : 0.1, 1, and 9.5 GeV. The contributions from IC scattering and bremsstrahlung clearly lead to an excess with respect to prompt emission below  $10^\circ$  at low energy.

weaker.

Investigating the morphology in the  $[0.1^\circ, 1^\circ]$  region, at energies below 0.1 GeV, may therefore enable one to discriminate between the  $b\bar{b}$  and pure leptonic final states.<sup>5</sup> We note that unresolved sources are likely to contribute to the flux in such a small angular region. Hence although the contribution from the leptonic scenario might not be large enough in the inner degree at low energy with respect to observations, the total flux may actually be compatible with the data.

However, this whole discussion is based on spectral analyses of the GCE relying on a NFW template associated with prompt emission. An updated analysis of the *Fermi* data accounting for the different spatial morphology of the secondary components in a self-consistent way is therefore needed, and this is the object of Chapter 6.

## 5.4 Conclusion

In this project, we have demonstrated that accounting for the  $\gamma$ -ray emission from DM-induced electrons and positrons drastically changes the interpretation of the *Fermi*-LAT excess, since the entire spectrum of the excess can be accounted for by DM annihilations into leptons only. Therefore,  $b\bar{b}$  is not the only viable channel, and we have rehabilitated the pure leptonic channel

<sup>5</sup>Note that 0.1 GeV is actually below the lowest data point for the excess (which is around 0.3–0.4 GeV).

containing a combination of leptons. More specifically, we have shown that the contributions of the  $e^+e^-$  and  $\mu^+\mu^-$  channels to IC and bremsstrahlung are very important. The reason for this improved fit to the *Fermi* excess is the IC and bremsstrahlung contributions, which give a  $\gamma$ -ray spectrum at slightly lower energies than prompt emission. The effect is strong for democratic annihilation into leptons, while it gets weaker (but definitely non-negligible) for the scenario favored by the latest constraints (Bringmann et al., 2014), with no electrons and a branching ratio into muons of 0.25. Possible additional constraints on this scenario involve the morphology of the  $\gamma$ -ray flux at low energy: our model is not in strong tension with the morphology of the excess in the energy range of the data, but looking at lower energies may help to discriminate between the leptonic and  $b\bar{b}$  scenarios. Therefore, in the absence of such a strong constraint, and should the excess be of DM origin, one would definitely need to account for these leptonic final states to determine the DM mass and the value of the self-annihilation cross-section, even though models may be harder to build than for a pure  $b\bar{b}$  final state (Boehm et al., 2014a).

It turns out that our approach is very promising since our conclusions are equally applicable to MSPs, which are also expected to produce electrons and positrons, subsequently leading to secondary  $\gamma$ -ray emission on top of the direct  $\gamma$ -ray emission that has been claimed to account for the GCE (see e.g. Yuan & Ioka, 2015). Studying secondary photon emission is therefore a very promising way to test models of the GCE and to go beyond the standard approach.

Finally, as discussed above, spatial morphology is a very important property that is exploited to further discriminate between different scenarios. Although we found the morphology of the total DM-induced emission for the leptonic channels to be qualitatively compatible with the observed morphology of the GCE, a more thorough treatment is needed to determine how this is modified when the secondary emission processes are included in the statistical analysis of the *Fermi*-LAT data in a self-consistent way. This is what we discuss in Chapter 6.



## Chapter 6

# The spatial morphology of the secondary emission in the Galactic center gamma-ray excess

As discussed in Chapter 5, the injection of secondary electrons and positrons into the interstellar medium by an unresolved population of MSPs or DM annihilations can lead to observable  $\gamma$ -ray emission via inverse Compton scattering or bremsstrahlung. In this chapter, adapted from Lacroix et al. (2015b), we investigate how to determine whether secondaries are important in a model for the GCE. We develop a method of testing model fit which accounts for the different spatial morphologies of the secondary emission. We examine several models which give secondary emission and illustrate a case where a broadband analysis is not sufficient to determine the need for secondary emission.

### Contents

---

<b>6.1</b>	<b>Introduction</b>	<b>102</b>
<b>6.2</b>	<b>Models for the gamma-ray emission</b>	<b>102</b>
<b>6.3</b>	<b>Data analysis</b>	<b>104</b>
6.3.1	Data selection	104
6.3.2	Analysis methods	105
<b>6.4</b>	<b>Models and procedure</b>	<b>107</b>
<b>6.5</b>	<b>Results and discussion</b>	<b>108</b>
6.5.1	<i>Model I</i> , democratic leptons	108
6.5.2	<i>Model II</i> , no electrons	109
6.5.3	<i>Model III</i> , millisecond pulsars	109
<b>6.6</b>	<b>Conclusions</b>	<b>110</b>

---

## 6.1 Introduction

Electrons and positrons ( $e^\pm$ ) would be injected into the interstellar medium either by an unresolved population of  $\sim 10^3$  MSPs or via DM annihilations, if either of these is responsible for the  $\gamma$ -ray excess seen towards the GC. The interaction of such particles with the ISRF, galactic magnetic fields and interstellar gas, would modify not only the energy spectrum but also the spatial morphology of the extended  $\gamma$ -ray source.

The model prediction from DM annihilation secondaries is discussed in [Cirelli et al. \(2013\)](#); [Buch et al. \(2015\)](#). The *Fermi*-LAT constraints on secondaries from DM annihilations in the GC were considered in [Gómez-Vargas et al. \(2013\)](#); [Lacroix et al. \(2014b\)](#); [Abazajian et al. \(2014\)](#); [Daylan et al. \(2016\)](#) but only the spectral changes were included in the likelihood analysis. [Abazajian et al. \(2015\)](#) non-parametrically accounted for different secondary spatial morphologies. They used a 20-cm component to model secondary emission from bremsstrahlung and a template based on infrared starlight emission to model secondary emission from IC scattering. They found the inclusion of both these templates to be preferred by the data. Here we take a more parametric approach which can in principle allow us to examine a greater range of interstellar medium (ISM) models. In the context of the MSP explanation of the GeV excess, [Petrović et al. \(2015\)](#); [Yuan & Ioka \(2015\)](#) have investigated the importance of secondary emission for multi-wavelength analyses as well as established a reliable MSP luminosity function.

In this chapter, we examine the importance of also including the different spatial morphology of the secondary emission which results from the diffusion of the secondary electrons. This has been done to some extent in [Calore et al. \(2015a,b\)](#); [Kaplinghat et al. \(2015\)](#) but they exclude  $|b| < 2^\circ$  and they do not use the full likelihood approach provided by the LAT Science Tools. We also examine different methods of determining whether secondaries make a significant difference to a model fit of the GCE.

## 6.2 Models for the gamma-ray emission

We compute the various components of the  $\gamma$ -ray emission from DM in the region of interest as follows. The prompt diffuse  $\gamma$ -ray intensity for annihilation channel  $f$  is given by the same expression as before:

$$E_\gamma^2 \frac{dn_f}{dE_\gamma d\Omega} \Big|_{\text{prompt}} = \frac{E_\gamma^2 \langle \sigma v \rangle_f}{4\pi 2m_{\text{DM}}^2} \frac{dN_{\gamma,f}}{dE_\gamma} \int_{\text{l.o.s.}} \rho^2(\vec{x}) ds. \quad (6.1)$$

To compute the secondary IC and bremsstrahlung  $\gamma$ -ray emissions, we first need to compute the  $e^\pm$  spectrum accounting for energy losses and spatial diffusion. In a steady state, this reads (see Chapter 4):

$$\psi_{e,f}(E, \vec{x}) = \frac{\kappa_f}{b_{\text{tot}}(E, \vec{x})} \int_E^{E_{\text{max}}} \tilde{I}_{\vec{x}}(\lambda_{\text{D}}(E, E_{\text{inj}})) \frac{dN_{e,f}}{dE_{\text{inj}}} dE_{\text{inj}}, \quad (6.2)$$

where  $\kappa_f = (1/2) \langle \sigma v \rangle_f (\rho_\odot/m_{\text{DM}})^2$ ,  $E_{\text{max}} = m_{\text{DM}}$ , and the total energy loss term  $b_{\text{tot}}(E, \vec{x})$  is the sum of the synchrotron, IC and bremsstrahlung losses, given in Chapter 4.

The losses are computed using GALPROP gas and ISRF maps (tabulated in [Buch et al., 2015](#)), and for the magnetic field we consider the following functional form which reads, in cylindrical coordinates:

$$B(\vec{x}) = B(r, z) = B_0 \exp\left(-\frac{r - r_\odot}{r_{\text{B}}} - \frac{|z|}{z_{\text{B}}}\right), \quad (6.3)$$

with  $B_0 \approx 5 \mu\text{G}$ ,  $r_\odot = 8.25 \text{ kpc}$ ,  $r_{\text{B}} = 10 \text{ kpc}$  and  $z_{\text{B}} = 2 \text{ kpc}$ . This is the standard model implemented in GALPROP ([Strong et al., 2000](#)) and it corresponds to  $B \approx 10 \mu\text{G}$  at the GC. The  $e^\pm$  injection spectrum for channel  $f$ ,  $dN_{e,f}/dE_{\text{inj}}$ , is tabulated in [Cirelli et al. \(2011\)](#). The halo

function  $\tilde{I}_{\vec{x}}(\lambda_D(E, E_{\text{inj}}))$  contains all the information on the way the DM profile is reshaped by spatial diffusion, through the diffusion length  $\lambda_D$ , given by (see Eq. (4.80))

$$\lambda_D^2(E, E_{\text{inj}}) = 4 \int_E^{E_{\text{inj}}} \frac{K(E')}{b_0(E')} dE', \quad (6.4)$$

where  $b_0$  is the energy loss term at the center,  $b_0(E) \equiv b_{\text{tot}}(E, \vec{0})$  and  $K$  is the diffusion coefficient, for which we make similar assumptions as in Cirelli et al. (2014a):<sup>1</sup>

$$K(E) = K_0 \left( \frac{E}{E_0} \right)^\delta, \quad (6.5)$$

with  $K_0 = 4.46 \times 10^{28} \text{ cm}^2 \text{ s}^{-1}$ ,  $E_0 = 3 \text{ GeV}$ . We take  $\delta = 0.33$ , corresponding to Kolmogorov turbulence.

We compute the halo function following the procedure of Sec. 4.3.7.6. We consider a half height of 4 kpc for the diffusion zone. Note that we treat inhomogeneous energy losses in a simplified way. More specifically, we keep the spatial dependence in the  $1/b_{\text{tot}}$  term in Eq. (6.2) and in the emission spectra  $P_{\text{IC}}$  and  $P_{\text{brems}}$ , but we compute the effect of the diffusion assuming homogeneous losses, given by the value of the loss rate at the center,  $b_0$ . This simplification, which allows us to avoid resorting to a full treatment of the inhomogeneous propagation equation, is justified by the fact that the DM profile is sharply peaked at the center, so the profile is essentially reshaped by diffusion according to the parameters of the ISM very close to the GC. Moreover, the spatial dependence of the losses only enters the diffusion length through a square root, so the spatial variation of the flux is dominated by the  $1/b_{\text{tot}}$  factor and the emission spectrum. On top of that, the energy losses vary only mildly over the region of interest.

In summary, we used a refined treatment of the secondary fluxes with respect to the standard semi-analytic approach of Sec. 4.3.7—where the whole calculation was done assuming homogeneous losses—but using the same accurate treatment of the steepness of the DM profile in the halo functions. For the case of interest this is a good approximation to the fully inhomogeneous resolution methods used e.g. in the GALPROP code, the DRAGON code, or in Buch et al. (2015), but more straightforward in terms of computation techniques. In Fig. 6.1, we compare our results to published results from DRAGON. The differences seen in the bremsstrahlung results, at high latitude, are not important as the order of magnitude is similar and in the cases we consider bremsstrahlung has a negligible contribution. Accounting for the uncertainties in the diffusion coefficient, ISRF and other relevant parameters, our IC results are a reasonable approximation to those found in Cirelli et al. (2014a). Therefore, using DRAGON, instead of our derivation of secondaries, would not significantly change our conclusions.

The spectrum  $\psi_{e,f}$  is then convolved with the emission spectrum  $P_{\text{IC}}$  or  $P_{\text{brems}}$  to obtain the photon emissivity. In practice, bremsstrahlung is subdominant compared to IC. This was not the case in Chapter 5, where we used a simplified model for the gas density, corresponding to higher bremsstrahlung losses than what is obtained here using the GALPROP maps. Finally, the intensity from secondary emissions is given by integrating the emissivity over the l.o.s. (Eq. (4.1)):

$$E_\gamma^2 \frac{dn_f}{dE_\gamma d\Omega} \Big|_{\text{sec}} = \frac{E_\gamma}{4\pi} \int_{\text{l.o.s.}} j_{\text{IC, brems}, f}(E_\gamma, \vec{x}) ds. \quad (6.6)$$

The derivation of the secondary  $e^+$  and  $e^-$  fluxes from MSPs is essentially the same as for DM annihilations, with  $E_{\text{max}}$  now given by the maximum injection energy. For pulsars, we use a monochromatic injection spectrum  $dN_e/dE_{\text{inj}} = \delta(E_{\text{inj}} - E_{\text{max}})$  with  $E_{\text{max}} = 20 \text{ GeV}$ , as suggested in Yuan & Ioka (2015) and discussed in the following. We parametrize the amplitude of the secondaries as the ratio ( $r$ ) of the energy of  $\gamma$ -rays observed from the secondary emission

<sup>1</sup>However, we consider a homogeneous diffusion coefficient.

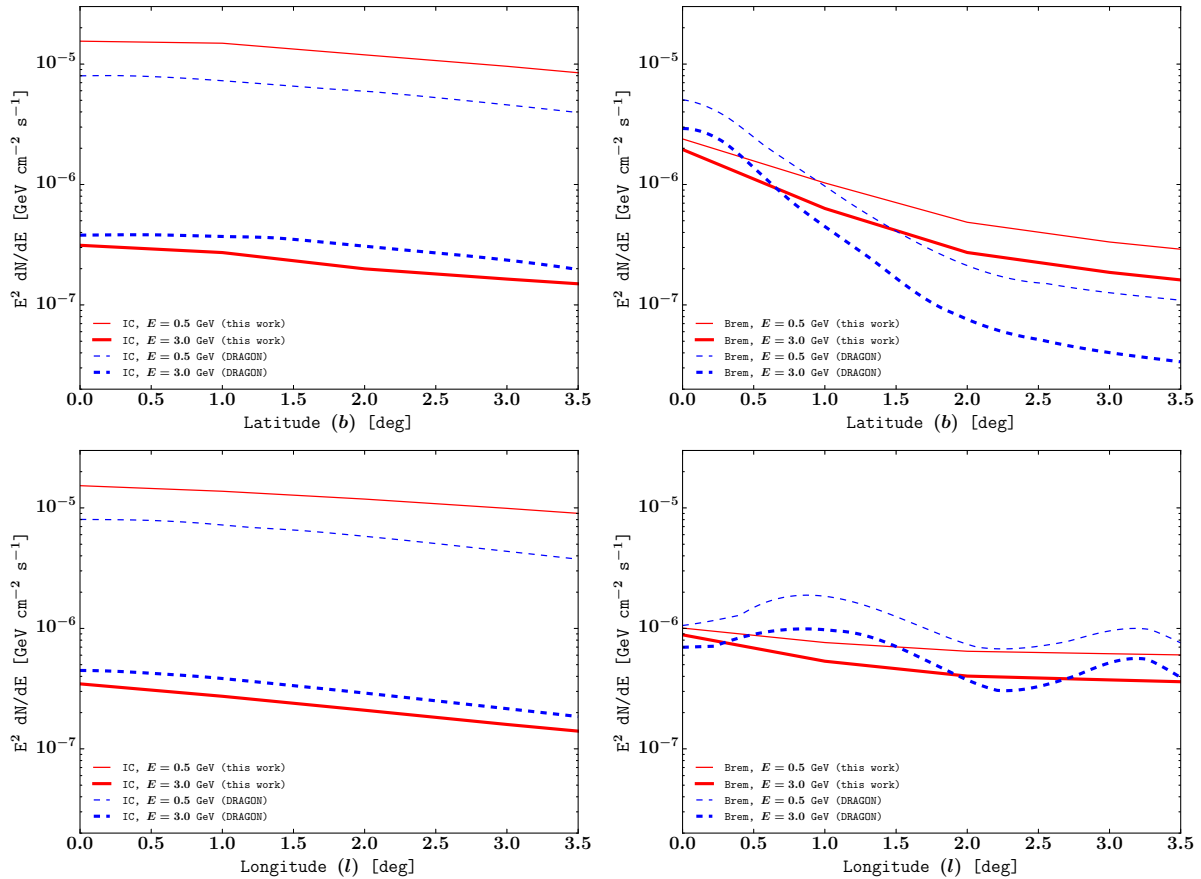


**Figure 6.1** – Comparison of our secondaries with those generated by DRAGON, for IC (**left**) and bremsstrahlung (**right**), averaging on  $|l| \leq 5^\circ$  (**top**) and  $|b| \leq 5^\circ$  (**bottom**). A model with DM mass of 9.4 GeV,  $\langle\sigma v\rangle = 3 \times 10^{-26} \text{ cm}^3 \text{ s}^{-1}$ , and an annihilation channel mix of 20%  $e^+e^- + 20\% \mu^+\mu^- + 60\% \tau^+\tau^-$  is used. The DRAGON predictions are taken from Fig. 2 of Cirelli et al. (2014a).

to the energy of  $\gamma$ -rays from the primary emission. Finally, the prompt  $\gamma$ -ray emission from MSPs is modeled as a power law with exponential cut-off:

$$\frac{dn}{dE_\gamma} = \mathcal{K} \left( \frac{E_\gamma}{E_0} \right)^{-\Gamma} \exp\left(-\frac{E_\gamma}{E_{\text{cut}}}\right), \quad (6.7)$$

where the photon index  $\Gamma$ , a cut-off energy  $E_{\text{cut}}$  and a normalization factor  $\mathcal{K}$  are free parameters, and  $E_0 \approx 1 \text{ GeV}$ .

## 6.3 Data analysis

In this section, we describe the data analysis procedure. This part of the project was carried out mostly by Oscar Macías and Chris Gordon.

### 6.3.1 Data selection

The *Fermi*-LAT is a  $\gamma$ -ray telescope sensitive to photon energies from 20 MeV to more than 300 GeV (Atwood et al., 2009). In operation since August 2008, this instrument makes all sky observations every  $\sim 3$  hours. The angular resolution of *Fermi*-LAT depends on the photon energy, improving as the energy increases (Atwood et al., 2009).

The analysis presented here was carried out with 45 months of observations from August 4, 2008–June 6, 2012<sup>2</sup>, using the LAT Pass-7 data. The SOURCE class events and the Instrument Response Functions (IRFs) P7SOURCE.V6 were used.

In this study, events were selected within a squared region of  $7^\circ \times 7^\circ$  centered on Sgr A\*, with energies greater than 300 MeV, and without making any distinction between *Front* and *Back* events. For energies lower than 300 MeV, the angular resolution of the LAT is poor and source confusion could introduce a large bias to the analysis, whereas above 100 GeV it is limited by low photon statistics.

The zenith angles were chosen to be smaller than  $100^\circ$  to reduce contamination from the Earth limb. Time intervals when the rocking angle was more than  $52^\circ$  and when the *Fermi* satellite was within the South Atlantic Anomaly were also excluded.

The sources spectra were computed using a binned likelihood technique (Acero et al., 2015) with the *pyLikelihood* analysis tool<sup>3</sup>, and the energy binning was set to 24 logarithmic evenly spaced bins. The LAT Science Tools<sup>4</sup> v9r33p0 was used.

### 6.3.2 Analysis methods

The spectral and spatial features of an extended  $\gamma$ -ray source are inherently correlated. Modifications to the spatial model would distort the source spectra and vice versa (Lande et al., 2012). It is therefore necessary to assess the impact of secondary  $\gamma$ -ray radiation in the fit to the GC. We use a fitting method that is fully 3D (comprising an energy axis for the third dimension) and that self-consistently considers the distinct morphological characteristics of the GC extended source in energy and space.

#### 6.3.2.1 Fitting procedure

The complex spectrum and spatial extension of the extended central source is represented as three constituents: (i) Prompt emission, (ii) IC and (iii) a bremsstrahlung component. For the first case, a 2D spatial map given by the square of a generalized NFW profile with an inner slope of  $\gamma = 1.2$  is used. The prompt energy spectrum depends on the final states and the different sources of the case of interest. The remaining two secondary components are modeled by spatially extended sources as explained in Sec. 6.2. Their corresponding spatial templates account for spatial variations in energy and are, in this sense, 3D MAPCUBE maps. All three spatial model components have been appropriately normalized<sup>5</sup> to input in the LAT Science Tools software package.

This work utilizes two different fitting methods; a broad-band fit analysis and a bin-by-bin analysis procedure:

- *Broad-band fit*: The fit to the entire energy range (0.3–100 GeV) is executed using a similar approach to that followed by the *Fermi* team in the analysis of the Crab pulsar in the construction of the 3FGL catalog (Acero et al., 2015). The global best fit for the three-component central source is reached iteratively, keeping fixed the parameters describing the spectral shape of the three different components in every iteration step. The flux normalization of the sources are adjusted in such a way that the flux ratio (predicted by our simulations) between the three components is always maintained for the DM case

<sup>2</sup>Pass-7 data has been superseded by Pass-8. However, the Galactic diffuse emission model corresponding to Pass-8 is not recommended for analysis of extended sources. Hence, we use the 193 weeks of Pass-7 data that are still available at <http://heasarc.gsfc.nasa.gov/FTP/fermi/data/lat/weekly/p7v6/photon/>. However, preliminary tests found similar results with Pass-8 data

<sup>3</sup><http://fermi.gsfc.nasa.gov/ssc/data/analysis/documentation/>

<sup>4</sup><http://fermi.gsfc.nasa.gov/ssc/data/analysis/>

<sup>5</sup>The reader is referred to the *Cicerone* <http://fermi.gsfc.nasa.gov/ssc/data/analysis/scitools/extended/extended.html> for details.

once the DM mass is fixed and for a given annihilation channel. For the MSP case we just maintain the IC to bremsstrahlung ratio and then leave the ratio to the prompt emission as a free parameter. In practice, this is accomplished by constructing a grid of  $\log(\mathcal{L})$  values versus the flux normalization, where  $\mathcal{L}$  represents the likelihood of observing the data given the model. A certain point of the grid is obtained in one iteration—which is automated in a dedicated computer cluster as this is a computationally intensive task.

- *Bin-by-bin fit*: The framework for this stage of the analysis is inherited from [Gordon & Macías \(2013\)](#); [Macías & Gordon \(2014\)](#). The importance of this step stems from the fact that it works as a form of data compression, allowing us to take into account the systematic uncertainties in the Galactic diffuse emission model. It also serves as a way to validate the spectral and spatial model fit—in the sense that this guarantees that not only the sources are optimized, but that the predictions of the models are consistent with the data. In cases where the secondaries are negligible, as in the case of DM annihilation to  $b\bar{b}$ , then the energy bins generated from a good fitting model, like a log-parabola spectrum, can be used. But for non-negligible secondaries we may need to account for the three-component nature of the extended source under scrutiny. As in [Gordon & Macías \(2013\)](#); [Macías & Gordon \(2014\)](#), the data are split in several energy bins and a maximum likelihood routine is run at each energy bin using the LAT Science Tools. The three-component source is treated similarly as it was done in the broad-band analysis, except that here, the source spectra are replaced by simple power laws with the spectral slope given by the tangent to the broad-band spectra at the logarithmic midpoint of the energy bin. Again, the flux ratio between the three components is kept fixed at all times and a grid of  $\log(\mathcal{L})$  values versus the flux normalization for each bin is constructed. In this case, the ratio of the secondaries to the prompt emission is also kept constant in the MSP case. This is necessary as the bin-by-bin fit does not explicitly incorporate changes to the best fit spatial morphology found in the broad-band fit. [Macías & Gordon \(2014\)](#) computed the systematic uncertainties in the Galactic diffuse emission model obtaining that these are space and energy dependent and of order 20%. The present study relies on similar analysis methods and assumes the same estimates for the systematic uncertainties.

### 6.3.2.2 Other sources included in the fits

In the broad-band fit, the spectral parameters of every source (other than the GCE) within  $5^\circ$  of Sgr A\* were freed, while in the bin-by-bin analysis, only their amplitudes were varied. All 2FGL ([Nolan et al., 2012](#)) point-sources present in the region of interest, plus the standard diffuse Galactic emission `gal_2yearp7v6_v0.fits` and the isotropic extra-galactic background model `iso_p7v6source.txt`, were employed.

Since the *Fermi* data used in this work comprises almost 4 years of data taking, while the 2FGL catalog ([Nolan et al., 2012](#)) was constructed with 2 years of data, making a search for new point-sources in the region of interest is required. The results of [Macías et al. \(2015\)](#), where two new faint point-sources were found, are used.

In addition to the GCE, an independent ridge-like GeV excess which is correlated with the H.E.S.S. TeV ridge ([Aharonian et al., 2006a](#)) has also been detected ([Hooper & Goodenough, 2011](#); [Yusef-Zadeh et al., 2013](#); [Macías & Gordon, 2014](#); [Abazajian et al., 2014](#)) and is thought to be due to cosmic rays interacting with molecular gas ([Yusef-Zadeh et al., 2013](#); [Macías & Gordon, 2014](#); [Yoast-Hull et al., 2014](#); [Macías et al., 2015](#)). This GC ridge-like emission template was also included in the analysis. The 2FGL point sources, “the Arc” (2FGL J1746.6-2851c) and “Sgr B” (2FGL J1747.3-2825c), are spatially coincident with our GC ridge map template. It is possible that these two point sources are the result of the interaction of cosmic rays with molecular gas clouds and are thus an integral part of the Galactic ridge. The template for the Galactic ridge source is obtained from a 20-cm map ([Yusef-Zadeh et al., 2013](#); [Macías & Gordon,](#)

2014) and for the spectra a broken power law was used (Macías et al., 2015). In the current project we are interested in the spherically symmetric GCE and so we want the best model for the ridge-like excess emission. Therefore, in this project the Arc and Sgr B point sources as well as the 20-cm template were included. This was also done in Macías & Gordon (2014) when the goal was to construct a bin-by-bin analysis for the spherically symmetric GCE.

## 6.4 Models and procedure

We study a set of well-motivated models for the GeV excess for which the propagation of secondary leptons can contribute appreciably to the total energy spectrum, and the resulting  $\gamma$ -ray spatial morphology can deviate from that given by the square of a generalized NFW profile<sup>6</sup> with an inner slope of  $\gamma = 1.2$ . The cases under scrutiny are:

- *Model I*: 10 GeV WIMPs self-annihilating democratically into leptons ( $\frac{1}{3}e^+e^- + \frac{1}{3}\mu^+\mu^- + \frac{1}{3}\tau^+\tau^-$ ). Based on a spectral fit to the GCE data, as explained in Chapter 5 and Lacroix et al. (2014b), we found this to be a good fitting model provided that the energy spectrum from secondaries was taken into consideration.
- *Model II*: 10 GeV WIMPs self-annihilating into  $0.25\mu^+\mu^- + 0.75\tau^+\tau^-$ . The stringent constraints on the  $e^\pm$  annihilation channel obtained by Bergström et al. (2013); Ibarra et al. (2014); Bringmann et al. (2014) motivate this model. In Chapter 5, we showed these particular branching ratios to be the most adequate mixture of leptonic final states other than  $e^+e^-$  that fits well the GC excess energy spectrum.
- *Model III*: An unresolved population of order  $10^3$  MSPs. These objects can release a significant amount of their total spin-down energy in  $e^\pm$  winds (Petrović et al., 2015; Yuan & Ioka, 2015). The diffusion of such leptons in the GC environment could not only modify the spatial morphology of the central source at  $\sim$  GeV energies but also potentially provide distinctive signatures at very high energies ( $\sim$  TeV). Here we focus on the situation where electrons are injected monochromatically (typically at  $\sim$  20 GeV) and are not further accelerated, i.e. in the absence of a shock region, as discussed in Yuan & Ioka (2015).

We start off by using a pure spectral analysis for comparison with previous results from the literature, e.g. those obtained in Chapter 5 and Lacroix et al. (2014b). Then, to determine whether a new model component is required, and more importantly to assess the actual importance of secondaries, we perform a 3D broad-band fit to evaluate the value of the test statistic  $TS = 2 \ln(\mathcal{L}_{\text{new}}/\mathcal{L}_{\text{old}})$ , where  $\mathcal{L}$  is the maximum likelihood and the subscript indicates whether or not the new parameters are included. In the case of DM the new parameter corresponds to  $\langle\sigma v\rangle$ . For the DM models we consider that the ratio of primary to secondary emission is fixed by the underlying theory and the assumed ISM parameters. In the MSP case we allow the ratio of primary to secondary emission to be a free parameter and we use the exponential cut-off for the MSP primary spectrum. Crucially the spatial and spectral aspects of the prompt and secondary emission are accounted for. The distinct morphologies of the secondary emissions are illustrated in Fig. 6.2.

Based on the examination of the sources near Cygnus, Orion and molecular clouds, the *Fermi* Collaboration (Nolan et al., 2012) stipulated that depending on the intensity of the diffuse background, sources near the galactic ridge need to have  $TS \gg 25$  to not be considered as simply corrections to the DGB model. A new source would need to have a  $TS \geq 80$  to be seriously considered for a multi-wavelength search and so we adopt that value as our necessary threshold for a model to explain the GCE. This criterion is based on 4 new parameters and if a source only has one new parameter, an equivalent p-value threshold is obtained by requiring  $TS \geq 68$ .

<sup>6</sup>Although in practice a power-law profile would give approximately the same results.

We can assign a TS for the secondary emission from a given model by comparing the best fit likelihood with and without the secondaries included. For models which have  $TS \geq 68$  secondary emission, we proceed to perform a bin-by-bin analysis, to check the consistency of the results as explained in Sec. 6.3.2.1. For the DM cases, there was only one degree of freedom,  $\langle\sigma v\rangle$ , in both the broadband and bin-by-bin fit. In the MSPs and log-parabola case the three parameters of the primary spectrum and the ratio of secondaries to primaries are allowed to vary in the broadband fit. If the secondary and primary morphology is assumed to be the same, then a pure spectral fit, to a previously evaluated primary only bin-by-bin spectrum, can be done with the MSP secondary to primary ratio allowed to vary. However, if the distinct secondary morphology is accounted for in the bin-by-bin fit, only the overall normalization of the total MSP model spectrum is allowed to vary. The other three parameters had to remain fixed, to the broadband best fit values, so as to preserve the underlying spatial morphology which is fixed in the bin-by-bin case.

## 6.5 Results and discussion

Table 6.1 summarizes the results of a spectral analysis. The results are plotted in Fig. 6.3. For the left-hand side (LHS) panels we used the bins from Macías & Gordon (2014) which were generated with a primary-emission only model. To further assess the need for secondaries, once the actual spatial morphology of the secondary emission was taken into account, we performed a 3D broad-band analysis, as described in Sec. 6.3.2.1. The results for the broadband analysis are shown in Table 6.2. 3D bin-by-bin analyses were also performed to assess the importance of systematic uncertainties introduced by the spatial morphology. In the right-hand side (RHS) panels of Fig. 6.3, the actual secondary emission spatial profiles were used to generate the bins, as explained in Sec. 6.3.2.1. Note that on the RHS there is one less significant ( $TS \geq 1$ ) bin compared to the LHS for *Model I* and *Model II*.

Model	spectrum, prompt only			spectrum, prompt+secondaries			spectrum+spatial, prompt+secondaries		
	$\chi^2$	d.o.f.	p-value	$\chi^2$	d.o.f.	p-value	$\chi^2$	d.o.f.	p-value
I	37.9	11	$8 \times 10^{-5}$	30.4	11	$1 \times 10^{-3}$	16.6	10	$8 \times 10^{-2}$
II	34.0	11	$4 \times 10^{-4}$	26.4	11	$6 \times 10^{-3}$	29.4	10	$1 \times 10^{-3}$
III	11.9	9	$2 \times 10^{-1}$	11.0	8	$2 \times 10^{-1}$	11.0	8	$2 \times 10^{-1}$

**Table 6.1** – Results of the spectral (bin-by-bin) analyses performed on the *Fermi* GeV excess emission as explained in Sec 6.3.2.1. In the “spectrum, prompt only” and “spectrum, prompt+secondaries” columns the secondary emission is assumed to have the same morphology as the primary emission and the bins to be fitted to were obtained from Macías & Gordon (2014).

### 6.5.1 *Model I*, democratic leptons

Table 6.1 shows that for *Model I*, the fit p-value is improved to the  $10^{-3}$  threshold when including secondaries and assuming that their morphology is the same as the morphology of the prompt emission. However, the improvement is significantly above that level once the distinct spatial morphology of the secondaries is accounted for. Table 6.2 shows that the democratic leptons case (*Model I*) has an overall  $TS \geq 68$  and so can be considered as a potential model for the GCE. Moreover, Table 6.2 shows that for this model, secondaries have  $TS \geq 68$ , so we conclude that for *Model I*, the need for secondaries is ascertained by the 3D analysis.

Interestingly, using a more non-parametric template-based fitting approach, Abazajian et al. (2015) also found evidence for secondary  $\gamma$ -rays originating from  $\sim 10$  GeV electrons, consistent with both the democratic leptons model and the MSP scenario. Their prediction for the

Model	$\text{TS}_{\text{base+prompt+sec}} - \text{TS}_{\text{base}}$	d.o.f. <sub>base</sub> - d.o.f.	$\text{TS}_{\text{base+prompt+sec}} - \text{TS}_{\text{base+prompt}}$
Base	0	0	–
I	435.1	1	101.7
II	343.8	1	6.5
III	512.0	4	41.7

**Table 6.2** – Results of the broad-band fits to the GCE as explained in Sec. 6.3.2.1. Different models for the GCE in the 300 MeV–100 GeV energy range are listed. Each model includes the base model and the extra prompt and secondary (sec) emission. The DM models each require one degree of freedom (d.o.f.) for the cross-section. The exponential cut-off model requires three parameters for the prompt spectrum and one for the prompt to secondary ratio if included. The spatial morphology of the prompt emission was modeled with a square of a generalized NFW profile with an inner slope of  $\gamma = 1.2$  (Gordon & Macías, 2013). Spatial templates for the IC and bremsstrahlung components as well as their respective spectra were obtained from our calculations discussed in Sec. 6.2.

democratic leptons bremsstrahlung component was somewhat higher than ours, which is likely due to their different approach of extracting the bremsstrahlung contribution from the data and different assumptions about the ISM.

### 6.5.2 Model II, no electrons

As can be seen from Table 6.1, if a spectral-only analysis is performed, the no-electron case (*Model II*) goes from bad-fitting to good-fitting (p-value  $\geq 10^{-3}$ ) if secondaries are included. When the distinct morphology of the secondaries is accounted for, the goodness of the fit decreases to just above the  $10^{-3}$  threshold. From this spectral analysis, we would be led to conclude that secondaries are needed in making *Model II* a good model for the GCE.

When moving to the full 3D broad-band analysis, although a significant overall TS value is obtained, the contribution of secondaries turns out to be negligible, as evidenced by the last column of Table 6.2. When deciding whether a new model component is needed by the data, evaluating the improvement in the likelihood (via a TS comparison) is a valuable tool. However, there can be cases in which the new model component improves some other aspect of the fit which does not significantly change the data likelihood. As we have seen that is what happens in the case of *Model II*. In that case secondaries do not significantly improve the TS (likelihood) but they do make the spectral fit acceptable. We therefore argue that the spatial bin-by-bin analysis shows that *Model II* does require secondaries even if they do not have a significant effect on the broadband TS.

### 6.5.3 Model III, millisecond pulsars

As seen from Table 6.1, the spectral-only analysis would not reveal the need for a secondary component for the MSP case (*Model III*) as the p-value is well above the  $10^{-3}$  threshold before or after adding the secondaries.

Table 6.2 shows that the TS of the MSP secondaries is higher than the traditional 25 threshold but not higher than the threshold of 80 needed to be accepted as a non-correction to the DGB. The best broadband analysis fit value for the secondary to primary  $\gamma$ -ray ratio was only  $r \sim 1\%$  and the other parameter values were consistent with the no-secondaries case considered in Macías & Gordon (2014). As seen from the bottom panels of Fig. 6.3, a larger best-fit value of  $r$  was obtained in the spectrum only analysis. But due to large degeneracies with the other parameters, it was less than  $3\sigma$  away from the no-secondary case of  $r = 0$ . Therefore, in this case both

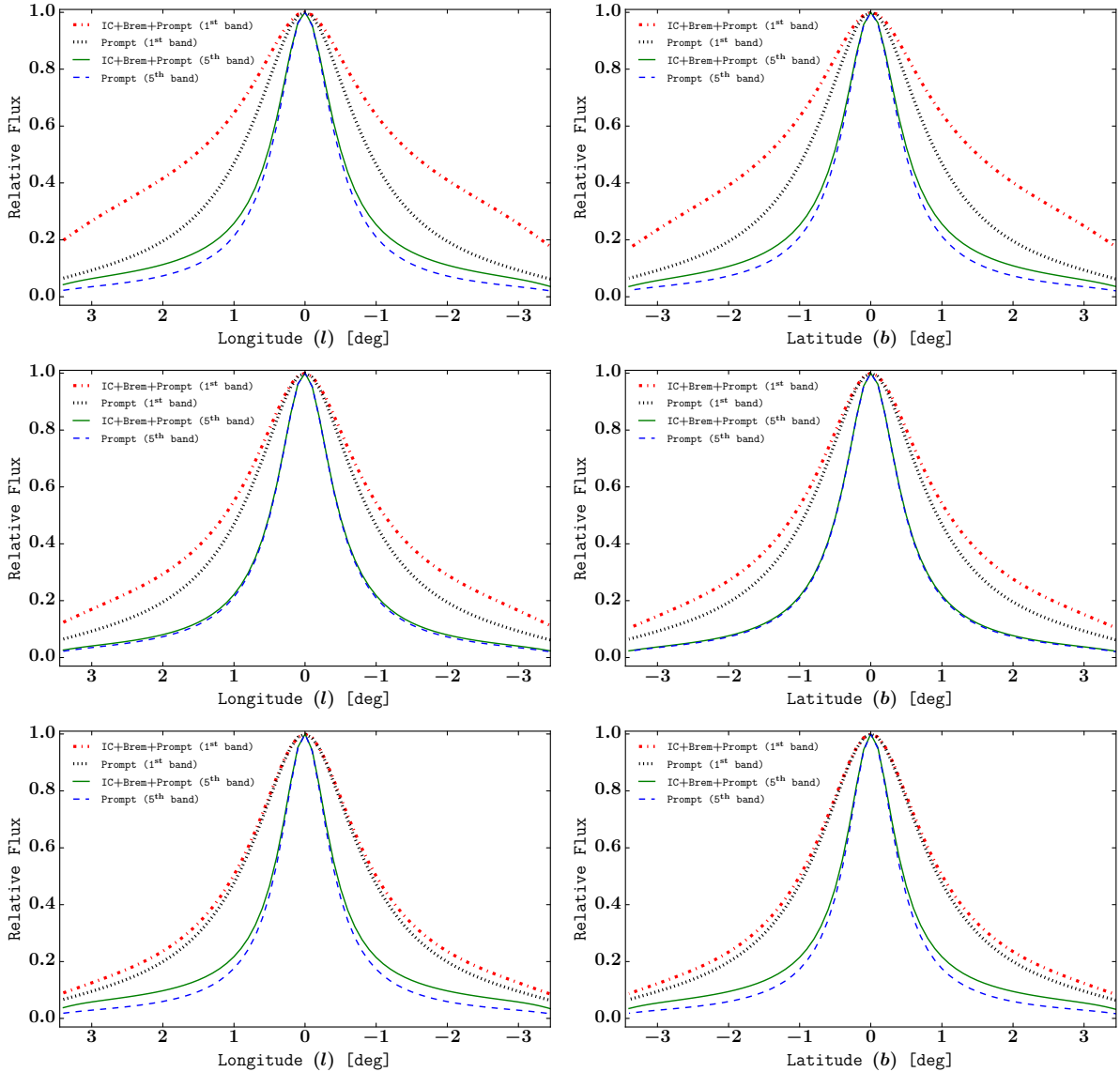


**Figure 6.2** – Spatial brightness profiles of the best fit GeV excess source associated to *Model I* (**top**), *Model II* (**middle**), and *Model III* (**bottom**). *Fermi*-LAT energy-dependent beam smoothing is included. The profiles are shown in two different energy bins; the 1<sup>st</sup> bin refers to the energy range 0.30–0.40 GeV (thick dotted lines) while the 5<sup>th</sup> one to 0.97–1.29 GeV (thin lines). At each energy bin we present the total emission (IC+Bremstrahlung+Prompt) and the prompt emission for comparison. Profiles correspond to  $b = 0^\circ$  (**left**) and  $l = 0^\circ$  (**right**). Fluxes are normalized to the maximum for display purposes. See Fig. 6.3 for details on the corresponding bin-by-bin analysis.

the spectral analysis and the full 3D broadband analysis show that the data do not require a secondary component. Similar results were found with a log-parabola model.

## 6.6 Conclusions

In this project, we have illustrated the importance of including the spatial morphology of secondary emission in a self-consistent analysis set-up when evaluating the validity of models for the GeV excess. The 3D broadband analysis took into account this spatial morphology and by

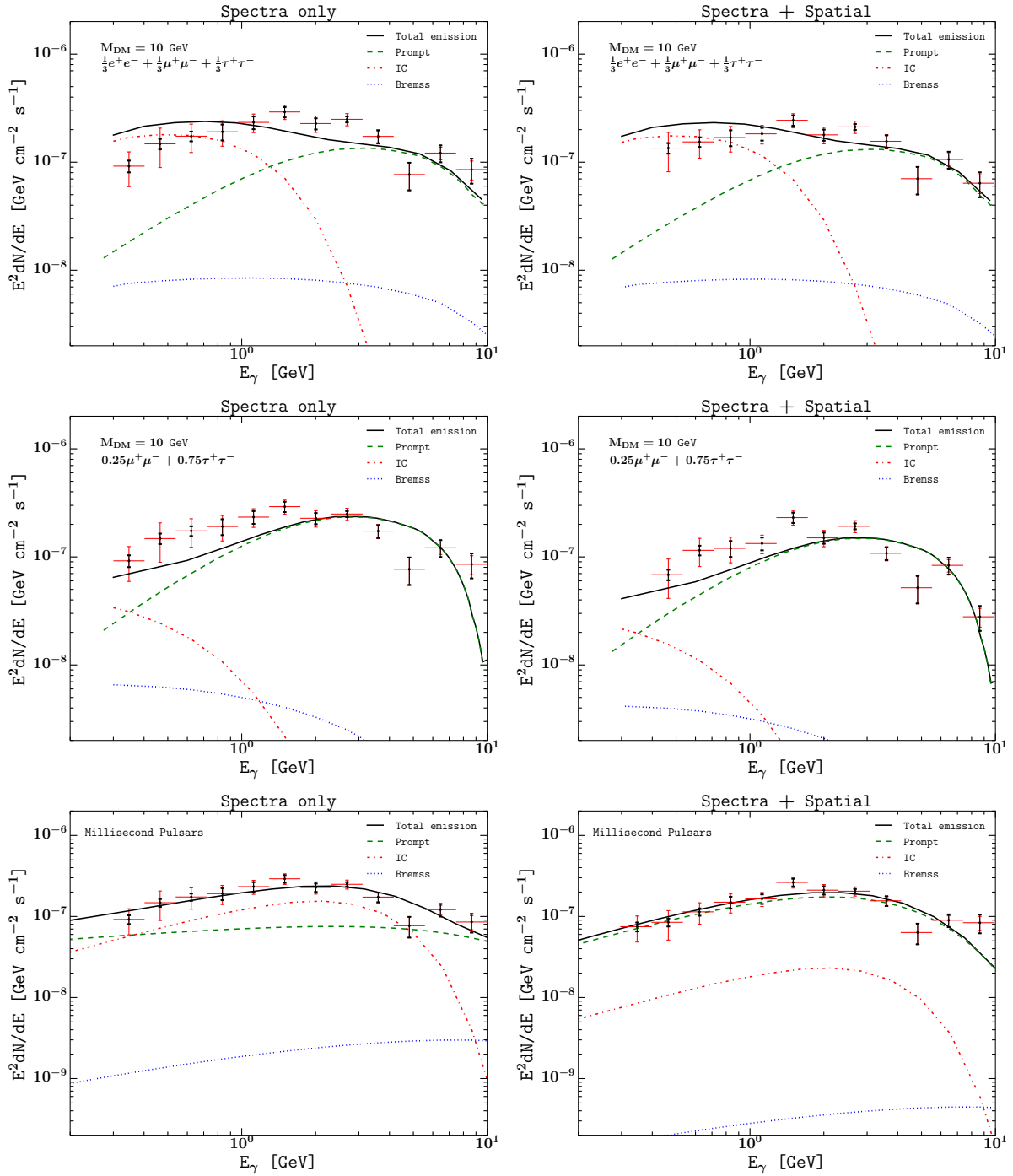


**Figure 6.3** – Spectral energy distribution for the GCE modelled with Spatial brightness profiles of *Model I* (**top**), *Model II* (**middle**), and *Model III* (**bottom**). IC and Brems stand for inverse Compton and bremsstrahlung emission respectively. Black and red error bars refer to the LAT ( $1\sigma$ ) statistical and systematic errors, respectively. The fit and plot only consider energy bins with  $TS \geq 1$ . **Left panel:** shows the results of a bin-by-bin analysis when the secondaries’ different morphologies were not accounted for in determining the bins. **Right panel:** Displays the results of the bin-by-bin analysis when the full spectral and spatial information from secondaries was considered.

requiring a high TS threshold, a secondary emission component was shown to be required in the democratic lepton case. This was also confirmed by a spectral analysis which accounted for the

different spatial morphologies of the secondaries.

In the no-electron case of *Model II*, the full broadband analysis did not support the need for secondaries. However, a spectral analysis showed that the model fit was below the  $10^{-3}$  p-value threshold unless secondaries were included. The TS only tells how much a model is improved by secondaries, but does not take into account how well the overall model fits. This illustrates the need to check model fit in addition to TS improvement. We have shown that a spectral approach to evaluating model fit can be adapted to the case where some components of the model have different spatial morphologies.

In future work, a full likelihood analysis will have to be performed to accurately determine the secondary model parameter uncertainties in the presence of DGB systematics. This will require to also generate a DGB template which varies with the ISM, as at least the IC component should also change when the ISM radiation field is adjusted.

## Part IV

# Phenomenology of dark matter spikes in the Milky Way



## Chapter 7

# Probing a dark matter spike at the Galactic center in the presence of spatial electron diffusion

In this chapter, adapted from [Lacroix et al. \(2014a\)](#), we use synchrotron emission to probe the DM energy distribution at the GC. The difficulty lies in the fact that the synchrotron signal is sensitive to propagation of electrons and positrons in the interstellar medium, which is essentially the result of the interplay between spatial diffusion and energy losses. In particular, spatial diffusion is poorly constrained in the inner region of the MW. In order to quantify the effect of spatial diffusion on a distribution of electrons and positrons injected with a spiky density profile ( $\rho(r) \propto r^{-7/3}$ ), we model electron diffusion on very small scales—typically smaller than  $10^{-3}$  pc—by using our new technique described in Sec. 4.3.7.6. This allows us to determine how a spiky profile affects the morphology and intensity of the synchrotron emission expected from DM. We illustrate our results using 10 and 800 GeV weakly interacting DM candidates annihilating directly into  $e^+e^-$ . Our most critical assumptions are that the DM is heavier than a few GeV and directly produces a reasonable amount of electrons and positrons in the Galaxy. We conclude that in the presence of significant spatial diffusion, astrophysical observations—including with the *Planck* experiment—could be used to shed light on the DM halo profile on scales that lie beyond the capability of any current numerical simulations.

### Contents

---

<b>7.1</b>	<b>Dark matter spike and electron diffusion . . . . .</b>	<b>116</b>
<b>7.2</b>	<b>Synchrotron emission from a dark matter spike with spatial diffusion</b>	<b>116</b>
<b>7.3</b>	<b>Constraining the existence of a dark matter spike . . . . .</b>	<b>117</b>
7.3.1	Morphology of the synchrotron emission: maps of the Galactic center with or without a spike . . . . .	118
7.3.2	Can we distinguish different inner profiles using their synchrotron emission?	118
7.3.3	Impact of the magnetic field . . . . .	123
7.3.4	Observability with <i>Planck</i> . . . . .	124
<b>7.4</b>	<b>Conclusion and perspectives . . . . .</b>	<b>126</b>

---

## 7.1 Dark matter spike and electron diffusion

The DM profile toward the center of the MW, i.e. at sub-kpc scales, is unknown. As discussed in Chapter 3, a DM spike may be present around the SMBH Sgr A\* at the GC, but this remains to be established, and the full range of dynamical effects has not been fully explored. In this project, we have focused on a range of possible very dense inner spike profiles and their effects on the millimeter/sub-millimeter emission induced by DM annihilation via synchrotron radiation. This enables us to determine whether present experiments can constrain the DM distribution very near to the GC.

Careful modeling of the propagation of DM-induced electrons and positrons is critical to accurately estimate the resulting photon intensity of synchrotron photons, as reviewed in Chapter 4. In particular, diffusion can significantly affect the spatial morphology of the synchrotron signal. However, the characteristics of spatial diffusion are poorly constrained at the GC and depend on the degree of turbulence in the magnetic field, as discussed e.g. in Regis & Ullio (2008). In particular, in the inner  $\sim 100$  pc the diffusion coefficient may differ significantly from the values corresponding to the usual MIN, MED and MAX set-ups derived from local cosmic-ray measurements. For instance, in the case of a highly turbulent magnetic field, corresponding to Bohm diffusion, the diffusion coefficient is smaller than the fiducial MIN, MED and MAX values by several orders of magnitude. Furthermore, even if the diffusion coefficient is large enough, if energy losses are too severe, for instance in the presence of a very large magnetic field, then electrons and positrons essentially lose their energy in place. This case was considered in Bertone et al. (2002); Aloisio et al. (2004); Regis & Ullio (2008), where the synchrotron emission induced by a DM spike at the GC was studied in the context of very large magnetic fields.

*In this project we have studied for the first time the impact of spatial diffusion on the synchrotron emission from electrons and positrons produced in a DM spike at the GC.* Considering the large uncertainty on spatial diffusion in the very inner region of the Galaxy, we have used the MIN, MED and MAX sets of diffusion parameters as benchmarks. The steepness of the source term in the diffusion-loss equation at very small scales due to the DM spike requires our specific resolution technique described in Sec. 4.3.7.6, relying on a careful treatment of the Green's functions by adapting the integration step to different regimes defined in terms of the distance from the GC.

To illustrate our point, we focus on 10 GeV DM particles but will also consider heavy (e.g. 800 GeV) DM candidates for the sake of completeness. At present, there are still claims of possible evidence for light annihilating DM particles (Boehm et al., 2004a) in the DAMA/LIBRA and marginally CoGeNT direct detection experiments, which are nevertheless in tension with null results from e.g. XENON100 and LUX (see Chapter 2). There are in addition constraints from radio signatures in galaxy clusters and the center of the Milky Way (Boehm et al., 2004a, 2010; Fornengo et al., 2012), as well as in off-center regions of the Milky Way (Mambrini et al., 2012). Light particles may nevertheless provide us with a possible explanation for the nonthermal radio filaments observed at the GC (Linden et al., 2011) and are also worth considering even just for illustrative purposes.

## 7.2 Synchrotron emission from a dark matter spike with spatial diffusion

The DM-induced synchrotron intensity is given by

$$I_{\nu,\text{syn}}(l, b) = \int_{\text{l.o.s.}} \frac{j_{\text{syn}}(\nu, r(s, l, b))}{4\pi} ds, \quad (7.1)$$

where the emissivity  $j_{\text{syn}}$  is computed following the procedure detailed in Chapter 4, using the dedicated method we developed to account for spatial diffusion for very steep source density

profiles like adiabatic spikes (see Sec. 4.3.7.6). Inverse Compton energy losses are computed exactly as in Chapter 5, and we use  $n_{\text{gas}} = 1 \text{ cm}^{-3}$  for bremsstrahlung and a constant magnetic field for synchrotron radiation.

We consider two types of DM halo profiles, namely a NFW+spike profile and a pure NFW profile without a spike. For the spiky profile we assume the following radial dependence, which is essentially equivalent to the spike profile given in Eq. (3.20):

$$\rho(r) = \begin{cases} \rho_{\text{sat}} & r < r_{\text{sat}} \\ \rho_{\text{sat}} \left( \frac{r}{r_{\text{sat}}} \right)^{-\gamma_{\text{sp}}} & r_{\text{sat}} \leq r < R_{\text{sp}} \\ \rho_{\odot} \frac{r_{\odot}}{r} \left( \frac{1 + r_{\odot}/r_s}{1 + r/r_s} \right)^2 & r \geq R_{\text{sp}}, \end{cases} \quad (7.2)$$

where  $\rho_{\odot} = 0.3 \text{ GeV cm}^{-3}$ ,  $r_{\odot} = 8.5 \text{ kpc}$  and we take  $r_s = 20 \text{ kpc}$  for the scale radius of the NFW profile. We keep some freedom on the spike radius  $R_{\text{sp}}$ , considering the uncertainties on the robustness of an adiabatic spike. The saturation density  $\rho_{\text{sat}}$  and the saturation radius  $r_{\text{sat}}$  are related by the equality  $\rho(r_{\text{sat}}) = \rho_{\text{sat}}$ . A natural value of  $\rho_{\text{sat}}$  is determined by the depletion of the central spike due to DM annihilations:  $\rho_{\text{sat}}^{\text{ann}} = m_{\text{DM}} / (\langle \sigma v \rangle t_{\text{BH}})$ . We assume a conservative value of the age of the BH,  $t_{\text{BH}} = 10^{10} \text{ yr}$ . When the values of the DM mass or annihilation cross-section are changed, the very inner part of the density profile is changed accordingly in a self-consistent way, since the saturation radius is given by

$$r_{\text{sat}}^{\text{ann}} = R_{\text{sp}} \left[ \frac{\rho_{\odot} r_{\odot}}{\rho_{\text{sat}} R_{\text{sp}}} \left( 1 + \frac{r_{\odot}}{r_s} \right)^2 \right]^{1/\gamma_{\text{sp}}}. \quad (7.3)$$

Taking  $m_{\text{DM}} = 10 \text{ GeV}$ , and assuming the canonical value of the cross-section  $\langle \sigma v \rangle = 3 \times 10^{-26} \text{ cm}^3 \text{ s}^{-1}$ , the saturation density given by annihilations is  $\rho_{\text{sat}}^{\text{ann}} \approx 1.1 \times 10^9 \text{ GeV cm}^{-3}$ . This leads to  $r_{\text{sat}}^{\text{ann}} \approx 5.3 \times 10^{-3} \text{ pc}$  for  $R_{\text{sp}} = 1 \text{ pc}$ ,  $\gamma_{\text{sp}} = 7/3$ . For the NFW profile without a spike, the saturation radius is much smaller:  $r_{\text{sat}}^{\text{ann}} \approx 4.9 \times 10^{-6} \text{ pc}$ .

For illustrative purposes, we also consider a spiky profile with a much smaller saturation radius, independent of the annihilation cross-section, and equal to the Schwarzschild radius of Sgr A\*,  $R_S = 4.2 \times 10^{-7} \text{ pc}$ , leading to a saturation density of the order of  $10^{18} \text{ GeV cm}^{-3}$ . This extreme case of a very small saturation radius is not very realistic but nevertheless illustrates for instance the case of a very small infall time of DM particles onto the BH.

The saturation radius provides a natural regularization of the divergence toward the GC for a spiky profile. Although such a prescription is in principle required for a NFW profile, it was shown in [Boehm & Lavalley \(2009\)](#) that the resolution of the instrument actually regularized the divergence.<sup>1</sup>

### 7.3 Constraining the existence of a dark matter spike

With our new dedicated technique for the treatment of spatial diffusion for steep DM profiles, we can now attempt to determine whether it is possible to distinguish a spiky DM halo profile from a NFW distribution and whether one can constrain the properties of the spike using synchrotron emission. In the next sections, we will mostly consider light DM particles (typically  $m_{\text{DM}} = 10 \text{ GeV}$ ), but we will show that our conclusions remain valid in the case of heavy DM particles.

<sup>1</sup>Ultimately, the Schwarzschild radius of the BH provides a natural cut-off scale.

### 7.3.1 Morphology of the synchrotron emission: maps of the Galactic center with or without a spike

The presence of a spike in the DM halo profile is expected to affect the morphology of the synchrotron emission coming from DM particles. The latter can be inferred by looking at synchrotron maps in terms of longitude  $l$  and latitude  $b$  (Delahaye et al., 2012). For a 10 GeV WIMP and relatively low values of the magnetic field, one expects a signal in the lowest frequency channels of the *Planck* low frequency instrument (LFI), in particular at 30 GHz, and no other signature in any of the *Planck* high frequency instrument (HFI) channels.

To establish these maps, we use the canonical value of  $3 \times 10^{-26} \text{ cm}^3 \text{ s}^{-1}$  for the annihilation cross-section, a constant value of  $3 \mu\text{G}$  for the magnetic field  $B$ , and the MED set of diffusion parameters unless stated otherwise. The results are shown in Fig. 7.1. The left panel shows the synchrotron emission for a NFW+spike profile with  $R_{\text{sp}} = 1 \text{ pc}$  and  $r_{\text{sat}} = r_{\text{sat}}^{\text{ann}} \approx 5.3 \times 10^{-3} \text{ pc}$ , while the NFW case is shown in the right panel.

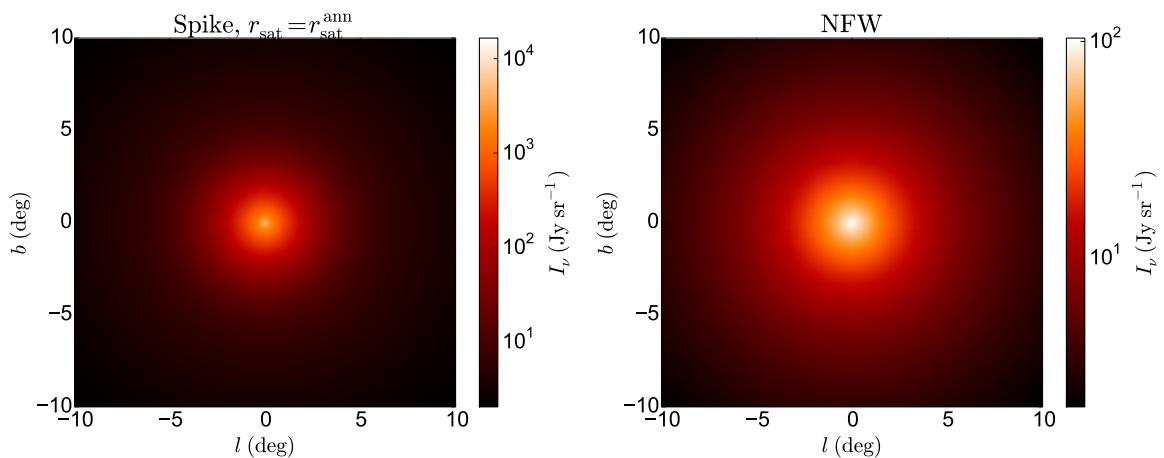


**Figure 7.1** – 30 GHz maps of the synchrotron intensity induced by 10 GeV DM particles, for  $\langle\sigma v\rangle = 3 \times 10^{-26} \text{ cm}^3 \text{ s}^{-1}$ ,  $B = 3 \mu\text{G}$ , and the MED set of propagation parameters. The DM profiles used are a spiky profile with  $\gamma_{\text{sp}} = 7/3$ ,  $R_{\text{sp}} = 1 \text{ pc}$ , with  $r_{\text{sat}} = r_{\text{sat}}^{\text{ann}}$  (**left panel**), and the NFW profile (**right panel**).

By comparing the left and right panels, we see that the emission in the case of a spiky profile is much more peaked than for a NFW profile. Hence, different DM halo profiles predict distinctive morphological signatures and synchrotron intensities. Therefore, the combination of both the normalization and the spatial morphology of the DM-induced emission could be used to probe the existence of a spike in the inner Galaxy.

This conclusion is in agreement with the results of Ascasibar et al. (2006); Boehm et al. (2010), where spatial morphology was used to distinguish decaying from annihilating DM scenarios (i.e.,  $\rho$  vs  $\rho^2$ ). But more importantly, these maps also indicate that very steep profiles in the GC have signatures visible on scales of a few degrees (i.e., at much larger scales than  $R_{\text{sp}}$ ).

As a result one may be able to probe the DM energy distribution in the very inner Galaxy, even in the absence of synchrotron measurements at these scales. This new and very important result already suggests that even the *Planck* data may have the potential to constrain spiky profiles.

### 7.3.2 Can we distinguish different inner profiles using their synchrotron emission?

Maps are well suited for highlighting the morphology of the signal, but not for quantitatively comparing the intensities associated with different profiles. Therefore, we now study the depen-

dence of the synchrotron intensity in terms of latitude. In practice, one should investigate the dependence in terms of  $l$  and  $b$ , but giving the results in terms of latitude is actually enough, considering the symmetry of the source (the latitude being slightly more relevant as the effects of the diffusion zone are more noticeable in this direction).

### 7.3.2.1 Large scales (a few degrees)

To begin with, we shall consider relatively large scales ( $0.1^\circ \lesssim b \lesssim 10^\circ$ ). Our synchrotron predictions for those scales are shown in Fig. 7.2, again assuming  $\langle\sigma v\rangle = 3 \times 10^{-26} \text{ cm}^3 \text{ s}^{-1}$  and  $B = 3 \mu\text{G}$ .

Since one should in principle account for the resolution of the detector, we first smooth out the intensity over the solid angle  $\Delta\Omega \approx \pi\theta_{\text{res}}^2$ , where  $\theta_{\text{res}}$  is the resolution of the instrument, namely 33 arcmin at 30 GHz for *Planck*/LFI (Aghanim et al., 2014). The corresponding result is shown as dotted lines in Fig. 7.2 (visible below  $1^\circ$ ) in the case of a spiky profile with  $R_{\text{sp}} = 1 \text{ pc}$ , the MED set of parameters, and  $r_{\text{sat}}$  equal to either  $R_{\text{S}}$  or  $r_{\text{sat}}^{\text{ann}}$ .

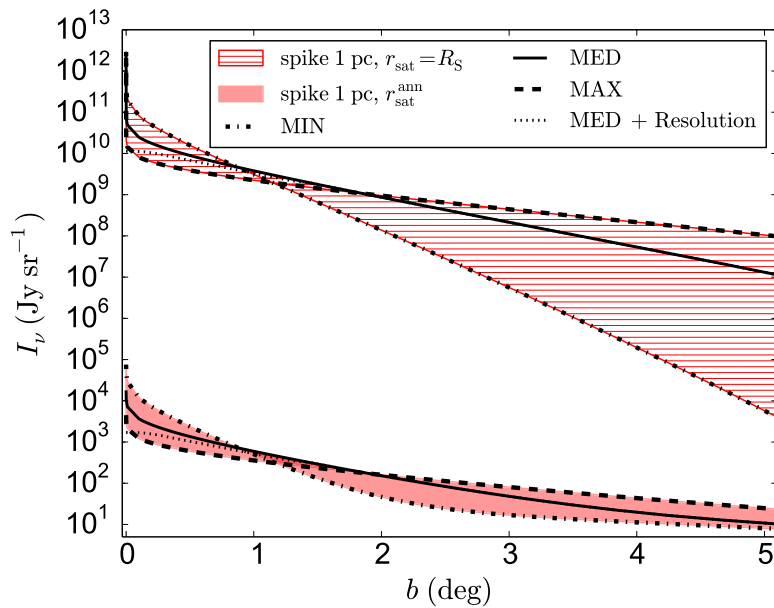


**Figure 7.2** – Synchrotron intensity as a function of latitude  $b$ , for 10 GeV DM particles,  $\langle\sigma v\rangle = 3 \times 10^{-26} \text{ cm}^3 \text{ s}^{-1}$ ,  $B = 3 \mu\text{G}$  and  $\nu = 30 \text{ GHz}$ . The red horizontally hatched and shaded areas represent the intensity for a spike with  $\gamma_{\text{sp}} = 7/3$  and  $R_{\text{sp}} = 1 \text{ pc}$ , respectively, for  $r_{\text{sat}} = R_{\text{S}}$  and  $r_{\text{sat}} = r_{\text{sat}}^{\text{ann}}$ . The uncertainty on the diffusion model is defined by the intensity for the MIN (dashed-dotted lines) and MAX (dashed lines) propagation parameters. The solid lines are associated with the MED set. The dotted lines represent the intensity for the MED set smoothed using the angular resolution of *Planck*/LFI at 30 GHz, namely, 33 arcmin.

In both cases, accounting for the angular resolution of *Planck* at 30 GHz reduces the intensity in the inner region by only less than 1 order of magnitude (making the emission look more extended). Since this does not have a significant impact on the estimates of the intensity and adding an extra integral slows down our calculations, we do not average over the resolution of the detector in the following. This also allows us to keep our results independent of a particular experiment.

Figure 7.2 also enables us to study the impact of the saturation radius. For  $R_{\text{sp}} = 1 \text{ pc}$ , we can compare the synchrotron intensities as a function of latitude for  $r_{\text{sat}} = r_{\text{sat}}^{\text{ann}}$  and  $r_{\text{sat}} = R_{\text{S}}$ . The spike with the extremely small saturation radius ( $r_{\text{sat}} = R_{\text{S}}$ ) leads to an intensity that is orders of magnitude greater than for the spike with  $r_{\text{sat}}^{\text{ann}}$ . This is true both at  $0.1^\circ$  and  $10^\circ$ . Since the value of  $r_{\text{sat}}$  affects the normalization of the intensity on visible scales, it should be possible

to distinguish spikes which have the same size but different saturation radii by measuring the synchrotron intensity at latitude  $b \sim 1^\circ$ .

Throughout the rest of this chapter, we fix the saturation radius  $r_{\text{sat}}$  to the usual annihilation-driven value  $r_{\text{sat}}^{\text{ann}}$ , which is more realistic than  $r_{\text{sat}} = R_{\text{S}}$ . Let us now study how the size of the spike  $R_{\text{sp}}$  affects the intensity. Figure 7.3 (top panel) shows that different values of  $R_{\text{sp}}$  induce a distinctive morphology: intensities indeed decrease differently with latitude depending on  $R_{\text{sp}}$ . The only exception is when  $R_{\text{sp}} = 0.1$  pc as the morphology of the intensity in this case is somewhat degenerated with the predictions for a NFW profile. For all the other profiles, it should be possible to determine the size of the spike  $R_{\text{sp}}$  by looking at the synchrotron intensity around  $b \sim 1^\circ$ . Therefore, one can constrain both the existence of a spike in the DM density profile at the GC and its size using both the intensity of synchrotron emission at degree scales and its global spatial morphology.

Our conclusions are similar in the case of heavy DM (Fig. 7.3, bottom panel). In this figure we show the synchrotron intensity for 800 GeV DM particles and a frequency of  $\nu = 857$  GHz (the highest frequency channel of *Planck*/HFI). As one can see, profiles with spikes of different sizes lead to a different spatial morphology below  $10^\circ$ . The main uncertainty on the value of the intensity actually arises from diffusion, since at such energies electrons can diffuse out to larger distances and reach outer regions of the Galaxy, and are thus more sensitive to the boundaries of the diffusion zone. However, keeping this caveat in mind, the morphology of the synchrotron emission can also be used to constrain the existence of a spike and its characteristics if DM is made of heavy particles.

### 7.3.2.2 Zooming in on the very center (sub-arcsecond scales)

Complementary information on the DM profile can be gained by looking at the very inner region of the Galaxy, typically at sub-arcsecond scales. By studying the emission at these small scales, one expects to be more sensitive to the characteristics of the spike. Our estimates of the intensities below  $0.1^\circ$  are given in Fig. 7.4, for spiky profiles of  $R_{\text{sp}} = 0.1, 1, 10$  pc. For comparison we also display the intensity for the NFW DM halo profile. As one expects, the intensities associated with spiky profiles become much larger toward the GC, and more interestingly the annihilation plateau of radius  $r_{\text{sat}}^{\text{ann}}$ , which depends on  $R_{\text{sp}}$ , is clearly visible below  $b \sim 0.1$  arcsec.

### 7.3.2.3 Combining small and large scales

On the one hand, one can determine the size of the saturation plateau  $r_{\text{sat}}$  by using the value of the intensity at sub-arcsec scales. On the other hand, one can infer the size of the spike  $R_{\text{sp}}$  by studying the spatial morphology at  $0.1^\circ \lesssim b \lesssim 10^\circ$  scales. As  $R_{\text{sp}}$  enters into the expression of the saturation radius, the combination of observations from small to large scales should provide us with a consistent picture of the DM inner profile, potentially also pointing toward the value of the cross-section if DM is indeed made of annihilating particles. These measurements could therefore be used to verify or infer the nature of DM.

Note that to draw our conclusions we used the canonical value of  $\langle\sigma v\rangle = 3 \times 10^{-26} \text{ cm}^3 \text{ s}^{-1}$ . To test the robustness of our claim, we now estimate the uncertainty on the intensity due to the lack of determination of the cross-section. We therefore consider two values  $\langle\sigma v\rangle = 3 \times 10^{-27} \text{ cm}^3 \text{ s}^{-1}$  and  $\langle\sigma v\rangle = 3 \times 10^{-25} \text{ cm}^3 \text{ s}^{-1}$  and assume the existence of a regeneration mechanism for DM particles when  $\langle\sigma v\rangle > 3 \times 10^{-26} \text{ cm}^3 \text{ s}^{-1}$  (Williams et al., 2012).

The uncertainty on the intensity due to both uncertainties in diffusion and the broader range for the annihilation cross-section is represented by the blue vertically hatched area in Fig. 7.4. From this figure we can see that the morphology inferred by using  $\langle\sigma v\rangle = 3 \times 10^{-26} \text{ cm}^3 \text{ s}^{-1}$  is unchanged when the cross-section is increased or decreased. Thus, changing the cross-section only affects the normalization of the intensity.

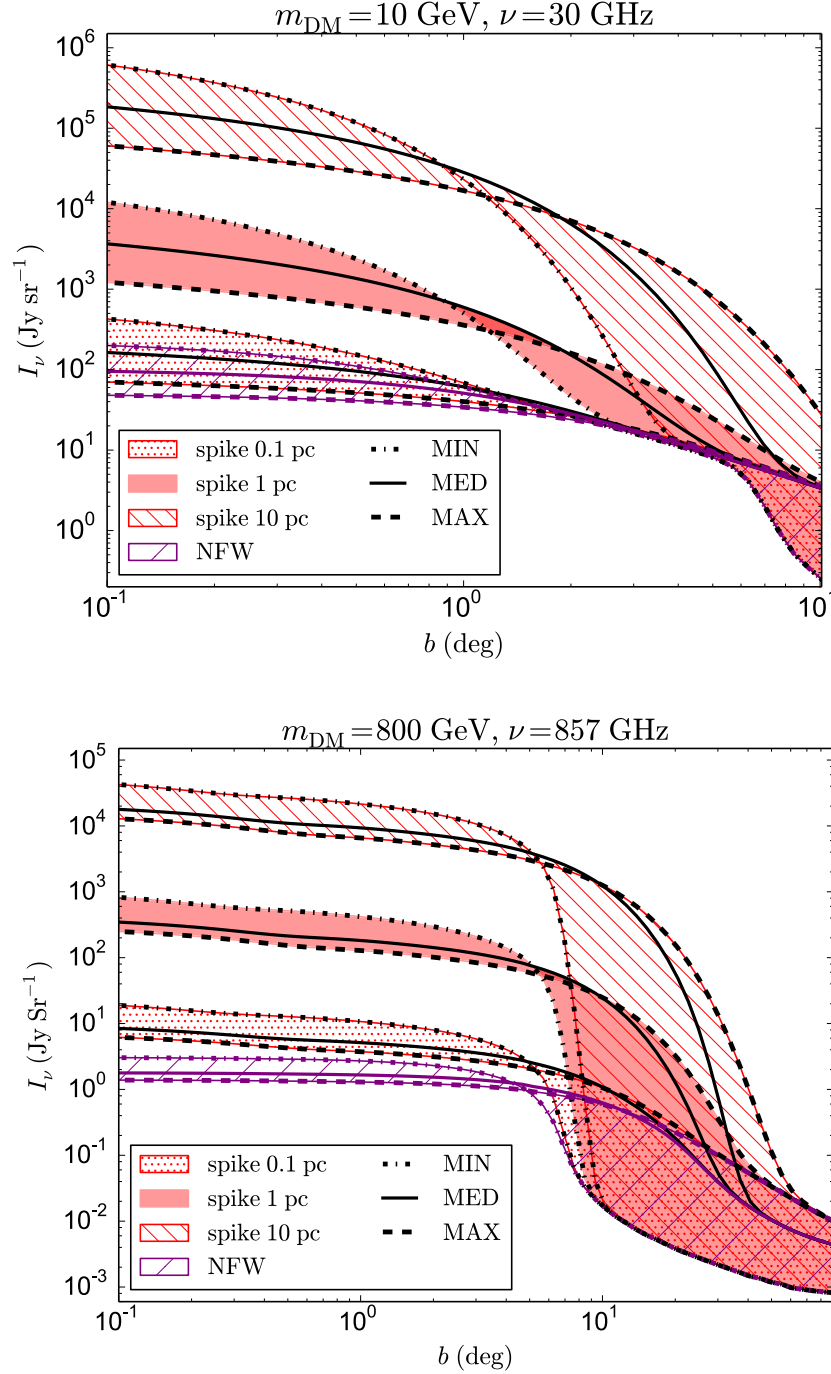


**Figure 7.3** – Synchrotron intensity as a function of latitude  $b$ , for  $\langle\sigma v\rangle = 3 \times 10^{-26} \text{ cm}^3 \text{ s}^{-1}$ , and  $B = 3 \mu\text{G}$ . The spikes are characterized by  $\gamma_{\text{spike}} = 7/3$ ,  $r_{\text{sat}} = r_{\text{sat}}^{\text{ann}}$ , and different values of  $R_{\text{sp}}$ . The **top panel** corresponds to  $m_{\text{DM}} = 10 \text{ GeV}$  and  $\nu = 30 \text{ GHz}$ , while the **bottom panel** corresponds to  $m_{\text{DM}} = 800 \text{ GeV}$  and  $\nu = 857 \text{ GHz}$ . The red dotted, shaded, and hatched areas represent the intensity for a spike of radius 0.1, 1 and 10 pc respectively. The purple hatched area is the intensity for the NFW profile without a spike.

In principle, not knowing the cross-section could lead to a misinterpretation of the spike characteristics: assuming the canonical cross-section, one could deduce the wrong values for  $R_{\text{sp}}$  or  $r_{\text{sat}}$ . However, since one can determine  $R_{\text{sp}}$  using the data at high latitudes and the morphology of the emission, the only possible source of degeneracy is between  $\langle\sigma v\rangle$  and  $r_{\text{sat}}$ . In

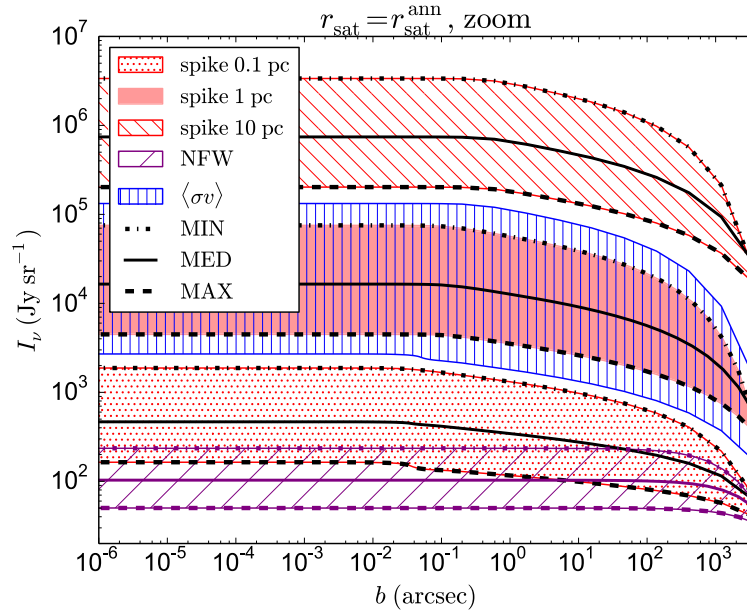


**Figure 7.4** – Synchrotron intensity from the inner part of the Galaxy as a function of latitude  $b$ , for 10 GeV DM particles,  $\langle\sigma v\rangle = 3 \times 10^{-26} \text{ cm}^3 \text{ s}^{-1}$ ,  $B = 3 \mu\text{G}$ , and  $\nu = 30 \text{ GHz}$ . The spikes are characterized by  $\gamma_{\text{sp}} = 7/3$ ,  $r_{\text{sat}} = r_{\text{sat}}^{\text{ann}}$ , and different values of  $R_{\text{sp}}$ . The blue vertically hatched area represents the additional uncertainty due to diffusion and the unknown cross-section, bracketed by the intensity for  $\langle\sigma v\rangle = 3 \times 10^{-27} \text{ cm}^3 \text{ s}^{-1}$  and  $\langle\sigma v\rangle = 3 \times 10^{-25} \text{ cm}^3 \text{ s}^{-1}$ .

the case of annihilating DM, this should not be a problem as both quantities are related. This is more problematic if there is no evidence that DM is annihilating, but one would not expect any anomalous synchrotron emission from the GC (unless DM is decaying, in which case the decay rate and  $r_{\text{sat}}$  should also be related).

As for distinguishing decaying from annihilating DM, for a given density profile, the morphology of the emission is different in both cases, as shown in [Ascasibar et al. \(2006\)](#); [Böehm et al. \(2010\)](#). One can therefore in principle discriminate between annihilating and decaying DM, but repeating a similar analysis for decaying DM is beyond the scope of our project. Annihilating and decaying DM are degenerate in terms of morphology only if the DM profile is twice as steep for decaying DM as for annihilating DM. However, in this work, we focus on the profile of annihilating DM, typically a spike with  $\gamma_{\text{sp}} = 7/3$ . Mimicking the morphology of the resulting emission with decaying DM would require a DM profile with a power-law index of the order of 5, which is unrealistic.

### 7.3.2.4 Heated spikes

So far, we only have considered adiabatic spikes with a slope  $\gamma_{\text{sp}} = 7/3$  that corresponds to the prescription of [Gondolo & Silk \(1999\)](#). However, for instance WIMPs scattering off stars in a dense star cluster at the GC may lead to shallower DM spikes with  $\gamma_{\text{sp}} = 3/2$ , as discussed in Chapter 3. Assuming  $\gamma_{\text{sp}} = 3/2$ , we obtain, however, essentially the same intensity as for a NFW profile for the masses of interest here. Our result is independent of the size of the spike and the latitude because the number of electrons injected in the center is small enough for diffusion to be efficient. Said differently, diffusion washes out the signature of a spike when the index is  $\gamma_{\text{sp}} = 3/2$ .

### 7.3.3 Impact of the magnetic field

We can now study the influence of the magnetic field on the intensity. To avoid possible degeneracies between the impact of a spike and spatial variations of the magnetic field, we will consider a constant field intensity over the whole diffusion zone. There is no established value of the magnetic field around Sgr A\*. Throughout our study we have used  $B = 3 \mu\text{G}$ , which is the expected value at large angular scales, but [Eatough et al. \(2013\)](#) suggest that  $B$  could actually be greater than 1 mG in the GC. To test the robustness of our conclusions, we now investigate the impact of the magnetic field intensity on the morphology of the synchrotron emission. Our results are shown in Fig. 7.5, and demonstrate that increasing the magnetic field from  $3 \mu\text{G}$  to 1 mG can significantly affect both the normalization and the morphology of the signal on scales of a few degrees.

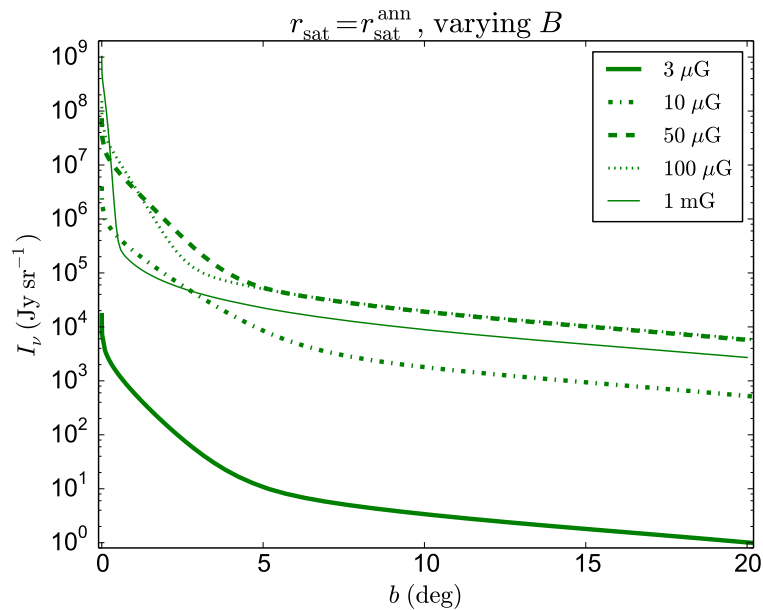


**Figure 7.5** – Synchrotron intensity as a function of latitude  $b$ , for 10 GeV DM particles,  $\langle\sigma v\rangle = 3 \times 10^{-26} \text{ cm}^3 \text{ s}^{-1}$ ,  $\nu = 30 \text{ GHz}$ , for a spike with  $\gamma_{\text{sp}} = 7/3$ ,  $r_{\text{sat}} = r_{\text{sat}}^{\text{ann}}$ , and for 5 values of the magnetic field between  $3 \mu\text{G}$  and 1 mG. The MED set of propagation parameters is used.

This can be understood as follows: the synchrotron intensity is the integral over the energy of the halo function times the ratio of the synchrotron power to the losses. All these quantities depend on the magnetic field but in different ways:

- (i) The synchrotron power depends on the magnetic field via  $P_{\text{syn}}(E) \propto B F_i(x)$ .
- (ii) The losses, being in the first approximation the sum of IC and synchrotron contributions, are dominated by one or the other depending on the value of the magnetic field; they are either almost independent of  $B$  when IC losses dominate or proportional to the magnetic field squared when the synchrotron losses are dominant.
- (iii) The halo function  $\tilde{I}$  is not directly proportional to the magnetic field. However, the larger the magnetic field, the more confined the electrons, so when the magnetic field increases, the calculation of  $\tilde{I}$  becomes essentially dominated by the very small values of the propagation length ( $\lambda_D \rightarrow 0$ ). The halo function is therefore related to the magnetic field in a nontrivial way.

In the regime in which the IC process is the dominant contribution to the loss term, the dependence of the synchrotron intensity on the magnetic field mostly arises through the synchrotron power  $P_{\text{syn}}$ . At 30 GHz and for  $B \in [3, 10] \mu\text{G}$ , we find that  $F_i(x) \propto B^p$  so  $P_{\text{syn}}(E) \propto B^{p+1}$  with  $p \approx 4$ , depending on the exact value of the energy. An increase in  $B$  thus induces a global increase in the intensity, as can be seen in Fig. 7.5 by comparing our predictions for  $B = 3 \mu\text{G}$

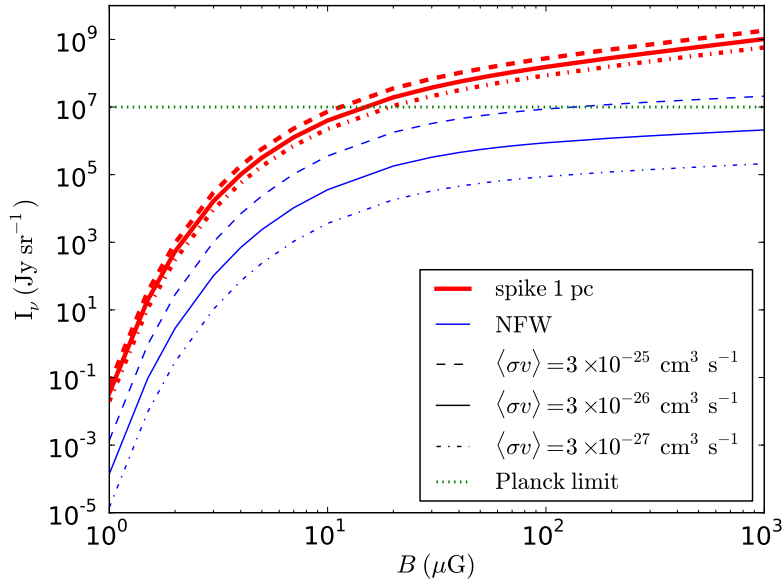


**Figure 7.6** – Synchrotron intensity from the direction of the GC ( $l = b = 0^\circ$ ) as a function of the magnetic field intensity, for 10 GeV DM particles,  $\nu = 30$  GHz, and for the NFW profile (blue thin lines) and the NFW+spike profile with  $\gamma_{\text{sp}} = 7/3$ ,  $R_{\text{sp}} = 1$  pc, and  $r_{\text{sat}} = r_{\text{sat}}^{\text{ann}}$  (red thick lines). The MED set of propagation parameters is used. The green dotted line represents the limit on the intensity given by *Planck*.

and  $B = 10 \mu\text{G}$ .

In the intermediate regime corresponding to  $B \in [10, 100] \mu\text{G}$ , IC and synchrotron losses are about the same order of magnitude, so the dependence of the intensity on  $B$  is more complex. It grows from  $B^0$  to  $B^2$  from 10 to 100  $\mu\text{G}$ . As a result, at high latitude where  $\tilde{I}$  is independent of  $E$  and  $B$ , the dependence of  $\int dEP_{\text{syn}}(E)\tilde{I}/b_{\text{tot}}(E)$  with the magnetic field decreases from  $B^5$  to  $1/\sqrt{B}$  (as discussed in [Boehm et al., 2010](#)), while at low latitude the electrons are more and more confined as  $B$  increases, so the morphology of the emission strongly depends on  $B$ . Finally in the regime where  $B \gtrsim 100 \mu\text{G}$ , the synchrotron losses are dominant so  $I_\nu \propto 1/\sqrt{B}$  at high latitude.

For a given value of the magnetic field, the intensity as a function of latitude follows the behavior of the halo function, which describes the outcome of the diffusion in terms of confinement. The latitude at which the intensity reaches its lower value is determined by the magnetic field. The stronger  $B$ , the smaller the confinement region and the earlier the intensity reaches its lower plateau in terms of latitude.

We now focus on the critical influence of the magnetic field on the strength of the synchrotron signal. As shown in Fig. 7.6 (and by comparing Fig. 7.3, top panel, to Fig. 7.7), the intensity varies by more than 4 orders of magnitude between 3  $\mu\text{G}$  and 1 mG. Consequently, the magnetic field has a huge impact on the constraints that one can set on the presence of a spike and its size. Large values of the magnetic field lead to a large intensity and thus potentially offer a scope for detectability of a steep inner profile.

### 7.3.4 Observability with *Planck*

We can now assess the potential for probing the existence of a spike with the *Planck* experiment. We estimate the total intensity at 30 GHz from the GC measured with *Planck* to be of order  $10^7 \text{ Jy sr}^{-1}$  ([Ade et al., 2014](#)). Since we do not account for the resolution of the detector, comparing our estimates of the intensity with this value only provides us with an indication of the synchrotron limit on these scenarios rather than a strict constraint. However, such a value turns out to be very useful in order to determine the ability of the *Planck* experiment to probe

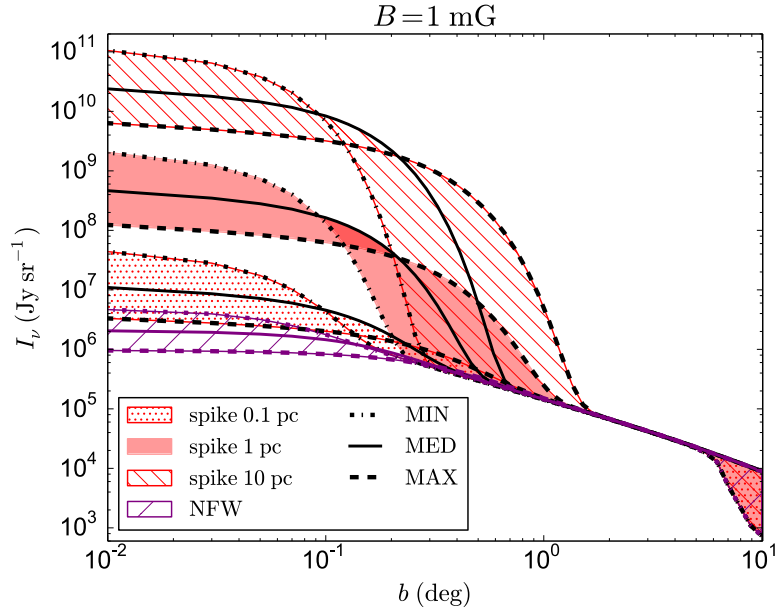


**Figure 7.7** – Synchrotron intensity as a function of latitude  $b$ , for 10 GeV DM particles,  $\langle\sigma v\rangle = 3 \times 10^{-26} \text{ cm}^3 \text{ s}^{-1}$ ,  $B = 1 \text{ mG}$ , and  $\nu = 30 \text{ GHz}$ , for spikes with  $\gamma_{\text{sp}} = 7/3$ ,  $r_{\text{sat}} = r_{\text{sat}}^{\text{ann}}$ , and different radii.

the existence of a spike.

From Fig. 7.2, we see that any spike with an extremely small saturation radius  $r_{\text{sat}} = R_{\text{S}}$  actually predicts a much larger intensity than what has been measured with *Planck*. Therefore, such profiles are likely to be excluded (especially since we used  $B = 3 \mu\text{G}$ , which is a conservative value). Inspecting Fig. 7.4 shows that spikes with a saturation radius of  $r_{\text{sat}} = r_{\text{sat}}^{\text{ann}}$  predict intensities below the *Planck* limit, thus indicating that it may not be possible to derive stringent constraints from the *Planck* results. However, our predictions assume  $B = 3 \mu\text{G}$  and the canonical value of the annihilation cross-section. Taking  $B \gtrsim \mathcal{O}(10) \mu\text{G}$  (or a larger cross-section value if one also assumes a regeneration mechanism, see Williams et al., 2012) increases our intensities by several orders of magnitude and typically implies that they exceed the *Planck* limit (see Fig. 7.6). Therefore, assuming a reasonable value of the magnetic field in the GC makes it possible to probe adiabatic spikes with *Planck*. This is illustrated in Fig. 7.7, where we display the synchrotron intensity for a large magnetic field ( $B = 1 \text{ mG}$ ) and the same parameters as in Fig. 7.3 (top panel). As one can readily see, spikes with radii 1 and 10 pc are excluded as their intensities exceed the *Planck* limit. Therefore, we conclude that the *Planck* experiment has the ability to constrain the presence of spiky DM halo profiles and discriminate between spikes of different sizes if there is a strong magnetic field in the GC.

The same types of conclusions hold for heavy (800 GeV) DM particles. At 857 GHz, the *Planck* limit on the emission from the GC is, however, of the order of  $10^9 \text{ Jy sr}^{-1}$  (Ade et al., 2014). Assuming  $B = 1 \text{ mG}$  and  $r_{\text{sat}} = r_{\text{sat}}^{\text{ann}}$ , we expect the synchrotron intensity (for  $\langle\sigma v\rangle = 3 \times 10^{-26} \text{ cm}^3 \text{ s}^{-1}$ ) to be about  $10^5 \text{ Jy sr}^{-1}$  (for MED). This is actually below the *Planck* limit, and so the presence of a spike would be difficult to assess in this case. However, a smaller saturation radius or an even larger magnetic field would increase the intensity.

Note that there could be additional constraints other than *Planck* on 10 GeV DM. For large values of the magnetic field, 10 GeV DM particles overproduce the synchrotron emission with respect to Sgr A\* at radio frequencies (300–400 MHz) and are therefore likely to be excluded (Boehm et al., 2004a, 2010). One important caveat, however, is that at such low frequencies one must account for the effects of advection and self-absorption of the synchrotron emission (e.g. Regis & Ullio, 2008), which were neglected in Boehm et al. (2004a, 2010). These effects

could reduce the radio flux and potentially weaken the radio constraints. Since such advection and self-absorption effects can be neglected at 30 GHz, using *Planck* data to constrain 10 GeV DM and the inner profile should provide us with a more robust method, although the foreground emission could then be problematic.

In our analysis, we have chosen a constant magnetic field over the whole Galaxy. Better modeling of  $B$  across the Galaxy would improve the analysis, but this was beyond the scope of this project. Also, we remark that our assumption of a very large (and homogeneous) magnetic field is not realistic as one expects  $B \sim 3 \mu\text{G}$  far away from the center. However, due to the confinement effect associated with large values of  $B$ , our conclusions should remain unchanged in that specific case.

## 7.4 Conclusion and perspectives

In this work, we have investigated whether it is possible to probe the DM energy distribution in the inner part of the Galaxy using synchrotron emission, in the presence of spatial diffusion of DM-induced electrons and positrons. We have focused on light (10 GeV) DM annihilating into  $e^+e^-$  but we also have investigated the case of heavy (800 GeV) DM. We have considered several DM halo profiles with different behaviors toward the GC, namely, NFW, NFW+spike with index  $\gamma_{\text{sp}} \sim 7/3$  and several sizes for the spike ( $R_{\text{sp}} = 0.1, 1, 10$  pc).

The standard propagation techniques that exist in the literature do not account for the steep increase in the electron number density close to the GC due to the presence of a spike. We have therefore modified the standard treatment of cosmic-ray propagation to account for a steep energy injection profile in the GC. Armed with the calculation of the electron and positron energy distribution accounting for propagation, we have been able to study the morphology of the synchrotron emission expected from annihilating DM candidates.

Our main conclusions are the following: first, we have shown that the size of the spike  $R_{\text{sp}}$  leaves an imprint on the synchrotron intensity at degree scales, and, second, the saturation radius  $r_{\text{sat}}$  can be inferred by zooming in on the GC. We thus find that the combination of small and large scales could enable one to probe the existence of a spiky DM halo distribution in the inner Galaxy. We also observe that using *Planck* data only could enable one to probe spikes of size greater than 1 pc, provided that the magnetic field is larger than  $\sim 20 \mu\text{G}$  in the inner region and that the cross-section is not too small. One can of course extend this analysis to other annihilation channels, but this was beyond the scope of this project.

In addition to probing the existence of a spike in the inner Galaxy, another application of this work could be to improve foreground modeling, in particular for *Planck*. Adding the emission induced by a DM spike to the astrophysical component might allow one to jointly constrain the properties of the spike and refine the foreground models.

In a follow-up project, we have used our new spatial diffusion technique to compute the inverse Compton  $\gamma$ -ray emission from a spike of annihilating DM, in the context of the recently detected H.E.S.S. diffuse emission at the GC. We describe this work in Chapter 8.

Finally, we note that the Event Horizon Telescope (EHT), with its micro-arcsec-scale angular resolution, will be able to probe very small scales in the MW and the M87 galaxy. This is particularly interesting since the effects of dynamical heating of DM by stars are likely to be unimportant in M87, so that a spike is more likely to have survived in that galaxy than in the MW, as discussed in Chapter 3. We discuss how to probe a DM spike at the center of M87 using the electromagnetic spectral energy distribution of the galaxy in Chapter 9, and we explore direct observation of a spike with the EHT in Chapter 11.

## Chapter 8

# New H.E.S.S. diffuse emission from the Galactic center: a combination of heavy dark matter and millisecond pulsars?

In this chapter, adapted from [Lacroix et al. \(2016\)](#), we show that the newly detected H.E.S.S.  $\gamma$ -ray diffuse emission from the Galactic center below  $0.45^\circ$  can be accounted for by inverse Compton emission from millisecond pulsars and heavy ( $\sim 100$  TeV) dark matter annihilating to electrons or muons with a thermal or sub-thermal cross-section, provided that the dark matter density profile features a supermassive black hole-induced spike on sub-pc scales. We discuss the impact of the interstellar radiation field, magnetic field and diffusion set-up on the spectral and spatial morphology of the resulting emission. For well-motivated parameters, we show that the DM-induced emission reproduces the spatial morphology of the H.E.S.S. signal above  $\sim 10$  TeV, while we obtain a more extended component from pulsars at lower energies, which could be used as a prediction for future H.E.S.S. observations.

### Contents

---

<b>8.1</b>	<b>Introduction</b>	<b>128</b>
<b>8.2</b>	<b>TeV gamma-rays from pulsars and dark matter annihilations</b>	<b>129</b>
8.2.1	Inverse Compton emission from millisecond pulsars	129
8.2.2	Annihilation signal from a dark matter spike	130
<b>8.3</b>	<b>Explaining the H.E.S.S. diffuse emission</b>	<b>132</b>
8.3.1	Spectral morphology	132
8.3.2	Spatial morphology	132
<b>8.4</b>	<b>Synchrotron emission and X-ray data</b>	<b>135</b>
<b>8.5</b>	<b>Conclusion</b>	<b>135</b>

---

## 8.1 Introduction

The H.E.S.S. collaboration has released the most detailed high-energy  $\gamma$ -ray view of the inner 300 pc of the GC region to date, thanks to improved statistics accumulated from 10 years of observation of the GC. In addition to the previously observed Galactic ridge emission (Aharonian et al., 2006a), a spherically symmetric diffuse emission has been detected between  $\sim 200$  GeV and 50 TeV (Abramowski et al., 2016). Specifically, this emission has been extracted in an open ring centered on the GC, with azimuthal size  $294^\circ$ , and inner and outer radii  $0.15^\circ$  and  $0.45^\circ$ , respectively, as shown in Fig. 8.1, taken from Abramowski et al. (2016). This corresponds to a solid angle of  $1.4 \times 10^{-4}$  sr. We refer to this new feature as the H.E.S.S. diffuse emission, which is distinct from the central point-like source HESS J1745-290 of size  $0.1^\circ$ .

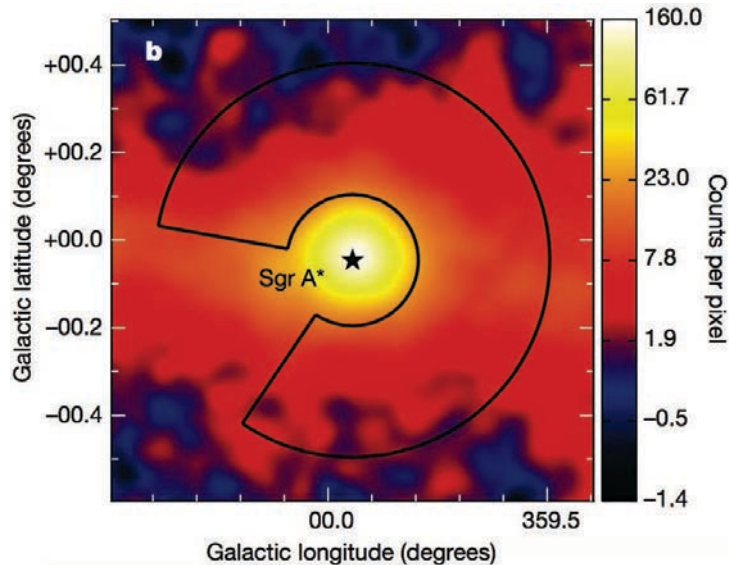


**Figure 8.1** – Very high-energy  $\gamma$ -ray image of the inner  $\sim 70$  pc around the GC, from Abramowski et al. (2016). Photon counts per  $0.02^\circ \times 0.02^\circ$  pixel are represented by the color scale. The star indicates the central BH Sgr A\*. The black contour defines the region where the diffuse emission has been extracted, excluding both the central point-like source HESS J1745-290 (corresponding to the yellow area) and a newly detected source to be reported by the H.E.S.S. Collaboration.

In the standard scenario, TeV  $\gamma$ -rays originate from the decay of neutral pions produced by collisions of protons accelerated by the central SMBH Sgr A\* with ambient gas (Abramowski et al., 2016). In this work, we explore a different interpretation which relates the H.E.S.S. diffuse emission to the excess of GeV  $\gamma$ -rays at the GC reported in the *Fermi*-LAT data. One of the leading explanations of the GeV excess is a population of millisecond pulsars (MSPs), as discussed in Part III. Here we point out that such a population of MSPs may also produce TeV  $\gamma$ -rays and thus significantly contribute to the H.E.S.S. diffuse emission.

A multi-TeV DM candidate would also produce  $\gamma$ -rays in the energy range of interest. However, as discussed in the following, the DM density profile must be strongly contracted in the very inner region in order for the associated flux to contribute significantly to the H.E.S.S. emission. A SMBH-induced density spike would provide the required enhancement of the annihilation signal.

In this chapter, we show that a combination of MSPs and a spike of heavy DM can explain the H.E.S.S. diffuse emission.<sup>1</sup>

<sup>1</sup>In the region of the H.E.S.S. diffuse signal lies the massive molecular cloud Sgr C (Abramowski et al., 2016). A  $\gamma$ -ray contamination of the diffuse signal, from a source located in this cloud, cannot be excluded. Our model of the overall diffuse signal in terms of a combination of MSPs and heavy DM should therefore be interpreted as an upper limit.

## 8.2 TeV gamma-rays from pulsars and dark matter annihilations

### 8.2.1 Inverse Compton emission from millisecond pulsars

The rotation energy of MSPs has been shown to power a high-energy  $e^\pm$  wind (Rees & Gunn, 1974). The interaction of this pulsar wind with the interstellar medium may create a shock which can accelerate  $e^\pm$  to very high energies (Bednarek & Sobczak, 2013; Yuan & Ioka, 2015). Their maximum energy  $E_{\max}$  is limited by their ability to escape the shock region, and by their synchrotron losses. However, this energy can be as high as a few tens of TeV (Bednarek & Sobczak, 2013). The resulting  $e^\pm$  injection spectrum follows a power law, with the maximum energy accounted for by an exponential cut-off:

$$\left. \frac{dN_e}{dE_{\text{inj}}} \right|_{\text{MSP}} \propto E_{\text{inj}}^{-2} \exp\left(-\frac{E_{\text{inj}}}{E_{\max}}\right), \quad (8.1)$$

where we take  $E_{\max} = 50$  TeV as in Bednarek & Sobczak (2013). The normalization is worked out by fitting the spectrum of the H.E.S.S. diffuse emission.

These  $e^\pm$  emit  $\gamma$ -rays by upscattering photons of the interstellar radiation field (ISRF) via the inverse Compton (IC) process. The resulting  $\gamma$ -ray spectrum can extend to very high energies, up to the range of interest for H.E.S.S. observations. This led Bednarek & Sobczak (2013); Yuan & Ioka (2015) to claim that IC emission from MSPs could be responsible for the H.E.S.S. central source data, based on a spectral analysis. In principle,  $e^\pm$  also emit bremsstrahlung by interacting with nuclei of the ambient gas, but this component is negligible with respect to IC over the energy range of interest.

The resulting IC flux is obtained by integrating the emissivity  $j_{\text{MSP}}$  over the line of sight (l.o.s.) coordinate  $s$  and the field of view (fov)  $\Delta\Omega$  (see Chapter 4):

$$E_\gamma^2 \left. \frac{dn}{dE_\gamma} \right|_{\text{MSP}}^{\text{IC}} = \int_{\Delta\Omega} E_\gamma^2 \left. \frac{dn}{dE_\gamma d\Omega} \right|_{\text{MSP}}^{\text{IC}} d\Omega = \frac{E_\gamma}{4\pi} \int_{\Delta\Omega} \int_{\text{l.o.s.}} j_{\text{MSP}}(E_\gamma, \vec{x}) ds d\Omega, \quad (8.2)$$

with the emissivity  $j_{\text{MSP}}$  given by the convolution of the MSP  $e^\pm$  spectrum after propagation  $\psi_{\text{MSP}}$  and the IC emission spectrum  $P_{\text{IC,G}}$  (the G subscript refers to the standard ISRF implemented in the GALPROP code):

$$j_{\text{MSP}}(E_\gamma, \vec{x}) = \int_{E_\gamma}^{E_{\max}} P_{\text{IC,G}}(E_\gamma, E_e, \vec{x}) \psi_{\text{MSP}}(E_e, \vec{x}) dE_e. \quad (8.3)$$

The integral over solid angle in Eq. (8.2) is performed over the fov of the H.E.S.S. diffuse emission,  $\Delta\Omega = 1.4 \times 10^{-4}$  sr.

The  $e^\pm$  spectrum from MSPs after propagation  $\psi_{\text{MSP}}$ , in a steady state and accounting for energy losses and spatial diffusion, reads, as described in Chapter 4,

$$\psi_{\text{MSP}}(E, \vec{x}) \propto \frac{1}{b_{\text{G}}(E, \vec{x})} \int_E^{E_{\max}} \tilde{I}_{\vec{x},\text{MSP}}(E, E_{\text{inj}}) \left. \frac{dN_e}{dE_{\text{inj}}} \right|_{\text{MSP}} dE_{\text{inj}}, \quad (8.4)$$

where  $b_{\text{G}}(E, \vec{x})$  is the sum of the synchrotron and IC loss rates, corresponding to the GALPROP losses tabulated in Buch et al. (2015). In particular the corresponding magnetic field is of order  $10 \mu\text{G}$ . The halo function  $\tilde{I}_{\vec{x},\text{MSP}}$  which models the effect of spatial diffusion on the MSP profile is computed exactly as in Sec. 4.3.7, assuming a diffusion set-up corresponding to the usual MED parametrization: a diffusion coefficient  $K(E) = K_0 (E/E_0)^\delta$ , with  $K_0 = 3.38 \times 10^{27} \text{ cm}^2 \text{ s}^{-1}$ ,  $E_0 = 1 \text{ GeV}$ ,  $\delta = 0.7$ , and a half height of  $L = 4 \text{ kpc}$  for the diffusion zone.<sup>2</sup> For the density that enters into the calculation of  $\tilde{I}_{\vec{x},\text{MSP}}$ , we use the same generalized NFW profile with slope  $\sim 1.2$ , consistent with the morphology of the GeV excess, as in Chapter 5.

<sup>2</sup>Incidentally, the diffusion coefficient is a factor 2 smaller at 1 TeV than the one used in Abramowski et al. (2016).

### 8.2.2 Annihilation signal from a dark matter spike

Following the prescription of [Gondolo & Silk \(1999\)](#) and the discussion of Chapter 3, we assume that a SMBH-induced adiabatic spike is present in the inner part of the DM density profile, with  $\rho(r) \propto r^{-\gamma_{\text{sp}}}$ , where  $\gamma_{\text{sp}} = 7/3$ , below a parsec-scale radius  $R_{\text{sp}}$ . We normalize the DM profile exactly as in Chapter 7.

#### 8.2.2.1 Prompt emission from dark matter annihilation

The prompt  $\gamma$ -ray flux for channel  $f$  reads as usual

$$E_\gamma^2 \frac{dn_f}{dE_\gamma} \Big|_{\text{DM}}^{\text{prompt}} = \frac{E_\gamma^2 \langle \sigma v \rangle_f}{4\pi 2m_{\text{DM}}^2} \frac{dN_{\gamma,f}}{dE_\gamma} \int_{\Delta\Omega_c} \int_{\text{l.o.s.}} \rho^2(\vec{x}) ds d\Omega, \quad (8.5)$$

with  $\rho(\vec{x})$  the DM density at position  $\vec{x}$ .  $\langle \sigma v \rangle_f$  the annihilation cross-section into channel  $f$  and  $dN_{\gamma,f}/dE_\gamma$  the  $\gamma$ -ray spectrum from this final state, taken once again from [Cirelli et al. \(2011\)](#). In practice, the DM profile is so steep that the integral depends weakly on the precise value of the fov  $\Delta\Omega_c$ , which we take equal to  $10^{-5}$  sr, the size of the central source HESS J1745-290.

#### 8.2.2.2 Inverse Compton emission from dark matter annihilation

Prompt emission from a DM spike is the dominant source of DM-induced  $\gamma$ -rays in the central parsec, but the corresponding spatial extension is too small to account for the H.E.S.S. diffuse emission detected up to  $0.45^\circ$ . However, in addition to prompt emission, we expect a significant amount of  $\gamma$ -rays to arise from IC emission from  $e^\pm$  produced in DM annihilations. Since  $e^\pm$  undergo spatial diffusion, the resulting  $\gamma$ -ray emission can be significantly more spatially extended than the initial DM profile, as discussed in Chapter 7.

Considering that with our DM spike model,  $e^\pm$  are produced by DM annihilations below parsec scales, we no longer use the GALPROP ISRF in this case, but the one computed in [Kistler \(2015\)](#) and referred to as the Kistler ISRF. This enhanced radiation field accounts for the strong sources of photons in the central parsec of the Galaxy, and is about three orders of magnitude larger than the GALPROP ISRF, as shown in Fig. 8.2. We also account for absorption of  $\gamma$ -rays from  $e^+e^-$  pair production on ISRF photons, using the attenuation factor computed in [Kistler \(2015\)](#). Absorption is essentially relevant above 10 TeV, and leads to a reduction of the flux of 10% at  $E_\gamma \sim 10$  TeV, down to 30% at 100 TeV.

The computation of the IC flux for channel  $f$  is similar to the MSP case:

$$E_\gamma^2 \frac{dn_f}{dE_\gamma} \Big|_{\text{DM}}^{\text{IC}} = \frac{E_\gamma}{4\pi} \int_{\Delta\Omega} \int_{\text{l.o.s.}} j_{\text{DM},f}(E_\gamma, \vec{x}) ds d\Omega, \quad (8.6)$$

where the IC emissivity reads

$$j_{\text{DM},f}(E_\gamma, \vec{x}) = 2 \int_{E_\gamma}^{m_{\text{DM}}} P_{\text{IC,K}}(E_\gamma, E_e, \vec{x}) \psi_{\text{DM},f}(E_e, \vec{x}) dE_e, \quad (8.7)$$

and the spectrum accounting for diffusion is given by

$$\psi_{\text{DM},f}(E_e, \vec{x}) = \frac{\kappa_f}{b_{\text{K}}(E_e)} \int_{E_e}^{E_{\text{max}}} \tilde{I}_{\vec{x},\text{DM}}(E_e, E_{\text{inj}}) \frac{dN_{e,f}}{dE_{\text{inj}}} \Big|_{\text{DM}} dE_{\text{inj}}, \quad (8.8)$$

where  $\kappa_f = 1/2 \langle \sigma v \rangle_f (\rho_\odot/m_{\text{DM}})^2$ , and  $b_{\text{K}}$  is the sum of synchrotron and IC losses in the central pc, where the K subscript stands for the Kistler ISRF. We assume a  $B = 0.1$  mG magnetic field in the central pc, following [Hinton & Aharonian \(2007\)](#); [Crocker et al. \(2010\)](#); [Kistler \(2015\)](#). The IC energy loss rate  $b_{\text{IC,K}}$  is computed following the procedure of [Cirelli & Panci](#)

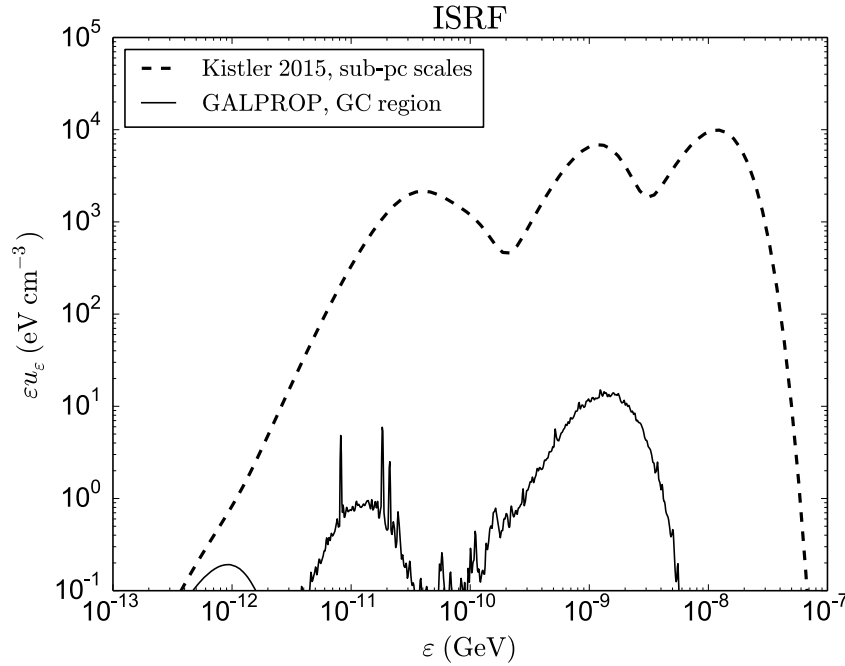


**Figure 8.2** – Comparison of the spectral energy distributions of the ISRF at the GC from Kistler (2015) and GALPROP. The GALPROP ISRF does not specifically account for photon sources below sub-parsec scales, which are nevertheless relevant when considering a DM spike.

(2009); Delahaye et al. (2010), which models the ISRF as a superposition of greybody spectra, as described in Sec. 4.3.5.1. The parameters of the various components of the radiation field from Kistler (2015) are given in Table 8.1. Considering the freedom we have on the poorly constrained diffusion set-up below  $\sim 100$  pc, we again use the benchmark MED set-up to compute the spike halo function  $\tilde{I}_{\vec{x},\text{DM}}$ . The electron injection spectrum  $dN_{e,f}/dE_{\text{inj}}|_{\text{DM}}$  is taken from Cirelli et al. (2011) and includes electroweak corrections, relevant at high energies.  $\tilde{I}_{\vec{x},\text{DM}}$  is computed using our dedicated method presented in Sec. 4.3.7.6, which accounts for the steepness of the source term in the diffusion-loss equation due to the DM spike.

**Table 8.1** – Temperatures  $T$ , blackbody energy densities  $w_{\text{bb}}$ , and ratios of energy density to energy density of a blackbody  $w/w_{\text{bb}}$  obtained by fitting the spectral energy distribution of the ISRF with greybody spectra in Kistler (2015).

$T$ (K)	$w_{\text{bb}}$ ( $10^{-9}$ GeV cm $^{-3}$ )	$w/w_{\text{bb}}$
2.725	0.26	1
40	$1.2 \times 10^4$	$2.0 \times 10^{-3}$
90	$3.1 \times 10^5$	$4.0 \times 10^{-3}$
120	$9.8 \times 10^5$	$1.2 \times 10^{-3}$
250	$1.8 \times 10^7$	$8.3 \times 10^{-5}$
3500	$7.1 \times 10^{11}$	$1.3 \times 10^{-8}$
35000	$7.1 \times 10^{15}$	$1.9 \times 10^{-12}$

## 8.3 Explaining the H.E.S.S. diffuse emission

### 8.3.1 Spectral morphology

Shown in Fig. 8.3 are the  $\gamma$ -ray spectra for the fov corresponding to the annulus of the H.E.S.S. diffuse emission,  $1.4 \times 10^{-4}$  sr (top panel, red) and the central source HESS J1745-290, i.e.  $10^{-5}$  sr (bottom panel, blue). The H.E.S.S. data points are taken from Abramowski et al. (2016). The dashed and dot-dashed lines represent our predictions of IC emission from MSPs and a DM spike of radius 0.1 pc, respectively. Prompt emission from the spike also contributes to the flux in the central source region (bottom panel, dotted line). We consider a DM candidate of mass  $m_{\text{DM}} = 100$  TeV, annihilating to  $e^+e^-$  with the canonical cross-section of  $\langle\sigma v\rangle = 3 \times 10^{-26}$  cm<sup>3</sup> s<sup>-1</sup>.<sup>3</sup>

The top panel of Fig. 8.3 shows that the H.E.S.S. diffuse emission can be accounted for by the sum of IC emission from MSPs and a DM spike, with the lower part of the H.E.S.S. spectrum associated with MSPs, and the high energy part above  $\sim 10$  TeV with DM. The reduced chi-squared is  $\chi^2/\text{d.o.f.} = 23.7/20 \approx 1.19$ , showing the quality of the fit.<sup>4</sup> As shown in the bottom panel of Fig. 8.3, our model is compatible with the data from the central source, in particular with the upper limits at the highest energies.

For an annihilation cross-section of  $3 \times 10^{-26}$  cm<sup>3</sup> s<sup>-1</sup>, we find that the spike radius  $R_{\text{sp}}$  must not be larger than  $\sim 0.1$  pc, otherwise the associated IC flux significantly overshoots both the diffuse and point source data. There is actually a degeneracy between the cross-section and the spike radius, but this is beyond the scope of this project.<sup>5</sup> For completeness we computed the IC flux from a heated spike with a 1.5 slope, but the result is roughly two orders of magnitude smaller than the H.E.S.S. flux. A SMBH-induced spike is therefore required for DM annihilations to significantly contribute to the H.E.S.S. diffuse emission.

We obtain similar results for DM annihilation into  $\mu^+\mu^-$ , with a slightly softer DM-induced IC spectrum, as shown in Fig. 8.4. We disregard softer channels like  $\tau^+\tau^-$  or  $b\bar{b}$ , for which the IC flux is too small in the H.E.S.S. extended region of interest while the associated prompt emission overshoots the central source data.

### 8.3.2 Spatial morphology

Shown in Fig. 8.5 are the IC intensities  $E_\gamma^2 dn/(dE_\gamma d\Omega)$  at 0.5 TeV (thin blue lines) and 23 TeV (thick black lines), as a function of angle  $\theta$  (or radius  $r$ ) from the center, for the same components (MSPs, dashed, and DM spike, dot-dashed) as in Fig. 8.3.

Fig. 8.5 shows that for the DM spike, which dominates above  $\sim 10$  TeV (see the spectrum in Fig. 8.3), the IC intensity drops steeply around  $0.3^\circ$  at 23 TeV and around  $1^\circ$  at 0.5 TeV. These specific scales correspond to the diffusion lengths associated with the losses and diffusion coefficient,<sup>6</sup> and turn out to be very similar to the characteristic size of the H.E.S.S. diffuse emission. For the MSP component, dominant below  $\sim 10$  TeV, the spatial extension of the IC emission is of order a few degrees, therefore larger than the H.E.S.S. region.

The diffuse emission has been detected by H.E.S.S. by accumulating statistics from a significant exposure time in this region. However, the emission might be even more extended, and future H.E.S.S. observations at Galactic latitudes  $|b| > 1^\circ$  would greatly help to discriminate between the proposed scenarios. In particular, according to our predictions, H.E.S.S. should observe an even more extended signal below  $\sim 10$  TeV, due to the MSP component.

<sup>3</sup>The value of  $\langle\sigma v\rangle$  considered here reaches the unitarity limit at 100 TeV (Griest & Kamionkowski, 1990). Models like minimal DM predict DM masses up to a few tens of TeV (see e.g. Del Nobile et al., 2015), but it is possible to go beyond the weak scale, up to very large masses, if for instance DM is part of a decoupled sector (Berlin et al., 2016).

<sup>4</sup>We have 22 data points and 2 free parameters, namely the normalization of the MSP flux and the size of the spike, so 20 degrees of freedom (d.o.f.).

<sup>5</sup>In particular, the cross-section needed for a larger spike radius would be smaller.

<sup>6</sup>For injection at  $\sim 100$  TeV and propagation down to 23 TeV, the diffusion length is  $\sim 50$  pc, i.e.  $\sim 0.3^\circ$ .

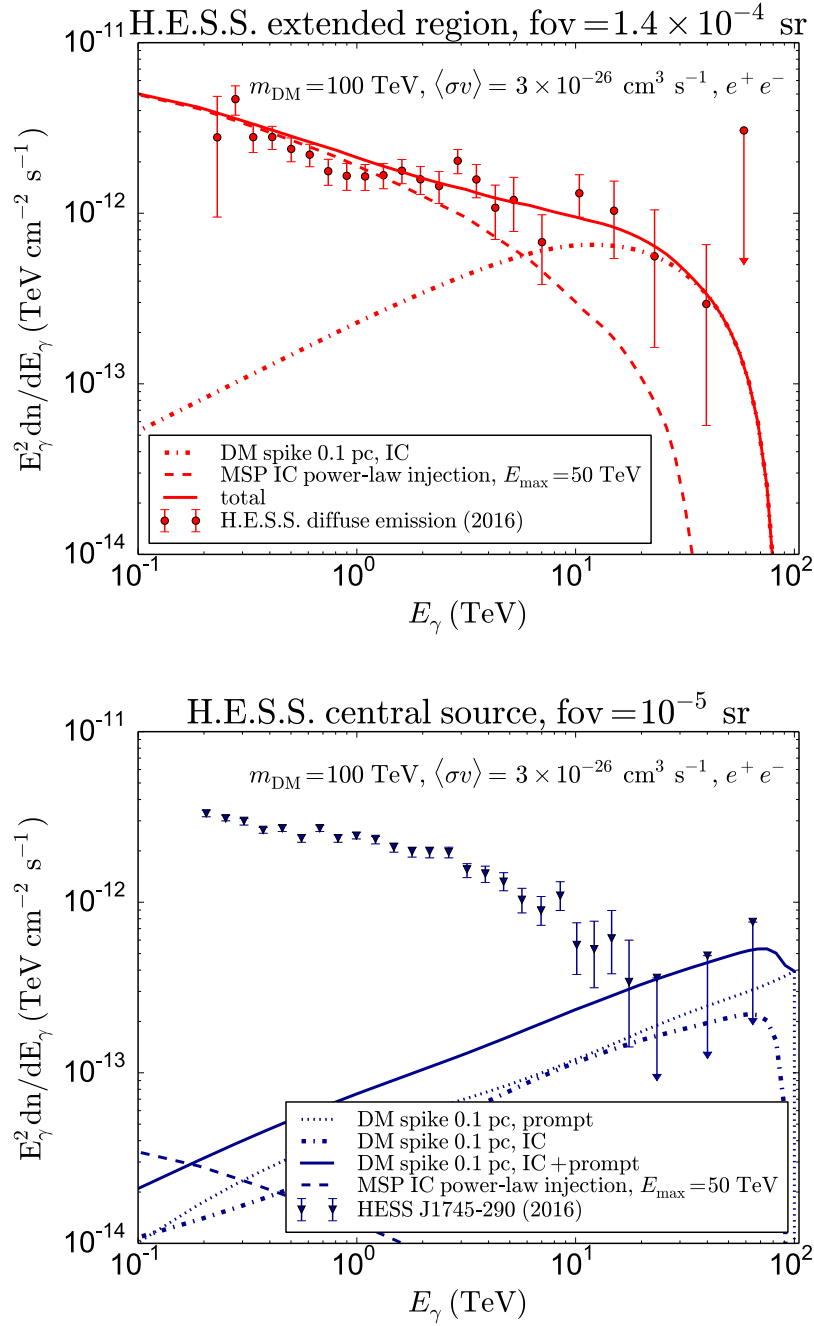


**Figure 8.3 – Top panel:**  $\gamma$ -ray spectra from 100 GeV to 100 TeV for a fov of  $1.4 \times 10^{-4}$  sr corresponding to the H.E.S.S. diffuse emission. IC emission from MSPs is depicted as a dashed line. IC emission from a spike of radius 0.1 pc, for a 100 TeV DM candidate annihilating exclusively to  $e^+e^-$  with the canonical cross-section of  $\langle\sigma v\rangle = 3 \times 10^{-26} \text{ cm}^3 \text{ s}^{-1}$  is shown as a dot-dashed line. The solid line represents the total spectrum. **Bottom panel:**  $\gamma$ -ray spectra from 100 GeV to 100 TeV for a fov of  $10^{-5}$  sr corresponding to the central source, HESS J1745-290. In addition to IC emission from MSPs (dashed) and a DM spike of radius 0.1 pc (dot-dashed), the central region features the sharply peaked prompt emission from the spike (dotted). The solid line is the total emission. The MSP and DM parameters are the same as for the top panel. The data points for both panels are taken from [Abramowski et al. \(2016\)](#).

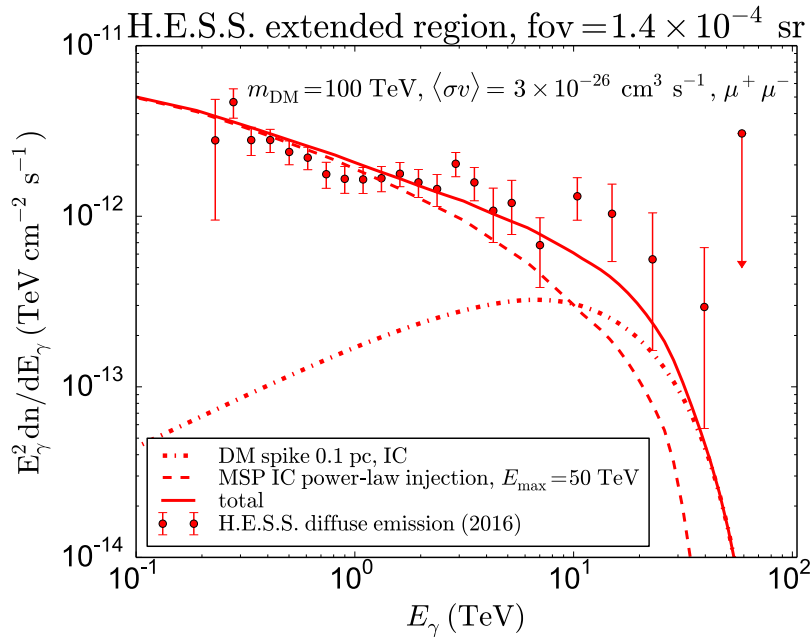


**Figure 8.4** – Same as Fig. 8.3 but for the  $\mu^+\mu^-$  channel. We do not show the associated emission in the central source region but the model is also compatible.

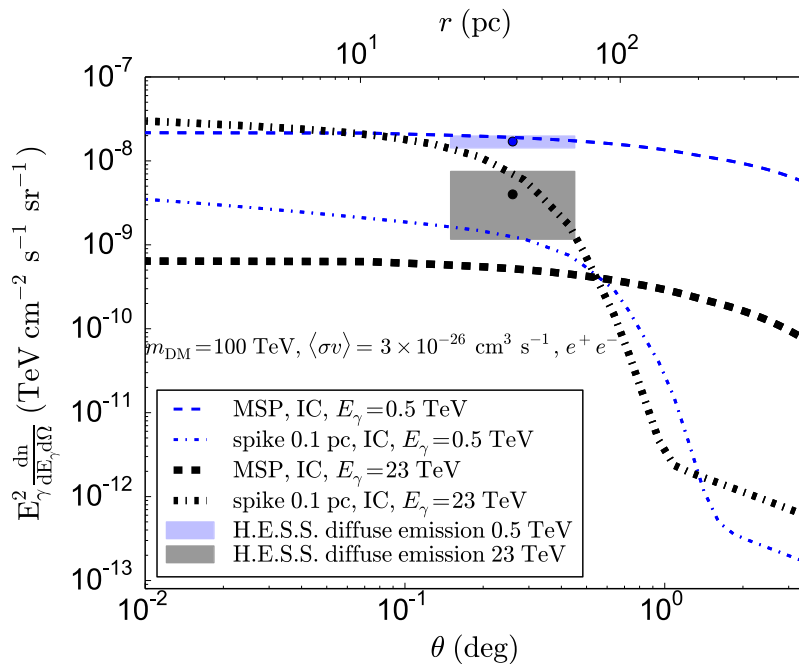


**Figure 8.5** – Intensity of IC emission from MSPs (dashed) and a 0.1 pc DM spike (dot-dashed) as a function of angular distance from the GC, at 0.5 TeV (thin blue) and 23 TeV (thick black). The data points at these energies and their error bars are depicted as shaded rectangles.

The IC flux from the DM spike is sensitive to the losses and diffusion coefficient in the central pc. On the one hand, a magnetic field in the mG range—larger than the 0.1 mG value we have considered—in the central pc, as suggested in [Eatough et al. \(2013\)](#), would lead to a factor  $\sim 100$  increase in synchrotron losses, thus significantly reducing the IC flux and spoiling the achievement of explaining the high-energy part of the H.E.S.S. diffuse emission. On the other hand, changing the diffusion coefficient from the MED to the MIN or MAX set-ups—which

usually quantify the uncertainty on diffusion on large scales—only changes the flux by a factor  $\sim 1.5$ , which does not affect our conclusions. However, if the diffusion coefficient was in fact much smaller, typically for Bohm diffusion (e.g. [Bednarek & Sobczak, 2013](#)), the spike-induced IC emission would be confined within the region corresponding to the central source and there would be no leakage into the diffuse emission region.

## 8.4 Synchrotron emission and X-ray data

Steady diffuse X-ray emission was recently detected with the [NuSTAR](#) satellite within a few pc of Sgr A\*, in the 20–40 keV band ([Mori et al., 2015](#); [Perez et al., 2015](#)). Considering that for  $e^\pm$  injected by  $\sim 100$  TeV DM, the typical synchrotron energy,

$$E_{\text{syn}} \sim 66 \left( \frac{E_e}{100 \text{ TeV}} \right)^2 \left( \frac{B}{0.1 \text{ mG}} \right) \text{ keV}, \quad (8.9)$$

falls in the hard X-ray domain, we checked that the  $e^\pm$  population needed to explain the H.E.S.S. diffuse emission does not overshoot the NuSTAR data by producing too much synchrotron radiation.

Within 40 arcsec of Sgr A\*, the flux measured with NuSTAR in the 20–40 keV band is  $\sim 2 \times 10^{-12} \text{ erg cm}^2 \text{ s}^{-1}$  ([Mori et al., 2015](#); [Perez et al., 2015](#)). In the same region, at 40 keV, and for  $B = 0.1$  mG, we find a synchrotron flux of  $\sim 7 \times 10^{-14} \text{ erg cm}^2 \text{ s}^{-1}$  for the  $e^+e^-$  annihilation channel. This is about 30 times smaller than the measured flux. The MSP component does not give a sizable contribution to the hard X-ray flux, due to a softer injection spectrum. Therefore our model of the H.E.S.S. diffuse emission is compatible with NuSTAR observations.

Interestingly, for a larger magnetic field, typically 5 mG, IC emission from the DM spike is subdominant, but the synchrotron flux is of the order of the NuSTAR flux. In addition, the corresponding synchrotron losses reduce the diffusion length—and thus the size of the emission region—to a few pc, similar to the NuSTAR region. As a result, if the magnetic field is in the mG range, the DM spike no longer accounts for the H.E.S.S. diffuse emission, but may instead contribute significantly to the hard X-ray emission measured with NuSTAR within a few pc of Sgr A\*, although DM is unlikely to account for the entire signal which is slightly asymmetric.

## 8.5 Conclusion

In this chapter, we have shown that the sum of IC emission from  $e^\pm$  produced by the same population of MSPs that can explain the *Fermi* GeV excess, and by annihilations of heavy ( $\sim 100$  TeV) DM particles in a SMBH-induced density spike, can account for the new diffuse emission observed at the GC with H.E.S.S.. Our model reproduces very well the spectrum of the emission, with MSPs accounting for observations below  $\sim 10$  TeV and DM accounting for the higher energy part of the spectrum. We have also discussed the associated spatial morphology. For well-motivated propagation parameters, we find that the DM-induced emission has the same extension as the observed signal, while the size of the MSP component is larger, reaching up to a few degrees. This can be used to test this scenario, depending on whether the current observed extension of  $\sim 0.45^\circ$  is the actual size of the emission region, or if more statistics will uncover a more extended signal.



## Part V

# Probing dark matter spikes in the M87 and Centaurus A galaxies



## Chapter 9

# Ruling out thermal dark matter with a black hole induced spiky profile in the M87 galaxy

In this chapter, using the spectral energy distribution of Messier 87 (M87), a nearby radio galaxy in the Virgo cluster, and assuming a supermassive black hole induced spike in the dark matter halo profile, we exclude any dark matter candidate with a velocity-independent (s-wave) annihilation cross-section of the order of  $\langle\sigma v\rangle \sim 10^{-26} \text{ cm}^3 \text{ s}^{-1}$  and a mass up to  $\mathcal{O}(100)$  TeV. These limits supersede all previous constraints on thermal, s-wave, annihilating dark matter candidates by orders of magnitude, and rule out the entire canonical mass range. We remark in addition that, under the assumption of a spike, dark matter particles with a mass of a few TeV and an annihilation cross-section of  $\sim 10^{-27} \text{ cm}^3 \text{ s}^{-1}$  could explain the TeV  $\gamma$ -ray emission observed in M87. A central dark matter spike is plausibly present around the supermassive black hole at the center of M87, for various, although not all, formation scenarios, and would have profound implications for our understanding of the dark matter microphysics. This chapter is adapted from [Lacroix et al. \(2015a\)](#).

### Contents

---

<b>9.1</b>	<b>Introduction</b>	<b>140</b>
<b>9.2</b>	<b>Diffuse emission in the presence of a dark matter spike in M87</b>	<b>140</b>
<b>9.3</b>	<b>Upper limits on the annihilation cross-section</b>	<b>142</b>
9.3.1	Methodology	142
9.3.2	Results	143
9.3.3	Robustness of our constraints	146
<b>9.4</b>	<b>DM spike and jet</b>	<b>147</b>
9.4.1	Jet emission	147
9.4.2	Upper limits on the annihilation cross-section with spike+jet	148
9.4.3	Explaining the TeV data with a dark matter spike	149
<b>9.5</b>	<b>Conclusion</b>	<b>152</b>

---

## 9.1 Introduction

In the absence of annihilation signatures in DM halos, stringent limits are placed on the DM self-annihilation cross-section as a function of the DM mass. Indirect searches already rule out the simplest<sup>1</sup> thermal, velocity independent, dark matter annihilation cross-section of about  $\langle\sigma v\rangle \simeq 3 \times 10^{-26} \text{ cm}^3 \text{ s}^{-1}$  for masses up to to  $\sim 100 \text{ GeV}$  as reviewed in Chapter 2, but here we show that one can go a step further. We use the spectral diffuse emission of M87, a nearby radio galaxy in the Virgo cluster located about 16 Mpc from us (Bird et al., 2010), to exclude heavier and more weakly interacting DM particles.

We observe that the presence of a SMBH in the core of M87 may increase the DM energy distribution so much toward the galactic center that the predicted flux expected from thermal DM particles would exceed observations. As discussed in Chapter 3, an adiabatic DM spike is more likely to have survived in M87, which is dynamically young, than in the MW. Therefore, in what follows, we assume that a spike has formed in M87 and has also survived until the present epoch. We study its impact on the electromagnetic signatures expected from DM annihilations and derive stringent constraints on the DM properties.

## 9.2 Diffuse emission in the presence of a dark matter spike in M87

We consider an adiabatic spike with  $\rho \propto r^{-7/3}$ , starting from the spike radius  $R_{\text{sp}}$ , down to the saturation radius  $r_{\text{sat}}$  determined by the DM mass and annihilation cross-section (see Chapter 3). Outside this inner region, i.e. for  $r > R_{\text{sp}}$ , we assume a NFW profile. Details on the normalization of the profile are given in Appendix A.2.1. In Fig. 9.1, we show the resulting profiles for two different values of the DM annihilation cross-section, so as to illustrate the impact of DM annihilations on the saturation plateau. As discussed in Chapter 3, a larger cross-section truncates the profile.

The DM contribution to the spectral energy distribution (SED) of M87 is essentially two-fold. Photons can be produced in the observed regime by prompt emission and secondary emission of  $e^\pm$  produced by DM annihilations, namely inverse Compton scattering (ICS) off low energy photons (CMB, infrared and starlight), as well as synchrotron radiation. We neglect any possible bremsstrahlung emission since M87 is deficient in cold gas (Young et al., 2011).

Prompt emission is independent of the galaxy dynamics and is only determined by the DM particle physics properties. On the contrary, synchrotron and ICS strongly depend on the properties of the interstellar medium in the galaxy, such as the magnetic field strength and interstellar radiation field. In the presence of a very strong magnetic field, synchrotron emission becomes the main source of low-energy photons but it is also the main energy loss for the electrons and positrons produced by the DM. As a result, we find that prompt emission dominates ICS and is therefore the dominant source of high energy gamma-rays, while synchrotron radiation is the dominant source of X-rays and lower-energy photons.

The assumption of a very strong magnetic field in this work is actually justified by the presence of a BH at the center of M87. In fact, we consider that the magnetic field distribution in the inner region is shaped by the accretion flow. Hence, unless stated otherwise, we assume that the radial dependence of the magnetic field is given by the equipartition model and thus goes as

---

<sup>1</sup>One exception to this conclusion being scenarios with co-annihilations, see e.g. Griest & Seckel (1991).

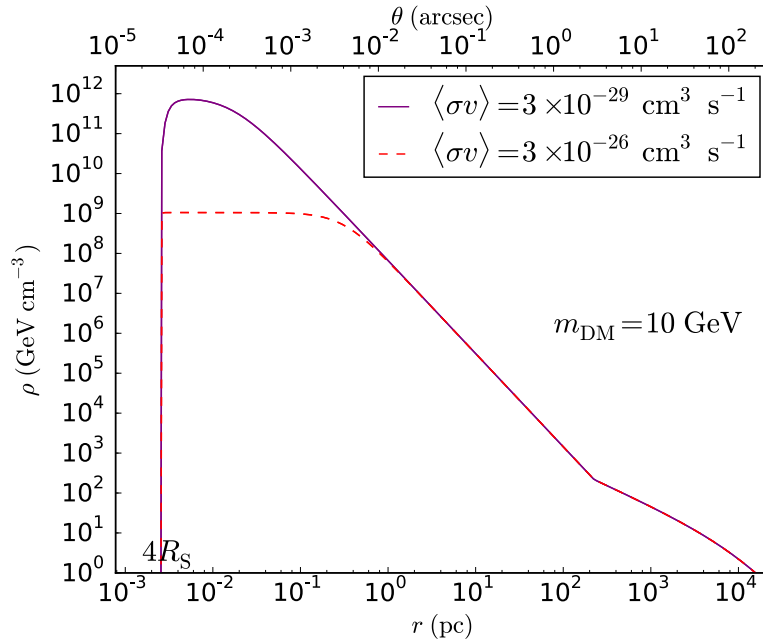


**Figure 9.1** – DM energy density as a function of the distance from the center, for a DM spike with  $\gamma_{\text{sp}} = 7/3$ . DM annihilations soften the central spike differently, depending on the DM mass and cross-section (as illustrated by the dashed and solid lines for a fixed DM mass and two different values of the annihilation cross-section).

$B(r) \propto r^{-5/4}$  toward the center, as discussed in [Aloisio et al. \(2004\)](#); [Regis & Ullio \(2008\)](#):

$$B(r) = \begin{cases} B_0 \left( \frac{r_c}{r_{\text{acc}}} \right)^2 \left( \frac{r}{r_{\text{acc}}} \right)^{-5/4} & r < r_{\text{acc}} \\ B_0 \left( \frac{r}{r_c} \right) & r_{\text{acc}} \leq r < r_c \\ B_0 & r \geq r_c. \end{cases} \quad (9.1)$$

We take  $B_0 = 10 \mu\text{G}$  for the large scale value of the magnetic field outside the inner cocoon of radius  $r_c \sim 10 \text{ kpc}$  observed for instance with [LOFAR \(de Gasperin et al., 2012\)](#). [Regis & Ullio \(2008\)](#) estimate the radius of the accretion region in the MW as  $r_{\text{acc}} = 2GM_{\text{BH}}/v_{\text{flow}}^2$ , where  $v_{\text{flow}} \sim 500\text{--}700 \text{ km s}^{-1}$  is the velocity of the Galactic wind at the center of the MW. Here we assume similar characteristics for the wind at the center of M87, so we just rescale the BH mass. For the MW, the size of the accretion region is  $\sim 0.04 \text{ pc}$ . Considering that the BH in M87 has a mass approximately  $1.5 \times 10^3$  times larger than Sgr A\*, we estimate  $r_{\text{acc}} \sim 60 \text{ pc}$  in M87. The resulting equipartition magnetic field can reach very large values at the center, typically up to  $10^{10}\text{--}10^{11} \mu\text{G}$  in the very inner region, which is at least eight orders of magnitude larger than the values usually considered in the MW.

Given the large values of the magnetic field that we consider here, energy losses are indeed dominated by synchrotron losses, so  $b_{\text{tot}}(E, r) = b_{\text{syn}}(E, r)$ . Moreover, due to the very large synchrotron losses, electrons and positrons produced in DM annihilations in the inner region are expected to stay confined to their site of injection, i.e. essentially in a sphere of radius  $R_{\text{sp}}$ . This means that we can safely disregard spatial diffusion.

We compute the prompt and synchrotron emission as explained in [Chapters 2 and 4](#) respectively. We recall the expression for the prompt diffuse  $\gamma$ -ray intensity,  $I_{\nu, f}^{\text{prompt}}(\theta)$  for annihilation channel  $f$ , at angle  $\theta$  from the center, given in [Eq. \(2.12\)](#):

$$\nu I_{\nu, f}^{\text{prompt}}(\theta) = E_\gamma^2 \frac{dn_f}{dE_\gamma d\Omega} \Big|_{\text{prompt}} = \frac{E_\gamma^2 \langle \sigma v \rangle_f}{4\pi \eta m_{\text{DM}}^2} \frac{dN_{\gamma, f}}{dE_\gamma} \int_{\text{l.o.s.}} \rho^2(r(s, \theta)) ds, \quad (9.2)$$

with  $\eta = 2$  for the case of self-conjugate DM considered here.  $s$  is the radial coordinate along the line of sight and  $r(s, \theta) = \sqrt{d^2 + s^2 - 2ds \cos \theta} \approx \sqrt{(d-s)^2 + ds\theta^2}$ . The approximation of small angles is justified since the characteristic radius  $R_{\text{M87}}$  of M87 (typically 50 kpc) is much smaller than the distance of M87,  $d = 16$  Mpc. Also in practice we perform the integral over the l.o.s. between  $d - R_{\text{M87}}$  and  $d + R_{\text{M87}}$ , considering the concentrated nature of the DM profile.

The synchrotron intensity reads

$$\nu I_{\nu,f}^{\text{syn}}(\theta) = \nu \int_{\text{l.o.s.}} \frac{j_{\text{syn},f}(\nu, r(s, \theta))}{4\pi} ds, \quad (9.3)$$

with the synchrotron emissivity  $j_{\text{syn}}$  computed as described in Chapter 4, using the  $e^\pm$  spectrum accounting for energy losses but neglecting spatial diffusion (Eq. (4.71)).

In principle, one should also account for the effect of advection of electrons and positrons toward the center by the accretion flow around the BH, which affects the synchrotron intensity close to the BH, typically in the range  $10^{12}$ – $10^{14}$  Hz (Aloisio et al., 2004). However, we disregard this effect throughout this chapter since most of our constraints come from higher frequencies, considering in particular the large magnetic field strengths we consider. Moreover, as discussed in Aloisio et al. (2004), including advection would in any case only change the SED by a factor of a few, and would not weaken our constraints but could even make them more stringent, depending on the exact radial dependence of the magnetic field.

### 9.3 Upper limits on the annihilation cross-section

Limits are set on the DM annihilation cross-section by comparing the expected emission from DM with the measured SED for M87. Most data points have actually been compiled by the *Fermi* Collaboration in Abdo et al. (2009). We use in particular:

- the historical measurements of the core emission from millimeter to X-rays (Biretta et al., 1991; Despringre et al., 1996; Tan et al., 2008; Shi et al., 2007; Perlman et al., 2001; Sparks et al., 1996; Marshall et al., 2002);
- the MOJAVE VLBA data point at 15 GHz which was derived in Abdo et al. (2009) (the data was reported in Lister et al. (2009));
- the 2009 X-ray data points which were derived in Abdo et al. (2009) from the 2009 *Chandra* measurements (Harris et al., 2009);
- the 2009 *Fermi*-LAT data (Abdo et al., 2009);
- the 2004 H.E.S.S. data (Aharonian et al., 2006b);
- the 2007 VERITAS data (Acciari et al., 2008);
- the 2011 MAGIC data (Aleksić et al., 2012);

which essentially give us the observed value of the electromagnetic flux between  $10^{10}$  and  $10^{27}$  Hz.

#### 9.3.1 Methodology

The DM contribution is estimated by integrating the prompt and synchrotron intensities  $\nu I_{\nu,f}^{\text{prompt,syn}}$ , given in Eqs. (9.2) and (9.3), over a field of view that is centered on the galactic center and set by the angular resolution  $\theta_{\text{res}}$  of the relevant experiment for a given frequency. Given the spherical symmetry of the spike, the prompt and synchrotron fluxes are given by

$$\nu F_{\nu,f}^{\text{prompt,syn}} = 2\pi \int_0^{\theta_{\text{res}}} \nu I_{\nu,f}^{\text{prompt,syn}}(\theta) \sin \theta d\theta. \quad (9.4)$$

We recall that *Chandra* has an angular resolution of 0.5 arcsec over the whole energy range considered here (Weisskopf et al., 2002) while the angular resolution of the *Fermi* experiment reads  $0.8^\circ \times E_{\text{GeV}}^{-0.8}$  (Abdo et al., 2009) where  $E_{\text{GeV}}$  is the energy of the  $\gamma$ -rays normalized to 1 GeV. H.E.S.S., VERITAS and MAGIC all have angular resolutions of the order of  $0.1^\circ$  (see Benbow, 2005; Holder, 2011; Colin et al., 2009). In practice though, the spike is contained in such a small region that the exact value of the upper bound of the integral in Eq. (9.4) does not significantly affect the result.

To set limits, we require that the synchrotron and prompt emission fluxes that are induced by the DM annihilations do not exceed the error bars on the flux for any measured data point. More specifically, we exclude any value of the annihilation cross-section that satisfies the following inequality for any observed frequency  $\nu$ :

$$S_\nu^{\text{model}} - (S_\nu^{\text{obs}} + \Delta S_\nu^{\text{obs}}) \geq \kappa (S_\nu^{\text{obs}} + \Delta S_\nu^{\text{obs}}), \quad (9.5)$$

with  $S_\nu \equiv \nu F_\nu$  and  $\kappa \ll 1$  (typically  $\kappa = 10^{-4}$ ). The terms  $S_\nu^{\text{model}}$ ,  $S_\nu^{\text{obs}}$  and  $\Delta S_\nu^{\text{obs}}$  represent respectively the expected DM contribution, the observed SED, and the  $1\sigma$  error bar at frequency  $\nu$ .

Note that large values of the annihilation cross-section, i.e.

$$\langle \sigma v \rangle \gg 10^{-27} \left( \frac{m_{\text{DM}}}{10 \text{ GeV}} \right) \text{ cm}^3 \text{ s}^{-1}, \quad (9.6)$$

flatten the inner part of the spike below a saturation radius given by

$$r_{\text{sat}} \sim 4 \times 10^{-2} \left( \frac{\langle \sigma v \rangle}{10^{-27} \text{ cm}^3 \text{ s}^{-1}} \right)^{1/2} \left( \frac{m_{\text{DM}}}{10 \text{ GeV}} \right)^{-1/2} \text{ pc}. \quad (9.7)$$

Therefore one cannot always rescale the flux for different values of  $\langle \sigma v \rangle$ , since in some cases the cross-section actually modifies the DM profile. For  $\langle \sigma v \rangle \lesssim 10^{-27} (m_{\text{DM}}/10 \text{ GeV}) \text{ cm}^3 \text{ s}^{-1}$ , on the other hand, the saturation radius is very small (below  $10^{-2} \text{ pc}$ ) and falls in the region where the DM profile vanishes close to the BH, so that in this regime the fluxes that we compute are simply proportional to the annihilation cross-section.

### 9.3.2 Results

In Fig. 9.2, we plot the largest allowed electromagnetic emission (prompt plus synchrotron) expected from DM annihilations for a 100 GeV DM candidate. The top panel shows the predictions for DM annihilations into  $\mu^+\mu^-$  while the bottom panel shows the predictions for annihilations into  $b\bar{b}$ . The two bumps correspond to the synchrotron (left) and prompt (right) emission. We also derive the constraints on the annihilation cross-section for any DM mass and eight annihilation channels ( $e^+e^-$ ,  $\mu^+\mu^-$ ,  $\tau^+\tau^-$ ,  $q\bar{q}$ ,  $b\bar{b}$ ,  $t\bar{t}$ ,  $ZZ$ ,  $hh$ , with  $h$  the standard model Higgs boson and  $q = u, d, s$ ), shown in Fig. 9.3. The top panel shows the constraints in the presence of a spike and the bottom panel shows the constraints without a spike (assuming a NFW profile).

The constraints in the case of a spike essentially rule out any DM candidate with a thermal (s-wave) cross-section, from a few GeV to a hundred TeV.<sup>2</sup> In other words, they rule out the entire mass range relevant for thermal DM. The only exceptions to our generic conclusions are for candidates which mostly annihilate into  $\mu^+\mu^-$  (the limit is then about 30 TeV) or which annihilate democratically into all channels (but the limit would still be close to 100 TeV nevertheless). We

<sup>2</sup>These constraints can be extended down to the MeV range for leptons and light quarks, provided the magnetic field is of the order of the equipartition value. Synchrotron emission then peaks around  $10^{10}$ – $10^{11}$  GHz. For smaller values of the magnetic field, the synchrotron peak falls below  $10^{10}$  GHz, i.e. in the radio range, where synchrotron self-absorption significantly reduces the flux (see e.g. Aloisio et al., 2004), thus preventing one from setting any constraints on the DM annihilation cross-section.

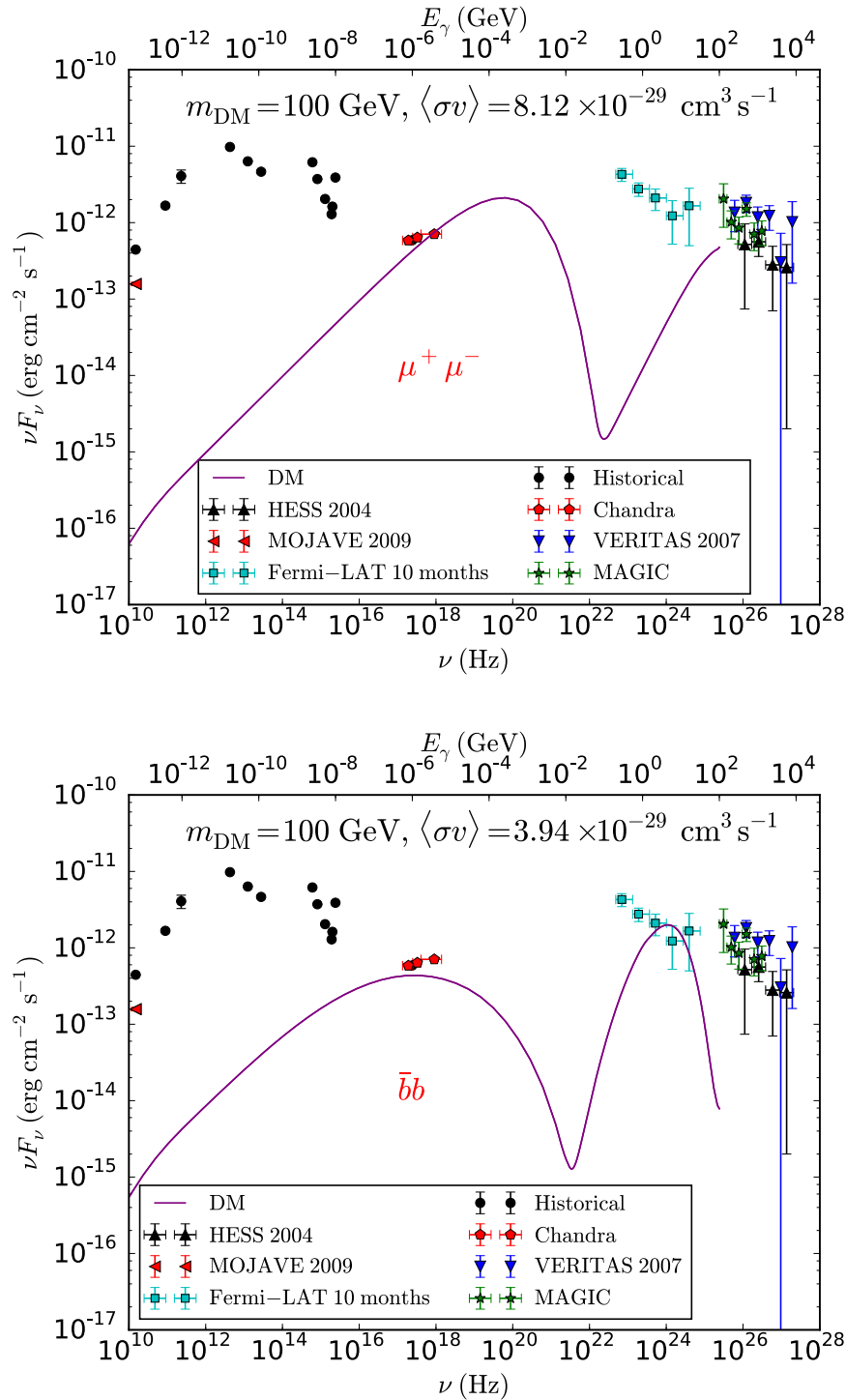


**Figure 9.2** – SED of M87 from the millimeter band to TeV  $\gamma$ -rays, from a DM spike, for 100 GeV DM particles annihilating into  $\mu^+\mu^-$  with  $\langle\sigma v\rangle = 8.12 \times 10^{-29} \text{ cm}^3 \text{ s}^{-1}$  (**top panel**), and into  $b\bar{b}$  with  $\langle\sigma v\rangle = 3.94 \times 10^{-29} \text{ cm}^3 \text{ s}^{-1}$  (**bottom panel**). These are the maximal values of the cross-section compatible with the data for a DM candidate of 100 GeV.

also confirm that thermal candidates with a p-wave suppressed annihilation cross-section are ruled out if they are much lighter than a few GeV. For comparison, our limits in the case of a pure NFW profile are considerably weaker, see Fig. 9.3 (bottom panel). They only rule out very light (below a few GeV) s-wave thermal DM candidates.

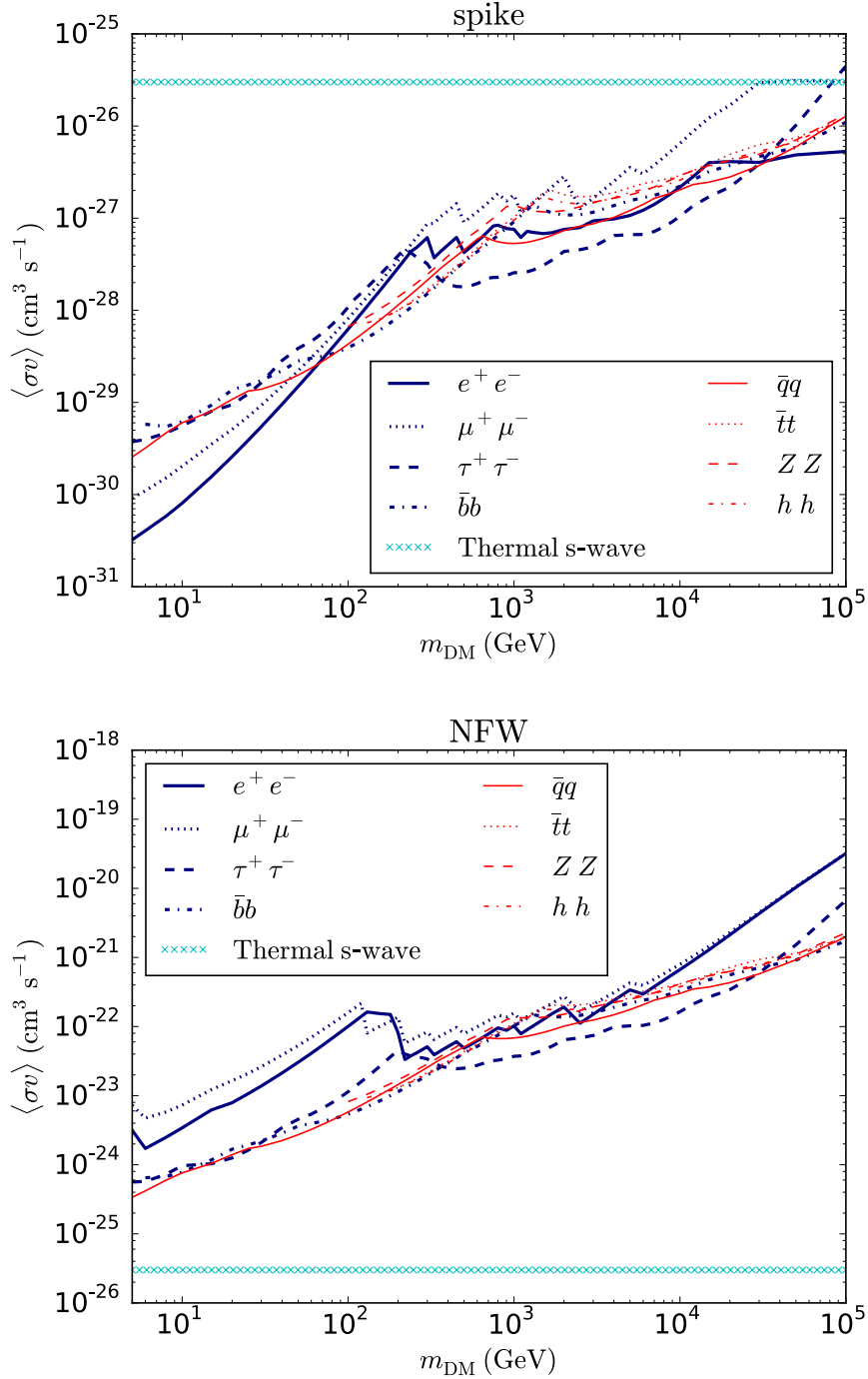


**Figure 9.3** – Upper limits on the annihilation cross-section as a function of DM mass for various annihilation channels. Constraints derived assuming a spike in the DM distribution are shown in the **top panel** while in the **bottom panel** we show the constraints obtained assuming a standard NFW cusp.

Of course our conclusions rely on the crucial assumption of the existence of a spike with  $\gamma_{\text{sp}} \sim 7/3$ . While this remains speculative, the stability of such a spike with respect to the scattering off stars is very likely. Hence, if the initial conditions were such that a spike could form in M87, our constraints would rule out a very large chunk of the thermal DM parameter space. An alternative interpretation of our results is that the discovery of a thermal s-wave DM candidate would rule out the existence of a spike in M87. This would in turn constrain the

evolution and formation of the SMBH at the center of M87.

### 9.3.3 Robustness of our constraints

In the previous sections, we have considered extremely large values of the magnetic field (several orders of magnitude with respect to the Milky Way) and we have neglected absorption. It is therefore legitimate to question the robustness of our limits with respect to the magnetic field model and absorption processes.

#### 9.3.3.1 Dependence on the magnetic field

Our most stringent limit on the DM contribution in M87 is set by the *Chandra* X-ray data. Since most of the DM induced X-ray signal originates from synchrotron radiation and synchrotron emission strongly depends on the magnetic field, a weaker magnetic field could weaken our constraints. This is particularly worrisome for the  $e^+e^-$  and  $\mu^+\mu^-$  final states which give the largest X-ray contribution in M87 when  $m_{\text{DM}} \lesssim 100$  GeV, as shown in Fig. 9.2, and which could become unconstrained.

However, a weaker magnetic field in the inner region, taken for example to be constant and about  $B = 10^5 \mu\text{G}$  (as suggested in [Neronov & Aharonian, 2007](#)), only weakens our constraints by about one order of magnitude below 30 GeV. We thus get  $\langle\sigma v\rangle < 10^{-29} \text{ cm}^3 \text{ s}^{-1}$  for  $e^+e^-$  and  $\mu^+\mu^-$  instead of  $\langle\sigma v\rangle < 10^{-30} \text{ cm}^3 \text{ s}^{-1}$ . Hence, even in the case of a weaker magnetic field in the inner region, we can rule out thermal s-wave DM. Note that decreasing the magnetic field to  $B = 1$  mG makes our constraints stronger again as the signal would be constrained by the MOJAVE data. Finally, as noted in [Aloisio et al. \(2004\)](#), if the magnetic field is significantly smaller than the equipartition value, synchrotron self-Compton emission decreases the DM-induced electron spectrum and thus also the synchrotron flux accordingly. Based on the results of [Aloisio et al. \(2004\)](#), we estimate that our limits for the  $e^+e^-$  and  $\mu^+\mu^-$  channels are weakened by an additional order of magnitude below  $\sim 100$  GeV for a magnetic field strength weaker than  $10^5 \mu\text{G}$ . However, this does not affect our conclusion since we can still exclude thermal s-wave DM.

A magnetic field of the order of  $10^5 \mu\text{G}$  also changes the limits for candidates with a mass above  $\sim 50$  TeV for the  $e^+e^-$  and  $\mu^+\mu^-$  channels. Indeed, the synchrotron peak then falls in the energy range [100 keV, 100 MeV] where there are no data points. In that case, the limit is given by the prompt component and weakened to the level of  $3 \times 10^{-25} \text{ cm}^3 \text{ s}^{-1}$ . As a reminder, in the case of a stronger magnetic field, we could rule out the canonical thermal cross-section for the  $e^+e^-$  channel. Thus, for such a value of the magnetic field, one can no longer exclude s-wave DM for particles heavier than 50 TeV. It is worth pointing out though that a smaller value of the magnetic field of e.g.  $10^3 \mu\text{G}$  would not alleviate our constraints as it would give rise to an excess in X-rays, which has not been observed. Such a value would therefore lead to an exclusion limit instead, similar to the one obtained for the equipartition magnetic field.

Finally, the annihilation channels which give a softer electron spectrum, e.g. the  $b\bar{b}$  channel, are unaffected by a weaker magnetic field since the prompt  $\gamma$ -ray emission dominates the synchrotron emission, see Fig. 9.2, and therefore our limits for these channels are independent of the magnetic field.

#### 9.3.3.2 Absorption

Absorption is another process that could weaken our conclusions. We may have overestimated the flux by not accounting for the photons which have been emitted by synchrotron radiation and absorbed by the same electron population that produced them. Relying on the results of [Aloisio et al. \(2004\)](#); [Regis & Ullio \(2008\)](#) that showed that this effect is only very efficient below  $10^{10}$  Hz, we cut the synchrotron emission below this critical frequency. This prevents us from

constraining the scenarios emitting in this energy range, i.e. candidates lighter than  $\mathcal{O}(1)$  GeV, unless the magnetic field is strong.

At the other end of the spectrum, high-energy  $\gamma$ -rays could also be absorbed via  $e^+e^-$  pair production with the background radiation field. However, [Neronov & Aharonian \(2007\)](#); [Brodatzki et al. \(2011\)](#) showed that the inner region of M87 is transparent to  $\gamma$ -rays below  $\sim 10$  TeV. Since we only have data below 10 TeV and absorption is relevant only above 10 TeV, we can neglect this effect for all candidates below 10 TeV. For the much heavier candidates, the lack of data above 10 TeV makes absorption irrelevant for the moment. Hence we have neglected absorption in our study.

## 9.4 DM spike and jet

In the previous section, we have investigated the DM contribution to the SED of M87 but neglected the contribution from the BH. In reality the jet emission associated with the BH must be taken into account. Indeed, to be observable, any putative emission from DM should be brighter than the emission from the jet.

### 9.4.1 Jet emission

The mechanism giving rise to high energy photons from the jet is not well known. It is unclear whether these photons have a leptonic or hadronic origin. In the most popular model, the  $\gamma$ -rays originate from electrons contained in a blob of plasma that moves relativistically and possesses a fairly strong magnetic field. This leptonic synchrotron self-Compton emission (SSC) proceeds in two steps: the electrons from the jet first produce photons in the infrared band due to synchrotron radiation in a strong magnetic field. Then, in a second step, these low energy photons are upscattered to  $\gamma$ -ray energies by ICS on the same electron population that produced them.

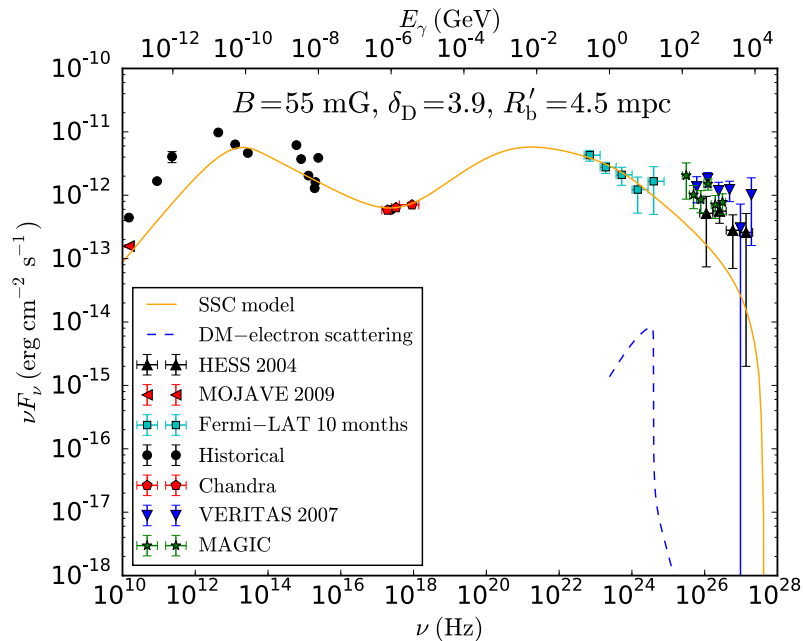


**Figure 9.4** – SED of M87 from the millimeter band to TeV  $\gamma$ -rays. The orange solid line represents the SSC model that best fits the data, for a 55 mG magnetic field in the plasma blob, a Doppler factor of 3.9, and a radius of 4.5 mpc for the blob in its rest frame, as found in [Abdo et al. \(2009\)](#). The blue dashed line corresponds to the signal expected from DM-jet scattering, as described in [Gorchtein et al. \(2010\)](#). Details on the parameters can be found in the text.

To take this effect into account and fit the spectral energy distribution of M87, we use the model described in [Finke et al. \(2008\)](#) and take the best-fit SSC parameters given in [Abdo et al. \(2009\)](#), see Appendix A.3. The parameters we consider are: a Doppler factor  $\delta_D = 3.9$ , a magnetic field  $B = 55$  mG, and a source radius  $R'_b = 4.5$  mpc in the rest frame of the blob. The data that have been used for the fit are the 2009 MOJAVE, *Chandra* and *Fermi*-LAT data. The best-fit value for the normalization of the electron distribution is  $K = 5.81 \times 10^{51}$ . The corresponding SSC emission for this set of parameters is shown in Fig. 9.4 as an orange solid line.

Note that the scattering of the DM particles off electrons and protons in the jet might also produce high energy photons ([Gorchtein et al., 2010](#)) and, consequently, lead to a characteristic signature in the *Fermi*-LAT data. The associated flux is proportional to the integral of the DM density over the line of sight ( $\delta_{DM}$ , as in [Gorchtein et al., 2010](#)), and the jet power ( $L$ ). For M87, the highest allowed jet power is  $L \sim 10^{45}$  erg s $^{-1}$  ([Abdo et al., 2009](#)). For an optimal configuration of the DM spike, i.e. for the largest possible DM energy density (correspondingly to the smallest possible saturation radius, typically  $\langle\sigma v\rangle \sim 10^{-30}$ – $10^{-29}$  cm $^3$  s $^{-1}$  for  $m_{DM} \sim 100$  GeV), the line-of-sight integration gives  $\delta_{DM} \sim 10^9$  M $_{\odot}$  pc $^{-2}$  which leads to a  $\gamma$ -ray flux of  $\sim 10^{-14}$  erg cm $^{-2}$  s $^{-1}$ . This is roughly two orders of magnitude below the *Fermi* data, as shown in Fig. 9.4 (blue dashed line). This process is therefore subdominant for M87, and we will disregard it in the following discussion.

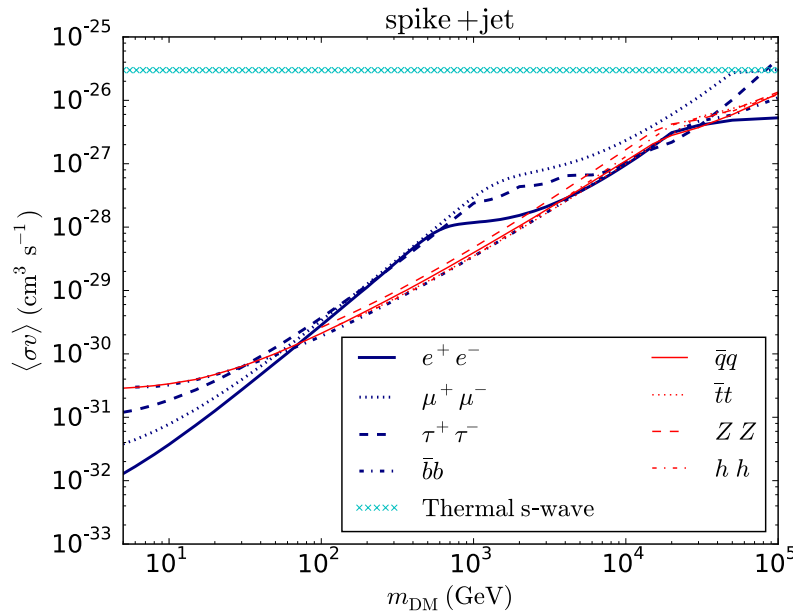


**Figure 9.5** – Upper limits on the annihilation cross-section as a function of DM mass for usual annihilation channels, obtained after summing the DM contribution to the photon emission expected from the jet (using the SSC model) and excluding cross-sections that depart from the best fit at  $2\sigma$ .

#### 9.4.2 Upper limits on the annihilation cross-section with spike+jet

Because the jet emission associated with the SSC model fits the data very well up to  $\gamma$ -ray energies of 100 GeV, there is little room for a dark matter contribution to the SED of M87 for candidates lighter than 20 TeV. Our results are shown in Fig. 9.5. We have excluded any values of the annihilation cross-section that cause the total flux to depart from the best fit to the *Chandra* and *Fermi* data by more than  $2\sigma$  and improved the limits by about one order of magnitude with respect to the constraints derived without considering the jet emission. Above  $E_\gamma \gtrsim 100$  GeV, a DM contribution improves the fit and prevents us from setting a better limit.

Note that we can also exclude thermal p-wave DM (corresponding to a cross-section of order of a few  $10^{-31} \text{ cm}^3 \text{ s}^{-1}$ ) up to  $\sim 40 \text{ GeV}$ .

Because the jet emission fits the whole spectrum up to  $100 \text{ GeV}$  and, in particular, fits the *Chandra* data which have the smallest error bars, any additional DM contribution—even small—tends to worsen the chi-square statistic and thus leads to stronger constraints. Since the *Chandra* data constrain the synchrotron contribution which is very sensitive to the magnetic field, these constraints strongly depend on the strength of the magnetic field.

Finally, let us recall that the limits derived in this section depend on the underlying jet model which, as we mentioned, is still very uncertain. Yet, the limits of Fig. 9.5 do illustrate the importance of including a model for the jet.

### 9.4.3 Explaining the TeV data with a dark matter spike

#### 9.4.3.1 Fits with a jet + DM spike

As shown in Fig. 9.4, the simplest SSC model does not explain the TeV emission measured by H.E.S.S., MAGIC and VERITAS (although some of the points are consistent with the jet model).<sup>3</sup> This led Saxena et al. (2011) to discuss the possibility that prompt emission from TeV DM may alleviate the discrepancy between the jet model and the TeV data. Assuming a NFW profile and the presence of DM clumps, they fit the data with a very large value of the annihilation cross-section (typically  $3 \times 10^{-24} \text{ cm}^3 \text{ s}^{-1}$ ) and a very large boost factor of almost 1000. However, as shown in Fig. 9.6, in the presence of a spike we can fit the TeV data for a value of the annihilation cross-section smaller than the thermal value and no additional boost factor is needed.

Using the *Chandra*, *Fermi*-LAT, VERITAS, MAGIC and H.E.S.S. data (namely 24 data points), our best fit for the jet emission model gives  $\chi^2 \approx 85.5$ , that is  $\chi^2/\text{d.o.f.} \approx 3.56$  for 24 degrees of freedom. Adding a DM contribution (modeled by 2 free parameters, namely the DM mass and annihilation cross-section) to this best fit background model considerably improves the quality of the fit. We obtain  $\chi^2 \approx 29.4$  ( $\chi^2/\text{d.o.f.} \approx 1.34$  for  $24 - 2$  d.o.f) for the  $b\bar{b}$  channel (Fig. 9.6, top panel) and  $\chi^2 \approx 28.7$  ( $\chi^2/\text{d.o.f.} \approx 1.30$ ) for the  $\tau^+\tau^-$  channel (Fig. 9.6, bottom panel). The corresponding best-fit values for the mass and cross-section are given in Table 9.1.

**Table 9.1** – Best-fit DM mass and annihilation cross-section, for various characteristic annihilation channels.

Channel	$m_{\text{DM}}$ (TeV)	$\langle\sigma v\rangle$ ( $\text{cm}^3 \text{ s}^{-1}$ )	$\chi^2/\text{d.o.f.}$
$b\bar{b}$	$23_{-8}^{+16}$	$3.9_{-1.4}^{+2.6} \times 10^{-27}$	1.34
$\tau^+\tau^-$	$2.1_{-0.5}^{+0.7}$	$4.4_{-0.9}^{+1.2} \times 10^{-28}$	1.30
$q\bar{q}$	$16_{-7}^{+14}$	$2.7_{-1.2}^{+2.3} \times 10^{-27}$	1.46
$t\bar{t}$	$31_{-12}^{+24}$	$6.0_{-2.3}^{+4.2} \times 10^{-27}$	1.33
$ZZ$	$18_{-7}^{+14}$	$3.9_{-1.5}^{+2.9} \times 10^{-27}$	1.29
$hh$	$22_{-8}^{+15}$	$4.3_{-1.4}^{+2.8} \times 10^{-27}$	1.25

The associated  $1\sigma$  and  $2\sigma$  confidence contour plots for both channels are shown in Fig. 9.7. For completeness, we also indicate the best-fit values obtained for other annihilation channels. Note that the  $c\bar{c}$  and  $gg$  channels are degenerate with the  $q\bar{q}$  channel, so the same conclusions apply. Similarly  $W^+W^-$  and  $ZZ$  are also degenerate.

<sup>3</sup>Also according to de Jong et al. (2015), it may be possible to refine the SSC model so as to fit the TeV data.

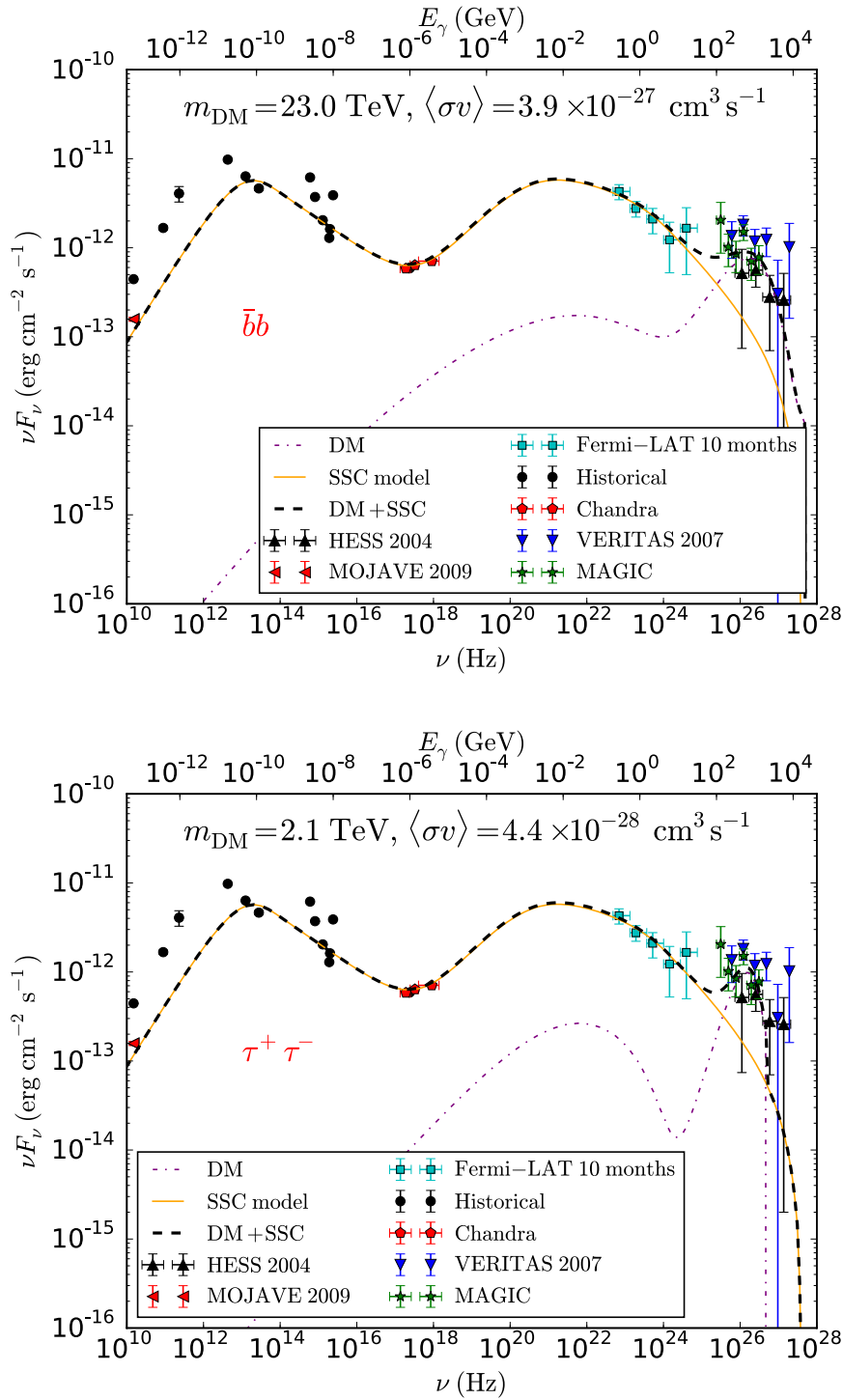


**Figure 9.6** – SED of M87 from the millimeter band to TeV  $\gamma$ -rays. The SSC model for the jet gives a double peak structure (orange solid line). The contribution from the DM spike is depicted by the purple dot-dashed line, for annihilations into  $b\bar{b}$  (**top panel**) and  $\tau^+\tau^-$  (**bottom panel**), with the synchrotron peak around  $10^{22}$  Hz and the prompt emission peak around  $10^{26}$  Hz. The black dashed line is the total SED.

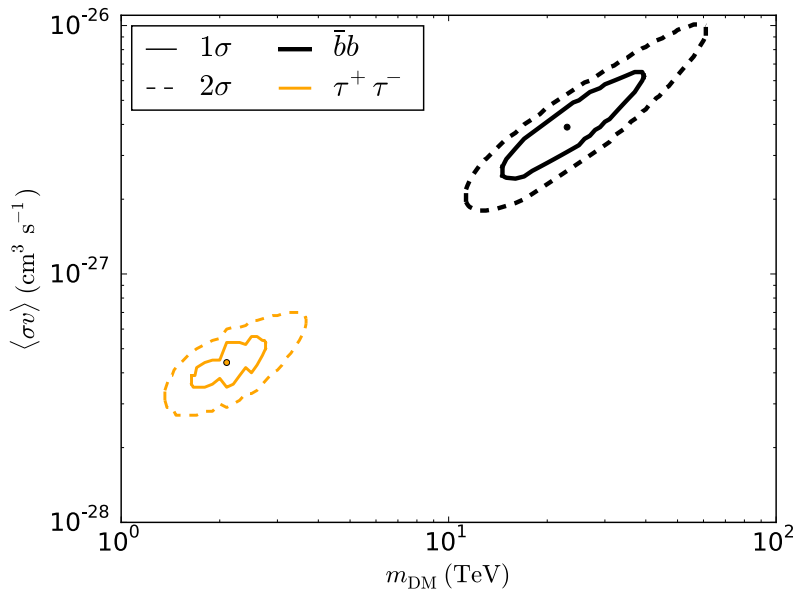


**Figure 9.7** – Confidence contours at the  $1\sigma$  and  $2\sigma$  levels, in the plane annihilation cross-section vs DM mass, for the  $b\bar{b}$  channel (black thick contours) and the  $\tau^+\tau^-$  channel (orange thin contours). The best fit points at the center of the contours correspond to  $m_{\text{DM}} = 23$  TeV,  $\langle\sigma v\rangle = 3.9 \times 10^{-27} \text{ cm}^3 \text{ s}^{-1}$  for  $b\bar{b}$ , and  $m_{\text{DM}} = 2.1$  TeV,  $\langle\sigma v\rangle = 4.4 \times 10^{-28} \text{ cm}^3 \text{ s}^{-1}$  for  $\tau^+\tau^-$ .

#### 9.4.3.2 Dependence on the magnetic field

The best-fit values displayed in Table 9.1 are obtained by assuming the same magnetic field intensity as in Sec. 9.2 and reflect the fact that very heavy DM candidates give rise to very high energy  $\gamma$ -rays. However, this statement depends on the magnetic field and heavy particles can induce photons at much lower energies. For example, we observe that a DM candidate with  $m_{\text{DM}} \sim 20$  TeV can lead to an excess of X-rays if the magnetic field is relatively weak (typically about  $10^5$ – $10^6 \mu\text{G}$ ) and be ruled out by the *Chandra* data.

Whether a candidate is ruled out or not, however, also depends on the model for the jet emission. By varying both the jet model and the DM component we can, for example, reconcile a DM candidate with  $m_{\text{DM}} \sim 20$  TeV (supposedly ruled out by the *Chandra* data in the presence of a relatively small magnetic field) with a possible noticeable contribution at TeV energies. Note that for such relatively small values of the magnetic field, ICS and SSC are still negligible.

If the magnetic field is even smaller, typically  $\sim 10^3 \mu\text{G}$  in the inner region, the synchrotron emission gives a signature at energies of a few eV corresponding to frequencies of about  $\sim 10^{15}$  Hz. In that case there is no tension with the X-ray data. However, ICS becomes non-negligible for moderate magnetic fields. The SSC emission could also be important but we expect it to be subdominant. For  $B \sim 10^3 \mu\text{G}$  and  $m_{\text{DM}} \sim 20$  TeV, we expect ICS to give an additional contribution at TeV energies, thus strengthening the case for an explanation of the observed high energy emission in terms of DM.

All these remarks show that the best-fit values obtained by fitting prompt  $\gamma$ -ray emission give a very good estimate of the contribution of annihilations from a DM spike to the TeV emission, fairly independently of the magnetic field and interstellar radiation field model. Therefore, our conclusion is that if there is indeed a DM spike in M87, then the subsequent annihilations can account for the TeV  $\gamma$ -ray emission, with annihilation cross-sections 10 times smaller than the thermal value or even smaller depending on the channel.

## 9.5 Conclusion

We believe that the case for a DM spike at the center of the M87 galaxy is very strong. One therefore expects a significant annihilation signal from thermal DM candidates. In this project, we have confronted the observed SED of M87 with the predicted emission from DM, and set extremely strong upper limits on the annihilation cross-section of DM particles as a function of the DM mass. These limits exclude thermal DM candidates with a velocity-independent (s-wave) cross-section and a mass up to  $\mathcal{O}(100)$  TeV. Our results are independent of the magnetic field distribution and absorption processes whatever the DM mass; the sole exception is for annihilations into light leptons but our conclusion remains valid for DM masses up to 50 TeV. Also we have shown that in the presence of a DM spike, TeV DM can explain the TeV  $\gamma$ -ray data for annihilation cross-sections smaller than the canonical value ( $\sim 10^{-27} \text{ cm}^3 \text{ s}^{-1}$ ).

We expect similar constraints for galaxies containing a SMBH with the same mass as in M87. Should evidence for such a spike be found, for example using stellar kinematics, one would exclude a very large chunk of the thermal DM parameter space. This opens up a new path in DM searches, with great potential to elucidate the nature of DM particles. These results provide a strong motivation to look for further evidence of DM spikes in galaxies.

## Chapter 10

# Discovery of a new extragalactic source population of energetic particles

Radio galaxies are active galactic nuclei (AGN) containing supermassive black holes with misaligned relativistic jets. Centaurus A (Cen A) is the closest known  $\gamma$ -ray emitting radio galaxy. This chapter draws from [Brown et al. \(2016\)](#), where the discovery of a hardening in the *Fermi*-LAT  $\gamma$ -ray spectrum of the core of Cen A above 2.4 GeV, at a significance of  $5\sigma$ , as well as evidence for variability below 2.4 GeV at 99%, are reported. These properties strongly support the hypothesis that the low energy component originates from leptons in the jet while the additional source of very high energy particles near the core of Cen A must originate from a different cosmic ray population. We show for the first time that the observed  $\gamma$ -ray spectrum is compatible with either a spike in the dark matter halo profile or a population of millisecond pulsars. A third explanation could be nevertheless the presence of a hadronic component injected by the jet. This work constitutes the first robust indication of new  $\gamma$ -ray production mechanisms in active galaxies and could provide tantalizing first evidence for the clustering of heavy dark matter particles around black holes.

### Contents

---

<b>10.1 Introduction</b>	<b>154</b>
<b>10.2 Analysis</b>	<b>154</b>
<b>10.3 Interpretation</b>	<b>155</b>
10.3.1 Dark matter	156
10.3.2 Millisecond pulsars	159
10.3.3 Diffused protons	160
<b>10.4 Conclusion</b>	<b>160</b>

---

## 10.1 Introduction

Due to its small distance of 3.8 Mpc (Rejkuba, 2004) and the off-axis nature of its jet, Cen A has been extensively studied at all wavelengths, including at  $\gamma$ -ray energies, where it has been found to emit radiation from 30 MeV to about 5 TeV (Sreekumar et al., 1999; Aharonian et al., 2009; Abdo et al., 2010a). A bright  $\gamma$ -ray core in Cen A was confirmed by observations with the *Fermi*-LAT (Abdo et al., 2010a) and a possible hardening of the gamma-ray emission above 4 GeV was hinted by Sahakyan et al. (2013). In addition, the *Fermi*-LAT observations revealed an extended  $\gamma$ -ray emission spatially coincident with Cen A’s giant radio lobes (Abdo et al., 2010b). Both core and lobe emissions appeared to have similar luminosities, and neither showed variability in their flux. This is at odds with observations of other prominent  $\gamma$ -ray bright radio galaxies, such as M87 and NGC 1275, whose fluxes vary on very short timescales, as little as days (Aharonian et al., 2006b; Brown & Adams, 2011).

In this work, we focus on the core emission of Cen A, taking advantage of the improvements afforded by the new PASS8 event characterisation of the *Fermi*-LAT data. Using a maximum likelihood analysis and 7.5 years of LAT data, the 0.1–300 GeV  $\gamma$ -ray spectrum in the central part of Cen A was determined by my colleagues with unprecedented sensitivity and precision.

After summarizing in Sec. 10.2 the analysis procedure used to establish a statistically significant hardening of the high-energy  $\gamma$ -ray emission in the core of Cen A and show evidence for variability of the low-energy component, we study in Sec. 10.3 two very promising interpretations. The first one involves a spike in the DM density profile and the second one MSPs. We also discuss a third hypothesis, namely protons injected by the jet.

## 10.2 Analysis

In the likelihood analysis, performed by my collaborators in Durham, both the Galactic and extragalactic diffuse emission were modeled, along with all nearby extended and point sources as defined by the third *Fermi*-LAT source catalog (3FGL). Cen A itself was modeled as a point source coincident with the Cen A core position (taken from the 3FGL), and a spatially extended emission as defined by the *Fermi*-LAT collaboration (see Appendix B for more details). The resulting spectrum can be seen in Fig. 10.1, and exhibits a clear hardening above  $\sim 2$  GeV.

To characterize the existence of possible spectral features, the 0.1–300 GeV spectrum was fitted with both power-law and broken power-law spectral models. This analysis shows that the broken power law is preferred over the power law at a statistically significant level (test statistic greater than 28), which equates to a significance slightly greater than  $5\sigma$ . The best-fit broken power law has a break energy of  $E_{\text{break}} = 2.420 \pm 0.003_{\text{stat}} \left( \begin{smallmatrix} +0.500 \\ -0.062 \end{smallmatrix} \right)_{\text{sys}}$  GeV, with a spectral index of  $\Gamma_1 = -2.766 \pm 0.001_{\text{stat}} \left( \begin{smallmatrix} +0.063 \\ -0.083 \end{smallmatrix} \right)_{\text{sys}}$  in the low energy regime and a spectral index of  $\Gamma_2 = -2.282 \pm 0.014_{\text{stat}} \left( \begin{smallmatrix} +0.075 \\ -0.000 \end{smallmatrix} \right)_{\text{sys}}$  above the break energy. We note that extrapolating the single power law found at low energy to the H.E.S.S. energies would under-predict the flux above 250 GeV by an order of magnitude, while the broken power-law model allows us to reconcile the *Fermi*-LAT spectrum found in this work with previous H.E.S.S. observations.

Deconvolving the two spectral components aforementioned yielded evidence that the  $\gamma$ -ray flux above and below the break energy originates from two different source populations. The  $\gamma$ -ray flux below the 2.4 GeV spectral break energy is inconsistent with a constant flux at 99% level of confidence, suggesting that the low energy component of the  $\gamma$ -ray flux in Cen A’s core is variable. Conversely, the emission above 2.4 GeV is consistent with a constant  $\gamma$ -ray flux. Assuming isotropic  $\gamma$ -ray emission and a luminosity distance of 3.8 Mpc, the luminosities ( $\mathcal{L}$ ) of the low and high energy components are found to be comparable, respectively  $\mathcal{L} \approx 9.9 \times 10^{38}$  erg  $\text{s}^{-1}$  and  $\mathcal{L} \approx 8.4 \times 10^{38}$  erg  $\text{s}^{-1}$ .

The hardening of the  $\gamma$ -ray spectrum above 2.4 GeV reported here confirms the trend that was suspected in Sahakyan et al. (2013). However, the significance of the hardening now amounts

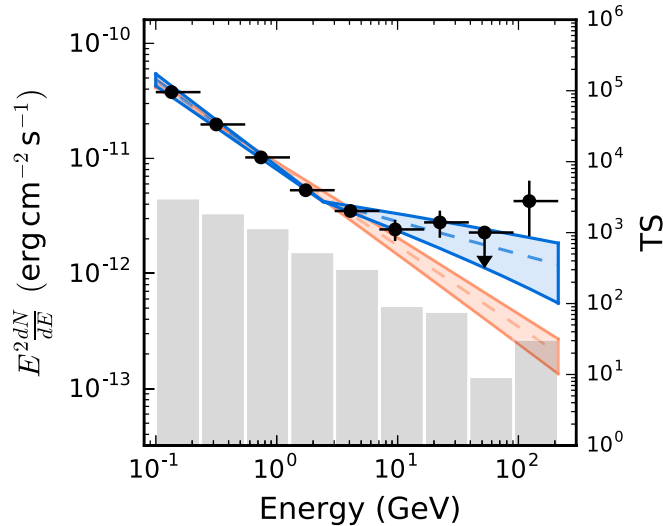


**Figure 10.1** – The 0.1 to 300 GeV spectrum of Cen A’s core, as seen by the *Fermi*-LAT detector. The broken power-law model, shown in blue, is preferred over the power-law model, shown in red, with a significance  $> 5\sigma$ . The grey histogram, with the right hand y axis, shows the TS value for each spectral bin. The bin with a TS  $< 25$ , is replaced with an upper limit at 95% confidence level.

to  $5\sigma$  instead of the  $\sim 2\sigma$  as obtained in Sahakyan et al. (2013). Unlike in Sahakyan et al. (2013) though, we now have evidence for the variability of the flux associated with the low energy component. Combining the two sets of information thus suggests a jet origin for the low energy component and establishes a new production mechanism of high energy  $\gamma$ -rays in the core of Cen A at  $5\sigma$  confidence level.

Indeed, previous explanations of the  $\gamma$ -ray emission below 10 GeV relied on a single zone population of relativistic electrons within the AGN jet that would up-scatter the synchrotron photon field via the inverse Compton process (Abdo et al., 2010a), usually cited as the synchrotron self-Compton (SSC) model. However, the spectral hardening above 2.4 GeV is inconsistent with the SSC model predictions (see Appendix B), especially given the latest X-ray observations (Fürst et al., 2016), and so is the lack of variability above 2.4 GeV. Indeed, high-energy electrons are expected to lose energy quickly and generate flux variability above the break energy, which is not observed.

### 10.3 Interpretation

There is a limited number of explanations for the non variable emission above 2.4 GeV (Rieger, 2012). Here we examine the case of DM, MSPs and protons injected by the jet. We disregard pulsar-like magnetospheric acceleration mechanisms of electrons since these models attribute the entire MeV–GeV  $\gamma$ -ray flux to curvature radiation from the same lepton population (Neronov & Aharonian, 2007), which is inconsistent with both the spectral break and the lack of flux variability above 2.4 GeV. Moreover these magnetospheric models predict that inverse-Compton luminosity,  $L_{IC}$ , is proportional to the SMBH mass  $M_{BH}$ , which is not observed across the mass range of prominent  $\gamma$ -ray bright radio galaxies (Brown & Adams, 2011).

Building on the apparent smooth transition between the data points above 2.4 GeV derived in this work and the H.E.S.S. data points from Aharonian et al. (2009), we discuss the validity

of models that can account for the spectral hardening by jointly fitting these data points. More specifically, we use the first three H.E.S.S. points, but we exclude the last three which are less statistically significant, and more likely to be modified with new observations and updated analyses. In any event, the last three points do not affect the best-fit spectrum due to their large error bars, but simply lead to a slight increase in the  $\chi^2$ .

### 10.3.1 Dark matter

While it is established that DM agglomerates in the cores of galaxies, its density profile near the central BH has yet to be characterized, as discussed in Chapter 3. Regardless of the precise characteristics of the DM profile, DM annihilations should produce high energy cosmic rays in the central parts of galaxies. The decay or hadronization of the particles injected by the DM are expected to produce  $\gamma$ -rays at an energy smaller than or equal to the DM mass (assuming they are charged and unstable).<sup>1</sup> Here we examine whether this prompt emission is sufficient to explain the anomalous spectral component between 2.4 GeV and  $\sim 5$  TeV. We compute the prompt flux the same way as in the previous chapters (see Sec. 2.3.3.1).<sup>2</sup>

In our analysis, the DM mass and annihilation cross-section as well as the normalization and slope of the spectral emission below 2.4 GeV are free parameters. We consider DM self-annihilations into leptons or quarks and test two DM density profiles, the NFW profile with  $\rho(r) \propto r^{-1}$ , and  $\rho(r) \propto r^{-7/3}$  corresponding to a central adiabatic DM spike (see Chapter 3). In particular, the presence of a central DM spike is very plausible for dynamically young galaxies like Cen A, for which the dynamical relaxation time is estimated from Eq. (3.26) to be  $t_r \sim 10^2$  Gyr (compared to  $\sim 2.5$  Gyr for the Milky Way), considering the mass of the central BH,  $M_{\text{BH}} = 5.5 \times 10^7 M_\odot$  (Neumayer, 2010). Details on the normalization of the DM profile can be found in Appendix A.2.2.

As shown in Fig. 10.2, our best fit favours a DM candidate with a mass of 3 TeV, annihilating into  $t\bar{t}$  with cross-section  $\langle\sigma v\rangle \simeq 1.6 \times 10^{-32} \text{ cm}^3 \text{ s}^{-1}$ , and a spike in the density profile. While the impact of a spike on the  $\gamma$ -ray emission from DM prompt emission in an AGN was first studied in Lacroix et al. (2015a) and Chapter 9, our work constitutes the first evidence that  $\gamma$ -ray observations have the mean to probe an anomalously high concentration of DM in the very inner core of AGNs. In addition, we note that the slope associated with the low energy contribution is about 2.77, which is remarkably consistent with relativistic Fermi acceleration in the presence of shock compressed turbulence (Lemoine & Revenu, 2006), and supports the hypothesis that the low energy emission has a jet origin.

The fit corresponding to annihilations into  $t\bar{t}$  (Fig. 10.2) gives  $\chi^2 = 1.7$ , for 11 spectral data points<sup>3</sup> and 4 free parameters ( $m_{\text{DM}}$ ,  $\langle\sigma v\rangle$  and the normalization and the slope of the power law spectrum below 2.4 GeV). This gives a reduced chi-square of  $\chi^2/\text{d.o.f} = 0.24$  which illustrates a remarkably good fit and suggests that it is dominated by statistical errors. Annihilations into  $b\bar{b}$  give  $\chi^2 = 3$ , i.e.  $\chi^2/\text{d.o.f} = 0.43$ , which also corresponds to a very good fit (see Fig. 10.3).<sup>4</sup> In Fig. 10.4, we show the best fit when considering DM particles annihilating into  $\tau^+\tau^-$ . Now the best-fit mass is  $\sim 400$  GeV, smaller than for hadronic channels. In this case, we find  $\chi^2/\text{d.o.f} = 2.14$ , so this channel gives a somehow less good fit than the previous cases, but it still reproduces the spectral hardening reported in this work. Note that for simplicity we have only focused on single annihilation channels. Depending on the underlying model, DM particles may annihilate into several different final states.

<sup>1</sup>Here we consider only prompt emission. We disregard any acceleration (Davis et al., 2015) or secondary emission that could distort the prompt spectrum.

<sup>2</sup>In practice we compute the flux from a region of size  $\sim 0.1$  deg corresponding to the optimal PSF of the instrument, although the bulk of the emission from the spike is contained in such a small region (typically below 1 pc, i.e. sub-arcsec scales) that the result is not very sensitive to the exact size of the region of interest.

<sup>3</sup>The points are taken from the *Fermi*-LAT analysis presented here and the first three data points from H.E.S.S. observations (Aharonian et al., 2009).

<sup>4</sup>If we include the last three H.E.S.S. points, we obtain  $\chi^2/\text{d.o.f} = 0.62$  for  $t\bar{t}$  and  $\chi^2/\text{d.o.f} = 0.87$  for  $b\bar{b}$ .

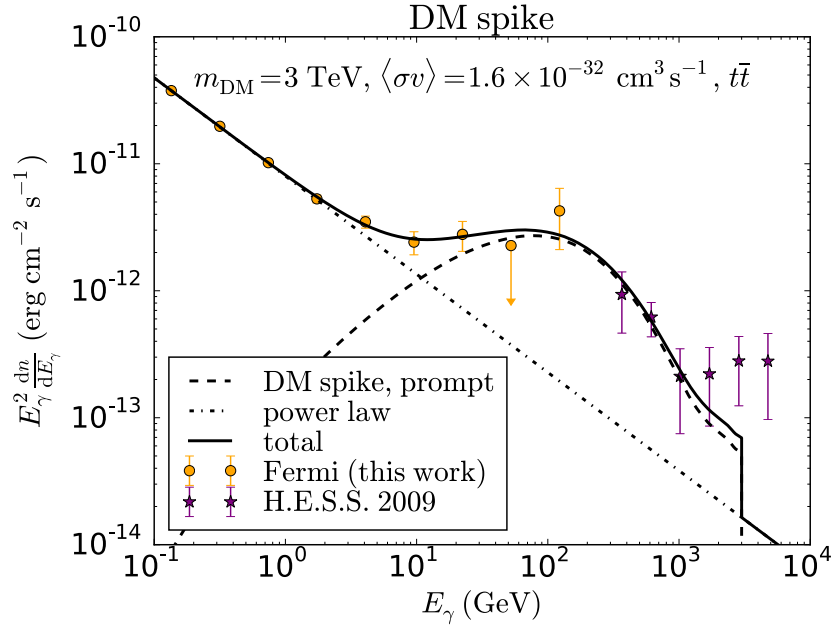


**Figure 10.2** – Best fit to the spectrum of the core of Cen A, obtained by assuming a single power law plus prompt emission from heavy DM particles annihilating into  $t\bar{t}$  and a spike in the DM density profile, with slope  $\gamma_{\text{sp}} = 7/3$ .

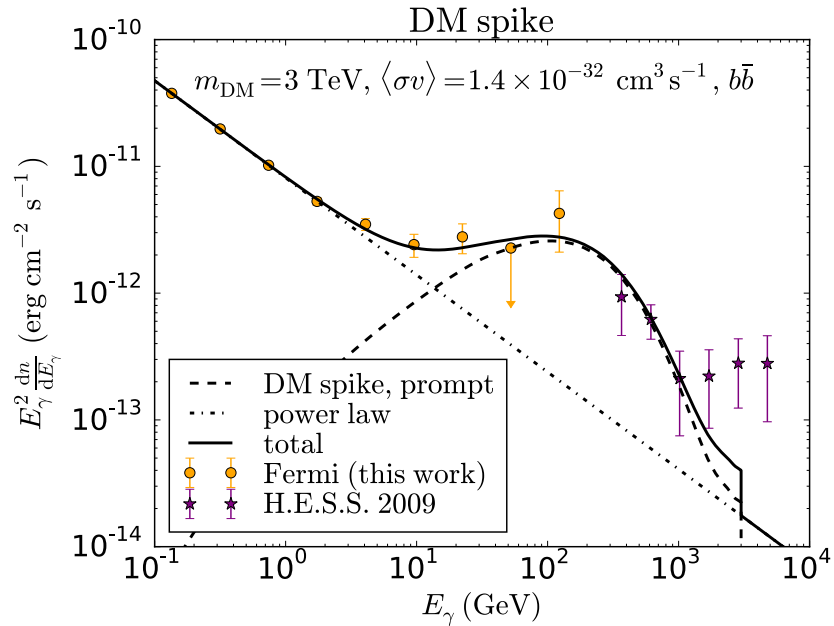


**Figure 10.3** – Best fit to the  $\gamma$ -ray spectrum of Cen A, obtained by assuming a single power law plus the prompt emission from 3 TeV DM particles annihilating into  $b\bar{b}$  with a cross-section of  $1.4 \times 10^{-32} \text{ cm}^3 \text{ s}^{-1}$ , and a spike in the DM density profile, with slope  $\gamma_{\text{sp}} = 7/3$ .

The hypothesis of a NFW profile with a thermal cross-section of  $\langle\sigma v\rangle \simeq 3 \times 10^{-26} \text{ cm}^3 \text{ s}^{-1}$  is excluded because the flux would be too strongly suppressed, as shown in Fig. 10.5. In practice a spike with slope  $\gtrsim 2$  is needed to account for the observed flux.

Our best-fit annihilation cross-section, of the order of  $\langle\sigma v\rangle \simeq 1.6 \times 10^{-32} \text{ cm}^3 \text{ s}^{-1}$ , is far too small to explain the observed fraction of DM in the Universe. However, this might simply be

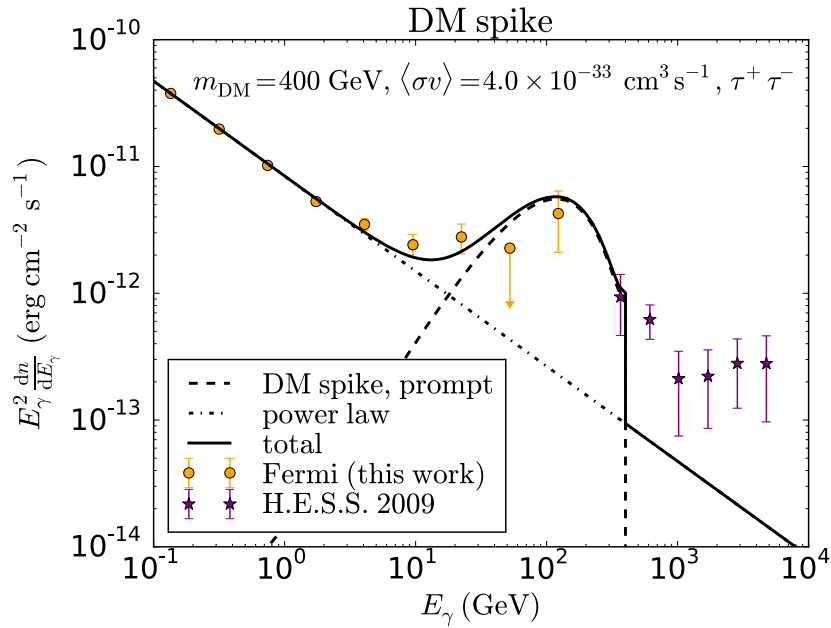


**Figure 10.4** – Best fit to the  $\gamma$ -ray spectrum of Cen A, obtained by assuming a single power law plus the prompt emission from 400 GeV DM particles annihilating into  $\tau^+\tau^-$  with a cross-section of  $4 \times 10^{-33} \text{ cm}^3 \text{ s}^{-1}$ , and a spike in the DM density profile, with slope  $\gamma_{\text{sp}} = 7/3$ .

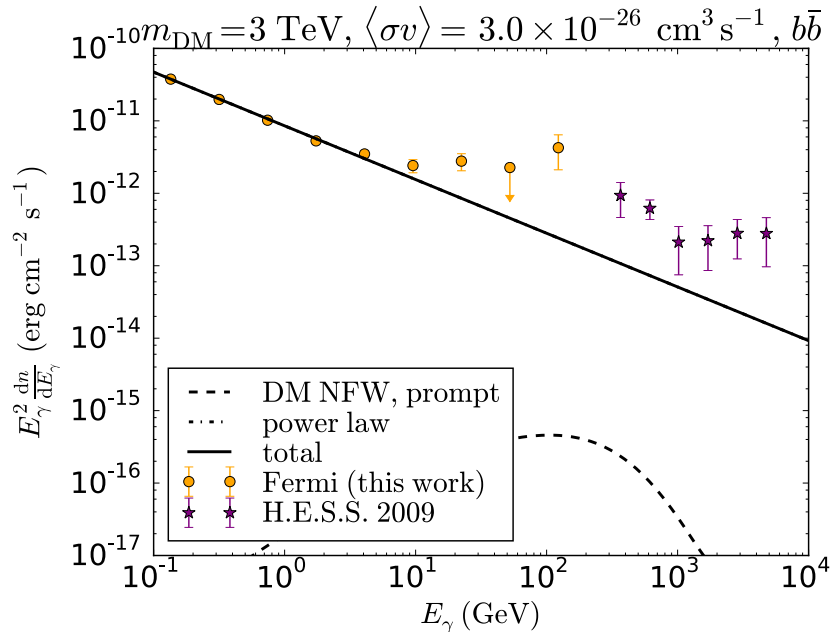


**Figure 10.5** – Contribution to the  $\gamma$ -ray spectrum of Cen A from a single power law plus the prompt emission from 3 TeV DM particles annihilating into  $b\bar{b}$  with the canonical cross-section of  $3 \times 10^{-26} \text{ cm}^3 \text{ s}^{-1}$ , for a DM density following the NFW profile. The DM-induced emission is several orders of magnitude below the data.

revealing the existence of a rich dark sector with several (non thermal) DM particles (Boehm et al., 2004b; Zurek, 2009),<sup>5</sup> or a combination of velocity-dependent and independent terms in

<sup>5</sup>Our estimate assumes a unique DM candidate. Sub-component DM particles might require efficient co-annihilation processes, see e.g. Boehm et al. (2000).

the annihilation cross section.<sup>6</sup> Either way, our findings would suggest the existence of heavy DM particles exchanging at least one heavy particle mediator. Such a mediator could be compatible with current hints of a 750 GeV boson at LHC (see e.g. Aad et al., 2015b), although our best fit requires hadronic processes, which may be inconsistent with LHC findings.

### 10.3.2 Millisecond pulsars

An alternative explanation to the DM model is MSPs, which are expected to form in high stellar density environments, typically in the central regions of galaxies. The expected GeV emission from MSPs is currently one of the leading explanations of the GC excess. It is estimated that around one to ten thousand MSPs are needed to explain the GeV excess in the GC (see Chapter 5). However, the  $\gamma$ -ray signature of MSPs can be broadened up to TeV energies by inverse Compton processes (Bednarek & Sobczak, 2013), when the electrons accelerated by MSP winds up-scatter the ambient soft photon field (e.g. in the UV and IR bands), as discussed in Chapter 8.

Two critical assumptions for our estimates of the very high-energy  $\gamma$ -ray emission from MSPs are an electron injection spectrum extending to a few tens of TeV (here we consider  $E_{\max} = 10$  TeV) and a large enough interstellar radiation field for the IC losses to dominate over synchrotron losses. Here we use the same propagation technique as for the MW. More specifically, we compute the IC flux from MSPs exactly as in Chapter 8. For the magnetic field, we assume a constant value of  $10 \mu\text{G}$  constrained by *Chandra* limits on synchrotron radiation from high energy electron-positron pairs and use a conservative power law,  $\rho_{\text{MSP}}(r) \propto r^{-1.2}$ , for the MSP density profile (consistent with the GC  $\gamma$ -ray excess). As for the DM analysis, we keep the normalization and slope of the jet contribution as free parameters.

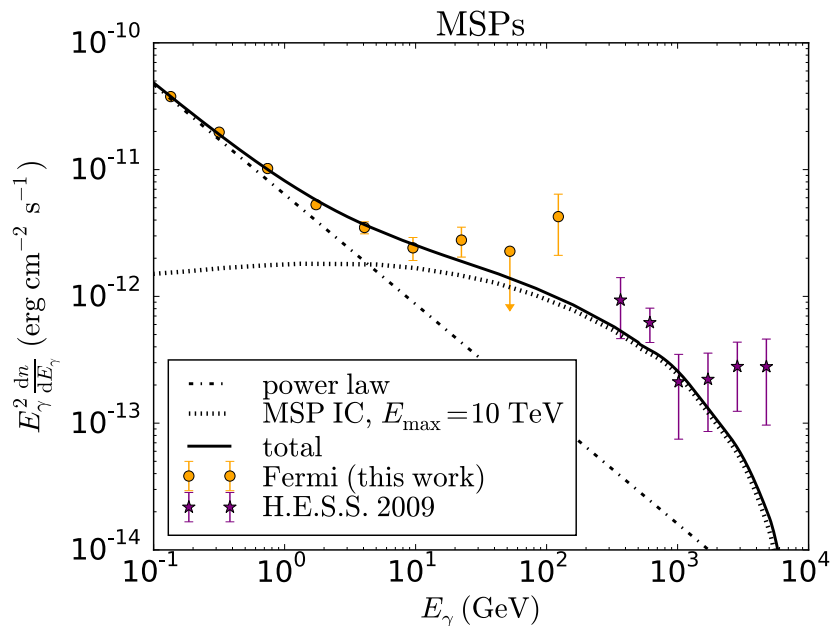


**Figure 10.6** – Best fit obtained with emission from a population of MSPs plus a power law.

Assuming the presence of a population of MSPs leads to the fit shown in Fig. 10.6, and  $\chi^2 \simeq 10$ , that is  $\chi^2/\text{d.o.f} \simeq 1.4$ . This fit is only slightly improved by the addition of a DM component at very high energy, as shown in Fig. 10.7 where we assumed a 30 TeV DM candidate annihilating into  $\tau^+\tau^-$ . While the reduced  $\chi^2$  is good, the poor knowledge of the MSPs density

<sup>6</sup>We note that there is a degeneracy between the annihilation cross-section and the spike characteristics (normalization, size, power-law index) which could affect our estimates.

profile, the soft-photon field and our rather crude model of the magnetic field severely limits our interpretation of the goodness of the fit.

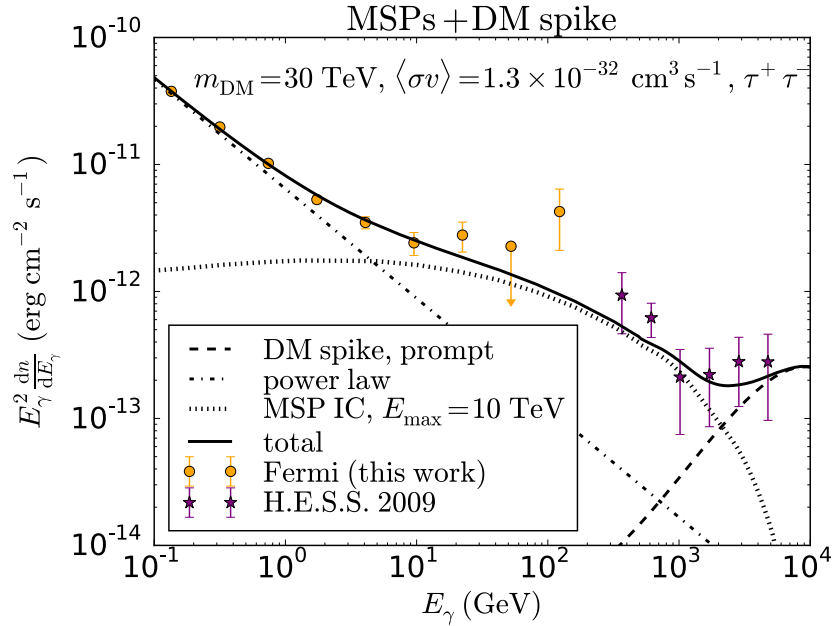


**Figure 10.7** – Best fit obtained by assuming a single power law plus IC emission from a population of MSPs and prompt emission from 30 TeV DM particles annihilating into  $\tau^+\tau^-$  and a spike in the DM density profile.

### 10.3.3 Diffused protons

Another explanation is that both  $\gamma$ -ray core emissions revealed in this project originate from the jet in Cen A, but are due to two different cosmic-ray populations. In an analysis of the very high energy  $\gamma$ -ray spectrum of the central region of the MW, [Chernyakova et al. \(2011\)](#) showed that accelerated protons from the jet could travel away from our GC, Sgr A\*, and emit enough  $\gamma$ -rays to explain the steady MW spectrum up to a few TeV. Probing this hypothesis in the case of Cen A requires a much better knowledge of the diffusive zone and cosmic ray propagation parameters in AGNs than currently available. Yet, in light of [Chernyakova et al. \(2011\)](#), further evidence that the jet is the dominant source of  $\gamma$ -ray emission in the core of Cen A would strengthen claims that the MW has been an active galaxy in the past ([Petrović et al., 2014](#); [Su et al., 2010](#)). The study of the morphology of Cen A’s core emission will thus be critical to answer this question.

## 10.4 Conclusion

In this project, we have reported a  $5\sigma$  evidence for a hardening of the *Fermi*-LAT  $\gamma$ -ray spectrum and showed that either heavy DM particles or a population of MSPs could explain this high-energy spectral feature. While we cannot rule out that the jet itself is at the origin of the hardening of the spectrum, the lack of variability of the emission above 2.4 GeV argues against jet-induced leptonic models (such as SSC). Hence, at the very least, our results are a strong indication that the modeling of  $\gamma$ -ray production mechanisms in active galaxies needs to be modified.

Our findings hint at new physics inside objects like Cen A or astrophysical objects that are rarely detected outside our Galaxy. Therefore the precise modelling of cosmic ray propagation, together with observations of Cen A’s  $\gamma$ -ray spectrum at TeV energies by H.E.S.S. and the Cherenkov Telescope Array, will be critical to determine the origin of the spectral break.

A DM explanation would reveal the existence of particles beyond the standard model of particle physics as well as spikes in the DM profile. While the existence of spikes is highly debated, Cen A is dynamically young, so such an enhancement may survive nuclear star cluster dynamics. If confirmed by other observations, our case for a boost of the DM annihilation signal will constitute the first evidence that DM clusters around BHs, and have central implications for our understanding of the feedback mechanisms between ordinary matter and DM in galactic cores.

Likewise, if the spectral hardening of Cen A's core reported here is due to a population of MSPs, then the  $\gamma$ -ray spectrum of Cen A constitutes the first insights into the pulsar population in another galaxy. Either way, these findings open up a new window on the physics of the cores of active galaxies and provide the prospect of more exciting discoveries.



## Chapter 11

# Probing a dark matter spike at the center of M87 with the Event Horizon Telescope

In this chapter, we investigate the potential of the Event Horizon Telescope for imaging the very inner part of the DM profile in M87, through the synchrotron emission induced by DM annihilations. We present preliminary results that show the unprecedented capabilities of the EHT to probe very weakly annihilating DM through the horizon-scale features introduced by a DM spike.

### Contents

---

<b>11.1 Introduction: beyond spectral information</b>	<b>164</b>
<b>11.2 The Event Horizon Telescope</b>	<b>164</b>
11.2.1 General features	164
11.2.2 Imaging the shadow of a black hole	164
<b>11.3 Probing dark matter at the center of M87 with the Event Horizon Telescope</b>	<b>166</b>
11.3.1 Electron propagation in the presence of advection	166
11.3.2 Relevance of advection	168
11.3.3 Dark synchrotron intensity in a curved spacetime	168
<b>11.4 Preliminary results</b>	<b>169</b>
<b>11.5 Summary</b>	<b>170</b>

---

## 11.1 Introduction: beyond spectral information

The plausible presence of a SMBH-induced DM spike at the center of M87 leads to a detectable signature of annihilations of thermal DM in the SED of M87, as discussed in Chapter 9. In particular, we were able to exclude DM candidates with a velocity independent (s-wave) annihilation cross-section  $\sim 3 \times 10^{-26} \text{ cm}^3 \text{ s}^{-1}$  for DM masses from a few GeV to about 100 TeV. For low-mass DM, typically 10 GeV, we could even constrain the cross-section down to the level of  $\sim 10^{-30} \text{ cm}^3 \text{ s}^{-1}$  using the observed SED. This seems to be the best achievable limit using spectral information.

However, it may be possible to probe even fainter DM-induced radiation by using the spatial morphology of the DM-induced signal. Still, by lack of angular resolution of existing facilities, a dedicated study has not been performed yet for objects such as M87, where the DM profile is plausibly sharply peaked on very small scales. However, things are about to change with the advent of the Event Horizon Telescope (EHT), with micro-arcsecond-scale angular resolution.

## 11.2 The Event Horizon Telescope

### 11.2.1 General features

The EHT is a network of millimeter and submillimeter facilities all around the world that relies on very long baseline interferometry (VLBI) to create an effective Earth-scale high angular resolution telescope (Doeleman, 2010; Lu et al., 2014). The goal of the collaboration is to test general relativity and shed light on physical processes taking place in the vicinity of supermassive black holes at the centers of galaxies. The array currently consists of the Submillimeter Telescope (SMT) in Arizona, the Combined Array for Research in Millimeter-wave Astronomy (CARMA), and a network of three facilities in Hawaii: the Caltech Submillimeter Observatory (CSO), the James Clerk Maxwell Telescope (JCMT), and the Submillimeter Array (SMA). The Atacama Large Millimeter/submillimeter Array (ALMA) in Chile is the latest addition to the network. So far, angular resolutions of the order of 30–40  $\mu\text{as}$  have been achieved at 230 GHz. Including an additional baseline between the Plateau de Bure interferometer and the South Pole Telescope (SPT) should improve the resolution to the level of 15  $\mu\text{as}$  at an additional higher frequency of 345 GHz. The characteristics of the EHT of interest in the context of this work are summarized in Table 11.1.

**Table 11.1** – Characteristics of the EHT.

	Frequency (GHz)	Angular resolution ( $\mu\text{as}$ )
Current	230	30–40
Planned	345	15

It turns out that the angular Schwarzschild radius of the SMBH at the center of M87 is about 8  $\mu\text{as}$ , very close to the corresponding radius of 10  $\mu\text{as}$  for Sgr A\* at the center of the MW. Therefore, while Sgr A\* is the prime target of the EHT, M87 is the second main target for observations of horizon-scale features (Lu et al., 2014).

### 11.2.2 Imaging the shadow of a black hole

The shadow of a BH is closely related to the gravitational lensing induced by the BH and more quantitatively to the deflection angle of light rays. Starting from the Schwarzschild metric, which describes the geometry of a non-rotating BH in a vacuum, one can derive the relation between

the impact parameter  $\mathfrak{b}$  and the closest approach distance  $r_m$  of a photon (Weinberg, 1972):

$$\mathfrak{b} = r_m \left( 1 - \frac{R_S}{r_m} \right)^{-\frac{1}{2}}, \quad (11.1)$$

where  $R_S$  is the Schwarzschild radius of the BH. It turns out that the deflection angle diverges for a particular value of the impact parameter, which defines the shadow of the BH. More precisely, this divergence corresponds to light rays infinitely bent by the BH and thus performing an infinite number of loops around it. Such orbits are unstable under small perturbations, which results in the photons eventually crossing the horizon and falling onto the singularity. Therefore, the shadow represents the minimum impact parameter of a photon escaping the attraction of the BH. Conversely, it is the minimum impact parameter of a photon coming from infinity for it to end up on the photon sphere (Bozza, 2010), as shown in Fig. 11.1. As a result of this gravitational lensing effect, for an observer looking at the BH, *the shadow is a disk of local darkness surrounded by a brighter ring*. The radius of the shadow can be determined analytically since it corresponds to the minimum of the function  $\mathfrak{b}(r_m)$ . The photon sphere has a radius of  $1.5R_S$ , obtained by minimizing  $\mathfrak{b}$ , and the corresponding value of the impact parameter yields the radius of the shadow:

$$r_{\text{shadow}} = \frac{3\sqrt{3}}{2}R_S \approx 2.6R_S. \quad (11.2)$$

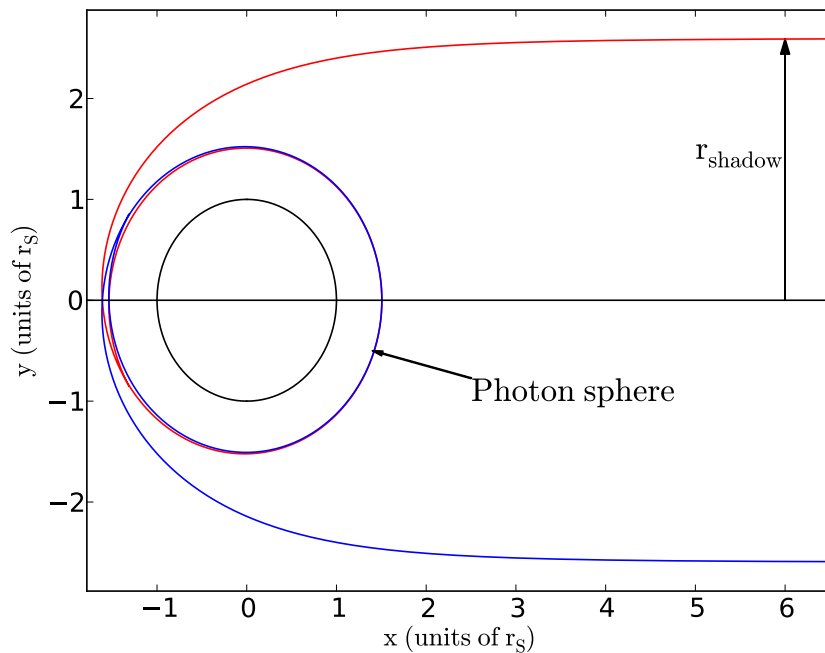


**Figure 11.1** – Diagram characterizing the shadow of a BH, from Lacroix & Silk (2013). The black circle represents the horizon. The radius of the shadow is the minimum impact parameter of a photon escaping the BH, so the shadow is a dark disk relatively to a brighter surrounding ring. The shadow or equivalently its bright silhouette represent the BH as seen by the observer.

Consequently, the shadow is the main observable feature of the BH via direct imaging. A simulated image of the shadow of Sgr A\* from Broderick et al. (2011) is shown in Fig. 11.2. This is what the EHT Collaboration aims to observe in the near future, in order for instance to test general relativity, characterize the properties of the accretion flow very close to the BH, and study high-energy astrophysical processes in a strong gravitational field. It turns out that horizon-scale features have already been observed at the GC (Fish et al., 2011) and at the center of M87 (Doeleman et al., 2012; Akiyama et al., 2015), which paves the way for even more exciting discoveries.

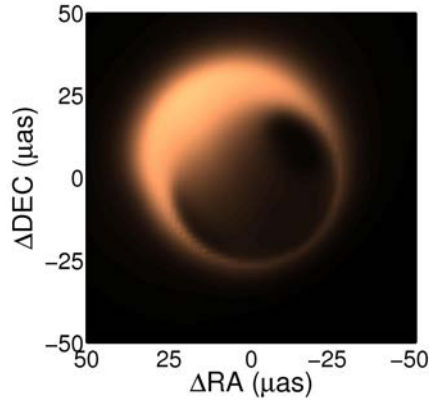


**Figure 11.2** – Simulated image of the shadow of Sgr A\* from Broderick et al. (2011). The bright ring is associated with the accretion flow, gravitationally lensed by the BH.

### 11.3 Probing dark matter at the center of M87 with the Event Horizon Telescope

In the context of the very good observational opportunities offered by the EHT, we now discuss the potential of this instrument in terms of DM searches. In particular, we study the observability of a DM spike at the center of M87, since such a sharply peaked morphological feature is expected to yield strong annihilation signals. At the frequencies of interest for the EHT, typically a few hundred GHz, the main DM signature comes from synchrotron radiation. Therefore, in order to assess the ability of the EHT to probe the inner part of the DM profile of M87, we need to compute the synchrotron emission of electrons and positrons produced in DM annihilations in the inner region. We make the following assumptions:

- The presence of a SMBH at the center is likely to lead to fairly strong magnetic fields, typically of the order of 1–10 G (Neronov & Aharonian, 2007; Brodatzki et al., 2011). As a result of such strong magnetic fields, synchrotron radiation and advection towards the central BH are the dominant physical processes by which DM-induced electrons and positrons lose or gain energy (Aloisio et al., 2004; Regis & Ullio, 2008), whereas inverse Compton scattering and bremsstrahlung are negligible. Additionally, the timescales associated with synchrotron radiation and advection are much shorter than that of spatial diffusion, so we disregard the latter in the following. Note that the magnetic field can be even higher—of the order of  $10^4$  G—if the equipartition scenario is realized, as discussed in Chapter 9. However, such an assumption, although plausible, has not been proven yet. Therefore, here we remain more conservative and we consider typically  $B \sim 10$  G.
- We also disregard two processes that can reduce the synchrotron intensity. First, the synchrotron self-Compton effect, which would lead to additional energy losses for electrons and positrons, is only relevant for magnetic fields smaller than 0.1 G (Aloisio et al., 2004). Then, synchrotron self-absorption is only relevant below  $\sim 10$  GHz (Aloisio et al., 2004; Regis & Ullio, 2008), so it can be neglected for the EHT frequency of 230 GHz.
- As for the DM profile, we assume that a spike effectively formed at early times and has survived until today (see the discussion in Chapter 3).

#### 11.3.1 Electron propagation in the presence of advection

To derive the intensity of DM-induced synchrotron radiation, we first need to compute the electron and positron spectrum from the DM annihilation rate. This is done by solving the propagation

equation of DM-induced electrons and positrons which, in the presence of synchrotron radiation and advection, and assuming a steady state reads (see e.g. Aloisio et al., 2004; Regis & Ullio, 2008):

$$v \frac{\partial f_i}{\partial r} - \frac{1}{3r^2} \frac{\partial}{\partial r} (r^2 v) p \frac{\partial f_i}{\partial p} + \frac{1}{p^2} \frac{\partial}{\partial p} (p^2 \dot{p} f_i) = Q_i, \quad (11.3)$$

with  $f_i(r, p)$  the distribution function of electrons and positrons in momentum space, at radius  $r$  and momentum  $p$ , for annihilation channel  $i$ . The first, second and third terms correspond to the advection current, the acceleration of electrons due to the adiabatic compression, and the loss term due to radiative losses, respectively.  $v(r) = -c (r/R_S)^{-1/2}$  is the radial infall velocity of electrons and positrons onto the BH in the accretion flow, where  $R_S$  is the Schwarzschild radius. The minus sign in the expression of the inflow velocity accounts for the direction of the flow, oriented towards the BH. Eq. (11.3) is the reformulation in terms of momentum  $p$  of the propagation equation in the presence of convection discussed in Sec. 4.3.2.

The source function  $Q_i(r, p)$  is the DM annihilation rate in momentum space for channel  $i$ , related to the annihilation rate  $q_i(r, E)$  in energy space via

$$Q_i(r, p) = \frac{c}{4\pi p^2} q_i(r, E) \quad (11.4)$$

in the ultra-relativistic (UR) regime where  $E = pc$ . The UR approximation can be safely used for electrons and positrons for the energy range relevant for this study. The usual annihilation rate in energy space reads (see Chapter 4):

$$q_i(r, E) = \frac{\langle \sigma v \rangle_i}{\eta} \left( \frac{\rho(r)}{m_{\text{DM}}} \right)^2 \frac{dN_{e,i}}{dE}(E), \quad (11.5)$$

where  $\eta = 2$  here. The injection spectrum  $dN_{e,i}/dE$  is taken from Cirelli et al. (2011).

For the DM density, we consider the following radial dependence, corresponding to a spiky profile (see Chapter 3)

$$\rho(r) = \begin{cases} 0 & r < R_S \\ \frac{\rho_{\text{sp}}(r) \rho_{\text{sat}}}{\rho_{\text{sp}}(r) + \rho_{\text{sat}}} & R_S \leq r < R_{\text{sp}} \\ \rho_0 \left( \frac{r}{r_0} \right)^{-1} \left( 1 + \frac{r}{r_0} \right)^{-2} & r \geq R_{\text{sp}}, \end{cases} \quad (11.6)$$

with  $r_0 = 20$  kpc. Note that one usually assumes that the DM profile vanishes below  $4R_S$  (or  $2R_S$  from the full relativistic calculation) due to DM particles captured by the BH. However, here we consider a DM spike that goes all the way down to the horizon of the BH, provided the saturation radius  $r_{\text{sat}}$ —for which  $\rho_{\text{sat}} = \rho(r_{\text{sat}})$ —is small enough, which is the case for small cross-sections like  $10^{-30} \text{ cm}^3 \text{ s}^{-1}$ . We use the same normalization of the profile as in Chapter 9, given in Appendix A.2.1. In particular we take  $\rho_0 \approx 2.5 \text{ GeV cm}^{-3}$ .

Since radiative losses are dominated by synchrotron losses, the total radiative loss term  $\dot{p} = dp/dt$  reduces to the synchrotron loss term (Eq. (4.62))

$$\dot{p}(r, p) = \dot{p}_{\text{syn}}(r, p) = -\frac{2\sigma_{\text{T}} B^2 p^2}{3\mu_0 (m_e c)^2}. \quad (11.7)$$

We assume the intensity of the magnetic field to be homogeneous, i.e.  $B \equiv B_0$ , over the accretion region, which has a size  $r_{\text{acc}}$  corresponding to the sphere of influence of the BH (Regis & Ullio, 2008), so typically  $\sim 60$  pc (as discussed in Chapter 9), which is also roughly the size of the spike.

The resolution of the propagation equation, Eq. (11.3), in the presence of synchrotron losses and advection, in the UR regime, and with the method of characteristics, yields the electron and positron spectrum in terms of the DM annihilation rate (Aloisio et al., 2004)

$$f_i(r, p) = \frac{1}{c} \left( \frac{r}{R_S} \right) \int_r^{r_{\text{acc}}} Q_i(R_{\text{inj}}, p_{\text{inj}}) \left( \frac{R_{\text{inj}}}{R_S} \right)^{\frac{5}{2}} \left( \frac{p_{\text{inj}}}{p} \right)^4 dR_{\text{inj}}, \quad (11.8)$$

where the injection momentum  $p_{\text{inj}} \equiv p_{\text{inj}}(R_{\text{inj}}; r, p)$  for a homogeneous magnetic field is given in Appendix A.4. From there, the electron and positron energy spectrum is given by:

$$\psi_i(r, E) = \frac{4\pi p^2}{c} f_i(r, p). \quad (11.9)$$

We then convolve  $\psi_i$  with the synchrotron power  $P_{\text{syn}}(\nu, E, r)$  to obtain the synchrotron emissivity:<sup>1</sup>

$$j_{\text{syn},i}(\nu, r) = 2 \int_{m_e}^{m_{\text{DM}}} P_{\text{syn}}(\nu, E, r) \psi_i(r, E) dE. \quad (11.10)$$

### 11.3.2 Relevance of advection

Advection shapes the inner part of the intensity profile by displacing electrons and positrons towards the BH and thus accelerating them. This effect is in competition with synchrotron losses. Therefore, depending on the magnetic field, electrons either lose their energy in place through synchrotron radiation, or are first advected towards the center. The dependence on the magnetic field of the size of the region where electrons are affected by advection is obtained by comparing the synchrotron loss term (Eq. (11.7)) with the momentum gain rate due to adiabatic compression (given in Eq. (4.66))

$$\dot{p}_{\text{ad}} = -\frac{1}{3r^2} \frac{\partial}{\partial r} (r^2 v(r)) p. \quad (11.11)$$

The shape of the emissivity profile is thus governed by advection for:

$$r < \left( \frac{3R_S^{\frac{1}{2}} \mu_0 m_e^2 c^4}{4\sigma_T B_0^2 E_{\text{syn}}} \right)^{\frac{2}{3}}, \quad (11.12)$$

where  $E_{\text{syn}} = (4\pi m_e^3 c^4 \nu / (3eB_0))^{1/2}$  is the peak synchrotron energy at the frequency  $\nu$  of interest (Longair, 2011). In terms of the angular distance from the center  $\theta \equiv r/d_{\text{M87}}$ —where  $d_{\text{M87}} \approx 16$  Mpc is the distance between Earth and the center of M87—this condition reads, for  $\nu = 230$  GHz,

$$\theta \lesssim 70 \left( \frac{B_0}{1 \text{ G}} \right)^{-1} \mu\text{as}. \quad (11.13)$$

It is therefore essential to include the advection process for  $B \lesssim 1$  G, since in that regime it has a strong impact on the synchrotron intensity in the region of interest for the EHT. For  $B \gtrsim 10$  G, advection is negligible since it would only dominate for radii smaller than the Schwarzschild radius of the BH.

### 11.3.3 Dark synchrotron intensity in a curved spacetime

The synchrotron intensity *for a flat spacetime* is computed as before by integrating the emissivity over the l.o.s.:

$$I_{\nu,i}^{\text{syn}}(\theta) = \int_{\text{l.o.s.}} \frac{j_{\text{syn},i}(\nu, r(s, \theta))}{4\pi} ds. \quad (11.14)$$

<sup>1</sup>In practice, energies smaller than  $\sim 100m_e$  fall in the exponential tail of the synchrotron spectrum, which justifies the UR approximation.

To determine whether a given value of the annihilation cross-section leads to a flux that does not overshoot the multi-spectral data, we also estimate as in Chapter 9 the contribution from DM-induced synchrotron radiation to the SED of M87 by integrating the synchrotron intensity given in Eq. (11.14) over a field of view centered on the galactic center and corresponding to the resolution  $\theta_{\text{res}}$  of the telescopes under consideration at a given frequency:

$$\nu F_{\nu,i}^{\text{syn}} = 2\pi \int_0^{\theta_{\text{res}}} \nu I_{\nu,i}^{\text{syn}}(\theta) \sin \theta d\theta. \quad (11.15)$$

However, the actual spacetime accounting for the presence of the SMBH at the center is characterized by the Schwarzschild or Kerr metric respectively if the BH is static or rotating. In these more realistic cases, the correct spatial morphology of the synchrotron signal is obtained using a ray-tracing technique that accounts for the gravitational lensing effect due to the BH. In our case, this is achieved thanks to the ray-tracing and radiative transfer technique described in Broderick (2006); Broderick & Loeb (2006a,b).

## 11.4 Preliminary results

In this section, we present the preliminary results obtained in collaboration with Avery Broderick's group. Shown in Fig. 11.3 is a color map corresponding to our prediction of the synchrotron intensity at 230 GHz from a DM spike with  $\gamma_{\text{sp}} = 7/3$ , assuming annihilation of 10 GeV DM particles into  $b\bar{b}$ , and a magnetic field of 10 G. We consider a cross-section of  $\sim 10^{-31} \text{ cm}^3 \text{ s}^{-1}$  which gives the maximal SED compatible with the multi-wavelength observed SED. The ray-tracing and radiative transfer scheme from Broderick (2006); Broderick & Loeb (2006a,b) was used to compute the intensity from our predicted emissivities, for a Schwarzschild spacetime corresponding to the assumption of a non-rotating BH. The bright ring of radius  $\sim 20 \mu\text{as}$  that surrounds the darker shadow of the BH is clearly visible. It is actually the main observable for very long baselines, since it introduces small-scale structure in the signal.

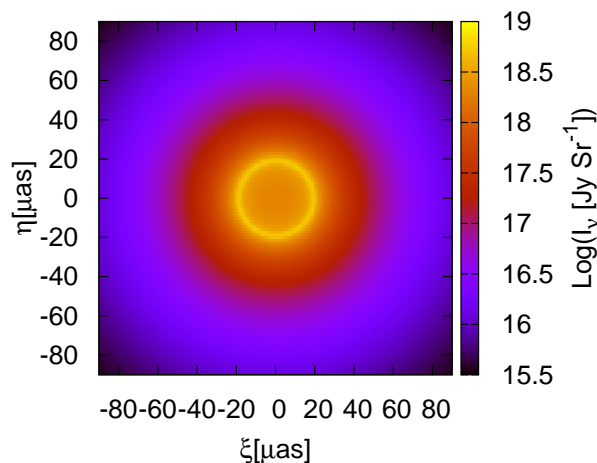


**Figure 11.3** – Color map of the predicted synchrotron intensity at 230 GHz from a DM spike with  $\gamma_{\text{sp}} = 7/3$  at the center of M87, for annihilation of 10 GeV DM particles into  $b\bar{b}$  with a cross-section  $\sim 10^{-31} \text{ cm}^3 \text{ s}^{-1}$ , and a magnetic field of 10 G. The ray-tracing and radiative transfer scheme from Broderick (2006); Broderick & Loeb (2006a,b) was used to compute the intensity in a Schwarzschild spacetime. The bright ring of radius  $\sim 20 \mu\text{as}$  that surrounds the darker shadow of the BH is clearly visible.

In practice, what is really observed via interferometry is the visibility amplitude, which is the spatial Fourier transform of the intensity. The visibility amplitude as a function of baseline

length is shown in Fig. 11.4, with predictions based on the synchrotron signal shown in Fig. 11.3, compared to EHT observations from Doeleman et al. (2012) and Akiyama et al. (2015).

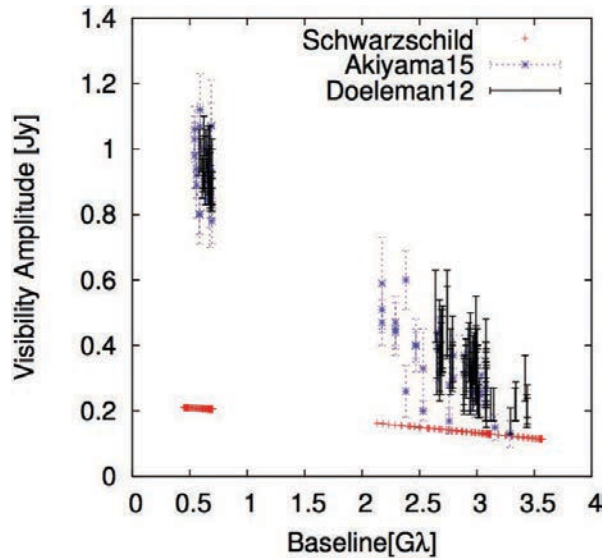


**Figure 11.4** – Visibility amplitude as a function of baseline length, for predictions based on the synchrotron signal from the spike that we derived. The data come from Doeleman et al. (2012) and Akiyama et al. (2015).

Fig. 11.4 shows that for the very small annihilation cross-section considered here, the synchrotron emission from a DM spike can give a sizable contribution to the small-scale structure of the emission detected by the EHT at the center of M87, as evidenced by the visibility for very long baselines. Therefore, although the spike is unlikely to account for the whole observed emission—as shown by the predicted visibility for small baselines which underestimates the data—, this result shows that the EHT can definitely probe the very inner DM profile of M87. We now need to investigate in more details the effect of the magnetic field, the DM mass and annihilation cross-section, as well as the properties of the BH (static vs rotating), but this already opens up a new path to explore the detectability of spikes of annihilating DM.

## 11.5 Summary

In this chapter, we have discussed the prospects for direct imaging of the synchrotron emission induced by a DM spike in the vicinity of the SMBH at the center of M87. We have shown preliminary results that strongly indicate that a DM spike can contribute significantly to the millimeter signal measured by the EHT, including for very small (potentially p-wave suppressed) annihilation cross-sections. In particular, the spike leads to a shadow feature, characteristic of the gravitational lensing effect induced by the central BH, which constitutes an observable feature for the very long baseline interferometer. This demonstrates that the EHT has great potential for detection of DM spikes, and shows unprecedented sensitivity to very weakly annihilating DM.

## Conclusion and outlook

In this thesis, I have focused on various aspects of indirect searches for dark matter particles in the central regions of galaxies. Nowadays, thanks to tremendous observational progress allowed by the advent of instruments like *Fermi*-LAT, H.E.S.S., or the even more spectacular Event Horizon Telescope, not only is it possible to search for signatures of dark matter annihilation in galactic halos at large, but also to zoom in on the very inner regions, in the vicinity of supermassive black holes.

In this context, it was timely to tackle the problem of the dark matter density profile at the centers of galaxies with novel methods, and this provided the main motivation of this thesis. In particular, the formation of supermassive black holes can lead, depending on the evolution of the host galaxy, to the formation of central dark matter density spikes on sub-parsec scales, via accretion of dark matter particles. In my thesis, I have investigated new ways of probing the very central part of dark matter halos, by exploiting the associated electromagnetic annihilation signatures over a wide range of frequencies, from prompt  $\gamma$ -ray emission to secondary photon emission via inverse Compton scattering, synchrotron radiation and bremsstrahlung. Most standard indirect searches actually focus on signatures from prompt  $\gamma$ -ray emission, but studying secondary emissions allows us to go one step further, and opens up new horizons to dive deeper into the parameter space of dark matter particles.

In order to model secondary photon emissions, I have developed my own cosmic-ray propagation code, to account for injection by spiky distributions of dark matter at the centers of galaxies. This dedicated technique is essential since existing propagation codes cannot cope with the small scales involved with dark matter density spikes below parsec scales.

I have applied my tools to the interpretation of the Galactic center excess reported in the *Fermi*-LAT  $\gamma$ -ray data, and I have obtained the important result that it is crucial to include secondary processes like inverse Compton scattering and bremsstrahlung when interpreting the *Fermi* excess. In particular, I have shown that once the secondary contributions are accounted for, the excess can be entirely explained by dark matter annihilation into leptonic final states, previously discarded based only on the associated prompt emission. Moreover, these leptonic annihilation channels prefer a mass of order 10 GeV, contrary to larger values favored by prompt-only studies. These results are based on the spectrum of the excess, but I have taken an additional step by studying with my collaborators the impact of accounting for the spatial morphology of the secondary components—affected in particular by spatial electron diffusion—in a fully self-consistent way in the analysis of the *Fermi* data. Actually, accounting for spatial morphology of the inverse Compton and bremsstrahlung contributions is essential to draw robust conclusions on the interpretation of the excess. In particular, we showed that a full 3D analysis reveals a more complex spatial morphology of the excess—with energy and spatial dependences entangled—than what is captured by a NFW template. This is illustrated for instance by the result that the 3D analysis prefers the presence of secondary extended emission in the democratic lepton model.

The new technique I have developed to model spatial diffusion for very sharply peaked sources has allowed me to quantify for the first time the effect of diffusion on a dark matter spike. I have shown that in the presence of diffusion, it is possible to probe the very inner part of the dark matter profile, way below scales within reach of numerical simulations, by measuring the induced synchrotron signal at microwave frequencies, since diffusion is able to increase the size of the

emission region. This project also served as a working example for the potential of studying spiky profiles in the presence of diffusion, which I have applied to the diffuse emission recently reported by the H.E.S.S. Collaboration. Of course, the techniques I have used are not restricted to the framework of dark matter, so I have also modeled the very high  $\gamma$ -ray emission from the population of millisecond pulsars that may account for the *Fermi* excess. I have shown that the diffuse emission recently reported by the H.E.S.S. Collaboration can be jointly accounted for by such a population of pulsars and a spike of heavy annihilating dark matter.

Furthermore, I have also started to explore the phenomenology of annihilating dark matter particles at the centers of active galaxies like M87 and Cen A. I have demonstrated that these galaxies are actually excellent laboratories in particular for indirect dark matter searches. Moreover, the centers of these galaxies are essentially unknown territory regarding the dark matter problem. This is due to the insufficient angular resolution of previous instruments, but the situation is going to change thanks to experiments like the Event Horizon Telescope, with micro-arcsecond-scale angular resolution. Dynamically young galaxies like M87 or Cen A are more likely to have conserved dark matter spikes in their central regions, which makes them ideal targets to search for strong annihilation signatures. In this context, I have developed novel models of the diffuse emission in the central region of M87. Comparing the spectral energy distribution expected from a dark matter spike with observations of the M87 galaxy has allowed me to derive extremely strong constraints on the annihilation cross-section as a function of dark matter mass, excluding thermal s-wave dark matter over the entire mass range relevant for WIMPs. My work therefore provides a strong motivation to perform more dedicated searches for dark matter spikes.

I have also investigated the interpretation of the spectral hardening that I reported in the *Fermi*  $\gamma$ -ray data of the core of Cen A and shown that the case for a new population of electrons and positrons injected either by a spike of annihilating TeV dark matter or a population of millisecond pulsars is very strong. This work paves the way for even more spectacular discoveries on high-energy astrophysical processes at the centers of galaxies.

Finally, one of the most exciting aspects of my thesis is certainly related to the Event Horizon Telescope, which thanks to its micro-arcsec-scale angular resolution, has the ability to image the shadow of the central black hole imprinted in the synchrotron emission induced by a dark matter spike. My predictions for M87 are extremely promising, showing that the Event Horizon Telescope can probe very weakly annihilating dark matter in the vicinity of the black hole. The Event Horizon Telescope is an outstanding instrument, with great potential to shed light on the complex regions surrounding supermassive black holes, and its relevance to the dark matter problem must be investigated further.

There are many potential applications of the formalism I have generated in this thesis. Much of the analysis I have developed could also be applied to decaying dark matter. Indeed, decaying DM is an interesting alternative for some of the phenomenology discussed here such as the positron excess. However, decaying dark matter cannot account for one of the central phenomena I have modeled, namely the morphology of the Galactic center excess(es). Another application is to the wide diversity of subhalo dark matter profiles encountered in the new generation of numerical simulations as a consequence of the complex baryonic physics. Yet another will be to refine the Event Horizon Telescope predictions to include more realistic jet physics, particle acceleration and diffusion.

To conclude, my work opens a new path towards a better understanding of the physical processes taking place at the centers of galaxies, including dark matter annihilation, but also astrophysical sources like pulsars. I have demonstrated that studying the very inner dark matter profile in galaxies is essential and can provide new information on the properties of dark matter. In this context, many directions need to be explored more thoroughly if we are to finally elucidate the nature of dark matter. The formation and evolution of spikes must be investigated, for instance using dedicated numerical simulations, since it can lead to more accurate predictions

regarding the observability of spikes, and I intend to get involved in projects dedicated to this task in the future. Quantifying the probability of survival of dark matter is also of great interest for the modeling of the isotropic  $\gamma$ -ray background, and may lead to strong constraints on the history of the Universe. Moreover, I intend to examine further the scattering of dark matter particles with relativistic particles in AGN jets, which can have very interesting implications including for non-annihilating dark matter. Finally, the tools and models I have developed in my thesis are also extremely relevant in the context of future experiments like the Cherenkov Telescope Array or future particle accelerators reaching 100 TeV center-of-mass energy, and satellite experiments like ATHENA.

Should the hint for a new mediator of interactions between dark and ordinary matter at LHC be confirmed, this would take us one step closer to the solution of the dark matter problem. In any event, exploiting new astrophysical probes will be instrumental in unraveling the mystery of dark matter.



# Appendices



# Appendix A

## Technical details

### Contents

---

<b>A.1</b>	<b>Integral over the line of sight</b>	<b>178</b>
A.1.1	Projection of a three-dimensional profile over the line of sight	178
A.1.2	Coordinate systems in the Milky Way	179
<b>A.2</b>	<b>Normalization of the dark matter profile in M87 and Centaurus A</b>	<b>179</b>
A.2.1	M87	179
A.2.2	Cen A	180
<b>A.3</b>	<b>Synchrotron self-Compton jet model</b>	<b>181</b>
<b>A.4</b>	<b>Solving the cosmic-ray equation with advection towards the black hole</b>	<b>182</b>

---

## A.1 Integral over the line of sight

### A.1.1 Projection of a three-dimensional profile over the line of sight

Here we present a simple way of projecting a three-dimensional (3D) profile along the line of sight (l.o.s.), which can be used as a consistency test when computing e.g. intensities of DM-induced signals at the center of galaxies. The geometry of the problem is illustrated in Fig. A.1.

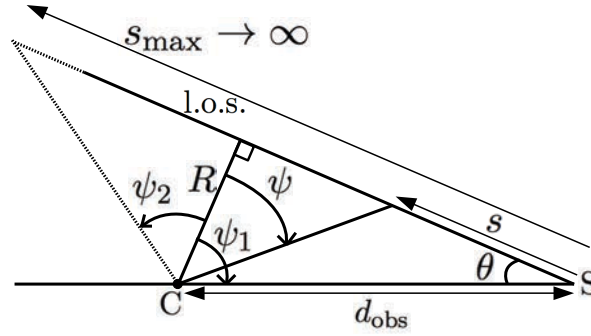


**Figure A.1** – Geometry of the problem for the line-of-sight projection of a 3D profile.

Let us consider a 3D profile  $j(r)$ .  $r$  is the radius associated with the 3D profile, related to the projected radius  $R$  and the angle  $\theta$  from the center via

$$r = \frac{R}{\cos \psi}. \quad (\text{A.1})$$

Since we are interested in practice in the inner region of a given galaxy, we consider the situation in which  $\theta \ll \pi/2$ . In this case,  $R \approx d_{\text{obs}}\theta$ , with  $d_{\text{obs}}$  the distance between the observer and the center of the galaxy. The l.o.s. coordinate can be written in terms of  $\psi$ :

$$s = -R \tan \psi_1 + R \tan \psi. \quad (\text{A.2})$$

Therefore the projected profile, given by the integral of the 3D profile over the l.o.s. coordinate, reads

$$I(R) = \int_0^\infty j(r) ds = \int_{\psi_1}^{\psi_2} j\left(\frac{R}{\cos \psi}\right) \frac{R}{\cos^2 \psi} d\psi, \quad (\text{A.3})$$

with  $\psi_1 = -(\pi/2 - \theta) \approx -\pi/2$  and  $\psi_2 = \pi/2$ . As a result, for a 3D profile following a power law,  $j(r) \propto r^{-\alpha}$ , the projected profile reads

$$\begin{aligned} I(R) &\propto \int_{-\pi/2}^{\pi/2} \left(\frac{R}{\cos \psi}\right)^{-\alpha} \frac{R}{\cos^2 \psi} d\psi \\ &\propto R^{-\alpha+1} \underbrace{\int_{-\pi/2}^{\pi/2} (\cos \psi)^{\alpha-2} d\psi}_{\text{independent of } R}. \end{aligned} \quad (\text{A.4})$$

Consequently, in terms of the angular projected radius  $\theta$ , the projected profile reads

$$I(\theta) \propto \theta^{-\alpha+1}. \quad (\text{A.5})$$

In particular, in the context of DM annihilation, the emissivity is usually proportional to the square of the DM density<sup>1</sup> which follows a power law,  $\rho \propto r^{-\gamma}$ , so the intensity is proportional to  $\theta^{-2\gamma+1}$ .

<sup>1</sup>This is the case e.g. for prompt emission or when spatial diffusion is negligible.

### A.1.2 Coordinate systems in the Milky Way

To compute photon intensities, we use the relations between the Cartesian coordinates and longitude  $l$  and latitude  $b$  obtained by considering the geometry of the diffusion zone (see Fig. A.2), which read for the MW:

$$\begin{aligned} x &= d_{\text{obs}} - s \cos b \cos l, \\ y &= -s \cos b \sin l, \\ z &= s \sin b, \end{aligned} \quad (\text{A.6})$$

with  $s$  the radial coordinate along the line of sight and  $d_{\text{obs}} \approx 8.5$  kpc is the distance between the Earth and the GC.

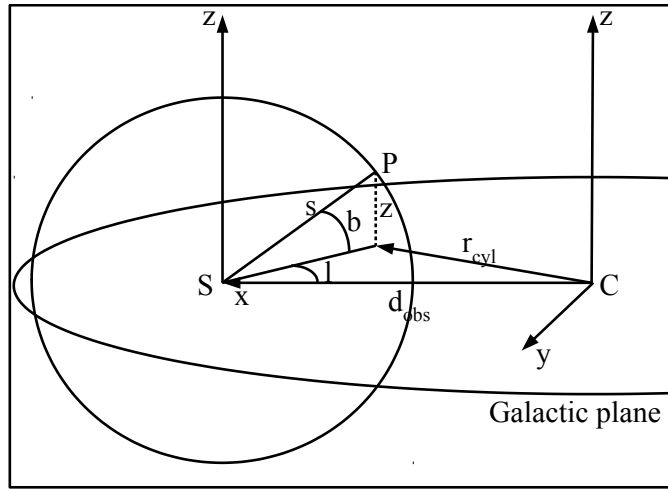


**Figure A.2** – Coordinate systems for cosmic rays in the Galaxy. For propagation, cylindrical coordinates centered on the GC denoted as C are used. Sky maps are based on spherical coordinates centered on the Sun S.  $l$  and  $b$  are the longitude and latitude of the observed point P, and  $s$  is the radial coordinate along the line of sight.

## A.2 Normalization of the dark matter profile in M87 and Centaurus A

### A.2.1 M87

Here we describe the way we normalize, for the M87 galaxy, the profile corresponding to a DM spike growing from an initial profile  $\propto \rho_0 (r/r_0)^{-\gamma}$ , described in Chapter 3:

$$\rho(r) = \begin{cases} 0 & r < 4R_S \\ \frac{\rho_{\text{sp}}(r)\rho_{\text{sat}}}{\rho_{\text{sp}}(r) + \rho_{\text{sat}}} & 4R_S \leq r < R_{\text{sp}} \\ \rho_0 \left(\frac{r}{r_0}\right)^{-\gamma} \left(1 + \frac{r}{r_0}\right)^{-2} & r \geq R_{\text{sp}}, \end{cases} \quad (\text{A.7})$$

where the saturation density determined by DM annihilations reads

$$\rho_{\text{sat}} = \frac{m_{\text{DM}}}{\langle \sigma v \rangle t_{\text{BH}}}, \quad (\text{A.8})$$

with  $m_{\text{DM}}$  and  $\langle\sigma v\rangle$  respectively the mass and annihilation cross-section of the DM particle, and  $t_{\text{BH}}$  the age of the BH. The spike profile reads

$$\rho_{\text{sp}}(r) = \rho_{\text{R}} g_{\gamma}(r) \left(\frac{R_{\text{sp}}}{r}\right)^{\gamma_{\text{sp}}}, \quad (\text{A.9})$$

where  $g_{\gamma}(r) \approx (1 - 4R_{\text{S}}/r)^3$ ,  $\rho_{\text{R}} = \rho_0 (R_{\text{sp}}/r_0)^{-\gamma}$ ,  $R_{\text{sp}} = \alpha_{\gamma} r_0 (M_{\text{BH}}/(\rho_0 r_0^3))^{\frac{1}{3-\gamma}}$  and  $\gamma_{\text{sp}} = (9 - 2\gamma)/(4 - \gamma)$ . We use  $M_{\text{BH}} = 6.4 \times 10^9 M_{\odot}$  for the mass of the BH (Gebhardt & Thomas, 2009), the corresponding Schwarzschild radius is  $R_{\text{S}} = 6 \times 10^{-4}$  pc, and we take  $\alpha_{\gamma} = 0.1$  and  $t_{\text{BH}} = 10^{10}$  yr. We fix  $r_0 = 20$  kpc for the halo (similarly to the Milky Way), and we must then determine the normalization  $\rho_0$ .

We choose  $\rho_0$  in such a way that the profile is compatible with both the total mass of the galaxy and the mass enclosed within the radius of influence of the BH, of order  $10^5 R_{\text{S}}$ . We thus follow the procedure described in Gorchtein et al. (2010): the DM mass within the region that is relevant for the determination of the BH mass, typically within  $R_0 = 10^5 R_{\text{S}}$ , must be smaller than the uncertainty on the BH mass  $\Delta M_{\text{BH}}$ .  $\rho_0$  is thus obtained by solving the following equation:

$$\int_{4R_{\text{S}}}^{10^5 R_{\text{S}}} 4\pi r^2 \rho(r) dr = \Delta M_{\text{BH}}, \quad (\text{A.10})$$

with  $\Delta M_{\text{BH}} = 5 \times 10^8 M_{\odot}$ . Considering the complex dependence of  $\rho$  on  $\rho_0$ , we use the fact that the mass is dominated by the contribution from  $r \gg R_{\text{S}}$ , i.e., typically  $r > R_{\text{min}} = \mathcal{O}(100R_{\text{S}})$ . In this regime we have  $\rho \sim \rho_{\text{sp}}(r)$ . We can also factorize the dependence on  $\rho_0$  in  $\rho_{\text{sp}}$ ,  $\rho_{\text{sp}}(r) = g_{\gamma}(r) \rho_0^{\frac{1}{4-\gamma}} (R'_{\text{sp}}/r_0)^{-\gamma} (R'_{\text{sp}}/r)^{\gamma_{\text{sp}}}$ , with  $R'_{\text{sp}} = \alpha_{\gamma} r_0 (M_{\text{BH}}/r_0^3)^{\frac{1}{3-\gamma}}$ , and we finally obtain

$$\rho_0 = \left( \frac{(3 - \gamma_{\text{sp}}) \Delta M_{\text{BH}}}{4\pi R_{\text{sp}}'^{\gamma_{\text{sp}}-\gamma} r_0^{\gamma} (R_0^{3-\gamma_{\text{sp}}} - R_{\text{min}}^{3-\gamma_{\text{sp}}})} \right)^{4-\gamma}. \quad (\text{A.11})$$

Numerically, we get  $\rho_0 \approx 2.5 \text{ GeV cm}^{-3}$  for  $\gamma = 1$ . Finally, the total mass within 50 kpc is  $\sim 4 \times 10^{12} M_{\odot}$ , compatible with the value derived from observations,  $6 \times 10^{12} M_{\odot}$  (Merritt & Tremblay, 1993).

For completeness, we also consider the case of a DM cusp without a spike. In that case the profile is given by:

$$\rho(r) = \begin{cases} 0 & r < 4R_{\text{S}} \\ \rho_{\text{sat}} & 4R_{\text{S}} \leq r < r_{\text{sat}} \\ \rho_0 \left(\frac{r}{r_0}\right)^{-\gamma} \left(1 + \frac{r}{r_0}\right)^{-2} & r \geq r_{\text{sat}}, \end{cases} \quad (\text{A.12})$$

where  $r_{\text{sat}} = r_0 (\rho_0/\rho_{\text{sat}})^{1/\gamma}$ , with the same value of  $\rho_0$  as in the presence of a spike.

In practice for M87 we take  $\gamma = 1$ , which corresponds to the NFW profile. The corresponding spike has a power-law index of  $\gamma_{\text{sp}} = 7/3$ .

### A.2.2 Cen A

For Cen A we use the same procedure to normalize the DM profile as for M87 (Sec. A.2.1). For numerical estimates, we use  $M_{\text{BH}} = 5.5 \times 10^7 M_{\odot}$  for the BH mass (Neumayer, 2010), the corresponding Schwarzschild radius is  $R_{\text{S}} = 5 \times 10^{-6}$  pc, and we take  $t_{\text{BH}} = 10^{10}$  yr. We fix  $r_0 = 20$  kpc for the halo (as for the Milky Way), and we must then determine the normalization of the spike, defined by  $\rho_0$ , by solving Eq. (A.10) with  $\Delta M_{\text{BH}} = 3 \times 10^7 M_{\odot}$  for Cen A. Numerically, we get  $\rho_0 \approx 1 \text{ GeV cm}^{-3}$  for  $\gamma = 1$ , while we take  $R_{\text{sp}} \approx 10^8 R_{\text{S}}$  for the spike radius so that the total mass of the galaxy within 50 kpc is equal to the measured mass of  $\sim 10^{12} M_{\odot}$  (Woodley et al., 2007).

The resulting DM profile featuring a spike with slope  $\gamma_{\text{sp}} = 7/3$ , for a DM mass of 3 TeV and annihilation cross-section  $\sim 10^{-32} \text{ cm}^3 \text{ s}^{-1}$  found to give the best fit to the  $\gamma$ -ray spectrum of the core of Cen A, is shown in Fig. A.3.

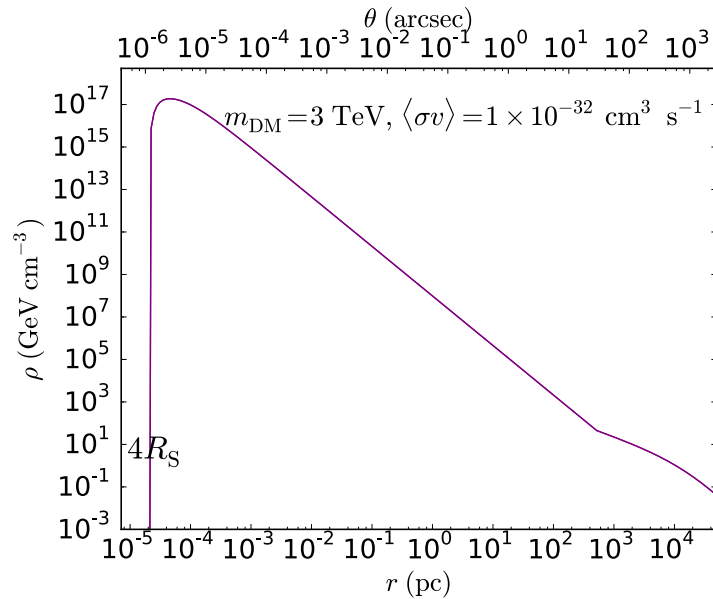


**Figure A.3** – DM profile in Cen A in the presence of a SMBH-induced spike with slope  $\gamma_{\text{sp}} = 7/3$ , for a DM mass of 3 TeV and annihilation cross-section  $\sim 10^{-32} \text{ cm}^3 \text{ s}^{-1}$  found to give the best fit to the  $\gamma$ -ray spectrum of the core of Cen A. For these DM parameters, the annihilation plateau characterized by the saturation density given in Eq. (A.8) falls below the horizon of the BH.

### A.3 Synchrotron self-Compton jet model

Here, we summarize the leptonic SSC model for the spectral energy distribution of M87 described in Finke et al. (2008) and used by the *Fermi* Collaboration in Abdo et al. (2009). All the primed quantities are defined in the rest frame of the plasma blob. Considering that the redshift of M87 is 0.00428,<sup>2</sup> we neglect redshift effects in our discussion. Following the notations of Finke et al. (2008), the observed synchrotron flux  $\nu F_\nu$  is denoted  $f_\epsilon$ , where  $\epsilon = h\nu/(m_e c^2)$  is the dimensionless energy of the emitted synchrotron in the observer’s frame. The observed synchrotron flux, rewritten in terms of dimensionless energies, and taking into account the Doppler boost, reads:

$$f_\epsilon^{\text{syn}} = \frac{\sqrt{3}\delta_D^4 \epsilon' e^3 B c}{4\pi h d^2} \int_1^\infty N'_e(\gamma') F_i(x(\epsilon', \gamma')), \quad (\text{A.13})$$

where  $\delta_D$  is the Doppler factor,  $\epsilon' = \epsilon/\delta_D$ , and  $d = 16 \text{ Mpc}$  is the distance of M87.  $N'_e = n'_e V'_b$  is the electron distribution in the rest frame of the blob, with  $n'_e$  the electron number density, and  $V'_b$  the volume of the blob.  $x = \nu'/\nu'_c$  is rewritten in terms of the dimensionless quantities:

$$x(\epsilon', \gamma') = \frac{4\pi \epsilon' m_e^2 c^2}{3e B h \gamma'^2}. \quad (\text{A.14})$$

Note that the intensity of the magnetic field  $B$  is not primed but is also defined in the rest frame of the blob. For the isotropic synchrotron emission spectrum  $F_i$ , we take the parametrization of Crusius & Schlickeiser (1986), also used in Finke et al. (2008). For the electron distribution, we

<sup>2</sup>[http://messier.seds.org/xtra/supp/m\\_NED.html](http://messier.seds.org/xtra/supp/m_NED.html)

consider as in [Abdo et al. \(2009\)](#) a broken power law:

$$N_e'(\gamma') = K \begin{cases} \gamma'^{-p_1} & 1 \leq \gamma' \leq \gamma'_1 \\ \gamma'_1^{p_2-p_1} \gamma'^{-p_2} & \gamma'_1 < \gamma' \leq \gamma'_2, \end{cases} \quad (\text{A.15})$$

where  $\gamma'_1 = 4 \times 10^3$  is the Lorentz factor at the break and  $\gamma'_2 = 10^7$  is the maximum Lorentz factor of the electrons.

From there, the observed SSC flux is given by [Finke et al. \(2008\)](#)

$$f_{\epsilon_s}^{\text{SSC}} = \frac{9\sigma_{\text{T}}\epsilon_s'^2}{16\pi\delta_{\text{D}}^2 c^2 t_{\text{v,min}}^2} \int_0^\infty \frac{f_\epsilon^{\text{syn}}}{\epsilon'^3} \int_{\gamma'_{\text{min}}}^{\gamma'_{\text{max}}} \frac{N_e'(\gamma')}{\gamma'^2} F_{\text{C}}(q, \Gamma) d\gamma' d\epsilon', \quad (\text{A.16})$$

where  $t_{\text{v,min}} = R'_b/(\delta_{\text{D}}c)$  is the variability time scale of the source,  $R'_b$  being the (comoving) radius of the blob.  $\epsilon'_s$  is the dimensionless energy of the scattered photon. The ICS process is encoded in  $F_{\text{C}}(q, \Gamma)$  which reads

$$F_{\text{C}}(q, \Gamma) = 2q \ln q + (1 + 2q)(1 - q) + \frac{(\Gamma q)^2}{2(1 + \Gamma q)}(1 - q) \quad (\text{A.17})$$

if  $1/(4\gamma'^2) \leq q \leq 1$  and  $F_{\text{C}}(q, \Gamma) = 0$  otherwise.  $q$  and  $\Gamma$  are given by:

$$q = \frac{\epsilon'_s/\gamma'}{\Gamma(1 - \epsilon'_s/\gamma')}, \quad \Gamma = 4\epsilon'\gamma'. \quad (\text{A.18})$$

The kinematically allowed range of values for  $q$  translates into the integration bounds in Eq. (A.16):

$$\gamma'_{\text{min}} = \frac{1}{2}\epsilon'_s \left( 1 + \sqrt{1 + \frac{1}{\epsilon'\epsilon'_s}} \right), \quad (\text{A.19})$$

$$\gamma'_{\text{max}} = \begin{cases} \frac{\epsilon'\epsilon'_s}{\epsilon' - \epsilon'_s} & \epsilon' > \epsilon'_s \\ \gamma'_2 & \epsilon' \leq \epsilon'_s. \end{cases} \quad (\text{A.20})$$

## A.4 Solving the cosmic-ray equation with advection towards the black hole

The propagation equation of electrons and positrons in the presence of advection and synchrotron losses,

$$v \frac{\partial f}{\partial r} - \frac{1}{3r^2} \frac{\partial}{\partial r} (r^2 v) p \frac{\partial f}{\partial p} + \frac{1}{p^2} \frac{\partial}{\partial p} (p^2 \dot{p} f) = Q, \quad (\text{A.21})$$

can be rewritten as:

$$\frac{\partial f}{\partial r} + \frac{\dot{p}_{\text{ad}} + \dot{p}_{\text{syn}}}{v} \frac{\partial f}{\partial p} = -\frac{1}{vp^2} \frac{\partial}{\partial p} (p^2 \dot{p}_{\text{syn}}) f + \frac{Q}{v}, \quad (\text{A.22})$$

where  $\dot{p}_{\text{ad}}$  is the momentum gain rate due to adiabatic compression in the advection process, and  $v(r)$  the velocity field of the accretion flow. The associated characteristic curves are obtained by solving the following differential equation:

$$\frac{dp}{dr} = \frac{\dot{p}_{\text{ad}} + \dot{p}_{\text{syn}}}{v}. \quad (\text{A.23})$$

Generalizing the method of [Aloisio et al. \(2004\)](#) to an arbitrary power-law profile for the magnetic field,  $B(r) = B_0 (r/R_{\text{S}})^{-\alpha/2}$ , solving Eq. (A.23) with initial condition  $p(R_{\text{inj}}) = p_{\text{inj}}$  leads to

$$p(r; R_{\text{inj}}, p_{\text{inj}}) = p_{\text{inj}} \left[ \frac{k_0 R_{\text{S}}^{\alpha-1/2}}{(\alpha-1)c} r^{\frac{3}{2}-\alpha} p_{\text{inj}} \left( 1 - \left( \frac{r}{R_{\text{inj}}} \right)^{\alpha-1} \right) + \left( \frac{r}{R_{\text{inj}}} \right)^{\frac{1}{2}} \right]^{-1}, \quad (\text{A.24})$$

where

$$k_0 = \frac{2\sigma_{\text{T}}B_0^2}{3\mu_0(m_e c)^2}. \quad (\text{A.25})$$

For  $\alpha = 5/2$  we recover the result for the equipartition magnetic field (Aloisio et al., 2004). Here we consider the case  $\alpha = 0$ , corresponding to a homogeneous magnetic field.

The solution of the propagation equation in the ultrarelativistic regime is then given by

$$f(r, p) = \frac{1}{c} \left( \frac{r}{R_S} \right) \int_r^{r_{\text{acc}}} Q_i(R_{\text{inj}}, p_{\text{inj}}) \left( \frac{R_{\text{inj}}}{R_S} \right)^{\frac{5}{2}} \left( \frac{p_{\text{inj}}}{p} \right)^4 dR_{\text{inj}}, \quad (\text{A.26})$$

where  $p_{\text{inj}} \equiv p_{\text{inj}}(R_{\text{inj}}; r, p)$  is the injection momentum of an electron injected at  $R_{\text{inj}} (\geq r)$  and arriving at  $r$  with momentum  $p$ . Using Eq. (A.24) and expressing  $p_{\text{inj}}$  as a function of  $p$ , we obtain, for  $\alpha = 0$ :

$$p_{\text{inj}}(R_{\text{inj}}; r, p) = p \left[ \frac{k_0 R_S^{-\frac{1}{2}}}{c} R_{\text{inj}}^{\frac{3}{2}} p \left( \frac{r}{R_{\text{inj}}} - 1 \right) + \left( \frac{R_{\text{inj}}}{r} \right)^{\frac{1}{2}} \right]^{-1}. \quad (\text{A.27})$$

Note that the denominator of  $p_{\text{inj}}$  can vanish and become negative, leading to nonphysical values of the injection momentum. This is related to the efficiency of the accretion flow and characterizes the region of the injection parameters  $(R_{\text{inj}}, p_{\text{inj}})$  corresponding to a given arrival point  $(r, p)$ . In practice,  $p_{\text{inj}}$  remains positive for  $R_{\text{inj}} < R_{\text{inj}}^0$  where

$$R_{\text{inj}}^0 = r + \frac{c}{k_0 p} \left( \frac{r}{R_S} \right)^{-\frac{1}{2}}. \quad (\text{A.28})$$

We then use this value as an effective upper bound for the integral of Eq. (A.26).



## Appendix B

# *Fermi*-LAT observations and data analysis of Cen A

Here we outline the analysis of the *Fermi*-LAT data of Cen A which led to the discovery of a hardening in the  $\gamma$ -ray spectrum.

### Contents

---

<b>B.1</b>	<b>Description of the data . . . . .</b>	<b>186</b>
<b>B.2</b>	<b>Models . . . . .</b>	<b>186</b>
<b>B.3</b>	<b>Spectrum . . . . .</b>	<b>188</b>
<b>B.4</b>	<b>Systematic error . . . . .</b>	<b>191</b>
<b>B.5</b>	<b>Luminosity . . . . .</b>	<b>193</b>
<b>B.6</b>	<b>Variability . . . . .</b>	<b>193</b>

---

## B.1 Description of the data

The data used in this study comprises all *Fermi*-LAT PASS8 event and spacecraft data taken during the first  $\sim 7.5$  years of *Fermi*-LAT operation, from 2008 August 4 to 2016 January 13. This time period equates to a Mission Elapsed Time (MET) of 239557417 to 474346804. Throughout the analysis *Fermi science tools* v10R0P5 were used in conjunction with the PASS8 instrument response functions (IRFs) of P8\_SOURCE\_V6.

All  $\gamma$ -ray events in the 0.1–300 GeV energy range were considered within a  $15^\circ$  radius of interest (ROI) centered on the core of Centaurus A ( $\alpha_{J2000}, \delta_{J2000}$ ) = ( $201^\circ.365, -43^\circ.0191$ ). In accordance with PASS8 data analysis criteria<sup>1</sup>, the raw data was first filtered by selecting events with EVENT TYPE=3 and EVENT CLASS=128. This filtering selects SOURCE  $\gamma$ -ray events and is recommended for analysis of point sources off the galactic plane. Once source events were selected, a cut on the maximum zenith angle of  $90^\circ$  was applied to remove  $\gamma$ -rays created by cosmic rays interacting with the Earth’s atmosphere. No ROI-based angle cut was applied again in accordance with PASS8 data analysis criteria. To further clean the data and select good time intervals, the (DATA\_QUAL > 0) && (LAT\_CONFIG == 1) filter expression was applied. A summary of the analysis criteria is given in Table B.1.

**Table B.1** – Summary of the criteria utilised in this analysis.

Science Tools version	v10R0P5
IRF	P8_SOURCE_V6
Event class	SOURCE, Pass 8
Photon Energies	0.1–300 GeV
RoI	$15^\circ$
Zenith angle cut	$< 90^\circ$
Data quality	$> 0$
LAT config	1
Galactic diffuse model	gll_iem_v06.fit
Isotropic diffuse model	iso_P8R2_SOURCE_V6_v06.txt

## B.2 Models

During the likelihood analyses used in our study, a model file consisting of diffuse, point and extended sources of  $\gamma$ -rays was employed. For the diffuse  $\gamma$ -ray emission, the most recent extragalactic, iso\_P8R2\_SOURCE\_V6\_v06.txt, and Galactic, gll\_iem\_v06.fit, models were used. The normalisation of both the Galactic and extragalactic diffuse models were left free to vary throughout the analysis. For the point source component of the model, all point sources within  $25^\circ$  of Cen A were considered, with the spectral shape and position of each source taken from the Third *Fermi* Source Catalog (3FGL; Acero et al. (2015)). The spectral indices and normalisations of all 66 of the 3FGL point sources within  $15^\circ$  of Cen A were left free to vary, while the 128 3FGL point sources within the  $15$ – $25^\circ$  annulus from Cen A had their spectral indices and normalisations frozen to their 3FGL values. In addition to Cen A’s radio lobes, there are two spatially extended sources of  $\gamma$ -rays within  $25^\circ$  of Cen A: HESS J1303-631 and MSH 15-52. The spatial profile of these sources were accounted for with the *Fermi*-LAT Collaboration’s HESSJ1303-631.FITS and MSH15-52.FITS templates respectively. Both HESS J1303-631 and MSH 15-52 are located in the  $15$ – $25^\circ$  annulus from Cen A’s core, and as such, had their spectral indices and normalisations frozen at their 3FGL values. Centaurus A itself was modelled as a combination of a point source

<sup>1</sup>See [http://fermi.gsfc.nasa.gov/ssc/data/analysis/documentation/Cicerone/Cicerone\\_Data\\_Exploration/Data\\_preparation.html](http://fermi.gsfc.nasa.gov/ssc/data/analysis/documentation/Cicerone/Cicerone_Data_Exploration/Data_preparation.html) for details on LAT data selection.

coincident with the core position taken from the 3FGL, and a spatially extended source coincident with the radio lobes of Cen A. The spectral index and normalisation of the spatial model of Cen A’s lobes were left free to vary during the likelihood fit.

To confirm the accuracy of the initial ‘diffuse + point + extended’ source model, a two-step BINNED likelihood analysis was undertaken. The first step involved an initial likelihood analysis. All point sources with a test statistic<sup>2</sup>, TS, less than 2 were then removed from the resultant best-fit model. This step was performed to remove any point sources that have reduced in flux to the extent that, over the 7.5 year period of our analysis, are insignificant sources. Thereafter, a second likelihood analysis was performed with this modified model. To confirm that all  $\gamma$ -ray sources present in the data are accounted for, the best-fit model from this second likelihood fit was used to construct a  $17^\circ \times 17^\circ$  ‘model map’ centered on  $(\alpha_{J2000}, \delta_{J2000}) = (201^\circ.365, -43^\circ.0191)$ . This model map was compared to the 7.5 year 0.1–300 GeV sky map to create a residuals count map<sup>3</sup>. Any positive excess in the residuals map above the expected statistical fluctuations indicates the presence of an additional source(s) present in the data that are not accounted for in the model. If new sources are present in the data, and not properly accounted for within the model file used during the likelihood analysis, they can create artifacts in Cen A’s spectrum.

The 0.1–300 GeV sky, model and residuals counts map for our analysis can be seen in Fig. B.1. In particular, with the largest positive excess being +0.1%, the residual map in Fig. B.1 shows no statistically significant excesses. This indicates that our initial ‘diffuse + point + extended’ source model accounts for all sources of  $\gamma$ -rays in our data set.

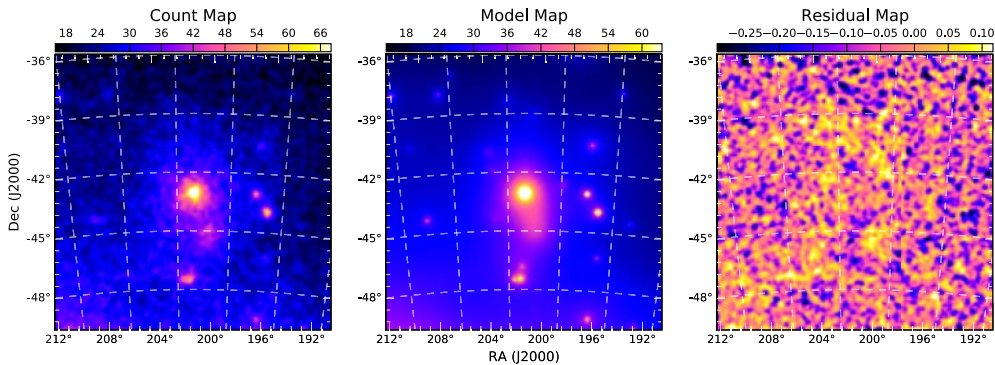


**Figure B.1 – Left:** A  $17^\circ \times 17^\circ$  sky map of all 0.1–300 GeV photons that passed the selection criteria, for the entire 7.5 year data set. The colour scale is in units of counts per pixel. **Middle:** A  $17^\circ \times 17^\circ$  model map of all 0.1–300 GeV photons produced with the *Fermi* tool GTMODEL, using the best-fit model from the 7.5 year binned likelihood analysis. The colour scale is in units of counts per pixel. **Right:** A  $17^\circ \times 17^\circ$  residuals map centered on the position of Cen A’s core. The residuals map is produced by  $((\text{sky map} - \text{model map}) / \text{model map})$  and is in units of percentage. The maximum positive excess is +0.1%, indicating that residuals map shows no evidence of new  $\gamma$ -ray sources beyond the ‘diffuse + point + extended’ source model used.

In addition to the sky, model and residuals maps of Fig. B.1, we also compared the  $\gamma$ -ray counts expected for the different components described in the model, taking a north-south and east-west slice across the lobes and core of Cen A, as done by the *Fermi*-LAT Collaboration in Abdo et al. (2010b). These slices can be seen in Fig. B.2, where  $0^\circ$  on both the top and bottom panel indicates the position of Cen A’s core. In Fig. B.2 we see that at  $0^\circ$ , above and below the break energy, the overall  $\gamma$ -ray counts are dominated by the flux component from Cen A’s core.

<sup>2</sup>The test statistic, TS, is defined as twice the difference between the log-likelihood of two different models,  $2[\log L - \log L_0]$ , where  $L$  and  $L_0$  are defined as the likelihood when the source is included or not respectively.

<sup>3</sup>The residuals count map was constructed via  $(\text{sky map} - \text{model map})$  divided by the model map (e.g. see Brown et al. (2015))

Furthermore, above the break energy, we see the total counts from the core region of Cen A is greater than low energy total counts from the same region.

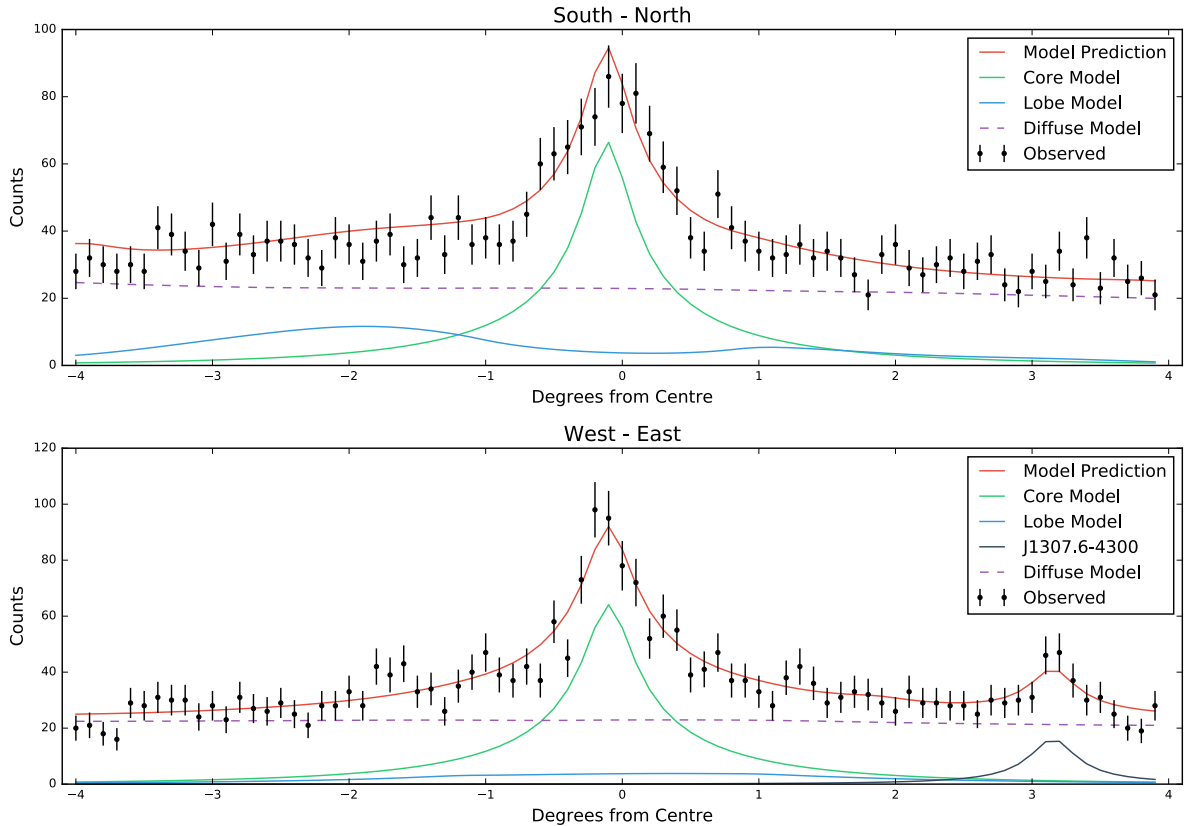


**Figure B.2 – Top:** A North-South slice in the counts map across Cen A’s core position. The counts are binned in  $0.1^\circ$  intervals, with all error bars represent a  $1\sigma$  level of statistical uncertainty. The total counts distribution predicted by the best-fit likelihood model is indicated by the red line. The dashed line indicates total contribution from the diffuse component of the model, with the green and blue lines representing the contribution from Cen A’s core and lobe emission respectively. **Bottom:** An East-West slice across the counts map. All contributions are shown as with the North-South slice, with the addition of the point source J1307.6-4300 which has a localised contribution to the observed counts at  $\sim 3^\circ$  east of Cen A’s core position.

### B.3 Spectrum

To investigate the  $\gamma$ -ray spectrum of Cen A’s core, the *Fermi* tool GTLIKE was used in conjunction with the best-fit model used for Fig. B.1, to analyse the 0.1–300 GeV data with ten logarithmically spaced energy bins. Of the ten energy bins, eight were detected with a  $TS > 25$ , equating to a  $> 5\sigma$  detection for each energy bin. The remaining bins,  $\sim 20$ –90 GeV and  $> 134$  GeV, were not detected at a statistically significant level, and as such we calculated an upper limit at a 95% confidence level. The resultant spectrum can be seen in Fig. B.3, with all error bars on the LAT data points representing a  $1\sigma$  level of statistical uncertainty.

Fig. B.3 shows a clear departure from the best-fit power law with a hardening of the spectrum above  $\sim 2$  GeV. To characterise this spectral feature, the likelihood analysis of the entire 0.1–300 GeV spectrum was performed assuming a broken power law spectral description of Cen A’s core. The likelihood of the broken-power law spectral description of Cen A’s core was compared to the likelihood of the power law fit via a likelihood ratio test. The resultant TS value of

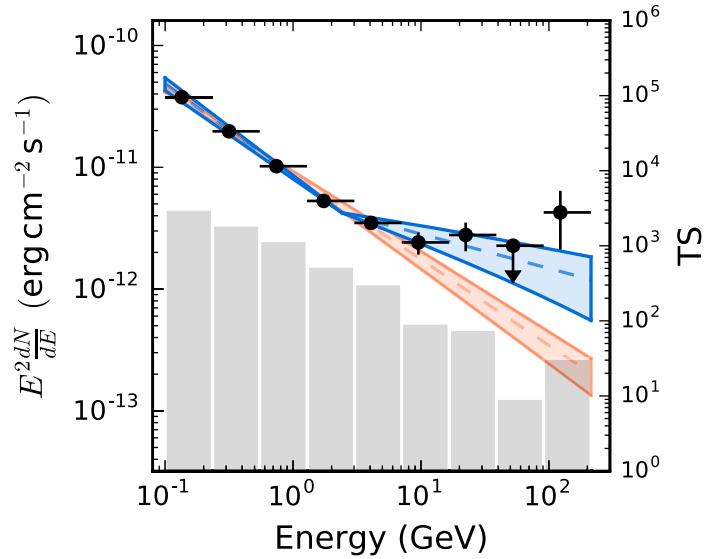


**Figure B.3** – The 0.1 to 300 GeV spectrum of Cen A’s core, as seen by the *Fermi*-LAT detector. The broken power-law model, shown in blue, is preferred over the power law model, shown in red, with a significance  $> 5\sigma$ . The grey histogram shows the TS value for each spectral bin. The bin with a TS  $< 25$ , is replaced with an upper limit at 95% confidence level.

this likelihood ratio test was  $TS \simeq 28$ , which equates to a significance of  $> 5\sigma$ , even after the increased number of free parameters of the broken power law are taken into consideration. As such, our analysis reveals the presence of a spectral hardening feature in the spectrum of Cen A’s core at a statistically significant level.

The best-fit broken power law has a break energy of  $E_{\text{break}} = (2.420 \pm 0.003_{\text{stat}})$  GeV, a lower energy spectral index of  $\Gamma_1 = -2.766 \pm 0.001_{\text{stat}}$  and a harder higher energy spectral index of  $\Gamma_2 = -2.282 \pm 0.014_{\text{stat}}$ . Meanwhile, the best-fit power law fit has a spectral index of  $\Gamma = -2.706 \pm 0.003_{\text{stat}}$ . Importantly, the broken power law model allows us to reconcile the *Fermi*-LAT data with previous H.E.S.S. observations, while extrapolating the single power law found at low energy would under predict the flux above 250 GeV by an order of magnitude. A combined *Fermi*-LAT and H.E.S.S. spectrum is shown in Fig. B.4.

With the statistical significance of spectral hardening feature verified, two additional likelihood analyses were undertaken below (0.1–2.4 GeV) and above (2.4–300 GeV) the break energy to search for faint sources in these energy bands that were missed by integrating over the larger 0.1–300 GeV energy range. As before, the best-fit model from these likelihood fits were used to construct a  $17^\circ \times 17^\circ$  ‘model map’ centered on  $(\alpha_{J2000}, \delta_{J2000}) = (201.365^\circ, -43.0191^\circ)$ . This model map was compared to the 7.5 year 0.1–300 GeV sky map to create a residuals count map. The sky, model and residuals map for the low energy component can be seen in Fig. B.5, while the maps for the high energy component can be seen in Fig. B.6. The maximum excess is 1% in the high energy residuals map, with the low energy residuals map showing a maximum excess of 0.2%. As such, fluctuations in the residuals maps for both components are consistent with statistical fluctuations, indicating that all  $\gamma$ -ray sources are accounted for and that the spectral hardening feature cannot be attributed to unmodelled point sources.

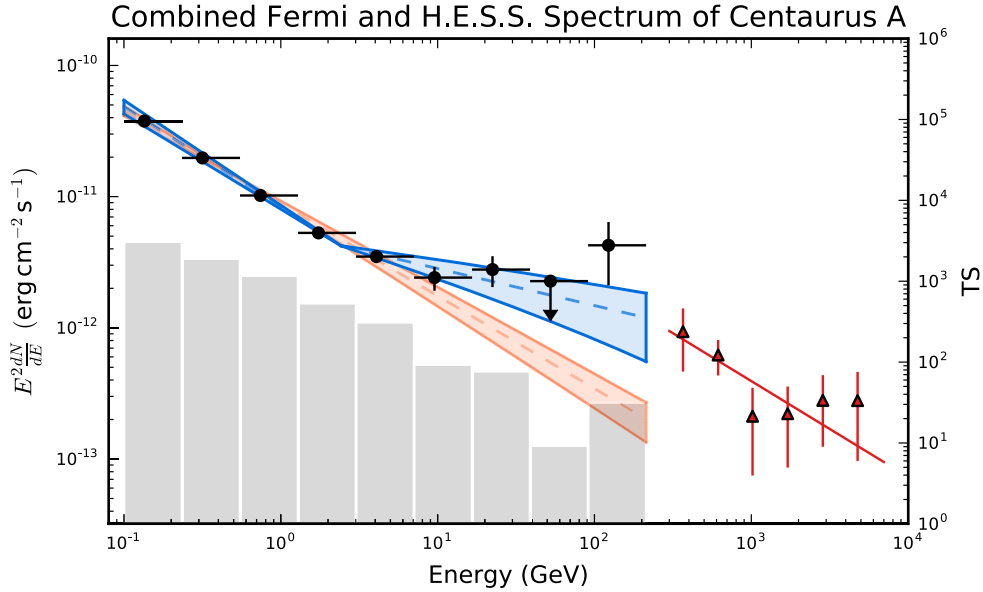


**Figure B.4** – A combined spectrum of our LAT analysis, shown with black circles, and the H.E.S.S. spectrum above  $E_\gamma = 250$  GeV, taken from [Aharonian et al. \(2009\)](#), shown in pink. The broken power-law model, shown in blue, is preferred over the power law model, shown in red, with a significance  $> 5\sigma$ . The grey histogram, with the right hand y axis, shows the TS value for each spectral bin for the LAT data points. The bin with a TS  $< 25$ , is replaced with an upper limit at 95% confidence level. Note that the last upper limit is not shown since it overlaps in energy with the H.E.S.S. data points. The broken power law fit allows for a smooth transition with the  $\gamma$ -ray spectrum reported here and the H.E.S.S. spectrum.

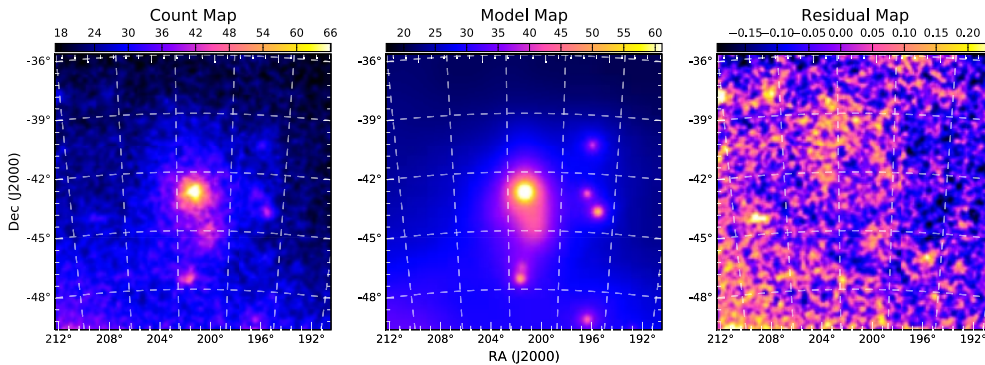


**Figure B.5** – **Left:** A  $17^\circ \times 17^\circ$  sky map of all 0.1–2.4 GeV photons that passed the selection criteria, for the entire 7.5 year data set. The colour scale is in units of counts per pixel. **Middle:** A  $17^\circ \times 17^\circ$  model map of all 0.1–2.4 GeV photons produced with the *Fermi* tool GTMODEL, using the best-fit model from the 7.5 year binned likelihood analysis. The colour scale is in units of counts per pixel. **Right:** A  $17^\circ \times 17^\circ$  residuals map of the low energy flux below the break energy, centered on the position of Cen A’s core. The residuals map is produced by (sky map–model map) divided by the model map and is in units of percentage. The residuals map shows no evidence of new 0.1–2.4  $\gamma$ -ray sources beyond the ‘diffuse + point + extended’ source model used.

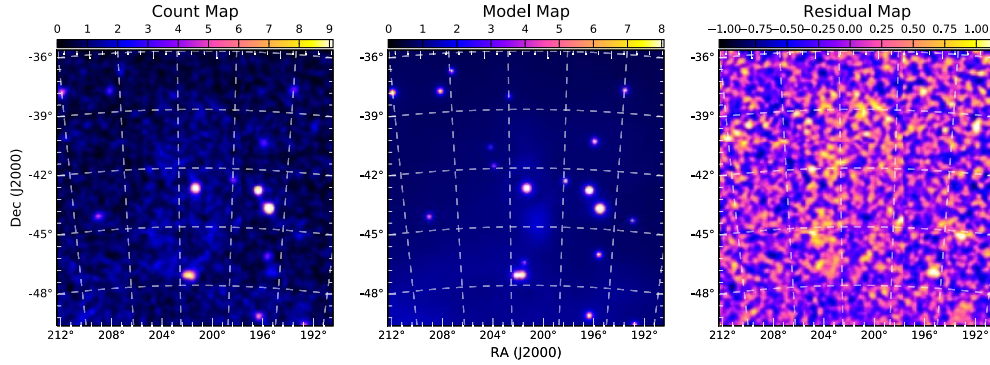


**Figure B.6** – **Left:** A  $17^\circ \times 17^\circ$  sky map of all 2.4–300 GeV photons that passed the selection criteria, for the entire 7.5 year data set. The colour scale is in units of counts per pixel. **Middle:** A  $17^\circ \times 17^\circ$  model map of all 2.4–300 GeV photons produced with the *Fermi* tool GTMODEL, using the best-fit model from the 7.5 year binned likelihood analysis. The colour scale is in units of counts per pixel. **Right:** A  $17^\circ \times 17^\circ$  residuals map of the high energy flux above the break energy, centered on the position of Cen A’s core. The residuals map is produced by (sky map–model map) divided by the model map and is in units of percentage. The residuals map shows no evidence of new 2.4–300  $\gamma$ -ray sources beyond the ‘diffuse + point + extended’ source model used.

## B.4 Systematic error

Following the approach of the *Fermi*-LAT Collaboration in [Ackermann et al. \(2012b\)](#), the systematic errors of our analysis were investigated. The main contribution to systematic error is the uncertainty in the LAT’s effective area  $A_{eff}$ , which matches Monte Carlo simulations to around 10% (and in most cases better). Taking this 10% value, and applying it to the *Fermi*-LAT IRFs, we have several options as to how to customize the energy dependence of  $A_{eff}$ .

If we have an uncertainty in the effective area of:

$$\epsilon(E) = \frac{\delta A_{eff}}{A_{eff}}, \quad (\text{B.1})$$

where  $\delta A_{eff}$  is the relative uncertainty on  $A_{eff}$ . By defining some bracketing functions  $B(E)$  which exist in the range  $[-1, +1]$ , we can define a modified  $A'_{eff}$  such as:

$$A'_{eff}(E, \theta) = A_{eff}(E, \theta) \cdot (1 + \epsilon(E)B(E)). \quad (\text{B.2})$$

There are two limiting cases to consider here:

- Limiting Fluxes – If we change  $A_{eff}$  by a flat multiplicative factor regardless of energy, we can find the maximised flux error of any given source. This corresponds to a bracketing function  $B(E) = \pm 1$
- Limiting Index – We can also alter  $A_{eff}$  maximally on either side of the decorrelation energy  $E_0$ , to maximise the error on the observed index. The bracketing function recommended in [Ackermann et al. \(2012b\)](#) is a tanh function such as:

$$B(E) = \pm \tanh \left( \frac{1}{k} \log \left( \frac{E}{E_0} \right) \right). \quad (\text{B.3})$$

The constant  $k$  determines the severity of the transition around  $E_0$ . A value of  $k = 0.13$  corresponds to smoothing over twice the LAT energy resolution.

We then applied these altered IRFs to our likelihood analysis of the spectrum of Cen A's core. Applying the same transformations of the IRFs as in Ackermann et al. (2012b) and re-analysing the central point source of Cen A, we investigated how the best fit power law transforms by finding the limiting fits for flux and index of a power law fit. These are plotted in the top and bottom panels of Fig. B.7 for  $\epsilon(E) = 0.1$ . Regardless of the fact that we investigated the worst case scenario for the systematic error, Fig. B.7 shows a clear excess in  $\gamma$ -ray events at the high energy tail of the spectrum when compared to a power law spectral model.

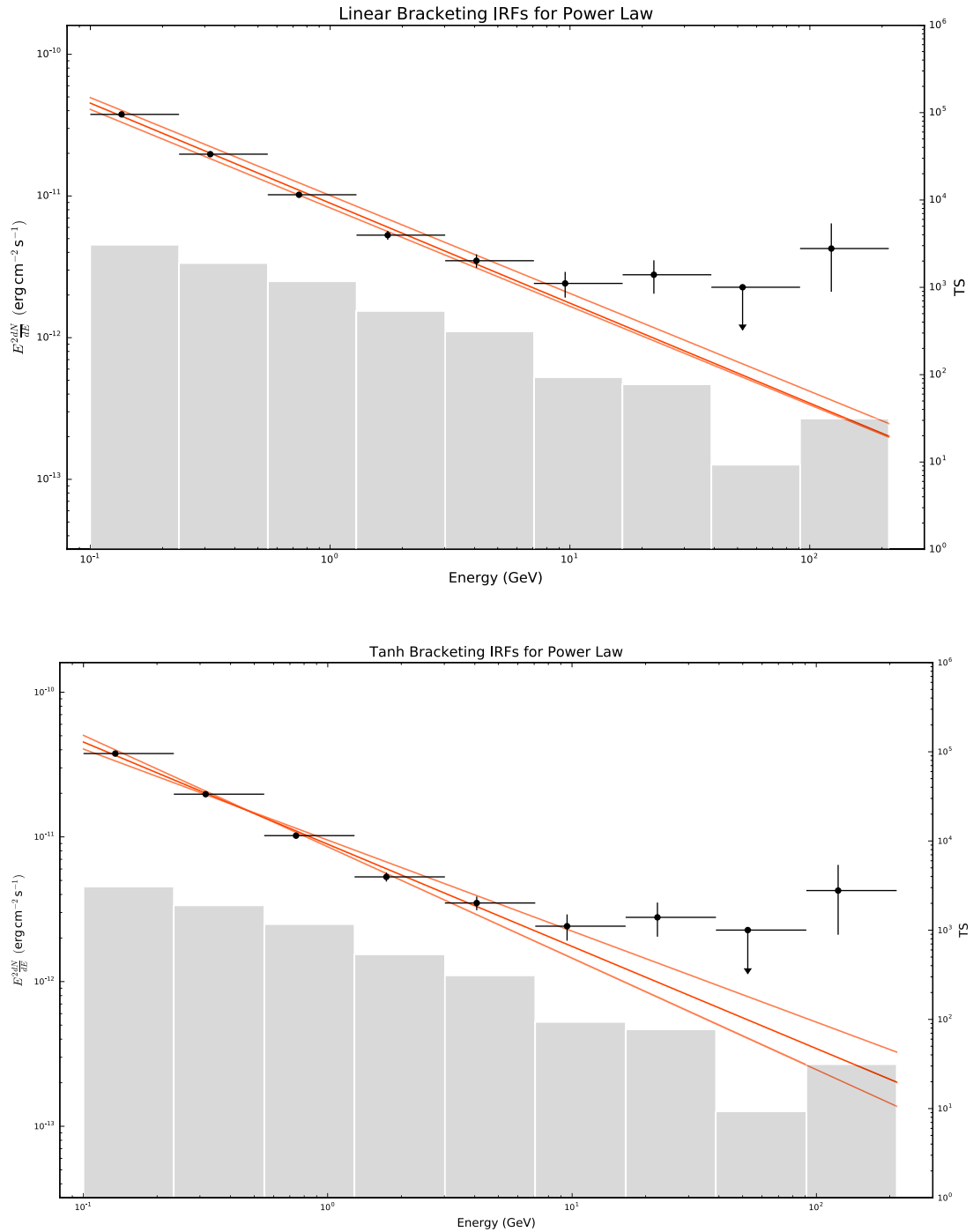


**Figure B.7 – Top:** The  $B(E) = \pm 1$  IRFs plotted either side of the naive  $B(E) = 0$  fit. **Bottom:** The tanh altered bracketing functions plotted either side of the naive  $B(E) = 0$  fit.

## B.5 Luminosity

Using the best-fit broken power law, the total energy flux from Cen A’s core in the 0.1–300 GeV energy range is  $\sim 1.1 \times 10^{-12}$  erg cm $^{-2}$  s $^{-1}$ . Assuming isotropic emission for the  $\gamma$ -ray emission and a luminosity distance of 3.8 million parsecs (1 parsec = 3.26 light years), the total luminosity of Cen A’s core in the 0.1–300 GeV is  $1.8 \times 10^{39}$  erg s $^{-1}$ . Interestingly, if we deconvolve the two spectral components, we find that the luminosity of the low and high energy components are comparable, with  $9.9 \times 10^{38}$  erg s $^{-1}$  and  $8.4 \times 10^{38}$  erg s $^{-1}$  respectively.

## B.6 Variability

To investigate the temporal characteristics of the two spectral components, we construct individual lightcurves for the  $\gamma$ -ray flux above and below the break energy. The 7.5 year data set was binned into 6 month temporal bins, with a likelihood analysis being applied to each bin separately. Only time intervals with a TS > 25 were considered. For temporal bins with TS < 25 an upper limit at the 95% confidence limit was calculated. The resultant lightcurves can be seen in Fig. B.8, with all error bars representing a  $1\sigma$  level of statistical uncertainty.

To determine if there was evidence for flux variability in either light curve, a constant flux value was fitted, with the normalisation left free to vary. The best-fit constant flux values are shown as a horizontal dashed line in each lightcurve. The constant flux value for the low energy lightcurve had a reduced  $\chi^2$  of 2.1 and a resultant probability of 1%. This indicates that the low energy lightcurve is variable at a 99% level of confidence. The constant flux value for the high energy lightcurve had a reduced  $\chi^2$  of 0.75, which illustrates a remarkably good fit and suggests that it is dominated by statistical errors. This goodness of fit suggests that, within the limitations of the statistical errors, that a constant flux is a good description of the high energy component of Cen A’s core.

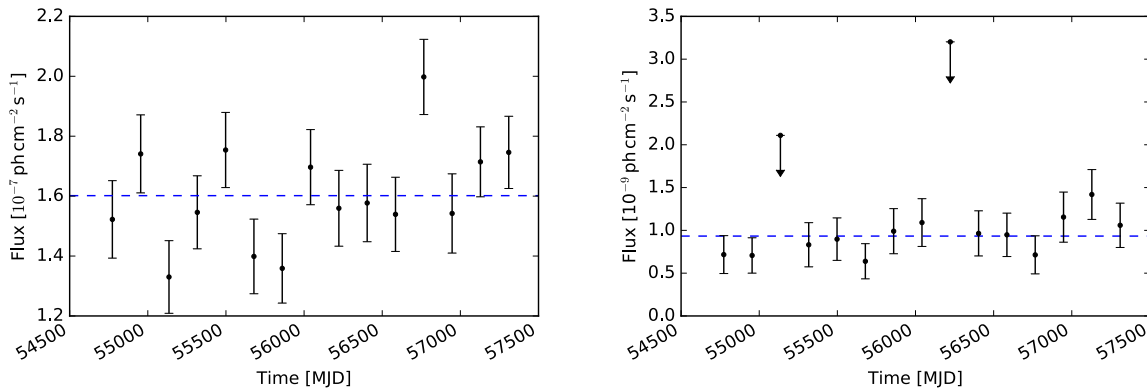


**Figure B.8** – **Left:** light curve of 0.1–2.4 GeV flux, binned in six month temporal bins. Each temporal bin has a TS > 25 and all error bars represent a  $1\sigma$  level of statistical uncertainty. The horizontal dashed line indicates the best-fit constant flux level. **Right:** light curve of 2.4–300 GeV flux, binned in six month temporal bins. All error bars represent a  $1\sigma$  level of statistical uncertainty. For temporal bins where the TS < 25, an upper limit was calculated at a 95% confidence level. The horizontal dashed line indicates the best-fit constant flux level.

The low energy light curve is the first indication that a component of the  $\gamma$ -ray flux from Cen A’s core is variable. There are a number of reasons why our analysis revealed this observational property while other studies of Cen A using the same *Fermi*-LAT observations did not (Abdo et al., 2010a). Firstly, this is the first study of Cen A’s core  $\gamma$ -ray emission with *Fermi*-LAT observations that use the PASS8 characterisation of events within the LAT detector. This new

PASS8 characterisation has resulted in a factor of  $\sim 2.3$  increase in photon acceptance at 100 MeV along with improved energy and angular resolution with reduced systematic errors (Atwood et al., 2013). These improvements in event characterisation allows the *Fermi*-LAT detector to be more sensitive to flux variation when compared to previous versions of data characterisation. Secondly, the light curve show in the left panel of Fig. B.8 shows a recent six month period where the flux is  $\sim 3.3\sigma$  away from the best-fit constant flux value, hinting at the possibility of recent flux variations.

## Appendix C

# Résumé détaillé en français

### C.1 Introduction

Élucider le mystère de la matière noire est l'un des plus grands défis de la physique moderne. Après un siècle de résultats inexpliqués en astrophysique, et malgré des progrès remarquables sur le plan des observations, des simulations numériques et de la théorie, cette substance invisible reste énigmatique. La matière noire est-elle constituée de particules inconnues ou peut-elle être expliquée par une extension de la théorie de la gravitation ? Le mystère reste entier et ces deux aspects pourraient bien être entremêlés.

L'approche dominante consiste à considérer que la matière noire est composée de particules exotiques dont il s'agit de déterminer les propriétés. On recherche ces particules grâce à différentes méthodes, qui vont de leur production dans les collisionneurs, à l'étude de leurs collisions avec des noyaux atomiques dans des expériences dédiées, en passant par une caractérisation indirecte à travers les signatures éventuelles dans les observations astrophysiques.

Dans cette thèse, je me suis concentré sur plusieurs aspects de la recherche indirecte des particules de matière noire, en m'appuyant sur les progrès technologiques récents et futurs dans le domaine des observations pour mettre au point des méthodes d'étude originales.

### C.2 La matière noire : du contexte historique aux recherches actuelles

#### C.2.1 Historique et candidats de la matière noire

##### C.2.1.1 Premières manifestations

**Dynamique des étoiles et galaxies.** Les premières indications de la présence de matière non lumineuse remontent au début du vingtième siècle, avec les premières études de la dynamique des étoiles dans le voisinage du Soleil. Dans les années 1930, Zwicky publie ses résultats célèbres sur l'existence d'une composante de *matière noire* (ou sombre) qu'il met en évidence dans l'amas de Coma grâce à la mesure de la dispersion de vitesse des galaxies de l'amas et à l'application du théorème du Viriel pour déterminer le potentiel gravitationnel. La problématique de la masse manquante prend ensuite de l'ampleur dans les années 1970, grâce aux mesures de plus en plus précises des courbes de rotation des galaxies, dont la platitude à grandes distances galactocentriques requiert la présence d'un halo de matière noire. Enfin, les premières simulations numériques dans les années 1970 montrent qu'une composante de matière noire est nécessaire pour stabiliser les disques stellaires auto-gravitants.

**Lentillage gravitationnel.** Les lentilles gravitationnelles ont également joué un rôle crucial dans la problématique de la matière noire, que ce soit l'effet de lentillage fort, qui donne lieu à

des images multiples déformées de galaxies d'arrière-plan sous forme d'arcs dans des observations d'amas de galaxies, mettant ainsi en évidence la présence de matière noire en grande quantité, ou le lentillage faible, dans le cadre duquel la distribution de matière noire sous-jacente est reconstruite statistiquement. Cette technique a été appliquée au célèbre amas de la balle de fusil, dont les observations contraignent très fortement les auto-interactions de la matière noire.

**Cosmologie.** En outre, la matière noire a un rôle central en cosmologie. C'est en particulier une composante majeure du modèle standard de la cosmologie,  $\Lambda$ CDM. L'observation du rayonnement fossile, et plus précisément des oscillations acoustiques des baryons sous forme de pics dans le spectre de puissance des anisotropies en température, est un argument très fort en faveur de l'existence de particules de matière noire. L'observation des oscillations acoustiques dans la trame cosmique à faible décalage spectral, ou encore la nucléosynthèse primordiale sont autant d'indications supplémentaires de la présence de matière noire dans l'Univers.

### C.2.1.2 Le scénario standard : la matière noire thermique

Dans l'approche standard, on suppose que la matière noire est formée de particules en équilibre thermique avec le plasma primordial. L'évolution de la densité numérique de particules de matière noire est décrite par l'équation de Boltzmann, qui permet de suivre l'histoire thermique de l'Univers. Les particules de matière noire sont initialement en équilibre thermique et chimique avec le plasma grâce au processus d'annihilation en particules ordinaires ; la réaction inverse a lieu tant que la température  $T$  est suffisamment élevée. Lorsque  $T$  devient inférieure à la masse des particules de matière noire, ces dernières deviennent non relativistes et l'énergie thermique devient insuffisante pour alimenter la réaction inverse. La densité des particules de matière noire diminue exponentiellement et de ce fait le taux d'annihilation par particule  $\Gamma_{\text{ann}} = n \langle \sigma v \rangle$  également.  $\langle \sigma v \rangle$  est la moyenne thermique de la section efficace d'annihilation multipliée par la vitesse relative de deux particules de matière noire. Lorsque  $\Gamma_{\text{ann}} = H$ , où  $H = \dot{a}/a$  est le paramètre de Hubble avec  $a$  le facteur d'échelle de l'Univers, les particules de matière noire se découplent chimiquement du bain thermique : c'est le gel des interactions ou freeze-out. En-deçà de la température correspondante  $T_F$ , les particules de matière noire ne peuvent plus s'annihiler efficacement et le nombre de particules  $na^3$  reste constant, donnant l'abondance relique de la matière noire de nos jours, que l'on peut écrire de manière approchée :

$$\Omega_{\text{DM}} h^2 \approx 0.1 \frac{3 \times 10^{-26} \text{ cm}^3 \text{ s}^{-1}}{\langle \sigma v \rangle}, \quad (\text{C.1})$$

avec  $h = H_0/(100 \text{ km s}^{-1} \text{ Mpc}^{-1})$  où  $H_0$  est la constante de Hubble aujourd'hui. L'équation (C.1) montre que pour  $\langle \sigma v \rangle \approx 3 \times 10^{-26} \text{ cm}^3 \text{ s}^{-1}$ , valeur caractéristique de l'interaction faible, la densité relique de particules de matière noire thermique reproduit l'abondance cosmologique mesurée par exemple avec *Planck*,  $\Omega_{\text{DM}} h^2 = 0.1198 \pm 0.0015$ . Par conséquent, ces arguments simples de cosmologie permettent d'obtenir des informations sur la nature des interactions de la matière noire et donnent lieu au scénario standard qui nécessite l'existence de particules massives interagissant faiblement (WIMPs en anglais). Ce résultat est désigné par l'expression "miracle des WIMPs", et fournit le point de départ des recherches de matière noire.

### C.2.1.3 Les principaux candidats

Des candidats nombreux et très variés ont été proposés, les plus célèbres étant les objets compacts sombres composés de matière ordinaires (les "MACHOs"), les neutrinos stériles, les WIMPs issus de la supersymétrie ou des théories de dimensions supplémentaires, ainsi que les axions.

### C.2.2 Recherches standards

**Détection directe.** Il s'agit d'utiliser des détecteurs ultra-sensibles pour mettre en évidence le recul d'un noyau atomique induit par une particule de matière noire arrivant dans le dispositif. Malgré quelques anomalies dans certains détecteurs, la majorité des expériences de détection directe a débouché sur des résultats négatifs, donnant lieu à des contraintes de plus en plus fortes sur la section efficace de diffusion WIMP-nucléon en fonction de la masse de la matière noire, les limites les plus restrictives provenant des expériences XENON100 et LUX utilisant du xénon liquide.

**Production en collisionneur.** Dans ce cas on cherche à produire des particules de matière noire qui sont donc invisibles et que l'on peut mettre en évidence en pratique sous la forme de particules ordinaires reculant face à de l'énergie transverse manquante. Les recherches dans les collisionneurs comme le Grand Collisionneur de Hadrons (LHC) n'ont pas révélé de résultats positifs.

**Détection indirecte.** Cette approche s'appuie sur les observations astrophysiques pour détecter les particules ordinaires produites dans les annihilations (ou désintégrations) de particules de matière noire : des positrons, des antiprotons, des antinoyaux, des photons  $\gamma$  et des neutrinos. Les signatures de ces particules sont recherchées notamment dans le rayonnement fossile, dans les flux de particules d'antimatière au voisinage de la Terre, ainsi que dans les observations de rayons  $\gamma$  et neutrinos dans de nombreuses régions du ciel. La plupart des observations donnent lieu à des contraintes sur les candidats de matière noire, bien qu'il y ait également quelques anomalies comme l'excès de rayons  $\gamma$  au GeV dans les données de *Fermi-LAT*.

## C.3 Recherche de la matière noire : au-delà des méthodes standards

La plupart des recherches indirectes de particules de matière noire sont effectuées de manière systématique par les grandes collaborations et se focalisent en particulier sur l'émission gamma prompte (provenant des cascades d'hadronisation et de désintégration à partir des particules chargées produites par les annihilations) et sur des profils de matière noire standards. Dans cette thèse je vais plus loin : j'explore de manière détaillée l'émission secondaire de photons par les électrons et positrons produits dans les annihilations de particules de matière noire, et j'étudie la phénoménologie de possibles pics de matière noire au centre des galaxies induits par les trous noirs supermassifs.

### C.3.1 Des pics de matière noire au centre des galaxies ?

**Le profil de matière noire au centre des galaxies : une situation débattue.** Il n'y a actuellement pas de consensus sur le profil de matière noire au centre des galaxies, les simulations numériques semblant indiquer la présence de profils en loi de puissance comme le profil de Navarro-Frenk-White (bien que des profils plus plats soient aussi obtenus) alors que les observations tendent à favoriser des profils plats (ou cœurs).

**Pic de matière noire induit par la croissance adiabatique d'un trou noir.** Il se trouve que la situation est encore plus incertaine à des échelles inférieures au parsec, inaccessibles tant aux simulations qu'aux observations. La présence d'un trou noir supermassif au centre de la plupart des galaxies a une influence significative sur le profil de matière noire. En particulier, la croissance adiabatique (c'est-à-dire lente) d'un trou noir supermassif au centre d'un halo de matière noire de densité  $\rho_i \propto r^{-\gamma}$  donne lieu à une augmentation extrêmement forte de la densité

en-dessous du parsec, avec une densité finale  $\rho_f \propto r^{-\gamma_{sp}}$ , avec  $\gamma_{sp} = (9 - 2\gamma)/(4 - \gamma)$ . Pour de tels “pics” de matière noire, la pente  $\gamma_{sp}$  est comprise entre 2.25 et 2.5 pour des pentes initiales  $0 < \gamma < 2$  attendues dans le contexte des simulations ou des observations. Naturellement, de tels profils très piqués donnent lieu à des signatures très fortes des annihilations de particules de matière noire.

**Les effets dynamiques en compétition.** Cependant, les pics adiabatiques sont controversés dans la mesure où ils sont affectés par un certain nombre de processus dynamiques négligés dans l’approche standard. En particulier, dans le cas de la croissance instantanée du trou noir, d’une fusion de trous noirs ou de formation excentrée du trou noir, le pic de matière noire qui en résulte est aplati de manière significative par rapport au cas adiabatique. En outre, la relaxation dynamique induite par les collisions avec les étoiles aplatit également le profil, mais ce processus est négligeable pour des galaxies dynamiquement jeunes comme par exemple M87 ou Cen A. Enfin, d’autres effets dynamiques, notamment liés à une possible triaxialité des halos de matière noire, ont pour effet de rendre la présence d’un pic proche du profil adiabatique plus plausible. Dans ma thèse, j’ai utilisé les possibilités offertes par les nouvelles technologies instrumentales pour étudier de tels profils très piqués au centre des galaxies.

### C.3.2 Émission de photons par des électrons et positrons

J’ai ensuite décrit les outils nécessaires à la modélisation des intensités de photons émis par les électrons et positrons produits notamment par les annihilations de matière noire, afin de pousser plus loin les recherches indirectes de particules de matière noire. Les processus radiatifs impliqués sont la *diffusion Compton inverse* (diffusion d’un électron de haute énergie par un photon de plus basse énergie du champ de radiation interstellaire), le *bremsstrahlung* (rayonnement d’un électron décéléré par le champ électrostatique d’un atome ou d’un ion) et l’émission *synchrotron* (interaction d’un électron avec un champ magnétique).

L’ingrédient principal dans le calcul de l’intensité est le spectre des électrons et positrons (densité numérique par unité d’énergie) tenant compte de tous les effets liés à la propagation, plus précisément les pertes radiatives et la diffusion spatiale. En particulier, j’ai mis au point une nouvelle méthode pour modéliser l’effet de la diffusion spatiale sur une source d’électrons et positrons présentant un profil très piqué (décrit dans la Section C.3.1) ; un problème qui ne peut pas être traité avec les codes de propagation des rayons cosmiques existants.

## C.4 L’excès *Fermi* de rayons gamma au centre Galactique

Plusieurs groupes indépendants ont mis en évidence un excès de rayons  $\gamma$  dans les données du télescope *Fermi*-LAT au-dessus du fond diffus Galactique dans une région de quelques degrés autour du centre Galactique. Le spectre de l’excès est une bosse centrée autour de 1–3 GeV. Cet excès au GeV est approximativement à symétrie sphérique et présente une morphologie spatiale en accord avec une émissivité spatiale en  $r^{-\gamma}$  avec  $\gamma \sim 1.2$ . Les principales explications possibles sont l’annihilation de particules de matière noire, une population d’environ  $10^3$ – $10^4$  pulsars milliseconde ou encore une injection soudaine d’électrons au centre Galactique lors d’un épisode éventuel d’activité intense dans le passé, bien que cette troisième possibilité semble nécessiter des ajustements significatifs pour fournir un scénario viable.

### C.4.1 De l’importance des électrons et positrons produits par la matière noire

Je me suis intéressé plus particulièrement à l’interprétation en terme de matière noire. Auparavant, le scénario le plus courant dans la littérature correspondait à l’annihilation de candidats d’environ 30 GeV principalement en  $b\bar{b}$ . Les canaux d’annihilation leptoniques ( $e^+e^-$ ,  $\mu^+\mu^-$ ,

$\tau^+\tau^-$ ) étaient rejetés dans la mesure où ils donnaient lieu à des spectres trop durs pour l'émission prompte. Cependant, ces conclusions ont précisément été obtenues en considérant uniquement l'émission prompte. J'ai montré qu'inclure l'émission secondaire par diffusion Compton inverse ou bremsstrahlung des électrons et positrons produits dans les annihilations change totalement l'interprétation de l'excès au GeV, puisqu'avec l'émission totale l'ensemble du spectre de l'excès peut être expliqué par des annihilations en leptons. J'ai donc montré que  $b\bar{b}$  n'était pas le seul canal et j'ai réhabilité les canaux leptoniques. Ces résultats sont d'autant plus intéressants qu'ils peuvent être appliqués à d'autres sources comme les pulsars milliseconde. En outre, l'émission secondaire présente une morphologie différente de l'émission prompte, en raison de la diffusion spatiale, ce qui peut être exploité pour tirer des informations supplémentaires dans l'analyse des données.

#### C.4.2 Morphologie spatiale de l'émission secondaire et excès au centre Galactique

Nous avons illustré l'importance d'inclure de manière cohérente la morphologie spatiale de l'émission secondaire dans l'analyse des données de *Fermi-LAT*, lorsqu'on évalue la validité de modèles de l'excès au GeV. Nous avons présenté une méthode permettant de déterminer la qualité de l'ajustement d'un modèle aux données en tenant compte de la morphologie spatiale des composantes Compton inverse et bremsstrahlung. Nous avons examiné plusieurs modèles donnant lieu à une émission secondaire significative (c'est-à-dire des scénarios contenant des leptons) et nous avons montré qu'une analyse à trois dimensions (deux dimensions spatiales plus une dimension spectrale) sur l'ensemble du spectre n'est pas forcément suffisante pour déterminer si les données requièrent une composante secondaire pour un modèle donné, et qu'une analyse par intervalle de fréquence, tenant compte de la morphologie spatiale, était nécessaire.

### C.5 Phénoménologie des pics de matière noire dans la Voie Lactée

#### C.5.1 Recherche d'un pic de matière noire au centre Galactique en présence de diffusion spatiale

J'ai utilisé l'émission synchrotron pour étudier le profil de matière noire au centre de la Voie Lactée. La difficulté réside dans le fait que le signal synchrotron dépend de manière significative de la propagation des électrons et positrons dans le milieu interstellaire, qui résulte essentiellement des effets de la diffusion spatiale et des pertes radiatives. En particulier, la diffusion spatiale est mal contrainte au centre Galactique. Afin de quantifier ses effets sur une distribution d'électrons et positrons injectés avec un profil très piqué ( $\rho(r) \propto r^{-7/3}$ ), j'ai utilisé la technique que j'ai développée pour modéliser la diffusion des électrons sur des petites échelles. La conclusion est qu'en présence de diffusion spatiale, les observations astrophysiques, et en particulier celles du satellite *Planck*, peuvent être utilisées pour explorer le profil de matière noire à des échelles inaccessibles notamment par les simulations numériques. Par exemple, les données *Planck* excluent des pics de matière noire pour la section efficace canonique  $\langle\sigma v\rangle \approx 3 \times 10^{-26} \text{ cm}^3 \text{ s}^{-1}$  et des candidats de masse 10 GeV s'annihilant en  $e^+e^-$ .

#### C.5.2 Nouvelle émission diffuse mesurée avec H.E.S.S. au centre Galactique : une combinaison de matière noire lourde et de pulsars milliseconde ?

Une émission  $\gamma$  diffuse dans une région comprise à l'intérieur de  $0.45^\circ$  autour du centre Galactique a été détectée avec le télescope H.E.S.S., entre  $\sim 200$  GeV et 50 TeV. Dans le scénario standard, ces rayons  $\gamma$  proviennent de la désintégration de pions neutres produits par l'interaction de protons accélérés par le trou noir central Sgr A\* avec le gaz du milieu interstellaire. Cependant,

j'ai exploré une interprétation différente qui relie l'émission diffuse au TeV de H.E.S.S. à l'excès au GeV, par le biais des pulsars milliseconde. J'ai démontré que l'émission diffuse de H.E.S.S. peut être expliquée par la somme de l'émission Compton inverse induite par une population de pulsars milliseconde et celle induite par l'annihilation de matière noire lourde ( $\sim 100$  TeV). La morphologie spatiale associée est particulièrement intéressante, avec notamment une composante due aux pulsars plus étendue que pour la matière noire. Ces propriétés peuvent être testées par de futures observations de H.E.S.S. à plus grande latitude.

## C.6 A la recherche de pics de matière noire dans les galaxies M87 et Centaurus A

### C.6.1 Exclusion de candidats thermiques en présence d'un pic de matière noire au centre de M87

Nous avons étudié les signatures de l'annihilation de particules de matière noire au centre de la galaxie M87, peu étudiées auparavant. En supposant la présence plausible d'un pic de matière noire au centre de la galaxie dynamiquement jeune M87, j'ai modélisé la distribution spectrale d'énergie induite par les annihilations, et en la comparant aux données multi-longueur d'onde de M87, j'ai établi des courbes d'exclusion pour la section efficace d'annihilation en fonction de la masse des particules de matière noire. Ces limites sont plus fortes que toutes les limites précédentes et excluent les candidats de matière noire avec une section efficace thermique et indépendante de la vitesse de l'ordre de  $10^{-26}$   $\text{cm}^3 \text{s}^{-1}$  et une masse allant jusqu'à  $\mathcal{O}(100)$  TeV. En outre, en présence d'un pic de matière noire, l'émission induite par les annihilations de particules ayant des masses de quelques TeV et une section efficace d'annihilation de l'ordre de  $10^{-27}$   $\text{cm}^3 \text{s}^{-1}$  pourrait expliquer l'émission au TeV dans M87.

Ces résultats sont très prometteurs pour l'étude de la microphysique de la matière noire. En effet, on s'attend à des contraintes similaires dans des galaxies présentant des trous noirs centraux de masse similaire au trou noir de M87. Par conséquent, si un pic de matière noire était découvert dans une telle galaxie, il serait alors possible d'exclure une portion significative de l'espace des paramètres des particules de matière noire pouvant s'annihiler. Cette approche ouvre une nouvelle voie pour l'exploration de la nature de la matière noire, et fournit une motivation forte pour des études supplémentaires dédiées aux pics de matière noire.

### C.6.2 Découverte d'une population extragalactique de particules énergétiques

Les radio-galaxies sont des galaxies actives, possédant un trou noir supermassif en leur centre et un jet décalé par rapport à la ligne de visée. Centaurus A (Cen A) est la plus proche radio-galaxie connue émettrice de rayons  $\gamma$ . Nous avons mis en évidence un durcissement du spectre  $\gamma$  du cœur de Cen A autour de 2.4 GeV, à un niveau de confiance de  $5\sigma$ , ainsi que la variabilité de l'émission en-dessous de 2.4 GeV à 99% de confiance. Ces propriétés favorisent fortement l'hypothèse selon laquelle la composante à basse énergie est due à une population de leptons dans le jet, tandis que l'émission au-dessus du durcissement spectral correspond à une population de rayons cosmiques différente. J'ai démontré pour la première fois que le spectre  $\gamma$  observé est compatible avec un pic de matière noire ou une population de pulsars milliseconde. Une troisième explication pourrait être reliée à une composante hadronique issue du jet. Ce travail met en évidence l'existence de nouveaux processus d'émission de rayons  $\gamma$  dans les galaxies actives et pourrait bien indiquer la présence de pics de matière noire lourde autour des trous noirs.

### C.6.3 Recherche d'un pic de matière noire au centre de M87 avec le Télescope de l'Horizon des Événements

Enfin, j'ai exploré le potentiel du Télescope de l'Horizon des Événements pour cartographier la partie centrale du profil de matière noire dans la galaxie M87, via l'émission synchrotron induite par les annihilations des particules de matière noire. Ce réseau de télescope utilise l'interférométrie à très longue base pour synthétiser un télescope de taille effective de l'ordre de celle de la Terre, ce qui permet d'atteindre une résolution angulaire de l'ordre de la microseconde d'arc. J'ai présenté des résultats préliminaires qui montrent les performances sans précédent de cet instrument novateur pour étudier les particules de matière noire s'annihilant avec des sections efficaces très faibles, à travers les signatures à l'échelle de l'horizon du trou noir introduites par un pic de matière noire. Plus précisément, le Télescope de l'Horizon des Événements se focalise sur l'ombre du trou noir, liée à l'effet de lentille gravitationnelle. Les prédictions que j'ai présentées sont très prometteuses, et le potentiel du Télescope de l'Horizon des Événements pour l'étude de la matière noire doit encore être exploré plus en profondeur, ce que je compte faire dans l'avenir.

## C.7 Conclusion

Grâce aux progrès observationnels permis par des instruments tels que *Fermi-LAT*, H.E.S.S. ou le Télescope de l'Horizon des Événements, il est possible non seulement de chercher des signatures des annihilations de particules de matière noire dans les halos des galaxies, mais également de zoomer sur les régions centrales des galaxies.

C'est dans ce contexte que je me suis attaqué au problème du profil de matière noire au centre des galaxies par de nouvelles méthodes, qui a servi de motivation principale à ma thèse. J'ai étudié en particulier la phénoménologie des pics de matière noire au centre de la Voie Lactée, mais également de galaxies actives comme M87 ou Cen A, et j'ai développé de nouveaux modèles de l'émission diffuse au centre de ces galaxies. Pour cela, j'ai mis au point une nouvelle méthode pour traiter le problème de la propagation des rayons cosmiques en présence d'une source très piquée au centre des galaxies. J'ai également appliqué les outils que j'ai développés à l'interprétation de l'excès de rayons  $\gamma$  au GeV mis en évidence dans les données de *Fermi-LAT*. Mes travaux m'ont permis d'aller au-delà des recherches standards des particules de matière noire.



# Bibliography

- Aad G. et al. (ATLAS Collaboration), *Observation of a new particle in the search for the Standard Model Higgs boson with the ATLAS detector at the LHC*, *Physics Letters B* **716**, 1-29 (2012), [arXiv:1207.7214](#). 36
- Aad G. et al. (ATLAS Collaboration), *Search for Dark Matter Candidates and Large Extra Dimensions in Events with a Photon and Missing Transverse Momentum in pp Collision Data at  $\sqrt{s} = 7$  TeV with the ATLAS Detector*, *Physical Review Letters* **110**, 011802 (2013a), [arXiv:1209.4625](#). 37
- Aad G. et al. (ATLAS Collaboration), *Search for dark matter candidates and large extra dimensions in events with a jet and missing transverse momentum with the ATLAS detector*, *Journal of High Energy Physics* **4**, 75 (2013b), [arXiv:1210.4491](#). 37
- Aad G. et al. (ATLAS Collaboration), *Search for dark matter in events with a hadronically decaying W or Z boson and missing transverse momentum in pp collisions at  $\sqrt{s} = 8$  TeV with the ATLAS detector*, *ArXiv e-prints* (2013c), [arXiv:1309.4017](#). 37
- Aad G. et al. (ATLAS Collaboration), *Search for dark matter in events with a Z boson and missing transverse momentum in pp collisions at  $\sqrt{s} = 8$  TeV with the ATLAS detector*, *Phys. Rev. D* **90**, 012004 (2014a), [arXiv:1404.0051](#). 37
- Aad G. et al. (ATLAS Collaboration), *Search for Invisible Decays of a Higgs Boson Produced in Association with a Z Boson in ATLAS*, *Physical Review Letters* **112**, 201802 (2014b), [arXiv:1402.3244](#). 38, 39
- Aad G. et al. (ATLAS Collaboration), *Constraints on new phenomena via Higgs boson couplings and invisible decays with the ATLAS detector*, *ArXiv e-prints* (2015a), [arXiv:1509.00672](#). 39
- Aad G. et al. (ATLAS Collaboration), *Search for resonances decaying to photon pairs in  $3.2 \text{ fb}^{-1}$  of pp collisions at  $\sqrt{s} = 13$  TeV with the ATLAS detector*, *ATLAS CONF Notes* **ATLAS-CONF-2015-081** (2015b). 39, 159
- Aalseth C. E. et al. (CoGeNT Collaboration), *CoGeNT: A search for low-mass dark matter using p-type point contact germanium detectors*, *Phys. Rev. D* **88**, 012002 (2013), [arXiv:1208.5737](#). 33
- Aalseth C. E. et al. (DarkSide-G2 Collaboration), *The darkside multiton detector for the direct dark matter search*, *Advances in High Energy Physics* **2015**, 541362 (2015). 33, 34
- Aartsen M. G. et al. (IceCube Collaboration), *Search for Dark Matter Annihilations in the Sun with the 79-String IceCube Detector*, *Physical Review Letters* **110**, 131302 (2013a), [arXiv:1212.4097](#). 36, 48
- Aartsen M. G. et al., *First Observation of PeV-Energy Neutrinos with IceCube*, *Physical Review Letters* **111**, 021103 (2013b), [arXiv:1304.5356](#). 48

- Aartsen M. G. et al. (IceCube Collaboration), *Multipole analysis of IceCube data to search for dark matter accumulated in the Galactic halo*, *European Physical Journal C* **75**, 20 (2015). 48
- Abazajian K., Fuller G. M., Patel M., *Sterile neutrino hot, warm, and cold dark matter*, *Phys. Rev. D* **64**, 023501 (2001a), arXiv:astro-ph/0101524. 22
- Abazajian K., Fuller G. M., Tucker W. H., *Direct Detection of Warm Dark Matter in the X-Ray*, *ApJ* **562**, 593-604 (2001b), arXiv:astro-ph/0106002. 22
- Abazajian K. N., *The consistency of Fermi-LAT observations of the galactic center with a millisecond pulsar population in the central stellar cluster*, *JCAP* **3**, 10 (2011), arXiv:1011.4275. 88
- Abazajian K. N., Acero M. A., Agarwalla S. K., Aguilar-Arevalo A. A., Albright C. H., Antusch S., Argüelles C. A., Balantekin A. B., Barenboim G., Barger V., Bernardini P., Bezrukov F., Bjaelde O. E., Bogacz S. A., Bowden N. S., Boyarsky A., Bravar A., Bravo Berguno D., Brice S. J., Bross A. D., Caccianiga B., Cavanna F., Chun E. J., Cleveland B. T., Collin A. P., Coloma P., Conrad J. M., Cribier M., Cucoanes A. S., D'Olivo J. C., Das S., de Gouvea A., Derbin A. V., Dharmapalan R., Diaz J. S., Ding X. J., Djurcic Z., Donini A., Duchesneau D., Ejiri H., Elliott S. R., Ernst D. J., Esmaili A., Evans J. J., Fernandez-Martinez E., Figueroa-Feliciano E., Fleming B. T., Formaggio J. A., Franco D., Gaffiot J., Gandhi R., Gao Y., Garvey G. T., Gavrin V. N., Ghoshal P., Gibin D., Giunti C., Gninenko S. N., Gorbachev V. V., Gorbunov D. S., Guenette R., Guglielmi A., Halzen F., Hamann J., Hannestad S., Haxton W., Heeger K. M., Henning R., Hernandez P., Huber P., Huelsnitz W., Ianni A., Ibragimova T. V., Karadzhov Y., Karagiorgi G., Keefer G., Kim Y. D., Kopp J., Kornoukhov V. N., Kusenko A., Kyberd P., Langacker P., Lasserre T., Laveder M., Letourneau A., Lhuillier D., Li Y. F., Lindner M., Link J. M., Littlejohn B. L., Lombardi P., Long K., Lopez-Pavon J., Louis W. C., Ludhova L., Lykken J. D., Machado P. A. N., Maltoni M., Mann W. A., Marfatia D., Mariani C., Matveev V. A., Mavromatos N. E., Melchiorri A., Meloni D., Mena O., Mention G., Merle A., Meroni E., Mezzetto M., Mills G. B., Minic D., Miramonti L., Mohapatra D., Mohapatra R. N., Montanari C., Mori Y., Mueller T. A., Mumm H. P., Muratova V., Nelson A. E., Nico J. S., Noah E., Nowak J., Smirnov O. Y., Obolensky M., Pakvasa S., Palamara O., Pallavicini M., Pascoli S., Patrizzii L., Pavlovic Z., Peres O. L. G., Pessard H., Pietropaolo F., Pitt M. L., Popovic M., Pradler J., Ranucci G., Ray H., Razaque S., Rebel B., Robertson R. G. H., Rodejohann W., Rountree S. D., Rubbia C., Ruchayskiy O., Sala P. R., Scholberg K., Schwetz T., Shaevitz M. H., Shaposhnikov M., Shrock R., Simone S., Skorokhvatov M., Sorel M., Sousa A., Spergel D. N., Spitz J., Stanco L., Stancu I., Suzuki A., Takeuchi T., Tamborra I., Tang J., Testera G., Tian X. C., Tonazzo A., Tunnell C. D., Van de Water R. G., Verde L., Veretenkin E. P., Vignoli C., Vivier M., Vogelaar R. B., Wascko M. O., Wilkerson J. F., Winter W., Wong Y. Y. Y., Yanagida T. T., Yasuda O., Yeh M., Yermia F., Yokley Z. W., Zeller G. P., Zhan L., Zhang H., *Light Sterile Neutrinos: A White Paper*, ArXiv e-prints (2012), arXiv:1204.5379. 21
- Abazajian K. N., Canac N., Horiuchi S., Kaplinghat M., *Astrophysical and dark matter interpretations of extended gamma-ray emission from the Galactic Center*, *Phys. Rev. D* **90**, 023526 (2014), arXiv:1402.4090. 87, 88, 90, 91, 92, 102, 106
- Abazajian K. N., Canac N., Horiuchi S., Kaplinghat M., Kwa A., *Discovery of a new galactic center excess consistent with upscattered starlight*, *JCAP* **7**, 13 (2015), arXiv:1410.6168. 102, 108
- Abazajian K. N., Kaplinghat M., *Detection of a gamma-ray source in the Galactic Center consistent with extended emission from dark matter annihilation and concentrated astrophysical emission*, *Phys. Rev. D* **86**, 083511 (2012), arXiv:1207.6047. 87, 88, 90

- Abazajian K. N., Kaplinghat M., *Erratum: Detection of a gamma-ray source in the Galactic Center consistent with extended emission from dark matter annihilation and concentrated astrophysical emission [Phys. Rev. D 86, 083511 (2012)]*, *Phys. Rev. D* **87**, 129902 (2013). [87](#), [88](#), [90](#)
- Abazajian K. N., Keeley R. E., *A Bright Gamma-ray Galactic Center Excess and Dark Dwarfs: Strong Tension for Dark Matter Annihilation Despite Milky Way Halo Profile and Diffuse Emission Uncertainties*, ArXiv e-prints (2015), [arXiv:1510.06424](#). [90](#)
- Abbasi R. et al. (IceCube Collaboration), *IceCube - Astrophysics and Astroparticle Physics at the South Pole*, ArXiv e-prints (2011), [arXiv:1111.5188](#). [48](#)
- Abbiendi G. et al. (OPAL Collaboration), *Photonic events with missing energy in  $e^+e^-$  collisions at  $\sqrt{s} = 189$  GeV*, *European Physical Journal C* **18**, 253-272 (2000), [arXiv:hep-ex/0005002](#). [37](#)
- Abbott B. P. et al. (LIGO Scientific and VIRGO Collaborations), *Observation of Gravitational Waves from a Binary Black Hole Merger*, *Physical Review Letters* **116**, 061102 (2016), [arXiv:1602.03837](#). [20](#)
- Abdo A. A. et al. (Fermi-LAT Collaboration), *Fermi Large Area Telescope Gamma-Ray Detection of the Radio Galaxy M87*, *ApJ* **707**, 55-60 (2009), [arXiv:0910.3565](#). [142](#), [143](#), [147](#), [148](#), [181](#), [182](#)
- Abdo A. A. et al. (Fermi-LAT Collaboration), *Fermi Large Area Telescope View of the Core of the Radio Galaxy Centaurus A*, *ApJ* **719**, 1433-1444 (2010a), [arXiv:1006.5463](#). [154](#), [155](#), [193](#)
- Abdo A. A. et al. (Fermi-LAT Collaboration), *Fermi Gamma-Ray Imaging of a Radio Galaxy*, *Science* **328**, 725 (2010b), [arXiv:1006.3986](#). [154](#), [187](#)
- Abdo A. A. et al. (Fermi-LAT Collaboration), *The Second Fermi Large Area Telescope Catalog of Gamma-Ray Pulsars*, *ApJS* **208**, 17 (2013), [arXiv:1305.4385](#). [88](#), [89](#)
- Abe K. et al. (XMASS Collaboration), *Light WIMP search in XMASS*, *Physics Letters B* **719**, 78-82 (2013a), [arXiv:1211.5404](#). [33](#)
- Abeysekara A. U., Alfaro R., Alvarez C., Álvarez J. D., Arceo R., Arteaga-Velázquez J. C., Ayala Solares H. A., Barber A. S., Baughman B. M., Bautista-Elivar N., Becerra Gonzalez J., Belmont E., BenZvi S. Y., Berley D., Bonilla Rosales M., Braun J., Caballero-Lopez R. A., Caballero-Mora K. S., Carramiñana A., Castillo M., Cotti U., Cotzomi J., de la Fuente E., De León C., DeYoung T., Diaz Hernandez R., Diaz-Cruz L., Díaz-Vélez J. C., Dings B. L., DuVernois M. A., Ellsworth R. W., Fiorino D. W., Fraija N., Galindo A., Garfias F., González M. M., Goodman J. A., Grabski V., Gussert M., Hampel-Arias Z., Harding J. P., Hui C. M., Hütemeyer P., Imran A., Iriarte A., Karn P., Kieda D., Kunde G. J., Lara A., Lauer R. J., Lee W. H., Lennarz D., León Vargas H., Linares E. C., Linnemann J. T., Longo M., Luna-Garcia R., Marinelli A., Martinez H., Martinez O., Martínez-Castro J., Matthews J. A. J., McEnery J., Mendoza Torres E., Miranda-Romagnoli P., Moreno E., Mostafá M., Nellen L., Newbold M., Noriega-Papaqui R., Oceguera-Becerra T., Patricelli B., Pelayo R., Pérez-Pérez E. G., Pretz J., Rivière C., Rosa-González D., Ryan J., Salazar H., Salesa F., Sanchez F. E., Sandoval A., Schneider M., Silich S., Sinnis G., Smith A. J., Sparks Woodle K., Springer R. W., Taboada I., Toale P. A., Tollefson K., Torres I., Ukwatta T. N., Villaseñor L., Weisgarber T., Westerhoff S., Wisher I. G., Wood J., Yodh G. B., Younk P. W., Zaborov D., Zepeda A., Zhou H., Abazajian K. N., *Sensitivity of HAWC to high-mass dark matter annihilations*, *Phys. Rev. D* **90**, 122002 (2014), [arXiv:1405.1730](#). [48](#)

- Abramowski A. et al. (H.E.S.S. Collaboration), *Search for a Dark Matter Annihilation Signal from the Galactic Center Halo with H.E.S.S.*, *Physical Review Letters* **106**, 161301 (2011a), [arXiv:1103.3266](#). 47
- Abramowski A. et al. (H.E.S.S. Collaboration), *H.E.S.S. Observations of the Globular Clusters NGC 6388 and M15 and Search for a Dark Matter Signal*, *ApJ* **735**, 12 (2011b), [arXiv:1104.2548](#). 47
- Abramowski A. et al. (H.E.S.S. Collaboration), *Search for Dark Matter Annihilation Signals from the Fornax Galaxy Cluster with H.E.S.S.*, *ApJ* **750**, 123 (2012), [arXiv:1202.5494](#). 47
- Abramowski A. et al. (H.E.S.S. Collaboration), *Search for Photon-Linelike Signatures from Dark Matter Annihilations with H.E.S.S.*, *Physical Review Letters* **110**, 041301 (2013), [arXiv:1301.1173](#). 46
- Abramowski A. et al. (H.E.S.S. Collaboration), *Search for dark matter annihilation signatures in H.E.S.S. observations of dwarf spheroidal galaxies*, *Phys. Rev. D* **90**, 112012 (2014), [arXiv:1410.2589](#). 47
- Abramowski A. et al. (H.E.S.S. Collaboration), *Acceleration of petaelectronvolt protons in the Galactic Centre*, *Nature* **531**, 476-479 (2016), [arXiv:1603.07730](#). 128, 129, 132, 133
- Abreu P. et al. (DELPHI Collaboration), *Photon events with missing energy at  $\sqrt{s} = 183$  to 189 GeV*, *European Physical Journal C* **17**, 53-65 (2000), [arXiv:hep-ex/0103044](#). 37
- Accardo L. et al., *High Statistics Measurement of the Positron Fraction in Primary Cosmic Rays of 0.5-500 GeV with the Alpha Magnetic Spectrometer on the International Space Station*, *Physical Review Letters* **113**, 121101 (2014). 41
- Acciari V. A. et al. (VERITAS Collaboration), *Observation of Gamma-Ray Emission from the Galaxy M87 above 250 GeV with VERITAS*, *ApJ* **679**, 397-403 (2008), [arXiv:0802.1951](#). 142
- Acero F. et al. (Fermi-LAT Collaboration), *Fermi Large Area Telescope Third Source Catalog*, *ApJS* **218**, 23 (2015), [arXiv:1501.02003](#). 105, 186
- Achard P. et al. (L3 Collaboration), *Single- and multi-photon events with missing energy in  $e^+e^-$  collisions at LEP*, *Physics Letters B* **587**, 16-32 (2004), [arXiv:hep-ex/0402002](#). 37
- Acharya B. S. et al. (CTA Collaboration), *Introducing the CTA concept*, *Astroparticle Physics* **43**, 3-18 (2013). 48
- Ackermann M. et al. (Fermi-LAT Collaboration), *Constraints on dark matter annihilation in clusters of galaxies with the Fermi large area telescope*, *JCAP* **5**, 025 (2010), [arXiv:1002.2239](#). 47
- Ackermann M. et al. (Fermi-LAT Collaboration), *Measurement of Separate Cosmic-Ray Electron and Positron Spectra with the Fermi Large Area Telescope*, *Physical Review Letters* **108**, 011103 (2012)a, [arXiv:1109.0521](#). 41
- Ackermann M. et al. (Fermi-LAT Collaboration), *The Fermi Large Area Telescope on Orbit: Event Classification, Instrument Response Functions, and Calibration*, *ApJS* **203**, 4 (2012)b, [arXiv:1206.1896](#). 191, 192
- Ackermann M. et al. (Fermi-LAT Collaboration), *Constraints on the Galactic Halo Dark Matter from Fermi-LAT Diffuse Measurements*, *ApJ* **761**, 91 (2012a), [arXiv:1205.6474](#). 47, 91
- Ackermann M. et al. (Fermi-LAT Collaboration), *Search for Dark Matter Satellites Using Fermi-LAT*, *ApJ* **747**, 121 (2012b), [arXiv:1201.2691](#). 47

- Ackermann M. et al. (Fermi-LAT Collaboration), *Fermi-LAT Observations of the Diffuse  $\gamma$ -Ray Emission: Implications for Cosmic Rays and the Interstellar Medium*, *ApJ* **750**, 3 (2012c), [arXiv:1202.4039](#). 74
- Ackermann M. et al. (Fermi-LAT Collaboration), *Search for Gamma-ray Spectral Lines with the Fermi Large Area Telescope and Dark Matter Implications*, ArXiv e-prints (2013), [arXiv:1305.5597](#). 46
- Ackermann M. et al. (Fermi-LAT Collaboration), *Searching for Dark Matter Annihilation from Milky Way Dwarf Spheroidal Galaxies with Six Years of Fermi Large Area Telescope Data*, *Physical Review Letters* **115**, 231301 (2015a), [arXiv:1503.02641](#). 47, 90
- Ackermann M. et al. (Fermi-LAT Collaboration), *Search for Extended Gamma-Ray Emission from the Virgo Galaxy Cluster with FERMI-LAT*, *ApJ* **812**, 159 (2015b), [arXiv:1510.00004](#). 47
- Ackermann M. et al. (Fermi-LAT Collaboration), *Limits on dark matter annihilation signals from the Fermi LAT 4-year measurement of the isotropic gamma-ray background*, *JCAP* **9**, 008 (2015c), [arXiv:1501.05464](#). 47
- Ackermann M. et al. (Fermi-LAT Collaboration), *Updated Search for Spectral Lines from Galactic Dark Matter Interactions with Pass 8 Data from the Fermi Large Area Telescope*, ArXiv e-prints (2015d), [arXiv:1506.00013](#). 46
- Ade P. A. R. et al. (Planck Collaboration), *Planck 2013 results. I. Overview of products and scientific results*, *A&A* **571**, A1 (2014), [arXiv:1303.5062](#). 124, 125
- Ade P. A. R. et al. (Planck Collaboration), *Planck 2015 results. I. Overview of products and scientific results*, ArXiv e-prints (2015a), [arXiv:1502.01582](#). 9, 10
- Ade P. A. R. et al. (Planck Collaboration), *Planck 2015 results. XIII. Cosmological parameters*, ArXiv e-prints (2015b), [arXiv:1502.01589](#). 9, 11, 12, 21, 41, 42
- Adrián-Martínez S. et al. (ANTARES Collaboration), *First results on dark matter annihilation in the Sun using the ANTARES neutrino telescope*, *JCAP* **11**, 032 (2013), [arXiv:1302.6516](#). 48
- Adrián-Martínez S. et al. (ANTARES Collaboration), *Search of dark matter annihilation in the galactic centre using the ANTARES neutrino telescope*, *JCAP* **10**, 068 (2015), [arXiv:1505.04866](#). 48
- Adriani O., Barbarino G. C., Bazilevskaya G. A., Bellotti R., Boezio M., Bogomolov E. A., Bonechi L., Bonghi M., Bonvicini V., Bottai S., Bruno A., Cafagna F., Campana D., Carlson P., Casolino M., Castellini G., de Pascale M. P., de Rosa G., de Simone N., di Felice V., Galper A. M., Grishantseva L., Hofverberg P., Koldashov S. V., Krutkov S. Y., Kvashnin A. N., Leonov A., Malvezzi V., Marcelli L., Menn W., Mikhailov V. V., Mocchiutti E., Orsi S., Osteria G., Papini P., Pearce M., Picozza P., Ricci M., Ricciarini S. B., Simon M., Sparvoli R., Spillantini P., Stozhkov Y. I., Vacchi A., Vannuccini E., Vasilyev G., Voronov S. A., Yurkin Y. T., Zampa G., Zampa N., Zverev V. G., *An anomalous positron abundance in cosmic rays with energies 1.5-100 GeV*, *Nature* **458**, 607-609 (2009a), [arXiv:0810.4995](#). 41
- Adriani O., Barbarino G. C., Bazilevskaya G. A., Bellotti R., Boezio M., Bogomolov E. A., Bonechi L., Bonghi M., Bonvicini V., Bottai S., Bruno A., Cafagna F., Campana D., Carlson P., Casolino M., Castellini G., de Pascale M. P., de Rosa G., Fedele D., Galper A. M., Grishantseva L., Hofverberg P., Leonov A., Koldashov S. V., Krutkov S. Y., Kvashnin A. N., Malvezzi V., Marcelli L., Menn W., Mikhailov V. V., Minori M., Mocchiutti E., Nagni M., Orsi S., Osteria G., Papini P., Pearce M., Picozza P., Ricci M., Ricciarini S. B., Simon M., Sparvoli R., Spillantini P., Stozhkov Y. I., Taddei E., Vacchi A., Vannuccini E., Vasilyev G., Voronov S. A., Yurkin

- Y. T., Zampa G., Zampa N., Zverev V. G., *New Measurement of the Antiproton-to-Proton Flux Ratio up to 100 GeV in the Cosmic Radiation*, *Physical Review Letters* **102**, 051101 (2009b), [arXiv:0810.4994](#). 43
- Adriani O., Bazilevskaya G. A., Barbarino G. C., Bellotti R., Boezio M., Bogomolov E. A., Bonvicini V., Bongi M., Bonechi L., Borisov S. V., Bottai S., Bruno A., Vacchi A., Vannuccini E., Vasilyev G. I., Voronov S. A., Wu J., Galper A. M., Grishantseva L. A., Danilchenko I. A., Gillard W., Jerse G., Zampa G., Zampa N., Zverev V. G., Casolino M., Campana D., Carbone R., Karelin A. V., Carlson P., Castellini G., Cafagna F., Kvashnin A. N., Koldashov S. V., Koldobskiy S. A., Krutkov S. Y., Consiglio L., Leonov A. A., Mayorov A. G., Malakhov V. V., Malvezzi W., Marcelli L., Menn W., Mikhailov V. V., Mocchiutti E., Monaco A., Mori N., Nikonov N. N., Osteria G., Palma F., Papini P., Pizzolotto C., de Pascale M. P., Picozza P., Pearce M., Ricci M., Ricciarini S., Rossetto L., Runtso M. F., De Santis C., Sarkar R., Simon M., De Simone N., Sparvoli R., Spillantini P., Stozhkov Y. I., Di Felice V., Yurkin Y. T., *Measurement of the flux of primary cosmic ray antiprotons with energies of 60 MeV to 350 GeV in the PAMELA experiment*, *Soviet Journal of Experimental and Theoretical Physics Letters* **96**, 621-627 (2013b). 43
- Adriani O. et al. (PAMELA Collaboration), *PAMELA Results on the Cosmic-Ray Antiproton Flux from 60 MeV to 180 GeV in Kinetic Energy*, *Physical Review Letters* **105**, 121101 (2010), [arXiv:1007.0821](#). 43
- Adriani O. et al. (PAMELA Collaboration), *Cosmic-Ray Positron Energy Spectrum Measured by PAMELA*, *Physical Review Letters* **111**, 081102 (2013a), [arXiv:1308.0133](#). 41
- Aghanim N. et al. (Planck Collaboration), *Planck 2013 results. IV. Low Frequency Instrument beams and window functions*, *A&A* **571**, A4 (2014), [arXiv:1303.5065](#). 119
- Agnes P. et al. (DarkSide Collaboration), *First results from the DarkSide-50 dark matter experiment at Laboratori Nazionali del Gran Sasso*, *Physics Letters B* **743**, 456-466 (2015), [arXiv:1410.0653](#). 33
- Agnese R. et al. (CDMS Collaboration), *Silicon detector results from the first five-tower run of CDMS II*, *Phys. Rev. D* **88**, 031104 (2013a), [arXiv:1304.3706](#). 33
- Agnese R. et al. (CDMS Collaboration), *Silicon Detector Dark Matter Results from the Final Exposure of CDMS II*, *ArXiv e-prints* (2013b), [arXiv:1304.4279](#). 33
- Agnese R. et al. (SuperCDMS Collaboration), *Search for Low-Mass Weakly Interacting Massive Particles Using Voltage-Assisted Calorimetric Ionization Detection in the SuperCDMS Experiment*, *Physical Review Letters* **112**, 041302 (2014a), [arXiv:1309.3259](#). 33
- Agnese R. et al. (SuperCDMS Collaboration), *Search for Low-Mass Weakly Interacting Massive Particles with SuperCDMS*, *Physical Review Letters* **112**, 241302 (2014b), [arXiv:1402.7137](#). 33
- Aguilar M. et al. (AMS-01 Collaboration), *Cosmic-ray positron fraction measurement from 1 to 30 GeV with AMS-01*, *Physics Letters B* **646**, 145-154 (2007), [arXiv:astro-ph/0703154](#). 41
- Aguilar M. et al. (AMS Collaboration), *First Result from the Alpha Magnetic Spectrometer on the International Space Station: Precision Measurement of the Positron Fraction in Primary Cosmic Rays of 0.5-350 GeV*, *Physical Review Letters* **110**, 141102 (2013). 41
- Aguilar-Arevalo A. et al. (DAMIC Collaboration), *The DAMIC dark matter experiment*, *ArXiv e-prints* (2015), [arXiv:1510.02126](#). 33
- Aharonian F. et al. (H.E.S.S. Collaboration), *Discovery of very-high-energy  $\gamma$ -rays from the Galactic Centre ridge*, *Nature* **439**, 695-698 (2006a), [arXiv:astro-ph/0603021](#). 106, 128

- Aharonian F. et al. (H.E.S.S. Collaboration), *Fast Variability of Tera-Electron Volt  $\gamma$  Rays from the Radio Galaxy M87*, *Science* **314**, 1424-1427 (2006b). [142](#), [154](#)
- Aharonian F. et al. (H.E.S.S. Collaboration), *Discovery of Very High Energy  $\gamma$ -Ray Emission from Centaurus a with H.E.S.S.*, *ApJL* **695**, L40-L44 (2009), [arXiv:0903.1582](#). [154](#), [155](#), [156](#), [190](#)
- Ahmed Z. et al. (CDMS-II Collaboration), *Dark Matter Search Results from the CDMS II Experiment*, *Science* **327**, 1619 (2010), [arXiv:0912.3592](#). [33](#)
- Ahmed Z. et al. (CDMS-II Collaboration), *Results from a Low-Energy Analysis of the CDMS II Germanium Data*, *Physical Review Letters* **106**, 131302 (2011), [arXiv:1011.2482](#). [33](#)
- Ajello M. et al. (Fermi-LAT Collaboration), *Fermi-LAT Observations of High-Energy Gamma-Ray Emission Toward the Galactic Center*, *ArXiv e-prints* (2015), [arXiv:1511.02938](#). [87](#), [88](#)
- Akerib D. S. et al. (LUX Collaboration), *First Results from the LUX Dark Matter Experiment at the Sanford Underground Research Facility*, *Physical Review Letters* **112**, 091303 (2014). [33](#)
- Akerib D. S. et al. (LZ Collaboration), *LUX-ZEPLIN (LZ) Conceptual Design Report*, *ArXiv e-prints* (2015), [arXiv:1509.02910](#). [34](#)
- Akimov D. Y. et al. (ZEPLIN-III Collaboration), *WIMP-nucleon cross-section results from the second science run of ZEPLIN-III*, *Physics Letters B* **709**, 14-20 (2012), [arXiv:1110.4769](#). [33](#), [36](#)
- Akiyama K., Lu R.-S., Fish V. L., Doeleman S. S., Broderick A. E., Dexter J., Hada K., Kino M., Nagai H., Honma M., Johnson M. D., Algaba J. C., Asada K., Brinkerink C., Blundell R., Bower G. C., Cappallo R., Crew G. B., *230 GHz VLBI Observations of M87: Event-horizon-scale Structure during an Enhanced Very-high-energy  $\gamma$ -Ray State in 2012*, *ApJ* **807**, 150 (2015), [arXiv:1505.03545](#). [165](#), [170](#)
- Aleksić J. et al. (MAGIC Collaboration), *MAGIC observations of the giant radio galaxy M 87 in a low-emission state between 2005 and 2007*, *A&A* **544**, A96 (2012), [arXiv:1207.2147](#). [142](#)
- Ali-Haïmoud Y., Chluba J., Kamionkowski M., *Constraints on Dark Matter Interactions with Standard Model Particles from Cosmic Microwave Background Spectral Distortions*, *Physical Review Letters* **115**, 071304 (2015), [arXiv:1506.04745](#). [41](#)
- Allahverdi R., Drees M., *Thermalization after inflation and production of massive stable particles*, *Phys. Rev. D* **66**, 063513 (2002), [arXiv:hep-ph/0205246](#). [15](#)
- Aloisio R., Blasi P., Olinto A. V., *Neutralino annihilation at the galactic centre revisited*, *JCAP* **5**, 7 (2004), [arXiv:astro-ph/0402588](#). [62](#), [116](#), [141](#), [142](#), [143](#), [146](#), [166](#), [167](#), [168](#), [182](#), [183](#)
- Alpher R. A., Follin J. W., Herman R. C., *Physical Conditions in the Initial Stages of the Expanding Universe*, *Physical Review* **92**, 1347-1361 (1953). [14](#)
- Alpher R. A., Herman R., *Evolution of the Universe*, *Nature* **162**, 774-775 (1948). [9](#)
- Altarelli G., *Collider Physics within the Standard Model: a Primer*, *ArXiv e-prints* (2013), [arXiv:1303.2842](#). [20](#)
- Amaudruz P.-A. et al. (DEAP Collaboration), *DEAP-3600 Dark Matter Search*, *ArXiv e-prints* (2014), [arXiv:1410.7673](#). [33](#)

- Anderson B., Zimmer S., Conrad J., Gustafsson M., Sánchez-Conde M., Caputo R., *Search for gamma-ray lines towards galaxy clusters with the Fermi-LAT*, *JCAP* **2**, 026 (2016), [arXiv:1511.00014](#). 46
- Anderson L., Aubourg É., Bailey S., Beutler F., Bhardwaj V., Blanton M., Bolton A. S., Brinkmann J., Brownstein J. R., Burden A., Chuang C.-H., Cuesta A. J., Dawson K. S., Eisenstein D. J., Escoffier S., Gunn J. E., Guo H., Ho S., Honscheid K., Howlett C., Kirkby D., Lupton R. H., Manera M., Maraston C., McBride C. K., Mena O., Montesano F., Nichol R. C., Nuza S. E., Olmstead M. D., Padmanabhan N., Palanque-Delabrouille N., Parejko J., Percival W. J., Petitjean P., Prada F., Price-Whelan A. M., Reid B., Roe N. A., Ross A. J., Ross N. P., Sabiu C. G., Saito S., Samushia L., Sánchez A. G., Schlegel D. J., Schneider D. P., Scoccola C. G., Seo H.-J., Skibba R. A., Strauss M. A., Swanson M. E. C., Thomas D., Tinker J. L., Tojeiro R., Magaña M. V., Verde L., Wake D. A., Weaver B. A., Weinberg D. H., White M., Xu X., Yèche C., Zehavi I., Zhao G.-B., *The clustering of galaxies in the SDSS-III Baryon Oscillation Spectroscopic Survey: baryon acoustic oscillations in the Data Releases 10 and 11 Galaxy samples*, *MNRAS* **441**, 24-62 (2014), [arXiv:1312.4877](#). 13, 15
- Angle J. et al. (XENON10 Collaboration), *Search for Light Dark Matter in XENON10 Data*, *Physical Review Letters* **107**, 051301 (2011), [arXiv:1104.3088](#). 33
- Angloher G. et al. (CRESST Collaboration), *Results from 730 kg days of the CRESST-II Dark Matter search*, *European Physical Journal C* **72**, 1971 (2012), [arXiv:1109.0702](#). 33
- Angloher G. et al. (CRESST Collaboration), *Results on low mass WIMPs using an upgraded CRESST-II detector*, *European Physical Journal C* **74**, 3184 (2014), [arXiv:1407.3146](#). 33
- Angloher G. et al. (CRESST Collaboration), *Results on light dark matter particles with a low-threshold CRESST-II detector*, *ArXiv e-prints* (2015), [arXiv:1509.01515](#). 33
- Appelquist T., Cheng H.-C., Dobrescu B. A., *Bounds on universal extra dimensions*, *Phys. Rev. D* **64**, 035002 (2001), [arXiv:hep-ph/0012100](#). 24
- Aprile E. (for the XENON1T Collaboration), *The XENON1T Dark Matter Search Experiment*, *ArXiv e-prints* (2012), [arXiv:1206.6288](#). 34
- Aprile E. et al. (XENON100 Collaboration), *Dark Matter Results from 100 Live Days of XENON100 Data*, *Physical Review Letters* **107**, 131302 (2011), [arXiv:1104.2549](#). 33
- Aprile E. et al. (XENON100 Collaboration), *Dark Matter Results from 225 Live Days of XENON100 Data*, *Physical Review Letters* **109**, 181301 (2012), [arXiv:1207.5988](#). 33
- Aprile E. et al. (XENON100 Collaboration), *Limits on Spin-Dependent WIMP-Nucleon Cross Sections from 225 Live Days of XENON100 Data*, *Physical Review Letters* **111**, 021301 (2013), [arXiv:1301.6620](#). 36
- Aprile E. et al. (XENON100 Collaboration), *First axion results from the XENON100 experiment*, *Phys. Rev. D* **90**, 062009 (2014). 36
- Archambault S. et al. (PICASSO Collaboration), *Constraints on low-mass WIMP interactions on  $^{19}\text{F}$  from PICASSO*, *Physics Letters B* **711**, 153-161 (2012), [arXiv:1202.1240](#). 36
- Arina C., Del Nobile E., Panci P., *Dark Matter with Pseudoscalar-Mediated Interactions Explains the DAMA Signal and the Galactic Center Excess*, *Physical Review Letters* **114**, 011301 (2015), [arXiv:1406.5542](#). 33

- Arlen T., Aune T., Beilicke M., Benbow W., Bouvier A., Buckley J. H., Bugaev V., Byrum K., Cannon A., Cesarini A., Ciupik L., Collins-Hughes E., Connolly M. P., Cui W., Dickherber R., Dumm J., Falcone A., Federici S., Feng Q., Finley J. P., Finnegan G., Fortson L., Furniss A., Galante N., Gall D., Godambe S., Griffin S., Grube J., Gyuk G., Holder J., Huan H., Hughes G., Humensky T. B., Imran A., Kaaret P., Karlsson N., Kertzman M., Khassen Y., Kieda D., Krawczynski H., Krennrich F., Lee K., Madhavan A. S., Maier G., Majumdar P., McArthur S., McCann A., Moriarty P., Mukherjee R., Nelson T., O'Faoláin de Bhróithe A., Ong R. A., Orr M., Otte A. N., Park N., Perkins J. S., Pohl M., Prokoph H., Quinn J., Ragan K., Reyes L. C., Reynolds P. T., Roache E., Ruppel J., Saxon D. B., Schroedter M., Sembroski G. H., Skole C., Smith A. W., Telezhinsky I., Tešić G., Theiling M., Thibadeau S., Tsurusaki K., Varlotta A., Vivier M., Wakely S. P., Ward J. E., Weinstein A., Welsing R., Williams D. A., Zitzer B., Pfrommer C., Pinzke A., *Constraints on Cosmic Rays, Magnetic Fields, and Dark Matter from Gamma-Ray Observations of the Coma Cluster of Galaxies with VERITAS and Fermi*, *ApJL* **757**, 123 (2012), arXiv:1208.0676. 47
- Armengaud E. et al. (EDELWEISS Collaboration), *Final results of the EDELWEISS-II WIMP search using a 4-kg array of cryogenic germanium detectors with interleaved electrodes*, *Physics Letters B* **702**, 329-335 (2011), arXiv:1103.4070. 33
- Armengaud E. et al. (EDELWEISS Collaboration), *Axion searches with the EDELWEISS-II experiment*, *JCAP* **11**, 067 (2013), arXiv:1307.1488. 36
- Arraki K. S., Klypin A., More S., Trujillo-Gomez S., *Effects of baryon removal on the structure of dwarf spheroidal galaxies*, *MNRAS* **438**, 1466-1482 (2014), arXiv:1212.6651. 27
- Arvanitaki A., Dimopoulos S., Dubovsky S., Kaloper N., March-Russell J., *String axiverse*, *Phys. Rev. D* **81**, 123530 (2010), arXiv:0905.4720. 25
- Asaka T., Blanchet S., Shaposhnikov M., *The  $\nu$ MSM, dark matter and neutrino masses [rapid communication]*, *Physics Letters B* **631**, 151-156 (2005), arXiv:hep-ph/0503065. 21, 22
- Ascasibar Y., Jean P., Boehm C., Knödseder J., *Constraints on dark matter and the shape of the Milky Way dark halo from the 511-keV line*, *MNRAS* **368**, 1695-1705 (2006), arXiv:astro-ph/0507142. 118, 122
- Askew A., Chauhan S., Penning B., Shepherd W., Tripathi M., *Searching for dark matter at hadron colliders*, *International Journal of Modern Physics A* **29**, 1430041 (2014), arXiv:1406.5662. 37, 38, 39, 40
- Asplund M., Grevesse N., Jacques Sauval A., *The solar chemical composition*, *Nuclear Physics A* **777**, 1-4 (2006), arXiv:astro-ph/0410214. 68
- Atre A., Han T., Pascoli S., Zhang B., *The search for heavy Majorana neutrinos*, *Journal of High Energy Physics* **5**, 030 (2009), arXiv:0901.3589. 21
- Atwood W., Albert A., Baldini L., Tinivella M., Bregeon J., Pesce-Rollins M., Sgrò C., Bruel P., Charles E., Drlica-Wagner A., Franckowiak A., Jogler T., Rochester L., Usher T., Wood M., Cohen-Tanugi J., S. Zimmer for the Fermi-LAT Collaboration, *Pass 8: Toward the Full Realization of the Fermi-LAT Scientific Potential*, ArXiv e-prints (2013), arXiv:1303.3514. 194
- Atwood W. B. et al. (Fermi-LAT Collaboration), *The Large Area Telescope on the Fermi Gamma-Ray Space Telescope Mission*, *ApJ* **697**, 1071-1102 (2009), arXiv:0902.1089. 44, 104
- Baer H., Choi K.-Y., Kim J. E., Roszkowski L., *Dark matter production in the early Universe: Beyond the thermal WIMP paradigm*, *Physics Reports* **555**, 1-60 (2015), arXiv:1407.0017. 15

- Bahcall J. N., Soneira R. M., *The universe at faint magnitudes. I - Models for the galaxy and the predicted star counts*, *ApJS* **44**, 73-110 (1980). 54
- Bahcall J. N., Wolf R. A., *Star distribution around a massive black hole in a globular cluster*, *ApJ* **209**, 214-232 (1976). 62
- Baker C. A., Doyle D. D., Geltenbort P., Green K., van der Grinten M. G. D., Harris P. G., Iaydjiev P., Ivanov S. N., May D. J. R., Pendlebury J. M., Richardson J. D., Shiers D., Smith K. F., *Improved Experimental Limit on the Electric Dipole Moment of the Neutron*, *Physical Review Letters* **97**, 131801 (2006), arXiv:hep-ex/0602020. 24
- Baltz E. A., Edsjö J., *Positron propagation and fluxes from neutralino annihilation in the halo*, *Phys. Rev. D* **59**, 023511 (1999), arXiv:astro-ph/9808243. 80
- Baluni V., *CP-nonconserving effects in quantum chromodynamics*, *Phys. Rev. D* **19**, 2227-2230 (1979). 24
- Barbieri R., Hall L. J., Rychkov V. S., *Improved naturalness with a heavy Higgs boson: An alternative road to CERN LHC physics*, *Phys. Rev. D* **74**, 015007 (2006), arXiv:hep-ph/0603188. 25
- Barreto J., Cease H., Diehl H. T., Estrada J., Flaughner B., Harrison N., Jones J., Kilminster B., Molina J., Smith J., Schwarz T., Sonnenschein A., *Direct search for low mass dark matter particles with CCDs*, *Physics Letters B* **711**, 264-269 (2012), arXiv:1105.5191. 33
- Bartels R., Krishnamurthy S., Weniger C., *Strong support for the millisecond pulsar origin of the Galactic center GeV excess*, ArXiv e-prints (2015), arXiv:1506.05104. 89
- Barwick S. W. et al. (HEAT Collaboration), *Measurements of the Cosmic-Ray Positron Fraction from 1 to 50 GeV*, *ApJL* **482**, L191-L194 (1997), arXiv:astro-ph/9703192. 41
- Bassett B., Hlozek R., *Baryon acoustic oscillations*, in *Dark Energy: Observational and Theoretical Approaches*, Cambridge University Press (2010), arXiv:0910.5224. 11, 12
- Batell B., Essig R., Surujon Z., *Strong Constraints on Sub-GeV Dark Sectors from SLAC Beam Dump E137*, *Physical Review Letters* **113**, 171802 (2014), arXiv:1406.2698. 34
- Battaglieri M. et al. (BDX Collaboration), *Dark matter search in a Beam-Dump eXperiment (BDX) at Jefferson Lab*, ArXiv e-prints (2014), arXiv:1406.3028. 34
- Battat J. B. R. et al. (DRIFT Collaboration), *First background-free limit from a directional dark matter experiment: Results from a fully fiducialised DRIFT detector*, *Physics of the Dark Universe* **9**, 1-7 (2015), arXiv:1410.7821. 34, 36
- Baudis L., *Direct dark matter detection: The next decade*, *Physics of the Dark Universe* **1**, 94-108 (2012), arXiv:1211.7222. 30, 31
- Baudis L., Ferella A., Kish A., Manalaysay A., Marrodán Undagoitia T., Schumann M., *Neutrino physics with multi-ton scale liquid xenon detectors*, *JCAP* **1**, 044 (2014), arXiv:1309.7024. 34
- Beck R., *Cosmic Magnetic Fields: Observations and Prospects*, *AIP Conference Proceedings* **1381**, 117-136 (2011), arXiv:1104.3749. 70
- Bednarek W., Sobczak T., *Gamma-rays from millisecond pulsar population within the central stellar cluster in the Galactic Centre*, *MNRAS* **435**, L14-L18 (2013), arXiv:1306.4760. 129, 135, 159

- Begeman K. G., Broeils A. H., Sanders R. H., *Extended rotation curves of spiral galaxies - Dark haloes and modified dynamics*, *MNRAS* **249**, 523-537 (1991). 5, 54
- Behnke E. et al. (COUPP Collaboration), *First dark matter search results from a 4-kg CF<sub>3</sub>I bubble chamber operated in a deep underground site*, *Phys. Rev. D* **86**, 052001 (2012), arXiv:1204.3094. 33, 36
- Bekenstein J. D., *Relativistic gravitation theory for the modified Newtonian dynamics paradigm*, *Phys. Rev. D* **70**, 083509 (2004), arXiv:astro-ph/0403694. 27
- Bekenstein J. D., *Erratum: Relativistic gravitation theory for the modified Newtonian dynamics paradigm [Phys. Rev. D 70, 083509 (2004)]*, *Phys. Rev. D* **71**, 069901 (2005). 27
- Bélançer G., *micrOMEGAs and the relic density in the MSSM*, ArXiv e-prints (2002), arXiv:hep-ph/0210350. 19
- Bélançer G., Boehm C., Cirelli M., Da Silva J., Pukhov A., *PAMELA and FERMI limits on the neutralino-chargino mass degeneracy*, *JCAP* **11**, 028 (2012), arXiv:1208.5009. 43
- Belikov A., Silk J., *Diffuse gamma ray background from annihilating dark matter in density spikes around supermassive black holes*, *Phys. Rev. D* **89**, 043520 (2014), arXiv:1312.0007. 62
- Belikov A. V., Zaharijas G., Silk J., *Study of the gamma-ray spectrum from the Galactic Center in view of multi-TeV dark matter candidates*, *Phys. Rev. D* **86**, 083516 (2012), arXiv:1207.2412. 62
- Benbow W., *The Status and Performance of H.E.S.S.*, *AIP Conf. Proc.* **745**, 611-616 (2005). 143
- Bennett C. L., Banday A. J., Gorski K. M., Hinshaw G., Jackson P., Keegstra P., Kogut A., Smoot G. F., Wilkinson D. T., Wright E. L., *Four-Year COBE DMR Cosmic Microwave Background Observations: Maps and Basic Results*, *ApJL* **464**, L1 (1996), arXiv:astro-ph/9601067. 9
- Bennett C. L., Larson D., Weiland J. L., Jarosik N., Hinshaw G., Odegard N., Smith K. M., Hill R. S., Gold B., Halpern M., Komatsu E., Nolte M. R., Page L., Spergel D. N., Wollack E., Dunkley J., Kogut A., Limon M., Meyer S. S., Tucker G. S., Wright E. L., *Nine-year Wilkinson Microwave Anisotropy Probe (WMAP) Observations: Final Maps and Results*, *ApJS* **208**, 20 (2013), arXiv:1212.5225. 9
- Berezinsky V. S., Bottino A., de Alfaro V., *Is it possible to detect the gamma-ray line from neutralino-neutralino annihilation?*, *Physics Letters B* **274**, 122-127 (1992). 44
- Bergström L., *Dark matter candidates*, *New Journal of Physics* **11**, 105006 (2009), arXiv:0903.4849. 21
- Bergström L., Bringmann T., Cholis I., Hooper D., Weniger C., *New Limits on Dark Matter Annihilation from Alpha Magnetic Spectrometer Cosmic Ray Positron Data*, *Physical Review Letters* **111**, 171101 (2013), arXiv:1306.3983. 42, 96, 107
- Bergström L., Bringmann T., Edsjö J., *New positron spectral features from supersymmetric dark matter: A way to explain the PAMELA data?*, *Phys. Rev. D* **78**, 103520 (2008), arXiv:0808.3725. 41
- Bergström L., Edsjö J., Ullio P., *Cosmic Antiprotons as a Probe for Supersymmetric Dark Matter?*, *ApJ-astro-ph/9902012*. 41
- Bergström L., Kaplan J., *Gamma ray lines from TeV dark matter*, *Astroparticle Physics:hep-ph/9403239*. 44

- Bergström L., Snellman H., *Observable monochromatic photons from cosmic photino annihilation*, *Phys. Rev. D* **37**, 3737-3741 (1988). 44
- Bergström L., Ullio P., Buckley J. H., *Observability of  $\gamma$  rays from dark matter neutralino annihilations in the Milky Way halo*, *Astroparticle Physics:astro-ph/9712318*. 40, 44
- Beringer J., Arguin J.-F., Barnett R. M., Copic K., Dahl O., Groom D. E., Lin C.-J., Lys J., Murayama H., Wohl C. G., Yao W.-M., Zyla P. A., Amsler C., Antonelli M., Asner D. M., Baer H., Band H. R., Basaglia T., Bauer C. W., Beatty J. J., Belousov V. I., Bergren E., Bernardi G., Bertl W., Bethke S., Bichsel H., Biebel O., Blucher E., Blusk S., Brooijmans G., Buchmueller O., Cahn R. N., Carena M., Ceccucci A., Chakraborty D., Chen M.-C., Chivukula R. S., Cowan G., D'Ambrosio G., Damour T., de Florian D., de Gouvêa A., DeGrand T., de Jong P., Dissertori G., Dobrescu B., Doser M., Drees M., Edwards D. A., Eidelman S., Erler J., Ezhela V. V., Fetscher W., Fields B. D., Foster B., Gaisser T. K., Garren L., Gerber H.-J., Gerbier G., Gherghetta T., Golwala S., Goodman M., Grab C., Gribsan A. V., Grivaz J.-F., Grünewald M., Gurtu A., Gutsche T., Haber H. E., Hagiwara K., Hagmann C., Hanhart C., Hashimoto S., Hayes K. G., Heffner M., Heltsley B., Hernández-Rey J. J., Hikasa K., Höcker A., Holder J., Holtkamp A., Huston J., Jackson J. D., Johnson K. F., Junk T., Karlen D., Kirkby D., Klein S. R., Klempt E., Kowalewski R. V., Krauss F., Kreps M., Krusche B., Kuyanov Y. V., Kwon Y., Lahav O., Laiho J., Langacker P., Liddle A., Ligeti Z., Liss T. M., Littenberg L., Lugovsky K. S., Lugovsky S. B., Mannel T., Manohar A. V., Marciano W. J., Martin A. D., Masoni A., Matthews J., Milstead D., Miquel R., Mönig K., Moortgat F., Nakamura K., Narain M., Nason P., Navas S., Neubert M., Nevski P., Nir Y., Olive K. A., Pape L., Parsons J., Patrignani C., Peacock J. A., Petcov S. T., Piepke A., Pomarol A., Punzi G., Quadt A., Raby S., Raffelt G., Ratcliff B. N., Richardson P., Roesler S., Rolli S., Romaniouk A., Rosenberg L. J., Rosner J. L., Sachrajda C. T., Sakai Y., Salam G. P., Sarkar S., Sauli F., Schneider O., Scholberg K., Scott D., Seligman W. G., Shaevitz M. H., Sharpe S. R., Silari M., Sjöstrand T., Skands P., Smith J. G., Smoot G. F., Spanier S., Spieler H., Stahl A., Stanev T., Stone S. L., Sumiyoshi T., Syphers M. J., Takahashi F., Tanabashi M., Terning J., Titov M., Tkachenko N. P., Törnqvist N. A., Tovey D., Valencia G., van Bibber K., Venanzoni G., Vincter M. G., Vogel P., Vogt A., Walkowiak W., Walter C. W., Ward D. R., Watari T., Weiglein G., Weinberg E. J., Wiencke L. R., Wolfenstein L., Womersley J., Woody C. L., Workman R. L., Yamamoto A., Zeller G. P., Zenin O. V., Zhang J., Zhu R.-Y., Harper G., Lugovsky V. S., Schaffner P., *Review of Particle Physics*, *Phys. Rev. D* **86**, 010001 (2012). 93
- Berlin A., Hooper D., Krnjaic G., *PeV-Scale Dark Matter as a Thermal Relic of a Decoupled Sector*, ArXiv e-prints (2016), [arXiv:1602.08490](https://arxiv.org/abs/1602.08490). 132
- Bernabei R., Belli P., Cerulli R., Montecchia F., Nozzoli F., Incicchitti A., Prosperi D., Dai C. J., He H. L., Kuang H. H., Ma J. M., Scopel S., *Search for solar axions by Primakoff effect in NaI crystals*, *Physics Letters B* **515**, 6-12 (2001). 36
- Bernabei R. et al. (DAMA/LIBRA Collaboration), *New results from DAMA/LIBRA*, *European Physical Journal C* **67**, 39-49 (2010), [arXiv:1002.1028](https://arxiv.org/abs/1002.1028). 33
- Bertone G., *Particle Dark Matter*, Cambridge University Press (2013). 21
- Bertone G., Hooper D., Silk J., *Particle dark matter: evidence, candidates and constraints*, *Physics Reports* **405**, 279-390 (2005), [arXiv:hep-ph/0404175](https://arxiv.org/abs/hep-ph/0404175). 21, 55
- Bertone G., Sigl G., Silk J., *Astrophysical limits on massive dark matter*, *MNRAS* **326**, 799-804 (2001), [arXiv:astro-ph/0101134](https://arxiv.org/abs/astro-ph/0101134). 62
- Bertone G., Sigl G., Silk J., *Annihilation radiation from a dark matter spike at the Galactic Centre*, *MNRAS* **337**, 98-102 (2002), [arXiv:astro-ph/0203488](https://arxiv.org/abs/astro-ph/0203488). 62, 116

- Bhattacharya D., van den Heuvel E. P. J., *Formation and evolution of binary and millisecond radio pulsars*, *Physics Reports* **203**, 1-124 (1991). 88
- Billard J., Figueroa-Feliciano E., Strigari L., *Implication of neutrino backgrounds on the reach of next generation dark matter direct detection experiments*, *Phys. Rev. D* **89**, 023524 (2014), arXiv:1307.5458. 34
- Binétruy P., Girardi G., Salati P., *Constraints on a system of two neutral fermions from cosmology*, *Nuclear Physics B* **237**, 285-306 (1984a). 15
- Binétruy P., Girardi G., Salati P., *Cosmological constraints on unstable heavy neutrinos*, *Physics Letters B* **134**, 174-178 (1984b). 15
- Binney J., Tremaine S., *Galactic dynamics*, Princeton University Press (1987). 61
- Binney J. J., Evans N. W., *Cuspy dark matter haloes and the Galaxy*, *MNRAS* **327**, L27-L31 (2001), arXiv:astro-ph/0108505. 54
- Bird S., Cholis I., Muñoz J. B., Ali-Haïmoud Y., Kamionkowski M., Kovetz E. D., Raccanelli A., Riess A. G., *Did LIGO detect dark matter?*, ArXiv e-prints (2016), arXiv:1603.00464. 20
- Bird S., Harris W. E., Blakeslee J. P., Flynn C., *The inner halo of M 87: a first direct view of the red-giant population*, *A&A* **524**, A71 (2010), arXiv:1009.3202. 140
- Biretta J. A., Stern C. P., Harris D. E., *The radio to X-ray spectrum of the M87 jet and nucleus*, *Astron. J.* **101**, 1632-1646 (1991). 142
- Blandford R., Eichler D., *Particle acceleration at astrophysical shocks: A theory of cosmic ray origin*, *Physics Reports* **154**, 1-75 (1987). 73
- Blumenthal G. R., Faber S. M., Flores R., Primack J. R., *Contraction of dark matter galactic halos due to baryonic infall*, *ApJ* **301**, 27-34 (1986). 55, 62, 90
- Blumenthal G. R., Faber S. M., Primack J. R., Rees M. J., *Formation of galaxies and large-scale structure with cold dark matter*, *Nature* **311**, 517-525 (1984). 12
- Blumenthal G. R., Gould R. J., *Bremsstrahlung, Synchrotron Radiation, and Compton Scattering of High-Energy Electrons Traversing Dilute Gases*, *Review of Modern Physics* **42**, 237-271 (1970). 65, 66, 68, 69
- Blumenthal G. R., Pagels H., Primack J. R., *Galaxy formation by dissipationless particles heavier than neutrinos*, *Nature* **299**, 37 (1982). 12
- Böehm C., Delahaye T., Silk J., *Can the Morphology of  $\gamma$ -Ray Emission Distinguish Annihilating from Decaying Dark Matter?*, *Physical Review Letters* **105**, 221301 (2010), arXiv:1003.1225. 118, 122
- Böehm C., Djouadi A., Drees M., *Light scalar top quarks and supersymmetric dark matter*, *Phys. Rev. D* **62**, 035012 (2000), arXiv:hep-ph/9911496. 158
- Böehm C., Dolan M. J., McCabe C., *A lower bound on the mass of cold thermal dark matter from Planck*, *JCAP* **8**, 041 (2013), arXiv:1303.6270. 18
- Böehm C., Dolan M. J., McCabe C., Spannowsky M., Wallace C. J., *Extended gamma-ray emission from Coy Dark Matter*, *JCAP* **5**, 009 (2014a), arXiv:1401.6458. 99
- Böehm C., Enßlin T. A., Silk J., *Can annihilating dark matter be lighter than a few GeVs?*, *Journal of Physics G Nuclear Physics* **30**, 279-285 (2004a), arXiv:astro-ph/0208458. 25, 47, 116, 125

- Boehm C., Fayet P., *Scalar dark matter candidates*, Nuclear Physics B **683**, 219-263 (2004), arXiv:hep-ph/0305261. 18, 25
- Boehm C., Fayet P., Schaeffer R., *Constraining dark matter candidates from structure formation*, Physics Letters B **518**, 8-14 (2001), arXiv:astro-ph/0012504. 12, 13, 41
- Boehm C., Fayet P., Silk J., *Light and heavy dark matter particles*, Phys. Rev. D **69**, 101302 (2004b), arXiv:hep-ph/0311143. 158
- Boehm C., Hooper D., Silk J., Casse M., Paul J., *MeV Dark Matter: Has It Been Detected?*, Physical Review Letters **92**, 101301 (2004c), arXiv:astro-ph/0309686. 46
- Boehm C., Lavallo J., *Clarifying the covariant formalism for the Sunyaev-Zel'dovich effect due to relativistic nonthermal electrons*, Phys. Rev. D **79**, 083505 (2009), arXiv:0812.3282. 117
- Boehm C., Mathis H., Devriendt J., Silk J., *Non-linear evolution of suppressed dark matter primordial power spectra*, MNRAS **360**, 282-287 (2005). 12, 13
- Boehm C., Riazuelo A., Hansen S. H., Schaeffer R., *Interacting dark matter disguised as warm dark matter*, Phys. Rev. D **66**, 083505 (2002), arXiv:astro-ph/0112522. 12, 13, 41
- Boehm C., Schaeffer R., *Constraints on Dark Matter interactions from structure formation: damping lengths*, A&A **438**, 419-442 (2005), arXiv:astro-ph/0410591. 12, 13, 41
- Boehm C., Schewtschenko J. A., Wilkinson R. J., Baugh C. M., Pascoli S., *Using the Milky Way satellites to study interactions between cold dark matter and radiation*, MNRAS **445**, L31-L35 (2014b), arXiv:1404.7012. 12, 13, 26
- Boehm C., Silk J., Ensslin T., *Radio observations of the Galactic Centre and the Coma cluster as a probe of light dark matter self-annihilations and decay*, ArXiv e-prints (2010), arXiv:1008.5175. 78, 116, 124, 125
- Boezio M., Barbiellini G., Bonvicini V., Schiavon P., Vacchi A., Zampa N., Bergström D., Carlson P., Francke T., Grinstein S., Weber N., Suffert M., Hof M., Kremer J., Menn W., Simon M., Stephens S. A., Ambriola M., Bellotti R., Cafagna F. S., Ciacio F., Circella M., De Marzo C., Finetti N., Papini P., Piccardi S., Spillantini P., Bartalucci S., Ricci M., Grimani C., Casolino M., De Pascale M. P., Morselli A., Picozza P., Sparvoli R., Mitchell J. W., Ormes J. F., Streitmatter R. E., Bravar U., Stochaj S. J., *Measurements of cosmic-ray electrons and positrons by the Wizard/CAPRICE collaboration*, Advances in Space Research **27**, 669-674 (2001). 42
- Bond J. R., Szalay A. S., Turner M. S., *Formation of galaxies in a gravitino-dominated universe*, Physical Review Letters **48**, 1636-1639 (1982). 13
- Borriello A., Salucci P., *The dark matter distribution in disc galaxies*, MNRAS **323**, 285-292 (2001), arXiv:astro-ph/0001082. 54
- Bosma A., van der Kruit P. C., *The local mass-to-light ratio in spiral galaxies*, A&A **79**, 281-286 (1979). 5
- Bou-Cabo M. (for the PICO Collaboration), *Dark matter searches using superheated liquid detectors*, in Talk at the Roma International Conference on Astroparticle Physics 2014, Noto, Italy (2014). 34
- Boudaud M., Aupetit S., Caroff S., Putze A., Belanger G., Genolini Y., Goy C., Poireau V., Poulin V., Rosier S., Salati P., Tao L., Vecchi M., *A new look at the cosmic ray positron fraction*, A&A **575**, A67 (2015a), arXiv:1410.3799. 42

- Boudaud M., Cirelli M., Giesen G., Salati P., *A fussy revisit of antiprotons as a tool for Dark Matter searches*, *JCAP* **5**, 013 (2015b), arXiv:1412.5696. 43
- Bouquet A., Casse M., Prantzos N., Salati P., *Weakly Interacting Massive Particles and Solar Neutrinos*, *International Cosmic Ray Conference* **4**, 365 (1987). 48
- Bouquet A., Salati P., *R-parity breaking and cosmological consequences*, *Nuclear Physics B* **284**, 557-588 (1987). 15
- Bouquet A., Salati P., Silk J.,  *$\gamma$ -ray lines as a probe for a cold-dark-matter halo*, *Phys. Rev. D* **40**, 3168-3186 (1989). 40, 44
- Bovy J., Tremaine S., *On the Local Dark Matter Density*, *ApJ* **756**, 89 (2012), arXiv:1205.4033. 4, 59
- Boyarsky A., Malyshev D., Ruchayskiy O., *A comment on the emission from the Galactic Center as seen by the Fermi telescope*, *Physics Letters B* **705**, 165-169 (2011), arXiv:1012.5839. 88
- Boyarsky A., Ruchayskiy O., Iakubovskiy D., Franse J., *Unidentified Line in X-Ray Spectra of the Andromeda Galaxy and Perseus Galaxy Cluster*, *Physical Review Letters* **113**, 251301 (2014), arXiv:1402.4119. 22
- Boyarsky A., Ruchayskiy O., Shaposhnikov M., *The Role of Sterile Neutrinos in Cosmology and Astrophysics*, *Annual Review of Nuclear and Particle Science* **59**, 191-214 (2009), arXiv:0901.0011. 21, 22
- Boylan-Kolchin M., Bullock J. S., Kaplinghat M., *Too big to fail? The puzzling darkness of massive Milky Way subhaloes*, *MNRAS* **415**, L40-L44 (2011), arXiv:1103.0007. 26
- Bozza V., *Gravitational lensing by black holes*, *General Relativity and Gravitation* **42**, 2269-2300 (2010), arXiv:0911.2187. 165
- Brandt T. D., Kocsis B., *Disrupted Globular Clusters Can Explain the Galactic Center Gamma-Ray Excess*, *ApJ* **812**, 15 (2015), arXiv:1507.05616. 89
- Bringmann T., Bergström L., Edsjö J., *New gamma-ray contributions to supersymmetric dark matter annihilation*, *Journal of High Energy Physics* **1**, 049 (2008), arXiv:0710.3169. 44
- Bringmann T., Donato F., Lineros R. A., *Radio data and synchrotron emission in consistent cosmic ray models*, *JCAP* **1**, 049 (2012b), arXiv:1106.4821. 74
- Bringmann T., Huang X., Ibarra A., Vogl S., Weniger C., *Fermi LAT search for internal bremsstrahlung signatures from dark matter annihilation*, *JCAP* **7**, 054 (2012), arXiv:1203.1312. 46
- Bringmann T., Vollmann M., Weniger C., *Updated cosmic-ray and radio constraints on light dark matter: Implications for the GeV gamma-ray excess at the Galactic Center*, *Phys. Rev. D* **90**, 123001 (2014), arXiv:1406.6027. 42, 90, 96, 97, 99, 107
- Bringmann T., Weniger C., *Gamma ray signals from dark matter: Concepts, status and prospects*, *Physics of the Dark Universe* **1**, 194-217 (2012), arXiv:1208.5481. 44, 46
- Brodatzki K. A., Pardy D. J. S., Becker J. K., Schlickeiser R., *Internal  $\gamma\gamma$  Opacity in Active Galactic Nuclei and the Consequences for the TeV Observations of M87 and Cen A*, *ApJ* **736**, 98 (2011), arXiv:1103.5552. 147, 166
- Broderick A. E., *Radiative transfer along rays in curved space-times*, *MNRAS* **366**, L10-L12 (2006), arXiv:astro-ph/0511515. 169

- Broderick A. E., Fish V. L., Doeleman S. S., Loeb A., *Evidence for Low Black Hole Spin and Physically Motivated Accretion Models from Millimeter-VLBI Observations of Sagittarius A\**, *ApJ* **735**, 110 (2011), arXiv:1011.2770. 165, 166
- Broderick A. E., Loeb A., *Frequency-dependent Shift in the Image Centroid of the Black Hole at the Galactic Center as a Test of General Relativity*, *ApJL* **636**, L109-L112 (2006a), arXiv:astro-ph/0508386. 169
- Broderick A. E., Loeb A., *Imaging optically-thin hotspots near the black hole horizon of Sgr A\* at radio and near-infrared wavelengths*, *MNRAS* **367**, 905-916 (2006b), arXiv:astro-ph/0509237. 169
- Brooks A., *Re-examining astrophysical constraints on the dark matter model*, *Annalen der Physik* **526**, 294-308 (2014), arXiv:1407.7544. 26, 55
- Brown A. M., Adams J., *High-energy  $\gamma$ -ray properties of the Fanaroff-Riley type I radio galaxy NGC 1275*, *MNRAS* **413**, 2785-2790 (2011), arXiv:1101.2687. 154, 155
- Brown A. M., Adams J., Chadwick P. M.,  *$\gamma$ -ray observations of extraterrestrial neutrino track events*, *MNRAS* **451**, 323-331 (2015), arXiv:1505.00935. 187
- Brown A. M., Boehm C., Graham J., Lacroix T., Chadwick P. M., Silk J., *Discovery of a new extragalactic source population of energetic particles*, ArXiv e-prints (2016), arXiv:1603.05469. 47, 153
- Buch J., Cirelli M., Giesen G., Taoso M., *PPPC 4 DM secondary: a Poor Particle Physicist Cookbook for secondary radiation from Dark Matter*, *JCAP* **9**, 37 (2015), arXiv:1505.01049. 78, 102, 103, 129
- Buchmüller W., Covi L., Hamaguchi K., Ibarra A., Yanagida T. T., *Gravitino dark matter in R-parity breaking vacua*, *Journal of High Energy Physics:hep-ph/0702184*. 40
- Bulbul E., Markevitch M., Foster A., Smith R. K., Loewenstein M., Randall S. W., *Detection of an Unidentified Emission Line in the Stacked X-Ray Spectrum of Galaxy Clusters*, *ApJ* **789**, 13 (2014), arXiv:1402.2301. 22
- Burkert A., *The Structure of Dark Matter Halos in Dwarf Galaxies*, *ApJL* **447**, L25 (1995), arXiv:astro-ph/9504041. 54
- Calore F., Cholis I., McCabe C., Weniger C., *A tale of tails: Dark matter interpretations of the Fermi GeV excess in light of background model systematics*, *Phys. Rev. D* **91**, 063003 (2015a), arXiv:1411.4647. 87, 90, 102
- Calore F., Cholis I., Weniger C., *Background model systematics for the Fermi GeV excess*, *JCAP* **3**, 038 (2015b), arXiv:1409.0042. 88, 102
- Carlson E., Coogan A., Linden T., Profumo S., Ibarra A., Wild S., *Antihelium from dark matter*, *Phys. Rev. D* **89**, 076005 (2014), arXiv:1401.2461. 44
- Carlson E., Linden T., Profumo S., *Putting Things Back Where They Belong: Tracing Cosmic-Ray Injection with H<sub>2</sub>*, ArXiv e-prints (2015), arXiv:1510.04698. 88
- Carlson E., Profumo S., *Cosmic ray protons in the inner Galaxy and the Galactic Center gamma-ray excess*, *Phys. Rev. D* **90**, 023015 (2014), arXiv:1405.7685. 89
- Carlson E. D., Machacek M. E., Hall L. J., *Self-interacting dark matter*, *ApJ* **398**, 43-52 (1992). 25

- Carr B. J., Kohri K., Sendouda Y., Yokoyama J., *New cosmological constraints on primordial black holes*, *Phys. Rev. D* **81**, 104019 (2010), arXiv:0912.5297. 19
- Casse F., Lemoine M., Pelletier G., *Transport of cosmic rays in chaotic magnetic fields*, *Phys. Rev. D* **65**, 023002 (2002), arXiv:astro-ph/0109223. 73
- Chatrchyan S. et al. (CMS Collaboration), *Observation of a new boson at a mass of 125 GeV with the CMS experiment at the LHC*, *Physics Letters B* **716**, 30-61 (2012a), arXiv:1207.7235. 36
- Chatrchyan S. et al. (CMS Collaboration), *Search for Dark Matter and Large Extra Dimensions in pp Collisions Yielding a Photon and Missing Transverse Energy*, *Physical Review Letters* **108**, 261803 (2012b), arXiv:1204.0821. 37
- Chatrchyan S. et al. (CMS Collaboration), *Search for dark matter and large extra dimensions in monojet events in pp collisions at  $\sqrt{s} = 7$  TeV*, *Journal of High Energy Physics* **9**, 94 (2012c), arXiv:1206.5663. 37
- Chatrchyan S. et al. (CMS Collaboration), *Search for dark matter in the mono-lepton channel with pp collision events at center-of-mass energy of 8 TeV*, Tech. Rep. **CMS-PAS-EXO-13-004** (2013). 37
- Chatrchyan S. et al. (CMS Collaboration), *Search for invisible decays of Higgs bosons in the vector boson fusion and associated ZH production modes*, ArXiv e-prints (2014), arXiv:1404.1344. 39
- Chatrchyan S. et al. (CMS Collaboration), *Search for new physics in high mass diphoton events in proton-proton collisions at 13TeV*, Tech. Rep. **CMS-PAS-EXO-15-004** (2015). 39
- Chen X., Kamionkowski M., *Particle decays during the cosmic dark ages*, *Phys. Rev. D:astro-ph*/0310473. 40
- Cheng H.-C., Feng J. L., Matchev K. T., *Kaluza-Klein Dark Matter*, *Physical Review Letters* **89**, 211301 (2002), arXiv:hep-ph/0207125. 24
- Chernyakova M., Malyshev D., Aharonian F. A., Crocker R. M., Jones D. I., *The High-energy, Arcminute-scale Galactic Center Gamma-ray Source*, *ApJ* **726**, 60 (2011), arXiv:1009.2630. 160
- Chluba J., *Which spectral distortions does  $\Lambda$ CDM actually predict?*, *MNRAS* (2016), arXiv:1603.02496. 41
- Chluba J., Sunyaev R. A., *The evolution of CMB spectral distortions in the early Universe*, *MNRAS* **419**, 1294-1314 (2012), arXiv:1109.6552. 41
- Choi K. et al. (Super-Kamiokande Collaboration), *Search for Neutrinos from Annihilation of Captured Low-Mass Dark Matter Particles in the Sun by Super-Kamiokande*, *Physical Review Letters* **114**, 141301 (2015). 48
- Cholis I., Evoli C., Calore F., Linden T., Weniger C., Hooper D., *The Galactic Center GeV excess from a series of leptonic cosmic-ray outbursts*, *JCAP* **12**, 005 (2015b), arXiv:1506.05119. 90
- Cholis I., Hooper D., *Dark matter and pulsar origins of the rising cosmic ray positron fraction in light of new data from the AMS*, *Phys. Rev. D* **88**, 023013 (2013), arXiv:1304.1840. 42
- Cholis I., Hooper D., Linden T., *A New Determination of the Spectra and Luminosity Function of Gamma-Ray Millisecond Pulsars*, ArXiv e-prints (2014), arXiv:1407.5583. 89

- Cholis I., Hooper D., Linden T., *Challenges in explaining the Galactic Center gamma-ray excess with millisecond pulsars*, *JCAP* **6**, 043 (2015a), arXiv:1407.5625. 89
- Chung D. J. H., Kolb E. W., Riotto A., *Production of massive particles during reheating*, *Phys. Rev. D* **60**, 063504 (1999), arXiv:hep-ph/9809453. 15
- Churazov E., Sunyaev R., Sazonov S., Revnivtsev M., Varshalovich D., *Positron annihilation spectrum from the Galactic Centre region observed by SPI/INTEGRAL*, *MNRAS* **357**, 1377-1386 (2005), arXiv:astro-ph/0411351. 46
- Cirelli M., *Status of Indirect (and Direct) Dark Matter searches*, ArXiv e-prints (2015), arXiv:1511.02031. 40, 42, 49
- Cirelli M., Corcella G., Hektor A., Hütsi G., Kadastik M., Panci P., Raidal M., Sala F., Strumia A., *PPPC 4 DM ID: a poor particle physicist cookbook for dark matter indirect detection*, *JCAP* **3**, 51 (2011), arXiv:1012.4515. 44, 45, 55, 79, 82, 102, 130, 131, 167
- Cirelli M., Fornengo N., Strumia A., *Minimal dark matter*, *Nuclear Physics B* **753**, 178-194 (2006), arXiv:hep-ph/0512090. 25
- Cirelli M., Fornengo N., Taoso M., Vittino A., *Anti-helium from dark matter annihilations*, *Journal of High Energy Physics* **8**, 9 (2014b), arXiv:1401.4017. 44
- Cirelli M., Gaggero D., Giesen G., Taoso M., Urbano A., *Antiproton constraints on the GeV gamma-ray excess: a comprehensive analysis*, *JCAP* **12**, 45 (2014a), arXiv:1407.2173. 90, 103, 104
- Cirelli M., Panci P., *Inverse Compton constraints on the Dark Matter  $e^+e^-$  excesses*, *Nuclear Physics B* **821**, 399-416 (2009), arXiv:0904.3830. 66, 67, 76, 130
- Cirelli M., Serpico P. D., Zaharijas G., *Bremsstrahlung gamma rays from light dark matter*, *JCAP* **11**, 035 (2013), arXiv:1307.7152. 68, 78, 102
- Clesse S., García-Bellido J., *Massive primordial black holes from hybrid inflation as dark matter and the seeds of galaxies*, *Phys. Rev. D* **92**, 023524 (2015), arXiv:1501.07565. 20
- Clesse S., García-Bellido J., *The clustering of massive Primordial Black Holes as Dark Matter: measuring their mass distribution with Advanced LIGO*, ArXiv e-prints (2016), arXiv:1603.05234. 20
- Clowe D., Bradač M., Gonzalez A. H., Markevitch M., Randall S. W., Jones C., Zaritsky D., *A Direct Empirical Proof of the Existence of Dark Matter*, *ApJL* **648**, L109-L113 (2006), arXiv:astro-ph/0608407. 7
- Clowe D., Gonzalez A., Markevitch M., *Weak-Lensing Mass Reconstruction of the Interacting Cluster 1E 0657-558: Direct Evidence for the Existence of Dark Matter*, *ApJ* **604**, 596-603 (2004), arXiv:astro-ph/0312273. 7
- Cole S. et al. (2dFGRS Collaboration), *The 2dF Galaxy Redshift Survey: power-spectrum analysis of the final data set and cosmological implications*, *MNRAS* **362**, 505-534 (2005), arXiv:astro-ph/0501174. 11, 13
- Colin P., Borla Tridon D., Carmona E., De Sabata F., Gaug M., Lombardi S., Majumdar P., Moralejo A., Scalzotto V., Sitarek J., *Performance of the MAGIC telescopes in stereoscopic mode*, ArXiv e-prints (2009), arXiv:0907.0960. 143
- Colless M. et al. (2dFGRS Collaboration), *The 2dF Galaxy Redshift Survey: spectra and redshifts*, *MNRAS* **328**, 1039-1063 (2001), arXiv:astro-ph/0106498. 13

- Collins M. L. M., Chapman S. C., Rich R. M., Ibata R. A., Martin N. F., Irwin M. J., Bate N. F., Lewis G. F., Peñarrubia J., Arimoto N., Casey C. M., Ferguson A. M. N., Koch A., McConnachie A. W., Tanvir N., *The Masses of Local Group Dwarf Spheroidal Galaxies: The Death of the Universal Mass Profile*, *ApJ* **783**, 7 (2014), arXiv:1309.3053. 26
- Conrad J., Cohen-Tanugi J., Strigari L. E., *Wimp searches with gamma rays in the Fermi era: Challenges, methods and results*, *Soviet Journal of Experimental and Theoretical Physics* **121**, 1104-1135 (2015), arXiv:1503.06348. 44
- Cooley J., *Overview of non-liquid noble direct detection dark matter experiments*, *Physics of the Dark Universe* **4**, 92-97 (2014), arXiv:1410.4960. 34
- Covi L., Grefe M., Ibarra A., Tran D., *Unstable gravitino dark matter and neutrino flux*, *JCAP* **1**, 029 (2009), arXiv:0809.5030. 40
- Covi L., Kim H. B., Kim J. E., Roszkowski L., *Axinos as dark matter*, *Journal of High Energy Physics* **5**, 033 (2001), arXiv:hep-ph/0101009. 15
- Covi L., Kim J. E., Roszkowski L., *Axinos as Cold Dark Matter*, *Physical Review Letters* **82**, 4180-4183 (1999), arXiv:hep-ph/9905212. 15
- Coyle P. (for the KM3NeT Collaboration), *The KM3NeT Neutrino Telescope and Prospects for Dark Matter Detection*, in Proceedings of Identification of Dark Matter 2008 (2008). 48
- Crewther R. J., di Vecchia P., Veneziano G., Witten E., *Chiral estimate of the electric dipole moment of the neutron in quantum chromodynamics*, *Physics Letters B* **88**, 123-127 (1979). 24
- Crocker R. M., Jones D. I., Melia F., Ott J., Protheroe R. J., *A lower limit of 50 microgauss for the magnetic field near the Galactic Centre*, *Nature* **463**, 65-67 (2010), arXiv:1001.1275. 130
- Crusius A., Schlickeiser R., *Synchrotron radiation in random magnetic fields*, *A&A* **164**, L16-L18 (1986). 181
- Cushman P., Galbiati C., McKinsey D. N., Robertson H., Tait T. M. P., Bauer D., Borgland A., Cabrera B., Calaprice F., Cooley J., Empl T., Essig R., Figueroa-Feliciano E., Gaitskell R., Golwala S., Hall J., Hill R., Hime A., Hoppe E., Hsu L., Hungerford E., Jacobsen R., Kelsey M., Lang R. F., Lippincott W. H., Loer B., Luitz S., Mandic V., Mardon J., Maricic J., Maruyama R., Mahapatra R., Nelson H., Orrell J., Palladino K., Pantic E., Partridge R., Ryd A., Saab T., Sadoulet B., Schnee R., Shepherd W., Sonnenschein A., Sorensen P., Szydagis M., Volansky T., Witherell M., Wright D., Zurek K., *Snowmass CF1 Summary: WIMP Dark Matter Direct Detection*, ArXiv e-prints (2013), arXiv:1310.8327. 35
- Davis J. H., McCabe C., Boehm C., *Quantifying the evidence for dark matter in CoGeNT data*, *JCAP* **8**, 014 (2014), arXiv:1405.0495. 33
- Davis J. H., Silk J., Boehm C., Kotera K., Norman C., *Shocking Signals of Dark Matter Annihilation*, ArXiv e-prints (2015), arXiv:1507.04962. 156
- Davis M., Efstathiou G., Frenk C. S., White S. D. M., *The evolution of large-scale structure in a universe dominated by cold dark matter*, *ApJ* **292**, 371-394 (1985). 12
- Daylan T., Finkbeiner D. P., Hooper D., Linden T., Portillo S. K. N., Rodd N. L., Slatyer T. R., *The characterization of the gamma-ray signal from the central Milky Way: A case for annihilating dark matter*, *Physics of the Dark Universe* **12**, 1-23 (2016), arXiv:1402.6703. 87, 88, 90, 91, 92, 97, 102

- de Blok W. J. G., Bosma A., *High-resolution rotation curves of low surface brightness galaxies*, *A&A* **385**, 816-846 (2002), arXiv:astro-ph/0201276. 54
- de Blok W. J. G., McGaugh S. S., Rubin V. C., *High-Resolution Rotation Curves of Low Surface Brightness Galaxies. II. Mass Models*, *The Astronomical Journal* **122**, 2396-2427 (2001). 54
- de Blok W. J. G., Walter F., Brinks E., Trachternach C., Oh S.-H., Kennicutt Jr. R. C., *High-Resolution Rotation Curves and Galaxy Mass Models from THINGS*, *The Astronomical Journal* **136**, 2648-2719 (2008), arXiv:0810.2100. 54
- de Boer W., Gebauer I., Kunz S., Neumann A., *Evidence for a hadronic origin of the Fermi Bubbles and the Galactic Excess*, ArXiv e-prints (2015), arXiv:1509.05310. 88
- de Gasperin F., Orrú E., Murgia M., Merloni A., Falcke H., Beck R., Beswick R., Bîrzan L., Bonafede A., Brügger M., Brunetti G., Chyży K., Conway J., Croston J. H., Enßlin T., Ferrari C., Heald G., Heidenreich S., Jackson N., Macario G., McKean J., Miley G., Morganti R., Offringa A., Pizzo R., Rafferty D., Röttgering H., Shulevski A., Steinmetz M., Tasse C., van der Tol S., van Driel W., van Weeren R. J., van Zwieten J. E., Alexov A., Anderson J., Asgekar A., Avruch M., Bell M., Bell M. R., Bentum M., Bernardi G., Best P., Breitling F., Broderick J. W., Butcher A., Ciardi B., Dettmar R. J., Eisloffel J., Frieswijk W., Gankema H., Garrett M., Gerbers M., Griessmeier J. M., Gunst A. W., Hassall T. E., Hessels J., Hoeft M., Horneffer A., Karastergiou A., Köhler J., Koopman Y., Kuniyoshi M., Kuper G., Maat P., Mann G., Mevius M., Mulcahy D. D., Munk H., Nijboer R., Noordam J., Paas H., Pandey M., Pandey V. N., Polatidis A., Reich W., Schoenmakers A. P., Sluman J., Smirnov O., Sobey C., Stappers B., Swinbank J., Tagger M., Tang Y., van Bemmell I., van Cappellen W., van Duin A. P., van Haarlem M., van Leeuwen J., Vermeulen R., Vocks C., White S., Wise M., Wucknitz O., Zarka P., *M 87 at metre wavelengths: the LOFAR picture*, *A&A* **547**, A56 (2012), arXiv:1210.1346. 141
- de Jong S., Beckmann V., Soldi S., Tramacere A., Gros A., *High-energy Emission Processes in M 87*, ArXiv e-prints (2015), arXiv:1504.06517. 149
- de Laix A. A., Scherrer R. J., Schaefer R. K., *Constraints on Self-interacting Dark Matter*, *ApJ* **452**, 495 (1995), arXiv:astro-ph/9502087. 25
- de Lapparent V., Geller M. J., Huchra J. P., *A slice of the universe*, *ApJL* **302**, L1-L5 (1986). 13
- de Souza R. S., Rodrigues L. F. S., Ishida E. E. O., Opher R., *The effect of a single supernova explosion on the cuspy density profile of a small-mass dark matter halo*, *MNRAS* **415**, 2969-2973 (2011), arXiv:1104.2850. 55
- Del Nobile E., Nardecchia M., Panci P., *Millicharge or Decay: A Critical Take on Minimal Dark Matter*, ArXiv e-prints (2015), arXiv:1512.05353. 132
- Delahaye T., Böhm C., Silk J., *Can Planck constrain indirect detection of dark matter in our Galaxy?*, *MNRAS* **422**, 16-20 (2012), arXiv:1105.4689. 118
- Delahaye T., Lavalle J., Lineros R., Donato F., Fornengo N., *Galactic electrons and positrons at the Earth: new estimate of the primary and secondary fluxes*, *A&A* **524**, A51 (2010), arXiv:1002.1910. 76, 131
- Delahaye T., Lineros R., Donato F., Fornengo N., Lavalle J., Salati P., Taillet R., *Galactic secondary positron flux at the Earth*, *A&A* **501**, 821-833 (2009), arXiv:0809.5268. 72, 73
- Delahaye T., Lineros R., Donato F., Fornengo N., Salati P., *Positrons from dark matter annihilation in the galactic halo: Theoretical uncertainties*, *Phys. Rev. D* **77**, 063527 (2008), arXiv:0712.2312. 73, 79, 80, 81, 82, 83

- D'Eramo F., de Vries J., Panci P., *A 750 GeV Portal: LHC Phenomenology and Dark Matter Candidates*, ArXiv e-prints (2016), [arXiv:1601.01571](#). 39
- Despringre V., Fraix-Burnet D., Davoust E., *First millimeter mapping of the jet and nucleus of M 87.*, *A&A* **309**, 375-380 (1996). 142
- Di Bernardo G., Evoli C., Gaggero D., Grasso D., Maccione L., *Cosmic ray electrons, positrons and the synchrotron emission of the Galaxy: consistent analysis and implications*, *JCAP* **3**, 036 (2013), [arXiv:1210.4546](#). 74
- Di Cintio A., Brook C. B., Macciò A. V., Stinson G. S., Knebe A., Dutton A. A., Wadsley J., *The dependence of dark matter profiles on the stellar-to-halo mass ratio: a prediction for cusps versus cores*, *MNRAS* **437**, 415-423 (2014), [arXiv:1306.0898](#). 55
- Di Cintio A., Knebe A., Libeskind N. I., Brook C., Yepes G., Gottlöber S., Hoffman Y., *Size matters: the non-universal density profile of subhaloes in SPH simulations and implications for the Milky Way's dSphs*, *MNRAS* **431**, 1220-1229 (2013), [arXiv:1204.0515](#). 27
- Di Mauro M., Donato F., Fornengo N., Lineros R., Vittino A., *Interpretation of AMS-02 electrons and positrons data*, *JCAP* **4**, 006 (2014), [arXiv:1402.0321](#). 74
- Diamanti R., Lopez-Honorez L., Mena O., Palomares-Ruiz S., Vincent A. C., *Constraining dark matter late-time energy injection: decays and p-wave annihilations*, *JCAP* **2**, 017 (2014), [arXiv:1308.2578](#). 41, 42
- Diamond M., Schuster P., *Searching for Light Dark Matter with the SLAC Millicharge Experiment*, *Physical Review Letters* **111**, 221803 (2013), [arXiv:1307.6861](#). 34
- Dicke R. H., Peebles P. J. E., Roll P. G., Wilkinson D. T., *Cosmic Black-Body Radiation.*, *ApJ* **142**, 414-419 (1965). 9
- Diemand J., Moore B., Stadel J., *Convergence and scatter of cluster density profiles*, *MNRAS* **353**, 624-632 (2004), [arXiv:astro-ph/0402267](#). 54
- Dimopoulos S., Georgi H., *Softly broken supersymmetry and SU(5)*, *Nuclear Physics B* **193**, 150-162 (1981). 23
- Dodelson S., Widrow L. M., *Sterile neutrinos as dark matter*, *Physical Review Letters* **72**, 17-20 (1994), [arXiv:hep-ph/9303287](#). 22
- Doeleman S., *Building an event horizon telescope: (sub)mm VLBI in the ALMA era*, in 10th European VLBI Network Symposium and EVN Users Meeting: VLBI and the New Generation of Radio Arrays (2010). 164
- Doeleman S. S., Fish V. L., Schenck D. E., Beaudoin C., Blundell R., Bower G. C., Broderick A. E., Chamberlin R., Freund R., Friberg P., Gurwell M. A., Ho P. T. P., Honma M., Inoue M., Krichbaum T. P., Lamb J., Loeb A., Lonsdale C., Marrone D. P., Moran J. M., Oyama T., Plambeck R., Primiani R. A., Rogers A. E. E., Smythe D. L., SooHoo J., Strittmatter P., Tilanus R. P. J., Titus M., Weintroub J., Wright M., Young K. H., Ziurys L. M., *Jet-Launching Structure Resolved Near the Supermassive Black Hole in M87*, *Science* **338**, 355 (2012), [arXiv:1210.6132](#). 165, 170
- Dolgov A. D., Hansen S. H., *Massive sterile neutrinos as warm dark matter*, *Astroparticle Physics* **16**, 339-344 (2002), [arXiv:hep-ph/0009083](#). 22
- Donato F., Fornengo N., Maurin D., Salati P., Taillet R., *Antiprotons in cosmic rays from neutralino annihilation*, *Phys. Rev. D* **69**, 063501 (2004), [arXiv:astro-ph/0306207](#). 74

- Donato F., Fornengo N., Salati P., *Antideuterons as a signature of supersymmetric dark matter*, *Phys. Rev. D* **62**, 043003 (2000), arXiv:hep-ph/9904481. 44
- D'Onghia E., Burkert A., *The Failure of Self-Interacting Dark Matter to Solve the Overabundance of Dark Satellites and the Soft Core Question*, *ApJ* **586**, 12-16 (2003), arXiv:astro-ph/0206125. 26
- Drees M., Nojiri M. M., *Neutralino relic density in minimal  $N=1$  supergravity*, *Phys. Rev. D* **47**, 376-408 (1993), arXiv:hep-ph/9207234. 15
- Drlica-Wagner A. et al. (DES and Fermi-LAT Collaborations), *Search for Gamma-Ray Emission from DES Dwarf Spheroidal Galaxy Candidates with Fermi-LAT Data*, *ApJL* **809**, L4 (2015), arXiv:1503.02632. 47
- Dutton A. A., *On the origin of exponential galaxy discs*, *MNRAS* **396**, 121-140 (2009), arXiv:0810.5164. 26
- Eatough R. P., Falcke H., Karuppusamy R., Lee K. J., Champion D. J., Keane E. F., Desvignes G., Schnitzeler D. H. F. M., Spitler L. G., Kramer M., Klein B., Bassa C., Bower G. C., Brunthaler A., Cognard I., Deller A. T., Demorest P. B., Freire P. C. C., Kraus A., Lyne A. G., Noutsos A., Stappers B., Wex N., *A strong magnetic field around the supermassive black hole at the centre of the Galaxy*, *Nature* **501**, 391-394 (2013), arXiv:1308.3147. 123, 134
- Edsjö J., Gondolo P., *Neutralino relic density including coannihilations*, *Phys. Rev. D* **56**, 1879-1894 (1997), arXiv:hep-ph/9704361. 19
- Eichler D., Idan R., Gavish E., *Ultrahigh Energy Cosmic Rays, The Diffuse High Energy Gamma Ray Background and Anti-protons*, ArXiv e-prints (2016), arXiv:1604.07398. 48
- Einasto J., Kaasik A., Saar E., *Dynamic evidence on massive coronas of galaxies*, *Nature* **250**, 309-310 (1974). 5
- Eisenstein D. J. et al. (SDSS Collaboration), *Detection of the Baryon Acoustic Peak in the Large-Scale Correlation Function of SDSS Luminous Red Galaxies*, *ApJ* **633**, 560-574 (2005), arXiv:astro-ph/0501171. 11, 13
- Eisenstein D. J., Hu W., *Baryonic Features in the Matter Transfer Function*, *ApJ* **496**, 605-614 (1998), arXiv:astro-ph/9709112. 11, 12
- Elbert O. D., Bullock J. S., Garrison-Kimmel S., Rocha M., Oñorbe J., Peter A. H. G., *Core formation in dwarf haloes with self-interacting dark matter: no fine-tuning necessary*, *MNRAS* **453**, 29-37 (2015), arXiv:1412.1477. 26
- Ellis J., Hagelin J. S., Nanopoulos D. V., Olive K., Srednicki M., *Supersymmetric relics from the big bang*, *Nuclear Physics B* **238**, 453-476 (1984). 23
- Englert F., Brout R., *Broken Symmetry and the Mass of Gauge Vector Mesons*, *Physical Review Letters* **13**, 321-323 (1964). 20
- Enqvist K., McDonald J., *MSSM dark matter constraints and decaying B-balls*, *Physics Letters B* **440**, 59-65 (1998), arXiv:hep-ph/9807269. 15
- Escudero M., Mena O., Vincent A. C., Wilkinson R. J., Boehm C., *Exploring dark matter microphysics with galaxy surveys*, *JCAP* **9**, 034 (2015), arXiv:1505.06735. 12, 13
- Evoli C., Gaggero D., Grasso D., *Secondary antiprotons as a Galactic Dark Matter probe*, *JCAP* **12**, 039 (2015), arXiv:1504.05175. 43

- Faham C. (for the LUX Collaboration), *First Dark Matter Search Results from the Large Underground Xenon (LUX) Experiment*, ArXiv e-prints (2014), [arXiv:1405.5906](#). 33
- Falk T., Olive K. A., Srednicki M., *Heavy sneutrinos as dark matter*, *Physics Letters B* **339**, 248-251 (1994), [arXiv:hep-ph/9409270](#). 23
- Farrar G. R., *A Stable H-Dibaryon: Dark Matter, Candidate Within QCD?*, *International Journal of Theoretical Physics* **42**, 1211–1218 (2003). 21
- Farrar G. R., Fayet P., *Phenomenology of the production, decay, and detection of new hadronic states associated with supersymmetry*, *Physics Letters B* **76**, 575-579 (1978). 23
- Fayet P., *Spontaneous supersymmetry breaking without gauge invariance\*1*, *Physics Letters B* **58**, 67-70 (1975a). 23
- Fayet P., *Supergauge invariant extension of the Higgs mechanism and a model for the electron and its neutrino*, *Nuclear Physics B* **90**, 104-124 (1975b). 23
- Fayet P., *Spontaneously broken supersymmetric theories of weak, electromagnetic and strong interactions*, *Physics Letters B* **69**, 489-494 (1977). 23
- Fayet P., Iliopoulos J., *Spontaneously broken supergauge symmetries and goldstone spinors*, *Physics Letters B* **51**, 461-464 (1974). 23
- Felizardo M. et al. (SIMPLE Collaboration), *Final Analysis and Results of the Phase II SIMPLE Dark Matter Search*, *Physical Review Letters* **108**, 201302 (2012), [arXiv:1106.3014](#). 33, 36
- Feng J. L., Rajaraman A., Takayama F., *Superweakly Interacting Massive Particles*, *Physical Review Letters* **91**, 011302 (2003), [arXiv:hep-ph/0302215](#). 23
- Ferrarese L., Ford H., *Supermassive Black Holes in Galactic Nuclei: Past, Present and Future Research*, *Space Science Reviews* **116**, 523-624 (2005), [arXiv:astro-ph/0411247](#). 61
- Finke J. D., Dermer C. D., Böttcher M., *Synchrotron Self-Compton Analysis of TeV X-Ray-Selected BL Lacertae Objects*, *ApJ* **686**, 181-194 (2008), [arXiv:0802.1529](#). 148, 181, 182
- Fish V. L., Doeleman S. S., Beaudoin C., Blundell R., Bolin D. E., Bower G. C., Chamberlin R., Freund R., Friberg P., Gurwell M. A., Honma M., Inoue M., Krichbaum T. P., Lamb J., Marrone D. P., Moran J. M., Oyama T., Plambeck R., Primiani R., Rogers A. E. E., Smythe D. L., SooHoo J., Strittmatter P., Tilanus R. P. J., Titus M., Weintroub J., Wright M., Woody D., Young K. H., Ziurys L. M., *1.3 mm Wavelength VLBI of Sagittarius A\*: Detection of Time-variable Emission on Event Horizon Scales*, *ApJL* **727**, L36 (2011), [arXiv:1011.2472](#). 165
- Fitzpatrick A. L., Haxton W., Katz E., Lubbers N., Xu Y., *The effective field theory of dark matter direct detection*, *JCAP* **2**, 004 (2013), [arXiv:1203.3542](#). 31
- Fixsen D. J., *The Temperature of the Cosmic Microwave Background*, *ApJ* **707**, 916-920 (2009), [arXiv:0911.1955](#). 9
- Fixsen D. J., Cheng E. S., Gales J. M., Mather J. C., Shafer R. A., Wright E. L., *The Cosmic Microwave Background Spectrum from the Full COBE FIRAS Data Set*, *ApJ* **473**, 576 (1996), [arXiv:astro-ph/9605054](#). 9
- Fornengo N., Lineros R. A., Regis M., Taoso M., *Galactic synchrotron emission from WIMPs at radio frequencies*, *JCAP* **1**, 5 (2012), [arXiv:1110.4337](#). 116
- Fornengo N., Lineros R. A., Regis M., Taoso M., *The isotropic radio background revisited*, *JCAP* **4**, 008 (2014), [arXiv:1402.2218](#). 74

- Fort B., Mellier Y., *Arc(let)s in clusters of galaxies*, *The Astronomy and Astrophysics Review* **5**, 239-292 (1994). 6
- Fox P., Pierce A., Thomas S., *Probing a QCD String Axion with Precision Cosmological Measurements*, ArXiv High Energy Physics - Theory e-prints (2004), arXiv:hep-th/0409059. 25
- Freeman K. C., *On the Disks of Spiral and so Galaxies*, *ApJ* **160**, 811 (1970). 4
- Friedmann A., *Über die Krümmung des Raumes*, *Zeitschrift für Physik* **10**, 377-386 (1922). 8
- Fujii M., Hamaguchi K., *Higgsino and wino dark matter from  $\bar{Q}$ -ball decay in Affleck-Dine baryogenesis*, *Physics Letters B* **525**, 143-149 (2002), arXiv:hep-ph/0110072. 15
- Fuke H., Maeno T., Abe K., Haino S., Makida Y., Matsuda S., Matsumoto H., Mitchell J. W., Moiseev A. A., Nishimura J., Nozaki M., Orito S., Ormes J. F., Sasaki M., Seo E. S., Shikaze Y., Streitmatter R. E., Suzuki J., Tanaka K., Tanizaki K., Yamagami T., Yamamoto A., Yamamoto Y., Yamato K., Yoshida T., Yoshimura K., *Search for Cosmic-Ray Antideuterons*, *Physical Review Letters* **95**, 081101 (2005), arXiv:astro-ph/0504361. 44
- Fukushige T., Makino J., *On the Origin of Cusps in Dark Matter Halos*, *ApJL* **477**, L9-L12 (1997), arXiv:astro-ph/9610005. 54
- Fürst F., Müller C., Madsen K. K., Lanz L., Rivers E., Brightman M., Arevalo P., Baloković M., Beuchert T., Boggs S. E., Christensen F. E., Craig W. W., Dauser T., Farrah D., Graefe C., Hailey C. J., Harrison F. A., Kadler M., King A., Krauß F., Madejski G., Matt G., Marinucci A., Markowitz A., Ogle P., Ojha R., Rothschild R., Stern D., Walton D. J., Wilms J., Zhang W., *NuSTAR and XMM-Newton Observations of the Hard X-Ray Spectrum of Centaurus A*, *ApJ* **819**, 150 (2016), arXiv:1511.01915. 155
- Gaggero D., Taoso M., Urbano A., Valli M., Ullio P., *Towards a realistic astrophysical interpretation of the gamma-ray Galactic center excess*, *JCAP* **12**, 056 (2015a), arXiv:1507.06129. 88
- Gaggero D., Urbano A., Valli M., Ullio P., *Gamma-ray sky points to radial gradients in cosmic-ray transport*, *Phys. Rev. D* **91**, 083012 (2015b), arXiv:1411.7623. 88
- Gamow G., *The Evolution of the Universe*, *Nature* **162**, 680-682 (1948). 9
- Gebhardt K., Thomas J., *The Black Hole Mass, Stellar Mass-to-Light Ratio, and Dark Halo in M87*, *ApJ* **700**, 1690-1701 (2009), arXiv:0906.1492. 61, 180
- Gell-Mann M., Ramond P., Slansky R., *Complex spinors and unified theories*, in *Supergravity: Proceedings of the Supergravity Workshop at Stony Brook, September 27-29, 1979*, Amsterdam: North-Holland Publishing Co. (1979), arXiv:1306.4669. 21
- Geller M. J., Huchra J. P., *Mapping the universe*, *Science* **246**, 897-903 (1989). 13
- Gentile G., Salucci P., Klein U., Granato G. L., *NGC 3741: the dark halo profile from the most extended rotation curve*, *MNRAS* **375**, 199-212 (2007), arXiv:astro-ph/0611355. 54
- Gerhard O. E., Binney J., *Triaxial galaxies containing massive black holes or central density cusps*, *MNRAS* **216**, 467-502 (1985). 62
- Geringer-Sameth A., Koushiappas S. M., Walker M. G., *Comprehensive search for dark matter annihilation in dwarf galaxies*, *Phys. Rev. D* **91**, 083535 (2015a), arXiv:1410.2242. 90

- Geringer-Sameth A., Walker M. G., Koushiappas S. M., Koposov S. E., Belokurov V., Torrealba G., Evans N. W., *Indication of Gamma-Ray Emission from the Newly Discovered Dwarf Galaxy Reticulum II*, *Physical Review Letters* **115**, 081101 (2015b), arXiv:1503.02320. 90
- Gershtein S. S., Zeldovich Ya. B., *Rest Mass of Muonic Neutrino and Cosmology*, *JETP Lett.* **4**, 120-122 (1966). 21
- Giesen G., Boudaud M., Génolini Y., Poulin V., Cirelli M., Salati P., Serpico P. D., *AMS-02 antiprotons, at last! Secondary astrophysical component and immediate implications for Dark Matter*, *JCAP* **9**, 023 (2015), arXiv:1504.04276. 43, 74
- Gillessen S., Eisenhauer F., Fritz T. K., Bartko H., Dodds-Eden K., Pfuhl O., Ott T., Genzel R., *The Orbit of the Star S2 Around SGR A\* from Very Large Telescope and Keck Data*, *ApJL* **707**, L114-L117 (2009), arXiv:0910.3069. 56, 81
- Ginzburg V. L., *Theoretical physics and astrophysics*, Oxford: Pergamon Press (1979). 77
- Giudice G. F., Griest K., *Rate for annihilation of galactic dark matter into two photons*, *Phys. Rev. D* **40**, 2549-2558 (1989). 44
- Glashow S. L., *Partial-symmetries of weak interactions*, *Nuclear Physics* **22**, 579-588 (1961). 20
- Gnedin O. Y., Primack J. R., *Dark Matter Profile in the Galactic Center*, *Phys. Rev. Lett.* **93**, 061302 (2004), arXiv:astro-ph/0308385. 60
- Golfand Yu. A., Likhtman E. P., *Extension of the Algebra of Poincare Group Generators and Violation of p Invariance*, *JETP Letters* **13**, 323-326 (1971). 22
- Gómez-Vargas G. A., Sánchez-Conde M. A., Huh J.-H., Peiró M., Prada F., Morselli A., Klypin A., Cerdeño D. G., Mambrini Y., Muñoz C., *Constraints on WIMP annihilation for contracted dark matter in the inner Galaxy with the Fermi-LAT*, *JCAP* **10**, 029 (2013), arXiv:1308.3515. 102
- Gondolo P., Edsjö J., Ullio P., Bergström L., Schelke M., Baltz E. A., *DarkSUSY: computing supersymmetric dark matter properties numerically*, *JCAP* **7**, 008 (2004), arXiv:astro-ph/0406204. 19
- Gondolo P., Gelmini G., *Cosmic abundances of stable particles: improved analysis.*, *Nucl. Phys. B* **360**, 145-179 (1991). 19
- Gondolo P., Silk J., *Dark Matter Annihilation at the Galactic Center*, *Phys. Rev. Lett.* **83**, 1719-1722 (1999), arXiv:astro-ph/9906391. 56, 57, 58, 59, 62, 122, 130
- Goodenough L., Hooper D., *Possible Evidence For Dark Matter Annihilation In The Inner Milky Way From The Fermi Gamma Ray Space Telescope*, *ArXiv e-prints* (2009), arXiv:0910.2998. 87, 90
- Goodman J., Ibe M., Rajaraman A., Shepherd W., Tait T. M. P., Yu H.-B., *Constraints on dark matter from colliders*, *Phys. Rev. D* **82**, 116010 (2010), arXiv:1008.1783. 37
- Gorchtein M., Profumo S., Ubaldi L., *Probing dark matter with active galactic nuclei jets*, *Phys. Rev. D* **82**, 083514 (2010), arXiv:1008.2230. 147, 148, 180
- Gordon C., Macías O., *Dark matter and pulsar model constraints from Galactic Center Fermi-LAT gamma-ray observations*, *Phys. Rev. D* **88**, 083521 (2013), arXiv:1306.5725. 87, 88, 89, 90, 91, 92, 93, 106, 109

- Gordon C., Macías O., *Erratum: Dark matter and pulsar model constraints from Galactic Center Fermi-LAT gamma-ray observations [Phys. Rev. D 88, 083521 (2013)]*, *Phys. Rev. D* **89**, 049901 (2014). 88
- Governato F., Brook C., Mayer L., Brooks A., Rhee G., Wadsley J., Jonsson P., Willman B., Stinson G., Quinn T., Madau P., *Bulgeless dwarf galaxies and dark matter cores from supernova-driven outflows*, *Nature* **463**, 203-206 (2010), arXiv:0911.2237. 27
- Graham P. W., Irastorza I. G., Lamoreaux S. K., Lindner A., van Bibber K. A., *Experimental Searches for the Axion and Axion-Like Particles*, *Annual Review of Nuclear and Particle Science* **65**, 150807173859001 (2015). 36
- Griest K., *Cross sections, relic abundance, and detection rates for neutralino dark matter*, *Phys. Rev. D* **38**, 2357-2375 (1988). 15
- Griest K., *Erratum: Cross sections, relic abundance, and detection rates for neutralino dark matter [Phys. Rev. D 38, 2357 (1988)]*, *Phys. Rev. D* **39**, 3802-3803 (1989). 15
- Griest K., Kamionkowski M., *Unitarity limits on the mass and radius of dark-matter particles*, *Physical Review Letters* **64**, 615-618 (1990). 18, 132
- Griest K., Seckel D., *Three exceptions in the calculation of relic abundances*, *Phys.Rev.* **D43**, 3191-3203 (1991). 140
- Grimani C., Stephens S. A., Cafagna F. S., Basini G., Bellotti R., Brunetti M. T., Circella M., Codino A., De Marzo C., De Pascale M. P., Finetti N., Golden R. L., Hof M., Menn W., Mitchell J. W., Morselli A., Ormes J. F., Papini P., Pfeifer C., Piccardi S., Picozza P., Ricci M., Simon M., Spillantini P., Stochaj S. J., Streitmatter R. E., *Measurements of the absolute energy spectra of cosmic-ray positrons and electrons above 7 GeV*, *A&A* **392**, 287-294 (2002). 42
- Gunn J. E., Lee B. W., Lerche I., Schramm D. N., Steigman G., *Some astrophysical consequences of the existence of a heavy stable neutral lepton*, *ApJ* **223**, 1015-1031 (1978). 40
- Guralnik G. S., Hagen C. R., Kibble T. W., *Global Conservation Laws and Massless Particles*, *Physical Review Letters* **13**, 585-587 (1964). 20
- Haber H. E., *The status of the minimal supersymmetric standard model and beyond*, *Nuclear Physics B Proceedings Supplements* **62**, 469-484 (1998), arXiv:hep-ph/9709450. 23
- Haber H. E., Kane G. L., *The search for supersymmetry: Probing physics beyond the standard model*, *Physics Reports* **117**, 75-263 (1985). 22
- Hagelin J. S., Kane G. L., *Cosmic ray antimatter from supersymmetric dark matter*, *Nuclear Physics B* **263**, 399-412 (1986). 40
- Harding A. K., Grenier I. A., Gonthier P. L., *The Geminga fraction*, *Astrophysics and Space Science* **309**, 221-230 (2007), arXiv:astro-ph/0703019. 88
- Harding J. P., Dingus B. (for the HAWC Collaboration), *Dark Matter Annihilation and Decay Searches with the High Altitude Water Cherenkov (HAWC) Observatory*, ArXiv e-prints (2015), arXiv:1508.04352. 48
- Harris D. E., Cheung C. C., Stawarz L., Biretta J. A., Perlmutter E. S., *Variability Timescales in the M87 Jet: Signatures of  $E^2$  Losses, Discovery of a Quasi Period in HST-1, and the Site of TeV Flaring*, *ApJ* **699**, 305-314 (2009), arXiv:0904.3925. 142

- Hawking S., *Gravitationally collapsed objects of very low mass*, *MNRAS* **152**, 75 (1971). 19
- Hawking S. W., *Particle creation by black holes*, *Communications in Mathematical Physics* **43**, 199-220 (1975). 19
- Hayashi C., *Proton-Neutron Concentration Ratio in the Expanding Universe at the Stages preceding the Formation of the Elements*, *Progress of Theoretical Physics* **5**, 224-235 (1950). 14
- Heister A. et al. (ALEPH Collaboration), *Single photon and multiphoton production in  $e^+e^-$  collisions at  $\sqrt{s}$  up to 209-GeV*, *European Physical Journal C* **28**, 1-13 (2003). 37
- Hennawi J. F., Ostriker J. P., *Observational Constraints on the Self-interacting Dark Matter Scenario and the Growth of Supermassive Black Holes*, *ApJ* **572**, 41-54 (2002), arXiv:astro-ph/0108203. 26
- Hernquist L., *An analytical model for spherical galaxies and bulges*, *ApJ* **356**, 359-364 (1990). 54
- Higgs P. W., *Broken symmetries, massless particles and gauge fields*, *Physics Letters* **12**, 132-133 (1964a). 20
- Higgs P. W., *Broken Symmetries and the Masses of Gauge Bosons*, *Physical Review Letters* **13**, 508-509 (1964b). 20
- Higgs P. W., *Spontaneous Symmetry Breakdown without Massless Bosons*, *Physical Review* **145**, 1156-1163 (1966). 20
- Hillas A. M., *Evolution of ground-based gamma-ray astronomy from the early days to the Cherenkov Telescope Arrays*, *Astroparticle Physics* **43**, 19-43 (2013). 44
- Hinshaw G., Weiland J. L., Hill R. S., Odegard N., Larson D., Bennett C. L., Dunkley J., Gold B., Greason M. R., Jarosik N., Komatsu E., Nolte M. R., Page L., Spergel D. N., Wollack E., Halpern M., Kogut A., Limon M., Meyer S. S., Tucker G. S., Wright E. L., *Five-Year Wilkinson Microwave Anisotropy Probe Observations: Data Processing, Sky Maps, and Basic Results*, *ApJS* **180**, 225-245 (2009), arXiv:0803.0732. 9
- Hinton J. A., Aharonian F. A., *Inverse Compton Scenarios for the TeV Gamma-Ray Emission of the Galactic Center*, *ApJ* **657**, 302-307 (2007), arXiv:astro-ph/0607557. 130
- Hoekstra H., Bartelmann M., Dahle H., Israel H., Limousin M., Meneghetti M., *Masses of Galaxy Clusters from Gravitational Lensing*, *Space Science Reviews* **177**, 75-118 (2013), arXiv:1303.3274. 7
- Holder J., *VERITAS: Status and Highlights*, *International Cosmic Ray Conference* **12**, 137 (2011), arXiv:1111.1225. 143
- Hooper D., Blasi P., Dario Serpico P., *Pulsars as the sources of high energy cosmic ray positrons*, *JCAP* **1**, 025 (2009), arXiv:0810.1527. 42
- Hooper D., Cholis I., Linden T., Siegal-Gaskins J. M., Slatyer T. R., *Millisecond pulsars cannot account for the inner Galaxy's GeV excess*, *Phys. Rev. D* **88**, 083009 (2013), arXiv:1305.0830. 89
- Hooper D., Goodenough L., *Dark matter annihilation in the Galactic Center as seen by the Fermi Gamma Ray Space Telescope*, *Physics Letters B* **697**, 412-428 (2011), arXiv:1010.2752. 87, 90, 106
- Hooper D., Linden T., *Origin of the gamma rays from the Galactic Center*, *Phys. Rev. D* **84**, 123005 (2011), arXiv:1110.0006. 87, 90, 91, 92

- Hooper D., Linden T., Mertsch P., *What does the PAMELA antiproton spectrum tell us about dark matter?*, *JCAP* **3**, 021 (2015), arXiv:1410.1527. 90
- Hooper D., Profumo S., *Dark matter and collider phenomenology of universal extra dimensions*, *Physics Reports* **453**, 29-115 (2007), arXiv:hep-ph/0701197. 24
- Hooper D., Slatyer T. R., *Two emission mechanisms in the Fermi Bubbles: A possible signal of annihilating dark matter*, *Physics of the Dark Universe* **2**, 118-138 (2013), arXiv:1302.6589. 88
- Hoyle F., Tayler R. J., *The Mystery of the Cosmic Helium Abundance*, *Nature* **203**, 1108 (1964). 14
- Hryczuk A., Cholis I., Iengo R., Tavakoli M., Ullio P., *Indirect detection analysis: wino dark matter case study*, *JCAP* **7**, 031 (2014), arXiv:1401.6212. 43
- Hu W., Silk J., *Thermalization constraints and spectral distortions for massive unstable relic particles*, *Physical Review Letters* **70**, 2661-2664 (1993). 41
- Hut P., *Limits on masses and number of neutral weakly interacting particles*, *Physics Letters B* **69**, 85-88 (1977). 15, 18
- Ibarra A., Lamperstorfer A. S., Silk J., *Dark matter annihilations and decays after the AMS-02 positron measurements*, *Phys. Rev. D* **89**, 063539 (2014), arXiv:1309.2570. 42, 96, 107
- Ibarra A., Tran D., *Gamma-Ray Spectrum from Gravitino Dark Matter Decay*, *Physical Review Letters* **100**, 061301 (2008a), arXiv:0709.4593. 40
- Ibarra A., Tran D., *Antimatter signatures of gravitino dark matter decay*, *JCAP* **7**, 002 (2008b), arXiv:0804.4596. 40
- Ibarra A., Tran D., *Decaying dark matter and the PAMELA anomaly*, *JCAP* **2**, 021 (2009), arXiv:0811.1555. 42
- Ibarra A., Tran D., Weniger C., *Indirect Searches for Decaying Dark Matter*, *International Journal of Modern Physics A* **28**, 1330040 (2013), arXiv:1307.6434. 42
- Ichimura K. (for the XMASS Collaboration), *XMASS1.5, the next step of the XMASS experiment*, in Proceedings of the 34th International Cosmic Ray Conference, The Hague, The Netherlands, Vol. 2015, Proceedings of Science (2015). 33
- Iocco F., Pato M., Bertone G., *Evidence for dark matter in the inner Milky Way*, *Nature Physics* **11**, 245-248 (2015), arXiv:1502.03821. 5
- Ipsier J. R., Sikivie P., *Estimates of the density of dark matter near the center of the Galaxy*, *Phys. Rev. D* **35**, 3695-3704 (1987). 56
- Ishiwata K., Matsumoto S., Moroi T., *High energy cosmic rays from the decay of gravitino dark matter*, *Phys. Rev. D* **78**, 063505 (2008), arXiv:0805.1133. 40
- Izaguirre E., Krnjaic G., Schuster P., Toro N., *New electron beam-dump experiments to search for MeV to few-GeV dark matter*, *Phys. Rev. D* **88**, 114015 (2013), arXiv:1307.6554. 34
- Izaguirre E., Krnjaic G., Schuster P., Toro N., *Physics motivation for a pilot dark matter search at Jefferson Laboratory*, *Phys. Rev. D* **90**, 014052 (2014), arXiv:1403.6826. 34
- Jansson R., Farrar G. R., *A New Model of the Galactic Magnetic Field*, *ApJ* **757**, 14 (2012a), arXiv:1204.3662. 70

- Jansson R., Farrar G. R., *The Galactic Magnetic Field*, *ApJL* **761**, L11 (2012b), arXiv:1210.7820. 70
- Jansson R., Farrar G. R., Waelkens A. H., Enßlin T. A., *Constraining models of the large scale Galactic magnetic field with WMAP5 polarization data and extragalactic rotation measure sources*, *JCAP* **7**, 021 (2009), arXiv:0905.2228. 70
- Jean P., Knödseder J., Gillard W., Guessoum N., Ferrière K., Marcowith A., Lonjou V., Roques J. P., *Spectral analysis of the Galactic  $e^+e^-$  annihilation emission*, *A&A* **445**, 579-589 (2006), arXiv:astro-ph/0509298. 46
- Jean P., Knödseder J., Lonjou V., Allain M., Roques J.-P., Skinner G. K., Teegarden B. J., Vedrenne G., von Ballmoos P., Cordier B., Caraveo P., Diehl R., Durouchoux P., Mandrou P., Matteson J., Gehrels N., Schönfelder V., Strong A. W., Ubertini P., Weidenspointner G., Winkler C., *Early SPI/INTEGRAL measurements of 511 keV line emission from the 4th quadrant of the Galaxy*, *A&A* **407**, L55-L58 (2003), arXiv:astro-ph/0309484. 46
- Jeannerot R., Zhang X., Brandenberger R., *Non-thermal production of neutralino cold dark matter from cosmic string decays*, *Journal of High Energy Physics* **12**, 003 (1999), arXiv:hep-ph/9901357. 15
- Jeans J. H., *The motions of stars in a Kapteyn universe*, *MNRAS* **82**, 122-132 (1922). 4
- Jedamzik K., Pospelov M., *Big Bang nucleosynthesis and particle dark matter*, *New Journal of Physics* **11**, 105028 (2009), arXiv:0906.2087. 49
- Jeltema T., Profumo S., *Discovery of a 3.5 keV line in the Galactic Centre and a critical look at the origin of the line across astronomical targets*, *MNRAS* **450**, 2143-2152 (2015), arXiv:1408.1699. 22
- Jungman G., Kamionkowski M., *Cosmic-ray antiprotons from neutralino annihilation into gluons*, *Phys. Rev. D* **49**, 2316-2321 (1994), arXiv:astro-ph/9310032. 40
- Jungman G., Kamionkowski M.,  *$\gamma$  rays from neutralino annihilation*, *Phys. Rev. D* **51**, 3121-3124 (1995), arXiv:hep-ph/9501365. 40, 44
- Jungman G., Kamionkowski M., Griest K., *Supersymmetric dark matter*, *Physics Reports* **267**, 195-373 (1996), arXiv:hep-ph/9506380. 19, 22, 30, 31
- Kaluza T., *On the Problem of Unity in Physics*, *Sitzungsber. Preuss. Akad. Wiss. Berlin (Math. Phys.)* **1921**, 966-972 (1921). 24
- Kamionkowski M., Turner M. S., *Thermal relics: Do we know their abundances?*, *Phys. Rev. D* **42**, 3310-3320 (1990). 15
- Kane G. L., Kolda C., Roszkowski L., Wells J. D., *Study of constrained minimal supersymmetry*, *Phys. Rev. D* **49**, 6173-6210 (1994), arXiv:hep-ph/9312272. 23
- Kaplinghat M., Linden T., Yu H.-B., *Galactic Center Excess in  $\gamma$  Rays from Annihilation of Self-Interacting Dark Matter*, *Physical Review Letters* **114**, 211303 (2015), arXiv:1501.03507. 102
- Kaplinghat M., Tulin S., Yu H.-B., *Dark Matter Halos as Particle Colliders: Unified Solution to Small-Scale Structure Puzzles from Dwarfs to Clusters*, *Physical Review Letters* **116**, 041302 (2016), arXiv:1508.03339. 27
- Kappl R., Reinert A., Winkler M. W., *AMS-02 antiprotons reloaded*, *JCAP* **10**, 034 (2015), arXiv:1506.04145. 43

- Kapteyn J. C., *First Attempt at a Theory of the Arrangement and Motion of the Sidereal System*, *ApJ* **55**, 302 (1922). 4
- Kawasaki M., Moroi T., Yanagida T., *Constraint on the reheating temperature from the decay of the Polonyi field*, *Physics Letters B* **370**, 52-58 (1996), arXiv:hep-ph/9509399. 15
- Kelvin B., *Baltimore lectures on molecular dynamics and the wave theory of light*, London, C. J. Clay and sons; Baltimore, Publication agency of the Johns Hopkins university (1904). 4
- Khalil S., Muñoz C., Torrente-Lujan E., *Relic neutralino density in scenarios with intermediate unification scale*, *New Journal of Physics* **4**, 27 (2002), arXiv:hep-ph/0202139. 15
- Kibble T. W., *Symmetry Breaking in Non-Abelian Gauge Theories*, *Physical Review* **155**, 1554-1561 (1967). 20
- Kieffer M., Dundas Mora K., Conrad J., Farnier C., Jacholkowska A., Veh J., Viana A. (for the H.E.S.S. Collaboration), *Search for Gamma-ray Line Signatures with H.E.S.S.*, ArXiv e-prints (2015), arXiv:1509.03514. 46
- Kim S. C. et al. (KIMS Collaboration), *New Limits on Interactions between Weakly Interacting Massive Particles and Nucleons Obtained with CsI(Tl) Crystal Detectors*, *Physical Review Letters* **108**, 181301 (2012), arXiv:1204.2646. 36
- Kissmann R., *PICARD: A novel code for the Galactic Cosmic Ray propagation problem*, *Astroparticle Physics* **55**, 37-50 (2014), arXiv:1401.4035. 79
- Kistler M. D., *Gamma Rays, Electrons, Hard X-Rays, and the Central Parsec of the Milky Way*, ArXiv e-prints (2015), arXiv:1511.00723. 130, 131
- Klein O., *Quantentheorie und fünfdimensionale Relativitätstheorie*, *Zeitschrift für Physik* **37**, 895-906 (1926). 24
- Klypin A., Kravtsov A. V., Valenzuela O., Prada F., *Where Are the Missing Galactic Satellites?*, *ApJ* **522**, 82-92 (1999), arXiv:astro-ph/9901240. 26
- Knödseder J., Jean P., Lonjou V., Weidenspointner G., Guessoum N., Gillard W., Skinner G., von Ballmoos P., Vedrenne G., Roques J.-P., Schanne S., Teegarden B., Schönfelder V., Winkler C., *The all-sky distribution of 511 keV electron-positron annihilation emission*, *A&A* **441**, 513-532 (2005), arXiv:astro-ph/0506026. 46
- Kolb E. W., Chung D. J. H., Riotto A., *WIMPZILLAS!*, in *Dark matter in Astrophysics and Particle Physics* (1999), arXiv:hep-ph/9810361. 25
- Kolb E. W., Turner M. S., *The early universe*, *Frontiers in Physics* (1990). 15, 16
- Kormendy J., Ho L., *Supermassive Black Holes in Inactive Galaxies*, in Murdin P., ed., *Encyclopedia of Astronomy and Astrophysics* (2001). 56
- Kounine A., *Latest Alpha Magnetic Spectrometer results: positron fraction and  $p\bar{p}/p$  ratio*, in *Proceedings of the 34th International Cosmic Ray Conference*, The Hague, The Netherlands, Vol. 2015, *Proceedings of Science* (2015). 43
- Krause M., *Magnetic Fields and Star Formation in Spiral Galaxies*, in *Revista Mexicana de Astronomía y Astrofísica Conference Series*, Vol. 36 of *Revista Mexicana de Astronomía y Astrofísica Conference Series* (2009), arXiv:0806.2060. 73, 74
- Kravtsov A. V., Klypin A. A., Bullock J. S., Primack J. R., *The Cores of Dark Matter-dominated Galaxies: Theory versus Observations*, *ApJ* **502**, 48-58 (1998), arXiv:astro-ph/9708176. 54

- Krumm N., Salpeter E. E., *Rotation curves, mass distributions and total masses of some spiral galaxies.*, *A&A* **56**, 465-468 (1977). [5](#)
- Kuijken K., Gilmore G., *The Mass Distribution in the Galactic Disc - II - Determination of the Surface Mass Density of the Galactic Disc Near the Sun*, *MNRAS* **239**, 605-649 (1989). [4](#)
- Kunnen J. (for the IceCube Collaboration), *A search for Dark Matter in the centre of the Earth with the IceCube neutrino detector*, in Proceedings of the 34th International Cosmic Ray Conference, The Hague, The Netherlands, Vol. 2015, Proceedings of Science (2015). [48](#)
- Kuzio de Naray R., McGaugh S. S., de Blok W. J. G., Bosma A., *High-Resolution Optical Velocity Fields of 11 Low Surface Brightness Galaxies*, *ApJS* **165**, 461-479 (2006), [arXiv:astro-ph/0604576](#). [54](#)
- Lacroix T., Boehm C., Silk J., *Probing a dark matter density spike at the Galactic Center*, *Phys. Rev. D* **89**, 063534 (2014a), [arXiv:1311.0139](#). [83](#), [115](#)
- Lacroix T., Boehm C., Silk J., *Fitting the Fermi-LAT GeV excess: On the importance of including the propagation of electrons from dark matter*, *Phys. Rev. D* **90**, 043508 (2014b), [arXiv:1403.1987](#). [91](#), [102](#), [107](#)
- Lacroix T., Boehm C., Silk J., *Ruling out thermal dark matter with a black hole induced spiky profile in the M87 galaxy*, *Phys. Rev. D* **92**, 043510 (2015a), [arXiv:1505.00785](#). [139](#), [156](#)
- Lacroix T., Macías O., Gordon C., Panci P., Boehm C., Silk J., *The Spatial Morphology of the Secondary Emission in the Galactic Center Gamma-Ray Excess*, *ArXiv e-prints* (2015b), [arXiv:1512.01846](#). [101](#)
- Lacroix T., Silk J., *Constraining the distribution of dark matter at the Galactic centre using the high-resolution Event Horizon Telescope*, *A&A* **554**, A36 (2013), [arXiv:1211.4861](#). [165](#)
- Lacroix T., Silk J., Moulin E., Boehm C., *New H.E.S.S. diffuse emission from the Galactic center: a combination of heavy dark matter and millisecond pulsars?*, *ArXiv e-prints* (2016), [arXiv:1603.05977](#). [127](#)
- Lage C., Farrar G., *Constrained Simulation of the Bullet Cluster*, *ApJ* **787**, 144 (2014). [7](#)
- Lande J., Ackermann M., Allafort A., Ballet J., Bechtol K., Burnett T. H., Cohen-Tanugi J., Drlica-Wagner A., Funk S., Giordano F., Grondin M.-H., Kerr M., Lemoine-Goumard M., *Search for Spatially Extended Fermi Large Area Telescope Sources Using Two Years of Data*, *ApJ* **756**, 5 (2012), [arXiv:1207.0027](#). [105](#)
- Lavalle J., Maurin D., Putze A., *Direct constraints on diffusion models from cosmic-ray positron data: Excluding the minimal model for dark matter searches*, *Phys. Rev. D* **90**, 081301 (2014), [arXiv:1407.2540](#). [74](#)
- Lavalle J., Pochon J., Salati P., Taillet R., *Clumpiness of dark matter and the positron annihilation signal*, *A&A* **462**, 827-840 (2007), [arXiv:astro-ph/0603796](#). [72](#), [79](#), [80](#)
- Lebedenko V. N. et al. (ZEPLIN-III Collaboration), *Limits on the Spin-Dependent WIMP-Nucleon Cross Sections from the First Science Run of the ZEPLIN-III Experiment*, *Physical Review Letters* **103**, 151302 (2009), [arXiv:0901.4348](#). [36](#)
- Lee B. W., Weinberg S., *Cosmological lower bound on heavy-neutrino masses*, *Phys. Rev. Lett.* **39**, 165-168 (1977). [15](#), [18](#)
- Lee S. K., Lisanti M., Safdi B. R., *Distinguishing dark matter from unresolved point sources in the Inner Galaxy with photon statistics*, *JCAP* **5**, 56 (2015), [arXiv:1412.6099](#). [89](#)

- Lee S. K., Lisanti M., Safdi B. R., Slatyer T. R., Xue W., *Evidence for Unresolved  $\gamma$ -Ray Point Sources in the Inner Galaxy*, *Physical Review Letters* **116**, 051103 (2016), [arXiv:1506.05124](#). 47, 89
- Lefranc V., Moulin E. (for the H.E.S.S. Collaboration), *Dark matter search in the inner Galactic halo with H.E.S.S. I and H.E.S.S. II*, ArXiv e-prints (2015), [arXiv:1509.04123](#). 47
- Lemaître G., *Un Univers homogène de masse constante et de rayon croissant rendant compte de la vitesse radiale des nébuleuses extra-galactiques*, *Annales de la Société Scientifique de Bruxelles* **47**, 49-59 (1927). 8
- Lemoine M., Revenu B., *Relativistic Fermi acceleration with shock compressed turbulence*, *MNRAS* **366**, 635-644 (2006), [arXiv:astro-ph/0510522](#). 156
- Leventhal M., MacCallum C. J., Stang P. D., *Detection of 511 keV positron annihilation radiation from the galactic center direction*, *ApJL* **225**, L11-L14 (1978). 46
- Lewin J. D., Smith P. F., *Review of mathematics, numerical factors, and corrections for dark matter experiments based on elastic nuclear recoil*, *Astroparticle Physics* **6**, 87-112 (1996). 31
- Lin W. B., Huang D. H., Zhang X., Brandenberger R., *Nonthermal Production of Weakly Interacting Massive Particles and the Subgalactic Structure of the Universe*, *Physical Review Letters* **86**, 954-957 (2001), [arXiv:astro-ph/0009003](#). 15
- Lindblad B., *Researches based on determinations of stellar luminosities*, *Uppsala Meddelanden* **11**, 30 (1926). 4
- Linden T., *Known Radio Pulsars Do Not Contribute to the Galactic Center Gamma-Ray Excess*, ArXiv e-prints (2015), [arXiv:1509.02928](#). 89
- Linden T., Hooper D., Yusef-Zadeh F., *Dark Matter and Synchrotron Emission from Galactic Center Radio Filaments*, *ApJ* **741**, 95 (2011), [arXiv:1106.5493](#). 116
- Lister M. L., Aller H. D., Aller M. F., Cohen M. H., Homan D. C., Kadler M., Kellermann K. I., Kovalev Y. Y., Ros E., Savolainen T., Zensus J. A., Vermeulen R. C., *MOJAVE: Monitoring of Jets in Active Galactic Nuclei with VLBA Experiments. V. Multi-Epoch VLBA Images*, *Astron. J.* **137**, 3718-3729 (2009), [arXiv:0812.3947](#). 142
- Longair M. S., *High Energy Astrophysics*, Cambridge University Press (2011). 64, 65, 69, 71, 72, 75, 77, 78, 168
- Lorimer D. R., *Binary and Millisecond Pulsars*, *Living Reviews in Relativity* **11** (2008), [arXiv:0811.0762](#). 88
- Lovell M. R., Frenk C. S., Eke V. R., Jenkins A., Gao L., Theuns T., *The properties of warm dark matter haloes*, *MNRAS* **439**, 300-317 (2014), [arXiv:1308.1399](#). 26
- Lu R.-S., Broderick A. E., Baron F., Monnier J. D., Fish V. L., Doeleman S. S., Pankratius V., *Imaging the Supermassive Black Hole Shadow and Jet Base of M87 with the Event Horizon Telescope*, *ApJ* **788**, 120 (2014), [arXiv:1404.7095](#). 164
- Ma E., *Verifiable radiative seesaw mechanism of neutrino mass and dark matter*, *Phys. Rev. D* **73**, 077301 (2006), [arXiv:hep-ph/0601225](#). 25
- Macciò A. V., Paduroiu S., Anderhalden D., Schneider A., Moore B., *Cores in warm dark matter haloes: a Catch 22 problem*, *MNRAS* **424**, 1105-1112 (2012), [arXiv:1202.1282](#). 26

- Machacek M. E., Carlson E. D., Hall L. J., *Self-Interacting Dark Matter: An Alternative Scenario?*, in Akerlof C. W., Srednicki M. A., eds, Texas/PASCOS '92: Relativistic Astrophysics and Particle Cosmology, Vol. 688 of Annals of the New York Academy of Sciences (1993). [25](#)
- Macías O., Gordon C., *Contribution of cosmic rays interacting with molecular clouds to the Galactic Center gamma-ray excess*, *Phys. Rev. D* **89**, 063515 (2014), [arXiv:1312.6671](#). [88](#), [90](#), [106](#), [107](#), [108](#), [109](#)
- Macías O., Gordon C., Crocker R. M., Profumo S., *Cosmic ray models of the ridge-like excess of gamma rays in the Galactic Centre*, *MNRAS* **451**, 1833-1847 (2015), [arXiv:1410.1678](#). [106](#), [107](#)
- Madhavacheril M. S., Sehgal N., Slatyer T. R., *Current dark matter annihilation constraints from CMB and low-redshift data*, *Phys. Rev. D* **89**, 103508 (2014), [arXiv:1310.3815](#). [42](#)
- MAGIC Collaboration, Aleksić J., Wood M., Anderson B., Bloom E. D., Cohen-Tanugi J., Drlica-Wagner A., Mazziotta M. N., Sánchez-Conde M., Strigari L., *Limits to dark matter annihilation cross-section from a combined analysis of MAGIC and Fermi-LAT observations of dwarf satellite galaxies*, ArXiv e-prints (2016), [arXiv:1601.06590](#). [47](#)
- MAGIC Collaboration, Ibarra A., *Optimized dark matter searches in deep observations of Segue 1 with MAGIC*, *JCAP* **2**, 008 (2014), [arXiv:1312.1535](#). [46](#), [47](#)
- Malaney R. A., Mathews G. J., *Probing the early universe: a review of primordial nucleosynthesis beyond the standard big bang*, *Physics Reports* **229**, 145-219 (1993). [15](#)
- Mambrini Y., Tytgat M. H. G., Zaharijas G., Zaldívar B., *Complementarity of Galactic radio and collider data in constraining WIMP dark matter models*, *JCAP* **11**, 038 (2012), [arXiv:1206.2352](#). [116](#)
- Markevitch M., *Chandra Observation of the Most Interesting Cluster in the Universe*, in The X-ray Universe 2005, Vol. 604 of ESA Special Publication, Wilson, A. (2006), [arXiv:astro-ph/0511345](#). [7](#)
- Markevitch M., Gonzalez A. H., Clowe D., Vikhlinin A., Forman W., Jones C., Murray S., Tucker W., *Direct Constraints on the Dark Matter Self-Interaction Cross Section from the Merging Galaxy Cluster 1E 0657-56*, *ApJ* **606**, 819-824 (2004), [arXiv:astro-ph/0309303](#). [7](#)
- Marsh D. J. E., *Axion Cosmology*, ArXiv e-prints (2015), [arXiv:1510.07633](#). [24](#)
- Marshall H. L., Miller B. P., Davis D. S., Perlman E. S., Wise M., Canizares C. R., Harris D. E., *A High-Resolution X-Ray Image of the Jet in M87*, *ApJ* **564**, 683-687 (2002), [arXiv:astro-ph/0109160](#). [142](#)
- Masi S., Ade P. A. R., Bock J. J., Bond J. R., Borrill J., Boscaleri A., Cabella P., Contaldi C. R., Crill B. P., de Bernardis P., de Gasperis G., de Oliveira-Costa A., de Troia G., di Stefano G., Ehlers P., Hivon E., Hristov V., Iacoangeli A., Jaffe A. H., Jones W. C., Kisner T. S., Lange A. E., MacTavish C. J., Marini Bettolo C., Mason P., Mauskopf P. D., Montroy T. E., Nati F., Nati L., Natoli P., Netterfield C. B., Pascale E., Piacentini F., Pogosyan D., Polenta G., Prunet S., Ricciardi S., Romeo G., Ruhl J. E., Santini P., Tegmark M., Torbet E., Veneziani M., Vittorio N., *Instrument, method, brightness, and polarization maps from the 2003 flight of BOOMERanG*, *A&A* **458**, 687-716 (2006), [arXiv:astro-ph/0507509](#). [9](#)
- Massey R., Kitching T., Richard J., *The dark matter of gravitational lensing*, *Reports on Progress in Physics* **73**, 086901 (2010), [arXiv:1001.1739](#). [6](#)

- Maurin D., Donato F., Taillet R., Salati P., *Cosmic Rays below  $Z=30$  in a Diffusion Model: New Constraints on Propagation Parameters*, *ApJ* **555**, 585-596 (2001), arXiv:astro-ph/0101231. 74
- Maurin D., Taillet R., Donato F., *New results on source and diffusion spectral features of Galactic cosmic rays: I B/C ratio*, *A&A* **394**, 1039-1056 (2002), arXiv:astro-ph/0206286. 74
- Mauskopf P. D., Ade P. A. R., de Bernardis P., Bock J. J., Borrill J., Boscaleri A., Crill B. P., DeGasperis G., De Troia G., Farese P., Ferreira P. G., Ganga K., Giacometti M., Hanany S., Hristov V. V., Iacoangeli A., Jaffe A. H., Lange A. E., Lee A. T., Masi S., Melchiorri A., Melchiorri F., Miglio L., Montroy T., Netterfield C. B., Pascale E., Piacentini F., Richards P. L., Romeo G., Ruhl J. E., Scannapieco E., Scaramuzzi F., Stompor R., Vittorio N., *Measurement of a Peak in the Cosmic Microwave Background Power Spectrum from the North American Test Flight of Boomerang*, *ApJL* **536**, L59-L62 (2000), arXiv:astro-ph/9911444. 12
- Mayet F., Billard J., *A review on the discovery reach of Dark Matter directional detection*, *Journal of Physics Conference Series* **469**, 012013 (2013), arXiv:1310.0214. 34
- Meneghetti M., Yoshida N., Bartelmann M., Moscardini L., Springel V., Tormen G., White S. D. M., *Giant cluster arcs as a constraint on the scattering cross-section of dark matter*, *MNRAS* **325**, 435-442 (2001), arXiv:astro-ph/0011405. 26
- Merritt D., *Evolution of the Dark Matter Distribution at the Galactic Center*, *Physical Review Letters* **92**, 201304 (2004), arXiv:astro-ph/0311594. 60, 61
- Merritt D., Graham A. W., Moore B., Diemand J., Terzić B., *Empirical Models for Dark Matter Halos. I. Nonparametric Construction of Density Profiles and Comparison with Parametric Models*, *The Astronomical Journal* **132**, 2685-2700 (2006), arXiv:astro-ph/0509417. 54
- Merritt D., Harfst S., Bertone G., *Collisionally regenerated dark matter structures in galactic nuclei*, *Phys. Rev. D* **75**, 043517 (2007), arXiv:astro-ph/0610425. 62
- Merritt D., Milosavljević M., Verde L., Jimenez R., *Dark Matter Spikes and Annihilation Radiation from the Galactic Center*, *Physical Review Letters* **88**, 191301 (2002), arXiv:astro-ph/0201376. 59
- Merritt D., Poon M. Y., *Chaotic Loss Cones and Black Hole Fueling*, *ApJ* **606**, 788-798 (2004), arXiv:astro-ph/0302296. 62
- Merritt D., Tremblay B., *The distribution of dark matter in the halo of M87*, *Astron. J.* **106**, 2229-2242 (1993). 180
- Milgrom M., *A modification of the Newtonian dynamics as a possible alternative to the hidden mass hypothesis*, *ApJ* **270**, 365-370 (1983a). 27
- Milgrom M., *A modification of the Newtonian dynamics - Implications for galaxies*, *ApJ* **270**, 371-389 (1983b). 27
- Milgrom M., *A Modification of the Newtonian Dynamics - Implications for Galaxy Systems*, *ApJ* **270**, 384 (1983c). 27
- Milgrom M., *MOND theory*, *Canadian Journal of Physics* **93**, 107-118 (2015), arXiv:1404.7661. 27
- Minkowski P.,  $\mu \rightarrow e \gamma$  at a rate of one out of  $10^9$  muon decays?, *Physics Letters B* **67**, 421-428 (1977). 21
- Mirabal N., *Dark matter versus pulsars: catching the impostor*, *MNRAS* **436**, 2461-2464 (2013), arXiv:1309.3428. 88

- Miralda-Escudé J., *A Test of the Collisional Dark Matter Hypothesis from Cluster Lensing*, *ApJ* **564**, 60-64 (2002), [arXiv:astro-ph/0002050](#). 26
- Mohapatra R. N., Antusch S., Babu K. S., Barenboim G., Chen M.-C., de Gouvêa A., de Holanda P., Dutta B., Grossman Y., Joshipura A., Kayser B., Kersten J., Keum Y. Y., King S. F., Langacker P., Lindner M., Loinaz W., Masina I., Mocioiu I., Mohanty S., Murayama H., Pascoli S., Petcov S. T., Pilaftsis A., Ramond P., Ratz M., Rodejohann W., Shrock R., Takeuchi T., Underwood T., Wolfenstein L., *Theory of neutrinos: a white paper*, *Reports on Progress in Physics* **70**, 1757-1867 (2007), [arXiv:hep-ph/0510213](#). 21
- Moniez M., *Review of results from EROS Microlensing search for Massive Compact Objects*, *ArXiv e-prints* (2009), [arXiv:0901.0985](#). 19
- Moore B., Ghigna S., Governato F., Lake G., Quinn T., Stadel J., Tozzi P., *Dark Matter Substructure within Galactic Halos*, *ApJL* **524**, L19-L22 (1999a), [arXiv:astro-ph/9907411](#). 26
- Moore B., Quinn T., Governato F., Stadel J., Lake G., *Cold collapse and the core catastrophe*, *MNRAS* **310**, 1147-1152 (1999b), [arXiv:astro-ph/9903164](#). 54
- Mori K., Hailey C. J., Krivonos R., Hong J., Ponti G., Bauer F., Perez K., Nynka M., Zhang S., Tomsick J. A., Alexander D. M., Baganoff F. K., Barret D., Barrière N., Boggs S. E., Canipe A. M., Christensen F. E., Craig W. W., Forster K., Giommi P., Grefenstette B. W., Grindlay J. E., Harrison F. A., Hornstrup A., Kitaguchi T., Koglin J. E., Luu V., Madsen K. K., Mao P. H., Miyasaka H., Perri M., Pivovarov M. J., Puccetti S., Rana V., Stern D., Westergaard N. J., Zhang W. W., Zoglauer A., *NuSTAR Hard X-Ray Survey of the Galactic Center Region I: Hard X-Ray Morphology and Spectroscopy of the Diffuse Emission*, *ApJ* **814**, 94 (2015), [arXiv:1510.04631](#). 135
- Moroi T., Randall L., *Wino cold dark matter from anomaly mediated SUSY breaking*, *Nuclear Physics B* **570**, 455-472 (2000), [arXiv:hep-ph/9906527](#). 15
- Moskalenko I. V., Strong A. W., *Production and Propagation of Cosmic-Ray Positrons and Electrons*, *ApJ* **493**, 694-707 (1998), [arXiv:astro-ph/9710124](#). 41
- Murase K., Laha R., Ando S., Ahlers M., *Testing the Dark Matter Scenario for PeV Neutrinos Observed in IceCube*, *Physical Review Letters* **115**, 071301 (2015), [arXiv:1503.04663](#). 48
- Murayama H., *Supersymmetry Phenomenology*, in Particle Physics, Proceedings of the 1999 Summer School, held in Trieste, Italy, 21 June - 9 July, 1999 (2000), [arXiv:hep-ph/0002232](#). 20
- Nakano T., Makino J., *On the Cusp around Central Black Holes in Luminous Elliptical Galaxies*, *ApJL* **525**, L77-L80 (1999), [arXiv:astro-ph/9906131](#). 60
- Navarro J. F., Eke V. R., Frenk C. S., *The cores of dwarf galaxy haloes*, *MNRAS* **283**, L72-L78 (1996b), [arXiv:astro-ph/9610187](#). 55
- Navarro J. F., Frenk C. S., White S. D. M., *The Structure of Cold Dark Matter Halos*, *ApJ* **462**, 563 (1996a), [arXiv:astro-ph/9508025](#). 54
- Navarro J. F., Frenk C. S., White S. D. M., *A Universal Density Profile from Hierarchical Clustering*, *ApJ* **490**, 493-508 (1997), [arXiv:astro-ph/9611107](#). 54
- Navarro J. F., Hayashi E., Power C., Jenkins A. R., Frenk C. S., White S. D. M., Springel V., Stadel J., Quinn T. R., *The inner structure of  $\Lambda$ CDM haloes - III. Universality and asymptotic slopes*, *MNRAS* **349**, 1039-1051 (2004), [arXiv:astro-ph/0311231](#). 54

- Navarro J. F., Ludlow A., Springel V., Wang J., Vogelsberger M., White S. D. M., Jenkins A., Frenk C. S., Helmi A., *The diversity and similarity of simulated cold dark matter haloes*, *MNRAS* **402**, 21-34 (2010), arXiv:0810.1522. 54
- Neronov A., Aharonian F. A., *Production of TeV Gamma Radiation in the Vicinity of the Supermassive Black Hole in the Giant Radio Galaxy M87*, *ApJ* **671**, 85-96 (2007), arXiv:0704.3282. 146, 147, 155, 166
- Neumayer N., *The Supermassive Black Hole at the Heart of Centaurus A: Revealed by the Kinematics of Gas and Stars*, *Publications of the Astronomical Society of Australia* **27**, 449-456 (2010), arXiv:1002.0965. 156, 180
- Nilles H. P., *Supersymmetry, supergravity and particle physics*, *Physics Reports* **110**, 1-162 (1984). 23
- Nolan P. L. et al. (Fermi-LAT Collaboration), *Fermi Large Area Telescope Second Source Catalog*, *ApJS* **199**, 31 (2012), arXiv:1108.1435. 106, 107
- Norman C., Silk J., *The dynamics and fueling of active nuclei*, *ApJ* **266**, 502-515 (1983). 62
- Nussinov S., *Technocosmology - could a technibaryon excess provide a "natural" missing mass candidate?*, *Physics Letters B* **165**, 55-58 (1985). 25
- Oh S.-H., Brook C., Governato F., Brinks E., Mayer L., de Blok W. J. G., Brooks A., Walter F., *The Central Slope of Dark Matter Cores in Dwarf Galaxies: Simulations versus THINGS*, *The Astronomical Journal* **142**, 24 (2011), arXiv:1011.2777. 54
- O'Leary R. M., Kistler M. D., Kerr M., Dexter J., *Young Pulsars and the Galactic Center GeV Gamma-ray Excess*, ArXiv e-prints (2015), arXiv:1504.02477. 89
- Olive K. A., Steigman G., Walker T. P., *Primordial nucleosynthesis: theory and observations*, *Physics Reports* **333**, 389-407 (2000), arXiv:astro-ph/9905320. 14
- Olive K. A., Turner M. S., *Cosmological bounds on the masses of stable, right-handed neutrinos*, *Phys. Rev. D* **25**, 213-216 (1982). 13
- Oort J. H., *The force exerted by the stellar system in the direction perpendicular to the galactic plane and some related problems*, *Bulletin of the Astronomical Institutes of the Netherlands* **6**, 249 (1932). 4
- O'Raiifeartaigh L., *Spontaneous symmetry breaking for chirals scalar superfields*, *Nuclear Physics B* **96**, 331-352 (1975). 23
- Orlando E., Strong A., *Galactic synchrotron emission with cosmic ray propagation models*, *MNRAS* **436**, 2127-2142 (2013), arXiv:1309.2947. 74
- Ostriker J. P., *Collisional Dark Matter and the Origin of Massive Black Holes*, *Physical Review Letters* **84**, 5258-5260 (2000), arXiv:astro-ph/9912548. 62
- Ostriker J. P., Peebles P. J. E., *A Numerical Study of the Stability of Flattened Galaxies: or, can Cold Galaxies Survive?*, *ApJ* **186**, 467-480 (1973). 5
- Ostriker J. P., Peebles P. J. E., Yahil A., *The size and mass of galaxies, and the mass of the universe*, *ApJL* **193**, L1-L4 (1974). 5
- Paczynski B., *Gravitational microlensing by the galactic halo*, *ApJ* **304**, 1-5 (1986). 19

- Padmanabhan N., Finkbeiner D. P., *Detecting dark matter annihilation with CMB polarization: Signatures and experimental prospects*, *Phys. Rev. D* **72**, 023508 (2005), arXiv:astro-ph/0503486. 41
- Panci P., *New Directions in Direct Dark Matter Searches*, ArXiv e-prints (2014), arXiv:1402.1507. 30
- Pani P., Loeb A., *Tidal capture of a primordial black hole by a neutron star: implications for constraints on dark matter*, *JCAP* **6**, 026 (2014), arXiv:1401.3025. 20
- Peccei R. D., *The Strong CP Problem and Axions*, in Kuster M., Raffelt G., Beltrán B., eds, *Axions*, Vol. 741 of *Lecture Notes in Physics*, Berlin Springer Verlag (2008), arXiv:hep-ph/0607268. 24
- Peccei R. D., Quinn H. R., *CP conservation in the presence of pseudoparticles*, *Physical Review Letters* **38**, 1440-1443 (1977a). 24, 25
- Peccei R. D., Quinn H. R., *Constraints imposed by CP conservation in the presence of pseudoparticles*, *Phys. Rev. D* **16**, 1791-1797 (1977b). 24, 25
- Peebles P. J., *Primeval Helium Abundance and the Primeval Fireball*, *Physical Review Letters* **16**, 410-413 (1966a). 14
- Peebles P. J. E., *Primordial Helium Abundance and the Primordial Fireball. II*, *ApJ* **146**, 542 (1966b). 14
- Peebles P. J. E., *Gravitational collapse and related phenomena from an empirical point of view, or, black holes are where you find them.*, *General Relativity and Gravitation* **3**, 63-82 (1972a). 56
- Peebles P. J. E., *Star Distribution Near a Collapsed Object*, *ApJ* **178**, 371-376 (1972b). 61
- Peebles P. J. E., *The large-scale structure of the universe*, Princeton University Press (1980). 7
- Peebles P. J. E., *Large-scale background temperature and mass fluctuations due to scale-invariant primeval perturbations*, *ApJL* **263**, L1-L5 (1982). 12
- Peebles P. J. E., *Dark matter and the origin of galaxies and globular star clusters*, *ApJ* **277**, 470-477 (1984). 12
- Peebles P. J. E., Yu J. T., *Primeval Adiabatic Perturbation in an Expanding Universe*, *ApJL* **162**, 815 (1970). 10
- Penzias A. A., Wilson R. W., *A Measurement of Excess Antenna Temperature at 4080 Mc/s.*, *Apj* **142**, 419-421 (1965). 9
- Perez K., Hailey C. J., Bauer F. E., Krivonos R. A., Mori K., Baganoff F. K., Barrière N. M., Boggs S. E., Christensen F. E., Craig W. W., Grefenstette B. W., Grindlay J. E., Harrison F. A., Hong J., Madsen K. K., Nynka M., Stern D., Tomsick J. A., Wik D. R., Zhang S., Zhang W. W., Zoglauer A., *Extended hard-X-ray emission in the inner few parsecs of the Galaxy*, *Nature* **520**, 646-649 (2015). 135
- Perlman E. S., Sparks W. B., Radomski J., Packham C., Fisher R. S., Piña R., Biretta J. A., *Deep 10 Micron Imaging of M87*, *ApJ* **561**, L51-L54 (2001). 142
- Peskin M. E., *Supersymmetric dark matter in the harsh light of the Large Hadron Collider*, *Proceedings of the National Academy of Science* **112**, 12256-12263 (2015). 37
- Peter P., Uzan J.-P., *Primordial Cosmology*, Oxford Graduate Texts (2009). 10, 14

- Petraki K., Volkas R. R., *Review of Asymmetric Dark Matter*, *International Journal of Modern Physics A* **28**, 1330028 (2013), arXiv:1305.4939. 25
- Petrou M., PhD thesis, Univ. of Cambridge (1981). 19
- Petrović J., Dario Serpico P., Zaharijaš G., *Galactic Center gamma-ray “excess” from an active past of the Galactic Centre?*, *JCAP* **10**, 052 (2014), arXiv:1405.7928. 89, 160
- Petrović J., Serpico P. D., Zaharijas G., *Millisecond pulsars and the Galactic Center gamma-ray excess: the importance of luminosity function and secondary emission*, *JCAP* **2**, 23 (2015), arXiv:1411.2980. 88, 89, 102, 107
- Poincaré H., Vergne H., *Leçons sur les hypothèses cosmogoniques professées à la Sorbonne*, A. Hermann et fils (1911). 4
- Pontzen A., Governato F., *How supernova feedback turns dark matter cusps into cores*, *MNRAS* **421**, 3464-3471 (2012), arXiv:1106.0499. 55
- Porter T. A., Moskalenko I. V., Strong A. W., Orlando E., Bouchet L., *Inverse Compton Origin of the Hard X-Ray and Soft Gamma-Ray Emission from the Galactic Ridge*, *ApJ* **682**, 400-407 (2008), arXiv:0804.1774. 67, 91
- Press W. H., Spergel D. N., *Capture by the sun of a galactic population of weakly interacting, massive particles*, *ApJ* **296**, 679-684 (1985). 48
- Primakoff H., *Photo-Production of Neutral Mesons in Nuclear Electric Fields and the Mean Life of the Neutral Meson*, *Physical Review* **81**, 899-899 (1951). 36
- Pshirkov M. S., Tinyakov P. G., Kronberg P. P., Newton-McGee K. J., *Deriving the Global Structure of the Galactic Magnetic Field from Faraday Rotation Measures of Extragalactic Sources*, *ApJ* **738**, 192 (2011), arXiv:1103.0814. 70
- Putze A., *The USINE cosmic-ray propagation code and recent results from an MCMC analysis*, *International Cosmic Ray Conference* **6**, 256 (2011). 79
- Putze A., Derome L., Maurin D., *A Markov Chain Monte Carlo technique to sample transport and source parameters of Galactic cosmic rays. II. Results for the diffusion model combining B/C and radioactive nuclei*, *A&A* **516**, A66 (2010), arXiv:1001.0551. 74
- Quinlan G. D., Hernquist L., Sigurdsson S., *Models of Galaxies with Central Black Holes: Adiabatic Growth in Spherical Galaxies*, *ApJ* **440**, 554 (1995), arXiv:astro-ph/9407005. 56, 57
- Randall S. W., Markevitch M., Clowe D., Gonzalez A. H., Bradač M., *Constraints on the Self-Interaction Cross Section of Dark Matter from Numerical Simulations of the Merging Galaxy Cluster 1E 0657–56*, *ApJ* **679**, 1173-1180 (2008), arXiv:0704.0261. 26
- Read J. I., *The local dark matter density*, *Journal of Physics G Nuclear Physics* **41**, 063101 (2014), arXiv:1404.1938. 4
- Read J. I., Gilmore G., *Mass loss from dwarf spheroidal galaxies: the origins of shallow dark matter cores and exponential surface brightness profiles*, *MNRAS* **356**, 107-124 (2005), arXiv:astro-ph/0409565. 55
- Rees M. J., Gunn J. E., *The origin of the magnetic field and relativistic particles in the Crab Nebula*, *MNRAS* **167**, 1-12 (1974). 129
- Regis M., Ullio P., *Multiwavelength signals of dark matter annihilations at the Galactic center*, *Phys. Rev. D* **78**, 043505 (2008), arXiv:0802.0234. 62, 73, 116, 125, 141, 146, 166, 167

- Rejkuba M., *The distance to the giant elliptical galaxy NGC 5128*, *A&A* **413**, 903-912 (2004), [arXiv:astro-ph/0310639](#). 154
- Rico J., Wood M., Drlica-Wagner A., Aleksić J. (for the MAGIC and Fermi-LAT Collaborations), *Limits to dark matter properties from a combined analysis of MAGIC and Fermi-LAT observations of dwarf satellite galaxies*, ArXiv e-prints (2015), [arXiv:1508.05827](#). 47
- Ricotti M., Ostriker J. P., Mack K. J., *Effect of Primordial Black Holes on the Cosmic Microwave Background and Cosmological Parameter Estimates*, *ApJ* **680**, 829-845 (2008), [arXiv:0709.0524](#). 19
- Rieger F. M., *Cen A as gamma - and UHE cosmic-ray source*, *Memorie della Societa Astronomica Italiana* **83**, 127 (2012), [arXiv:1108.4565](#). 155
- Ringwald A., *Exploring the role of axions and other WISPs in the dark universe*, *Physics of the Dark Universe* **1**, 116-135 (2012), [arXiv:1210.5081](#). 24, 25
- Roberts M. S., *The Rotation Curve of Galaxies*, in Hayli A., ed., *Dynamics of the Solar Systems*, Vol. 69 of IAU Symposium (1975). 5
- Roberts M. S., Rots A. H., *Comparison of Rotation Curves of Different Galaxy Types*, *A&A* **26**, 483-485 (1973). 5
- Robertson H. P., *On the Foundations of Relativistic Cosmology*, *Proceedings of the National Academy of Science* **15**, 822-829 (1929). 8
- Robertson H. P., *Kinematics and World-Structure*, *ApJ* **82**, 284 (1935). 8
- Robertson H. P., *Kinematics and World-Structure II.*, *ApJ* **83**, 187 (1936a). 8
- Robertson H. P., *Kinematics and World-Structure III.*, *ApJ* **83**, 257 (1936b). 8
- Rocha M., Peter A. H. G., Bullock J. S., Kaplinghat M., Garrison-Kimmel S., Oñorbe J., Moustakas L. A., *Cosmological simulations with self-interacting dark matter - I. Constant-density cores and substructure*, *MNRAS* **430**, 81-104 (2013), [arXiv:1208.3025](#). 26
- Rogstad D. H., Shostak G. S., *Gross Properties of Five Scd Galaxies as Determined from 21-CENTIMETER Observations*, *ApJ* **176**, 315 (1972). 5
- Ross S. (for the D<sup>3</sup> Collaboration), *Recent Progress on D<sup>3</sup> - The Directional Dark Matter Detector*, ArXiv e-prints (2014), [arXiv:1402.0043](#). 34
- Rothstein I. Z., Schwetz T., Zupan J., *Phenomenology of dark matter annihilation into a long-lived intermediate state*, *JCAP* **7**, 018 (2009), [arXiv:0903.3116](#). 82
- Rubin V. C., Ford Jr. W. K., *Rotation of the Andromeda Nebula from a Spectroscopic Survey of Emission Regions*, *ApJ* **159**, 379 (1970). 4
- Rubin V. C., Ford W. K. J., Thonnard N., *Rotational properties of 21 SC galaxies with a large range of luminosities and radii, from NGC 4605 (R = 4kpc) to UGC 2885 (R = 122 kpc)*, *ApJ* **238**, 471-487 (1980). 5
- Ruhl J. E., Ade P. A. R., Bock J. J., Bond J. R., Borrill J., Boscaleri A., Contaldi C. R., Crill B. P., de Bernardis P., De Troia G., Ganga K., Giacometti M., Hivon E., Hristov V. V., Iacoangeli A., Jaffe A. H., Jones W. C., Lange A. E., Masi S., Mason P., Mauskopf P. D., Melchiorri A., Montroy T., Netterfield C. B., Pascale E., Piacentini F., Pogosyan D., Polenta G., Prunet S., Romeo G., *Improved Measurement of the Angular Power Spectrum of Temperature Anisotropy in the Cosmic Microwave Background from Two New Analyses of BOOMERANG Observations*, *ApJ* **599**, 786-805 (2003), [arXiv:astro-ph/0212229](#). 9

- Rybicki G. B., Lightman A. P., *Radiative processes in astrophysics*, John Wiley & Sons (1979). 64, 65, 69
- Sadeghian L., Ferrer F., Will C. M., *Dark-matter distributions around massive black holes: A general relativistic analysis*, *Phys. Rev. D* **88**, 063522 (2013), arXiv:1305.2619. 58
- Sahakyan N., Yang R., Aharonian F. A., Rieger F. M., *Evidence for a Second Component in the High-energy Core Emission from Centaurus A?*, *ApJL* **770**, L6 (2013), arXiv:1302.7173. 154, 155
- Salam A., *Weak and electromagnetic interactions*, in *Elementary Particle Theory: Relativistic Groups and Analyticity*, Proceedings of the Eighth Nobel Symposium, Almquist & Wiksell (1968). 20
- Salati P., *The distortions of the microwave background radiation, heavy neutral decaying leptons and decaying gravitinos*, *Physics Letters B* **163**, 236-242 (1985). 41
- Salati P., *Indirect and direct dark matter detection*, Proceedings of Science **CARGESE2007**, 009 (2007). 73
- Salati P., *Dark matter annihilation in the universe*, *International Journal of Modern Physics Conference Series* **30**, 1460256 (2014), arXiv:1403.4495. 40
- Salucci P., Burkert A., *Dark Matter Scaling Relations*, *ApJL* **537**, L9-L12 (2000), arXiv:astro-ph/0004397. 54
- Sarkar S., *Big bang nucleosynthesis and physics beyond the standard model*, *Reports on Progress in Physics* **59**, 1493-1609 (1996), arXiv:hep-ph/9602260. 14, 15, 49
- Saxena S., Summa A., Elsässer D., Rürger M., Mannheim K., *Constraints on dark matter annihilation from M87. Signatures of prompt and inverse-Compton gamma rays*, *European Physical Journal C* **71**, 1815 (2011), arXiv:1111.3868. 149
- Schaeffer R., Silk J., *Cold, warm, or hot dark matter - Biased galaxy formation and pancakes*, *ApJ* **332**, 1-16 (1988). 13
- Schewtschenko J. A., Baugh C. M., Wilkinson R. J., Boehm C., Pascoli S., Sawala T., *Dark matter-radiation interactions: the structure of Milky Way satellite galaxies*, ArXiv e-prints (2015b), arXiv:1512.06774. 12, 13
- Schewtschenko J. A., Wilkinson R. J., Baugh C. M., Boehm C., Pascoli S., *Dark matter-radiation interactions: the impact on dark matter haloes*, *MNRAS* **449**, 3587-3596 (2015a), arXiv:1412.4905. 12, 13
- Schlickeiser R., *Cosmic Ray Astrophysics*, Springer (2002). 73
- Schumann M., *Dark Matter 2014*, in *European Physical Journal Web of Conferences*, Vol. 96 of *European Physical Journal Web of Conferences* (2015), arXiv:1501.01200. 30
- Scorza S. (for the SuperCDMS Collaboration), *Recent results from CDMS II, Status and future of the SuperCDMS experiment*, in *Talk at the New Perspectives on Dark Matter workshop*, Lyon, France (2013). 33
- Servant G., Tait T. M. P., *Is the lightest Kaluza-Klein particle a viable dark matter candidate?*, *Nuclear Physics B* **650**, 391-419 (2003), arXiv:hep-ph/0206071. 24
- Shi X., Fuller G. M., *New Dark Matter Candidate: Nonthermal Sterile Neutrinos*, *Physical Review Letters* **82**, 2832-2835 (1999), arXiv:astro-ph/9810076. 22

- Shi Y., Rieke G. H., Hines D. C., Gordon K. D., Egami E., *Thermal and Nonthermal Infrared Emission from M87*, *ApJ* **655**, 781-789 (2007), [arXiv:astro-ph/0610494](#). 142
- Shokair T. M., Root J., van Bibber K. A., Brubaker B., Gurevich Y. V., Cahn S. B., Lamoreaux S. K., Anil M. A., Lehnert K. W., Mitchell B. K., Reed A., Carosi G., *Future directions in the microwave cavity search for dark matter axions*, *International Journal of Modern Physics A* **29**, 1443004 (2014), [arXiv:1405.3685](#). 36
- Siegert T., Diehl R., Khachatryan G., Krause M. G. H., Guglielmetti F., Greiner J., Strong A. W., Zhang X., *Gamma-ray spectroscopy of positron annihilation in the Milky Way*, *A&A* **586**, A84 (2016), [arXiv:1512.00325](#). 46
- Sikivie P., *Axion Cosmology*, in *Axions*, Vol. 741 of *Lecture Notes in Physics*, Berlin Springer Verlag (2008), [arXiv:astro-ph/0610440](#). 24, 25
- Silk J., *Cosmic Black-Body Radiation and Galaxy Formation*, *ApJ* **151**, 459 (1968). 10, 12
- Silk J., Srednicki M., *Cosmic-ray antiprotons as a probe of a photino-dominated universe*, *Physical Review Letters* **53**, 624-627 (1984). 40
- Simon J. D., Bolatto A. D., Leroy A., Blitz L., *High-Resolution Measurements of the Dark Matter Halo of NGC 2976: Evidence for a Shallow Density Profile*, *ApJ* **596**, 957-981 (2003), [arXiv:astro-ph/0307154](#). 54
- Sivertsson S., Edsjö J., *Publisher's Note: WIMP diffusion in the solar system including solar WIMP-nucleon scattering [Phys. Rev. D 85, 123514 (2012)]*, *Phys. Rev. D* **85**, 129905 (2012), [arXiv:1201.1895](#). 48
- Sjöstrand T., Mrenna S., Skands P., *PYTHIA 6.4 physics and manual*, *Journal of High Energy Physics* **5**, 026 (2006), [arXiv:hep-ph/0603175](#). 44
- Skordis C., Mota D. F., Ferreira P. G., Boehm C., *Large Scale Structure in Bekenstein's Theory of Relativistic Modified Newtonian Dynamics*, *Physical Review Letters* **96**, 011301 (2006), [arXiv:astro-ph/0505519](#). 27
- Slatyer T. R., *Indirect dark matter signatures in the cosmic dark ages. I. Generalizing the bound on s-wave dark matter annihilation from Planck results*, *Phys. Rev. D* **93**, 023527 (2016), [arXiv:1506.03811](#). 41, 42
- Spano M., Marcelin M., Amram P., Carignan C., Epinat B., Hernandez O., *GHASP: an H $\alpha$  kinematic survey of spiral and irregular galaxies - V. Dark matter distribution in 36 nearby spiral galaxies*, *MNRAS* **383**, 297-316 (2008), [arXiv:0710.1345](#). 54
- Sparks W. B., Biretta J. A., Macchetto F., *The Jet of M87 at Tenth-Arcsecond Resolution: Optical, Ultraviolet, and Radio Observations*, *ApJ* **473**, 254 (1996). 142
- Spergel D. N., Steinhardt P. J., *Observational Evidence for Self-Interacting Cold Dark Matter*, *Physical Review Letters* **84**, 3760-3763 (2000), [arXiv:astro-ph/9909386](#). 25, 26
- Springel V., Frenk C. S., White S. D. M., *The large-scale structure of the Universe*, *Nature* **440**, 1137-1144 (2006), [arXiv:astro-ph/0604561](#). 13, 14
- Springel V., Wang J., Vogelsberger M., Ludlow A., Jenkins A., Helmi A., Navarro J. F., Frenk C. S., White S. D. M., *The Aquarius Project: the subhaloes of galactic haloes*, *MNRAS* **391**, 1685-1711 (2008), [arXiv:0809.0898](#). 54

- Springel V., White S. D. M., Jenkins A., Frenk C. S., Yoshida N., Gao L., Navarro J., Thacker R., Croton D., Helly J., Peacock J. A., Cole S., Thomas P., Couchman H., Evrard A., Colberg J., Pearce F., *Simulations of the formation, evolution and clustering of galaxies and quasars*, *Nature* **435**, 629-636 (2005), arXiv:astro-ph/0504097. 13
- Srednicki M., Olive K. A., Silk J., *High-energy neutrinos from the sun and cold dark matter*, *Nuclear Physics B* **279**, 804-823 (1987). 48
- Srednicki M., Watkins R., Olive K. A., *Calculations of relic densities in the early universe*, *Nuclear Physics B* **310**, 693-713 (1988). 15
- Sreekumar P., Bertsch D. L., Hartman R. C., Nolan P. L., Thompson D. J., *GeV emission from the nearby radio galaxy Centaurus A*, *Astroparticle Physics* **11**, 221-223 (1999), arXiv:astro-ph/9901277. 154
- Stecker F. W., *The cosmic gamma-ray background from the annihilation of primordial stable neutral heavy leptons*, *ApJ* **223**, 1032-1036 (1978). 40
- Stecker F. W., Rudaz S., Walsh T. F., *Galactic antiprotons from photinos*, *Physical Review Letters* **55**, 2622-2625 (1985). 40
- Steigman G., Dasgupta B., Beacom J. F., *Precise relic WIMP abundance and its impact on searches for dark matter annihilation*, *Phys. Rev. D* **86**, 023506 (2012), arXiv:1204.3622. 18
- Strong A. W., Moskalenko I. V., *Propagation of Cosmic-Ray Nucleons in the Galaxy*, *ApJ* **509**, 212-228 (1998), arXiv:astro-ph/9807150. 79
- Strong A. W., Moskalenko I. V., Ptuskin V. S., *Cosmic-Ray Propagation and Interactions in the Galaxy*, *Annu. Rev. Nucl. Part. Sci.* **57**, 285-327 (2007), arXiv:astro-ph/0701517. 72
- Strong A. W., Moskalenko I. V., Reimer O., *Diffuse Continuum Gamma Rays from the Galaxy*, *ApJ* **537**, 763-784 (2000), arXiv:astro-ph/9811296. 78, 102
- Su M., Finkbeiner D. P., *Strong Evidence for Gamma-ray Line Emission from the Inner Galaxy*, ArXiv e-prints (2012), arXiv:1206.1616. 46
- Su M., Slatyer T. R., Finkbeiner D. P., *Giant Gamma-ray Bubbles from Fermi-LAT: Active Galactic Nucleus Activity or Bipolar Galactic Wind?*, *ApJ* **724**, 1044-1082 (2010), arXiv:1005.5480. 160
- Sun X.-H., Reich W., *The Galactic halo magnetic field revisited*, *Research in Astronomy and Astrophysics* **10**, 1287-1297 (2010), arXiv:1010.4394. 70
- Sunyaev R. A., Zeldovich Y. B., *Small-Scale Fluctuations of Relic Radiation*, *Astrophysics and Space Science* **7**, 3-19 (1970). 10
- Swaters R. A., Madore B. F., van den Bosch F. C., Balcells M., *The Central Mass Distribution in Dwarf and Low Surface Brightness Galaxies*, *ApJ* **583**, 732-751 (2003), arXiv:astro-ph/0210152. 54
- Tan J. C., Beuther H., Walter F., Blackman E. G., *A Search for Molecular Gas in the Nucleus of M87 and Implications for the Fueling of Supermassive Black Holes*, *ApJ* **689**, 775-781 (2008), arXiv:astro-ph/0610488. 142
- Teyssier R., Pontzen A., Dubois Y., Read J. I., *Cusp-core transformations in dwarf galaxies: observational predictions*, *MNRAS* **429**, 3068-3078 (2013), arXiv:1206.4895. 55

- Tisserand P. et al. (EROS-2 Collaboration), *Limits on the Macho content of the Galactic Halo from the EROS-2 Survey of the Magellanic Clouds*, *A&A* **469**, 387-404 (2007), [arXiv:astro-ph/0607207](#). 19
- Tollerud E. J., Beaton R. L., Geha M. C., Bullock J. S., Guhathakurta P., Kalirai J. S., Majewski S. R., Kirby E. N., Gilbert K. M., Yniguez B., Patterson R. J., Ostheimer J. C., Cooke J., Dorman C. E., Choudhury A., Cooper M. C., *The SPLASH Survey: Spectroscopy of 15 M31 Dwarf Spheroidal Satellite Galaxies*, *ApJ* **752**, 45 (2012), [arXiv:1112.1067](#). 26
- Torrente-Lujan E., *Neutralino relic density from direct non-equilibrium production and intermediate scales*, *ArXiv High Energy Physics - Phenomenology e-prints* (2002), [arXiv:hep-ph/0210036](#). 15
- Trachternach C., de Blok W. J. G., Walter F., Brinks E., Kennicutt Jr. R. C., *Dynamical Centers and Noncircular Motions in THINGS Galaxies: Implications for Dark Matter Halos*, *The Astronomical Journal* **136**, 2720-2760 (2008), [arXiv:0810.2116](#). 54
- Tremaine S., Gunn J. E., *Dynamical role of light neutral leptons in cosmology*, *Physical Review Letters* **42**, 407-410 (1979). 22
- Ullio P., Zhao H., Kamionkowski M., *Dark-matter spike at the galactic center?*, *Phys. Rev. D* **64**, 043504 (2001), [arXiv:astro-ph/0101481](#). 57, 59, 60, 62
- Urban M., Bouquet A., Degrange B., Fleury P., Kaplan J., Melchior A. L., Paré E., *Searching for TeV dark matter by atmospheric Čerenkov techniques*, *Physics Letters B* **293**, 149-156 (1992), [arXiv:hep-ph/9208255](#). 44
- van den Bosch F. C., Burkert A., Swaters R. A., *The angular momentum content of dwarf galaxies: new challenges for the theory of galaxy formation*, *MNRAS* **326**, 1205-1215 (2001), [arXiv:astro-ph/0105082](#). 26
- van den Bosch F. C., Robertson B. E., Dalcanton J. J., de Blok W. J. G., *Constraints on the Structure of Dark Matter Halos from the Rotation Curves of Low Surface Brightness Galaxies*, *The Astronomical Journal:astro-ph*/9911372. 54
- Vasiliev E., Zelnikov M., *Dark matter dynamics in the galactic center*, *Phys. Rev. D* **78**, 083506 (2008), [arXiv:0803.0002](#). 60, 61
- Vitale V., Morselli A., for the Fermi/LAT Collaboration, *Indirect Search for Dark Matter from the center of the Milky Way with the Fermi-Large Area Telescope*, *ArXiv e-prints* (2009), [arXiv:0912.3828](#). 87
- Vladimirov A. E., Digel S. W., Jóhannesson G., Michelson P. F., Moskalenko I. V., Nolan P. L., Orlando E., Porter T. A., Strong A. W., *GALPROP WebRun: An internet-based service for calculating galactic cosmic ray propagation and associated photon emissions*, *Computer Physics Communications* **182**, 1156-1161 (2011), [arXiv:1008.3642](#). 67
- Vogelsberger M., Zavala J., Loeb A., *Subhaloes in self-interacting galactic dark matter haloes*, *MNRAS* **423**, 3740-3752 (2012), [arXiv:1201.5892](#). 26
- Vogelsberger M., Zavala J., Simpson C., Jenkins A., *Dwarf galaxies in CDM and SIDM with baryons: observational probes of the nature of dark matter*, *MNRAS* **444**, 3684-3698 (2014), [arXiv:1405.5216](#). 27
- Volkov D. V., Akulov V. P., *Is the neutrino a goldstone particle?*, *Physics Letters B* **46**, 109-110 (1973). 22

- von Doetinchem P., Aramaki T., Boggs S., Fuke H., Hailey C. J., Mognet S. I., Ong R. A., Perez K., Zweerink J., *GAPS - Dark matter search with low-energy cosmic-ray antideuterons and antiprotons*, ArXiv e-prints (2015), [arXiv:1507.02717](#). 44
- Wagoner R. V., Fowler W. A., Hoyle F., *On the Synthesis of Elements at Very High Temperatures*, *ApJ* **148**, 3 (1967). 14
- Walker A. G., *On Milne's Theory of World-Structure*, *Proceedings of the London Mathematical Society* **s2-42**, 90-127 (1937). 8
- Walsh D., Carswell R. F., Weymann R. J., *0957 + 561 A, B - Twin quasistellar objects or gravitational lens*, *Nature* **279**, 381-384 (1979). 6
- Weidenspointner G., Shrader C. R., Knödlseeder J., Jean P., Lonjou V., Guessoum N., Diehl R., Gillard W., Harris M. J., Skinner G. K., von Ballmoos P., Vedrenne G., Roques J.-P., Schanne S., Sizun P., Teegarden B. J., Schönfelder V., Winkler C., *The sky distribution of positronium annihilation continuum emission measured with SPI/INTEGRAL*, *A&A* **450**, 1013-1021 (2006), [arXiv:astro-ph/0601673](#). 46
- Weinberg S., *A Model of Leptons*, *Physical Review Letters* **19**, 1264-1266 (1967). 20
- Weinberg S., *Gravitation and Cosmology: Principles and Applications of the General Theory of Relativity*, Wiley (1972). 165
- Weinberg S., *A new light boson?*, *Physical Review Letters* **40**, 223-226 (1978). 25
- Weisskopf M. C., Brinkman B., Canizares C., Garmire G., Murray S., Van Speybroeck L. P., *An Overview of the Performance and Scientific Results from the Chandra X-Ray Observatory*, *Publ. Astron. Soc. Pac.* **114**, 1-24 (2002), [arXiv:astro-ph/0110308](#). 143
- Weldrake D. T. F., de Blok W. J. G., Walter F., *A high-resolution rotation curve of NGC 6822: a test-case for cold dark matter*, *MNRAS* **340**, 12-28 (2003), [arXiv:astro-ph/0210568](#). 54
- Weniger C., *A tentative gamma-ray line from Dark Matter annihilation at the Fermi Large Area Telescope*, *JCAP* **8**, 007 (2012), [arXiv:1204.2797](#). 46
- Wess J., Zumino B., *Supergauge transformations in four dimensions*, *Nuclear Physics B* **70**, 39-50 (1974). 22
- Wharton R. S., Chatterjee S., Cordes J. M., Deneva J. S., Lazio T. J. W., *Multiwavelength Constraints on Pulsar Populations in the Galactic Center*, *ApJ* **753**, 108 (2012), [arXiv:1111.4216](#). 88
- Whitehurst R. N., Roberts M. S., *High-Velocity Neutral Hydrogen in the Central Region of the Andromeda Galaxy*, *ApJ* **175**, 347 (1972). 5
- Wilkinson R. J., Boehm C., Lesgourgues J., *Constraining dark matter-neutrino interactions using the CMB and large-scale structure*, *JCAP* **5**, 011 (2014b), [arXiv:1401.7597](#). 12, 13, 41
- Wilkinson R. J., Lesgourgues J., Boehm C., *Using the CMB angular power spectrum to study Dark Matter-photon interactions*, *JCAP* **4**, 026 (2014a), [arXiv:1309.7588](#). 12, 13, 41
- Wilkinson R. J., Vincent A. C., Boehm C., McCabe C., *Ruling out the light WIMP explanation of the galactic 511 keV line*, ArXiv e-prints (2016), [arXiv:1602.01114](#). 46
- Williams A. J., Boehm C., West S. M., Albornoz Vásquez D., *Regenerating WIMPs in the light of direct and indirect detection*, *Phys. Rev. D* **86**, 055018 (2012), [arXiv:1204.3727](#). 120, 125

- Wood M., Buckley J., Digel S., Funk S., Nieto D., Sanchez-Conde M. A., *Prospects for Indirect Detection of Dark Matter with CTA*, ArXiv e-prints (2013), [arXiv:1305.0302](#). 48
- Woodley K. A., Harris W. E., Beasley M. A., Peng E. W., Bridges T. J., Forbes D. A., Harris G. L. H., *The Kinematics and Dynamics of the Globular Clusters and Planetary Nebulae of NGC 5128*, *The Astronomical Journal* **134**, 494-510 (2007), [arXiv:0704.1189](#). 180
- Wyithe J. S. B., Turner E. L., Spergel D. N., *Gravitational Lens Statistics for Generalized NFW Profiles: Parameter Degeneracy and Implications for Self-Interacting Cold Dark Matter*, *ApJ* **555**, 504-523 (2001), [arXiv:astro-ph/0007354](#). 26
- Wyse R. F. G., *The Merging History of the Milky Way Disk*, in *Galaxy Disks and Disk Galaxies*, Vol. 230 of *Astronomical Society of the Pacific Conference Series* (2001), [arXiv:astro-ph/0012270](#). 59
- Xiao M. et al. (PandaX Collaboration), *First dark matter search results from the PandaX-I experiment*, *Science China Physics, Mechanics, and Astronomy* **57**, 2024-2030 (2014). 33
- Yanagida T., *Horizontal gauge symmetry and masses of neutrinos*, in *Proceedings of the Workshop on Unified Theory and Baryon Number of the Universe*, KEK, Japan (1979). 21
- Yang R.-z., Aharonian F., *On the GeV excess in the diffuse  $\gamma$ -ray emission towards the Galactic Center*, ArXiv e-prints (2016), [arXiv:1602.06764](#). 88
- Yoast-Hull T. M., Gallagher III J. S., Zweibel E. G., *The Cosmic-Ray Population of the Galactic Central Molecular Zone*, *ApJ* **790**, 86 (2014), [arXiv:1405.7059](#). 106
- York D. G. et al. (SDSS Collaboration), *The Sloan Digital Sky Survey: Technical Summary*, *The Astronomical Journal* **120**, 1579-1587 (2000), [arXiv:astro-ph/0006396](#). 13
- Yoshida N., Springel V., White S. D. M., Tormen G., *Collisional Dark Matter and the Structure of Dark Halos*, *ApJL* **535**, L103-L106 (2000), [arXiv:astro-ph/0002362](#). 25
- Young L. M., Bureau M., Davis T. A., Combes F., McDermid R. M., Alatalo K., Blitz L., Bois M., Bournaud F., Cappellari M., Davies R. L., de Zeeuw P. T., Emsellem E., Khochfar S., Krajnović D., Kuntschner H., Lablanche P.-Y., Morganti R., Naab T., Oosterloo T., Sarzi M., Scott N., Serra P., Weijmans A.-M., *The ATLAS<sup>3D</sup> project - IV. The molecular gas content of early-type galaxies*, *MNRAS* **414**, 940-967 (2011), [arXiv:1102.4633](#). 140
- Young P., *Numerical models of star clusters with a central black hole. I - Adiabatic models*, *ApJ* **242**, 1232-1237 (1980). 56
- Yuan Q., Ioka K., *Testing the Millisecond Pulsar Scenario of the Galactic Center Gamma-Ray Excess With Very High Energy Gamma-Rays*, *ApJ* **802**, 124 (2015), [arXiv:1411.4363](#). 99, 102, 103, 107, 129
- Yuan Q., Zhang B., *Millisecond pulsar interpretation of the Galactic center gamma-ray excess*, *Journal of High Energy Astrophysics* **3**, 1-8 (2014), [arXiv:1404.2318](#). 88, 89
- Yusef-Zadeh F., Hewitt J. W., Wardle M., Tatischeff V., Roberts D. A., Cotton W., Uchiyama H., Nobukawa M., Tsuru T. G., Heinke C., Royster M., *Interacting Cosmic Rays with Molecular Clouds: A Bremsstrahlung Origin of Diffuse High-energy Emission from the Inner  $2^\circ \times 1^\circ$  of the Galactic Center*, *ApJ* **762**, 33 (2013), [arXiv:1206.6882](#). 106
- Zavala J., Vogelsberger M., Walker M. G., *Constraining self-interacting dark matter with the Milky Way's dwarf spheroidals*, *MNRAS* **431**, L20-L24 (2013), [arXiv:1211.6426](#). 26

- Zeldovich Y. B., Sunyaev R. A., *The Interaction of Matter and Radiation in a Hot-Model Universe*, *Astrophysics and Space Science* **4**, 301-316 (1969). [41](#)
- Zhang Jian-Zu, *Wess-Zumino-type effective action for technions with light gauge bosons in a chiral-anomaly technicolor model*, *Phys. Rev. D* **39**, 354-357 (1989). [44](#)
- Zhao H., *Analytical models for galactic nuclei*, *MNRAS* **278**, 488-496 (1996), [arXiv:astro-ph/9509122](#). [54](#)
- Zhao H., Haehnelt M. G., Rees M. J., *Feeding black holes at galactic centres by capture from isothermal cusps*, *New Astronomy* **7**, 385-394 (2002), [arXiv:astro-ph/0112096](#). [62](#)
- Zhou B., Liang Y.-F., Huang X., Li X., Fan Y.-Z., Feng L., Chang J., *GeV excess in the Milky Way: The role of diffuse galactic gamma-ray emission templates*, *Phys. Rev. D* **91**, 123010 (2015), [arXiv:1406.6948](#). [88](#)
- Zitner B. (for the VERITAS Collaboration), *Search for Dark Matter from Dwarf Galaxies using VERITAS*, ArXiv e-prints (2015), [arXiv:1509.01105](#). [47](#)
- Zolotov A., Brooks A. M., Willman B., Governato F., Pontzen A., Christensen C., Dekel A., Quinn T., Shen S., Wadsley J., *Baryons Matter: Why Luminous Satellite Galaxies have Reduced Central Masses*, *ApJ* **761**, 71 (2012), [arXiv:1207.0007](#). [27](#)
- Zurek K. M., *Multicomponent dark matter*, *Phys. Rev. D* **79**, 115002 (2009), [arXiv:0811.4429](#). [158](#)
- Zwicky F., *Die Rotverschiebung von extragalaktischen Nebeln*, *Helvetica Physica Acta* **6**, 110-127 (1933). [4](#)
- Zwicky F., *On the Masses of Nebulae and of Clusters of Nebulae*, *ApJ* **86**, 217 (1937). [4](#)
- Zwicky F., *Republication of: The redshift of extragalactic nebulae*, *General Relativity and Gravitation* **41**, 207-224 (2009). [4](#)

---

## **Phenomenology of dark matter particles at the centers of galaxies**

Unveiling the nature of dark matter is one of the greatest challenges of modern physics, at the interface between astrophysics, cosmology and particle physics. In this thesis, I tackle various aspects of indirect searches for dark matter particles, which provide a complementary approach to direct detection or collider experiments. We are now entering into an era of instruments with outstanding capabilities, so it was timely to tackle the problem of the dark matter density profile at the centers of galaxies with novel methods, which motivated this thesis. Taking advantage of these technological advances, I investigate new ways of probing the very central part of dark matter halos, especially focusing on dark matter spikes, i.e. very strong enhancements of the dark matter density that can form around supermassive black holes. I show that we can go beyond standard dark matter searches by studying photon emission from electrons and positrons produced in dark matter annihilation processes. In this context, I describe a new cosmic-ray propagation technique to account for injection by spiky distributions at the centers of galaxies. I develop novel models of the diffuse emission in the central regions of galaxies, focusing not only on the center of the Milky Way, but on the central regions of other galaxies as well. This allows me to explain recently reported observations and make predictions for future observations.

---

## **Phénoménologie des particules de matière noire au centre des galaxies**

Élucider le mystère de la matière noire est l'un des plus grands défis de la physique moderne, à l'interface entre l'astrophysique, la cosmologie et la physique des particules. Dans cette thèse, j'aborde différents aspects de la recherche indirecte des particules de matière noire, approche complémentaire à la détection directe et à la production dans des collisionneurs. Nous entrons dans une nouvelle ère grâce à des instruments remarquables et c'était donc le moment opportun pour s'attaquer au problème du profil de densité de matière noire au centre des galaxies par des méthodes originales. C'est la motivation principale de ma thèse. Dans ce travail, je tire parti des avancées technologiques afin d'explorer de nouvelles façons d'étudier la région centrale des halos de matière noire. Je me concentre en particulier sur les pics de matière noire, qui correspondent à des augmentations extrêmement fortes de la densité de matière noire pouvant être induites par les trous noirs supermassifs. Je montre qu'il est possible d'aller au-delà des recherches standards en étudiant les photons émis par des électrons et positrons produits dans les processus d'annihilation des particules de matière noire. Dans ce contexte, je décris une nouvelle technique pour modéliser la propagation des rayons cosmiques pour des profils d'injection très piqués. Je développe des modèles originaux de l'émission diffuse dans les régions centrales des galaxies, non seulement pour la Voie Lactée mais également pour d'autres galaxies, ce qui me permet d'expliquer certaines observations récentes et de faire des prédictions pour des observations futures.

---